FEB 1950

THE

PHYSICAL REVIEW

Second Series — VOLUME

...RY 15, 1950

Published by the

AMERICAN PHYSICAL SOCIETY

under the

AUSPICES OF THE NATIONAL

...ew York, N. Y.

THE PHYSICAL REVIEW

A journal of experimental and theoretical physics established by E. L. Nichols in 1893

Published by the American Institute of Physics for the

AMERICAN PHYSICAL SOCIETY

Officers

President

F. W. Loomis
University of Illinois
Urbana, Illinois

Vice-President

I. I. Rabi
Columbia University
New York, New York

Secretary

K. K. Darrow
Bell Telephone Laboratories
Office:
Columbia University
New York 27, New York

Treasurer

G. B. Pegram
Columbia University
New York 27, New York

Local Secretary for the Pacific Coast

J. Kaplan
University of California at Los Angeles
Los Angeles, California

Managing Editor

John T. Tate
University of Minnesota
Minneapolis, Minnesota

BOARD OF EDITORS

Editor

John T. Tate

Assistant Editor

J. W. Buchta

Associate Editors

H. A. Bethe	S. A. Goudsmit	W. E. Lamb, Jr.
A. H. Compton	E. M. Purcell	R. G. Sachs
W. W. Hansen	I. I. Rabi	J. Schwinger
W. W. Watson	H. M. Skarsgard	E. U. Condon
R. T. Birge	V. F. Weisskopf	

Manuscripts for publication should be submitted to John T. Tate, University of Minnesota, Minneapolis, Minnesota. The authors' institutions are requested to pay a publication charge of $8 per page which, if honored, entitles them to 100 free reprints. Instructions will be sent with galley proofs.

Proof and all correspondence concerning papers in the process of publication should be addressed to the Publication Manager, American Institute of Physics, 57 East 55 Street, New York 22, New York.

Subscription Price

United States and Canada.....$12.00
Members.....$7.50

Back Numbers[1]

Yearly back number rate when complete year is available:
Prior to 1949: $20.00
Thereafter: $27.00

Single copies: $2.00 each, prior to July, 1929;
$1.00 each, July, 1929–December, 1941;
$2.00 each, January, 1942–December, 1946;
$3.00 each, January, 1947–December, 1948;
$3.25 each, thereafter.

General index, 1893–1920: $4.00.

Subscriptions and orders for back numbers should be addressed to Prince and Lemon Streets, Lancaster, Pennsylvania, or to the American Institute of Physics, 57 East 55 Street, New York 22, New York.

Changes of address in the case of members of the American Physical Society should be addressed to the Treasurer; in the case of other subscribers, to the Circulation Manager, American Institute of Physics.

[1] See Series 1 Issues of Physics Department, Cornell University, Ithaca, New York.

The Physical Review is published monthly on Prince and Lemon Streets, Lancaster, Pennsylvania.

Entered as second-class matter March [illegible], at the Post Office at Lancaster, Pennsylvania, under the Act of March 3, 1879.

Acceptance for mailing at special rate of postage provided for in paragraph d, Section 538, P. L. & R., authorized January 27, 1925.

THE
PHYSICAL REVIEW

A journal of experimental and theoretical physics established by E. L. Nichols in 1893

SECOND SERIES, VOL. 77, NO. 2 JANUARY 15, 1950

Conversion Electrons of Radium D

LAWRENCE CRANBERG*
University of Pennsylvania, Philadelphia, Pennsylvania
(Received September 6, 1949)

The conversion electrons of radium D have been studied with thin sources on thin backings in a beta-ray spectrograph using calibrated photographic emulsions. The number of conversion electrons due to the 47-kev gamma-ray has been measured to be 74±5 per hundred disintegrations. The $L:M:N$ ratio is 1:0.26:0.077. This implies a complex decay scheme for radium D, since earlier results give 3.5 unconverted 47-kev gamma-rays per hundred disintegrations.

INTRODUCTION

DESPITE numerous studies of the radiations of radium D, doubt remains regarding some of the main features of the decay because of the softness of these radiations.

Measurements on the primary beta-spectrum[1] indicates an endpoint less than 30 kev, but with large uncertainty. Most definite are the conversion lines associated with a 47-kev gamma-ray, for which the previous results are summarized in Table I. The gamma-ray is insufficiently energetic to convert in the K shell. Momentum is in gauss-cm. Intensities given in Table I are estimated from a photographic record, without correction for energy dependence of the emulsion sensitivity.

To determine the fraction of the decays associated with the 47-kev transition, several measurements have been made of the fraction of the decays associated with the unconverted gamma-ray, and the fraction associated with excited atomic levels of the radium E (bismuth^{210}) atom due to internal conversion of the gamma-ray. In addition to clarifying the decay scheme, these measurements give the conversion coefficient of the gamma-ray.[2]

The results of various workers on the number of unconverted gamma-rays per hundred disintegrations are in good agreement. These have been given as follows:[3] Bramson, 3.1; Gray, 4.0; Von Droste, 3.5; Stahel, 3.8.

The results on the number of excited atomic levels caused by conversion of the 47-kev gamma-ray vary widely. Those obtained from measurements on the conversion electrons directly have given low results, of the order of 10 per hundred disintegrations,[4] implying that the 47-kev excited state is a relatively minor feature of the decay. Several measurements by an indirect method have given much higher results. This method involves determination of (a) the number of L x-rays produced due to internal conversion in the L shell, (b) the fraction of excited L levels which yields x-rays (the remainder decaying by Auger effect), and (c) the contribution of the L excited states to the total number of excited levels due to the 47-kev gamma-ray.

According to Stahel[3] (a) is 25.1 per hundred disintegrations, (b) is 42 percent, using a result of Lay,[5] and (c) is 60 percent from the results of Curtiss in Table I. This implies conversion occurs in about 99 percent of the disintegrations. Very recently Kinsey[6] obtained for (b) 47.5 percent, and estimated for (c) 75 percent from the known results for the 40-kev gamma-ray of thorium C. He notes Curtiss' figure must be too small because of the correction necessary for the dependence of photographic darkening on energy.

* This work was carried out in partial fulfillment of the requirements for the degree of Doctor of Philosophy.

[1] H. O. W. Richardson and A. Leigh-Smith, Proc. Roy. Soc. A160, 454 (1937); W. F. Libby and D. D. Lee, Phys. Rev. 55, 852 (1939); A. Saha, Proc. Nat. Acad. Sci., India 12, 159 (1946).

[2] According to private communication from Dr. M. E. Rose theoretical calculations of the conversion coefficients for the L shells for different multipoles are in progress.

[3] S. Bramson, Zeits. f. Physik 66, 721 (1930); J. Gray, Nature 130, 738 (1932); G. Von Droste, Zeits. f. Physik 34, 17 (1933); E. Stahel, Helv. Phys. Acta 8, 651 (1935).

[4] T. San-Tsiang, Phys. Rev. 69, 38 (1946).

[5] H. Lay, Zeits. f. Physik 90, 533 (1934).

[6] B. Kinsey, Can. J. Research 26, 421 (1948).

TABLE I. Previous results for the momenta of the β-ray conversion lines associated with the 47-kev gamma-ray from radium D.*

Conversion level	Danysz p	Ellis p	Ellis i	Meitner p	Black p	Curtiss p	Curtiss i
$L\,I$	602	600	1.00	602	600	594.3	1.00
$L\,II$	607	605	0.04	...	606	600.3	0.06
$L\,III$	...	628	0.01	...	...	...	
M	718	717	0.40	718	714	709.1	0.50
N	743	742	0.20	741	738	735.2	0.20
O	...	...		...	...	742.5	0.01

* J. Danysz, Le. Rad. 2, 16 (1912); C. Ellis, Proc. Camb. Phil. Soc. 21, 121 (1921–23); L. Meitner, Zeits. f. Physik 9, 131 (1922); D. Black, Proc. Roy. Soc. A109, 166 (1925); L. Curtiss, Phys. Rev. 27, 672 (1926).

These results imply 71 percent of the decays give conversion electrons.

These conflicting results indicate the desirability of a direct measurement of the number of conversion electrons produced in the radium D disintegration, with special attention to minimizing self-absorption effects in the source, as these may have caused serious errors in the earlier work.

Still to be fitted into the decay scheme are the data on several weak, low energy gamma-rays recently reported recorded with a Cauchois spectrograph.[4]

EXPERIMENTAL PROCEDURE

The spectrum of radium D has been examined with thin uniform sources on thin backings by exposure in a conventional 180 degree beta-ray spectrograph using photographic detection. The dependence of photographic darkening on energy and exposure has been determined previously[7] for the emulsions used in this work.

To calculate the number of conversion electrons per disintegration from the spectrum, the geometry of the spectrograph and the disintegration rate of the source are measured. These data, together with the sensitivity

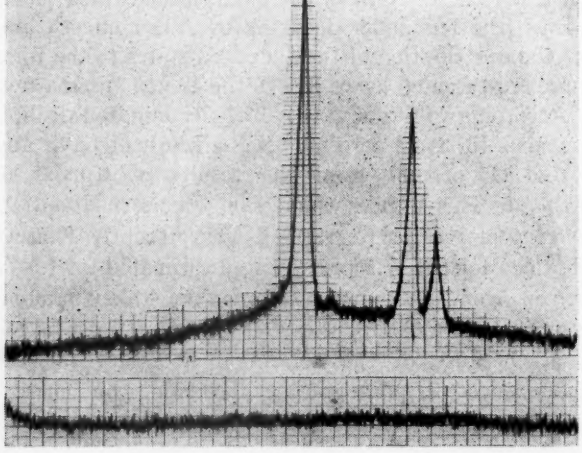

FIG. 1. Low energy spectrum of electrons from radium D and radium E in equilibrium.

[7] L. Cranberg and J. Halpern, Rev. Sci. Inst. 20, 641 (1949).

TABLE II. Comparison of primary and secondary standards with progressively greater thickness of absorber next to the counter window.

Primary std.	Secondary std.	Ratio
6.78	252	37.0
1.47	59.5	40.5
1.10	46.0	41.8
0.85	34.2	41.6
0.49	20.5	41.9

of the emulsion used give C, the percentage of the disintegrations accompanied by the conversion electrons in a given line, according to the following equation:

$$C=100\cdot\frac{2\pi^2\rho}{\theta}\cdot S\int_{l_1}^{l_2} Ddl\cdot\frac{1}{\phi t}, \qquad (1)$$

where ρ is the radius of curvature to the center of the line in cm, θ is the semi-angle subtended by the width of the spectrograph slit at the source, S is the sensitivity of the emulsion in electrons/cm^2 per unit density for the electron energy involved, l_1, l_2 are the lower and upper endpoints of the line, D is the density above background at any point in the line, l is distance measured along the film in cm, ϕ is the disintegration rate of the source per second, t is the exposure time in seconds.

This calculation assumes (1) the lines are sharp, (2) the emission from the source is isotropic, (3) there is no loss of electrons due to self-absorption, (4) the photographic reciprocity law is obeyed, (5) the density-exposure relation is linear, and (6) fading is negligible. To satisfy the first three assumptions sources as thin and uniform as possible were prepared. Previous work[8] supports assumption (4). Most of the exposures were run so that densities were in the linear density-exposure range. For a few exposures the darkening due to the $L\,I$ line extended into the non-linear region. Appropriate corrections were then made based on density-exposure data taken with the electron gun at the energy of the $L\,I$ line. Fading was checked for nine-day exposure, which was the longest exposure time used. This was done by exposing a calibrating strip in the electron gun at the beginning and end of a nine-day period, during all of which time the strip was in vacuum, and comparing densities of the two sets of exposures. Fading was negligible.

The sensitivity S was determined each time a spectrograph exposure was processed by processing simultaneously, in the same container, a calibrating strip cut from the same sheet of film as the spectrograph strip. The calibrating strip was exposed to a known number of electrons in an electron gun, at the energy of the $L\,I$ line, with the apparatus and procedures described elsewhere.[7]

The spectrograph film and calibrating strips were run

[8] O. Klemperer, *Einführung in der Elektronik* (M. S. Rosenberg, New York, 1944).

through a Leeds and Northrup recording microphotometer and the integral of Eq. (1) was evaluated graphically from the recording.

The spectrograph and magnet used have been previously described.[9] To minimize scattering all exposed surfaces of the spectrograph camera have been lined with polyethylene, and a shutter was installed to prevent exposure during the interval in which the camera is being evacuated.

DETERMINATION OF SOURCE ACTIVITY

To determine the disintegration rate of a source, the following procedure was adopted. Aliquots of radium D salt solution were delivered at the same time to the spectrograph source support and to a silver disk furnished by the Bureau of Standards. After equilibrium was reached between the radium D and radium E (f an equilibrium mixture was not used to begin with) the activity on the disk was determined by comparison with a radium D–radium E equilibrium standard whose disintegration rate is furnished by the Bureau of Standards, with a 3 percent uncertainty.

The aliquot delivered to the disk was evaporated, giving a small ring-shaped deposit whose average thickness, estimated from a weighed aliquot, was always within a factor of 5 of the average thickness, 1 mg/cm², of the primary standard provided by the Bureau. To prevent loss of activity the secondary standards were covered with 5 μg/cm² zapon films.

To minimize the effect of differences in area of primary and secondary standards when making activity comparisons, the source-to-counter distance was made sufficiently large, 2.5 inches, so that counting rate was insensitive to source area. This was checked by varying the position of a small source. To minimize differences between the primary and secondary standards in regard to self-scattering and self-absorption, comparisons were made with progressively greater thickness of absorber placed next to the counter window. Table II shows the results of such a series of comparisons, the statistical uncertainty in the counting rates being 2 percent.

It is to be expected that the absorption curves should run parallel with greater absorber thickness, since then only the most energetic electrons are counted and these are the least affected by self-scattering and self-absorption. Hence the value taken[10] for the correct ratio from the data of Table II is 42.0±1.0.

SOURCE PREPARATION

The radium D used in these measurements was furnished in the form of lead nitrate by the Eldorado Mining and Refining, Ltd., of Canada. Evaporation of the material with excess hydrochloric acid converted this to the chloride. The radioactive purity of the material was checked by carrying out a separation of the radium E by the Erbacher[11] method. The activity of a separated sample was followed for forty days, the ratio of the final to initial activities being 20 to 1, the rate of growth corresponding to the half-life of radium E. These measurements were made with about 10 mg/cm² of absorber to eliminate the radium D radiations. Samples separated by a new method[12] gave a ratio of 70 to 1 on one test, implying a maximum contamination of 1.4 percent.

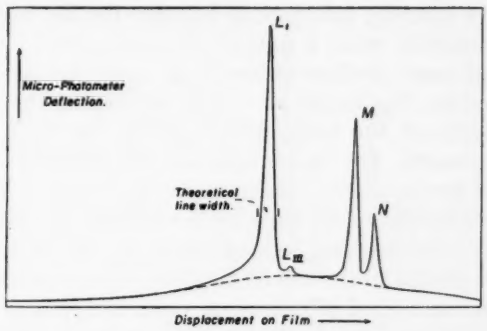

FIG. 2. Tracing of radium D–radium E low energy electron spectrum, showing estimated continuum.

The sources were prepared on zapon films of 5 μg/cm² by delivery of 10 to 15 microliters of radioactive solution, exposing to an atmosphere of ammonia for about 2 minutes to precipitate the lead as hydroxide, followed by evaporation in vacuum. The most uniform sources were obtained when the radioactive solution did not solidify in the vacuum, but evaporated from the liquid state. With the best technique, microscopic examination of a source after evaporation showed at least 90 percent of the nominal area of the source was actually covered with material in a uniform manner.

RESULTS AND CONCLUSIONS

Figure 1 is a reproduction of a photometric record of the low energy electron spectrum of radium D and radium E in equilibrium, taken with a source of average thickness of 43 μg/cm². Accompanying it is the record of the background density taken in the unexposed portion of the film. Figure 2 is a tracing obtained from this record by averaging the fluctuations due to granularity, above a base-line corresponding to the average background. Figure 3 is a replot of the region about the *L I* line in which account is taken of the density-exposure relation to show the true

[9] Plesset, Harnwell, and Seidl, Rev. Sci. Inst. **13**, 351 (1942).

[10] This procedure has been corroborated by another method by Dr. B. Burtt of the Brookhaven National Laboratories.

[11] O. Erbacher, Zeits. f. physik. Chemie **A156**, 142 (1931).

[12] Such efficient separation of radium D from radium E was obtained under the following circumstances. Radium D in the form of $PbCl_2$ solution in doubly distilled water was left undisturbed for about 24 hours. Samples of 10 to 20 microliters pipetted from the top of the solution were found on half a dozen tests to have less than 5 percent of the equilibrium amount of radium E, as determined from the growth of RaE activity, whereas the radioactive material was old enough for secular equilibrium to have been established in the mother solution. A one-cc glass beaker was used, half-filled with solution having a concentration of about 1 mc/cc.

relative intensity relationship between the line and the continuum on which it appears superimposed.

In all cases the lines observed are superimposed on a continuum, the height of which, relative to the peak intensities of the lines, differs greatly for thick and thin sources. For three thin sources, however, the results are very similar to those shown in Fig. 1. There is a rise in density approaching the *L I* line, an approximately constant level between the *L* and *M* lines, then a slow decline to the end of the film, which corresponds to a momentum of 850 gauss cm, or an energy of 60 kev.

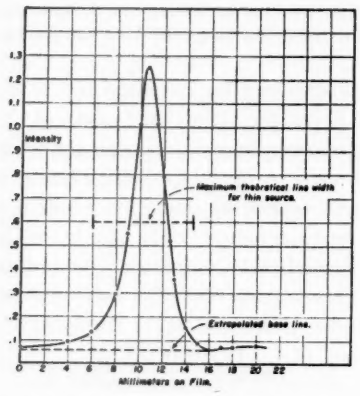

FIG. 3. True relative intensities of line *L I* and continuum.

Reference is made below to possible interpretation of this continuum. Its outline is indicated by the dashed lines of Figs. 2 and 3. Also shown on these figures are the maximum line widths calculated from the geometries of the source and spectrograph. Low energy tails are evident due, undoubtedly, to source-thickness effects. The continuum is distinguishable from these tails on the assumption that the former may be estimated by extrapolation from the high energy sides of the lines as shown in the figures.

A. Relative Line Intensities

The weak lines *L II* and *O* are not resolved in Figs. 1 and 2 because of the unfavorable combination of wide source and fast scanning of the record. To obtain these lines special runs were taken with a narrow source, and much slower speeds of scanning with the microphotometer. Line intensities were taken relative to the *L I* line, using the three thinnest and most uniform sources.

TABLE III. Intensities of the conversion lines relative to the intensity of *L I*.

Line	Density ratio, weighted average	Resolution correction	Film correction	Relative intensity
L I	1.0	1.0	1.0	1.0
L II	0.09 ±0.015	1.01	0.98	0.090±0.015
L III	0.019±0.004	1.05	0.93	0.019±0.004
M	0.38 ±0.02	1.19	0.65	0.29 ±0.02
N	0.115±0.015	1.24	0.60	0.085±0.01
O	0.029±0.01	1.25	0.58	0.021±0.007

The results are summarized in Table III. The "film correction" factor, which takes account of the energy dependence of the film sensitivity, was obtained with the procedure and apparatus described before.[7] With some sources more than one exposure was obtained. The weighted averages represent the results of three or more exposures for the strong lines. The uncertainties are due almost entirely to uncertainty in estimating the position of the continuum.

From Table III the number of conversions in the *L* shells is 73±2 percent of the total, in good agreement with Kinsey's estimate based on the thorium *C* 40-kev gamma-ray.

B. Absolute Intensities of Lines *L I* Plus *L II*

Because of the difficulty of resolving lines *L I* and *L II* with the dimensions of source it was desired to use for this phase of the work, measurements were made from records on which the lines were not resolved. From the preceding results the separate intensities may be calculated.

In Table IV are given the values of the measured quantities from which the quantity *C* is computed for lines *L I* plus *L II* according to Eq. (1). The results are given for four sources exposed a total of 6 times. All runs were taken with No-screen x-ray film, except that marked with an asterisk, for which Ilford B-2 plates of 50 micron emulsion thickness were used. The transmission of the spectrograph was the same in all cases, amounting to 0.0715 percent for the *L I* line. This is the reciprocal of the geometric factor in Eq. (1). The activity of source 12 is given as an upper limit because contamination of the apparatus was evident after the first run, and the source had visibly deteriorated; the calculated value of *C* is consequently a lower limit. The estimated uncertainties for the individual measurements are 5 percent in *S*, 4 percent in ϕ, and 5 to 10 percent in the integral, being greatest for the smallest values of the integral. The consistency of the results for a range of source thicknesses is to be particularly noted.

Taking account of the *L III* line, 54 percent of the disintegrations are accompanied by conversion in the *L* shell. Taking a value of 3.5 percent for the unconverted 47-kev gamma-ray, the ratio of the number of

TABLE IV. Values of the measured quantities from which the quantity *C* is computed for lines *L I* plus *L II*.

Source	t sec. 10^4	S electrons / den. cm 10^7	ϕ sec.$^{-1}$ 10^6	$\int D dl$ den. cm	*C*%	Average source thickness μg/cm²
11	9.40	2.15	1.84	0.31	54	101
12	8.65	2.45	<1.73	0.16	>37	207
	14.7	2.16	<1.73	0.30	>36	
17	*17.9	11.6	1.26	0.068	49	68
	7.39	2.20	1.26	0.16	53	
18	78.5	2.50	0.37	0.44	53	43
			Weighted average		53±3	

internal conversion electrons from the L shell to the number of unconverted gamma-rays is 15.5.

The total number of conversion electrons is 74 ± 5. Adding to this the number of unconverted gammas gives 77.5 ± 5 for the percentage of the decays associated with the 47-kev excited state of radium E. Thus there must be an alternative decay scheme accounting for approximately 20 percent of the decays. These results are in good agreement with the results of Kinsey based on the indirect method, involving measurement of the L x-rays. The results of Kinsey and Stahel taken together with those reported here comprise a set of mutually consistent data which may be interpreted as lending support to whichever of the following three quantities is least certain: the number of L conversion electrons, the number of L x-rays, or the yield of L x-rays caused by internal conversion (fluorescence yield).

C. Possible Additional Conversion Line

Figure 4 shows the record obtained with a source on which only one exposure was run, after which the zapon film deteriorated seriously. There is indication here of a weak line at 470 ± 10 gauss cm, corresponding to an energy of 19 ± 1 kev. The same indication was found on three scans over different portions of the exposure. An upper limit to the intensity of this line relative to the $L\,I$ line is about 2.5 percent. The uncertainty in the intensity is of the same order, however. A similar upper limit may be placed on the strengths of any other lines, down to an energy of about 15 kev. Below this energy the sensitivity of the emulsions used was very low. Assuming a line at 19 kev is due to conversion in the $L\,I$ shell, the energy of the gamma-ray is 35.4 ± 1 kev, in agreement with one of the new gamma-rays reported by San-Tsiang.[4]

D. The Continuum

Comparison was made of the continua obtained with a source in which radium D and radium E were in equilibrium, and a source in which the radium E had on the average only 20 percent of its equilibrium value during the exposure. In both cases the continua bore approximately the same intensity relation to the lines,

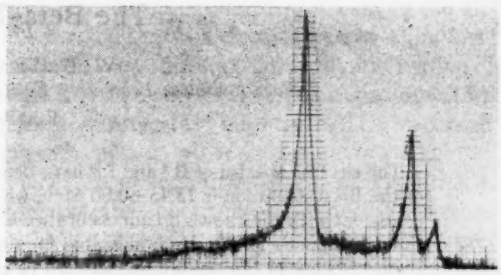

FIG. 4. Radium D electron spectrum with indication of additional line.

the electrons recorded between the centers of the $L\,I$ and M lines accounting for about 25 percent of the disintegrations. This eliminates the possibility that the radium E contamination is responsible for any appreciable portion of the continuum. The continuum can be interpreted as evidence of a more energetic primary beta-spectrum than has been hitherto been reported but also it may be due to scattering of conversion electrons, probably from the side-walls of the spectrograph.

ACKNOWLEDGMENTS

Thanks are due Professor P. Morrison for bringing the author's attention to radium D, and to Dr. K. Krieger for advice on chemical problems. The assistance of Mr. H. Mohr on mechanical problems is gratefully acknowledged. This research was supported in part by a joint program of the Office of Naval Research and the Atomic Energy Commission. The beta-ray spectrograph was constructed under a grant from the American Philosophical Society. The Faculty Research Committee of the University of Pennsylvania also contributed assistance.

Special thanks for helpful criticism, encouragement, and suggestions are due to Professors J. Halpern and W. E. Stephens.

The author was assisted during a portion of this work by an AEC predoctoral fellowship, and subsequently was Mary Amanda Wood Research Associate of the University of Pennsylvania.

The Beta-Decay of B^{12} and Li^8

W. F. HORNYAK* AND T. LAURITSEN
Kellogg Radiation Laboratory, California Institute of Technology, Pasadena, California
(Received October 13, 1949)

The electron spectra of B^{12} and Li^8 have been studied, using a magnetic lens spectrometer. The end point of the B^{12} distribution is 13.43±0.06 Mev, while the Li^8 spectrum tails off gradually with a shape which is consistent with the known broadness of the excited state of Be^8 to which the decay occurs. Neither distribution corresponds to the shape indicated for simple "allowed" transitions, but it seems probable that more than one state of the residual nuclei may be involved in the decay schemes. The discrepancy between the observed end point of the B^{12} spectrum and the mass differences suggests the existence of an excited state at 0.9 Mev either in B^{12} or C^{12}.

INTRODUCTION

RADIOACTIVE Li^8, produced in the bombardment of Li^7 by deuterons, disintegrates by electron emission, with a half-life of 0.89 sec., predominantly to a broad excited state in Be^8 at approximately 3 Mev which in turn decays in $\sim 10^{-21}$ sec. into two alpha-particles. The beta-decay of Li^8 to the ground state of Be^8 is apparently forbidden. The electron spectrum was studied by Crane, Delsasso, Fowler, and Lauritsen[1] and by Bayley and Crane[2] using cloud-chamber methods. The latter investigators found a maximum energy of 12.0±0.6 Mev. The alpha-particle distribution has been investigated most recently by Bonner, Evans, Malich, and Risser[3] who summarize the earlier literature. Radioactive B^{12}, which has a half-life of 0.025 sec., is produced by deuteron bombardment of B^{11} and decays by electron emission, presumably to the ground state of C^{12}. This spectrum was also investigated by Bayley and Crane with a cloud chamber, and was found to have an end point of 12.0±0.6 Mev. More recently Hereford,[4] using an absorption technique, has reported 13.3±0.5 Mev for the end point.

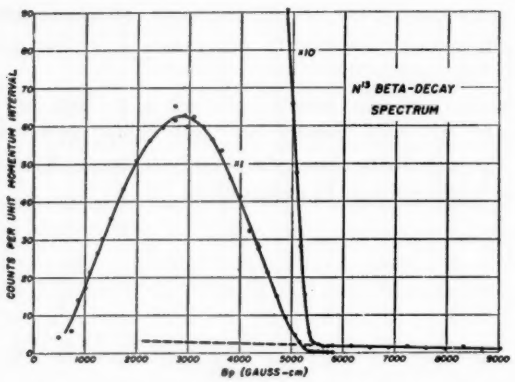

FIG. 1. Momentum spectrum of N^{13} positrons. The ordinate scale is in arbitrary units in this and following figures.

In view of the interest in obtaining more precise information on these spectra, we have studied the electron momentum distributions using a magnetic lens type spectrometer, with considerably better statistics than was possible in the earlier cloud-chamber work. As a check on the performance of the spectrometer, particularly with respect to scattering, the spectrum of N^{13} was also run. A preliminary account of these results has appeared in a Letter to the Editor.[5]

EXPERIMENTAL METHOD

The beta-ray spectrometer used in this investigation was described in an earlier paper.[6] The spectrometer stops were set for ring focusing with a resolution of 2.6 percent. The momentum calibration was obtained from the internal conversion "X" line of Th-D, $B\rho = 10{,}000$ gauss-cm. The compensation for the vertical component of the earth's magnetic field and other stray magnetic fields was checked both at the beginning and the end of the experiment and was found to be satisfactory down to the internal conversion "I" line of Th-C, corresponding to a kinetic energy of approximately 200 kev. The deuteron beam from an electrostatic accelerator was brought directly into the vacuum chamber of the spectrometer to bombard suitable targets placed at the source position for the production of the radioactive elements. In order to eliminate the effects of prompt radiation produced during bombardment of the target, observations were made with the beam off. For the N^{13},

TABLE I: Summary of N^{13} β-decay spectrum end-point energies.

End-point energy (Mev)	Date	Observers
1.198±0.006	1939	Lyman[a]
1.218±0.004	1940	Townsend[b]
1.24 ±0.02	1945	Siegbahn and Slatis[c]
1.25 ±0.03	1948	Cook, Langer, Price, and Sampson[d]
1.202±0.005		This experiment

[a] E. R. Lyman, Phys. Rev. 55, 234 (1939).
[b] A. A. Townsend, Proc. Roy. Soc. A177, 357 (1940–41).
[c] K. Siegbahn and H. Slätis, Arkiv. f. Ast. Math. Fys. 32A, No. 9, (1945).
[d] See reference 7.

* Now at Brookhaven National Laboratory, Upton, Long Island, New York.
[1] Crane, Delsasso, Fowler, and Lauritsen, Phys. Rev. 47, 971 (1935).
[2] D. S. Bayley and H. R. Crane, Phys. Rev. 52, 604 (1937).
[3] Bonner, Evans, Malich, and Risser, Phys. Rev. 73, 885 (1948).
[4] F. L. Hereford, Phys. Rev. 74, 574 (1948).
[5] Hornyak, Dougherty, and Lauritsen, Phys. Rev. 74, 1727 (1948).
[6] Hornyak, Lauritsen, and Rasmussen, Phys. Rev. 76, 731 (1949).

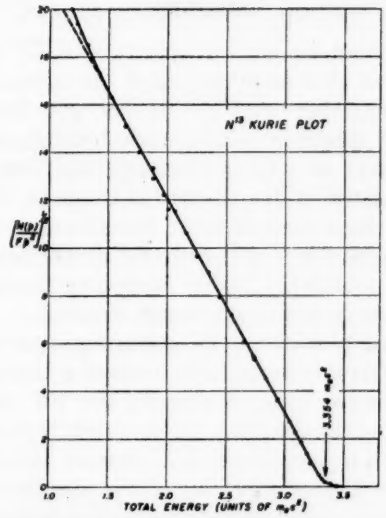

FIG. 2. Kurie plot of N^{13} positron spectrum.

the target was bombarded for fifteen minutes, the accelerator shut down and counting carried out over two or three half-lives. Corrections for decay and normalization for successive runs were ascertained by frequent repetition of certain points in the spectrum. In the cases of Li^8 and B^{12}, because of the short half-lives, the accelerator was run continuously and the deuteron beam periodically intercepted, either mechanically or by means of an electrostatic deflecting plate. In the former method, used in some of the Li^8 experiments, a quartz shutter was interposed in the beam during a one-second counting period and removed for a one-second bombardment. Suitable interlocks cut the counter off during the bombardment period. For the shorter lived B^{12} and for some of the later Li^8 work, an electrostatic deflector was used, operated by a 3000-volt, 60-cycle square wave supply, interlocked with the counting system by means of a simple coincidence circuit. During the counting period, the beam struck a brass target several feet from the spectrometer. Check

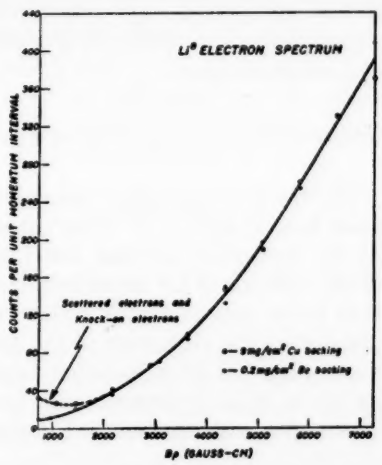

FIG. 3. Low energy end of Li^8 electron momentum spectrum.

runs with the intense prompt radiation of the $Be^9(dn)$ reaction showed that the circuits were working properly and rendered the counters completely insensitive during the bombardment period. The beam was monitored by a separate gamma-ray counter which recorded the prompt radiation.

Primarily to ascertain the extent of scattering in the spectrometer, the spectrum of N^{13} decay positrons was run, using a thin soot target sandwiched between two layers of 0.2 mg/cm² Be foil.* The resulting momentum

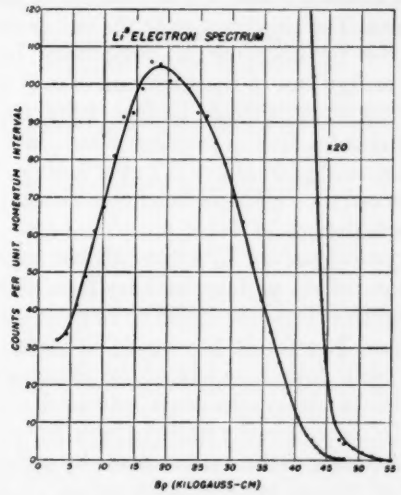

FIG. 4. Momentum spectrum of Li^8 electrons.

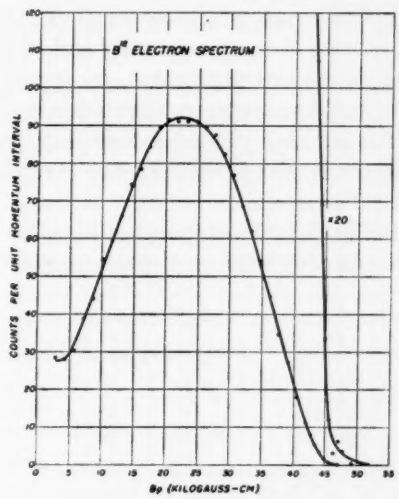

FIG. 5. Momentum spectrum of B^{12} electrons.

spectrum after cosmic-ray and local background have been subtracted is shown in Fig. 1. A background which is slightly field sensitive and of the order of cosmic-ray background is still apparent above the end point of the β-spectrum, indicating a slight diffusion of the radioactive nitrogen from the target and possibly a small degree of scattering in the spectrometer. In connection

* We are indebted to Dr. H. Bradner for the Be foils.

with the former point, it may be mentioned that an appreciable increase in background was observed with non-sandwiched targets when the pumping speed was reduced by turning off the oil diffusion pump on the spectrometer. That no great diffusion of the radioactive nitrogen occurs with sandwiched targets is indicated by the agreement of the half-life of 10.05±0.1 minutes observed here with the values reported in the literature.

When the slight correction for the residual background is made, the Kurie plot of the data, Fig. 2, is linear from about 0.2-Mev kinetic energy to just below the end point. The curvature near the end point can be accounted for by instrumental resolution. The shape of the low energy end of the spectrum is in good agreement with the work of Cook, Langer, Price, and Sampson[7] and indicates that scattering effects in the spectrometer are negligible above 0.2 or 0.3 Mev. The end point observed in this experiment is compared with other determinations in Table I.

For the production of Li^8, thin lithium metal layers were evaporated on various backing foils. Copper foil of 9 mg/cm² thickness was found to be most convenient and was used in most of the work. No detectable activity was found from bare foils at the deuteron energies used. Since the decay electrons traversed the copper before being focused in the spectrograph, a check on the effect of scattering in the foil was made by using a target consisting of lithium metal evaporated on a 0.2 mg/cm² Be foil. The resulting distributions in the low energy range, shown in Fig. 3, are identical for momenta greater than 2000 gauss-cm. Below this limit, the copper foil gives evidence of some scattering and of knock-on electrons. A subsequent experiment, made with a radically different spectrometer configuration and with a beryllium foil backing yielded satisfactory agreement with the present results in the region re-examined, from 5000 to 35,000 gauss-cm.

In the B^{12} work, thin evaporated films of B_2O_3 on 9 mg/cm² copper foil were used throughout.

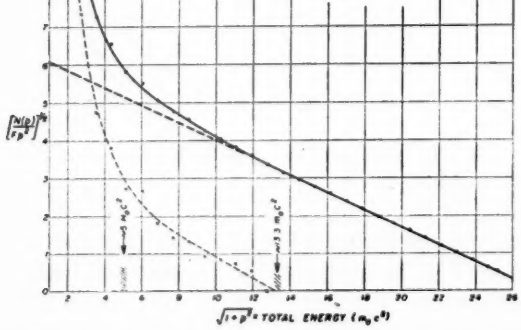

FIG. 6. Kurie plot of B^{12} electron spectrum. The dashed curves indicate a possible decomposition into simple spectra.

RESULTS

The observed momentum spectrum of Li^8 is shown in Fig. 4 and that of B^{12} in Fig. 5. As compared with the cloud-chamber work of Bayley and Crane, the present Li^8 spectrum is somewhat broader, having a larger number of both low energy and high energy electrons relative to the number at the peak. The present peak occurs at somewhat lower energy. The B^{12} spectrum agrees less well with the earlier work, indicating a considerably higher energy at the peak and relatively many more high energy electrons.

The Kurie plot of the B^{12} spectrum is presented in Figs. 6 and 7, the latter curve indicating the end point on an expanded scale. A straight line fits the higher energy end of the spectrum from a total electron energy of 12 m_0c^2 to the end point of 27.30 m_0c^2. The slight tail just at the high energy end of the spectrum can be accounted for almost entirely by the instrument resolution. The deviation of the experimental curve from a straight line below a total energy of 12 m_0c^2 is very marked. The Kurie plot for the spectrum of Li^8 is shown in Figs. 8 and 9. It will be seen that there is no extensive linear portion in the experimental curve and in particular the deviation from linearity in the neighborhood of the upper energy limit is much more pronounced than for the B^{12} data and cannot be ascribed to the instrumental resolution. Although no sharp end point exists in the usual sense, one may take the extrapolation of the best straight line fit to the spectrum as an effective mean "end point." The "end point" thus obtained is

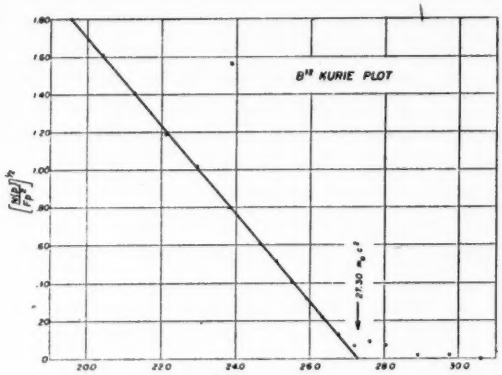

FIG. 7. Kurie plot of B^{12} electron spectrum near end point.

~26 m_0c^2 (~13-Mev kinetic energy). Since the Li^8-Be^8 mass difference from Q and mass value calculations is 16.02 Mev,[8] the indication is that the high energy transition in the β-decay of Li^8 is predominantly to an excited state in Be^8 at approximately 3 Mev rather than to the ground state. The curvature of the plot in this region indicates that this level is rather broad. These observations are in good agreement with the existing knowledge from other experiments. The deviation from

[7] Cook, Langer, Price, and Sampson, Phys. Rev. 74, 502 (1948).

[8] Using $Li^7(dp)Li^8 = -0.19$ Mev; $Be^8 \rightarrow 2He^4 = 0.09$ Mev.

linearity of the experimental data below a total energy of 12 m_0c^2 (Fig. 8), as in the case of B^{12}, is quite marked.

DISCUSSION

A proposed disintegration scheme for Li^8 is illustrated in Fig. 10. The α-particle distribution has been observed to extend up to an energy $E_\alpha=7.75$ Mev[9] and has a maximum intensity at $2E_\alpha=3.3$ Mev.[3] By analysis of the α-particle spectrum, Bonner *et al.* found that the distribution can best be accounted for by taking the major part of the β-decay to an excited state in Be^8 at 3.1 Mev having a width of 0.8 Mev. There was also some indication that a broad state at 7–9 Mev may be

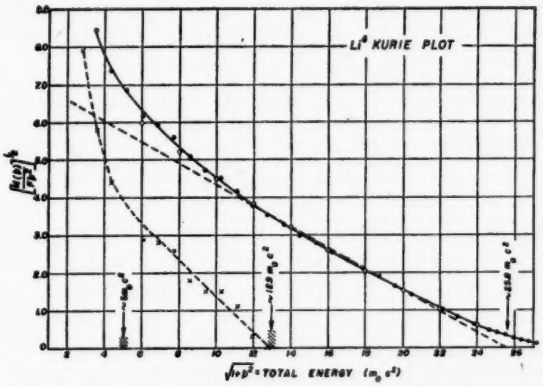

FIG. 8. Kurie plot of Li^8 electron spectrum: Open circles calculated from alpha-particle distribution of Fig. 11. The dashed curves indicate a possible decomposition into simple spectra.

involved in the decay scheme. Their data are reproduced in Fig. 11; the solid curve shown is a reasonable fit to these points at low and intermediate energies and follows approximately the work of Smith and Chang at high energies. As has been pointed out by Bayley and Crane,[2] the electron decay spectrum can be predicted from the α-particle distribution by assuming that the latter, with an appropriate energy-dependent normalization, gives the density of states available in Be^8 for the β-transitions. This assumption is equivalent to stating that the principal mode of decay of the excited states in which Be^8 is left following the Li^8 break-up is by α-particle emission and that γ-radiation can be neglected. The Fermi theory for allowed β-decay then gives the electron distribution:

$$N(W)dW=F[W^2-1]^{\frac{1}{2}}WdW \times\int_0^{Q'-W} A(E)[Q'-E-W]^2dE, \quad (1)$$

where W is the total electron energy in units of m_0c^2, E is the combined kinetic energy of the alpha-particles ($E=2E_\alpha$), and Q' is the total energy available (atomic mass difference, Li^8-2He^4, plus m_0c^2). The function

[9] C. L. Smith and W. Y. Chang, Proc. Roy. Soc. **166**, 415 (1938).

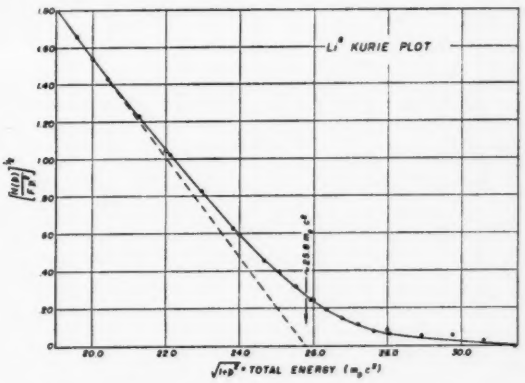

FIG. 9. Kurie plot of Li^8 electron spectrum near end point: Open circles calculated from alpha-particle distribution of Fig. 11.

$A(E)$ is the density of states, given by

$$A(E)dE\int_0^{Q'-E}[Q'-E-W]^2 \times[W^2-1]^{\frac{1}{2}}WdW=N_\alpha(E)dE. \quad (2)$$

The distribution predicted from Eq. (1) using the solid curve of Fig. 11 for the alpha-particle spectrum, is indicated by the open circles of Figs. 8 and 9. The value of Q' which gave the best fit was 32.8 m_0c^2 or 16.75 Mev, which is about 0.13 Mev higher than the value expected from the masses.

The agreement between predicted and observed points is quite satisfactory above a total energy of 12 m_0c^2 and indicates that the electrons observed in this region are adequately accounted for by the observed alpha-particles. The deviations below 12 m_0c^2 appear to require relatively more high energy alpha-particles than have been observed and may suggest that gamma-ray emitting states may be involved in the decay. Delayed gamma-radiation certainly occurs but it is not known to what extent the observed effects may be accounted for by bremsstrahlung. Decomposition of the spectrum of Fig. 8 indicates that about 10 percent of the β-transitions occur to states of Be^8 at $\sim$10 and $\sim$13 Mev and 90 percent to the 3.1-Mev state. From the limit of error associated with the points just at the end point where the spectrum merges with the background, it is estimated that less than 2 percent of the entire β-decay is to the ground state. A less certain estimate is that no more than 5 percent of the β-decay is to the known γ-ray emitting state at 4.8 Mev. If the component

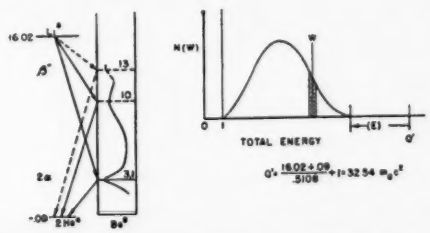

FIG. 10. Suggested disintegration scheme for Li^8 decay.

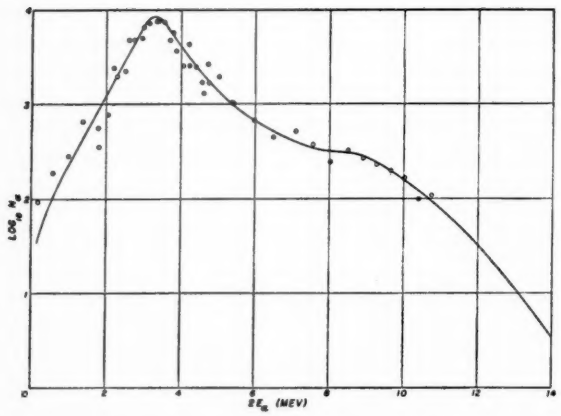

FIG. 11. Alpha-particle distribution from decay of Li^8. Circles represent data of Bonner *et al.* (see reference 3); high energy extrapolation follows approximately work of Smith and Chang (see reference 12).

spectra are of "forbidden" or "unfavored" types, as might be expected from the relatively long half-life, these relative intensity estimates may be considerably modified.

The extrapolated end point of the Kurie plot for B^{12} (Fig. 7) gives 27.30 ± 0.10 m_0c^2 for the total energy or 13.43 ± 0.06-Mev kinetic energy, in agreement with the value 13.3 ± 0.5 Mev obtained by Hereford. If the high energy end of the β-spectrum corresponds to a decay to the ground state of C^{12} then the observed end point, combined with the mass[10] of C^{12} gives 12.01827 ±0.00009 a.m.u. for the mass of B^{12}. From an analysis of the nuclear binding energies Barkas[11] predicts a mass of 12.0188 a.m.u. for B^{12}. Using the observed end point as the decay energy to the ground state of C^{12} and the mass tables of Mattauch and Flammersfeld,[12] the Q of the reaction $B^{11}(dp)B^{12}$ is found to be $+1.07$ Mev. The early work of Cockroft and Lewis[13,14] indicated that the bombardment of boron targets with deuterons of 0.55 Mev yielded no group with range greater than 2.7 cm, implying that the Q of the reaction is probably less than $\sim$0.8 Mev. Recently Hudspeth and Swann[15] have made a direct determination, yielding $Q=0.15$ Mev, based on the analysis of the yield curve for B^{12} and on the measurement of the range in photographic emulsion of a particle group ascribed to this reaction. The discrepancy of 0.92 Mev is too large to be accounted for by the mass uncertainties and appears to indicate either that the decay of B^{12} proceeds mainly to a level in C^{12} at $\sim$0.9 Mev excitation, the transition to the ground state being forbidden, or that the B^{12} is initially formed in an excited state, emitting a gamma-ray before the β-decay. The observation by Hudspeth and Swann of $\beta-\gamma$-coincidences would favor the first hypothesis, although the evidence is not entirely clear.

Note added in proof.—In a more recent paper, E. L. Hudspeth and C. P. Swann, Phys. Rev. **76**, 1150 (1949), report the discovery of a weak, higher energy proton group (corresponding to $Q=1.25$ Mev). It thus appears that the second hypothesis is the correct one.

If 5 percent of the β-decay is assumed to go to a level in C^{12} at $\sim$7.1 Mev and possibly to a broad or composite level at $\sim$11 Mev (Fig. 6), the observed nonlinearity of the Kurie plot below 12 m_0c^2 total energy can be accounted for. A decay of 5 percent or less to the 4.3-Mev level in C^{12} cannot be excluded. It should be pointed out that if the primary decay of B^{12} occurs to an excited state in C^{12} then the estimated energy of the excited states in C^{12} involved in the possible complex decay of B^{12} must be raised from 7.1 to 8.0 Mev and from 11 to 12 Mev.

ACKNOWLEDGMENTS

The authors' thanks are due Professors C. C. Lauritsen, W. A. Fowler, and R. F. Christy for much helpful advice and assistance in connection with this problem. Mr. C. B. Dougherty was an active participant in the early part of the work. This work was assisted by the Joint Program of ONR and AEC.

[10] R. Cohen and W. F. Hornyak, Phys. Rev. **72**, 1127 (1947).
[11] W. H. Barkas, Phys. Rev. **55**, 691 (1939).
[12] Mattauch and Flammersfeld, Isotopic Report, Special Issue, Zeits. f. Naturforschung (1949).
[13] J. D. Crockroft and W. B. Lewis, Proc. Roy. Soc. **A154**, 246 (1936).
[14] M. S. Livingston and H. A. Bethe, Rev. Mod. Phys. **9**, 326 (1937).
[15] E. L. Hudspeth and C. P. Swann, Phys. Rev. **74**, 1722 (1948).

Determination of the Energy Distribution of Bremsstrahlung from 19.5-Mev Electrons*

H. W. Koch** and R. E. Carter***
Physics Department, University of Illinois, Urbana, Illinois
(Received September 23, 1949)

The conventional target of a 22-Mev betatron has been replaced by a 0.005-in. platinum target and the intensity spectrum of x-rays produced in the platinum by betatron-accelerated electrons has been measured. The kinetic energy of the monoenergetic electrons at the time of expansion was 19.5 Mev. The x-rays were collimated and observed in the forward direction by studying the electron-positron pairs produced in a cloud chamber filled with air. About 1300 pairs were measured. The intensity spectrum of x-rays is calculated from the pair energy distribution and is compared with the bremsstrahlung theory of Bethe and Heitler. The experimental intensity in the region of 10 Mev is found to be higher than the theoretical value by an amount which is larger than the statistical uncertainty of the experiment. Some details of the pair production process are given, and methods of correcting for instrumental discrimination are discussed and applied.

INTRODUCTION

THE non-relativistic wave-mechanical treatment of bremsstrahlung production has been developed in detail by Sommerfeld,[1] Sommerfeld and Maue,[2] and Weinstock.[3] The theory was confirmed by the experiments of Nicholas,[4] Kulenkampff,[5] and Harworth and Kirkpatrick.[6] There was agreement on the existence of a finite number of quanta at the high energy end of the spectrum produced by monoenergetic electrons impinging on a thin target.

In 1934, Bethe and Heitler[7] developed a theory of bremsstrahlung which should be valid for electrons in the relativistic region. In addition, this theory gave the cross section for electron-positron pair production. The theory has been carried out only to the extent of the Born approximation and the validity of its predictions are thus limited. The theory has not been compared with a direct detailed experiment in the past, although some parts of it have been investigated. In particular, Lanzl, Laughlin, and Skaggs[8] have shown that the ratio of the bremsstrahlung production cross sections for tantalum and copper was larger than the theoretical Z^2 factor by about eight percent for quanta having energies between 10.9 and 16 Mev.

The form of the theory which described the cross section for pair production has been investigated in the work of Adams,[9] of Lawson,[10] and of Walker[11] on x-ray absorption coefficients. They found discrepancies with the theory for high Z absorbers, and ascribed these to the part of the absorption which resulted in the production of pairs.

A partial but more direct examination of the bremsstrahlung spectrum theory at energies of the order of 2 Mev was reported by Miller and Waldman.[12] They determined the spectral distribution at the high energy x-ray end and found a finite and constant intensity of radiation within several hundred kilovolts of the upper energy tip. Their experiment differed from the present one in that they had a monochromatic detector, and varied the electron energy. The result of the experiment was predicted by Guth,[13] who used the Bethe-Heitler theory and applied a correction which was intended to remove the error due to the Born approximation.

Two reports have been published on previous determinations of betatron x-ray spectra, which are similar in principle to the present work. The first[14] was the investigation of the Compton recoil electrons produced in a carbon radiator in a cloud chamber by the x-rays from a 2.8-Mev betatron. The intensity spectrum obtained by these authors is very different from that predicted.

The second spectrum experiment,[15] which was done with a 20-Mev betatron, involved the two energy distribution determinations of the electron-positron pairs from a lead foil in a cloud chamber and the photoprotons in deuterium-loaded emulsions. The authors point out that unfortunately their measured spectrum "is not the spectrum that would be obtained if only the target radiation were measured."

Therefore, neither of the two reports permits a conclusive test of the Bethe-Heitler theory when it is applied to the radiation from 19.5-Mev electrons.

Several other methods have been proposed for the determination of betatron x-ray spectra by Baldwin and Klaiber,[16] and by Lawson.[17]

* Assisted by the Joint Program of the ONR and the AEC.
** Present address: X-Ray Section, National Bureau of Standards, Washington, D.C.
*** Present address: Los Alamos Scientific Laboratory, Los Alamos, New Mexico.

[1] A. Sommerfeld, Ann. d. Physik **11**, 257 (1931).
[2] A. Sommerfeld and A. W. Maue, Ann. d. Physik **23**, 589 (1935).
[3] R. Weinstock, Phys. Rev. **61**, 584 (1942); **64**, 276 (1943).
[4] W. W. Nicholas, Bur. Stand. J. Research **2**, 837 (1929).
[5] H. Kulenkampff, *Handbuch der Physik* (1933), Vol. 23, p. 2.
[6] K. Harworth and P. Kirkpatrick, Phys. Rev. **62**, 334 (1942).
[7] H. Bethe and W. Heitler, Proc. Roy. Soc. **146**, 83 (1934).
[8] Lanzl, Laughlin, and Skaggs, Phys. Rev. **74**, 1261 (1948).
[9] G. D. Adams, Phys. Rev. **74**, 1707 (1948).
[10] J. L. Lawson, Phys. Rev. **75**, 433 (1949).
[11] R. Walker, Phys. Rev. **76**, 527 (1949).
[12] W. C. Miller and B. Waldman, Phys. Rev. **75**, 425 (1949).
[13] E. Guth, Phys. Rev. **59**, 325 (1941).
[14] W. B. Lasich and L. Riddiford, J. Sci. Inst. **24**, 177 (1947).
[15] Bosley, Craggs, Nash, and Payne, Nature **161**, 1022 (1948).
[16] G. C. Baldwin and G. S. Klaiber, Phys. Rev. **71**, 554 (1947).
[17] J. L. Lawson *et al.*, ONR Quarterly Progress Report, General Electric Company (September, 1948).

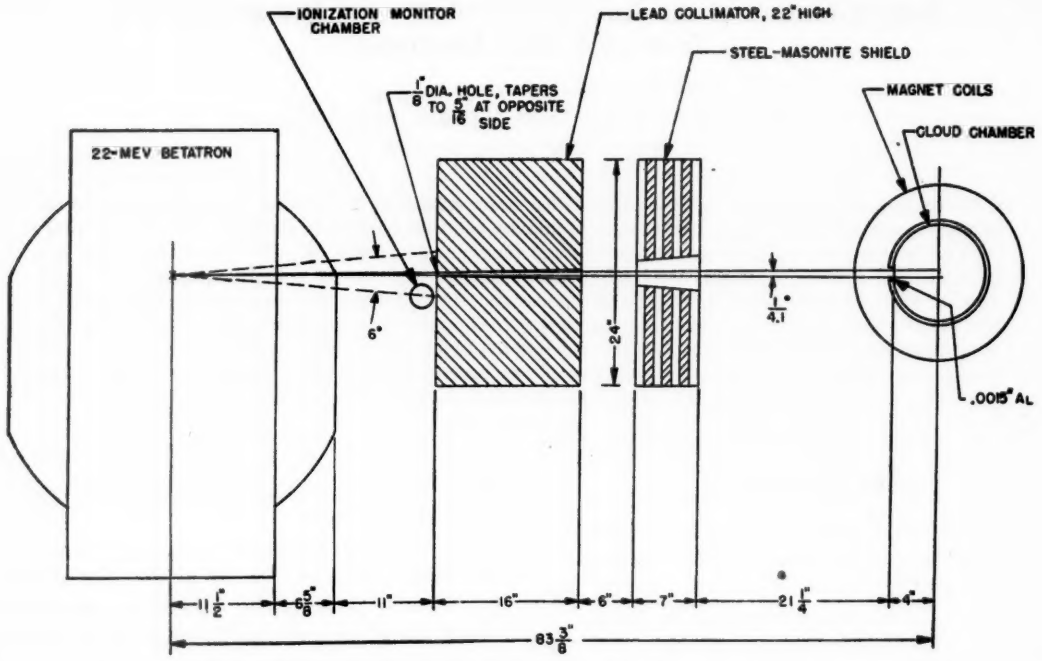

FIG. 1. Schematic diagram of the experimental arrangement.

The present experiment[18] determined the energy distribution of bremsstrahlung, which was produced in a thin target of platinum by electrons accelerated in a 22-Mev betatron.[19] Pair electrons were created in the gas of a cloud chamber by the betatron x-rays. The x-ray intensity distribution was calculated from the pair energy distribution, which was measured.

The principal purpose of the experiment was to obtain a set of experimental data which could be compared with the predictions of the Bethe-Heitler bremsstrahlung theory. The betatron is obviously ideal as a source of x-rays, because it produces a monoenergetic beam of high energy electrons. However, other requirements also had to be satisfied in order to permit a valid test of the theory by the experiment. The following were regarded as essential in the present work:

(1) The x-ray target was thin.
(2) The x-rays were finely collimated so that only quanta, originating in the target and going in the forward direction from the target, entered the cloud chamber through a thin window.
(3) The electron-positron pairs were produced in a low Z gas, so that the use of the theoretical pair production cross section would permit the accurate conversion of the pair energy distribution into the x-ray intensity distribution.
(4) The pair particle characteristics were examined in detail experimentally, in order to make a rough test of the theoretical description of the pair production process and also to eliminate instrumental discrimination against certain energy groups of pairs.

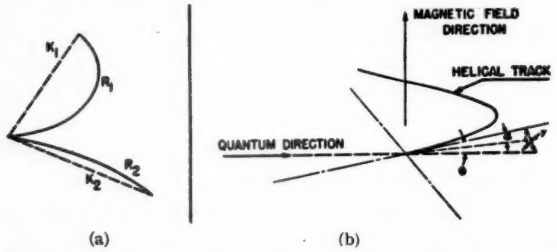

FIG. 2. Schematic drawing showing typical pair tracks. (a) Reprojection onto horizontal plane, in which the quantities measured were: (1) X–Y coordinates of pair origin; (2) conically projected radius, R; (3) chord length, K, of particle arc with measured R. (b) Reprojection into three dimensions in which the quantities measured were: (1) Z coordinate of pair origin; (2) dip angle of particle helix, α; (3) angle, θ, of particle with respect to quantum direction.

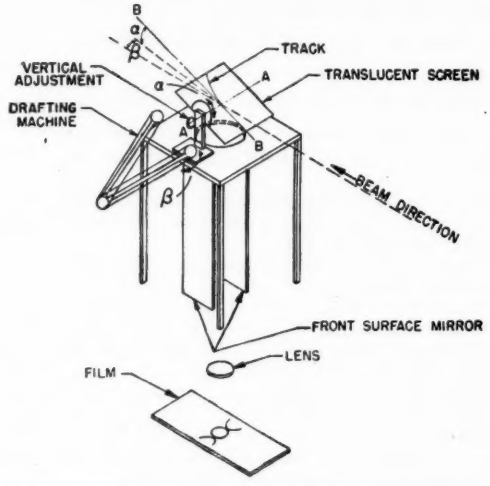

FIG. 3. Schematic drawing showing the apparatus used in the three-dimensional analysis of tracks.

[18] Preliminary reports have been given in Koch, Carter, and Robinson, Phys. Rev. 75, 172A (1949); and H. W. Koch and R. E. Carter, Phys. Rev. 75, 1950 (1949).
[19] D. W. Kerst, Rev. Sci. Inst. 13, 387 (1942).

It must be emphasized that an intensity spectrum result can only be applied to experiments in which a similar experimental arrangement is used. For example, the result in this paper is not applicable to an uncollimated beam of betatron x-rays emanating from a conventionally thick target.

APPARATUS

The experimental apparatus can be described in two parts: (1) The equipment required to produce a collimated beam of x-rays from the 22-Mev betatron; and (2) the equipment required to detect, photograph, and analyze the pair electrons.

1. The X-Ray Source

Figure 1 shows schematically the cloud-chamber arrangement in front of the 22-Mev betatron. The betatron was pulse-operated[20] so as to produce electrons with a kinetic energy of 19.5 Mev. The electron energy was accurately determined by the energy control built by Mr. H. Palevsky and described in principle in previous papers.[21]

After acceleration to the peak energy, the electrons bombarded a platinum target ($Z=78$), which was 0.005 in. thick. Electrons with energies of 19.5 Mev will lose approximately $\frac{1}{2}$ Mev energy due to ionization loss in going through the target. Therefore, the x-radiation produced by the electron bombardment of the platinum is considered thin target radiation.

The target was a relatively large flag, $\frac{3}{16}$ by $\frac{1}{4}$ by 0.005 in. thick, in order to insure that the x-rays being studied in the cloud chamber of Fig. 1 were emanating from the platinum target and not from other parts of the betatron vacuum chamber. The target projected out from the injector structure $\frac{3}{16}$ in. in the direction of the electron orbit. No obvious reduction in the x-ray intensity was observed as compared to that obtained from standard thicker targets.

The target thickness was tested by determining the total angle of the x-ray cone. Copper foils placed normal to the x-ray beam direction were used and the total angle of the half-intensity value of the copper activity was 6° for a betatron energy of 19.5 Mev. To within experimental error this is in good agreement with the

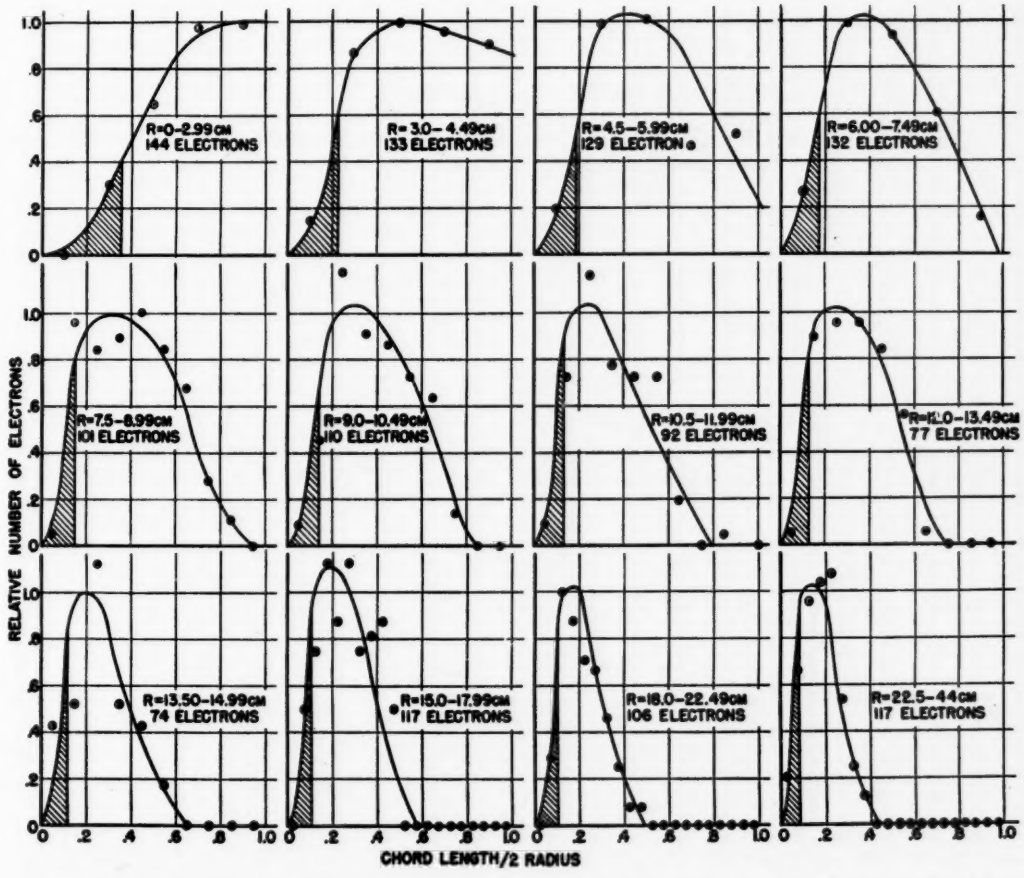

FIG. 4. Relative number of electrons whose radii of curvature fall within a certain interval, plotted as a function of chord length/2 radius. This is shown for several intervals of radius. The vertical line defining the right side of the shaded area in each plot corresponds to the minimum length of chord which was acceptable. All tracks falling in the shaded areas were discarded.

[20] H. W. Koch and C. S. Robinson, Rev. Sci. Inst. **19**, 37 (1948).
[21] See McElhinney, Hanson, Becker, Duffield, and Diven, Phys. Rev. **75**, 542 (1949).

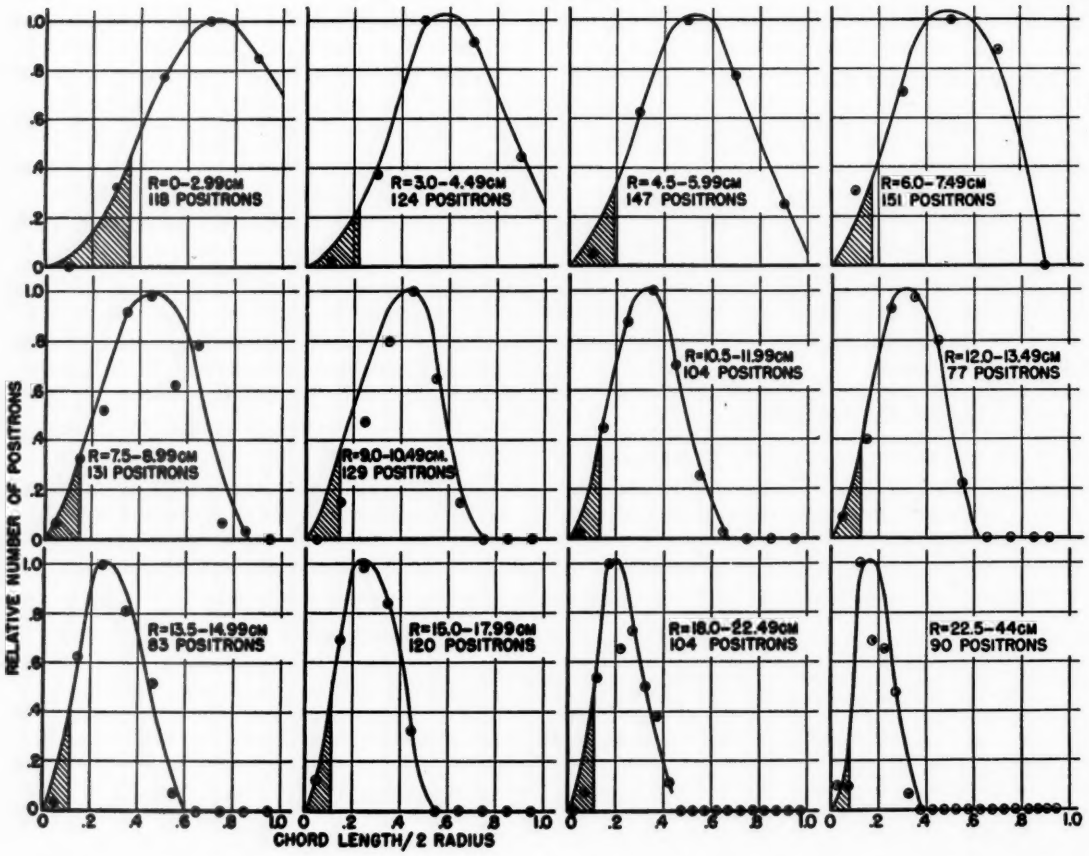

FIG. 5. Relative number of positrons whose radii of curvature fall within a certain interval, plotted as a function of chord length/2 radius. This is shown for several intervals of radius. The vertical line defining the right side of the shaded area in each plot corresponds to the minimum length of chord which was acceptable. All tracks falling in the shaded areas were discarded.

value predicted by Schiff[22] for a 0.005-in. thick tungsten target.

Tests were also made on the focal spot size and the time duration of the x-ray burst. The focal spot size was measured by the use of a pinhole camera at several electron energy values. The spot size was 1.3 mm high by 0.3 mm wide. No other images were observed. Therefore, it is believed that only the platinum target was serving as a source of x-rays.

The x-ray burst time width was examined by means of a 931 photo-multiplier tube plus a fast amplifier circuit. Mr. G. W. Rodeback built the circuits and showed that the x-ray burst for 19.5-Mev electrons was

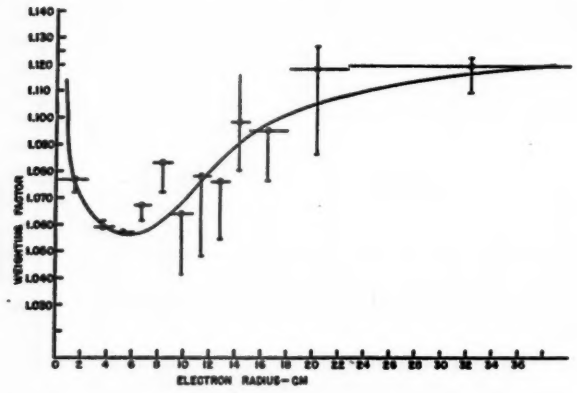

FIG. 6. Chord length weighting factor calculated for electrons to correct for effects of discrimination.

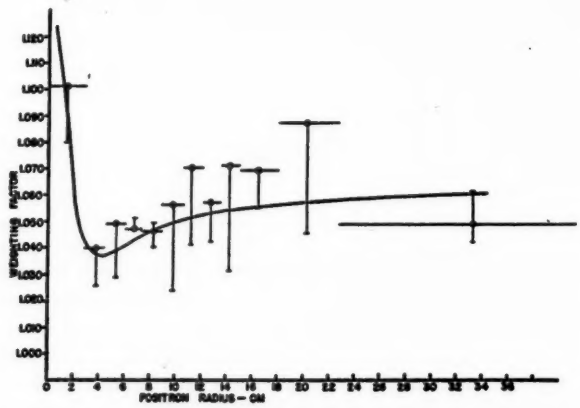

FIG. 7. Chord length weighting factor calculated for positrons to correct for effects of discrimination.

[22] L. I. Schiff, Phys. Rev. 70, 87 (1946).

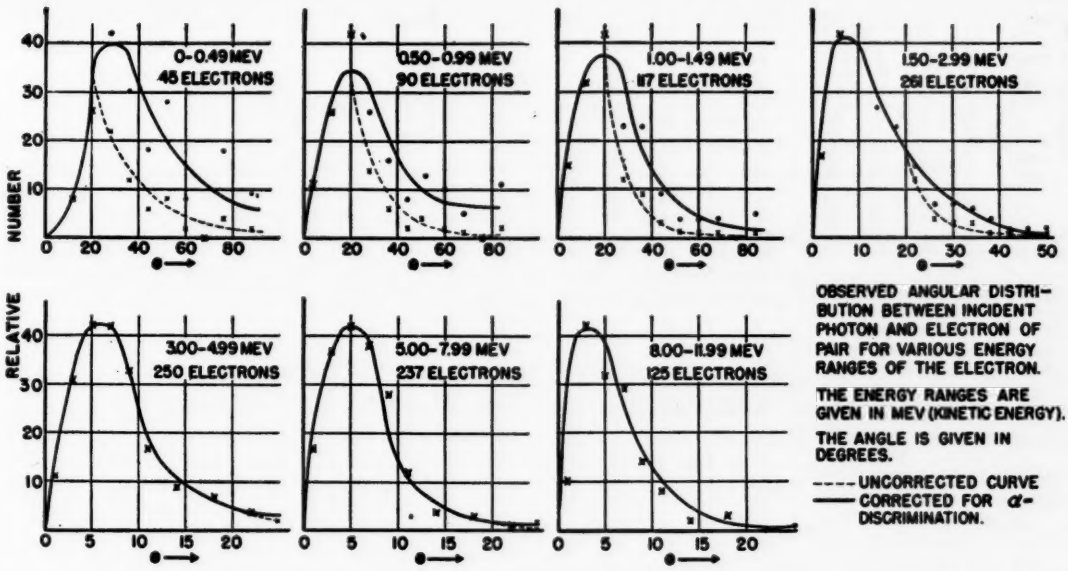

FIG. 8. Relative number of electrons in certain energy intervals plotted as a function of the angle (θ) they made with respect to the incident quantum.

a single burst and not a multiple burst as found previously[23] at one other energy.

Integral x-ray intensity measurements were made for each x-ray burst by means of a high pressure argon-filled ionization chamber and a charge integrating circuit.[24] The integrator readings were recorded on an Esterline-Angus recorder, which permitted the monitoring of the x-ray yield from the betatron during the entire period of the cloud-chamber exposures. The yield at the chamber position was approximately 1.9×10^{-6} R per pulse as measured with a thick-walled ionization chamber. The argon chamber monitor was located between the betatron and the x-ray collimator as shown in Fig. 1.

The x-rays from the platinum target pass through a $\frac{3}{8}$-in. thick wall of procelain before reaching the collimator, which consisted of a 16-in. thick lead wall (Fig. 1). The x-rays were collimated by means of the tapered hole in the lead, whose defining aperture for the betatron x-rays was $\frac{1}{8}$ in. in diameter at the entrance

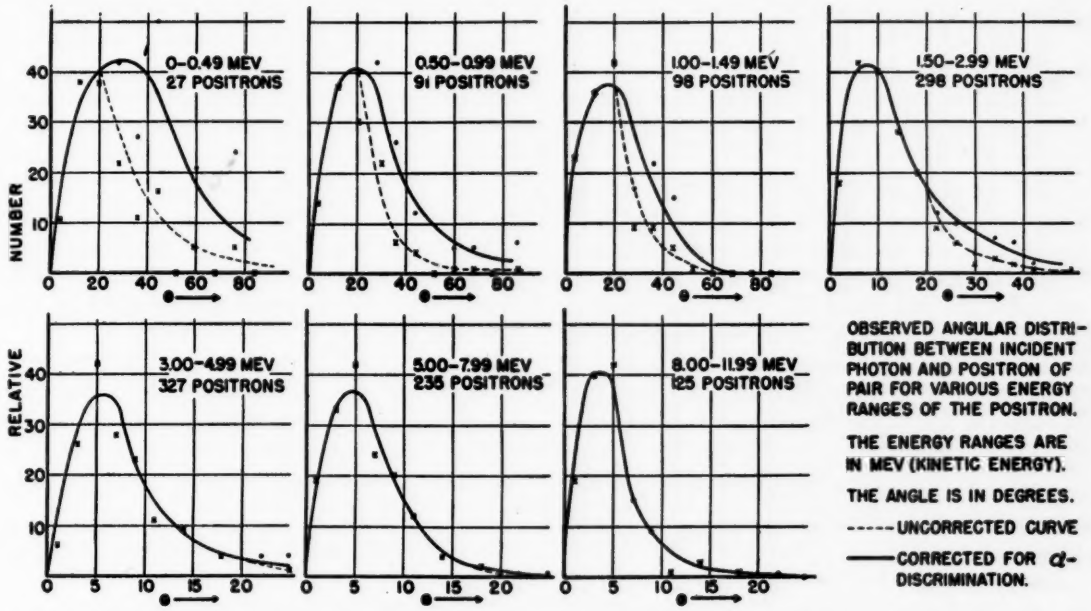

FIG. 9. Relative number of positrons in certain energy intervals plotted as a function of the angle (θ) they made with respect to the incident quantum.

[23] D. W. Kerst and H. W. Koch, Rev. Sci. Inst. 18, 681 (1947).
[24] J. S. Allen and D. E. Hudson, A.E.C.D. 2052, L.A.D.C. 232 (May, 1945).

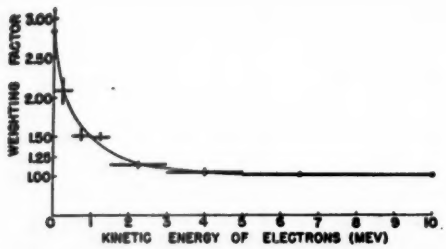

FIG. 10. Weighting factor necessary to correct for discrimination against electron tracks because of the selection criterion on the angle α.

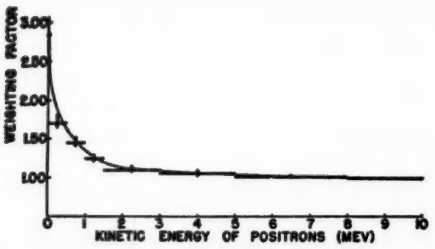

FIG. 11. Weighting factor necessary to correct for discrimination against positron tracks because of the selection criterion on the angle α.

end of the collimator. The primary beam so collimated was a cone whose whole angle was 0.24°. Since the exit aperture of the hole was $\frac{5}{16}$ in. in diameter, the secondary rays produced in the entrance end of the collimator were confined to a cone whose whole angle was 1.6°. Thus the collimator served two functions:

1. It insured that the x-rays that entered the cloud chamber were x-rays that came from the thin betatron target;
2. It reduced the number of secondary collimator rays that enter the cloud chamber. It also permitted an evaluation of the number of secondaries as indicated in the discussion section.

2. Detection, Photography, and Analysis of Pairs

Pair electrons were produced in the gas of the cloud chamber by the betatron x-rays. The gas consisted of 1.4 atmos. of air saturated with a three to one ratio of ethyl alcohol and water vapor. The temperature regulated chamber was 8 in. in diameter and 1.5 in. deep with an illuminated region $\frac{1}{2}$ in. high. The x-rays at the chamber position were confined to an approximate cylinder whose diameter was $\frac{3}{8}$ in. and which was located centrally in the illuminated region. The beam was admitted to the chamber through a 0.0015-in. Duralumin window in order to increase the ratio of pair electrons produced in the gas to background electrons from the wall.

The chamber magnetic field was pulsed on for 1.5 sec. once every 30 sec. by the field control circuit of a 25-kw motor generator set. The chamber field current was kept constant at 59.0 ($\pm$0.2) amp. at the time that the x-ray burst entered the cloud chamber. The field intensity corresponding to this current value was 1540 gausses as calibrated by means of the proton magnetic field detector similar to that described by Roberts.[25] The field was constant within the illuminated volume of the chamber to $\pm$0.3 percent.[26]

Synchronized with the x-ray burst, which bombarded the cloud chamber once every 30 sec., were the shutters of two mercury arc lamps and of a specially built 35-mm camera. The lamps were GE H-6 lamps and the camera lens was a Kodak Eklar $f/1.9$ lens, 50-mm focal length, which was operated at $f/3.5$ in order to obtain sufficient depth of field. Forty thousand stereoscopic pictures were taken during a three-week period.

After the pictures were taken and the film was developed in D-11 developer, the film was examined, either by replacing and reprojecting the film in the original camera-mirror system to produce three-dimensional pictures of the pairs photographed, or by reprojecting the film on to a horizontal plane. Both methods were used to examine 10,300 of the frames. The analysis procedure is schematically described in Fig. 2.

The tracks in the horizontal plane projection are helices which are conically projected by the optics of the original camera system. The principal quantity measured is R, the average radius of the arc whose chord length was also measured. The chord lengths are limited by multiple scattering, by the tracks going out of the lighted region, and by the tracks going out through the walls of the cloud chamber. The classification of a chord length into one of these three categories was recorded. In addition, the x and y coordinates of the origin of the pair as well as quantities describing the accuracy of the measurements were noted.

In order to describe fully the electrons and positrons in space, the related angles had to be measured. These were obtained from the three-dimensional reprojection system described in Fig. 2(b). The quantities measured are α, which determines the component of momentum being acted on by the magnetic field, and β, which together with α, describes the angle θ between the outgoing electron or positron and the incoming quantum.

Figure 3 shows the three-dimensional analysis arrangement which is similar to that used by Brueckner, Hartsough, Hayward, and Powell.[27]

In the selection of tracks to be measured and in their measurement, certain selection criteria were applied to insure that all particle energies used in the final data have a probable error less than a given tolerable maximum. The selection criteria center around the values of α and R and could conceivably produce a marked discrimination against certain energy ranges of pairs.

In the case of the radius, R, the selection criterion arises from the fact that the length of the arc determines

[25] A. Roberts, Rev. Sci. Inst. 18, 845 (1947).
[26] H. W. Koch, J. App. Phys. (to be published).
[27] Brueckner, Hartsough, Hayward, and Powell, Phys. Rev. 75, 555 (1949).

the accuracy with which an arc of a given radius of curvature can be measured. The radius of curvature of a track was measured by a comparison of the arc with standard arcs scribed on a thin sheet of Lucite. This type of comparison is based on the observer being able to detect a difference ΔS in the sagitta for the arc being measured and the standard curve. Since the sagitta is related to the radius and the chord length, K, by the equation

$$S=K^2/8R, \tag{1}$$

the differential form for a given K becomes

$$K^2=8R\Delta S/(\Delta R/R). \tag{2}$$

An experiment on known arcs was made with several observers to determine the error in R, $(\Delta R/R)$, as a function of chord length and radius. It was found that ΔS could be determined and was approximately a constant. From these results, it was possible to fix the minimum chord length required for a given radius in order to insure that the probable error in the measured radius would be five percent. The chord length criterion that was used in the selection or omission of pair components was

$$K_{\min}=0.978\times R^{\frac{1}{2}}. \tag{3}$$

The application of this criterion might be expected to result in discarding more tracks in one energy region than in another. In order to look for such discrimination, the relative number of tracks having radii of curvature within a certain interval was plotted as a function of chord length. This was done for several intervals of radii of curvature. Figure 4 contains such a plot for all electrons which were judged, by two or more observers, to be one of the components of a true pair. The same information concerning the positrons is contained in Fig. 5. For convenience, the abscissas are made $K/2R$, instead of simply K.

On both sets of curves the minimum acceptable values of $K/2R$ are indicated by the vertical line defining the right side of the shaded area. All tracks whose measurements caused them to fall in the shaded areas were discarded. In order to correct for the pairs which have been discarded due to the chord length

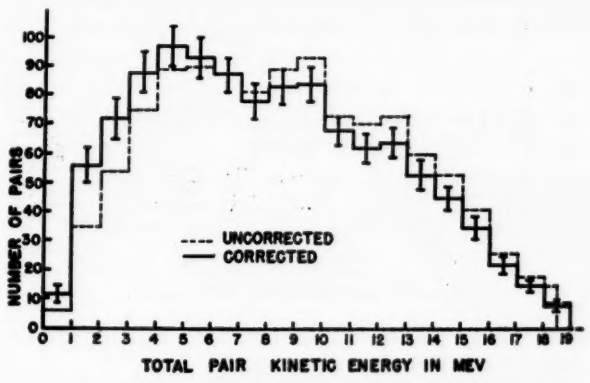

FIG. 12. Electron pair energy spectrum.

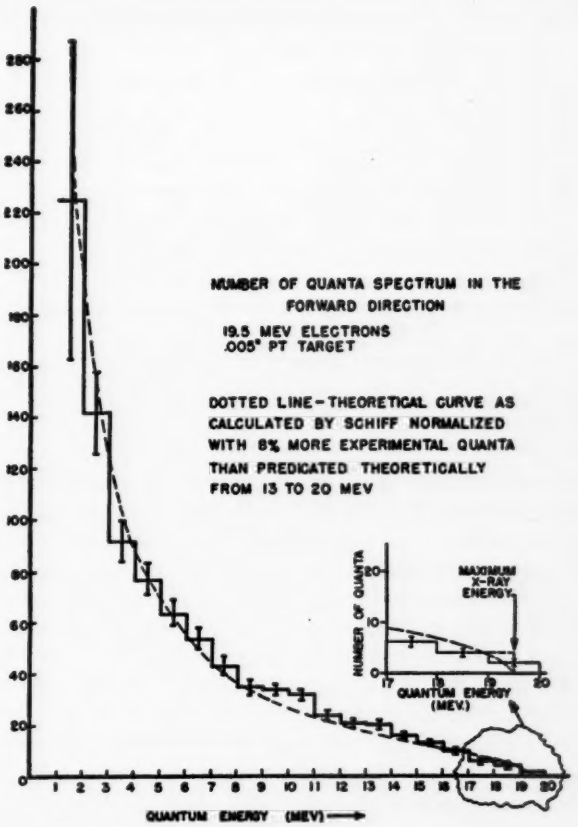
NUMBER OF QUANTA SPECTRUM IN THE FORWARD DIRECTION
19.5 MEV ELECTRONS
.005" PT TARGET
DOTTED LINE - THEORETICAL CURVE AS CALCULATED BY SCHIFF NORMALIZED WITH 8% MORE EXPERIMENTAL QUANTA THAN PREDICATED THEORETICALLY FROM 13 TO 20 MEV
NUMBER OF QUANTA
MAXIMUM X-RAY ENERGY
QUANTUM ENERGY (MEV)
QUANTUM ENERGY (MEV)

FIG. 13. Number of quanta as a function of energy, obtained by dividing the curve in Fig. 12 by the theoretical pair production cross section for air.

criterion applied to the electrons or positrons, a weighting factor has been calculated from the ratio of the total area of a given curve to the area representing those electrons that are kept for the final data. The weighting factors for electrons are therefore defined as

$$W\cdot F_E{}^K=(N_{SE}{}^K+N_{DE}{}^K)/N_{SE}{}^K, \tag{4}$$

where $N_{SE}{}^K$=number of electrons in the K sample, $N_{DE}{}^K$=number of electrons discarded from the K

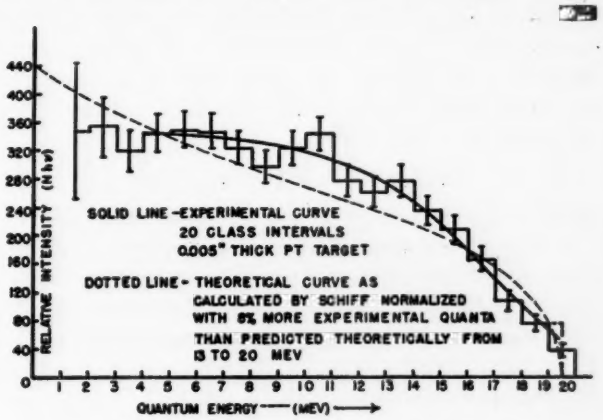
RELATIVE INTENSITY (ARB.)
SOLID LINE - EXPERIMENTAL CURVE
20 GLASS INTERVALS
0.005" THICK PT TARGET
DOTTED LINE - THEORETICAL CURVE AS CALCULATED BY SCHIFF NORMALIZED WITH 8% MORE EXPERIMENTAL QUANTA THAN PREDICTED THEORETICALLY FROM 13 TO 20 MEV
QUANTUM ENERGY (MEV)

FIG. 14. Intensity spectrum in forward direction, 19.5-Mev electrons.

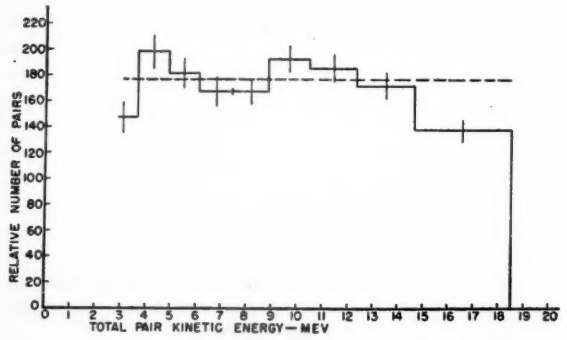

FIG. 15. Experimental electron pair spectrum with unequal energy intervals. For the width and position of the energy intervals as used, the theoretically predicted spectrum is rectangular in shape.

sample. A similar set of weighting factors was calculated for positrons. The chord length weighting factor has been plotted as a function of radius for electrons in Fig. 6 and for positrons in Fig. 7.

In the case of α, the dip angle of a track, the selection of allowable tracks depends upon the size of the angle. Since α is measured essentially by drawing a straight line from the track origin to a point further up the helical track the measured value is always greater than the true value and the error in the measurement increases with α. The selection criterion applied to the α-values was $-20°\leqq\alpha\leqq+20°$. Any particle whose absolute value of α was greater than 20° was discarded. More low energy pairs than high energy pairs were discarded due to the α-criterion on the individual electron tracks. In order to check the discrimination, the distributions of θ, the angle between the electron or positron and the incoming quantum were plotted. The dotted curves in Fig. 8 for electrons and in Fig. 9 for positrons represent the uncorrected data. The correction factor at any given value is obtained from the particular azimuthal angle, γ (see Fig. 2(b)), which is limited by the 20° α-criterion. All γ-angles are assumed equally probable. This is permissible unless the x-ray beam is polarized.

As in the case of the chord length distribution curves, weighting factors are calculated for electrons and for positrons as a function of the particle energies from the relative areas under the corrected and uncorrected curves of Figs. 8 and 9. The α-weighting factors for electrons are defined as

$$\text{W.F.}_{E^\alpha}=(N_{SE^\alpha}+N_{DE^\alpha})/N_{SE^\alpha} \qquad (5)$$

and are plotted in Fig. 10 and for positrons in Fig. 11.

If the K discrimination is first applied to all the pairs and if the number of electrons or positrons is not greatly reduced at a given energy by α-discrimination, then it can be shown that the true number of pairs of a given total energy and of a given distribution in energy between positron and electron is given by

$$N_T{}^P=N_{SP^\alpha}\{1+[\text{W.F.}_{E^K}+\text{W.F.}_{E^\alpha}+\text{W.F.}_{P_0{}^K}+\text{W.F.}_{P_0{}^\alpha}-4]\}. \qquad (6)$$

N_{SP^α} is the number of pairs in the sample which have survived both the K and α-discriminations. N_{SP^α} is always equal to 1, since the pair weighting factor, $N_T{}^P/N_{SP^\alpha}$ is applied to each individual pair.

As can be seen from a comparison of Figs. 6 and 7, and 10 and 11, the discrimination due to the α-selection criterion is more important than that due to the chord length criterion.

RESULTS

From the 10,300 pictures that have been analyzed, data were obtained on approximately 1300 pair electrons produced in the field of a nucleus and 33 pair electrons produced in the field of an electron. The principal purpose of the present experiment was to determine the x-ray spectral distribution when a thin platinum target is bombarded by monoenergetic electrons. Therefore, the details of the pair production and triplet production processes are presented here only to enlarge upon the x-ray spectrum interpretations.

The dotted histogram of Fig. 12 gives the distribution of 1122 pairs which survived the K and α-selection criteria. The solid histogram is corrected for the K and α-discriminations by applying the weighting factors of Figs. 6–11, to the individual pairs that were used to plot the uncorrected, dotted histogram. The abscissa scale is in terms of pair kinetic energy. Since the betatron for this experiment was operated so as to produce a peak x-ray energy of 19.5 Mev, the maximum obtainable pair energy was 18.5 Mev. Therefore, the number of pairs in the last 1-Mev interval of Fig. 12 should be doubled and the energy interval width should be plotted as a $\frac{1}{2}$-Mev interval. This is indicated in Fig. 12 as a dark-dotted rectangular interval and is the procedure which will be followed in the subsequent x-ray energy distributions.

Since the pair electrons were produced in a low Z material, air, the pair production cross section given by Heitler[28] was assumed correct.[29] Dividing each ordinate

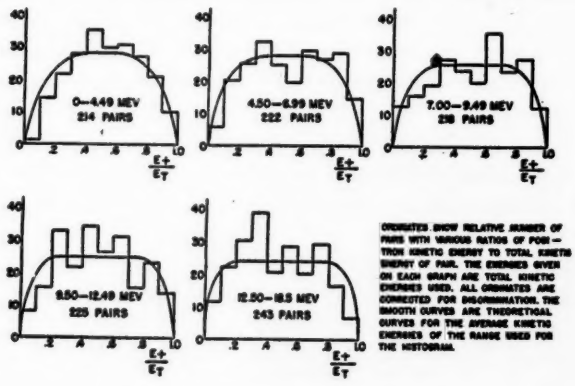

FIG. 16. Energy distribution of pairs.

[28] W. Heitler, *Quantum Theory of Radiation* (Oxford University Press, London, 1936), first edition, p. 200.

[29] See G. D. Adams, Phys. Rev. 74, 1707 (1948); C. L. Cowan, Phys. Rev. 74, 1841 (1948); and R. L. Walker, Phys. Rev. 76, 527

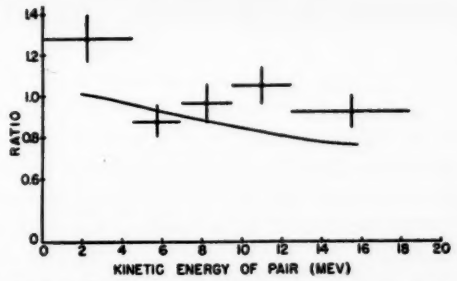

FIG. 17. Ratio of number of positrons with 0.3 to 0.7 of the total kinetic energy of the pair to remaining number of positrons.

on the corrected histogram of Fig. 12 by the corresponding pair production cross section gives the spectrum of quanta Fig. 13. A small correction has also been made for the x-ray absorption in the betatron vacuum chamber wall. The dotted line is the theoretically predicted intensity spectrum in the forward direction and for a thin platinum target as calculated by Schiff using the Bethe-Heitler theory.[30] The theoretical curve has been normalized by providing for eight percent more experimental quanta than are theoretically predicted from 13 to 20 Mev.[31]

A more conventional plot of the data is shown in the intensity plot of Fig. 14. The emphasis of the low energy end in the number of quanta spectrum is removed in the intensity spectrum. The most apparent difference in shape between the theoretical and experimental curves of Fig. 14 occurs near the middle energy ranges, where the experimental intensity is relatively higher than the theoretical curve at a quantum energy of 10 Mev. At the higher energy tip of the spectrum the statistics are too poor to state definitely that the intensity is constant for 1 Mev below the maximum energy, although the experimental points do not contradict such a statement. Because of the uncertainty, the solid curve of Fig. 14, which best represents the experiment, has not been drawn above 19.3 Mev.

The solid curve has also not been drawn for quantum energy values below 4 Mev. Below this energy the values are believed unreliable because the weighting factor principle for pairs is not valid when the probability for pairs being discarded becomes appreciable. This latter condition occurs below pair kinetic energies of 3 Mev.

Since the discrepancy between experiment and theory in the middle energy ranges of Fig. 14 depends on the normalization method used for the theoretical curve, the electron pair energy distribution has been replotted in Fig. 15, in order to permit an actual comparison of shapes independent of normalization. In this plot, the width and position of the energy intervals of Fig. 12 are selected so as to transform the theoretically predicted pair spectrum in to a rectangular distribution. The best fitting theoretical curve, which is now a horizontal straight line, has been drawn between the energies of 3 and 18.5 Mev. Obviously, the theoretical shape does not best represent the experiment especially near the high energy tip. The conclusion drawn from the curves in Fig. 14, that the theoretical prediction is low in the middle energy region, would be consistent with Fig. 15.

The great advantage to the unequal width interval plot is the ease with which tests can be made of the adequacy of the experimental statistics. If the theory best represented the experiment, then the experimental points would fall within a band of the theoretical horizontal line. The band width above and below the line would be determined by the statistical accuracy of the points. In the present experiment, no straight line fits the experimental data. Therefore, the statistical accuracy of the experiment is sufficient to prove a discrepancy with the theory in the middle energy ranges.

Other tests have given the same indications. For example, the spectral distribution of pairs determined for the front half and for the back half of the cloud chamber were very similar in shape. Also, plots have been made using 30 energy intervals in place of the 20 1-Mev intervals used in Fig. 12 and again there are more pairs in the middle energy ranges than are predicted.

The results[32] on the details of the pair and triplet production processes are given in Figs. 18 and 16–19.

The plots in Fig. 16 are frequency histograms of the ratio of the positron energy to the total pair energy for five ranges of the total pair energies. The theoretical fractional energy curves of Bethe and Heitler[7] have been drawn on each histogram.

To test the relative shapes between the experimental and theoretical curves a calculation was made of the

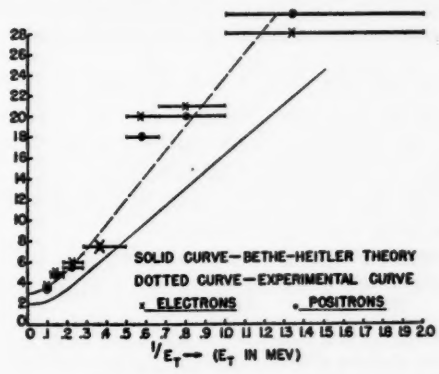

FIG. 18. Plot of θ_{max} *versus* $1/E_t$.

(1949) for the latest results and the references in the literature. The theoretical pair production cross section for air is within three percent of the experimental value at energies between 10.9 and 18.7 Mev according to the results of the first reference.

[30] L. I. Schiff (private communication). See also reference 22.

[31] The normalization procedure used in reference 18 provided for 10 percent more quanta experimentally than theoretically predicted between 12 and 20 Mev. The figures of eight percent and 13 to 20 Mev which are used in the present report are a more correct interpretation of the results given by Skaggs *et al.* in reference 8.

[32] A very complete report of similar results at an x-ray energy of 2.6 Mev is given in L. V. Groshev, J. Phys. U.S.S.R. 5, 115 (1941).

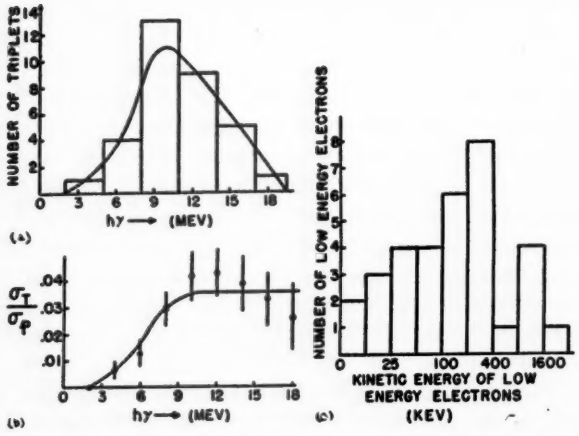

FIG. 19. Data for air concerning pair production in the field of an electron. (Data collected from 33 observed triplets.) (a) Energy distribution of the triplets. (b) Ratio of the triplet-to-pair production cross sections at a given quantum energy as obtained from Figs. 19(a) and 12. (c) Energy distribution of the low energy electrons of triplets. The minimum detectable energy was of the order of 10 kv.

ratio of the number of positrons with 0.3 to 0.7 of the total pair kinetic energy to the remaining number of positrons. The ratio has been plotted in Fig. 17. The smooth curve shows the theoretical ratios, which in general are lower than the experimental points.

According to Bethe and Heitler[7] there should be an energy difference between the average positron energy and the average electron energy. The difference will be of the order of $2\,mc^2\,Z/137$ for small quantum energies; for higher $h\nu$ the difference will be smaller. Since $2\,mc^2\,Z/137$ is approximately 60 kv for a Z of 8, no difference could be determined in the present experiment. The experiment was thus not in disagreement with the prediction, since calculated values of $\overline{E_+/E_T}$ and $\bar{E}_+/\bar{E}_T$ showed no detectable asymmetry in the positron and electron energies.

The distributions of the angle between the individual particle and the incoming quantum direction have already been presented in Figs. 8 and 9. A comparison with the theoretical expression[33]

$$\theta^2 d\theta/(\theta_0^2+\theta^2)^2 \ln[\{(\theta_0^2+\theta^2)/\theta_0^2\}+B], \qquad (7)$$

where $\theta_0=mc^2/E_T$ and B is a constant, was made in Fig. 18 by plotting the angles of the maxima[34] of Figs. 8 and 9 as a function of the particle total energy. The θ_{max} calculated from Eq. (7) is drawn as a smooth curve. The experimental values are all higher than the corresponding theoretical values.

The data on triplets are very poor statistically, since only 33 triplets were found in the pictures that contained 1300 pairs. However, the little data on triplets is consistent and indicates that very few triplets could have been mistaken for pairs and included in the pair energy distribution of Fig. 12. A smooth curve best representing the data has been drawn on the triplet energy spectrum of Fig. 19(a). A division of the number of triplets on the smooth curve at a given quantum energy by the number of pairs found at the same energy results in the ratio of the triplet production to pair production cross sections. The cross-section ratios *versus* quantum energy are plotted in Fig. 19(b). The smooth curve has been drawn leveling off at energies above 10 Mev as would be expected from any of the triplet production theories.

The value for the cross-section ratio that Phillips and Kruger[35] found at 6.5 Mev was 0.035, which is not in disagreement with the ratio of 0.022 found in the present experiment (Fig. 19(b)).

Figure 19(c) is the frequency distribution of energy for the low energy electron of the 33 triplets. The histogram is plotted on a logarithmic energy scale and has a shape very similar to that found by Phillips and Kruger for their triplets. The shape is also similar to that found for the nuclear recoils produced by the pairs in the present experiment and discussed in the following paper.

DISCUSSION

The possible criticisms of the present work center around the effect of secondaries from the collimator and around the statistical uncertainties in the interpretation of an x-ray spectrum based on 1122 pairs.

It was pointed out in the discussion of the collimator that the secondary rays from the collimator were emitted into a cone whose angle was 1.6° as compared to the primary cone of angle 0.24°. The measurement of the X, Y, and Z coordinates of the pair origins showed that only four pairs were produced in the cloud-chamber external to the primary beam. These must have been produced by scattered quanta which did not come directly from the target. It was then calculated that not more than six pairs were formed in the region of the primary beam by other scattered secondary quanta, which are emitted from the collimator into a cone whose whole angle is greater than 6°.

The statistics in the present experiment are admittedly poor and should be improved. However, the conclusion that in the energy range from 8 to 12 Mev, the experimental number of quanta is relatively greater than the Bethe-Heitler prediction seems clear. This cannot be ascribed entirely to poor statistics.

The authors are indebted to Professors C. S. Robinson, A. T. Nordsieck, and D. W. Kerst for their invaluable suggestions and help. Mr. George Modesitt capably performed much of the tedious analysis.

[33] H. Bethe and W. Heitler, Proc. Camb. Phil. Soc. **30**, 559 (1934). See also the comments of J. C. Jaeger and H. R. Hulme, Nature **142**, 573 (1938).

[34] Some of the experimental average angles are given in the following paper by G. Modesitt and H. W. Koch, Phys. Rev. **77**, 177 (1950).

[35] J. Phillips and P. G. Kruger, Phys. Rev. **76**, 1471 (1949).

Nuclear Impulse in Electron Pair Creation*

G. E. MODESITT AND H. W. KOCH**
Physics Department, University of Illinois, Urbana, Illinois
(Received September 23, 1949)

The nuclear impulses were studied for electron pairs produced in an air-filled cloud chamber by the continuous spectrum of x-rays from a 22-Mev betatron. Less than one-third of the momentum transfers to the nucleus were found to consist of values less than mc. The probability $\Phi(P_n)$ of a momentum transfer P_n was found to decrease rapidly with decreasing P_n for $P_n<mc$.

INTRODUCTION

IN pair production the momentum K of the photon is always greater than the sum of the momenta of the pair electron and positron, i.e.,

$$K>P_1+P_2. \tag{1}$$

A certain momentum $\mathbf{P}_n$ is transferred to the nucleus,[1] where

$$\mathbf{P}_n=\mathbf{K}-\mathbf{P}_p \quad \text{and} \quad \mathbf{P}_p=\mathbf{P}_1+\mathbf{P}_2. \tag{2}$$

The nuclear impulse will have its smallest value when all momenta are parallel; in this case, P_n is equal to

$$(P_n)_{\min}=\delta=K-P_P=K-P_1-P_2. \tag{3}$$

The distribution of the values of the nuclear momenta can be calculated theoretically.[2-4] These calculations indicate that most of the pair creations involve momentum transfer values between δ and mc to the nucleus and that the probability $\Phi(P_n)$ of a momentum transfer P_n is proportional to $1/P_n$ in this region. Groshev and Frank[5] and Groshev[6,7] investigated the formation of pairs in N, Kr, and Xe in a Wilson chamber by gamma-rays from ThC'' and computed the nuclear momentum for 76 of the pairs formed in N and for 29 formed in Kr. No other experimental work on nuclear impulse during pair formation has been reported in the literature.

METHOD

Photons from a betatron operating with a peak x-ray energy of 19.5 Mev were used to create electron pairs in an air-filled cloud chamber. The determination of the momentum of each pair particle from the cloud-chamber photographs is described in the preceding paper,[8] henceforth referred to as A. From the momenta of the pair components the energy of the incident photon was determined. Since the momenta of three of the four particles involved in each pair creation were known, the momentum of the fourth particle, the nucleus, could be calculated from (2).

For each pair, a rectangular set of axes (Fig. 1(a)) was employed having its origin at the origin of the pair, its y axis along the photon direction, and its z axis parallel to the magnetic field of the cloud chamber. The diagram in Fig. 1(a) shows the vectors $\mathbf{P}_1$ and $\mathbf{P}_2$ representing the momenta of the electron and the positron, respectively. The angles α and β are identical with those described in A. Also shown (Fig. 1(b)) are the nuclear momentum $\mathbf{P}_n$, the pair momentum vector $\mathbf{P}_p$, the angle θ_p between $\mathbf{K}$ and $\mathbf{P}_p$, and the angle θ_n between $\mathbf{K}$ and $\mathbf{P}_n$. The components of $\mathbf{P}_n$ in terms of α and β are:

$$\begin{aligned}(P_n)_x&=-(P_1\cos\alpha_1\sin\beta_1+P_2\cos\alpha_2\sin\beta_2),\\ (P_n)_y&=K-(P_1\cos\alpha_1\cos\beta_1+P_2\cos\alpha_2\cos\beta_2),\\ (P_n)_z&=-(P_1\sin\alpha_1+P_2\sin\alpha_2).\end{aligned} \tag{4}$$

From these components the values for P_n and θ_n were computed.

An important source of possible error in determining P_n was the uncertainty of the order of $\pm1°$ involved in the measurements of α and β. Since P_1 and P_2 increase with increasing x-ray energies, an error in angle measurement becomes more serious with increasing photon energies. A statement of the angle errors will be given in the discussion section.

Another source of possible error was introduced by

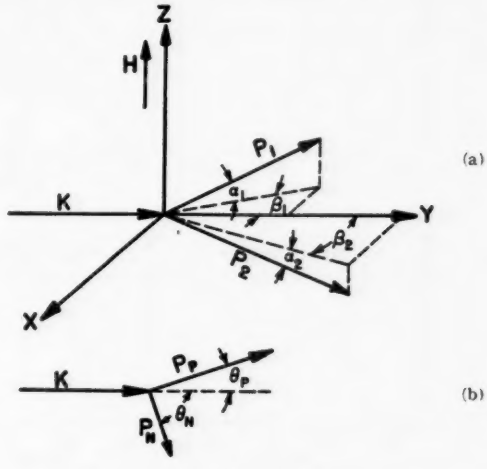

FIG. 1. Momentum vector diagrams.

* Assisted by the Joint Program of the ONR and the AEC.
** Present address: X-Ray Section, National Bureau of Standards, Washington, D. C.
[1] Pair production in the field of the electron ("triplet" production) will not be considered here.
[2] H. Bethe and W. Heitler, Proc. Roy. Soc. **146A**, 83 (1934).
[3] H. Bethe, Proc. Camb. Phil. Soc. **30**, 524 (1934).
[4] J. Wheeler and W. Lamb, Phys. Rev. **55**, 858 (1939).
[5] L. Groshev and I. Frank, Comptes Rendus U.S.S.R. **19**, 49 (1938).
[6] L. Groshev, Comptes Rendus U.S.S.R. **26**, 424 (1940).
[7] L. Groshev, J. Phys. U.S.S.R. **5**, 115 (1941).
[8] H. W. Koch and R. E. Carter, Phys. Rev. **77**, 166 (1949).

TABLE I. Number of pairs as a function of photon energy.

Photon energy range (Mev)	Mean value of $h\nu$ (Mev)	Number of pairs Observed	Number of pairs Corrected for α-discrimination
1.02–2.99	2.4	41	91
3.00–4.99	4.1	129	209
5.00–7.99	6.5	266	362
8.00–10.99	9.6	263	313
11.00–13.99	12.5	216	244
14.00–16.99	15.4	154	166
17.00–19.50	18.2	54	56
		1123	

TABLE II. Numerical data obtained from Figs. 2 and 4.

Photon energy range (Mev)	Percentage of events with: $P_n<mc$	$P>2.3mc$	Median value of P_n
1.02–2.99	16	13	1.6
3.00–4.99	25	32	1.6
5.00–7.99	29	27	1.5
8.00–10.99	27	25	1.6
11.00–13.99	31	32	1.5
14.00–16.99	23	32	1.6
17.00–19.50	27	29	1.6
1.02–19.50	27	28	1.6

the practice of discarding all pairs with either α_1 or α_2 greater than 20° (see the "α-discrimination" discussion in A). The fraction of pairs discarded increases with decreasing energy as shown in Table I, which lists the total number of pairs in each energy range corrected for the α-discrimination together with the number of pairs for which measurements were made. Thus, although the values of P_n computed by (4) were more accurate for low energies because of the smaller effect of possible angle errors, a greater portion of the total number of momentum transfers had to be computed by another method.

The values of P_n for the discarded pairs were obtained by observing the distribution of nuclear momenta for which β_1 or β_2 was greater than 20°. There is no reason to believe that the α- and β-distribution should be dissimilar. Values of nuclear momentum for pairs having more than one angle (α_1, α_2, β_1, or β_2) greater than 20° were more difficult to estimate, but they represented a small portion of the total (except for the lowest x-ray energy range) and had little effect.

The uncorrected curves (Figs. 2 and 3) represent those values of P_n computed from (4), whereas the corrected curves show, in addition, values of P_n corrected for α-discrimination as has been described. Other sources of discrimination described in A have no effect on the nuclear momentum distribution.

These arguments indicate that the values of P_n are most reliable in the middle energy ranges (at x-ray energies of the order 10 Mev).

RESULTS

Values of P_n and θ_n were computed for x-ray energies ($h\nu$) between 1.02 and 19.5 Mev. Table I lists the mean value of $h\nu$ for each interval and the number of pairs, corrected and uncorrected, in each interval. The distributions of P_n and θ_n are plotted for seven different ranges of $h\nu$ in Figs. 2 and 3. Corrected curves showing the nuclear momentum distribution for the entire $h\nu$ range from 1.02 to 19.5 Mev have been plotted in Fig. 4. Similarities in the nuclear momentum distributions (Figs. 2 and 4) may be observed with the aid of Table II. With the exception of the lowest energy range, each group fell within ±4 percent of having 25 percent of the momentum transfers below mc, and within ±3 percent of having 29 percent of the P_n values above 2.3 mc. With one other exception, each energy interval had 45±2 percent of the nuclear momentum between mc and 2.3 mc. In the range $h\nu$=11.0–13.99 Mev, this

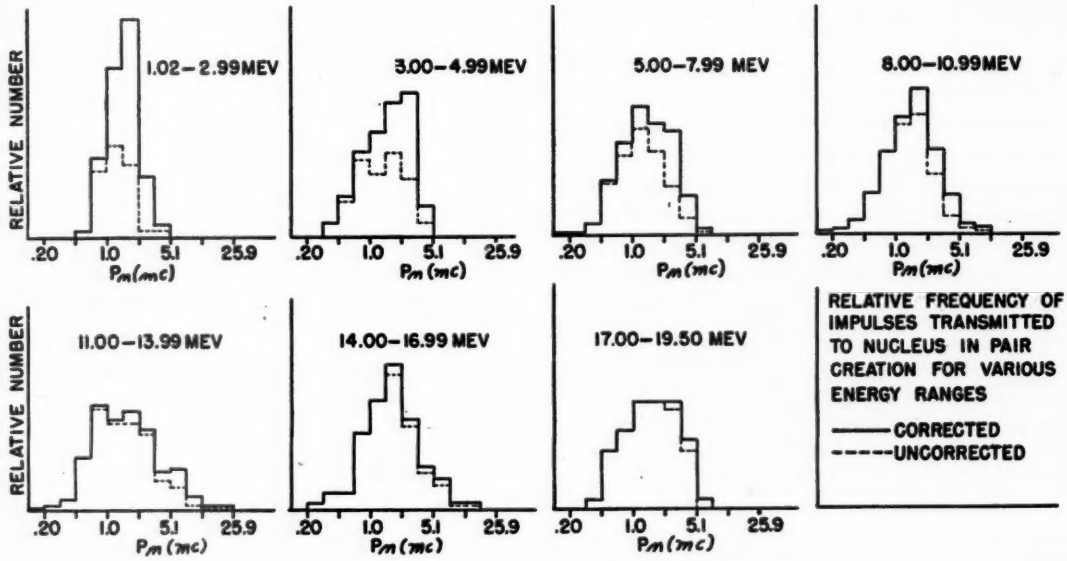

FIG. 2. Nuclear momentum distribution.

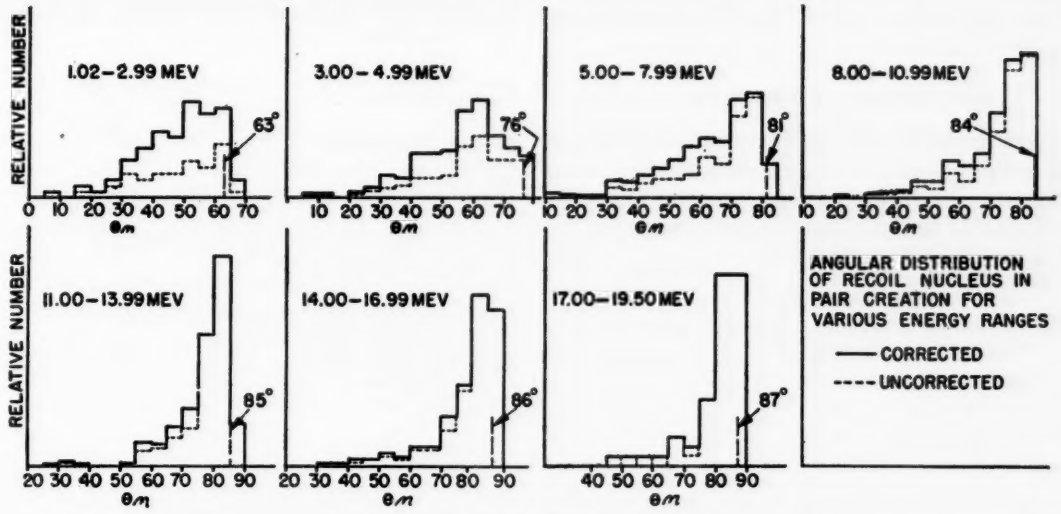

FIG. 3. Angular distribution of recoil nucleus.

figure mounted to 36 percent. The interval $h\nu = 1.02$–2.99 Mev is more peaked than the others, with 71 percent of the values of P_n falling between mc and 2.3 mc. The median value of P_n was within 0.1 mc of 1.6 mc in every group.

The average values of P_n in each of the intervals (Fig. 5(a)) seemed to vary more than would be expected from the data in Table II. The experimental curve for P_n becomes uncertain at both energy extremes because of the large effect of α-discrimination at the low energies and because of the importance of angle uncertainties at high energies. The downward trend at the high energies is probably not significant, but the values of P_n must approach 2 mc at the low energies. This can be seen from the table of minimum and maximum values of nuclear momenta given with the curve. The minimum value ($\delta_{\min}$) can be obtained from (3) with $P_1 = P_2$. The maximum value of the nuclear momentum will arise when the pair electrons have equal energies and are directed opposite to the incident photon direction. The mean value of all momentum transfers in the x-ray range from 1.02 to 19.5 Mev was 2.0 mc (1.7 mc when uncorrected for α-discrimination). The most probable value was near mc (Fig. 4(b)).

When studying the values of θ_n, the angle between $\mathbf{K}$ and $\mathbf{P}_n$ (Figs. 3 and 5(b)), one should note that there is an upper limit to these values for a given photon energy depending upon the energy distribution and direction of emission of the pair particles. The angle θ_n will be at a maximum when

$$\theta_P = \cos^{-1}(P_P/K), \tag{5}$$

where θ_P is the angle between $\mathbf{K}$ and $\mathbf{P}_P$. When $P_1 = P_2$, the angle θ_n will have its largest possible value. Calling this upper limit τ, we have

$$\tau = \tan^{-1}(P_P/2\mu), \tag{6}$$

where $\mu = mc$. The smooth curve in Fig. 5(b) shows τ as a function of $h\nu$. The vertical dotted lines indicated on each histogram of Fig. 3 show the average value of τ for the energy range being considered.

The values of θ_n (Fig. 3) show a definite trend toward becoming more peaked near the maximum possible angle (τ) with increasing energies. The effect is more pronounced than would appear from the curves as drawn because some of the angles in each energy interval are greater than the average τ for the interval. The values of θ_n plotted in Fig. 5(b) show the same tendency for θ_n to approach τ with increasing x-ray energies, as would be expected from Fig. 3. The dotted

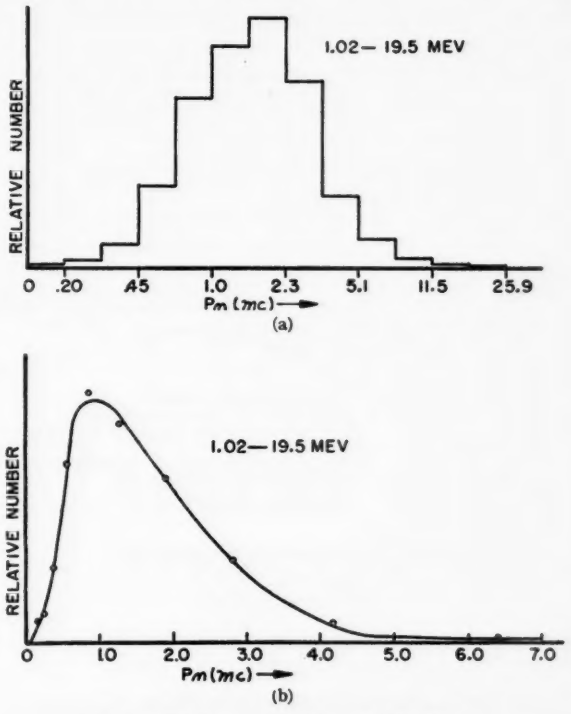

FIG. 4. Nuclear momentum distribution.

part of the experimental curve (Fig. 5(b)) shows that $\theta_n \to 0°$ as $h\nu \to 1.02$ Mev.

DISCUSSION OF RESULTS

Since screening of the atomic field due to the atomic electrons is unimportant in this experiment,[9] the probability that a momentum between P_n and P_n+dP_n will be transferred to the nucleus in pair production for $h\nu \gg mc^2$ is theoretically given as [2,3]

$$\Phi(P_n)dP_n = \text{const.}\frac{dP_n}{P_n}\left(\frac{P_n-\delta}{P_n}\right)^2 \quad (P_n \sim \delta), \tag{7}$$

$$\Phi(P_n)dP_n = \frac{c}{P_n}dP_n \quad (\delta \ll P_n \ll \mu), \tag{8}$$

$$\Phi(P_n)dP_n = a\frac{dP_n}{P_n^3}\left(\log\frac{P_n}{\mu}+b\right) \quad (P_n \gg \mu), \tag{9}$$

where a, b, and c are constants. The equations indicate that the main part of the pair creations is connected with a momentum transfer between δ and mc to the nucleus, and that the probability of a momentum transfer P_n is proportional to $1/P_n$ in this region.

The experimental results indicated a most probable value of momentum transfer near mc and a rapid decrease in probability in both directions away from mc. In no instance was a probability proportional to $1/P_n$ noted for momentum transfers below mc. This disagreement is emphasized by the use of equal logarithmic intervals for P_n (as in Figs. 2 and 4(a)). Equation (8) predicts an equal number of momentum transfers in each of the logarithmic intervals in a region between δ and mc.

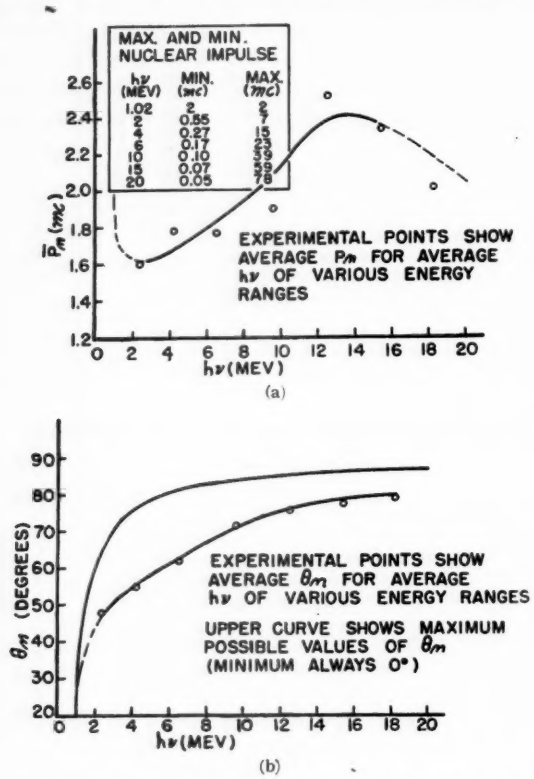
MAX. AND MIN. NUCLEAR IMPULSE
hν (MEV) MIN. (mc) MAX. (mc)
1.02 2 2
2 0.55 7
4 0.27 15
6 0.17 23
10 0.10 39
15 0.07 59
20 0.05 78
EXPERIMENTAL POINTS SHOW AVERAGE Pn FOR AVERAGE hν OF VARIOUS ENERGY RANGES
Pn (mc)
hν(MEV)
(a)
EXPERIMENTAL POINTS SHOW AVERAGE θn FOR AVERAGE hν OF VARIOUS ENERGY RANGES
UPPER CURVE SHOWS MAXIMUM POSSIBLE VALUES OF θn (MINIMUM ALWAYS 0°)
θn (DEGREES)
hν(MEV)
(b)

FIG. 5. Mean values of (a) nuclear momentum and (b) angle of recoil.

[9] Screening is unimportant when $S \gg 1$, where $S=(100mc^3h\nu/(E_+E_-Z^{\frac{1}{3}}))$.

TABLE III. Comparison of two experiments at 2.6 Mev.

	Groshev and Frank		Present experiment
Gas	N	Kr	Air
Percentage of values of $P_n<mc$	24	10	20
Mean value of P_n	1.5 mc	1.7 mc	1.6 mc
Mean value of θ_n	49°	not given	48°

TABLE IV. Mean values of θ and $(P_n)_s$.

Mean particle momentum (mc)	$\frac{\bar{\theta}_1+\bar{\theta}_2}{2}$	Mean sideways component of particle momentum (mc)
1.4	30°	0.7
2.0	27°	0.9
9	7.0°	1.1
14	5.8°	1.4
21	4.1°	1.5

The theoretical expressions (7)–(9) are not applicable to energies of the order mc^2. For example, at the threshold energy for electron pair production ($h\nu=2\,mc^2=1.02$ Mev), only one momentum transfer (2 mc) is possible, and near threshold the distribution in values of P_n is necessarily more peaked. This could explain the shape of the nuclear momentum distribution in Fig. 2 for the lowest energy interval ($h\nu=1.02$–2.99 Mev). Between $h\nu=3.00$ Mev and $h\nu=19.50$ Mev, the distributions of the experimental values of P_n have been shown to be similar for each energy interval.

The results obtained agree very well with the work done by Groshev and Frank, who investigated pairs formed by photons from the principal line of ThC″ ($h\nu=2.6$ Mev).[5–7] They computed P_n for 29 pairs in Kr and 76 pairs in N and found approximately the same distributions of nuclear impulses for the two gases. They also calculated the values of θ_n for the 76 pairs formed in N. The distributions of P_n and θ_n which they found were similar to those reported here. The percentages of values of $P_n<mc$ indicated by the experiments of Groshev and Frank are compared with the percentage found in the present experiment at 2.6 Mev (Table III). Also compared are mean values of P_n and θ_n.

Perhaps with the exception of the lower energy ranges, the present experiment seems to show larger values of momentum transfers than predicted by theory. Some increase in the nuclear impulses above the predicted values was anticipated before calculations were begun because the experimental values of θ_1 and θ_2

were larger than theoretically predicted (see A). The components of nuclear momentum both along and perpendicular to the photon direction increase with increasing θ_1 and θ_2.

A qualitative indication of the effect of larger θ_1 and θ_2 values on P_n can be obtained by considering only the sideways momentum of the pair particles, since the forward component of nuclear momentum decreases with increasing energy and is small compared with mc for $h\nu \gg mc^2$. According to Bethe, the average sideways momentum of each of the pair particles is of the order mc for $h\nu \gg mc^2$. The experimental mean values of the sideways momenta of the pair particles were obtained from the average of the mean values of θ_1 and θ_2 and are listed in Table IV.

In addition, for nuclear momentum transfers near δ it is in general necessary that the sideways momenta of the pair particles be directed nearly opposite to each other. The sideways momentum of the nuclear recoil equals

$$(P_n)_s=[P_1^2(1-\cos^2\theta_1)+P_2^2(1-\cos^2\theta_2) +2P_1P_2\sin\theta_1\sin\theta_2\cos\phi]^{\frac{1}{2}}, \quad (10)$$

where ϕ is the angle between the planes $(\mathbf{K}, \mathbf{P}_1)$ and $(\mathbf{K}, \mathbf{P}_2)$. If one assumes a favorable case for producing a small value of $(P_n)_s$ by setting the sideways momentum of the pair particles equal to each other, Eq. (10) may be reduced to

$$(P_n)_s=\sqrt{2}(P_1)_s(1+\cos\phi)^{\frac{1}{2}}, \quad (11)$$

where $(P_1)_s$ is the sideways momentum of the pair electron (equal to $(P_2)_s$).

Equation (11) shows that even in favorable cases it is necessary that the values of ϕ be near π. Groshev[7] found good agreement between the theoretical and experimental distributions of ϕ in the experiment previously discussed. His experiment showed 50 percent

TABLE V. Experimental dihedral angle data.

X-ray energy range (Mev)	1.0–5.5	5.5–9.0	9.0–18.5	1.0–18.5
Percentage of ϕ between 120° and 180°	53	58	57	57

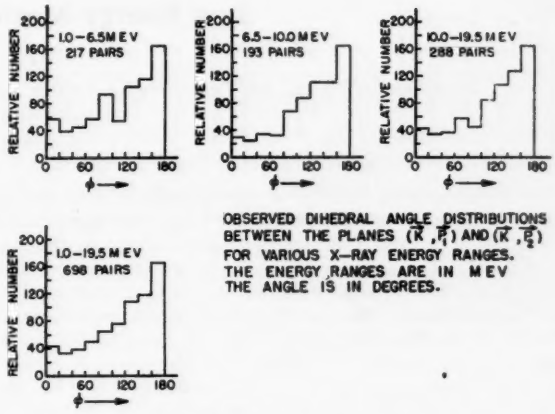
RELATIVE NUMBER
1.0–6.5 MEV
217 PAIRS
6.5–10.0 MEV
193 PAIRS
10.0–19.5 MEV
288 PAIRS
1.0–19.5 MEV
698 PAIRS
OBSERVED DIHEDRAL ANGLE DISTRIBUTIONS BETWEEN THE PLANES $(\vec{K},\vec{P}_1)$ AND $(\vec{K},\vec{P}_2)$ FOR VARIOUS X-RAY ENERGY RANGES. THE ENERGY RANGES ARE IN MEV THE ANGLE IS IN DEGREES.

FIG. 6. Angular distributions.

of the values of ϕ falling between 120° and 180° for pairs formed in N and Kr. The distributions of ϕ found in the present experiment (Fig. 6 and Table V) are very similar to the results given by Groshev. The fact that the experimental values of ϕ (Fig. 6) are not concentrated near π is consistent with the large values of nuclear momentum found in the present experiment.

For comparable energy ranges (2.6 Mev) the present experiment agreed in every field of comparison with the work done by Groshev and Frank, and it has been shown that no significant changes in the distribution of the values of nuclear momentum were found for x-ray energy ranges up to 19.5 Mev.

No quantitative estimate of errors has been given, although a brief statement of the causes of errors was presented in the method section. Specifically, the error in P_n increases approximately as the square of the ratio P_1/P_n and as the first power of $\theta_1\Delta\theta_1$. For the case of $P_1=P_2=10\ mc$, $P_n=2\ mc$, $\theta_1=\theta_2=6°$, $\Delta\theta_1=\Delta\theta_2=\pm1°$, and $\Delta P_1/P_1=0.05$, the probable error in P_n is 12 percent. In no energy range is the probable error great enough to explain the apparent disagreement with the theoretical prediction of an increasing probability $\Phi(P_n)$ with decreasing values of momentum transfers for $P_n<mc$.

The authors acknowledge the stimulating discussions with Professor A. Nordsieck.

Low Energy Mesons in the Atmosphere*

MATTHEW SANDS
Department of Physics and Laboratory for Nuclear Science and Engineering, Massachusetts Institute of Technology, Cambridge, Massachusetts

(Received October 5, 1949)

The dependence on altitude of the intensity of slow mesons, mesons with ranges less than 100 g cm^{-2}, has been measured by the method of delayed coincidences for atmospheric depths down to 250 g cm^{-2}. The intensity at this depth is thirty times that at sea level, and the variation with the depth x is approximately as $\exp(-x/\alpha)$ where α is 220 g cm^{-2}. The differential range spectrum of mesons at sea level has been measured by the same method for ranges between 10 g cm^{-2} and 200 g cm^{-2}. The spectrum is nearly flat in this interval, the value at the lower limit being 0.9 of that at the upper limit. The data which are available in the literature have been examined to obtain the differential range spectrum of mesons whose ranges are greater than 100 g cm^{-2} and less than 3×10^4 g cm^{-2}, and to obtain the variation with altitude of the intensity of fast mesons—mesons with ranges greater than 100 g cm^{-2}.

The experimental results can be explained with the assumption that the number of mesons produced in the depth interval dx at the depth x with ranges in dR at R varies as $G(R)dR\exp(-x/L)dx$. Using 125 g cm^{-2} for L we have arrived at a production spectrum $G(R)$ which is compatible with the experiment data. In the computations, the exact energy-range relation and an empirical atmospheric pressure-altitude relation were used.

The spectrum obtained can be represented approximately by $G(R)=(R+\alpha)^{-2.9}$, where $\alpha=210$ g cm^{-2}. The exact spectrum is of the same form for ranges larger than 100 g cm^2 but falls about 40 percent lower for ranges of 100 g cm^{-2} and less. The observed spectra which result from the derived production spectrum have been computed for several altitudes.

I. INTRODUCTION

LITTLE direct experimental evidence is available concerning the distribution-in-energy of ordinary mesons (mass = 200 electron masses) as they are produced in the atmosphere. It is possible, however, to infer the production spectrum from measurements of the distribution-in-energy of mesons at various locations in the atmosphere, using the known disintegration-probability and energy-loss relations. Various workers have used the measured sea level spectrum of mesons,[1–4] the altitude dependence of the hard component,[5–9] the latitude effect of the hard component,[5–7,10] or the angular dependence and the East–West effect[3,10] to arrive at a production spectrum. Still others[6,11] have obtained production spectra from a knowledge of the spectrum of the primary particles coupled with theoretical reasoning on the nature of the interaction of nucleons. In order to simplify the computations, all of these authors have taken one or more of the following assumptions: (1) That production occurs at one altitude in the atmosphere;[1,3,5,6,9,10] (2) that the energy loss of mesons is independent of their energy[1–3,5,6,8–10] or (3) that the distribution-in-energy at the place of production depends on a negative power of the energy.[1–5,8–10] These approximations are, in general, satisfactory for computations related to the intensity of high energy mesons at sea level, but cannot be expected to give quantitative results concerning measurements on high energy mesons in the upper atmosphere or on low energy mesons ($E<3\mu c^2$) at any altitude.

Although mesons produced with low energy do contribute to the intensity observed at sea level, the contribution is small, and any accurate information about the production spectrum at low energies must be inferred from the slow meson intensity at higher altitudes. In the present work we have attempted to obtain the distribution-in-energy of mesons as they are produced—particularly for low energies—using experimental information on meson intensities. To do this, it was necessary to augment the experimental data available on low energy mesons, and to perform the computations in a manner applicable to such mesons.

In an earlier paper[12] we have reported the results of some measurements of the relative intensity of slow mesons at altitudes up to 10,700 meters. The accuracy of the measurements was impaired at the highest altitudes by the large numbers of spurious events observed. In Part II of the present paper we report the results of some improved high altitude measurements and also of further measurements at sea level made to establish the absolute value of the slow meson intensity.

In reference 12 we reported the results of some preliminary computations which indicated that the slow increase of the low energy meson intensity with altitude implied less production of low energy mesons than would be inferred by an extrapolation to low energies of the production spectrum at high energies. In Part III of

* Most of the material presented here was taken from a thesis submitted in 1948 to the Physics Department, M.I.T., and has appeared also in Technical Report No. 28 (1949) of the Laboratory for Nuclear Science and Engineering. The work was assisted by the Joint Program of the ONR and the AEC.

[1] H. Euler and W. Heisenberg, Ergeb. d. exact. Naturwiss. **17**, 1 (1938).
[2] L. Janossy and J. G. Wilson, Nature **158**, 450 (1946).
[3] E. M. Bruins, Proc. Akad. Wetensch, Amsterdam **42**, 740 (1939).
[4] M. E. Rose, J. Frank. Inst. **236**, 9 (1943).
[5] W. F. G. Swann, J. Frank. Inst. **236**, 111 (1943).
[6] Hamilton, Heitler, and Peng, Phys. Rev. **64**, 78 (1943).
[7] G. Chew, Phys. Rev. **73**, 1128 (1948).
[8] I. Bloch, Phys. Rev. **69**, 575 (1946).
[9] M. Schein and J. Steinberger, Phys. Rev. **72**, 734 (1947).
[10] L. Janossy and P. Nicolson, Proc. Roy. Soc. **192A**, 98 (1947).
[11] Lewis, Oppenheimer, and Wouthuysen, Phys. Rev. **73**, 127 (1948).
[12] Rossi, Sands, and Sard, Phys. Rev. **72**, 120 (1947).

this paper we describe an attempt to synthesize a suitable production spectrum, taking into account the production at all altitudes, the more exact energy-loss relations, and the deviation of the atmosphere from an ideal exponential one. Only those mesons are considered whose trajectories are near the vertical, and lateral scattering effects are neglected.

II. EXPERIMENTS AND EXPERIMENTAL RESULTS

The Altitude Dependence of the Slow Meson Intensity

The experimental results obtained in the previous work[12] suffered the defect that at the highest altitude the counting rate due to mesons was less than that due to chance coincidences. A second set of measurements was made, therefore, with a modified experimental arrangement which is shown in Fig. 1, and which we shall call Arrangement II. The counter tube trays A, B, C, and D correspond to those of the previous set-up and were connected to an identical circuit. Thus, mesons were detected which traversed trays A and B, stopped in the 2.5-cm thick brass absorber S, and gave rise to a disintegration product which traversed both trays C and D in the time interval from 0.9 μsec. to 8.1 μsec. after the arrival of the meson.

With the new arrangement, the delayed coincidence rate due to mesons stopped in S was about the same as before, but the rate of spurious delayed coincidences was less for the following reasons: (a) The rate of twofold coincidences (A, B) was lower because a smaller area and solid angle were subtended by the two trays, and because the layer of lead between trays A and B absorbed much of the very soft electronic component present at high altitudes; (b) the fraction of twofold coincidences (A, B) *not accompanied by the discharge of a tube in tray* C was less, because of the increased extent of tray C; and (c) the rate of twofold coincidences (C, D) was no greater, despite the increased size of the trays, because these trays were shielded by lead at the sides. With Arrangement II, most of the spurious delayed coincidences were due to rays (other than mesons) which traversed trays A and B and stopped in the absorber S.

In order to determine whether the small increase with altitude observed in the first measurements was characteristic only of mesons at the end of their range, or whether it would also hold for mesons of somewhat greater energy, measurements were made with a third arrangement, "Arrangement III," which consisted of Arrangement II with the addition of a 7.5-cm thick layer of lead above in the position indicated by T in Fig. 1.

Seven high altitude flights were made in the summer of 1947 with Arrangements II and III. For these flights the apparatus was mounted in the rear, pressurized cabin of a B-29 aircraft. All flights were made at the latitude of Cambridge. During each flight data were taken at each of two or more altitudes, and at each altitude, with and without the lead in position above the apparatus. The combined data from all flights and from the ground runs are given in Table I for Arrangement II. The data obtained with Arrangement III are given in Table II. The spurious, delayed coincidence rates for all altitudes were computed from the measured twofold and threefold coincidence rates by means of the formula given in reference 12.

The corrected delayed coincidence rates given in Tables I and II depend on the directional intensity of the slow mesons over a rather large angle. Since the angular dependence of the intensity is not known we shall assume that it does not change greatly over the altitudes where the measurements were taken, and that the corrected delayed coincidence rates are, therefore, proportional to the vertical intensity of mesons which could stop in the absorber S. The ratios of the rates at the higher elevations to those at sea level are given in Table III for each arrangement. Included also in Table III are the results from reference 12 under the heading "Arrangement I."

Each of the three experimental arrangements used was sensitive to mesons of different ranges. Table IV gives for each arrangement the mean minimum and maximum ranges in air for mesons which could enter from the vertical and stop in the absorber S. All of the mesons detected are in the "soft component."

It will be seen from Table II that the relative intensities obtained with the three arrangements agree within the errors except for the value obtained with Arrangement II at the lowest atmospheric pressure. Because of

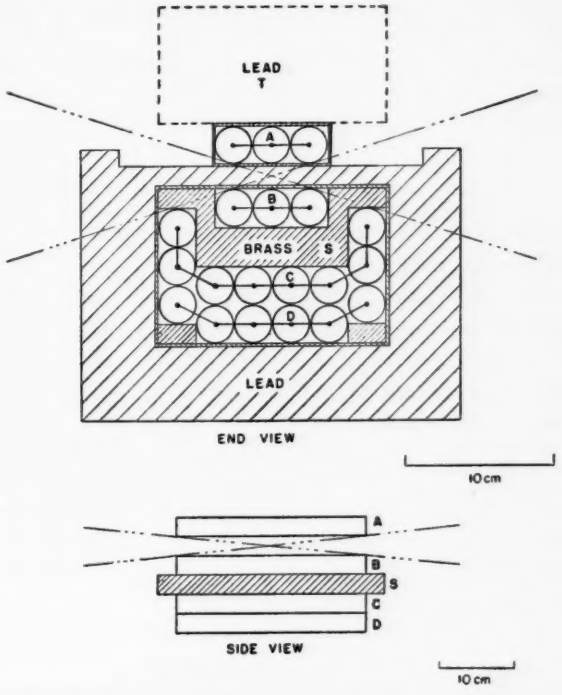

FIG. 1. Experimental Arrangement II.

TABLE I. Experimental results with Arrangement II.

Pressure (g cm^{-2})	1030	610	390	310	250
Approx. alt. (meters)	0	4260	7620	9150	10,700
Twofold coincidences (A, B) (min.$^{-1}$)	107	349	1100	1680	2540
Twofold coincidences (C, D) (min.$^{-1}$)	278	853	2730	4420	5960
Threefold coincidences (A, B, $C+D$) (min.$^{-1}$)	89	260	745	1100	1510
Fourfold coincidences (A, B, C, D) (min.$^{-1}$)	65	188	513	772	1018
Delayed coincidence rate (hr.$^{-1}$)					
0.9–2.7 μsec.	0.61	5.6	10	20	29
2.7–4.5 μsec.	0.33	1.1	6.3	5.2	19
4.5–6.3 μsec.	0.15	1.1	4.2	8.1	13
6.3–8.1 μsec.	0.092	0.4	2.1	6.7	4
Spurious delay rate, each channel (hr.$^{-1}$)	0.009	0.14	1.74	4.6	11
True delay rate, 0.9–8.1 μsec. (hr.$^{-1}$)	1.14±0.03	7.5±1.9	15.3±1.8	22±4.4	20±9
Duration of observations (hr.)	546	2.7	6.7	2.1	0.70

the small number of counts obtained in this measurement the disparity must be allowed as a statistical fluctuation. Thus, we can conclude that within the accuracy of the data the differential intensity of mesons at atmospheric depths down to 250 g cm^{-2} is independent of the range for ranges between 5 and 80 g cm^{-2}, and that the best value for the intensity relative to that at sea level of mesons in the soft component is given by the average of the several determinations at each altitude. Such an average, weighted according to the errors, is given in the last column of Table III. The data of Table III were used in constructing Fig. 7 of Rossi's survey article.[13]

The Intensity of Slow Mesons at Sea Level

The high altitude experiments described above give information about only the relative intensity of slow mesons at the various altitudes. In order to establish an absolute value for the intensity, measurements were made at sea level with experimental Arrangement IV, which is shown in Fig. 2. The counter trays A and B were connected to one of the coincidence circuits, used in the previous experiments. All of the remaining counters were connected in parallel and to *both* of the input terminals of the second coincidence circuit.† The two coincidence circuits were connected to a delay discriminator as before. The delay discriminator was of the same construction as the one used in the previous measurements, but due to a slight variation in the circuit parameters the first channel began at 1.0 μsec. Thus mesons which entered the absorber S via trays A and B were detected if their disintegration product traversed any one of the counters C during the selected time interval. The heavy broken lines in the figure show the locations of a 15-cm thick and a 30-cm thick lead moderator which could be placed in the entrant meson beam. The absorber S in this arrangement was a block of carbon whose density was 1.5 g cm^{-3}.

The condition that the disintegration product produce a coincidence was relaxed, as the equipment was operated only at sea level where the spurious, delayed coincidence rate due to pairs of unrelated rays

TABLE II. Experimental results with Arrangement III.

Pressure (g cm^{-2})	1030	610	390	310	250
Approx. alt. (meters)	0	4260	7620	9150	10,700
Twofold coincidences (A, B) (min.$^{-1}$)	94	251	643	943	1380
Twofold coincidences (C, D) (min.$^{-1}$)	247	662	1800	2700	4000
Threefold coincidences (A, B, $C+D$) (min.$^{-1}$)	85	210	503	709	1000
Fourfold coincidences (A, B, C, D) (min.$^{-1}$)	60	151	359	508	710
Delayed coincidence rate (hr.$^{-1}$)					
0.9–2.7 μsec.	0.58	5.0	7.8	16	23
2.7–4.5 μsec.	0.26	0.4	4.0	5.2	14
4.5–6.3 μsec.	0.15	0	1.8	4.0	7.5
6.3–8.1 μsec.	0.12	0	1.1	2.8	2.5
Spurious delay rate each channel (hr.$^{-1}$)	0.004	0.05	0.45	1.14	2.7
True delay rate, 0.9–8.1 μsec. (hr.$^{-1}$)	1.1±0.07	5.2±1.6	13.0±1.6	23.1±3.3	35±7
Duration of observations (hr.)	216	2.4	5.5	2.5	0.80

[13] B. Rossi, Rev. Mod. Phys. 20, 537 (1948).

† Actually a preamplifier was interposed between the tubes and the coincidence circuit to compensate for the reduction in signal amplitude which results from connecting many tubes in parallel.

TABLE III. Slow meson intensity relative to that at sea level.

Atmospheric pressure (g cm^{-2})	Relative intensity Arr. I	Arr. II	Arr. III	Average
250	37±6	18±7	32±7	30.5±3.9
310	——	19±4	21±3	20.5±2.6
390	16.1±2.0	13.4±1.9	11.8±1.6	13.5±1.1
610	5.3±0.6	6.6±1.8	4.7±1.5	5.3±0.6
1030	1.00	1.00	1.00	1.00

was negligible. Since all penetrating rays which traversed both trays A and B had to traverse also two counters of tray C, the rate of spurious delayed coincidences due to delays in the discharge of the G-M tubes can be shown to be negligible by the same considerations as before.[12] The experimental results show that the spurious delays are indeed negligible.

Arrangement IV was set up in Cambridge under a wooden roof whose average thickness was about 2 cm, and operated from October 6, 1947 to January 16, 1948. Data were taken with no lead, and with lead moderators 15 cm and 30 cm thick. With each lead thickness data were taken also with the carbon absorber S removed. The following data were taken for each measuring period: (a) The number of twofold coincidences (A, B); (b) the number of threefold coincidences (A, B, C); (c) the number of delayed coincidences (A, B, C_{del}) in each channel; and (d) the counting rate of tray C, which rate was recorded continuously by means of a counting-rate meter. The difference between (a) and (b) gives the number of anticoincidences $(A, B, -C)$, that is, the number of particles which traverse A and B but either stop in S or otherwise fail to trigger a tube in tray C. It will be noted that, while the anticoincidence rate is obtained as a difference, its accuracy does not suffer, because the difference is of two quantities obtained concurrently.

The spurious delayed-coincidence rate due to random pairs of events can be shown to be given for this arrangement by

$$\{A, B, -C\}\cdot\{C\}\cdot\tau, \qquad (1)$$

where $\{A, B, -C\}$ is the counting rate for anticoincidences, $\{C\}$ is the counting rate of tray C, and τ is the width of the interval in which delays are detected.

The data obtained with Arrangement IV are given in Table V. Those obtained with the absorber S removed are given in Table VI.

With no lead moderator the mesons which can be detected must penetrate three G-M tube walls and must stop in the carbon absorber or the walls of G-M tubes immediately adjoining it. With the lead in place the entering mesons must penetrate the additional lead thickness but must stop in the same thickness as before. The mean thickness in the vertical direction of material in which mesons can stop and be detected is equivalent (for mesons) to 16.5 g cm^{-2} of air. The mean range of mesons detected with no moderator is 10 g cm^{-2} of air; with 15 cm of lead it is 100 g cm^{-2}; and with 30 cm of lead it is 200 g cm^{-2}.

TABLE IV. Ranges of mesons which stopped in the absorbers. The ranges are given in g cm^{-2} of air.

Arrangement	Min. range	Max. range
I	5	21
II	13	33
III	63	83

The data indicate that the number of spurious delayed coincidences is negligible. From line 11 in Table VI we see that with the absorber S removed, a total of 14 delayed coincidences were obtained in 299 hr., giving the rate of 0.05 per hr. With the absorber S in place the average delayed coincidence rate is 0.5 per hr. Now, even with absorber S removed, there still remain the walls of the G-M tubes in which mesons can be stopped and give delayed coincidences. The ratio of the thicknesses of stopping material in the two cases is about 0.15. If we assume that the efficiency for detecting disintegration products from the tube walls and from the absorber S is the same, but take into account the fact that, while all mesons which stop in carbon disintegrate, in brass only one-half disintegrate,[14] we conclude that the number of delayed coincidences, to be expected from mesons with S removed, is $(0.5)(0.15)(0.5)=0.03$ per hr. We can therefore conclude that at most 0.02 delayed coincidences per hr. can be due to spontaneous delays in G-M tubes. This is less than the accuracy of the measurements with absorber S in position, and, since presumably it does not depend on the lead thickness, it does not affect appreciably the ratios of counting rates withd ifferent moderators. The above calculation is quite rough, so that the results have not been used to correct the data.

The corrected delayed coincidence rates given in line 13 of Table V are proportional to the differential

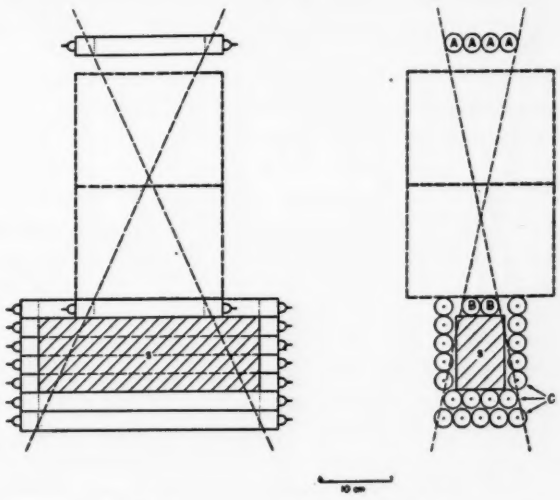

FIG. 2. Experimental Arrangement IV.

[14] G. E. Valley, Phys. Rev. **72**, 772 (1947); **73**, 177 (1948).

intensity of mesons with ranges of 10 g cm^{-2}, 100 g cm^{-2}, and 200 g cm^{-2}. We can obtain from the data the absolute values of the intensities in three more or less independent ways.

(a) We assume that all rays which cause twofold coincidences (A, B) through 15 cm of lead are mesons. Then the difference between the twofold coincidence rates with 15 cm of lead and with 30 cm of lead is a measure of the average, differential intensity of mesons with ranges between 100 and 200 g cm^{-2}. Thus, if we let N_1 and N_2 be the coincidence rates with 15 cm and 30 cm of lead, respectively, R_1 and R_2 the corresponding minimum ranges for mesons detected, and I_0 the vertical intensity of mesons with ranges greater than R_1, the average differential intensity is

$$\bar{\imath}=(I_0/N_1)\cdot(N_1-N_2)/(R_2-R_1). \qquad (2)$$

Unfortunately, fluctuations in meson intensity are a source of error, since the data for different thicknesses of lead were taken at different times. The sets of data were, however, taken over sufficiently long periods that the short period fluctuations should average out. Perhaps the largest remaining effect is due to those fluctuations which are correlated with changes in barometric pressure, and we can make a correction for this. With each day's data the mean barometric pressure for the day was obtained from the U. S. Weather Bureau. From these data the average barometric pressures given in line 14 of Table V were obtained. From the same data and from the daily average counting rates it was found that the average fluctuation with both moderator thicknesses was -13 coincidences per minute for each inch of mercury increase of pressure.‡ If we use this figure to normalize the twofold coincidence data to 30.00 in. of mercury, we find that $(N_1-N_2)=13.3\pm1.0$ (hr.$^{-1}$). We have further that $N_1=198$ (hr.$^{-1}$), and that $(R_2-R_1)=100$ (g cm^{-2}). So we have

$$\bar{\imath}=I_0\frac{13.3}{198(100)}=6.71\times10^{-4}I_0 \text{ g}^{-1}\text{ cm}^2 \text{ of air},$$

with a statistical error of eight percent. If we use the data of Greisen[15] (extrapolated to sea level) we obtain for I_0 the value 0.49 min.$^{-1}$ cm^{-2} sterad.$^{-1}$ Then

$$\bar{\imath}=(3.3\pm0.3)\times10^{-4} \text{ min.}^{-1}\text{ sterad.}^{-1}\text{ g}^{-1}\text{ (of air)}.$$

From the corrected, delayed coincidence rates and the average intensity just computed, we obtain the differential intensities given in the second column of Table VII.

(b) Delayed coincidences are produced by mesons which stop in S, which disintegrate more than 1.0 μsec. but less than 8.2 μsec. after stopping, and whose disintegration product discharges a G-M tube of tray C. If we let f represent the fraction of mesons which disintegrate in the time interval (1.0–8.2) μsec., and g represent the fraction whose disintegration products discharge tray C, then the delayed coincidence rate n is related to the rate n_0 at which mesons stop in S by the equation $n_0=n/fg$. Evidently

$$f=\exp(-1.0/2.2)-\exp(-8.2/2.2)=0.61.$$

An evaluation of g can be made from the known geometry of the counting arrangement and the range in carbon of the disintegration product. We have computed g under the assumption that the range of the disintegration product is 13 cm (20 g cm^{-2}) of carbon, which range is approximately that of an electron whose energy

TABLE V. Data obtained with Arrangement IV, absorber S in place.

(1) Moderator thickness (cm)	0	15	30
(2) Duration of measurement (hr.)	606	284	529
(3) Twofold coincidences (A, B)	176,898	55,861	97,936
(4) Coincidence rate (hr.$^{-1}$)	291.9	196.9	185.1
(5) Counting rate in tray C, (min.$^{-1}$)	2300	2100	1950
(6) Threefold coincidences (A, B, C)	150,054	55,164	96,652
(7) Coincidence rate (hr.$^{-1}$)	247.5	194.4	182.7
(8) Anticoincidences (A, B, $-C$)	26,844	697	1284
(9) Anticoincidence rate (hr.$^{-1}$)	44.3	2.46±0.09	2.43±0.07
(10) Delayed coincidences			
1.0–2.8 μsec.	175	84	168
2.8–4.6 μsec.	77	39	78
4.6–6.4 μsec.	24	13	30
6.4–8.2 μsec.	16	7	12
(11) Total	292	143	288
(12) Spurious delayed coincidences, 1.0–8.2 μsec.	7	0.2	0.3
(13) Corrected delayed coincidence rate (hr.$^{-1}$), 1.0–8.2 μsec.	0.47±0.03	6.50±0.04	0.54±0.03
(14) Average barometric pressure (in. of mercury)	30.07	30.11	29.99

TABLE VI. Data obtained with Arrangement IV, absorber S removed.

(1) Moderator thickness (cm)	0	15	30
(2) Duration of measurement (hr.)	69.6	133.4	95.7
(3) Twofold coincidences (A, B)	19,902	26,700	18,065
(4) Coincidence rate (hr.$^{-1}$)	286	200	189
(5) Counting rate in tray C (min.$^{-1}$)	2300	2100	1950
(6) Threefold coincidences (A, B, C)	18,692	26,512	17,944
(7) Coincidence rate (hr.$^{-1}$)	269	197	188
(8) Anticoincidences (A, B, $-C$)	1210	188	121
(9) Anticoincidence rate (hr.$^{-1}$)	17.4±0.5	1.41±0.10	1.26±0.11
(10) Delayed coincidences			
1.0–2.8 μsec.	0	7	1
2.8–4.6 μsec.	1	2	1
4.6–6.4 μsec.	0	1	1
6.4–8.2 μsec.	0	0	0
(11) Total	1	10	3
(12) Spurious delayed coincidences, 1.0–8.2 μsec.	0.3	0.1	0.1
(13) Delayed coincidence rate (hr.$^{-1}$), 1.0–8.2 μsec.	0.01	0.07	0.03

‡ This value agrees with the results of other workers. See, for instance, Rossi, Hilberry, and Hoag, Phys. Rev. **57**, 461 (1940).

[15] K. I. Greisen, Phys. Rev. **61**, 212 (1942).

is 5×10^7 ev. We obtained for g the value 0.7.¶ Using these values for f and g we find that $n_0=2.3\ n$.

The differential intensity of the mesons which stop in S is then given by

$$i=(n_0I_0)/(N_1t), \tag{3}$$

where N_1 and I_0 are the same quantities used above and t is the thickness (in the vertical direction) of the absorber S. Using the values for N_1 and I_0 above and for t the value 16 g cm^{-2}, we find that

$$i=0.0215\ n\ (\text{g}^{-1}\ \text{sterad.}^{-1}).$$

The intensities obtained from this relation and the data in line 13 of Table V are shown in the third column of Table VII.

(c) We can get values for the differential intensity of mesons with ranges of 100 g cm^{-2} and 200 g cm^{-2} in still another way by using the prompt coincidence data. Twofold coincidences (A, B) not accompanied by threefold coincidences (A, B, C) can arise from the following events: (i) Mesons which traverse trays A and B, and stop in S, but either disintegrate after 1.0 μsec., or give rise to disintegration products which do not traverse tray C; (ii) mesons which traverse A and B and do not stop in S but fail for some reason to discharge C within 1.0 μsec.; (iii) mesons which stop just above tray B and give rise to a disintegration product which traverses B within 1.0 μsec. but are absorbed in S or, otherwise fail to discharge C.

The counting rate of anticoincidences $(A, B, -C)$ due to effect (ii) and to those products considered in (iii) which are not absorbed in S is just the rate given in line 9 of Table VII. An estimate of the rate due to the disintegration products considered in (iii) which do stop in S can be made as follows: Let the range of the disintegration product be 12 g cm^{-2} of lead. The number of mesons which stop in this thickness is equal to the number which would stop in 6 g cm^{-2} of carbon, or 6/15 of the number which stop in S. Of these mesons only 0.5 disintegrate in lead, and of these only $1-\exp(-1/2.2)=0.3$ disintegrate before 1.0 μsec. Of all the disintegration products about 0.3 will traverse tray B and of these about 0.5 will stop in S. From the results of (b) we know that under the 15-cm moderator about $2.2\times0.50=1.1$ mesons stop in S each hour. Thus the anticoincidence rate due to mesons which stop in the lead and whose disintegration products are absorbed by S is approximately $(1.1)(6/15)(0.5)(0.3)(0.3)=0.02$ (hr.$^{-1}$). Since the quantity is small compared to the observed anticoincidence rate with S removed, the crudeness of the estimate will have a negligible effect on the accuracy of the final result. The total anticoincidence rate due to events of the types (i) and (ii) is

¶ The range used was based on the early work of M. Conversi and O. Piccioni, Phys. Rev. **70**, 874 (1946). More recent results of Leighton, Anderson, and Seriff, Phys. Rev. **75**, 1432 (1949), show that a somewhat smaller average range should be used. An estimate using a single range one-half that used above gives for g a value only 15 percent less.

TABLE VII. Differential intensities obtained in three ways.

Mean range (g cm^{-2} of air)	Differential intensity $\times10^{-4}$ min.$^{-1}$ sterad.$^{-1}$ g^{-1} (of air) Method (a)	Method (b)	Method (c)
10	3.0±0.3	1.7±0.1	——
100	3.2±0.3	1.8±0.1	1.8±0.2
200	3.4±0.3	1.9±0.1	1.9±0.2

then (with the 15-cm moderator)

$$(1.41\pm0.10)-0.02=1.39\pm0.10\ (\text{hr.}^{-1}).$$

The observed anticoincidence rate with S in place is 2.46±0.09 hr.$^{-1}$. That due to mesons stopped by S is evidently

$$(2.46\pm0.09)-(1.39\pm0.10)=1.07\pm0.13\ (\text{hr.}^{-1}).$$

This quantity can now be substituted for n_0 in Eq. (3) to obtain the differential intensity. The differential intensities obtained in this way for both moderator thicknesses are given in the last column of Table VII.

The excellent agreement between the results obtained by Methods (b) and (c) is undoubtedly fortuitous. The principle source of error in the determination made by Method (b) is the estimate of the geometric efficiency into which the uncertain range of the disintegration product enters. Also the errors in the values determined by Method (c) are conceivably somewhat larger than the statistical ones since the results depend on the difference between two anticoincidence rates taken at different times. These rates are very sensitive to small changes in the properties of the apparatus, especially to the detection efficiency of tray C. Some confidence in the results, however, may be derived from the fact that Koenig[16] in a similar measurement obtained the value $(2.2\pm0.1)\times10^{-4}$ for the differential intensity of mesons with ranges near 100 g cm^{-2} of air, and that our results agree for both moderator thicknesses. Within the uncertain errors we can conclude from the results of (b) and (c) that all rays which stop under 15 cm and 30 cm of lead are mesons which disintegrate in carbon.

A disturbing feature of the results is the disagreement between the result obtained by the absorption method in (a) and the results obtained by other methods. This discrepancy seems to be larger than can be accounted for by any of the errors in the measurements. It is possible, though it would seem unlikely, that lateral scattering effects are responsible. Mesons of such energy that they should stop in the carbon may be scattered into tray C and produce prompt, threefold coincidences and thus escape detection. The effect is in the proper direction, but it would not account for Koenig's result since the geometry he used was not affected by this kind of scattering. It would seem that the explanation lies elsewhere, and further experiments are necessary to clear up the matter.** At the present time it is probably

[16] H. P. Koenig, Phys. Rev. **69**, 590 (1946).

** For more information on this point see W. Kraushaar, Phys. Rev. **76**, 1045 (1949).

best to assume that the coincidence experiments give the proper absolute value for the differential intensity at ranges greater than 100 g cm^{-2}, and that the delayed coincidence data determine only the relative values for lower ranges. The data of Table VII have been included in Fig. 6 of reference 13.

III. THE PRODUCTION SPECTRUM

The General Problem

We consider the problem of a beam of mesons traveling vertically downward through the atmosphere. We consider the manner in which this beam is enriched by production, is degraded by energy losses, and is depleted by disintegration. For convenience we shall consider a beam of unit cross section (1 cm^2) and by the "number of mesons" in the beam at a level, we shall mean the number which cross that level in a unit of time (1 min.). Depths below the top of the atmosphere and ranges of mesons are measured in terms of the mass per unit area of an equivalent thickness of air. Our unit of thickness will be 100 g cm^{-2}.

The energy of a meson at the atmospheric depth x can be specified by its range $R(x)$ at that depth. Since $dR/dx=-1$, we may write $R(x)=x_0-x$ where x_0 is then a constant which specifies the energy of a given meson at all depths. The depth x_0 will be called the *end point* of a meson. Let $H(R, x)dRdx$ be the number of mesons added to the beam between the depths x and $x+dx$ with ranges (at x) between R and $R+dR$. Then the number of mesons added in dx with end points between x_0 and x_0+dx_0 is $H(x_0-x, x)dx_0dx$. Also let $w(x, s, x_0)$ be the probability that a meson which has the end point x_0 and which is known to be at x will arrive at the depth s before disintegrating. Then, if $F(s, x_0)dx_0$ represents the number of mesons at the depth s which have end points between x_0 and x_0+dx_0, we have

$$F(s, x_0)=\int_{x=0}^{s} H(x_0-x, x)w(x, s, x_0)dx. \quad (s<x_0) \quad (4)$$

The probability $w(x, s, x_0)$ depends only on the energy loss and mean life of mesons and on the properties of the atmosphere. Its computation is carried out below. Equation (4) then relates F, the observable end-point spectrum, to H, the production function of mesons. In what follows an attempt is made to derive H from the experimental data.

The Survival Probability

If we let $p(x, x_0)$ represent the momentum (in units of μc) at x of a meson whose end point is x_0, and $\rho(x)$ the density of air at x; then the probability that the meson survives from the depth r to the depth s is given by the equation

$$-\ln w(r, s, x_0)=\frac{1}{\tau c}\int_r^s \frac{dx}{p(x, x_0)\rho(x)}, \quad (r<s<x_0), \quad (5)$$

where τ is the mean life of a meson at rest and c is the velocity of light. Consider now the function $w(x, x_0)\equiv w(x, x_0, x_0)$, which is the probability that a meson survives from x to its end point. It follows from Eq. (5) that

$$\ln w(r, s, x_0)=\ln w(r, x_0)-\ln w(s, x_0), \quad (6)$$

and that

$$-\ln w(x, x_0)=\frac{1}{\tau c}\int_x^{x_0} \frac{dx'}{p(x', x_0)\rho(x')}, \quad (7)$$

Thus the problem of evaluating the probability function of three variables is reduced to that of taking differences of values of a function of two variables.

The function $p(x, x_0)$ represents the momentum-range relation of mesons in air. The dependence of the range on the density of the air can be neglected,[17] we can, therefore, write $p(x, x_0)=p(x_0-x)$. Also, it is convenient to write

$$\rho(x)=x/[\tau c\zeta(x)],$$

where $\zeta(x)$ is then a slowly varying function of x. Equation (7) takes the form

$$-\ln w(x, x_0)=\int_0^{x_0} \frac{\zeta(x')dx'}{x'p(x_0-x')}. \quad (8)$$

The integral of Eq. (9) has been evaluated for values of x between 0.1 and 10 ($\times$100 g cm^{-2}) and for values of x_0 between 2 and 35 ($\times$100 g cm^{-2}). For vaiues of $x_0>10$, that is, for end points below sea level, we have set $w(10, x_0)\equiv 1$. This is in no way a compromise with accuracy, as it can be shown that, for mesons in solid materials, the probability that a mesons will disintegrate before being brought to rest is negligible compared with any other effects considered here. In order to achieve as great an accuracy as possible, the rest of the integration was carried out numerically using the best available information for p and for ζ.

The function $p(R)$ was obtained from the energy-range relation tabulated by Smith[18] using 10^8 ev/c^2 for the mass of the meson. The function $\zeta(x)$ was computed from the altitude-pressure tables of the National Advisory Committee for Aeronautics for the "United States standard atmosphere"[19] using also $\tau c=6.6\times10^4$ cm. The standard atmosphere tables represent closely the yearly average atmospheric conditions in the Northern United States. A graph of the function $p(R)$ which we have used appears in Fig. 22 of reference 13. In Fig. 21 of the same paper there is given a graph of the function $x/\rho(x)=\tau c\zeta(x)$.

For a large momenta, that is, for $(x_0-x)>1$, we can evaluate the integral of Eq. (9) in relatively large steps (whose size depends on x_0).

[17] O. Halpern and H. Hall, Phys. Rev. 73, 477 (1948).
[18] J. H. Smith, Phys. Rev. 71, 32 (1947).
[19] W. G. Brombacher, N.A.C.A. Report No. 538 (1942).

Consider the partial integral

$$\int^{s} \zeta(x)dx/xp(x_0-x); \quad (r<s<x_0-1). \tag{9}$$

We choose the interval $(s-r)$ as large as possible under the conditions that within the desired accuracy

$$\zeta(x)=\zeta(r)=\zeta(s)$$

and

$$p(x_0-x)=p(x_0-s)+(s-x)\alpha, \tag{10}$$

where α is a constant. The integral (9) can then be evaluated analytically,[1] and becomes

$$\frac{\zeta(s)}{p(x_0-r)+r\alpha}\ln\left[\frac{s}{r}\cdot\frac{p(x_0-r)}{p(x_0-s)}\right], \tag{11}$$

where α depends on the particular x_0, r, and s according to (10). A somewhat larger interval can be used if we take for ζ a mean value between $\zeta(s)$ and $\zeta(r)$.

For small momenta, that is, for $(x_0-x)<1$, it is convenient to rewrite Eq. (9) as

$$-\ln w(x, x_0)=\int_0^{x_0-x}\zeta(x_0-R)dR/(x_0-R)p(R). \tag{12}$$

For $R<0.01$ we can, to a good approximation, set $p(R)=p(0.01)(R/0.01)^{\frac{1}{2}}$ and $x_0-R=x_0$ and evaluate the integral analytically. For $0.01<R<1$ the integrals (12) have been evaluated by straightforward numerical methods.

The probability integrals for $x<x_0-1$ have been obtained from sums of integrals like (12) and terms computed by means of (11). A table of all the values of $w(x, x_0)$ that have been computed is available.[20] A graph of some of the results is given in Fig. 3. In the graph we have plotted $-\ln w(x,x_0)$ against x_0 for various values of x. The probability that a meson whose end point is x_0 will survive between the depths x_1 and x_2 is thus given (see Eq. (6)) by the vertical distance between the curves for x_1 and x_2 at the abscissa x_0.

The Available Data

As the probability function w is completely determined, it is possible in principle to determine the production function H if given sufficient information about the mesons observed in the atmosphere, i.e., about $F(x, x_0)$. The complete range spectrum of mesons at sea level has been measured. (See Part II and reference 13.) We take the solid curve of Fig. 6 in reference 13 to represent $F(s, x_0)$ for $s=10$ ($\times 100$ g cm^{-2}) and for $x_0=R+10$. From the data of Ehmert[21] and of Wilson[22] one sees that this curve can be extrapolated by a straight line to $R=300$ ($\times 100$ g cm^{-2}). We have also information about the altitude dependence of slow mesons (Part II) which give us $F(x_0-0.1, x_0)$ for values of x_0 from 3 to 10 ($\times 100$ g cm^{-2}). In addition, we have information concerning the total hard component at all altitudes.[23] This gives unfortunately little information about the intensity of hard mesons until we make some assumptions about the contributions due to effects other than mesons.

It is assumed here, therefore, that mesons of all energies are produced mainly in the upper atmosphere by the primary radiation and/or by its products. Measurements on the production of penetrating showers and on ionization bursts probably detect the events in which mesons are produced. From an analysis of the data of Janossy[24] and of Tinlot[25] on penetrating showers and of Bridge[26] and Hulsizer[27] one can conclude[13] that events of this type vary with the depth x in the atmosphere in a manner proportional to $\exp(-x/L)$ where L is about 1.25 ($\times 100$ g cm^{-2}). We assume then that the production of mesons in the atmosphere varies also as $\exp(-x/L)$. Since there is not sufficient evidence to decide otherwise we assume further that the mean production depth L is the same for all energies and is 1.25 ($\times 100$ g cm^{-2}).†† We write

$$H(R, x)=G(R)e^{-x/L}. \tag{13}$$

This assumption not only simplifies our task to that of obtaining the energy-dependent part of the production function, but also allows us to obtain the altitude dependence of the intensity of high energy mesons from the hard component measurements. We follow Rossi and take curve *fm* of Fig. 16 in reference 13 to represent the vertical intensity of fast mesons, i.e., mesons with ranges greater than 1($\times 100$ g cm^{-2} of air).

With the assumption we have made regarding the independence of production on depth it is possible in principle to determine the complete production spectrum from the observed, sea level distribution-in-x_0. The method is not practical, however, because it requires a completely impossible accuracy of the experimental data. A more practical method would involve performing the synthesis on the basis of the sea level data and the data on the variation with altitude of the intensity of mesons at the end of their range. Such a method places a large burden on the somewhat uncertain absolute value of the slow meson intensity. In what follows we have therefore attacked the problem in the following way. We have used the sea level spec-

[20] Tech. Report No. 28, see reference *.
[21] A. Ehmert, Zeits. f. Physik **106**, 751 (1937).
[22] V. C. Wilson, Phys. Rev. **53**, 337 (1938).
[23] See Section 3 of reference 13.
[24] L. Janossy, Proc. Roy. Soc. **179A**, 361 (1942).
[25] J. Tinlot, Phys. Rev. **73**, 1476 (1948).
[26] H. Bridge and B. Rossi, Phys. Rev. **71**, 379 (1947).
[27] R. Hulsizer, Phys. Rev. **73**, 1252 (1948).

†† Our assumption implies essentially (a) that the cross section for nuclear interactions of the primary radiation is independent of energy and (b) that the primaries undergo but one meson-producing collision. If there exists a secondary component capable of producing mesons, it is likely that the spectrum of the total meson-producing radiation varies with depth and hence that our separation is not justified.

trum to determine the nature of $G(R)$ for ranges larger than $10(\times 100$ g cm$^{-2})$. The form of $G(R)$ for smaller ranges has then been determined in such a way as to satisfy the data on the altitude dependence of both slow and fast mesons.

The Production Spectrum for Large Energies

In the earlier works mentioned in Part I the authors have shown that if one assumes that all mesons are produced at one altitude—usually taken to be the depth of 1 ($\times 100$ g cm^{-2}), one can explain the observed intensities at sea level for ranges greater than a few $\times 100$ g/cm^{-2} by taking a production spectrum which varies as $R^{-\gamma}$, where γ is about 3. We shall now describe a refinement of this method which not only enables us to obtain the production spectrum for high energies from the sea level data but also points up the limitations in the previous approach.

Consider mesons all of range R produced exponentially in the atmosphere so that the number produced in dx at x is proportional to $\exp(-x/L)dx$. Of those produced in dx the number which arrive at the depth s greater than x but less than R is

$$\phi(x, R, s)dx = e^{-x/L}w(x, s, x+R)dx. \tag{14}$$

Thus, for each meson produced at all depths less than s the number which arrive at s is

$$P(R, s) = \int_0^s \phi(x, R, s)dx. \tag{15}$$

Those mesons which do arrive at s are produced on the average at the depth

$$\bar{x}(R, s) = \int_0^s x\phi(x, R, s)dx \Big/ P(R, s). \tag{16}$$

We are interested in the case where $s=10$ (sea level). In this case it turns out that if $R=10$ the main part of the integrals come from values of x near $\bar{x}$. We can then say approximately that, insofar as the effect at sea level, is concerned, all mesons of range R are produced at the depth $\bar{x}(R, 10)$ and have the probability $P(R, 10)$ of surviving to sea level.

Mesons produced at x with the range R have the end point $x_0=R+x$, or on the average the end point $x_0=R-\bar{x}$. Since this x_0 depends only on R, we can argue as follows: Mesons observed at $s=10$ with end points in dx_0 at x_0 were produced with ranges in $dR=dx_0$ with R given by $R+\bar{x}(R)=x_0$, and were produced at the depth $\bar{x}(R)$ in the number $1/p$ of that observed. By application of this argument we can construct the production spectrum $G(R)$ for $R>10$ from the observed sea level spectrum $F(10, x_0)$ from the relation

$$G(R) = \frac{F(10, R+\bar{x})}{P(R, 10)}. \tag{17}$$

The integrals of Eqs. (15) and (16) have been computed numerically for $s=10$, $L=1.0$,‡‡ and for values of R between 10 and 35 (all$\times 100$ g cm^{-2}). The functions $\bar{x}/L$ and P have been plotted against $x_0=R+\bar{x}$ in the graph of Fig. 4. It is evident that the assumption that all production takes place at $x=L$ is not satisfactory for mesons observed at sea level with end points less than about 12, i.e., with ranges less than two. It is interesting, however, that for all values plotted P is within five percent of $w(1, x_0)$.

The distribution-in-x_0 of mesons observed at sea level has been plotted as curve $i(x_0)$ in Fig. 5. This curve was obtained from the curve of Fig. 6, reference 13, by setting $x_0=R+10$. The curve $G(R)$ was obtained from the curve $i(x_0)$ by application of relation (17). The relation is indicated for a few points by lines joining the two curves. The curve for $G(R)$ obtained in this way is a straight line between $R=10$ and $R=35$. If this line is extended toward larger R's, as indicated by the broken line portion of the curve, it becomes coincident with the curve of $i(x_0)$ at about $R=100$. The data for $i(x_0)$ for x_0's up to 300 (not plotted) also lie on the extrapolated curve of $G(R)$. Since from the curves of Fig. 4, $\bar{x}$ and P both approach one for large R, this is precisely the behavior we would expect if the production spectrum obeyed by a power law. We conclude, therefore, that for ranges between 10 and 300 the distribution-in-range of mesons as they are produced is of the form

$$G(R) = A(R/R_0)^{\gamma}, \tag{18}$$

where $R_0=100$ g cm^{-2}. From the curve of $G(R)$ we find that $\gamma=2.91$, and that if $R_0=100$ g cm^{-2}, $A=207$ min.$^{-1}$ sterad.$^{-1}$ cm^{-2} (100 g cm^{-2})$^{-2}$.

It can be shown that if we had chosen the mean production depth L to be 1.25 ($\times 100$ g cm^{-2}), the above analysis would give a value for γ not significantly different but that A becomes 154 min.$^{-1}$ sterad.$^{-1}$ cm^{-2} (100 g cm^{-2})$^{-2}$.

The curve of $i(x_0)$ suddenly becomes much more steep for values of x_0 greater than 300. From our considerations this would indicate that for high energies the production spectrum no longer obeys the simple law above. Whether this is the case or whether some other phenomena comes into play is not clear. (See, for instance, the discussion of Greisen.[28])

The method of this section is not suitable for determining the production spectrum for ranges less than 10. The difficulty lies in the fact that the function $\phi(x, R, s)$ deviates radically from the general form of an exponential when R and s are less than 10. Thus the integrals (15) and (16) do not receive their main contribution from values of x remote from s and the succeeding arguments are invalidated.

‡‡ At the time these computations were done, $L=1.0$ was the best available value for the mean depth of production. The conclusions of this section would not have been greatly different if the new accepted value, 1.25, had been used.

[28] K. Greisen, Phys. Rev. 73, 521 (1948).

The Production Spectrum for Small R

Referring to Eqs. (4) and (13), it is evident that if we know the production spectrum $G(R)$ we can compute the observed distribution-in-x_0 at any depth s from the equation

$$F(s, x_0)=\int_0^s G(x_0-x)e^{-x/L}w(x, s, x_0)dx. \quad (19)$$

We shall take the measurements of the intensity of slow mesons to give the values of $F(s, s-0.1)\equiv f(s)$. The intensity $I(s)$ of mesons in the hard component at the depth s is related to $G(R)$ by the equation

$$I(s)=\int_{x_0=s+1}^{\infty}\int_{x=0}^{s} G(x_0-x)e^{-x/L}w(x, s, x_0)dxdx_0. \quad (20)$$

The task of evaluating $G(R)$ from $f(s)$ and $I(s)$ in a direct manner by means of Eqs. (19) and (20) is a formidable one. We have, therefore, instead, attempted to select a function $G(R)$ which takes on the form given by (18) for $R>10$ and when entered in Eqs. (19) and (20) yield results in agreement with the data. The process of arriving at a suitable G is made easier by the fact that Eqs. (19) and (20) are linear. Thus, if G_1 yields f_1 and I_1 and G_2 yields f_2 and i_2, then (G_1+G_2) yields (f_1+f_2) and (I_1+I_2). Once the numerical integrations of Eqs. (19) and (20) have been performed for several trial spectra G, these spectra can be used as components of a more complex spectrum with the weights of the various components adjusted so as to give the best fit.

To limit the number of integrations to a finite one, they were carried out only for $s=3$, $s=6$, and $s=10$, where it was felt the experimental data were most reliable. Also this removed the danger of overdetermination of the function G. Of course, G is now underdetermined but requirements of smoothness and reasonableness can carry a share of the burden. The six experimental points which we try to fit by the choice of the production spectrum are given in the first line of Table VIII.

It is evident, from the start, that the production spectrum cannot be given by (18) for all R since then the number and hence the energy of the mesons formed in any finite layer of the atmosphere would be infinite. The first trial functions used were

$$G(R)=10^2\times\begin{cases}R_c^{-2.91}; & R\leq R_c\\ R^{-2.91}; & R\geq R_c,\end{cases}$$

(where all R's are measured in units of 100 g cm^{-2}). Four values were taken for R_c: 1, 2, 4, and 8. These spectra will be referred to be the designations I, II, III, and IV, respectively. The resulting values for $I(s)$ and

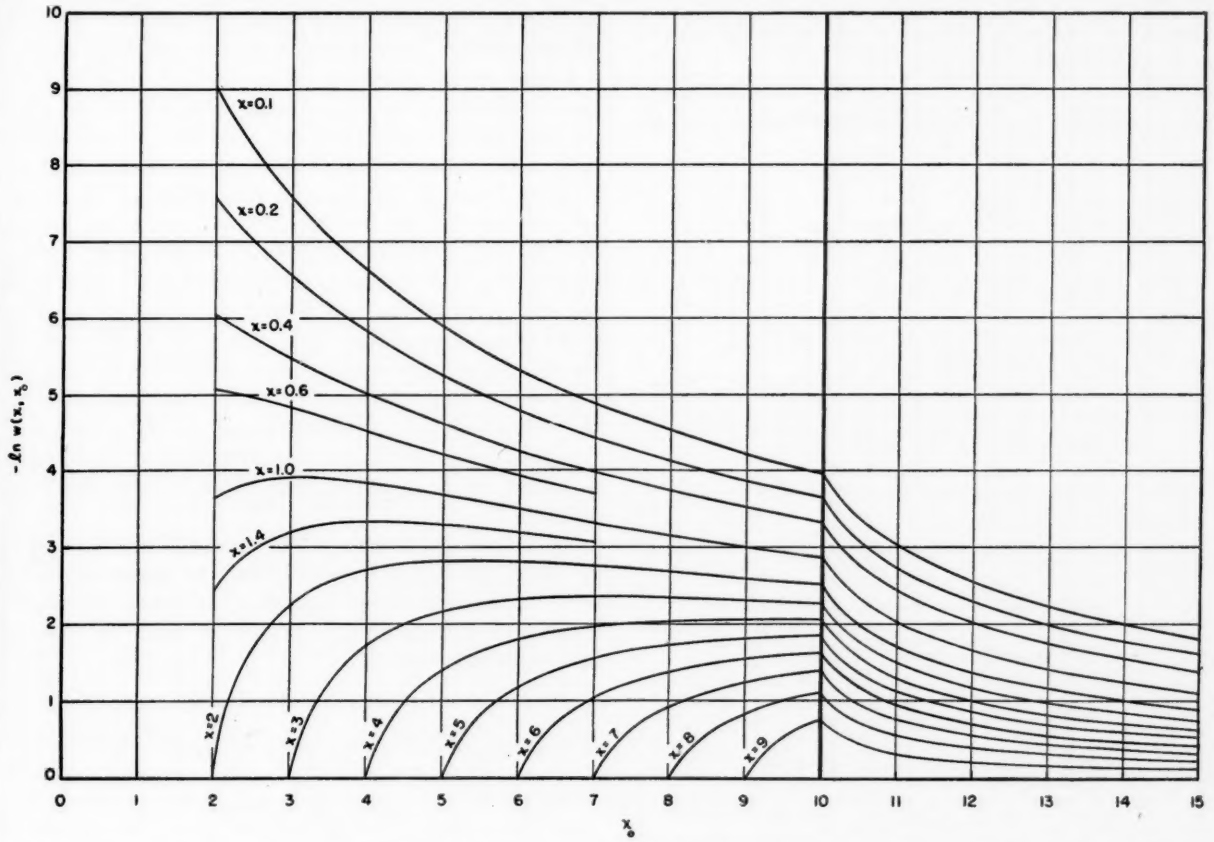

FIG. 3. The survival probabilities. The function $w(x, x_0)$ is the probability that a meson will survive from x to the end of its range at x_0. All depths are measured in units of 100 g cm^{-2}.

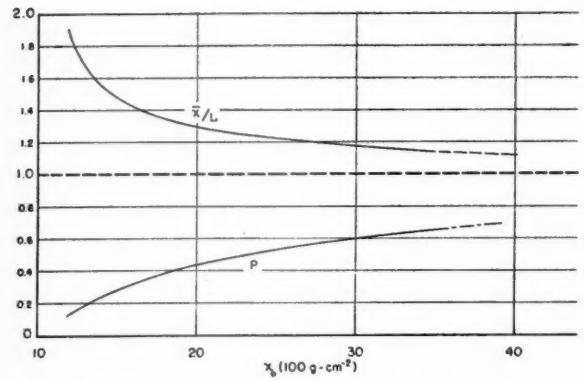

FIG. 4. Mean survival probability and mean depth of production for mesons observed at sea level.

$f(s)$ are given in Table VIII. None of these spectra can be considered as satisfactory, but certainly the general character of the desired spectrum is approached by *III*. It can be shown also that no linear combination of the four spectra is satisfactory.

In order to be able to effect perturbations on the four spectra above for values of R_c less than eight, four other trial functions were used. These are

$$G(R)=10^2\times\begin{cases}(1/R_c^2)(R_c-R); & R<R_c\\ 0; & R>R_c.\end{cases}$$

They are the spectra *V*, *VI*, *VII*, and *VIII* for R_c 1, 2, 4, and 8, respectively. The resulting values for I and f are given in Table VIII.

Since we are trying to fit only six experimental points we can certainly do so with a linear combination of any

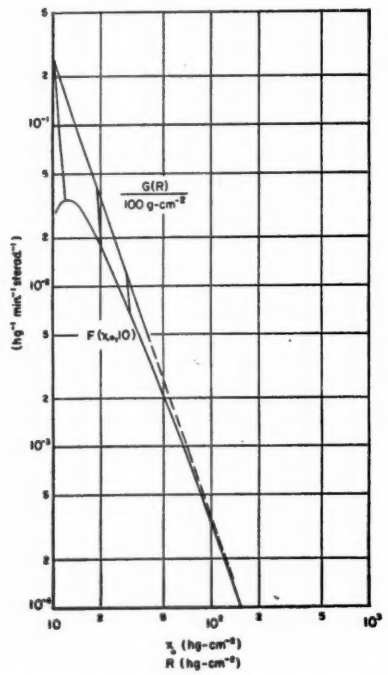

FIG. 5. Distribution-in-x_0 for sea level mesons and the production spectrum for high energies. (Note: hg = 100 g.)

TABLE VIII. Observable computed from the various assumed spectra. The number $f(s)$ is the differential intensity of slow mesons at the atmospheric depth s (in 100 g cm^{-2}). $I(s)$ is the intensity of mesons of the hard component at the depth s. The unit for f is min.$^{-1}$ sterad.$^{-1}$ (100 g)$^{-1}$. The unit for I is min.$^{-1}$ sterad.$^{-1}$ cm^{-2}.

	$f(3)$	$f(6)$	$f(10)$	$I(3)$	$I(6)$	$I(10)$
Experimental	0.57	0.142	0.0280	2.40	1.19	0.51
Spectrum *I*	5.10	0.951	0.748	4.11	1.39	0.373
Spectrum *II*	0.91	0.294	0.0395	3.56	1.30	0.371
Spectrum *III*	0.130	0.093	0.0262	2.07	1.00	0.361
Spectrum *IV*	0.0174	0.0153	0.0158	0.86	0.76	0.344
Spectrum *V*	2.20	0.273	0.0134	0	0	0
Spectrum *VI*	2.23	0.287	0.0156	0.49	0.055	0.0038
Spectrum *VII*	1.35	0.345	0.0230	2.75	0.544	0.0231
Spectrum *VIII*	0.1792	0.437	0.077	7.2	2.06	0.158
Spectrum *IX*	0.57	0.151	0.036	2.40	1.34	0.52
Spectrum *X*	0.54	0.124	0.022	1.77	0.81	0.37
Spectrum *XI*	0.56	0.138	0.0278	2.33	1.09	0.50

six of the eight trial spectra we have chosen. We can try to find a suitable combination by inspection. One combination, which was found in this way to give a reasonable fit, yields the spectrum

$$G_{VIII}(R)=0.96G_{III}+0.50G_{IV}+0.20G_V. \qquad (21)$$

The consequences of this spectrum are given with spectrum *VIII* in Table VIII. The computed values agree with the experimental within 30 percent, and the production spectrum is reasonably smooth, being a monatomically decreasing function for all R.

Linear combinations of any six of the trial spectra can be found which give results agreeing exactly with the six experimental values. Five sets of weighting factors for such compound spectra have been obtained (see reference 20 for details). But although all of the spectra so formed fit the six experimental points exactly, and also have the proper form for large R, they could not be considered as satisfactory. First, they were not smooth functions, and second, the resulting function $G(R)$ takes on negative values for some R. The taking on of negative values and the irregularity of the spectra obtained cannot represent the true situation and must be attributed to the properties of the particular trial spectra used. The gross characteristics of all the spectra obtained seem to agree with those of the spectrum given in Eq. (21).

In order to try to abstract the essential characteristics of the compound spectra obtained, we investigated for each (i) the behavior for large R, (ii) the total number of mesons produced. For R larger than eight the spectra all can be expressed

$$G(R)=AR^{-2.91}(R>8).$$

The total number of mesons produced is given by

$$N=L\int_0^\infty G(R)dR.$$

The quantities A for the five compound spectra inves-

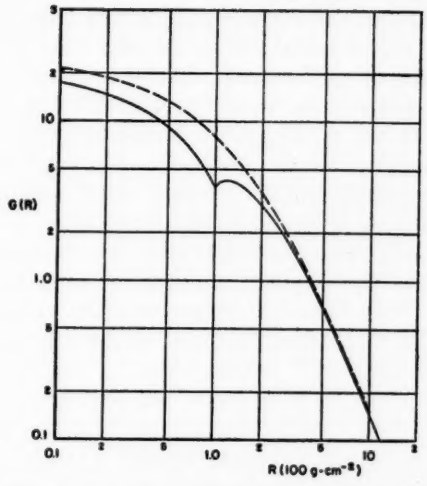

FIG. 6. Distribution-in-range of mesons as they are produced.

tigated all lay near 150, which is in agreement with the value obtained for A in Eq. (18), and the values of N ranged from 23 and 25. We can probably conclude then that the correct spectrum has a value for $A=150$ and for $N=24$.

With this in mind it would seem advisable to try to find a simple, smooth function which is similar to the spectra above and which gives these values for A and N. A function of the form $G(R)=A(R+\alpha)^{-2.91}$ has the general nature of the combined spectra above. The constant A is the same as above and α can be chosen to make the total number of mesons produced be 24. We thus get a new trial spectrum

$$G_X(R)=150(R+2.1)^{-2.91}.$$

The values of $I(s)$ and $b(s)$ resulting from this spectrum are given in line 11 of Table VIII. It is evident that the fit is not very good. Part of the discrepancy can be accounted for by the fact that our requirement that A be the same in this case is too strong. The function G_X differs quite appreciably from $R^{-2.91}$ even for ranges of R as large as 10 or 20. The results also indicate, however, that it is unlikely that a smooth spectrum can be found to fit the data.

As a final attempt we have tried to build a spectrum from a linear combination spectrum X and one of the first eight spectra. The best fit was obtained with the spectrum

$$G_{XI}(R)=1.4G_X-0.04G_I.$$

The consequences of this spectrum are also given in Table VII. The agreement with the experimental data is within three percent for all values but one where it differs by eight percent. The disparity is of the same order as both the experimental errors and the cumulative errors in the numerical computations. We shall therefore consider case XI as our "best" spectrum insofar as the agreement with the altitude data is concerned. It is probably significant that this spectrum gives $N=26$ in close agreement with the "invariant" value obtained for the other combined spectra.

The spectrum $G_{XI}(R)$ has been plotted against R as the solid line in Fig. 6. For comparison the broken-line curve gives $1.4G_X$. The nature of the perturbation $-0.04G_I$ is evident.

It is not clear whether some peculiarity such as the dip at $R=1.0$ in the spectrum of Fig. 6 is necessary in any spectrum compatible with our assumptions. Whether the actual production spectrum is like this, or whether it is due to the inaccuracies of the experimental data, or to one of our basic assumptions cannot be determined by the methods we have used. It is probable, however, that our "best" spectrum represents on the average something close to the true production spectrum averaged over all depths at which production occurs.

Discussion

The properties of the spectrum XI are given in Table IX. The range at production is R in units of 100 g cm^{-2}; the corresponding momentum is $p(R)$ and the total (relativistic) energy $E(R)$, measured in units of μc and μc^2, respectively; $G(R)$ gives the differential range spectrum at production, i.e., $G(R)\exp(-x/L)dxdR$ is the number of mesons produced in dx at x with ranges

TABLE IX. Properties of the production spectrum.

R	$p(R)$	$E(R)$	$G(R)$	$g(R)$	$G_\pi(p)$	$G_E(E)$
0	0	1	20.42	20.86	0	0
0.1	1.017	1.426	17.34	18.98	4.593	6.450
0.2	1.339	1.671	14.76	17.39	5.246	6.568
0.3	1.601	1.888	12.58	16.02	5.158	6.064
0.4	1.831	2.086	10.73	14.85	4.796	5.419
0.5	2.047	2.278	9.15	13.86	4.300	4.776
0.6	2.256	2.468	7.78	20.46	3.797	4.147
0.7	2.459	2.655	6.60	12.30	3.313	3.571
0.8	2.657	2.839	5.58	11.70	2.845	3.051
0.9	2.852	3.022	4.68	11.19	2.415	2.575
1.0	3.045	3.205	3.89	10.76	2.025	2.142
1.2	3.427	3.570	4.230	9.951	2.220	2.343
1.4	3.806	3.935	4.044	9.119	2.135	2.266
1.6	4.184	4.302	3.701	8.399	1.961	2.036
1.8	4.563	4.671	3.330	7.639	1.761	1.821
2.0	4.941	5.041	2.973	7.008	1.570	1.614
2.2	5.322	5.415	2.650	6.445	1.397	1.425
2.4	5.706	5.793	2.364	5.948	1.241	1.265
2.6	6.089	6.171	2.110	5.495	1.103	1.123
2.8	6.475	6.552	1.890	5.097	0.985	0.998
3.0	6.863	6.935	1.698	4.740	0.8793	0.8878
4	8.835	8.891	1.037	3.409	0.5237	0.5269
5	10.86	10.91	0.6762	2.568	0.3347	0.3361
6	12.92	12.96	0.4650	2.007	0.2260	0.2260
7	15.07	15.10	0.3334	1.613	0.1590	0.1590
8	17.17	17.20	0.2472	1.325	0.1157	0.1157
9	19.38	19.41	0.1884	1.109	0.0871	0.0871
10	21.58	21.60	0.1471	0.9421	0.06708	0.06708
12	26.08	26.10	0.09464	0.7074	0.04221	0.04221
14	30.73	30.75	0.06454	0.5490	0.02814	0.02814
16	35.41	35.42	0.04602	0.4398	0.01970	0.01970
18	40.21	40.22	0.03398	0.3605	0.01430	0.01430
20	44.99	45.00	0.02585	0.3014	0.01073	0.01073
25	57.29	57.30	0.01433	0.2048	0.005731	0.005731
30	69.99	70.00	$0.8774\ 10^{-2}$	0.1484	0.003422	0.003422
35	82.99	83.00	$0.5770\ 10^{-2}$	0.1128	0.002192	0.002192
40	96.00	96.01	$0.4001\ 10^{-2}$	0.0888	0.001488	0.001488

in dR at R (min.$^{-1}$ sterad.$^{-1}$ cm^{-2}) where dx and dR are measured in units of 100 g cm^{-2}. The integral range spectrum is

$$g(R)=\int_R^\infty G(R')dR',$$

and $G_p(p)$ and $G_E(E)$ are the differential momentum and energy spectra, respectively. The differential energy spectrum is also plotted in Fig. 7 as a function of the *kinetic* energy. For comparison the corresponding curve for $1.4\times G_X$ is plotted as the broken line. It will be noted that the differential energy spectrum takes for high energies approximately the form $G_E(E)=kE^{-2.5}$.

For comparison with other data we have plotted by the solid curves in Fig. 8 the differential range spectra of mesons observed at the depths 3, 6, and 10, as a consequence of our final spectrum. We give also, by the broken curve near the $s=10$ curve, the experimental data on mesons at sea level (from Fig. 6, reference 13). That the experimental curve lies below the computed one can be explained in part by the fact that the computations were for the depth 1000 g cm^{-2} and the experimental curve refers to the depth 1030 g cm^{-2}. The broken-line curve near the curve for $s=3$ represents the experimental data obtained by Anderson and co-workers,[29] by momentum measurements at this altitude. For $R>1$ the agreement is within the statistical errors, and for $R<1$ the disagreement probably is due to the fact that no careful separation was made in the experiments of mesons of this range and electrons of the same momentum.

Another check with experiment can be made. Rossi[13] has computed the total energy lost by mesons throughout the atmosphere by the mechanism of collision and disintegration. These computations are based on the complete experimental curves for the fast and slow meson intensities. He finds that the energy lost by mesons is 183 μc^2 min.$^{-1}$ cm^{-2} sterad.$^{-1}$ We can compute the total energy which goes *into* mesons in the atmosphere according to our production spectrum. We find that this energy is 177 μc^2 min.$^{-1}$ cm^{-2} sterad.$^{-1}$ The agreement cannot be completely fortuitous.

From our production spectrum we can obtain a number for the average multiplicity of meson production. From Table IX we see that the vertical "intensity" of all mesons produced in the atmosphere is $L\times g(0.1)=24$ min.$^{-1}$ sterad.$^{-1}$ cm^{-2}. From an examination of the high altitude measurements Rossi[13] concludes that the vertical intensity of the primary radiation is at these latitudes 4.2 min.$^{-1}$ sterad.$^{-1}$ cm^{-2}. We conclude that on the average each primary ray gives rise to $24/4.2=5.7$ mesons.

The results of some of the intermediate steps in our computations show the importance of the contribution to measured intensities of production near the point of observation. Let the integrand of Eq. (19) be represented by $\phi(x, s, x_0)$. Then for a given s and x_0, and hence for mesons of a given range at the point of observation, the magnitude of ϕ at any x is proportional to the contribution to the measured intensity by mesons produced at x. In Fig. 9 we give some of the results from the computation of ϕ. In the figure we have plotted $\phi(x, s, x_0)/F(s, x_0)$ against x for a few values of s and x_0. Then for mesons observed at s with the range x_0-s the ordinate gives the fraction of these mesons that are produced at the depth x (per 100 g cm^{-2} interval). It is evident from these curves that production near the point of observation is predominant for mesons observed at the depth of 300 g cm^{-2} with ranges up to 400 g cm^{-2}; for mesons observed at 600 g cm^{-2} with

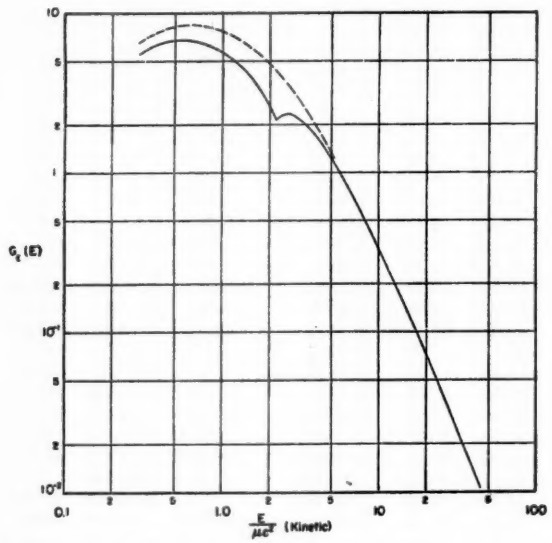

FIG. 7. Distribution-in-energy of mesons as they are produced.

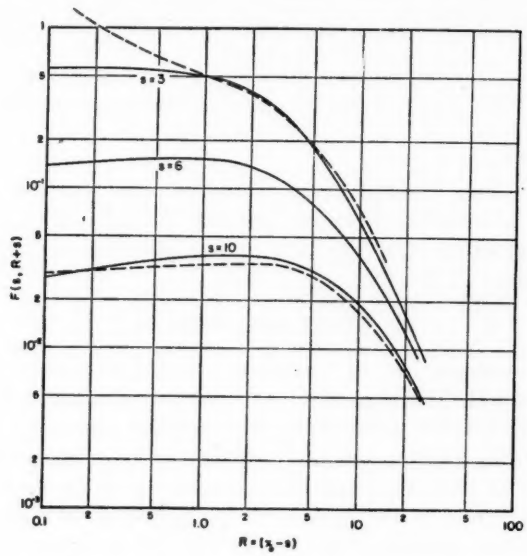

FIG. 8. Predicted differential range spectra of mesons at several altitudes. All thicknesses are in units of 100 g/cm^{-2}.

[29] Anderson, Adams, Lloyd, and Rau, Phys. Rev. 72, 724 (1947).

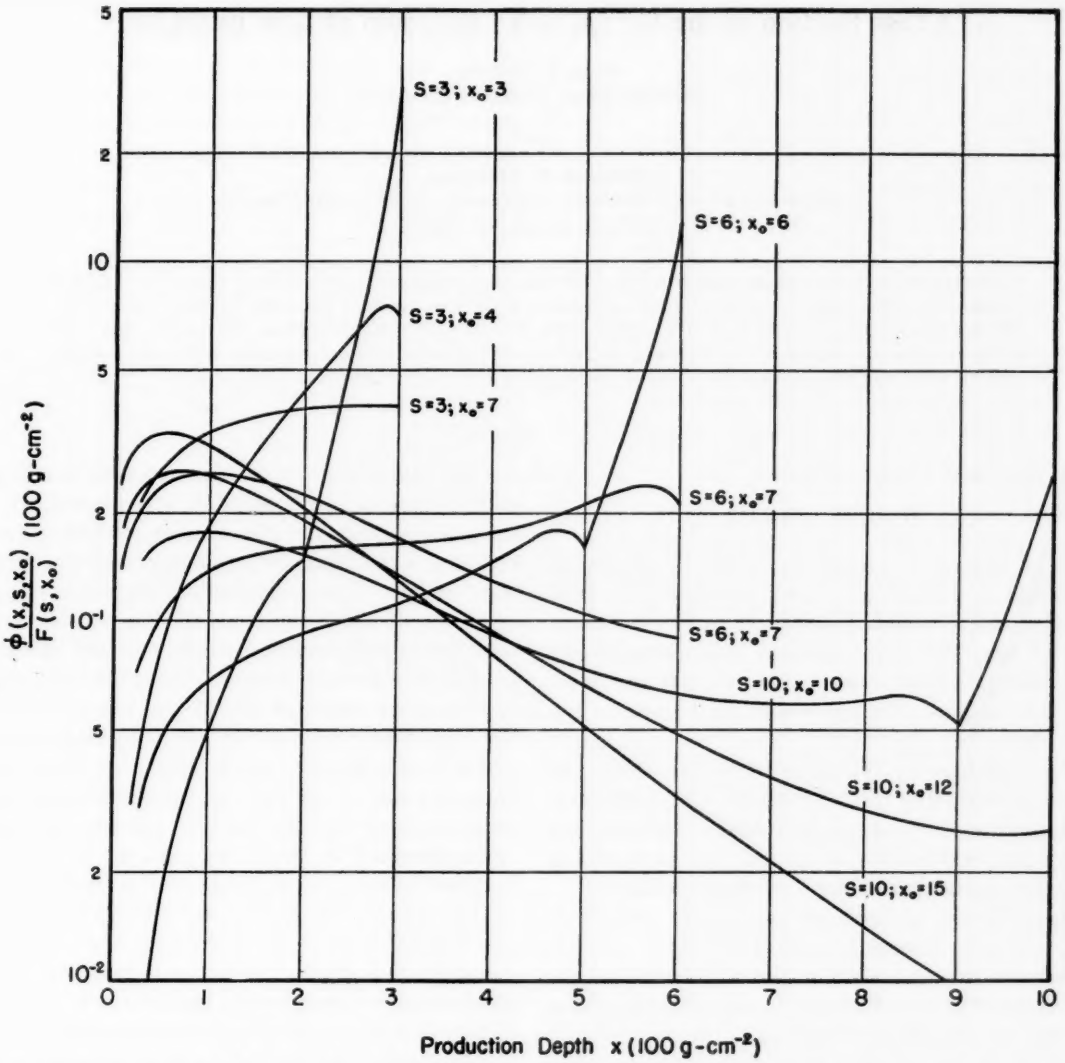

FIG. 9. Production efficiency at various depths for mesons observed at the depth s with the residual range (x_0-s). Note: Near the top of the ordinate scale 10 should read 1.0.

ranges somewhat above 100 g cm^{-2}, and that even at sea level local production cannot be neglected for mesons observed near the end of their range.

CONCLUSIONS

We have shown that it is possible to explain the available data on mesons in the atmosphere under the assumption that the dependences of production on depth and on energy are separable, and that the dependence on depth is as $\exp(-x/1.25)$. A production spectrum has been found which is compatible with these assumptions and with the experimental data. It is not presumed that this spectrum is unique in its details but only that it exhibits the gross properties of any suitable spectrum.

ACKNOWLEDGMENTS

The author is grateful to Professor Bruno Rossi under whose guidance this work was done and to Professor Street of Harvard University whose cooperation contributed to the success of the sea level measurements. P. Bowland, L. Shepard, W. Olney, and W. B. Smith made special contributions to various phases of the work.

Cross Section of the C^{12} $(p, \gamma)N^{13}$ Reaction at Low Energies

CARL L. BAILEY
Concordia College, Moorhead, Minnesota

AND

WILLIAM R. STRATTON
Department of Physics, University of Minnesota, Minneapolis, Minnesota

(Received October 14, 1949)

The efficiency of the nuclear reaction $C^{12}(p, \gamma)N^{13}$ has been measured over the energy range from 125 kev to 200 kev, with results which are in good agreement with those recently published by Hall and Fowler. The cross section ranges from 1.0×10^{-33} cm² at 128 kev to 23×10^{-33} cm² at 194 kev. The thick-target yield of the reaction was measured, by detecting the N^{13} positron activity with an absolutely calibrated counter, and the cross sections were obtained by differentiation of the thick-target yield curve.

THE efficiency of the nuclear reaction

$$C^{12}+H^1\rightarrow N^{13}\rightarrow C^{13}+\beta^+,$$

which is of interest in connection with the theory of stellar energy,[1,2] has recently been determined by Hall and Fowler[2] in the neighborhood of 88 to 128 kev bombarding energy. We have extended this measurement over the energy region between 125 and 200 kev, with results which are in good agreement with those of the above authors.

In our experiments, the yield of the reaction was measured by detecting the N^{13} activity. This method is feasible because N^{13} has a convenient half-life (10 minutes) and because no other activity is produced when carbon is bombarded by low energy protons.

A target of pure, natural isotopic carbon (graphite), 0.5 mm thick, was fastened to a hollow copper cylinder, by electroplating the back side of the carbon with copper and soldering to the cylinder. A mica-window β-ray Geiger counter (Radiation Counter Laboratories Mark 1, Model 2) was mounted so that the carbon could be placed 2.5 mm from the mica window, and so that the bombarding protons struck a spot 180° opposed to the position of the counter. The copper cylinder was filled with water to cool the carbon, and the whole assembly mounted on the target end of a 200-kev accelerator.

The experimental procedure was as follows: The target was bombarded for 20 minutes (two half-lives of N^{13}) by protons of a specified energy from the accelerator. Then the beam was shut off, the target rotated through 180°, and the total β-ray count (n^*) during the next 20 minutes determined (n^* equals gross count minus background). Under these conditions, it can easily be shown that the thick-target yield of the reaction, in disintegrations per proton, is given by

$$Y=\int_0^{E_B}(\sigma/\epsilon)dE=16\lambda e n^*/9FI. \qquad (1)$$

In this expression, σ is the reaction cross section; $\epsilon=(1/N)dE/dx$ is the stopping cross section of carbon for protons, and N is the number of carbon nuclei per cm³; E_B is the bombarding energy; λ is the decay constant of N^{13}; e is the electronic charge; F is the over-all efficiency of the β-ray counter (the number of counts recorded divided by the number of N^{13} nuclei which decay); and I is the average proton current. Small corrections were made to Eq. (1), to account for drift of the proton current and for the delay between the end of the bombardment and the beginning of the counting. Enough time was left between the successive bombardments to insure that residual N^{13} activity was negligible.

Background in the β-ray counter was important, because in some of the runs the intensity was below background. It was lowered by a 4-inch lead shield, and was further reduced by arranging eleven large Geiger counters in a semicircle in the hemisphere above the β-ray counter, and connecting them all in anti-coincidence with the latter. Accidental coincidences between the shielding counters and the β-ray counter were taken into account.

In determining the fraction F, it was not necessary to consider stopping of the electrons in the counter window or in the carbon target, because the counter window was only 2 or 3 mg/cm² thick and the range of protons in the target is less than 0.2 mg/cm², while the β-rays of N^{13} have an end-point energy of 1.2 Mev[3] and an energy spectrum[3] such that less than 1 percent have ranges of less than 10 mg/cm² of aluminum. The counter was calibrated by placing a RaD-RaE standard β-ray source (obtained from the National Bureau of Standards) at the same distance as the carbon target from the counter. By covering this source with lead sheet having holes of various sizes, it was determined that the efficiency F was sensibly independent of the size of the active deposit, as would be expected for distances as small as 2.5 mm. This circumstance made it unnecessary to make any correction for variations in the diameter of the proton beam.

[1] H. A. Bethe, Phys. Rev. 55, 434 (1939).
[2] R. N. Hall and W. A. Fowler, Phys. Rev. 77, 197 (1949); see also Phys. Rev. 74, 1558A (1948), and Phys. Rev. 75, 1462A (1949).
[3] Hornyak, Dougherty, and Lauritsen, Phys. Rev. 74, 1727 (1948).

A correction was necessary for the back-scattering of β-rays, from the carbon target and from the silver disk on which the standard was mounted. The size of this correction was determined experimentally by depositing a thin film of uranyl nitrate on a 1.5 mg/cm² Nylon foil and placing this source at the standard 2.5-mm distance from the counter window. Then the counting rate of the uranium β-rays was determined with and without the carbon target behind the source, and also with and without a clean silver disk of the same size as that on which the RaD-RaE calibrating source was mounted. While the spectrum of the uranium β-rays is not the same as that of the RaD-RaE standard or that of the N^{13}, Burt[4] has shown that the β-ray reflecting power is independent of energy over the range which we need consider. The values of F finally obtained were 0.385 $\pm$0.016 for one counter, and 0.365$\pm$0.015 for another.

The scattering of β-rays is, in general, a quite serious factor[4] in absolute β-ray counting; in this auxiliary experiment we observed that the carbon (plus copper backing) increased the counting rate by 31 percent, and the silver disk increased it by 37 percent.

The proton energy was measured by a high resistance voltmeter, reliable to 2 percent. In measuring the proton current, care was taken to prevent errors due to secondary electron emission.

The thick-target yields are shown in Fig. 1. The two sets of data shown by the dots and crosses were obtained with different counters and different sets of beam energies. In the first set, a thick-target yield was obtained at 121 kev, and then others were taken at higher energies separated by intervals of 13 or 14 kev. In the second set, the same procedure was followed except that the first point was taken at 126 kev.

The cross sections were calculated by subtracting successive measured values of Y and dividing the differences by $\Delta E/\epsilon$. They are shown in Fig. 1 and tabulated in Table I. The two sets of thick-target yields were analyzed independently, so that there are two sets of cross sections.

In the calculations, the constant value $\epsilon=20\times10^{-15}$ cm² volt was used, in accordance with the proton range-energy measurements of Parkinson *et al.*,[5] and with the value 0.97 for the atomic stopping power of carbon relative to air. Included in the adopted value of ϵ is a 1 percent correction for the fact that the target was only 99 percent C^{12}.

TABLE I. Measured cross section of the $C^{13}(p,\gamma)N^{13}$ reaction at various energies. The two sets of data were taken independently.

Bombarding energy (Kev)	First set	σ (in 10^{-33} cm² unit) Second set
128	1.0±0.2	
133		1.7±0.2
141	1.8±0.2	
147		2.5±0.2
155	3.8±0.3	
161		5.0±0.3
168	7.2±0.5	
175		9.6±0.6
181	16±1	
189		14.2±0.9
194	23±2	
202		20±1

[4] B. P. Burt, Nucleonics 5, 28 (1949).

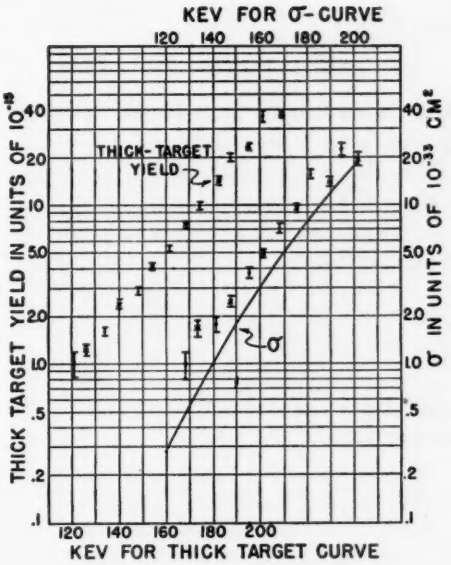

FIG. 1. Thick-target yield and cross section for the reaction $C^{13}(p,\gamma)N^{13}$. The left ordinate and lower abscissa refer to the thick-target yield; the right ordinate and upper abscissa refer to the cross section.

The statistical fluctuations, plus the uncertainty in F and the uncertainty involved in subtracting thick-target yields, allow an assignment of 5 percent to 10 percent error to each value of σ; the 10 percent uncertainty in ϵ imposes an additional latitude which is not indicated in the graph or table. The proton energy calibration does not introduce serious error, except as it effects ΔE, because a change in the energy calibration would just imply a shift of the thick-target yield curve along the energy axis.

At the highest energy the measured yield is very likely affected by evaporation of N^{13} from the target due to heating under bombardment, although we looked for such an effect by varying the proton current and found no clear-cut evidence.

The agreement with the results of Hall and Fowler is satisfactory. For example, at 120 kev they give the value 0.6×10^{-33} cm² for σ, and at 95 kev they give 0.1×10^{-33} cm². Examination of Fig. 1 shows that these values agree with an extrapolation of our results.

The solid cross-section curve in Fig. 1 is an extrapolation from the well-known 456-kev resonance in this reaction,[6] calculated using the one-level Breit-Wigner

[5] Parkinson, Herb, Bellamy, and Hudson, Phys. Rev. 52, 75 (1937); F. T. Rogers and M. M. Rogers, Phys. Rev. 53, 713 (1938).

[6] Fowler, Lauritsen, and Lauritsen, Rev. Mod. Phys. 20, 236 (1948); W. A. Fowler and C. C. Lauritsen, Phys. Rev. 76, 314 (1949).

formula,

$$\sigma=\pi\lambda^2[\omega\Gamma_P\Gamma_\gamma/(E-E_R)^2+\tfrac{1}{4}\Gamma^2], \quad (2)$$

where λ is the de Broglie wave-length in the center-of-mass system, ω is a weight factor, Γ_P is the proton width, Γ_γ is the γ-ray width, E is the center-of-mass energy, E_R is the resonance energy, and Γ is the total width. At resonance, one has $\sigma=\sigma_R$, $\lambda=\lambda_R$, $\Gamma_P=\Gamma_{PR}$, and $\Gamma=\Gamma_R$, so that

$$\sigma_R=4\pi\lambda_R^2\frac{\omega\Gamma_{PR}\Gamma_\gamma}{\Gamma_R^2}. \quad (3)$$

Dividing (2) by (3), and using the fact that $\Gamma^2\ll(E-E_R)^2$ in our energy region,

$$\sigma=\frac{1}{4}\frac{E_R}{E}\frac{\Gamma_P}{\Gamma_{PR}}\frac{\Gamma_R^2}{(E-E_R)^2}\sigma_R, \quad (4)$$

assuming that Γ_γ and ω are independent of energy. The constants are:[6] $\sigma_R=1.2\times10^{-28}$ cm^2, $E_R=421$ kev (center-of-mass energy), $\Gamma_{PR}=35$ kev, $\Gamma_\gamma=0.63$ ev, $\Gamma_R\cong35$ kev. The ratio of proton widths is involved, and if we take Γ_P to be of the form $\Gamma_P=$const. penetrability, it is only necessary to find the ratio of the penetrabilities in order to evaluate Γ_P/Γ_{PR}. The penetrabilities were read from the curves of Christy and Latter.[7]

If the theoretical expression used by Bethe[1] in his calculations on stellar energy is used to calculate the cross section in the energy region covered by our measurements, a result approximately 100 times smaller than the measured value is obtained. This discrepancy does not alter the main points of the stellar energy theory, but only the calculations of lifetimes and relative abundances of elements in stars. A detailed discussion of this matter is given by Hall and Fowler.[2]

We are indebted to Dr. J. H. Williams for his continued interest and suggestions, and to Dr. W. A. Fowler for communication of his results prior to publication. This research was done with the partial support of the ONR, Contract N5ori-147. It was also materially assisted by the University of Minnesota Technical Research Fund subscribed to by General Mills, Inc., Minneapolis Honeywell Regulator Company, Minneapolis Star Journal and Tribune Company, Minnesota Mining and Manufacturing Company, and Northern States Power Company.

[7] R. Christy and R. Latter, Rev. Mod. Phys. **20**, 185 (1948).

The Cross Section for the Radiative Capture of Protons by C^{12} near 100 Kev

ROBERT NOEL HALL AND WILLIAM ALFRED FOWLER
Kellogg Radiation Laboratory, California Institute of Technology, Pasadena, California
(Received September 15, 1949)

A low voltage accelerator and high current ion source has been used to determine the cross section of the reaction $C^{12}(p\gamma)N^{13}$ over the energy range from 88 to 128 kev. A counter arrangement is described which detects 26 percent of all the positrons from the decay of the N^{13} produced in the reaction and which has a low background rate of 5.5 counts per minute. With this accelerator and detector, yields of the order of 10^{-16} positron per proton and cross sections as low as 10^{-30} barn or 10^{-34} cm^2 can be measured with errors of the order of ± 20 percent. The cross section for the $C^{12}(p\gamma)N^{13}$ reaction has been found to fit the semi-empirical expression $\sigma = 0.0024E^{-1}\exp[-6E^{-\frac{1}{2}}]$ barn with E in Mev over the energy range measured. This is in satisfactory agreement with the Breit-Wigner one-level dispersion formula using constants determined at the 456-kev resonance. The astrophysical implications of these results in connection with the carbon-nitrogen cycle of nuclear reactions in stellar interiors are discussed.

INTRODUCTION

IN 1938 H. A. Bethe[1] showed that the most important source of energy in ordinary stars is the nuclear reactions of carbon and nitrogen with protons. These reactions which form a cycle in which the original nucleus is reproduced are as follows:

$$\begin{aligned} &C^{12}+H^1\rightarrow N^{13}+\gamma, && N^{13}\rightarrow C^{13}+\beta^++\nu,\\ &C^{13}+H^1\rightarrow N^{14}+\gamma, && \\ &N^{14}+H^1\rightarrow O^{15}+\gamma, && O^{15}\rightarrow N^{15}+\beta^++\nu.\\ &N^{15}+H^1\rightarrow C^{12}+He^4 && \end{aligned} \qquad (1)$$

Thus the carbon and nitrogen isotopes serve as catalysts for the combination of four protons into an alpha-particle, two positrons (β^+) and presumably two neutrinos (ν). The mass energy difference of 28 Mev per cycle (0.8 percent of the mass energy of the four protons involved) appears in the form of gamma-radiation (γ) or as kinetic energy of the alpha-particle, positrons, and neutrinos. Only 1.5 Mev is lost as kinetic energy of the neutrinos and is thus not convertible by presently known mechanisms except inverse β-decay into the general energy content of the star.

Of the nuclear reactions which might serve as sources of nuclear energy those involving hydrogen are favored by its large abundance, by its large mass excess which makes a considerable energy evolution possible, and by its small charge and mass which enable it to penetrate easily through nuclear potential barriers. Neutrons, with no barriers, react too rapidly to yield observed stellar lifetimes! Of the reactions involving hydrogen, the carbon-nitrogen processes are unique in their cyclical character. In general nuclei lighter than carbon are permanently destroyed by alpha-particle emission in reactions with protons and those heavier disappear through radiative capture of the protons and the formation of heavier stable nuclei.

On the basis of relatively meager experimental evidence available at the time on nuclear reaction rates or cross sections, Bethe showed that the process described above is the only one consistent with the known evolution of energy in the bright stars of the main sequence, including the sun, and with the central temperature of these stars as calculated by integration of the Eddington equations ($\sim 2\times 10^7$ degrees). For fainter stars with lower central temperatures the reaction

$$H^1+H^1\rightarrow D^2+\beta^++\nu, \qquad (2)$$

and the reactions following it were suggested[2] as being mainly responsible for the energy production.

The essential point of Bethe's argument cannot be questioned in spite of the fact that nuclear reaction rates at stellar temperatures can be only roughly estimated from existing experimental data at laboratory energies. However, it was felt that additional and more accurate experimental evidence should be obtained on these reactions, in particular at energies as close as possible to the effective stellar energies. It is the purpose of this paper to present such evidence on the first reaction given above, namely $C^{12}(p\gamma)N^{13}$.

EXPERIMENTAL ARRANGEMENTS

The proton energy at which a thermo-nuclear reaction is most probable in the carbon-nitrogen cycle is determined by the maximum in the product of the Maxwellian velocity distribution among the protons multiplied by the cross section for the reaction. This product reaches its maximum at roughly 30 kilovolts proton energy for stellar temperatures of 2×10^7 degrees when the charge of the capturing nucleus is 6 or 7. The cross sections (10^{-40} cm^2) at this energy are far too small to be measured in the laboratory with existing techniques, so the data obtained at higher energies must be extrapolated to 30 kev. A low voltage accelerator shown in Fig. 1 powered by a conventional x-ray tube transformer-condenser rectified supply[3] has been used to extend the measurement of the cross section of $C^{12}(p\gamma)$

[1] H. A. Bethe, Phys. Rev. **55**, 103, 434 (1939); Astrophys. J. **94**, 37 (1940).

[2] H. A. Bethe and C. L. Critchfield, Phys. Rev. **54**, 248, 862 (1938).

[3] R. N. Hall, Rev. Sci. Inst. **19**, 905 (1948). The results reported in this paper were described briefly by W. A. Fowler and R. N. Hall, Phys. Rev. **74**, 1558(A) (1948).

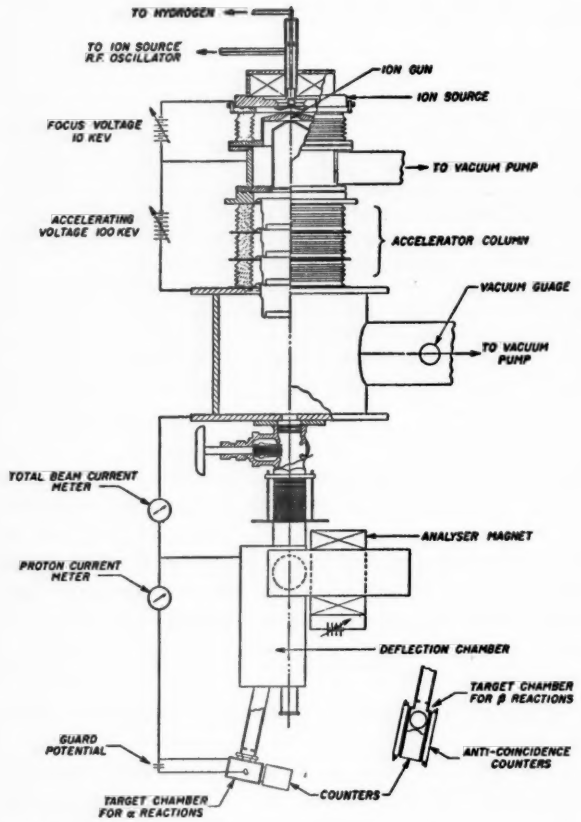

FIG. 1. Schematic arrangement of the 100-kev accelerator, high frequency ion source, magnetic analyzer, and detector used in these experiments.

down to bombarding energies as low as 88 kev, whereas previously reported data had been taken in the neighborhood of the 456-kilovolt resonance and above. This extension was made possible by the large current ($\sim$250 μa) of focused and monoenergetic protons which could be obtained from the radiofrequency ion source especially constructed for this purpose.[3]

The $C^{12}(p\gamma)N^{13}$ reaction has been studied by several investigators[4] in the energy region from 0.3 to 1.3 Mev. A well defined resonance exists at 456$\pm$2 kev having a proton width of 35 kev and a gamma-ray width of 0.63 electron volt.[5] The proton width corresponds to the measured breadth at half-maximum of the resonance, while the gamma-ray width, which is calculated from the cross section at resonance, represents the probability that radiation will follow capture of the incident proton. This information may be used in the dispersion formula to calculate the low energy cross section, but the results are open to question since they involve a considerable extrapolation from resonance. In the first place, higher energy resonances may contribute appreciably to the cross section. In the second place, the simple one-level dispersion formula itself is not necessarily valid except in the neighborhood of a resonance.

The N^{13} produced in this reaction has a positron radioactivity with a 10.13$\pm$0.1 minute half-life.[6] The recent results of W. F. Hornyak, C. B. Dougherty, and T. Lauritsen[7] show that the positron spectrum has a simple Fermi distribution with a maximum energy of 1.202$\pm$0.005 Mev. No gamma-radiation other than that from the annihilation of the positrons has been established with certainty, indicating the absence of K-capture or of any other positron groups. The presence of C^{13} in the target does not give rise to any radioactivity since the N^{14} formed by the $C^{13}(p\gamma)$ reaction is stable. It follows that for every proton captured by C^{12}, there is emitted one positron which is accompanied by no other activity.

In order to obtain a measurable yield at as low an energy as possible, a large bombardment current, together with a high counting efficiency in the presence of a low background, is necessary. Using the proton source described in reference 3, magnetically analyzed proton currents of 250 μa were focused upon an area of about two square millimeters of the target.

Since the counting efficiency for the 2.8-Mev gamma-rays produced in the $C^{12}(p\gamma)N^{13}$ is low ($\sim$1.5 percent) the yield was determined by counting the positrons emitted by the N^{13}. It is essentially the fact that a radioactive isotope is produced in this reaction which makes establishment of the cross section at a very low value possible. Due to the high background produced by x-rays and sparking during bombardment, it was necessary to measure the induced radioactivity after the beam was turned off.

The target and detector arrangement shown in Fig. 2 was used for these measurements. The carbon target, consisting in a few cases of a soot deposit and in most cases of a graphite disk, was mounted on the water-cooled brass target sphere. After the bombardment period, the sphere was rotated 180° so as to bring the target before the opening of a mica-window beta-ray counter sealed into the vacuum system. With this arrangement, a large solid angle was obtained with a minimum amount of absorbing material between the target and the sensitive volume of the counter.

The counter used was made by the Radiation Counter Laboratory, Chicago, Illinois, and was constructed with the sensitive volume reduced in length relative to that of their standard pressure seal mica window counter, Mark 1, Model 2. This reduction was accomplished by extending the glass sleeve surrounding the central wire to within a half-inch of the mica window (See Fig. 2). This modification reduced the background

[4] Cockcroft, Gilbert, and Walton, Proc. Roy. Soc. **A148**, 225 (1935); L. R. Hafstad and M. A. Tuve, Phys. Rev. **48**, 306 (1935); R. B. Roberts and N. P. Heydenburg, Phys. Rev. **53**, 374 (1938); Curran, Dee, and Petrzilka, Proc. Roy. Soc. **A169**, 269 (1938); Fowler, Lauritsen, and Lauritsen, Rev. Mod. Phys. **20**, 236 (1948); R. Tangen, Kgl. Norske Vid. Sels. Skrifter NR 1 (1946).

[5] W. A. Fowler and C. C. Lauritsen, Phys. Rev. **76**, 314 (1949).

[6] K. Seigbahn and H. Slatis, Arkiv. f. Ast. Math. Fys. **32A**, No. 9 (1945).

[7] Hornyak, Dougherty, and Lauritsen, Phys. Rev. **74**, 1727 (1948).

counting rate by a factor of two without appreciably altering the sensitivity of the counter to beta-radiation incident on the window. Although the "plateau" of these counters extends only over an interval of 100 volts, they behave very stably under standard voltage regulation techniques.

To reduce the cosmic-ray background, the counter was surrounded by 2 inches of lead on the ends and underside, 4 inches on the sides, and $4\frac{1}{2}$ inches on top. A further reduction in the background was made by using a belt of ten anti-coincidence counters mounted as shown in Fig. 2. These measures reduced the background counting rate to $5\frac{1}{2}$ counts per minute. This extremely low rate was maintained in several counters over an extended period of time. Counting rates appreciably above background were measured above 90-kev bombarding energy. Bombarding energies were limited to a maximum of 128 kev by the high voltage rectifier arrangement used, and by breakdown of the accelerating column.

YIELD MEASUREMENTS

The thick target yield curve obtained is shown in Fig. 3. Different runs were made with different bombardment periods and proton currents. In order that all of the results might be plotted on the same curve for comparison, the data have been corrected to give the values which would have been obtained if the bombardment had been made for an infinite length of time using 100 μa of proton current. The results thus give the saturation yield in disintegrations per minute for this current or the counts per 6000 microcoulombs of protons. The probable error indicated represents the statistical fluctuation due to the small numbers of counts recorded. The curve which is drawn through the points is a calculated thick target yield curve fitted near 110 kev. It will be discussed in more detail in a later section.

Since the counting rates measured were only slightly above background, the statistical errors involved were large, and considerable thought was given to the problem of making the measurements in such a way as to obtain the greatest accuracy. A fundamental consideration was the fact that observations could be made only with the high voltage supply completely cut off. Methods of rapidly alternating bombarding and observing periods were not considered practical because of the necessity of stabilizing the voltage and focusing the beam for each run. It was arbitrarily decided to bombard for a reasonable period of time, usually three half-lives with the maximum available current. The problem then reduced to choosing the time of observation, T, so that the statistical error in the yield measurement was a minimum when background was taken into account by subtracting the average number of background counts expected during T from the observed number of counts. That T has an optimum value is clear from the fact that for small T a large error arises from the large random fluctuations in the true counts while for large T the absolute (not relative!) statistical fluctuations in the background introduce an excessive error.

To make the calculation more explicit we assume an average exponential decay rate $\bar{n}$ during observation

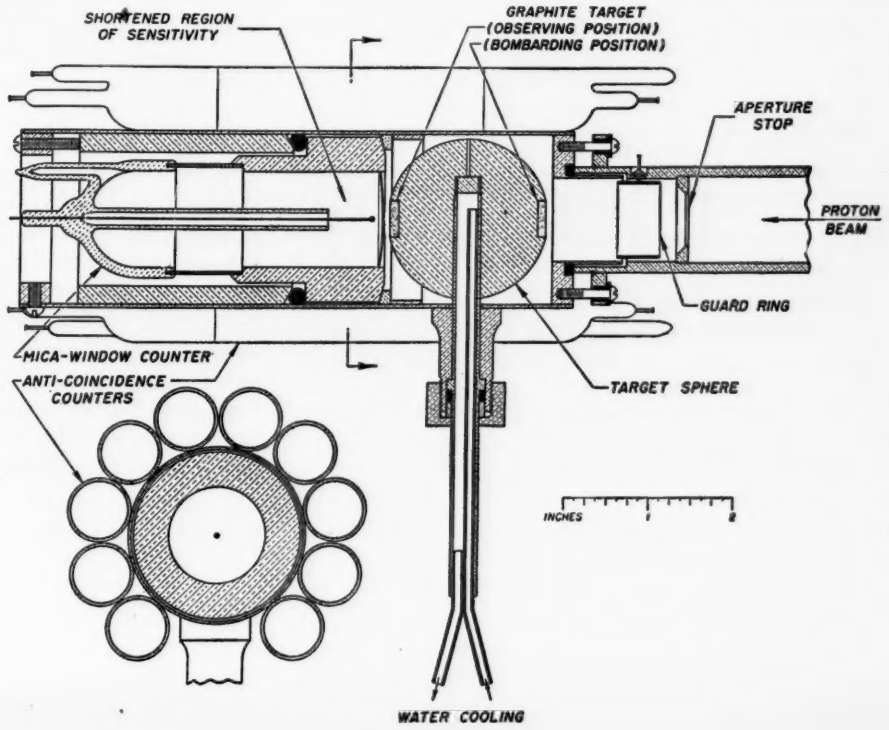

FIG. 2. Target support and detecting arrangement.

given by

$$\bar{n}=\bar{n}_0 e^{-t/\tau} \tag{3}$$

in the presence of an average background rate $\bar{n}_b$, which has been accurately determined in auxiliary measurements. The mean life of the activity, 14.6 minutes, is designated by τ. It is desired to determine as accurately as possible the average counting rate, $\bar{n}_0$, at the end of bombardment or the beginning of observation. The time elapsed between shutting off the high voltage and starting the counters was negligible. If $\bar{N}$ is the average total number of counts observed in time T, then $\bar{n}_0$ is given by

$$\bar{n}_0=[\bar{N}-\bar{n}_b T]/[\tau(1-e^{-T/\tau})]. \tag{4}$$

The relative probable error, δ, in $\bar{n}_0$ is given by the square root of the sum of the squares of the errors in $\bar{N}$ and $\bar{n}_b T$ divided by the counts above background and is thus given by probability theory as

$$\delta=0.6745\frac{(\bar{N}+\bar{n}_b T)^{\frac{1}{2}}}{\bar{N}-\bar{n}_b T}$$

$$=0.6745\frac{[2\bar{n}_b T+\bar{n}_0\tau(1-e^{-T/\tau})]^{\frac{1}{2}}}{[\bar{n}_0\tau^{\frac{1}{2}}(1-e^{-T/\tau})]}. \tag{5}$$

Choosing T so as to make the relative error a minimum,

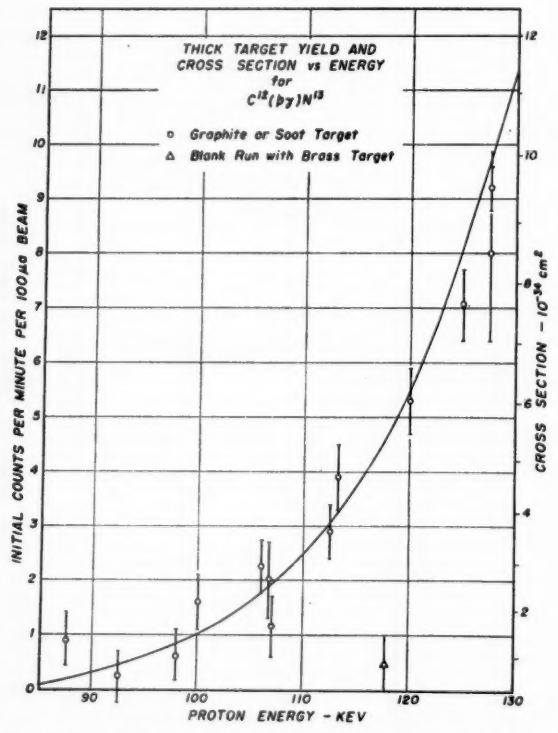

FIG. 3. Thick target yield curve for the reaction $C^{12}(p\gamma)N^{13}$ showing the initial counting rate in positrons from N^{13} per minute per 100 μa beam as a function of proton energy in the laboratory system. The left-hand ordinate also gives approximately the yield in positrons per 10^{16} protons over the whole sphere while the right-hand ordinate has been adjusted to give the cross section of the reaction.

results in the equation

$$\frac{\bar{n}_0}{\bar{n}_b}=2\frac{e^x-1-2x}{1-e^{-x}}, \tag{6}$$

where x is the optimum T expressed in mean lives. The minimum error is given by

$$\delta_{\min}=0.6745\left[\frac{1}{2\bar{n}_b\tau}\frac{e^x-1-x}{(e^x-1-2x)^2}\right]^{\frac{1}{2}}$$

$$=0.6745\left[\frac{1}{\bar{n}_0\tau}\frac{(e^x-1-x)(1-e^{-x})}{(e^x-1-2x)}\right]^{\frac{1}{2}}. \tag{7}$$

The optimum counting time expressed in mean lives is determined by the initial decay rate divided by the background counting rate. Solution of the above equation for x indicates that for initial counting rates less than or equal to several times the background the minimum error is obtained if counts are recorded for approximately 1.4 mean lives or two half-lives. In this time three-quarters of the maximum possible number of counts will be recorded. Under these conditions the percentage error is approximately equal to $1.2\,(\bar{N}-\bar{n}_b T)^{-\frac{1}{2}}$ for $\bar{n}_0\sim\bar{n}_b$ or approximately twice that expected for no background.

In order to obtain the thick target yield in disintegrations per proton, a number of corrections must be made. The initial decay rate given by Eq. (4) must be increased by a factor

$$\bar{n}_0(\infty)/\bar{n}_0(t)=1/(1-e^{-t/\tau}) \tag{8}$$

to account for the fact that the equilibrium concentration of N^{13} nuclei was not attained during the finite bombardment time t. For t equal to three half-lives as used in most of these measurements

$$\bar{n}_0(\infty)/\bar{n}_0(t)=1.14. \tag{8'}$$

In what follows a factor f will be used to represent the fraction of the disintegration positrons which are registered by the counting circuits. This factor takes into account the solid angle subtended by the counter, the counter efficiency, backscattering in the target and the fraction of the positrons which are missed due to absorption in the mica window and to the N^{13} nuclei which escape from the target before disintegrating. Because of the low counting rates involved, a resolving time correction is not necessary. The equilibrium decay rate is, therefore, given by

$$\bar{n}_0(\infty)=\frac{\bar{N}_t-\bar{n}_b T}{\tau(1-e^{-T/\tau})(1-e^{-t/\tau})}, \tag{9}$$

and the thick target yield by

$$Y=\bar{n}_0(\infty)/fI\times 0.267\times 10^{-14}, \tag{10}$$

where I is the analyzed proton current in micro-amps.

It will be noted that $\bar{n}_0(\infty)$ is expressed in counts per minute. The left-hand ordinate of Fig. 3 gives the yield, Y, in disintegrations per 10^{16} protons to a good approximation.

DETERMINATION OF THE COUNTING EFFICIENCY

The factor f representing the fraction of disintegrations which are observed will now be discussed. The positron spectrum[7] shows that less than 1 percent of the positrons have energies below 100 kev. The mica window of the counter has a thickness of 2 mg/cm^2 which is capable of stopping only a small fraction of the positrons having this energy. Absorption in the counter window may, therefore, be neglected.

There is considerable evidence that only a small amount of N^{13} leaves the target. Roberts and Heydenburg[4] estimate that the counting rate is decreased about 10 percent by the loss of active nitrogen. In their investigation of the carbon reaction above 300 kev, Fowler, Lauritsen, and Lauritsen[4] found no evidence for any loss greater than 10 percent as long as the targets remained at room temperature under bombardment. In order to reduce any loss of nitrogen in the low voltage experiments, the target sphere was water-cooled. The same yields were obtained within experimental error for targets made of graphite, soot, and the black deposit formed on the brass surface of the sphere by prolonged bombardments. The fact that the yield is independent of the physical form of the carbon is some evidence that no large amount of active nitrogen leaves the target.

Evidence concerning the N^{13} loss can also be obtained from the rate of rise of activity during bombardment and from the rate of decay after bombardment. In these experiments most of the bombardment times were 30 minutes but these gave results not significantly different than the few taken at 10 and 20 minutes on the assumption of a 10-minute half-life. Records were kept of the counts after bombardment *versus* time in all individual measurements with the results that 649 ± 17 positrons were counted in the first ten minutes after bombardment, 283 ± 11 in the second ten minutes and 141 ± 8 in the third ten minutes. These results establish a half-life of 9 ± 1 minutes again consistent within 10 percent of the known value.

Back-scattering of a fraction of those positrons which leave the surface layer in the direction of the target away from the counter will increase the number of counts. This subject has been investigated experimentally for RaE β-rays by Schonland for normal angles of incidence and corrected by Chalmers for all angles as in an active surface layer on a backing. The results indicate reflection corrections of 26 percent for Al and 58 percent for Cu.[8] Since the RaE β-rays are not markedly different than those from N^{13} we estimate a correction of 15 percent for N^{13} in the carbon targets. As this correction is of the same order of magnitude and opposite to that for N^{13} loss we have not made any over-all correction for the two effects.

The effective aperture and counter efficiency were examined in the experiment illustrated in Fig. 4. The beta-particles from a RaD source were collimated by a lead canal so as to produce a beam having a width of about one millimeter. The alpha-particles were stopped by a thin aluminum foil so that the resulting beam consisted only of beta-particles having an energy comparable to that of the N^{13} positrons. The source and collimator could be rotated about an axis perpendicular to the beam and to the axis of the counter. This axis was located 3 mm from the plane of the periphery of the mica window so that the particles from the beam entered the counter at the same angles as did the N^{13} positrons. The counting rate was measured as a function of the angle of incidence of the beam, giving the curves shown in Fig. 4. Three counters were measured in this fashion. The special low background counter used in the measurements of the carbon reaction and having 13 mm of exposed central wire was compared with two standard counters having 50 mm of exposed wire.

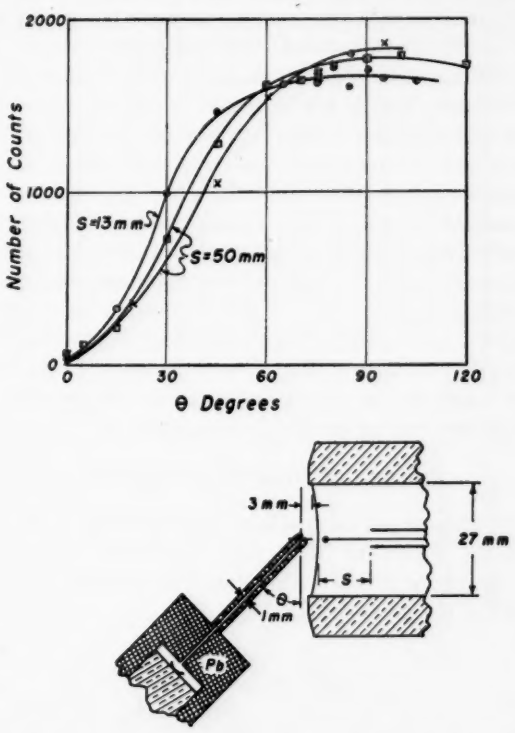

FIG. 4. Measurement of the counting efficiency. The sensitivity of mica-window beta-ray counters was explored with a collimated beam of RaD beta-particles. The special low background counter used in measuring the N^{13} activity had 13 mm of exposed central wire. Sensitivity curves for two standard counters having 50 mm of exposed wire are shown for comparison.

The maximum counting rate is nearly the same for each of the standard counters but is slightly less for the special low background counter. This difference indicates that the active volume of the low background

[8] Rutherford, Chadwick, and Ellis, *Radiations from Radioactive Substances* (Cambridge University Press, London, 1930), p. 420.

counter is sufficiently shallow that an appreciable fraction of the beta-particles pass through without being counted. It is also to be noted that the curve of the low background counter rises more sharply than do those of the standard counters. This arises from the fact that this counter was filled to slightly higher gas pressure. The curve for the low background counter reaches half-sensitivity at an angle of 27° corresponding to a path length within the counter of 7 mm. Since the active length of this counter is likely to be not much greater than the 13 mm length of exposed center wire, it is not unreasonable that an appreciable fraction of the particles pass through this counter without being counted. On the other hand, particles entering along the axis of the standard counters are almost certain to be counted.

The curve for the low background counter represents its counting efficiency as a function of the angle of incidence, the maximum of the standard counter curves corresponding to 100 percent efficiency. Using this curve as a weight function and integrating over all angles gives the effective aperture of the counter. A solid angle of 3.3 steradians is thus obtained corresponding to a counting efficiency of 26 percent on the assumption that the positrons are emitted with intensity independent of angle. The curves of Fig. 4, and hence the efficiency, were found to be nearly independent of the counter voltage within the limits of the plateau.

CROSS-SECTION CALCULATIONS

For purposes of comparison with the results obtained from the resonance in the $C^{12}(p\gamma)N^{13}$ reaction at 456 kev we use the Breit-Wigner one-level dispersion formula for the cross section, *viz*:

$$\sigma=\pi\lambda^2\frac{\omega\Gamma_\gamma\Gamma_p}{(E_R-E)^2+\Gamma^2/4}, \tag{11}$$

where λ=wave-length of incident protons in CM system, Γ_γ=gamma-ray width, Γ_p=proton width, $\Gamma=\Gamma_p+\Gamma_\gamma$, E=proton energy, E_R=proton energy at resonance.

The statistical factor ω is given by

$$\omega=[2J+1]/[(2s+1)(2i+1)],$$

where J=spin of compound nucleus, s=spin of incident particle, i=spin of target nucleus. For C^{12}, $i=0$ and hence for s wave protons, $J=s$ and $\omega=1$.

At low energies both Γ_p and Γ_γ are negligible compared with E_R and so

$$\sigma=\pi\lambda^2[(\omega\Gamma_\gamma\Gamma_p)/(E_R-E)^2]. \tag{11'}$$

Γ_γ is nearly independent of E since it depends essentially on the quantum energy which increases only slowly with E. However Γ_p is proportional to the Gamow barrier penetration factor, P, and the proton velocity and can be written as

$$\Gamma_p=\gamma_p E^{\frac{1}{2}}P, \tag{12}$$

where γ_p is the width without barrier evaluated at a velocity corresponding to an energy of 1 Mev if E is in Mev.[9] It is independent of E.

For low energies P is given approximately by

$$P=(g/g+1)(E_B/E)^{\frac{1}{2}}\exp(-\pi g[(E_B/E)^{\frac{1}{2}}-4/\pi]), \tag{13}$$

where

$$g=\left(\frac{2\mu Z_1Z_0e^2R}{\hbar}\right)^{\frac{1}{2}}=0.312\left(Z_1Z_0A_1A_0\frac{A_1^{\frac{1}{3}}+A_0^{\frac{1}{3}}}{A_1+A_0}\right)^{\frac{1}{2}}$$

$\approx 0.55Z_0^{\frac{1}{2}}$ for light elements under proton bombardment, and

$$E_B=2m_0c^2\frac{Z_1Z_0}{A_0}\frac{A_1+A_0}{A_1^{\frac{1}{3}}+A_0^{\frac{1}{3}}}=1.02\frac{Z_1Z_0}{A_0}\frac{A_1+A_0}{A_1^{\frac{1}{3}}+A_0^{\frac{1}{3}}}\text{ Mev}$$

$\approx 0.33Z_0$ Mev for light elements under proton bomment.

In the above expressions subscripts zero refer to target nuclei, subscripts one to incident particle, μ is the reduced mass of the system, R the radius at which nuclear forces set in, E_B is the barrier height or Coulomb potential at R and g is a function independent of E but not of the charge Z and atomic weight A of the interacting nuclei. E_B and E are measured in the laboratory system.

For any given reaction we can thus write Γ_p as a function of energy of the proton as

$$\Gamma_p=a\gamma_p\exp(-bE^{-\frac{1}{2}}), \tag{14}$$

where

$$a=\frac{g}{g+1}e^{A_0}E_B^{\frac{1}{2}}\approx\frac{0.32Z_0}{0.55Z_0^{\frac{1}{3}}+1}\exp(2.2Z_0^{\frac{1}{3}}),$$

$$b=\pi gE_B^{\frac{1}{2}}\approx Z_0\text{ Mev}.$$

Both a and b are independent of E. Since the term multiplying the exponential in a is ~ 1 for light elements under proton bombardment, we can write as a very rough approximation

$$\Gamma_p\approx\gamma_p\exp(-Z_0E^{-\frac{1}{2}}+2.2Z_0^{\frac{1}{3}}) \tag{14'}$$
$$=\gamma_p\exp(-6E^{-\frac{1}{2}}+5.4)\quad\text{for}\quad C^{12}+H^1.$$

The quantity $\pi\lambda^2$ is given by

$$\pi\lambda^2=(\pi\hbar^2/2\mu E)(A_1/A_0+1) \tag{15}$$
$$=0.65/A_1E(A_1/A_0+1)^2\text{ barns},$$

so that

$$\sigma=(k\Gamma_\gamma\gamma_p/E)\exp(-bE^{-\frac{1}{2}}), \tag{16}$$

where

$$k=\frac{0.65}{A_1}\left(\frac{A_1+A_0}{A_0}\right)^2\frac{\omega a}{(E_R-E)^2}\sim\frac{\omega e^{2.2Z_0^{\frac{1}{3}}}}{E_R^2}.$$

[9] R. F. Christy and R. Latter, Rev. Mod. Phys. **20**, 185 (1948).

k is substantially independent of E for E_R not in the stellar range.

The thick target yield is obtained by integrating the ratio of the disintegration cross section to the stopping cross section per disintegrable nucleus, ϵ, over the energy of the incident particle, *viz*:

$$Y=\int_0^E \frac{\sigma}{\epsilon}dE. \tag{17}$$

In the region near 100 kev the stopping cross section of protons in air is approximately constant and the stopping power of carbon relative to air is not greatly dependent on E so that ϵ can be taken as a constant and one obtains, substituting $b\approx Z_0$,

$$Y=2\sigma(E^{\frac{1}{2}}/\epsilon Z_0)(1-E^{\frac{1}{2}}/Z_0+\cdots). \tag{18}$$

From the yield one can thus determine σ as

$$\sigma=Y(\epsilon Z_0/2E^{\frac{1}{2}})(1+E^{\frac{1}{2}}/Z_0+\cdots)$$
$$=3Y(\epsilon/E^{\frac{1}{2}})(1+E^{\frac{1}{2}}/6+\cdots) \tag{18'}$$

for $C^{12}+H^1$ with E in Mev

and ϵ in Mev-cm^2. The stopping cross section for air[10] at 100 kev is 1.51×10^{-20} Mev-cm^2 while the stopping power of carbon is 0.96. The stopping cross section of carbon per C^{12} nucleus (98.9 percent) is thus $1.51\times0.96/0.989\times10^{-20}=1.46\times10^{-20}$ Mev-cm^2. In Fig. 3 the right-hand scale has been corrected to read directly in cross section using the coefficients of Y in the above expression for σ. The curve drawn through the data is of the form of (18) for Y or (16) for σ. It has been fitted over the lower half of the energy range and can be expressed with numerical coefficients as:

$$Y=5.6E^{\frac{1}{2}}(1-E^{\frac{1}{2}}/6)\exp(-6E^{-\frac{1}{2}})\times10^{-8}\beta^+/p, \tag{19}$$

or

$$\sigma=(0.0024/E)\exp(-6E^{-\frac{1}{2}})\text{ barn}. \tag{20}$$

The cross section is 1.0×10^{-10} barn at 96 kev and rises to $8.5\pm1\times10^{-10}$ barn at 128 kev. The empirical curve is slightly high at 128 kev.

The cross section constants evaluated at the 456-kev resonance[5] are $\Gamma_\gamma=0.63$ ev, $\Gamma_p=35$ kev and $\gamma_p=1680$ kev. Using these constants one calculates a numerical coefficient of 0.0014 in Eq. (20). This agreement within a factor of two is satisfactory considering the single level approximation made above. As we have neglected the dependence of Γ_γ on E as well as the resonance denominator $(E_R-E)^{-2}$ in the approximations leading to (20) it is clear that the variation of σ with E is not completely described by the single level dispersion formula. The data are consistent with the inclusion of an interference term $(E_R-E)/[(E_R-E)^2+\Gamma^2/4]$ in σ but is not accurate enough to give quantitative details. Extrapolating expression (20) to lower energies, it is found that $\sigma=10^{-16}$ barn$=10^{-40}$ cm^2 at 30 kev.

EXPERIMENTAL ERRORS

A number of sources of error are involved, most of which may be placed within fairly well defined limits. Certain other sources of error are believed to be small but are not easily estimated; these are all such as to give too small a computed cross section.

Examination of Fig. 3 shows that the yield is very sensitive to the proton energy; a 1 percent error in the voltage measurement is equivalent to a 10 percent error in the yield. A Type K potentiometer was used to measure the voltage developed across a precision resistor by the current from a 120-megohm stack of high voltage resistors in parallel with the accelerator. The calibration depends upon the accuracy of the 20-megohm precision resistor (<1 percent error) which was used as a standard to measure the 120-megohm stack. This 120-megohm stack was constructed from 1 percent accuracy 1-megohm wirewound resistors and the measurement of each section agreed within a few tenths of one percent of the nominal value. The voltage was continuously adjusted during each run so as to maintain a steady value. Corona currents to junctions between the sections of the 120-megohm stack were eliminated by maintaining large clearances between the stack and other conductors, and by wrapping the junctions with dental dam. It is believed that errors in cross section due to inaccuracy in the voltage measurement amount to less than 10 percent.

The proton current meter was calibrated and introduces negligible uncertainty. The stopping cross section for carbon may be in error by 10 percent according to Livingston and Bethe.[10] The measurement of the fraction of counts recorded would appear to introduce only a few percent error.

Blank runs have been made using the brass target sphere as a target instead of carbon. It was necessary to install a dry ice trap in the vacuum system to reduce the deposition of carbon upon the brass. The trap decreased the pressure indicated by the ion gauge by a factor of four, and bombardment periods of over ten minutes could be used without forming a detectable carbon deposit. One such blank run is shown in Fig. 3.

The positron radiation is not believed to be accompanied by any other kind of radioactivity which could cause spurious counts. The counter pulses were watched on an oscilloscope to check on the possibility of counter breakdown. The counter plateau was checked at frequent intervals to make sure that the counter was performing properly. The negative results obtained from the blank runs further indicate that the counters were functioning properly. The guard-ring potential of the target holder was adjusted so as to be well above the value required to return all secondary electrons to the target.

The statistical errors involved are indicated in Fig. 3. If it is assumed that the slope of the thick target yield curve is given correctly by Eq. (18') over the energy range explored, the cross section at 100 kev may be evaluated with an uncertainty of about 20 percent arising from statistical errors.

[10] M. S. Livingston and H. A. Bethe Rev. Mod. Phys. **9**, 245, (1937).

DISCUSSION

Any discussion of the astrophysical implications of the results reported here must begin by emphasizing the fact that these results constitute but a small fragment of the data which must be obtained in order to reach a detailed understanding of the operation of the carbon-nitrogen cycle in stellar interiors. Ideally one requires for such an understanding the variation of all the cross sections with energy over the entire range of energies which may be significant in the stellar problem say from a few kilovolts up to 100 kev. Only in this way will the contributions of resonances lying in this region be determined with certainty. This aspect of the problem has been discussed by Gamow and Teller.[11] In these experiments an attempt has been made to extend the direct cross-section measurements for one of the reactions of the carbon-nitrogen cycle to the lowest possible energies at which statistically reliable results could be obtained with the techniques developed and to compare these results with those calculated from constants determined at the 456-kev resonance using the Breit-Wigner single level dispersion formula. The measured cross section is somewhat less than twice that calculated and taking all possible sources of uncertainty into consideration one cannot exclude the possibility that the 456-kev resonance alone contributes to the yield near 100 kev. At the same time it is clear that in this region the effect of other resonances is at most of the same order of magnitude as that of the 456-kev resonance. Professor R. F. Christy has considered the implications of this fact in regard to stellar cross sections, bearing in mind that resonances in a limited region above the mean stellar energies may contribute markedly to stellar processes and yet not be more important in the thick target yield at 100 kev than the 456-kev resonance. He concludes that resonances which would completely invalidate the extrapolation of Eq. (20) to stellar temperatures cannot be excluded in the region from 10 to 40 kev. Since the average level spacing in the compound nucleus, N^{13}, for the low excitations available from $C^{12}+H^1$ is at least as great as 1 Mev experimentally, and with good theoretical justification, it can be argued that the chance of a level falling within this narrow region is small but this small chance must not be overlooked in discussions of the astrophysical implications. The experimental evidence is that no resonance levels other than the 456-kev resonance (2.34-Mev excitation in N^{13}) have been found in the $C^{12}(p\gamma)N^{13}$ reaction from 0.3 to 1.3 Mev* and no evidence of excited states in N^{13} has been found in the $C^{12}(dn)N^{13}$ reaction in spite of the fact that neutrons could be emitted accompanying excited states up to 2.0 Mev.

It has been pointed out by Fowler, Lauritsen, and Lauritsen that the single level resonance formula using constants determined at the 456-kev resonance gives a stellar cross section for $C^{12}(p\gamma)$ about 40 times that used by Bethe in his original calculations. The results reported here confirm this high value and actually indicate a somewhat larger cross section. The lifetime of the individual C^{12} nucleus under Bethe's conditions in the center of the sun is to be taken as $\sim 5\times 10^4$ years rather than 2.5×10^6 years.

The reaction $C^{13}(p\gamma)N^{14}$ shows resonance[5] at 554 kev with constants $\Gamma_\gamma = 15$ ev, $\Gamma_p = 40$ kev, and $\gamma_p = 880$ kev. With these constants the *single-level* formula predicts a rate for this reaction 8.5 times that for $C^{12}(p\gamma)N^{13}$ at stellar temperature and thus an abundance ratio of 8.5:1 for $C^{12}:C^{13}$ in stellar interiors. The results reported here would lower this figure somewhat. It has not been found possible to measure the $C^{13}(p\gamma)$ cross section at low voltages because it is not followed by radioactivity. It will remain for investigations of such reactions as $C^{13}(dn)N^{14}$ with 3.0-Mev deuterons and $B^{11}(\alpha n)N^{14}$ with 10-Mev alpha-particles to reveal details of the energy levels in N^{14} in the relevant energy range. It is probable, however, that the single-level expression will not give correct results since the average level separation[12] in N^{14}, the compound nucleus, is certainly less than 0.5 Mev at the high excitation, ~ 8 Mev, produced by $C^{13}+H^1$. A considerably higher cross section for $C^{13}(p\gamma)$ at stellar energies than that given by the single level expression based on the level at 554 kev is not to be ruled out. Considerations of level density and resonance effects aside, the C^{13} cross section should be higher than that for C^{12} by the ratio of the cube of the quantum energies of the capture radiations assuming both to be electric dipole and with the same dipole moment. This ratio is $(8.07/2.33)^3 = 41$. The experimental radiation widths are in the ratio $15/0.63 = 24$. For this reason, as originally pointed out by Bethe, the terrestrial abundance $C^{12}:C^{13} = 90$ and the abundance ratio observed in most stars $C^{12}:C^{13} \geqslant 50$ are not in contradiction with the carbon-nitrogen cycle. We must emphasize, however, that only by measurements at low energy can the cross sections and thus the abundances in stellar interiors be determined. In addition we must note that there is considerable question as to whether terrestrial abundances or those in stellar atmospheres should correspond to those in stellar interiors.

Experiments now under way in this laboratory may clarify these problems and this paper is to be considered a report on progress to date and a discussion of the experimental problems arising in the investigation of the carbon-nitrogen cycle. It is a pleasure to acknowledge discussions of the contents of this paper with Professors C. C. Lauritsen, R. F. Christy, Jesse L. Greenstein and Father J. D. O'Reilly.

This work was assisted by the Joint Program of the ONR and the AEC.

[11] G. Gamow and E. Teller, Phys. Rev. **53**, 608 (1938).

* A level at 1.697 Mev has been recently found by the MIT Nuclear Cross Sections Group (Progress Report, July 1, 1949). This level has a width of 74±9 kev and a thick target yield 1.3 times that at 456 kev. These results give $\gamma_p = 127$ kev and $\Gamma_\gamma = 1.3$ ev. The contribution to low energy cross sections is <1 percent that of the 456-kev level.

[12] T. Lauritsen, "Energy Levels of Light Nuclei," Preliminary Report No. 5, Nuclear Science Series, National Research Council.

On the Angular Distribution of Two-Photon Annihilation Radiation[1]

S. DeBenedetti,* C. E. Cowan,** W. R. Konneker, and H. Primakoff
*Department of Physics, Washington University,*** St. Louis, Missouri*

(Received August 11, 1949)

An experimental determination, using anthracene scintillation counters in coincidence, has been made of the departure from antiparallelism of the two photons in the pair annihilation process in an Au absorber. The observed mean angular departure, $\approx 1/137$ radians, arises from the motion of the centers of mass of the annihilating pairs; the mean momentum of these is found from the experimental data to be equal to 1,2 mc/137, a value to be compared with a lower limit of 0.8 mc/137 obtained from an included theoretical discussion in which the momentum probability amplitudes of the annihilating electrons and positrons (in the absorbing metal) are estimated and appropriately combined. In these estimates it is shown that the positrons become thermalized by collisions with the vibrating lattice atoms in times considerably shorter than the annihilation time, so that only their zero point motions, together with the zero point motions of the annihilating (valence) electrons, effectively contribute to the momenta of the centers of mass of the annihilating pairs.

WHILE testing with annihilation radiation a circuit selecting the coincident pulses from two scintillation counters, it was realized that the angular correlation between the two annihilation photons could easily be measured with far greater accuracy than previously reported.[2] As a result, it was considered that a precise measurement of the angular correlation, which would throw some light on the momentum distribution of the centers of mass of the annihilating pairs, and hence, on their mean momentum, was worth attempting. In particular, it was thought of interest to investigate the agreement of the so deduced value for the mean momentum of the centers of mass with the value for the same quantity recently obtained by DuMond, Lind, and Watson from an analysis of the shape of the annihilation γ-ray line.[3] It was also thought of interest to present a theoretical treatment and to compare the results of theory and experiment.

EXPERIMENTAL ARRANGEMENT AND RESULTS

Two anthracene detectors[4] were used with type 1P-21 photo-multipliers, whose pulses were amplified with amplifiers of 0.2 μsec. rise time, and fed to a coincidence circuit of 0.3 μsec. resolving time.

The pieces of anthracene were in contact with the envelope of the multiplier tubes. In order to minimize the effect of scattering, light tightness was insured by wrapping the tubes with rubber tape, and the pieces of anthracene were covered only with an aluminum foil 1 mil thick. The surfaces of the anthracene samples located directly under the aluminum foil were plane and their positions could easily be located from the outside.

The source of positrons consisted of thin "shavings" (two or three pieces 1×3 mm and a few mils thick) from a deuteron-bombarded copper target, rich in the 14-hour Cu^{64} activity. The copper "shavings" were introduced in a small gold tube, obtained by wrapping sixfold a 1 mil gold foil. This tube was subsequently flattened and effectively constituted a source of annihilation gamma-rays of thickness of only a few tenths of a mm, since, as is easily seen, most of the positrons were absorbed in the inner layers of the gold.

Several measurements of the angular distribution were performed with the source at different distances from the detectors. During the final experiments, whose results are shown in Fig. 1, the distance between the source and either detector was 120 cm (Fig. 2). For maximum efficiency and best angular definition, the gamma-rays from the source were made to traverse the detectors along their longest dimension. In these conditions the detectors, seen from the source, subtended an angle of 4×10^{-3} rad. $= 15'$ in the vertical direction, and an angle of 10^{-2} rad. $= 40'$ in the horizontal direction; while the source, seen from the detectors, covered an angle of only a few minutes in the vertical direction and of about $15'$ in the horizontal direction. The vertical alignment of the apparatus was made by means of a cathetometer and the measurements were performed by displacing one of the detectors vertically. The displacements were measured with the cathetometer from the position where the source and the upper surfaces of the detectors were in the same horizontal line; this position corresponds to the zero on the abscissas of Fig. 1, downward displacement of the detector being taken as positive.

The peak of the curve occurs for a negative displacement of about 0.6 cm, corresponding to the position at which the line joining the centers of the detectors passes through the source. The coincidence rate was ≈ 60 c/m at the peak, and ≈ 1 c/m at a displacement 3 cm away from the peak. The curve is practically symmetrical about the peak; however, some errors

[1] Preliminary note in Phys. Rev. **76**, 440 (1949).
* Now at Carnegie Institute of Technology, Pittsburgh, Pennsylvania.
** Now at Los Alamos Scientific Laboratory, Los Alamos, New Mexico.
*** Assisted by the Joint Program of the ONR and the AEC.
[2] R. Beringer and C. G. Montgomery, Phys. Rev. **61**, 222 (1942). A note by I. Pomeranchuk, J. Exp. Theor. Phys. (Russian) **19**, 183 (1949) on the "Mean life of slow positrons," received here after the present work was largely completed, contains a very brief discussion of the theory and mentions experiments by N. A. Vlassov and E. A. Tzirelson (Dokl. Akad. Nauk U.S.S.R. **59**, 879 (1948)) with results apparently in agreement with ours.
[3] DuMond, Lind, and Watson, Phys. Rev. **75**, 1226 (1949).
[4] Kindly supplied by P. R. Bell of the Oak Ridge National Laboratory.

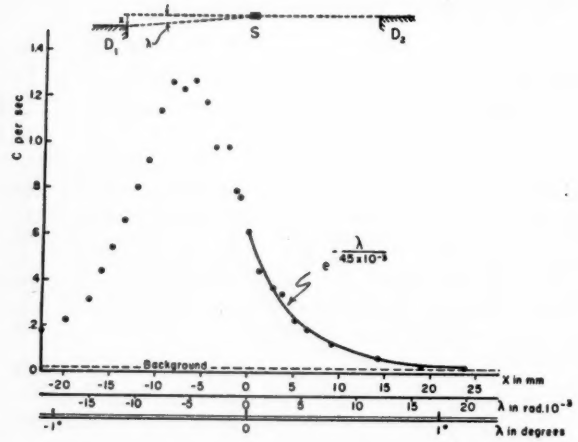

FIG. 1. Photon-photon coincidences as a function of the position of one of the detecting counters.

(due to imperfect alignment of the lower surface of the detectors, to scattering from the multiplier tubes, and to the direct response of the multipliers to gamma-rays) were expected on the negative side, and only the positive (right-hand) side of the peak was carefully studied. The fact that the counting rate does not vanish for positive displacements conclusively indicates that the annihilation gamma-rays are not always emitted in exactly opposite directions.

The possible influence of Compton scattering on the annihilation gamma-rays was studied experimentally by increasing the thickness of the gold absorber and by inserting a number of thin aluminum and paper foils along the path of the gamma-rays. Since the shape of the curve for positive displacements was not sensibly affected, we feel justified in assuming that the effect of Compton scattering can be neglected in the analysis of the observed distribution.[5]

THE MEAN MOMENTUM OF THE CENTERS OF MASS OF THE ANNIHILATING PAIRS

Let us call λ the experimentally measured angle between the lines connecting the source with the upper surfaces of the two detectors, ω the vertical angular width of the detectors, and $C(\lambda)$ the observed coincidence counting rate. Let us call $N(p)dp$ the number of annihilating pairs having center of mass momentum of magnitude between p and $p+dp$. We want to find a relation between the measured quantities and the function $N(p)$.

For this purpose let us first consider the function $N_z(p_z)$ expressing the distribution of the annihilating pairs according to their z (vertical) components of center of mass momentum, and observe that the horizontal angular aperture of our detectors is, on the one hand, so small that its square can be neglected, but, on the other, still so large compared to the angular aperture of the annihilation quanta that the problem can be treated in a vertical plane without too large errors. Then, since, p_z/mc is numerically equal to the vertical angle α (in radians) measuring the departure from 180° of the annihilation quanta, we can write:

$$C(\lambda)=\text{const.}\int_0^{\omega} d\beta \int_{\beta+\lambda}^{\beta+\omega+\lambda} N_z(\alpha)d\alpha,$$

so that after double differentiation, and apart from trivial constants,

$$[d^2C(\lambda)]/d\lambda^2=N_z(2\omega+\lambda)-2N_z(\omega+\lambda)+N_z(\lambda). \quad (1)$$

After $N_z(p_z)$ is obtained by means of this relation, $N(p)$ may be immediately computed from:

$$N(p)=-2p[dN_z(p)/dp].$$

The accuracy of our data hardly justifies the detailed application of this procedure, which will be used only as a guide in what follows. Since the experimentally determined $C(\lambda)$, for $\lambda>0$, can be closely approximated by (const.) $e^{-\lambda/\lambda_0}$, with $\lambda_0=4.5\times10^{-3}$ rad. (see Fig. 1), solution of the difference Eq. (1) immediately yields

$$N_z(\lambda)=(\text{const.})\lambda_0^{-2}(e^{-\omega/\lambda_0}-1)^{-2}e^{-\lambda/\lambda_0}$$
$$=(\text{const.}')e^{-\lambda/\lambda_0}. \quad (2)$$

Thus we can write $N(p)=(\text{const.})p\exp(-p/4.5\times10^{-3}$ mc). We will use this expression only for the determination of the average value of p, with the result

$$\bar{p}_{Au}=2\times4.5\times10^{-3}\text{ mc}=1.2\text{ mc}/137. \quad (3)$$

This value is in order of magnitude agreement with that obtained by DuMond, Lind, and Watson, from an analysis of the shape of the annihilation γ-ray line from a Cu absorber, viz.:

$$\bar{p}_{Cu}=8\times10^{-3}\text{ mc}=1.1\text{ mc}/137. \quad (4)$$

THEORETICAL ESTIMATE OF THE MEAN MOMENTUM OF THE CENTERS OF MASS OF THE ANNIHILATING PAIRS

In order to obtain a theoretical estimate of the mean momentum of the centers of mass of the annihilating pairs, $\bar{p}$, it is convenient to treat separately the contributions of the electron and of the positron.

Let us consider the positron first. We note that approximately 98 percent of the positrons reach the end of their "path of ionization" without suffering annihilation.[6] At the end of this path the positron kinetic

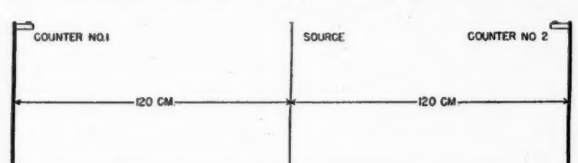

FIG. 2. Location of source and detecting counters in the final experiments.

[5] See also, DuMond, Lind, and Watson, reference 3, and J. W. M. DuMond, Phys. Rev. 75, 1266 (1949).

[6] W. Heitler, *Quantum Theory of Radiation* (Oxford University Press, London, 1944), p. 230 ff.

energy is of the same order of magnitude as that of the fastest electrons in the degenerate electron gas in the metal. Subsequent energy losses for the positron are then possible largely through inelastic collisions with the thermal lattice vibrations of the metal atoms. We shall show in what follows (see Appendix I) that, as a result of such inelastic collisions, the positrons attain thermal equilibrium with the lattice in a time short compared with the mean time for annihilation. Once thermalized, the positrons diffuse randomly through the metal without any further energy gain or loss on the average, and are eventually annihilated.

During their diffusion, the thermalized positrons preferentially occupy interstitial positions in the lattice as a consequence of the Coulomb repulsion of the positive metallic ions. We, therefore, describe the motion of these positrons by a wave-function which is essentially different from zero (and roughly constant), within any atomic polyhedron, only at distances from the nucleus greater than the positive ion radius. Thus, only electrons whose wave functions appreciably extend beyond the ionic volumes will effectively combine with the positrons in the annihilation process.[7] In the present case of Au, such electrons are those occupying the bands arising from the 6*s*, and, possibly the 5*d*, atomic orbitals.

We next present arguments (see below) indicating that, to a sufficient approximation for the purpose at hand, we may describe the motion of the 6*s* electrons by plane wave wave functions outside the ionic volumes, and may neglect the overlap between the 5*d* electron and the positron wave functions. With the electron and positron wave functions so specified we turn our attention to the matrix element for the two photon annihilation transition; this matrix element is seen, in accordance with radiation theory, to involve the above-mentioned electron and positron wave functions and the plane waves associated with the two emitted photons. The evaluation of the integral for this matrix element then yields, by standard perturbation theory, the probability for the annihilation of an electron and positron of given energies (or rather given wave numbers) with the simultaneous emission of two photons of given total momentum. Finally, we average this annihilation probability over the energy distributions (Fermi and Boltzmann, respectively) of the annihilating electrons and positrons; the result is $\mathfrak{N}(\mathbf{p})d\mathbf{p}$, the probability that the annihilation occurs with the total momentum $\mathbf{p}$ of the two emitted photons lying in the range $d\mathbf{p}$. Since $\mathbf{p}$, from the conservation of momentum in (any particular) annihilation process, is also the total momentum of the (particular) annihilating electron and positron, i.e., the momentum of the center of mass of the corresponding annihilating pair, a knowledge of $\mathfrak{N}(\mathbf{p})d\mathbf{p}$ immediately yields the pair's mean center of mass momentum, $\bar{p}$.

[7] See DuMond, Lind, and Watson, reference 3; Pomeranchuk, reference 2.

We may now proceed to obtain quantitative estimates of $\mathfrak{N}(\mathbf{p})$ and $\bar{p}$ in accordance with the scheme outlined in the preceding two paragraphs. First of all, ordinary statistical considerations indicate that:

$$\mathfrak{N}(\mathbf{p})d\mathbf{p}=\text{const.}\sum_{\mathbf{k}_+,\mathbf{k}_-}F_+(\mathbf{k}_+)F_-(\mathbf{k}_-)\,|\Phi_{\mathbf{k}_+,\mathbf{k}_-}(\mathbf{p})|^2d\mathbf{p}. \quad (5)$$

In Eq. (5), $F_\mp(\mathbf{k}_\mp)$ is the probability of the annihilating electron (positron) being in a state with wave number $\mathbf{k}_\mp$. Thus, since the positrons are supposed thermalized,

$$F_+(\mathbf{k}_+)=(\text{const.})\exp[-\epsilon_+(\mathbf{k}_+)/\kappa T],$$

while $F_-(\mathbf{k}_-)=\text{const.}$, for electron states in the completely filled $1s$, $2s$, $\cdots$, $5d$ bands, and

$$F_-(\mathbf{k}_-)=(\text{const.})\left\{\exp\left[\frac{\epsilon_-(\mathbf{k}_-)-\zeta(T)}{\kappa T}\right]+1\right\}^{-1}$$

for states in the half-filled $6s$ band; $\epsilon_\mp(\mathbf{k}_\mp)\approx\hbar^2k^2_\mp/2m$ is the energy of the $\mathbf{k}_\mp$ states (reckoned relative to the corresponding bottom-of-the-band zero-point energy).[8] The quantity $\Phi_{\mathbf{k}_+,\mathbf{k}_-}(\mathbf{p})$ is, apart from a constant, the matrix element (i.e. essentially the probability amplitude) for the emission of two photons with total momentum $\mathbf{p}$, as a result of the annihilation of an electron and a positron with wave numbers $\mathbf{k}_-$, $\mathbf{k}_+$.

Further, radiation theory indicates that (see Appendix II)

$$\Phi_{\mathbf{k}_+,\mathbf{k}_-}(\mathbf{p})=\int\psi_{\mathbf{k}_+}{}^*(\mathbf{r})\psi_{\mathbf{k}_-}(\mathbf{r})\exp(-i\mathbf{p}\cdot\mathbf{r})d\mathbf{r}. \quad (6)[9]$$

or, alternatively,

$$\Phi_{\mathbf{k}_+,\mathbf{k}_-}(\mathbf{p})=(2\pi)^3\int\varphi_{\mathbf{k}_+}{}^*(\mathbf{p}_+)\varphi_{\mathbf{k}_-}(\mathbf{p}_-)\times\delta(\mathbf{p}_++\mathbf{p}_--\mathbf{p})d\mathbf{p}_+d\mathbf{p}_-. \quad (7)$$

In Eqs. (6), (7), $\psi_{\mathbf{k}_\mp}(\mathbf{r})$, $\varphi_{\mathbf{k}_\mp}(\mathbf{r})$ are, respectively, the coordinate space and the momentum space wave functions of the annihilating electron and positron, appropriate to states of motion in the periodic potential of the lattice specified by wave number $\mathbf{k}_\mp$. The δ function in the integral of Eq. (7) expresses the conservation of momentum in any particular annihilation and justifies the additional interpretation of $\Phi_{\mathbf{k}_+,\mathbf{k}_-}(\mathbf{p})$ as the probability amplitude for the center of mass of the annihilating electron and positron (with wave numbers, $\mathbf{k}_-$, $\mathbf{k}_+$) having the momentum value $\mathbf{p}$.

[8] To a sufficient approximation, we may take throughout, as the effective crystal lattice mass of both the valence $6s$ electron and the positron, the free electron mass, m. This assumption is roughly justified, for the electron by the work of Krutter in reference 13 on the homologous case of Cu, and for the positron, by Eq. (23)–(25), below. It may also be mentioned that the general description used of the motion of a charged particle in the crystal lattice, the Bloch model, is an even better approximation for the positron than for the valence electron. This follows because of the absence, in the positron case, of exchange interactions (in the ordinary sense) with the electrons of the solid.

[9] Wave number units are used for the momenta $\mathbf{p}$, $\mathbf{p}_-$, $\mathbf{p}_+$.

To evaluate the integrals in Eq. (6) or in Eq. (7) for $\Phi_{\mathbf{k}+,\mathbf{k}-}(\mathbf{p})$ one recalls the Fourier expansions of coordinate space and momentum space wave functions in a periodic potential:

$$\psi_{\mathbf{k}\mp}(\mathbf{r})=\exp(i\mathbf{k}_{\mp}\cdot\mathbf{r})\sum_{\mathbf{g}\mp} v^{-1}\Big[\int_v \psi_{\mathbf{k}\mp}(\mathbf{r}') \times\exp[-i(\mathbf{k}_{\mp}\cdot\mathbf{r}'+2\pi\mathbf{g}_{\mp}\cdot\mathbf{r}')]d\mathbf{r}'\Big] \times\exp(2\pi i\mathbf{g}_{\mp}\cdot\mathbf{r}), \quad (8)$$

$$\varphi_{\mathbf{k}\mp}(\mathbf{p}_{\mp})=\sum_{\mathbf{g}\mp} v^{-1}\Big[\int_v \psi_{\mathbf{k}\mp}(\mathbf{r}') \times\exp[-i(\mathbf{k}_{\mp}\cdot\mathbf{r}'+2\pi\mathbf{g}_{\mp}\cdot\mathbf{r}')]d\mathbf{r}'\Big] \times\delta(\mathbf{k}_{\mp}+2\pi\mathbf{g}_{\mp}-\mathbf{p}_{\mp}), \quad (9)$$

v, and $\mathbf{g}_-$, $\mathbf{g}_+$, $\mathbf{g}$, being the volume of a unit cell, and reciprocal lattice vectors, respectively. Substituting Eq. (9) into Eq. (7), one then obtains:

$$\Phi_{\mathbf{k}+,\mathbf{k}-}(\mathbf{p})=(2\pi)^3\sum_{\mathbf{g}} v^{-1}\Big[\int_v \psi_{\mathbf{k}+}{}^*(r)\psi_{\mathbf{k}-}(\mathbf{r}) \times\exp[-i(\mathbf{k}_+ +\mathbf{k}_- +2\pi\mathbf{g})\cdot\mathbf{r}]d\mathbf{r}\Big] \times\delta(\mathbf{k}_+ +\mathbf{k}_- +2\pi\mathbf{g}-\mathbf{p}). \quad (10)$$

As already noted above, the integral in Eq. (10) for $\Phi_{\mathbf{k}+,\mathbf{k}-}(\mathbf{p})$ indicates that the annihilation probability effectively vanishes for all electrons except those in the $6s$ and, perhaps, the $5d$ bands, since it is only for these last that the corresponding $\psi_{\mathbf{k}-}(\mathbf{r})$ can overlap appreciably with the $\psi_{\mathbf{k}+}(\mathbf{r})$.

We must now specify quantitatively the $6s$ and the $5d$ electron wave functions and the positron wave function within a unit cell of the metal's crystal lattice. In accord with our previous assumption about the positron wave function and with the general method of Wigner and Seitz,[10] we may take:

$$\psi_{\mathbf{k}+}(\mathbf{r})\exp(-i\mathbf{k}_+\cdot\mathbf{r}) \quad (a)$$

spherically symmetric within the atomic polyhedron constituting the unit cell;

$$\psi_{\mathbf{k}+}(\mathbf{r})\exp(-i\mathbf{k}_+\cdot\mathbf{r})=0 \text{ for } r\leq r_i; \quad (b)$$

$$\partial/\partial r[\psi_{\mathbf{k}+}(\mathbf{r})\exp(-i\mathbf{k}_+\cdot\mathbf{r})]=0 \text{ at } r=r_p; \quad (c)$$

r_i and r_p are, respectively, the radii of the Au^+ ion and of a sphere equivoluminal with the atomic polyhedron. The conditions (a), (b), (c), yield for $r_i<r<r_p$,

$$\psi_{\mathbf{k}+}(\mathbf{r})\exp(-i\mathbf{k}_+\cdot\mathbf{r})=(\text{const.})\sin[\alpha(r-r_i)]/\alpha r$$

with $\alpha r_p=\tan[\alpha(r_p-r_i)]$,[11] which, for $(r_i)_{Au}\approx 1.0$ A° (see footnote 17), and $(r_p)_{Au}\approx 1.6$ A°, is not too badly approximated by replacing $\sin[\alpha(r-r_i)]/\alpha r$ by 1. This last approximation, which is adopted below, may actually be closer to the true $\psi_{\mathbf{k}+}(\mathbf{r})$ than the previous expression since: (a) the outer shells of the ion cannot be considered as absolutely impenetrable to the positron, and (b) once the positron does penetrate the ion more deeply it encounters an effective nuclear repulsion increasing much faster than (distance)$^{-2}$; both (a) and (b) tend to produce a more precipitate variation of $\psi_{\mathbf{k}+}(\mathbf{r})\exp[-i\mathbf{k}_+\cdot\mathbf{r})$ for $r\approx r_i$ than is described by $\sin[\alpha(r-r_i)]/\alpha r$,

As regards the Au $6s$ electron wave function, Wigner-Seitz-Slater type[12] calculations by Krutter[13] and by Tibbs[14] for the homologous case of Cu, indicate that for $r_i<r<r_p$, i.e. outside the Au^+ ion, $\psi_{\mathbf{k}-}(\mathbf{r})$ will be quite well approximated by the free electron solution: (const.) $\exp(-i\mathbf{k}_-\cdot r)$. Within the ion ($r<r_i$) the form of $\psi_{\mathbf{k}-}(\mathbf{r})$ approximates to an isolated atom $6s$ $(+5d+\cdots)$ wave function, but in any case, is irrelevant for our calculation; this follows from the effective vanishing of $\psi_{\mathbf{k}+}(\mathbf{r})$ for $r<r_i$ and the resultant absence of electron-positron wave function overlap in the ion interior, in the integral of Eq. (10) for $\Phi_{\mathbf{k}+,\mathbf{k}-}(\mathbf{p})$.

It remains to determine the Au $5d$ electron wave functions. Krutter's calculations for Cu[13] indicate that the energy *vs.* wave number dependence for the electrons in the $3d$ band is rather more appropriate to tightly than to loosely bound electrons and so imply a form for $\psi_{\mathbf{k}-}(\mathbf{r})$ (within any particular atomic polyhedron) not too different from that for an isolated atom $3d$ wave function.[14a] Now in an isolated Cu^+ ion, Hartree type calculations show rather small extension of the $3d$ wave function beyond the ion radius;[15] in the absence of definite information to the contrary we assume that the same situation holds in the analogous case of the $5d$ electrons in an isolated Au^+ ion and, so, in an Au^+ ion in the metal. It would then seem not too poor an approximation to suppose a very small effective overlap between $[\psi_{\mathbf{k}-}(\mathbf{r})]_{5d}$ and $\psi_{\mathbf{k}+}(\mathbf{r})$, and hence to neglect completely the $5d$ electron contribution to the annihilation probability. This procedure should at least give a reasonable lower limit to the theoretical $\bar{p}_{Au}$ and really cannot be avoided in the absence of any actual calculations of the Au metallic $5d$ wave functions.

[10] E. Wigner and F. Seitz, Phys. Rev. **43**, 804 (1933); **46**, 509 (1934).

[11] In accordance with the general theory of reference 10 one has: positron energy in state $\psi_{\mathbf{k}+}\approx(\hbar^2\alpha^2/2m)+(\hbar^2k_+^2/2m)$.

[12] See reference 10 and J. C. Slater, Phys. Rev. **45**, 794 (1934); Rev. Mod. Phys. **6**, 209 (1934).

[13] H. M. Krutter, Phys. Rev. **48**, 664 (1935).

[14] S. R. Tibbs, Proc. Camb. Phil. Soc. **34**, 89 (1938).

[14a] *Note added in proof.*—A similar implication may be drawn from an examination of Fig. 1 in a note of Steinberger and Wick (Phys. Rev. **76**, 994 (1949)) where plots are given of the $3d$ electron wave function in an isolated Fe atom and in metallic Fe.

[15] D. R. Hartree, Proc. Roy. Soc. **141**, 282 (1933); see particularly Table III on p. 297.

Our $\psi_{\mathbf{k}+}$ and $\psi_{\mathbf{k}-}$ having been specified, it is now a straightforward matter to evaluate the integral in Eq. (10) for $\Phi_{\mathbf{k}+,\mathbf{k}-}(\mathbf{p})$, and, then, the sums in Eq. (5) for $\mathfrak{N}(\mathbf{p})$. We obtain:

$$\Phi_{\mathbf{k}+,\mathbf{k}-}(\mathbf{p})=\text{const.}\sum_{\mathbf{g}}\Big[\delta_{\mathbf{g},0}-\frac{v_i}{v}\Big\{\Big[\sin(2\pi g r_i)-(2\pi g r_i)\cos(2\pi g r_i)\Big]\frac{3}{(2\pi g r_i)^3}\Big\}\Big]\times\delta(\mathbf{k}_+ +\mathbf{k}_- +2\pi\mathbf{g}-\mathbf{p}) \quad (11)$$

and

$$N(p)=4\pi p^2\mathfrak{N}(\mathbf{p})\approx\text{const.}4\pi p^2\Big[\eta_{k_{\max}}(p)\Big(1-\frac{2v_i}{v}\Big)+\frac{1}{2}\Big(\frac{v_i}{v}\Big)^2\exp\Big(-\frac{2}{\pi^2}r_i^2p^2\Big)\Big], \quad (12)$$

several purely mathematical approximations being introduced to carry out the sums over $\mathbf{k}_-$ and $\mathbf{k}_+$ in Eq. (5).[16] In Eqs. (11), (12), v_i and v are, respectively, the volumes of the Au^+ ion and the Au atomic polyhedron (unit cell); $k_{\max}=2\pi(3/(8\pi v))^{\frac{1}{3}}$ is the maximum value of $|\mathbf{k}_-|$ for an electron in the half-filled 6*s* band (at $T=0$);

$$\eta_{k_{\max}}(p)=1 \text{ if } p<k_{\max} \text{ and } \eta_{k_{\max}}(p)=0 \text{ if } p>k_{\max}.$$

As in the case of the experimental $N(p)$ distribution, we shall use the (qualitatively similar) theoretical $N(p)$ distribution only to calculate the mean momentum of the annihilating pair centers of mass. Equation (12) then yields,

$$\bar{p}=\int_0^\infty pN(p)dp\Big/\int_0^\infty N(p)dp=-\frac{3}{4}\hbar k_{\max}\Big[\frac{1-2v_i/v+1.80(v_i/v)^{\frac{1}{3}}}{1-2v_i/v+1.03(v_i/v)}\Big], \quad (13)$$

whence, using $v=1/4$ (Au lattice constant)$^3=1/4$ (4.07 A°)^3 and $v_i/v=1/4$ ($r_i=1.0$ A°), we obtain:[17]

$$\bar{p}_{\text{Au}}=\tfrac{3}{4}\hbar k_{\max}[1.6]=0.8 \text{ mc}/137. \quad (14)$$

It will be noted from Eqs. (12), (13), that $\frac{3}{4}\hbar k_{\max}$ (0.5 mc/137 for Au) is the value of $\bar{p}_{\text{Au}}$ obtained in the limit $v_i/v\to 0$ i.e., obtained on the assumption that both the 6*s* electron and the positron have wave functions which are of the free particle form:

$$\psi_{\mathbf{k}\mp}(\mathbf{r})=(\text{const.})\exp(i\mathbf{k}_\mp\cdot\mathbf{r})$$

throughout the whole volume of the metal (including the ionic interiors). Thus, the factor in the square brackets in Eqs. (13), (14), arises from the deviation of $\psi_{\mathbf{k}\mp}(\mathbf{r})$ from the free particle form, i.e., from the approach of $\psi_{\mathbf{k}-}(\mathbf{r})$ to the isolated atom 6*s* wave function within the ionic interior and from the effective vanishing of $\psi_{\mathbf{k}+}(\mathbf{r})$ in this interior. In accordance with the comment made in footnote 16, practically the whole observed value of $\bar{p}$ at room temperature arises from the zero-point motion of the electrons and the positrons, the temperature variation of $\bar{p}$ being very slight

$$(\langle p(T)\rangle_{\text{Av}}=\langle p(0)\rangle_{\text{Av}}[1+\gamma(\kappa T/\hbar^2k_{\max}^2/2m)^2] \text{ with } \gamma\sim 1).$$

A point worthy of examination is the possible effect on the annihilation photon angular distribution of the so far neglected Coulomb attraction between the members of the annihilating pair. It would seem that there is no such effect, at least in first order, since the operator corresponding to the pair's center of mass momentum commutes with the pair's Coulomb energy operator.[18] For the sake of completeness, we should also mention the possibility of the formation of positronium atoms within the solid with an ultimate two photon self-annihilation out of their ground ^1S states.[19] Here it appears possible that the angular distribution of the two annihilation photons might be shifted in a direction appropriate to smaller apparent electron-positron center of mass momenta. Such a shift will occur if, (a): the center of mass momentum of the positronium atom upon formation, (equal to the vector sum of the momenta of the combining electron and positron

[16] These mathematical approximations break down if v_i/v is too close to $\frac{1}{2}$ (or between $\frac{1}{2}$ and 1). Another method must then be used. It should also be noted that strictly speaking, the $N(p)$ of Eq. (12) is the annihilating pair center of mass momentum distribution calculated at the absolute zero of temperature; i.e. we have taken $F_+(\mathbf{k}_+)=(\text{const})\delta(\mathbf{k}_+)$ and $F_-(\mathbf{k}_-)=(\text{const})\eta_{k_{\max}}(\mathbf{k}_-)$. The $N(p)$ distribution at room temperature however is not very different from that at $T=0$ since $\kappa T_{\text{room}}\ll\hbar^2k_{\max}^2/2m$.

[17] The numerical value of r_i which we employ is obtained from the location of the 5*d* electron charge density maximum in Au^+ by using Slater's (isolated atom) hydrogenic wave functions. See J. C. Slater, Phys. Rev. **36**, 57 (1930). However, as emphasized by H. Jones (Physica **15**, 13 (1949)) the large excess of the observed value of the bulk modulus in Au over that calculated from the $\epsilon_-(\mathbf{k}_-)$ *vs.* $\mathbf{k}_-$ dependence for the 6*s* valence electrons, indicates a relatively large (repulsive) interionic overlap energy and hence a relatively large value of v_i/v, probably $>\frac{1}{2}$. Such a value of v_i/v would increase the theoretical value of $\bar{p}_{\text{Au}}$ (Eqs. (13), (14)) and would thus improve its agreement with the experimental value (Eq. (3)).

[18] This Coulomb attraction may, however, be expected to decrease somewhat the positron mean life for annihilation by increasing the electron density near the positron. See Pomeranchuk, reference 2; J. W. Shearer and M. Deutsch, Phys. Rev. **76**, 462 (1949), and the comment in footnote 31.

[19] J. Pirenne, Arch. D. Sci. Phys. et Natur. **28**, 273 (1946); **29**, 121 (1947); J. A. Wheeler, Ann. New York Acad. Sci. **48**, 219 (1946); A. Ore and J. L. Powell, Phys. Rev. **75**, 1696 (1949); L. D. Landau, Dokl. Akad. Nauk. U.S.S.R. **60**, 207 (1948); E. M. Lifshitz, Dokl. Akad. Nauk. U.S.S.R. **60**, 211 (1948); I. Pomeranchuk, Dokl. Akad. Nauk. U.S.S.R. **60**, 213 (1948). These authors also show that if any positronium annihilates itself out of the ground ^3S state, three photons are simultaneously emitted. Further Ore and Powell show that the ratio of the total cross sections for three and for two photon annihilation of slowly moving (but mutually unbound) electrons and positrons is $\approx 1/370$. Remembering in addition, the roughly isotropic three photon angular distribution and the solid angle factor, it is seen that the contribution of the three photon process to the observed breadth (and background) of the two photon angular distribution ($C(\lambda)$ of Eq. (11)) must be completely negligible.

$\sim mc/137$), is decreased to values $\sim(4m\kappa T)^{\frac{1}{2}}$ by thermalizing collisions with lattice atom vibrations, in a time short compared with that required for annihilation,[20] and (b), the positronium atom is not dissociated in any of these collisions. Item (b), however, is rather doubtful since the positronium atom in the crystal lattice probably has a very small positive or even a negative binding energy and is thus quite unstable. This last conclusion follows from the fact that the (isolated) positronium first Bohr orbit diameter (2 A°) is not much smaller than the distance between nearest neighbor Au lattice ions; the positronium wave function is then greatly compressed to enable the atom to fit into and move through the lattice, and such a compression involves a very large decrease in binding energy.[21]

DISCUSSION

The agreement between the experimental value and the (lower limit on the) theoretical value of $\bar{p}_{Au}$ (Eqs. (3) and (14)) is perhaps as good as can be expected considering the rough and preliminary nature of both. Several obvious uncertainties affect our theoretical formulas, in particular a somewhat dubious numerical value for v_i/v $(=1/4)$ has been used (see comment in footnote 17). On the other hand, our expression for $\bar{p}$ (Eq. (13)) is not too sensitively dependent on the necessarily somewhat arbitrary magnitude of v_i/v; values of this ratio of 1/5 and 1/3, for example, yield values of $\bar{p}_{Au}$ of 0.75 mc/137 and 0.9 mc/137, respectively. Nevertheless it is quite clear that any really quantitatively reliable values of $\bar{p}$ and $N(p)$ will necessitate Wigner-Seitz type calculations (with the proper ion core fields in the individual atomic polyhedra) for the appropriate electron and positron wave functions.

Certain additional experiments are immediately suggested by the general form of Eq. (13) for $\bar{p}$. Thus, if one should use as positron absorbers the members of a chemically homologous series of solids possessing the same crystal structure, e.g., the various alkali metals; Li, Na, K, Rb, Cs, one could expect about the same value of v_i/v for the different members of the series,[21a] so that their $\bar{p}$ would vary directly with their k_{max} or inversely with their lattice constant. Since the lattice constant increases by a factor of 1.75 from Li to Cs, the corresponding decrease of $\bar{p}$ should be easily observable. Another interesting test would involve the use of two series of alkali halides, e.g.: (a) Li^+Cl^-, Na^+Cl^-, K^+Cl^-, Rb^+Cl^-, and (b) Na^+F^- Na^+Cl^-, Na^+Br^-, Na^+I^-. Then, since one expects that, to a first approximation, the positron annihilates only against the fairly tightly bound outer shell electrons of the negatively charged halogen ions, and has a wave function immediately before annihilation determined mainly by the electrostatic potential of these ions, one should find about the same value of $\bar{p}$ for all the members of the (a) series and a monotonic variation in $\bar{p}$ along the (b) series. In general, it is clear that the study of the angular distribution of annihilation radiation with scintillation counters in coincidence will help throw light on electronic momentum distributions, in the atoms and molecules of gases and in liquids and solids.

[20] The ground ^1S state annihilation of positronium has a mean life of 1.25×10^{-10} sec. (see reference 19).

[21] Thus, A. Sommerfeld and H. Welker, Ann. d. Physik 32, 56 (1938), show that the lowest discrete energy of the H-atom becomes positive if the atom is confined in an impenetrable sphere centered at the atom's center of mass and having a radius $\leqq 1.835$, the radius of the (isolated) H-atom Bohr orbit.

[21a] For a discussion and criticism of such an expectation, see e.g. F. Seitz, *Modern Theory of Solids* (McGraw-Hill Book Company, Inc., New York, 1940), Chapter 2.

APPENDIX I

Thermalization Time of the Positron

In conclusion, we shall present an estimate of the time interval τ, required for the thermalization of positrons in a metallic solid. It will be recalled that practically all the positrons survive the atom ionization (and excitation) process without annihilation; then, having ceased to lose energy by kicking electrons from the half-filled 6*s* and the all-filled 5*d*, 5*p*, $\cdots$, 2*s*, 1*s* bands into unoccupied states in the overlapping 6*s*, 6*p*, $\cdots$ bands ($p_+<\sim mc/137$), the positrons begin to lose energy by collisions with the thermally vibrating lattice atoms (or ions) exciting these into states of higher vibrational energy. The net rate of positron energy loss as a result of such collisions is given, on the average, by

$$-\frac{d}{dt}\epsilon_+(\mathbf{k}_+)=\sum_{\mathbf{g}}\int\frac{d\sigma}{(2\pi)^3}\Big\{\frac{2\pi}{\hbar}\Big|(\mathbf{k}_+|H_{\text{inter}}|\mathbf{k}_+-\boldsymbol{\sigma}-2\pi\mathbf{g})\Big|^2 \times\delta(\epsilon_+(\mathbf{k}_+)-\epsilon_+(\mathbf{k}_+-\boldsymbol{\sigma}-2\pi\mathbf{g})-\hbar\omega(\boldsymbol{\sigma})) -\frac{2\pi}{\hbar}\Big|(\mathbf{k}_+|H_{\text{inter}}|\mathbf{k}_++\boldsymbol{\sigma}+2\pi\mathbf{g})\Big|^2 \times\delta(\epsilon_+(\mathbf{k}_+)-\epsilon_+(\mathbf{k}_++\boldsymbol{\sigma}+2\pi\mathbf{g})+\hbar\omega(\boldsymbol{\sigma}))\Big\}\hbar\omega(\boldsymbol{\sigma}). \quad (15)$$

In Eq. (15), the first term describes the mean rate of positron energy loss in collisions in which a vibrational quantum of wave number $\boldsymbol{\sigma}$ and energy $\hbar\omega(\boldsymbol{\sigma})$ is transferred from the positron to the lattice vibration, the positron making a transition from a state $\psi_{\mathbf{k}_+}$ to a state $\psi_{\mathbf{k}_+'}=\psi_{\mathbf{k}_+-\boldsymbol{\sigma}-2\pi\mathbf{g}}$; $\mathbf{g}$, as before, is a reciprocal lattice vector, the transitions to the states $\psi_{\mathbf{k}_+'}$ mentioned being the only allowed by the linear momentum conservation selection rule.[22] In a similar way, the second term in Eq. (15) describes the mean rate of positron energy gain in the "inverse" collisions where a vibrational quantum is transferred from the lattice vibration to the positron. The transition probabilities for both these types of collisions are given by the absolute squares of the corresponding matrix elements,

$$|(\mathbf{k}_+|H_{\text{inter}}|\mathbf{k}_+\mp\boldsymbol{\sigma}\mp2\pi\mathbf{g})|^2,$$

multiplied by $2\pi/\hbar$ and by the appropriate δ functions which maintain the conservation of (unperturbed) energy in the collisions.

The matrix elements in Eq. (15) may be expressed in accordance with the usual methods of the theory of metals,[23] by

$$(\mathbf{k}_+|H_{\text{inter}}|\mathbf{k}_+\mp\boldsymbol{\sigma}\mp2\pi\mathbf{g})=\Big[\int\psi_{\mathbf{k}_+}^*(\mathbf{r})\{\exp(\pm i\boldsymbol{\sigma}\cdot\mathbf{r})\mathbf{a}_{\boldsymbol{\sigma}}\cdot\operatorname{grad}V(\mathbf{r})\} \times\psi_{\mathbf{k}_+\mp\boldsymbol{\sigma}\mp2\pi\mathbf{g}}(\mathbf{r})d\tau\Big]v^{\frac{1}{2}}\Big(\frac{\hbar}{2M\omega(\boldsymbol{\sigma})}\Big[\begin{matrix}n(\boldsymbol{\sigma})+1\\ \text{or } n(\boldsymbol{\sigma})\end{matrix}\Big]\Big)^{\frac{1}{2}} \quad (16)$$

[22] See Eq. (9), where $\varphi_{\mathbf{k}_+}(\mathbf{p}_+)$ and $\varphi_{\mathbf{k}_+'}(\mathbf{p}_+')$ vanish unless $\mathbf{p}_+=\mathbf{p}_++2\pi\mathbf{g}_+$, $\mathbf{p}_+'=\mathbf{k}_+'+2\pi\mathbf{g}_+'$. Then, since one must have $\mathbf{p}_+'=\mathbf{p}_+\mp\boldsymbol{\sigma}$, one immediately obtains $\mathbf{k}_+'=\mathbf{k}_+\mp\boldsymbol{\sigma}+2\pi(\mathbf{g}_+-\mathbf{g}_+')$.

[23] F. Bloch, Zeits. f. Physik 52, 555 (1928); A. Sommerfeld and H. A. Bethe, *Handbuch der Physik* 24, II (J. Springer, Berlin,

the positron—lattice interaction potential, H_{inter}, being taken appropriate to the Bloch deformable ion approximation[24] as

$$v^{\frac{1}{2}}\mathbf{A}(\boldsymbol{\sigma})\exp(i\boldsymbol{\sigma}\cdot\mathbf{r})\,\text{grad}V(\mathbf{r})+\text{comp. conj.}$$

Here, $V(\mathbf{r})$ is the time average (static) periodic potential of the lattice. $\mathbf{A}(\boldsymbol{\sigma})$ is the $\boldsymbol{\sigma}$-normal mode lattice vibration amplitude. The quantity $v^{\frac{1}{2}}$ appears because of our present normalization: $\int_v|\psi_{\mathbf{k}+}(\mathbf{r})|^2d\mathbf{r}=1$. The square root in Eq. (16) times $\mathbf{a}_{\boldsymbol{\sigma}}$, the $\boldsymbol{\sigma}$-normal mode polarization unit vector, is just the matrix element of $\mathbf{A}(\boldsymbol{\sigma})$ with respect to the vibrational eigenfunctions in transitions in which a vibration quantum is created or destroyed; in this square root, M is the vibrating atom mass and $n(\boldsymbol{\sigma})=[\exp(\hbar\omega(\boldsymbol{\sigma})/\kappa T)-1]^{-1}$ is the number of vibrational quanta of energy $\hbar\omega(\boldsymbol{\sigma})$ and wave number $\boldsymbol{\sigma}$ present just before the occurrence of the transition.

In the case $\mathbf{g}=0$, the integrals in the matrix elements of Eq. (16) may be transformed by an integration by parts and use of the Schrödinger equation satisfied by $\psi_{\mathbf{k}+}(\mathbf{r})$; assuming in addition that in a given atomic polyhedron (unit cell) $\psi_{\mathbf{k}+}(\mathbf{r})\exp(-i\mathbf{k}_+\cdot\mathbf{r})$ satisfies the Wigner-Seitz boundary conditions, is spherically symmetric, and depends only weakly on $\mathbf{k}_+$, one obtains,[25]

$$\begin{aligned}\int_v\psi_{\mathbf{k}+}^*(r)[\exp(\pm i\boldsymbol{\sigma}\cdot\mathbf{r})\mathbf{a}_{\boldsymbol{\sigma}}\cdot\text{grad}V(\mathbf{r})]\psi_{\mathbf{k}\mp\boldsymbol{\sigma}}(\mathbf{r})d\mathbf{r}\\ =\pm\frac{2}{3}i\sigma\left[\frac{\hbar^2}{2m}\int_v|\text{grad}\psi_{\mathbf{k}+}(\mathbf{r})\exp(-i\mathbf{k}_+\cdot\mathbf{r})|^2d\mathbf{r}\right]\\ =\frac{2i}{3}\sigma\left(\frac{\langle p_+^2\rangle_{Av}}{2m}\right),\end{aligned}\tag{17}$$

where $\langle p_+^2\rangle_{Av}$ is the mean square positron momentum in the state with $\mathbf{k}_+=0$, so that $\langle p_+^2\rangle_{Av}/2m$ is just the positron's bottom-of-the-band zero-point kinetic energy. On the other hand, when $\mathbf{g}\neq0$, it does not seem possible to obtain a simplified expression for the matrix elements in Eq. (16). We confine ourselves, therefore, to the remark that in this case, the oscillating factor $\exp(\mp2\pi i\mathbf{g}\cdot\mathbf{r})$ in the integral over v (arising from $\psi_{\mathbf{k}_+\mp\boldsymbol{\sigma}\mp2\pi\mathbf{g}}$) will tend to decrease this integral's value (at least, for fairly large $\mathbf{g}$); in addition, the energy and momentum conservation laws governing the collisions, yield:[26]

$$1\geqslant\left|\frac{\mathbf{k}_+\cdot(\boldsymbol{\sigma}+2\pi\mathbf{g})}{|\mathbf{k}_+||\boldsymbol{\sigma}+2\pi\mathbf{g}|}\right|=\left|\frac{|\boldsymbol{\sigma}+2\pi\mathbf{g}|}{2|\mathbf{k}_+|}\pm\frac{m\omega(\boldsymbol{\sigma})}{\hbar|\mathbf{k}_+||\boldsymbol{\sigma}+2\pi\mathbf{g}|}\right|$$

and this condition cannot be satisfied, even for the smallest non-vanishing $2\pi g$, once $\hbar k_+$ becomes smaller than $\approx\frac{1}{2}\hbar\sigma_{\max}$[27] (which is, $\approx\frac{1}{2}$mc/137 for Au). Thus it would seem as if our subsequent complete neglect of the $\mathbf{g}\neq0$ collisions will yield a positron (net) average energy loss correct for $(2m\kappa T)^{\frac{1}{2}}<\hbar k_+<\approx\frac{1}{2}$mc/137 and somewhat underestimated for $\hbar k_+>\frac{1}{2}$mc/137; since most of the time required for thermalization, however, is spent in the range of positron momenta from $\frac{1}{2}$mc/137 to $(2m\kappa T)^{\frac{1}{2}}$ (see footnote 30) it is clear that the ultimate overestimate of τ will not be large.

We may now use Eqs. (17) and (16) for the collision matrix elements in the energy loss Eq. (15). With $\cos\theta_\sigma\equiv\mathbf{k}\cdot\boldsymbol{\sigma}/k\sigma$, one has,[28]

$$\begin{aligned}-\frac{d}{dt}\epsilon_+(\mathbf{k}_+)=\int_0^\infty d\sigma\sigma^2\eta_{\sigma\max}(\sigma)\int_0^\pi\left(\frac{2\pi d\theta_\sigma\sin\theta_\sigma}{(2\pi)^3}\right)\frac{2\pi}{\hbar}\\ \times\left(v\frac{\hbar}{2M\omega(\boldsymbol{\sigma})}\frac{4}{9}\sigma^2\left(\frac{\langle p_{\tau}^2\rangle_{Av}}{2m}\right)^2\right)\hbar\omega(\boldsymbol{\sigma})\\ \times\left[(n(\boldsymbol{\sigma})+1)\delta\left(\frac{\hbar^2}{2m}2k_+\sigma\cos\theta_\sigma-\frac{\hbar^2\sigma^2}{2m}-\hbar\omega(\boldsymbol{\sigma})\right)\right.\\ \left.-n(\boldsymbol{\sigma})\delta\left(\frac{-\hbar^2}{2m}2k_+\sigma\cos\theta_\sigma-\frac{\hbar^2\sigma^2}{2m}+\hbar\omega(\boldsymbol{\sigma})\right)\right]\end{aligned}\tag{18}$$

and, carrying out the integration over θ_σ,

$$\begin{aligned}-\frac{d}{dt}\epsilon_+(\mathbf{k}_+)=\frac{v(\langle p_+^2\rangle_{Av}/2m)^2}{9\pi\hbar k_+}\frac{m}{M}\left[\int_0^\infty d\sigma\sigma^3\eta_{\sigma\max}(\sigma)\right.\\ \left.\times\{\eta_{2k_+-\alpha}(\sigma)-n(\sigma)(\eta_{2k_++\alpha}(\sigma)-\eta_{|2k_+-\alpha|}(\sigma)\}\right],\end{aligned}\tag{19}$$

where $\alpha=2mv_{ac}/\hbar$, $v_{ac}=\omega(\boldsymbol{\sigma})/\sigma$, being the (longitudinal) acoustic wave velocity $=1.8\times10^5$ cm/sec. for Au.

Equation (19) indicates that there are four distinct cases in the energy loss expression; I: $2k_+\geqq\sigma_{\max}+\alpha$; II: $\sigma_{\max}+\alpha>2k_+>\sigma_{\max}-\alpha$; III: $\sigma_{\max}-\alpha\geqq2k_+>\alpha$; IV: $\alpha\geqq2k_+$; and, since $\sigma_{\max}\gg\alpha$, these essentially reduce to three: I′: $k_+>\sigma_{\max}/2$; II′: $\sigma_{\max}/2\geqq k_+>mv_{ac}/\hbar$. III′: $mv_{ac}/\hbar\geqq k_+$. Evaluating the integral over σ in Eq. (19) gives explicitly, with

$$A\equiv\frac{4}{9\pi}\hbar^{-1}\left(\frac{\langle p_+^2\rangle_{Av}}{2m}\right)^2\frac{m}{M}v(\sigma_{\max}/2)^3,$$

$$-\frac{d}{dt}\epsilon_+(\mathbf{k}_+)=A\frac{\sigma_{\max}}{2k_+};\quad\hbar k_+>\hbar\sigma_{\max}/2,\tag{20-I′}$$

$$\begin{aligned}-\frac{d}{dt}\epsilon_+(\mathbf{k}_+)=A\left(\frac{2k_+}{\sigma_{\max}}\right)^3\left\{\left(1-\frac{mv_{ac}}{\hbar k_+}\right)^4\right.\\ \left.-8\frac{mv_{ac}}{\hbar k_+}\left(\exp\left[\frac{\hbar v_{ac}2k_+}{\kappa T}\right]-1\right)^{-1}\right\};\\ \hbar\sigma_{\max}/2\geqq\hbar k_+>mv_{ac},\end{aligned}\tag{20-II′}$$

$$\begin{aligned}+\frac{d}{dt}\epsilon_+(\mathbf{k}_+)=A\left(\frac{2mv_{ac}}{\hbar\sigma_{\max}}\right)^3 8\left(\exp\left[\frac{2mv_{ac}^2}{\kappa T}\right]-1\right)^{-1};\\ mv_{ac}\geqq\hbar k_+,\end{aligned}\tag{20-III′}$$

where, for $T\gg\hbar v_{ac}\sigma_{\max}/\kappa\equiv T_{\text{Debye}}\gg2mv_{ac}^2/\kappa$ one can expand both exponentials in the usual way.[29] The second inequality is easily satisfied in Au, and indeed in all metals. The thermalization time τ, is now given by,

$$\begin{aligned}\tau=\int_{\text{mc}^2/2\cdot137^2}^{\kappa T}\frac{d\epsilon_+}{[d\epsilon_+/dt]}\approx\frac{2}{Am\hbar\sigma_{\max}^2}\int_{\hbar\sigma_{\max}/2}^{\text{mc}/137}(\hbar k_+)^2d(\hbar k_+)\\ +\left(\frac{\hbar^3\sigma_{\max}^3}{Am8}\right)\int_{(2m\kappa T)^{\frac{1}{2}}}^{\hbar\sigma_{\max}/2}\frac{d(\hbar k_+)}{(\hbar k_+)^2}\\ =\frac{3}{2\pi}\frac{\hbar}{\langle p_+^2\rangle_{Av}/m}\frac{M}{m}\frac{(\hbar\sigma_{\max})^2}{\langle p_+^2\rangle_{Av}}\frac{\hbar\sigma_{\max}}{(2m\kappa T)^{\frac{1}{2}}}\\ \times\left[1+\frac{(2m\kappa T)^{\frac{1}{2}}}{\hbar\sigma_{\max}}\frac{8}{3}\left[2\left(\frac{mc}{137\hbar\sigma_{\max}}\right)^2-1\right]\right]\\ =0.15\times10^{-10}\left[\frac{mc^2/137^2}{\langle p_+^2\rangle_{Av}/2m}\right]^2\text{sec.},\end{aligned}\tag{21}$$

1933); J. Bardeen, Phys. Rev. **52**, 688 (1937); F. Seitz, Phys. Rev. **73**, 549 (1948). In Seitz's paper, Peierls' criterion for the validity of the general type of time-dependent perturbation theory used, is given in convenient form. It may be verified that this criterion is satisfied in the situation which we consider.

[24] See particularly J. Bardeen, reference 23.

[25] See A. Sommerfeld and H. A. Bethe, reference 23, pp. 512, 513, for the wholly analogous calculation in the case of metallic electronic conduction.

[26] This condition gives those $\boldsymbol{\sigma}$ and $\mathbf{g}$ values for which the argument of the δ functions in Eq. (15) vanishes, and which, therefore, specify the allowed collisions that make a contribution to the $\Sigma_{\mathbf{g}}\int d\boldsymbol{\sigma}\cdots$.

[27] This conclusion is a consequence of the fact that, for example, in a face centered cubic lattice like Au,

$$2\pi g_{\min}=\frac{2\pi\sqrt{3}}{(4v)^{\frac{1}{3}}}>\sigma_{\max}=\frac{2\pi}{(4v)^{\frac{1}{3}}}\left(\frac{3}{\pi}\right)^{\frac{1}{2}}.$$

and so, the first term on the right-hand side of the inequality will necessarily be greater than 1, for all possible $\boldsymbol{\sigma}$ and $2\pi\mathbf{g}\neq0$ if $k_+<\frac{1}{2}(\sqrt{3}-(3/\pi)^{\frac{1}{2}})\sigma_{\max}$. As regards the second term, it is numerically negligible for all $\hbar k_+$ of interest $[\hbar k_+\geqq(2m\kappa T)^{\frac{1}{2}}]$.

[28] As before, $\eta_{x_0}(x)=1$ if $x<x_0$; $\eta_{x_0}(x)=0$ if $x>x_0$.

[29] Equations for the energy loss of an electron in an almost empty conduction band of an electrical non-conductor, entirely analogous to our Eqs. (20-I′, II′, III′), have been independently derived by Mr. W. R. Heller of this laboratory in the course of an investigation on the dielectric breakdown of non-polar insulators (to be published). *Note added in proof.*—F. Seitz (Phys. Rev. **76**, 1376 (1949)) has also independently derived essentially these equations (for the energy loss of an electron) in his work on electron multiplication in crystals.

where, to obtain the last expression, we have used $T=300°\text{K}$ and $\hbar\sigma_{\max}]_{\text{Au}}=0.8$ mc/137. Then, with $\langle p_+^2\rangle_{\text{Av}}/2m]_{\text{Au}}\approx 0.22$ mc^2/137^2 (see below) we finally have[30]

$$\tau\approx 3\times 10^{-10}\text{ sec.} \tag{22}$$

It may be mentioned that, according to Eq. (21), τ is relatively insensitive to variations in temperature.

On the other hand, the mean life for slow positron annihilation, assuming that only the $6s$ valence electrons are accessible to the positrons, is

$$\left\{\frac{1}{v}\pi\left(\frac{e^2}{mc^2}\right)^2 c\right\}^{-1}=25\times 10^{-10}\text{ sec.}\approx 8\tau.^{31}$$

It is thus indeed quite probable that, as we have supposed throughout, the instant of annihilation will find the positron occupying states with $\hbar k_+\sim(2m\kappa T)^{\frac{1}{2}}$; such thermalized positrons possess therefore a total momentum very close to the bottom-of-the-band zero-point value, which, on a root-mean-square basis, is the $(\langle p_+^2\rangle_{\text{Av}})^{\frac{1}{2}}$ used above.

It remains to justify the formula $\langle p_+^2\rangle_{\text{Av}}/2m]_{\text{Au}}\approx 0.22$ mc^2/137^2. We have, with our choice of $\psi_{\mathbf{k}+}(\mathbf{r})$ and with Eq. (9),

$$|\varphi_{\mathbf{k}+}(\mathbf{p}_+)|^2=\text{const.}\sum_{\mathbf{g}_+}\Big[\delta_{\mathbf{g}_+,0}\Big(1-\frac{2v_i}{v}\Big)+\Big(\frac{v_i}{v}\Big)^2\Big\{\Big[\sin(2\pi g_+r_i)-(2\pi g_+r_i)\cos(2\pi g_+r_i)\Big]^2\frac{9}{(2\pi g_+r_i)^6}\Big\}\Big]\delta\Big(\mathbf{k}_++2\pi\mathbf{g}_+-\mathbf{p}_+\Big). \tag{23}$$

Thus, recalling that for a face-centered cubic lattice (like Au) the $\mathbf{g}_+$ of smallest magnitude are 0;

$$\pm a^{-1}(\mathbf{e}_1+\mathbf{e}_2-\mathbf{e}_3),\ \pm a^{-1}(\mathbf{e}_2+\mathbf{e}_3-\mathbf{e}_1),\ \pm a^{-1}(\mathbf{e}_3+\mathbf{e}_1-\mathbf{e}_2),\ a^{-1}(\mathbf{e}_1+\mathbf{e}_2+\mathbf{e}_3);\ \pm 2a^{-1}\mathbf{e}_1,\ \pm 2a^{-1}\mathbf{e}_2,\ \pm 2a^{-1}\mathbf{e}_3;$$

etc. (here a is the lattice constant $=(4v)^{\frac{1}{3}}$ and, $\mathbf{e}_1$, $\mathbf{e}_2$, $\mathbf{e}_3$, unit vectors along the cubic axes), one gets with $v_i/v=\frac{1}{4}$, $r_i=1.0$A°, $P(p_+)$, the probability of the positron momentum having the value p_+:[32]

$$P(p_+=k_+)=\frac{|\varphi_{\mathbf{k}+}(p_+=k_+)|^2}{\Sigma_{\mathbf{p}_+}|\varphi_{\mathbf{k}+}(\mathbf{p}_+)|^2}=0.81,$$

$$P\Big(p_+=\Big|\frac{2\pi\sqrt{3}}{a}\frac{\mathbf{g}_+}{g_+}+\mathbf{k}_+\Big|\Big)\approx\frac{8|\varphi_{\mathbf{k}+}(p_+=2\pi\sqrt{3}a^{-1})|^2}{\Sigma_{\mathbf{p}_+}|\varphi_{\mathbf{k}+}(\mathbf{p}_+)|^2}=0.14, \tag{24}$$

$$P\Big(p_+=\Big|\frac{2\pi 2}{a}\frac{\mathbf{g}_+}{g_+}+\mathbf{k}_+\Big|\Big)\approx\frac{6|\varphi_{\mathbf{k}+}(p_+=2\pi 2a^{-1})|^2}{\Sigma_{\mathbf{p}_+}|\varphi_{\mathbf{k}+}(\mathbf{p}_+)|^2}=0.05,$$

$$P(p_+\approx 2\pi g_+>2\pi 2/a)\approx 0.$$

Thus, the mean square positron momentum in the state $\psi_{\mathbf{k}+}$ is

$$\langle p_+^2\rangle_{\mathbf{k}+}\approx 0.81(\hbar k_+)^2+0.14(2\pi\sqrt{3}a^{-1})^2+0.05(2\pi 2a^{-1})^2, \tag{25}$$

and the mean square zero-point positron kinetic energy $\langle p_+^2\rangle_{\text{Av}}/2m$, becomes, using $a]_{\text{Au}}=4.07\text{A}°=7.7\times 137\hbar/\text{mc}$,

$$\frac{\langle p_+^2\rangle_{\text{Av}}}{2m}=\frac{\langle p_+^2\rangle_{\mathbf{k}+}}{2m}-\frac{0.81(\hbar k_+)^2}{2m}\approx 0.22\frac{\text{mc}^2}{137^2}. \tag{26}$$

We may conclude by noting that it is not quite correct, to assume that the electrons alone contribute to the center of mass momentum of the annihilating pairs and thus to picture the positrons as effectively stationary targets for annihilation.[3] This follows since, as we have just seen, even a thermalized positron has probabilities of the order of 14 percent and 5 percent, respectively, for possessing momenta as large as $2\pi\sqrt{3}a^{-1}=1.4$ mc/137 and $2\pi 2a^{-1}=1.6$ mc/137. Indeed, our discussion makes use of no such assumption and obtains the probability amplitude for the momentum of the center of mass of the annihilating pairs, directly from the corresponding electron and positron coordinate space or momentum space wave functions (Eqs. (6), (7)).

APPENDIX II

The Annihilation Matrix Element

The integral of Eq. (6) for $\Phi_{\mathbf{k}+,\mathbf{k}-}(\mathbf{p})$ is proportional to the matrix element of the annihilation transition in which an electron jumps from an originally occupied initial state with wave number $\mathbf{k}_-$, energy $\approx mc^2$ to an originally unoccupied final state with wave number $-\mathbf{k}_+$, energy $\approx -mc^2$, with the simultaneous emission of two photons with total momentum $\mathbf{p}$. This can be straightforwardly shown from the usual two-step perturbation theory derivation of the annihilation probability based on the interaction of a Dirac electron with the quantized radiation field (see, e.g. W. Heitler, reference 6, pp. 204–208) provided that, (a): the wave functions of the intermediate (virtual) states of the process are treated in the free particle approximation, and (b): the wave functions of the initial and final states are treated non-relativistically, i.e. replaced by the corresponding Schrödinger wave functions ($\psi_{\mathbf{k}-}(\mathbf{r})$, $\psi_{\mathbf{k}+}{}^*(\mathbf{r})$ which appear in Eq. (6)) times

$$\begin{vmatrix}1\\0\\0\\0\end{vmatrix}\quad\text{and}\quad\begin{vmatrix}0\\0\\1\\0\end{vmatrix},$$

respectively. Then, remembering that the electronic momenta involved in the intermediate states ($\sim mc$) are much greater than those involved in the initial and final states ($\sim mc/137$), and, using the orthonormality of the space parts of the intermediate state free particle wave functions, one can perform the sum over all the possible intermediate states and obtain Eq. (6) for $\Phi_{\mathbf{k}+,\mathbf{k}-}(\mathbf{p})$. Eq. (7) for $\Phi_{\mathbf{k}+,\mathbf{k}-}(\mathbf{p})$ follows immediately from Eq. (6) by use of the Fourier transform relations between $\psi_{\mathbf{k}\mp}(\mathbf{r})$ and $\varphi_{\mathbf{k}\mp}(\mathbf{p}_\mp)$. It may also be mentioned that the above method yields most readily the known result[19] that the matrix element of the two-photon annihilation is proportional to the sine of the angle between the photon polarization vectors.

---

[30] From a calculation analogous to that in Eq. (21), the time required for the positron to slow down from a momentum

$$\tfrac{1}{3}\hbar\sigma_{\max}\approx\tfrac{1}{4}(\text{mc}/137)\text{ for Au,}$$

to a momentum $(2m\kappa T)^{\frac{1}{2}}$ is only 35 percent shorter than τ. This justifies the statement made previously , in the discussion of the neglect of the collisions with $2\pi\mathbf{g}\neq 0$.

[31] The fact that one should use, in the Dirac formula for the annihilation mean life, the number of valence electrons per unit volume, and not the total number of electrons per unit volume, was first pointed out by Pomeranchuk, reference 2. It should, however, be mentioned that our estimate of the annihilation time may be too long by a factor of 2 to 4, because of the possibility of occasional annihilation against a $5d$ electron and because of the neglect of the Coulomb attraction between the annihilating electron and positron (involving multiplication of the annihilation rate by

$$\sim\Big\langle\frac{2\pi e^2 m}{\hbar|\mathbf{p}_--\mathbf{p}_+|}\Big(1-\exp\Big[-\frac{2\pi e^2 m}{\hbar|\mathbf{p}_--\mathbf{p}_+|}\Big]\Big)\Big\rangle_{\text{Av}}\Big)$$

We may also note that our time for annihilation is short compared to a reasonable estimate of the time required to trap the positron at a lattice defect (i.e. an Au^+ vacancy, etc. For analogous estimates in the case of electron trapping, see N. F. Mott and R. W. Gurney, *Electronic Processes in Ionic Crystals* (Oxford University Press, London, 1940), p. 131 ff.).

[32] We have used, in the first approximate equalities, the fact that for the positrons of interest, $k_+\approx\hbar^{-1}(2m\kappa T)^{\frac{1}{2}}\ll 2\pi\sqrt{3}a^{-1}$, etc.

High Energy Photons from Proton-Nucleon Collisions

R. BJORKLUND, W. E. CRANDALL, B. J. MOYER, AND H. F. YORK
Radiation Laboratory, Department of Physics, University of California, Berkeley, California

(Received September 19, 1949)

High energy photons (up to 200 Mev) are emitted by various cyclotron targets when these are bombarded by protons with energies greater than 180 Mev. Spectral distributions, angular distributions, and yields are given for various proton energies and targets. Various possible origins are discussed in the light of the experimental observations.

I. INTRODUCTION

IN view of the success of the 184-inch synchrocyclotron in producing the π-mesons observed in high altitude cosmic-ray observations, it seemed worth while to search also for possible evidence bearing on the origin of the soft component of cosmic rays in the collisions of the 340-Mev protons with matter.

The mixed showers investigated by Chao[1] and by Fretter[2] indicate the generation of electronic radiation associated with the events which produce meson showers. One may speculate that this can arise through charge acceleration[3,4] (bremsstrahlung) of the primary proton and of the charged particles ejected in the event,[5] or through the production and self-decay of neutral mesons,[6] or by the excitation of very high energy nuclear states, or by some unidentified process whereby electrons or photons are directly projected from the collision event.

Evidence is here presented for the production of high energy photons in the collision of protons of energies over 175 Mev with the cyclotron target. The yield and the spectrum seem to exclude a bremsstrahlung origin, and a Doppler shift effect excludes a nuclear origin. The observations are consistent with a source associated with proton-nucleon impacts (as distinguished from proton-nucleus collisions).

Although the data at this stage are meager and without high precision, it is considered that they demonstrate an effect worth reporting in preliminary form. Because of extensive development of instrumentation required for further work, a considerable time will be required before a more thorough study can be presented. In the present report experimental details will be minimized, since these must be comprehensively treated in such a subsequent paper.

II. EXPERIMENTAL ARRANGEMENTS

A. Instrumentation

Through the ten-foot concrete shielding of the cyclotron two holes have been provided whose primary purpose is to permit collimated beams of neutrons to emerge from two different target radii. These have been here employed as ports for viewing the target with a pair counter.[7] In Fig. 1 the plan view of the arrangement is evident, and in Fig. 2 a plan view of the pair counter is shown.

For materializing the photons thin sheets of Ta were employed, and for counting the pair electrons proportional counters were used in quadruple coincidence. The fact that the cyclotron beam is pulsed dictates the use of proportional counters rather than Geiger counters with their long dead-time, since the pulse duration of the beam at the target is in the neighborhood of 100 μsec.

As the magnetic flux density is varied, to allow detection of pair electrons of different total energies, the detection efficiency will not remain constant, due to scattering of electrons in the material of the Ta radiator. It would be necessary to correct for this variation in scattering loss by calculations based upon multiple-scattering analysis if a single radiator were employed at various energies. Instead of this, however, in the data presented in Fig. 3 the radiator thickness was adjusted for each mean energy in such a manner as to keep the mean squared angle of scattering constant. This angle is given by

$$\langle\theta^2\rangle_{Av}=a(t/E^2)\ \ln bt,$$

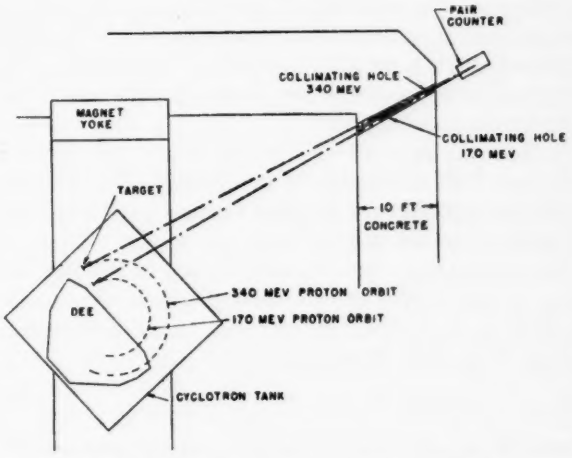

FIG. 1. Plan view of experimental arrangement.

[1] C. Y. Chao, Phys. Rev. **75**, 581 (1949).
[2] W. B. Fretter, Phys. Rev. **76**, 511 (1949).
[3] S. Hayakawa, Phys. Rev. **75**, 1759 (1949).
[4] J. Ashkin and R. E. Marshak, Phys. Rev. **76**, 58 (1949).
[5] L. I. Schiff, Phys. Rev. **76**, 89 (1949).
[6] Lewis, Oppenheimer, and Wouthuysen, Phys. Rev. **73**, 127 (1948).
[7] MacDaniel, von Dardel, and Walker, Phys. Rev. **72**, 985 (1947).

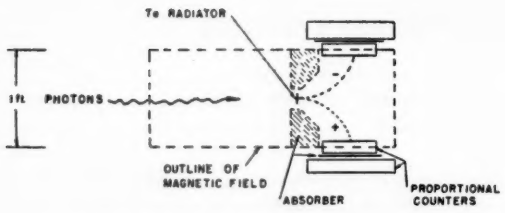

FIG. 2. Plan view of pair counters.

where a and b are constants; and the values of E at which data were taken were so related to the t values of 0.001 in., 0.002 in., 0.004 in., and 0.006 in. as to provide constant $\langle\theta^2\rangle_{Av}$.

The magnetic field dimensions were 12 in.×30 in. ×1¾ in. When used as shown in Fig. 2, the first half of the field is effective in clearing out electron pairs from the preceding air column and collimating fixtures. This was a necessary precaution with radiators of the thickness and size employed, the radiating area of the tantalum being restricted by their size and by beam collimation to a ½ in.×1 in. rectangle.

B. Corrections to Data

The following factors must be accounted for in obtaining from the monitored quadruple counting rates the data which are presented in Figs. 4 and 5 and in Table I.

1. Scattering losses, unless these are made constant as described above, must be relatively calculated. For the absolute yield data given later the scattering loss must be numerically evaluated.

2. The energy breadth detected varies with the mean energy. Since at relativistic electron energies, $E=300B\rho$ and since the geometry is the same for all energies, $\Delta E/E$ is a constant. For the arrangement of Fig. 2, ΔE is approximately $\frac{1}{3}E$.

3. The photon energy is not uniquely divided between the two electrons of the pair, but will range in its partition all the way from 0 percent and 100 percent for the electron and positron, respectively, to the other extreme; and it is possible to accept in the counters only the fraction allowed by the range of radii which the counter dimensions define.

4. The efficiency of pair production in the radiator will vary with the energy of the photons. Pair production cross sections calculated by Heitler[8] have been used for evaluating the effect of this.

In summarizing these items involved in treating the data, the formula relating counting rate to photon flux incident upon the radiator per unit range of energy at energy E may be expressed as:

$$F(E)=R/(N\sigma_{pp}t)\cdot\Delta E\cdot f\cdot\eta(E,t), \qquad (1)$$

where R=quadruple coincidence counts per second, $\eta(E,t)$=fraction of pairs not lost by scattering, ΔE =energy breadth detected, f=fraction of pairs which are detected, and $N\sigma_{pp}t$=pair production efficiency of radiator.

[8] W. Heitler, *Quantum Theory of Radiation* (Oxford University Press, New York, 1936). Second edition.

C. Energy and Angle-of-View Arrangements

The two neutron holes shown in Fig. 1 allow a limited range of proton energies and angles of view to be achieved. The hole directed along the tangent line of the 340-Mev orbit allows, by reversal of the proton beam, angles of view of 0° and 180° with respect to the beam direction. The hole directed along the tangent to the 170-Mev orbit allows targets to be placed at energies between 170 and 340 Mev.

An array of targets which could be raised into position by flip coils was placed along this line of view, with careful attention given to their equivalence from the standpoint of thickness, orientation, and visibility by the pair counter. The energies and associated angles of view for this array were:

175 Mev	2° and 178°
230 Mev	20° and 160°
290 Mev	41° and 139°
340 Mev	47° and 133°.

D. Cyclotron Targets

The high energy photons were observed from any target material, and the relative yields are discussed later. For the array of targets at various energies, each was of carbon, ½ in. thick. The target for which the absolute yield data were most carefully measured was of beryllium, 2 inches in thickness. The energy loss of the 340-Mev protons in 2 inches of beryllium is about 25 Mev.

III. RESULTS

A. Proof of Photon Identity

In order to establish the fact that the quadruple coincidences observed were indeed due to photon-produced pairs, the following kinds of separate observa-

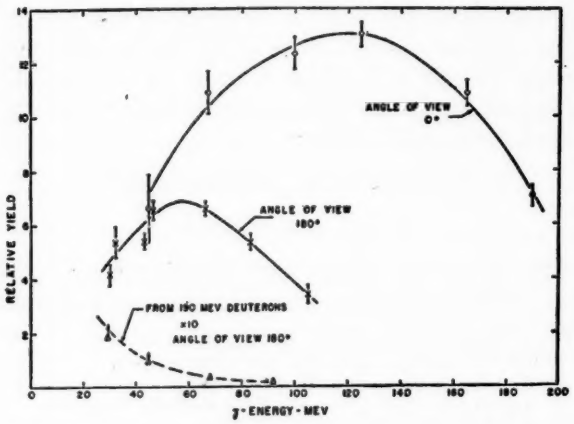

FIG. 3. Relative gamma-yield *vs.* energy from 2-in. Be target, bombarded with 350-Mev protons.

tions were made and repeated whenever deemed necessary.

1. Tantalum radiator removed. This always reduced the quadruple counting rate to a small number appropriate to pairs from the air plus accidental coincidences.

2. Magnetic field reduced to zero. This left only counts due to accidental coincidences, amounting to 0.1 percent to 1 percent of the normal quadruple counting rate, depending upon the mean energy for which the field is adjusted.

3. Absorber placed in path of one of the pair electrons, with same results as in 2.

4. Attenuation of the photons by Pb and Al studied in good geometry. The measured cross sections for attenuating the pair-producing radiation agree with Lawson's[9] values and are not consistent with any other known radiation.

B. The Photon Spectra and Relative Yields at 0° and 180°

In Figs. 3 and 4 the energy distribution is shown, as calculated relatively from the counting rates by use of Eq. (1), with $\eta(E, l)$ constant as described earlier. The Doppler shift effect upon the relative yields and the positions of the maximum intensity, due to reversal of the beam, is evident and will be discussed in later sections. The data in Fig. 3 also include the spectrum of photons yielded by bombardment of a ½-in. Be target with 190-Mev deuterons. Both the yield, when calculated on an absolute basis, and the spectrum, in the case of deuterons, are consistent with bremsstrahlung.

It will be shown in Section IV that the energy distributions and yields for 0° and 180° become apparently identical when transformed into a coordinate system moving with a relative velocity of $\beta=v/c=0.32$ with respect to the laboratory in the direction of the incident proton beam.

The relative yields in the 0° and 180° direction were approximately measured by successive runs of the same duration on identical carbon targets, which were then monitored for the annihilation gammas of the 20-minute C^{11} activity produced by the proton beam. The relative activities were considered to indicate relative beam strengths, making possible a comparison of the photon yields. By working in the 340-Mev position at 133°, a comparison with this direction was also included. In Table I, the results are related to those predicted by considering the photons to be emitted with spherical symmetry in a system moving in the proton beam direction with $\beta=v/c=0.32$, and applying the Doppler corrections to solid angle and energy interval.

C. Photon Yield *versus* Energy

For evident reasons it is not possible with present facilities to employ various proton energies without also changing the angle of view. The angles of view associated with the energies are given in Section II-C, and indicated in Fig. 4.

In order to compute yield *versus* energy data from the curves of Fig. 4, it would be necessary to know the angular distribution of the photons in the laboratory system for each proton energy. The meager data presented, however, indicate a yield rising steeply with energy. At 175 Mev the magnitude and spectrum of the photon emission are roughly consistent with proton bremsstrahlung; whereas at the next energy, 230 Mev, the yield has greatly exceeded bremsstrahlung predictions and the spectrum begins to show the characteristic maximum region, departing distinctly from the $1/E$ distribution.

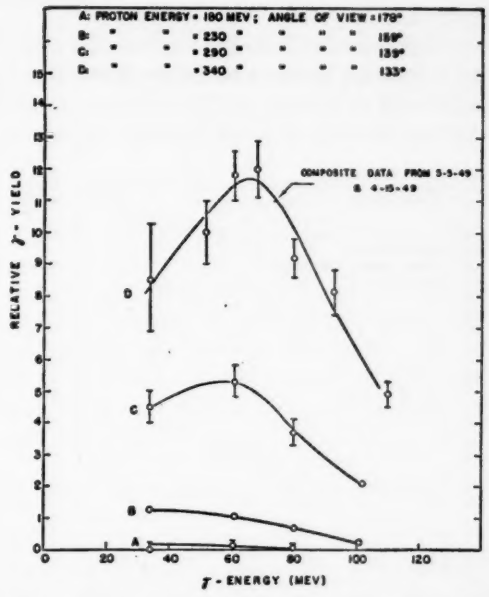
A: PROTON ENERGY = 180 MEV; ANGLE OF VIEW = 179°
B: " " = 230 " " " = 159°
C: " " = 290 " " " = 139°
D: " " = 340 " " " = 133°
COMPOSITE DATA FROM 5-5-49 & 4-15-49
RELATIVE γ - YIELD
γ - ENERGY (MEV)
0
20
40
60
80
100
120

FIG. 4a. Relative gamma-yield from ½-in. carbon target at various proton energies.

It appears reasonable to state that the onset of the emission of the radiation in question occurs somewhere between 175- and 200-Mev proton energy. Because of the momentum distribution of the nucleons in the target nuclei, a sharp threshold is not to be expected until an experiment with a hydrogen target is performed.

D. Yield *versus* Target Element

In Table II are presented data comparing the relative yields of photons with the relative cross sections for inelastic collision with high energy neutrons for a few elements distributed widely in atomic number.

It will be noted that the bremsstrahlung from deuterons at 190 Mev (proton energy of 95 Mev) gives relative yields similar to the relative inelastic cross sections, whereas the photon emission in the case of the 340-Mev protons increases with Z much more slowly than the cross section for inelastic collision. This suggests that the processes giving rise to the photons are different in the two cases.

[9] J. Lawson, Phys. Rev. **75**, 443 (1949).

E. Absolute Yield Data

The curves of Fig. 3 can be given absolute ordinates by evaluation of $\eta(E, t)$. From the proton beam current, target data (2-in. Be), and solid angle data, a cross section for the Be nucleus for production of the photons is computed.

The evaluation of $\eta(E, t)$ was performed by applying multiple scattering analysis to the contribution of electron pairs from an element of the radiator of thickness dx at depth x, finding the mean squared scattering angle

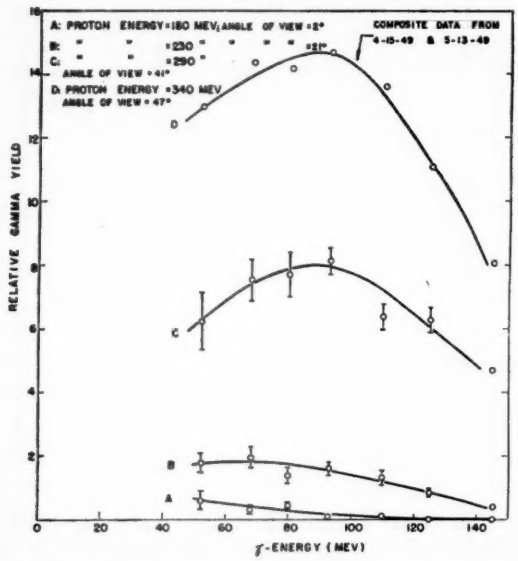

FIG. 4b. Relative gamma-yield from ½-in. carbon target at various proton energies.

with which they emerge, and their probability of both recording in the counters. The fraction of pairs surviving scattering loss is then found by integration (graphical) over the radiator thickness, t. In the case of 0° angle of view, the value of $\eta(E, t)$ was 0.97. It was made approximately constant at all energies by the method mentioned in II-A. In the case of 180° angle of view, $\eta(E, t)$ was 0.84.

The proton current was determined by measuring the C^{11} activity produced in the cyclotron target and using the $C^{12}(p, pn)C^{11}$ cross section at 345 Mev as determined by Peterson.[10]

The resulting cross sections are tabulated in Table III. The coordinate system with $\beta=0.32$ is the system for which the 0° and 180° distributions transform into a unique energy distribution. There is also some evidence for spherical symmetry of photon emission in this system, and this has been assumed in giving the value for total production cross section.

The values in Table III are not good in an absolute sense to the accuracy indicated, but the relative accuracy warrants the figures given. In an absolute sense, these are not to be trusted more closely than a factor of two or three.

[10] V. Peterson (to be published).

IV. ANALYSIS OF RESULTS

If there is some unique coordinate system with velocity βc, in which the photons (or some intermediate particle) are emitted with a spherically symmetric angular distribution, and if $I_c(E)$ is the spectrum of the photons in that system, then the spectrum in the laboratory system at an angle θ will be

$$I(E, \theta)=\frac{(1-\beta^2)^{\frac{1}{2}}}{1-\beta\cos\theta} I_c\left(\frac{1-\beta\cos\theta}{(1-\beta^2)^{\frac{1}{2}}}E\right),$$

where the Doppler shift and aberration effects have been taken into account. The spectra shown in Figs. 3 and 4, in the case of 340-Mev protons, all satisfy the above condition, within the experimental accuracy, if we choose $\beta=0.32$. Figure 5 shows the four 340-Mev spectra of Figs. 3 and 4 transformed to this moving coordinate system. (For the sake of clarity, all curves are normalized so as to have the same value at the peak. Table I gives the measured relative values at the peak.) The reasonableness of this value of β may be seen from the following considerations: The velocity of a 340-Mev proton is 0.67c, and hence, the β of the center of mass of such a proton and a stationary nucleon is 0.39. The nucleons in the target nucleus are not stationary, however, since they have kinetic energies up to about 25 Mev, and hence velocities up to about 0.22c. Now, as shown in Fig. 4, the process leading to the production of these photons is very energy sensitive, and hence, the production of photons presumably occurs predominately in those collisions where the largest amount of energy is available. These collisions are those which take place between a 340-Mev proton and a nuclear nucleon moving in the opposite direction, and hence those which lead to lower values for the velocity of the center of momentum. Since, as mentioned above, nuclear nucleons may have β's of the order of 0.2, a mean effective center of momentum velocity in the range 0.30c–0.35c is quite reasonable.

Figure 4 shows that the yield of photons increases by a factor of about 100 as the proton energy increases from 175 Mev to 350 Mev. The yield for 175-Mev protons is about the same as the yield for 190-Mev deuterons and is consistent with proton bremsstrahlung. If the large increase which occurs beyond this energy is due to some other process, then the threshold for this other process, as has already been mentioned, is somewhere in the neighborhood of 175–200 Mev. If we take 25 Mev as the maximum energy of nucleons in the target nucleus, then the maximum energy available for inelastic processes produced by 175-Mev incident protons is about 170 Mev. This energy is about twice the mean energy of the photons observed and suggests, perhaps, that the photons are produced in pairs, or that an intermediate particle with a rest mass equivalent to

twice the photon energy is involved. It may also be noted that the threshold for producing π-mesons is also about 175 Mev, and that the yield *vs.* energy results are similar.

V. INTERPRETATION OF RESULTS

In this section we shall discuss various possible interpretations of the origin of these photons, and examine how they fit the experimental data at hand.

A. Nuclear Excitation

This possibility may be eliminated almost immediately on theoretical grounds. It may also be eliminated on the basis of some of our results. A very strong evidence against nuclear excitation is the pronounced Doppler shift observed. The shift could not conceivably be appropriate to velocities possessed by a nucleus. Further, if this process were due to some nuclear excitation, then the yield from 390-Mev alpha-particle bombardment would be expected to be greater than the yield from 340-Mev proton bombardment, since the alpha-particle will in general lead to a more highly excited nucleus than the proton. The opposite has been found to be true; 340-Mev protons give a photon yield some 10^3 times greater than 390-Mev alphas.

B. Bremsstrahlung

Calculations by Hayakawa,[3] Marshak and Ashkin,[4] and Serber[11] lead to the result that about one photon in the region of interest of these experiments will be produced in about 10^4 proton-nucleon interactions. In the case of beryllium, which has an inelastic cross section of about 10^{-25} cm^2 (1.0×10^{-25} for 280-Mev neutrons),[12] these results lead to a cross section for high energy photon production of 10^{-29} cm. This is in agreement with our observed cross sections for 175-Mev protons and 190-Mev deuterons. The observed cross section at 350 Mev, however, is about 100 times larger than this predicted value. Further, the shape of the spectra and, in particular, the rapid increase in yield with proton energy do not conform to any known type of bremsstrahlung.

TABLE I. Photon yields as a function of angle.

Lab. angle of view	Relative photon yield	Predicted relative yield
0°	2.1 ±0.3	2.0
133°	1.1 ±0.2	1.2
180°	1.00	1.00

TABLE II. Comparisons of yields and cross sections for different elements.

	Be	Cu	Ta
Relative yield per nucleus of 70-Mev photons from 340-Mev incident protons (180° angle of view)	1	2.8	4
Relative inelastic collision cross sections for 280-Mev neutrons	1	5	11
Relative yield per nucleus of photons from 190-Mev deuteron bombardment	1	—	9±1
Relative inelastic collision cross sections for 90-Mev neutrons	1	4.3	8.7

[11] R. Serber (private communication).
[12] J. DeJuren (to be published).

TABLE III. Cross sections per C nucleus for production of photons.

	Lab. system	$\beta=0.32$ system
Differential cross section in cm^2 per Mev per steradian for yield in 0° direction (at the peak)	1.2×10^{-30}	0.85×10^{-30}
Same for yield in 180° direction	0.6×10^{-30}	0.85×10^{-30}
Integrated over spectrum observed at 0° in cm^2 per steradian	1.5×10^{-28}	0.75×10^{-28}
Same for 180° direction	0.35×10^{-28}	0.70×10^{-28}
Total cross section for producing photons, assuming spherical symmetry, in cm^2		1×10^{-27}

C. Nucleon Isobars (Excited Nucleons)

In this process it is assumed that in the proton-nucleon collision one of the nucleons becomes excited and then subsequently loses its excitation through photon emission. If it is assumed that in the coordinate system in which the isobar is at rest the photons are mono-energetic, or at least have an energy spread narrow compared to the observed spread shown in Fig. 5, this possibility may also be ruled out by the following considerations. Analysis of Fig. 5 shows that the energy of the excited state would in this case be about 80 Mev. Figure 3 shows that 40-Mev photons are observed in the forward (0°) direction. This requires that there be isobars moving in a direction opposite to that of the bombarding proton with a velocity of 0.6c. This can only

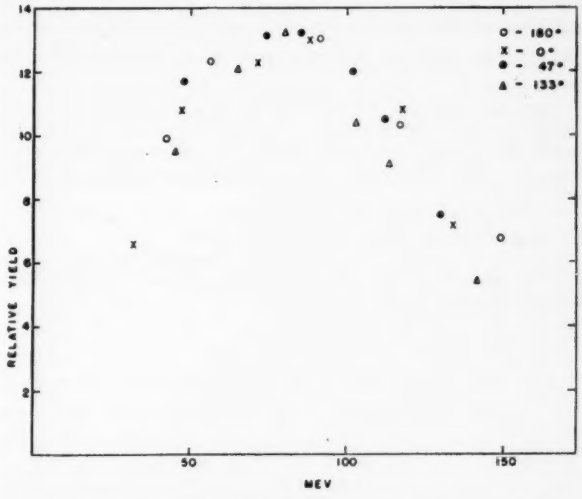

FIG. 5. Energy distributions transformed to system with $\beta=0.32$ in direction of protons.

happen if there are nucleons in the nucleus with momenta corresponding to energies in excess of 250 Mev.*

D. Excited State of a π-Meson

This possibility is not completely excluded, if the lifetime of the excited level is sufficiently short. However, the threshold occurring for available energy values below 200 Mev does not agree well with the mass of π-meson plus the mass equivalent of an 80-Mev photon.

E. Neutral Mesons

In this process it is assumed that the proton nucleon collision results in the production of a neutral meson which then decays into two photons. Such a process has been suggested by Lewis, Oppenheimer, and Wouthuysen[6] as a possible origin of the soft component in cosmic radiation.

On the basis of this assumption, the observations lead to mass of about 300 electron masses for the neutral meson involved. A particle of this type, with a half-life of less than 10^{-11} sec., fits all of our present observations. Since this particle is so light compared to a proton, velocities of 0.8c in the center of momentum system of the collision are allowed, and hence the broad distribution of photon energies may be explained. The apparent threshold near 175 Mev and the rapid rise in yield from 175 Mev to 350 Mev is also about what would be expected for this process, and the yield at 340 Mev is the same order of magnitude as the meson yield at this energy. Calculations by Taylor[13] and Marshak[14] of the expected photon spectra from this process are very similar to those observed.** The neutral meson hypothesis is also in agreement, as is also the isobar hypothesis, with the experimental observation that the energy of the peak of the photon spectrum occurs at approximately the same value, independent of the proton energy, when transformed to the proper coordinate system.

The existence of a neutral meson is clearly not required at the present stage of the experiments, but is the only one of the above five hypotheses which seems to fit the experimental data.

A planned experiment to determine whether the photons are emitted singly or in pairs will distinguish clearly between D and E, as well as between C and E.

VI. EXPERIMENTS IN PREPARATION

Several significant experimental tests are clearly implied by the foregoing results and discussion.

1. A liquid hydrogen target experiment is considered to determine a threshold without the uncertainties due to the momenta of nucleons in nuclei. This will also give the p-p collision yield, to be compared with the mixture of p-p and p-n collision yields from other light nuclei.

2. A specifically designed pair counter is in design with which more precise energy and angle distributions can be obtained in reasonable counting periods. From such measurements better information on the proper photon energy spectrum can be obtained, with consequent improvement of information about the existence and mass of an intermediate particle, and better data on absolute yield.

3. A cloud-chamber experimental program has been started, in cooperation with Dr. E. Hayward, seeking the answer about whether the photons are emitted singly or in pairs.

4. Simple experiments geometrically defining the region of emission of the photons have already shown the lifetime of any intermediate particle to be $<10^{-11}$ sec. This type of experiment will be improved.

VII. ACKNOWLEDGMENTS

The authors wish to express their appreciation of the stimulating interest of Professor E. O. Lawrence, and of the cooperation of the cyclotron crew under James Vale and the electronics staff under H. D. Farnsworth.

This work was done under the auspices of the AEC.

* The essential idea here is that the struck nucleon acts independently of the others present, except that it has considerable kinetic energy due to its being bound. See for instance R. Serber, Phys. Rev. 72, 1114 (1947) and M. L. Goldberger, Phys. Rev. 74, 1269 (1948).

[13] T. Taylor (private communication).

[14] R. E. Marshak (private communication).

** It may be noted that the energy distribution of the hypothetical neutral mesons could be calculated from better data of the type given in Fig. 5.

PHYSICAL REVIEW VOLUME 77, NUMBER 2 JANUARY 15, 1950

Quantum Theory of Non-Local Fields. Part I. Free Fields

HIDEKI YUKAWA*
Columbia University, New York, New York
(Received September 27, 1949)

The possibility of a theory of non-local fields, which is free from the restriction that field quantities are always point functions in the ordinary space, is investigated. Certain types of non-local fields, each satisfying a set of mutually compatible commutation relations, which can be obtained by extending familiar field equations for local fields in conformity with the principle of reciprocity, are considered in detail. Thus a scalar non-local field is obtained, which represents an assembly of particles with the mass, radius and spin 0, provided that the field is quantized according to the procedure similar to the method of second quantization in the usual field theory. Non-local vector and spinor fields corresponding to assemblies of particles with the finite radius and the spins 1 and ½ respectively are obtained in the similar way.

I. INTRODUCTION

IT has been generally believed for years that well-known divergence difficulties in quantum theory of wave fields could be solved only by taking into account the finite size of the elementary particles consistently. Recent success of quantum electrodynamics, which took advantage of the relativistic covariance to the utmost,[1] however, seemed to have weakened to some extent the necessity of introducing so-called universal length or any substitute for it into field theory. In fact, all infinities which had been familiar in previous formulations of quantum electrodynamics were reduced to unobservable renormalization factors for the mass and the electric charge in the newer formalism. Furthermore, in order to get rid of the remaining difficulties that these renormalization factors were still either infinite or indefinite, main efforts were concentrated in the direction of introducing various kinds of auxiliary fields, either real or only formal, rather than in the direction of introducing explicitly the universal length or the finite radius of the elementary particles. So far as the results of the investigations in the former direction are concerned, however, the prospect is not so encouraging. Namely, an ingenious method of regulators, which was investigated by Pauli extensively,[2] can be regarded as a formalistic generalization of the theory of mixed fields,[3] but cannot be replaced by a combination of neutral vector fields and charged spinor fields with different masses, unless we admit the introduction of bosons with negative energies and fermions with imaginary charges as pointed out by Feldman.[4] More generally, according to recent investigations by Umezawa and others[5] and by Feldman,[4] no combination of quantized fields with spins 0, ½, and 1 can be free from all of the divergence difficulties, as long as only *positive* energy states for bosons and *real* coupling constants for the interactions between fermions and bosons are taken into account.

Nevertheless, the difficulties remaining in quantum electrodynamics are not so serious as those which appear in meson theory. In the latter case, we know that straightforward calculations very often lead to divergent results for directly observable quantities such as the probabilities of certain types of meson decay.[6] Although the application of Pauli's regulators to meson theory was found useful for obtaining finite results, it can hardly be considered as a satisfactory solution of the problem for reasons mentioned above. It seems to the present author that, at least, a part of the defect of the present meson theory is due to the lack of a consistent method of dealing with the finite extension of the elementary particle such as the nucleon, whereas the effect of the finite extension is usually very small so far as electrodynamical phenomena in the narrowest sense are concerned, except for its decisive effect on the renormalizations of the mass and the electric charge.

Under these circumstances, it seems worth while to investigate again the possibility of extension of the present field theory in the direction of introducing the finite radius of the elementary particle. In this paper, as the continuation of the preceding papers,[7] the possibility of a theory of quantized *non-local* fields, which is free from the restriction that field quantities are always point functions in the ordinary space, will be discussed in detail. One may be very sceptical about the necessity of such a drastic change in field theory, because

* On leave of absence from Kyoto University, Kyoto, Japan.

[1] As to the list of recent works by Tomonaga, Schwinger and others, see V. Weisskopf, Rev. Mod. Phys. **21**, 305 (1949).

[2] W. Pauli and F. Villars, Rev. Mod. Phys. **21**, 433 (1949). The method of regulators is an extension of cut-off procedures by R. P. Feynman, Phys. Rev. **74**, 1430 (1948) and by D. Rivier and E. C. G. Stueckelberg, Phys. Rev. **74**, 218 (1948).

[3] Field theories by Bopp, Podolsky, Dirac, and others are more formalistic in that negative energy bosons are taken into account, whereas those by Pais, Sakata, and Hara are more realistic.

[4] D. Feldman, Phys. Rev. **76**, 1369 (1949). The author is indebted to Dr. Feldman for discussing the subject before publication of his paper.

[5] Umezawa, Yukawa, and Yamada, Prog. Theor. Phys. **4**, 25, 113 (1949). See also R. Jost and J. Rayski, Helv. Phys. Acta **22**, 457 (1949).

[6] H. Fukuda, and Y. Miyamoto, Prog. Theor. Phys. **4**, 235 (1949); Sasaki, Oneda, and Ozaki, Prog. Theor. Phys. (to be published); J. Steinberger, Phys. Rev. **76**, 1180 (1949). See further a comprehensive survey of recent works on meson theory by H. Yukawa, Rev. Mod. Phys. **21**, 474 (1949).

[7] A preliminary account of the content of this paper was published in H. Yukawa, Phys. Rev. **76**, 300 (1949), which will be cited as I.

other possibilities such as the introduction of *local* fields corresponding to particles with spins higher than 1 are not yet fully investigated. However, present theory of elementary particles with spins higher than 1 suffers from the difficulty associated with the necessity of of auxiliary conditions, and even if this is overcome by some revision of the formalism as proposed by Bhabha,[8] we can hardly expect a satisfactory solution of the whole problem, because the admixture of higher spin fields may well give rise to newer types of divergence in return for the elimination of more familiar ones. Moreover, it does not seem to the present author that the theory of non-local fields is necessarily contradictory to the theory of mixed local fields. They can rather be complementary to each other in that a non-local field may well happen to be approximately equivalent to some mixture of local fields. The most essential point, which is in favor of the non-local field, is that the convergence of field theory might be guaranteed by introducing a new type of *irreducible* field instead of a mixture, which is *reducible*.

In this paper, as in the preceding papers, we confine our attention to certain types of non-local field, each satisfying a set of mutually compatible commutation relations, which can be obtained by extending familiar field equations for local fields in conformity with the principle of reciprocity. The solutions of these operator equations can be interpreted as a field-theoretical representation of assemblies of elementary particles, each having a definite mass and a definite radius. In this connection, recent attempt by Born and Green[9] is interesting particularly in that they made use of the principle of reciprocity as a postulate for determining possible masses of elementary particles of various types. However, it is not yet clear whether their method of density operators contains something essentially different from the usual theory of mixture of local fields. The most important question of the interaction of two or more non-local fields will be discussed in Part II of this paper.

II. AN EXAMPLE OF THE NON-LOCAL SCALAR FIELD

In order to see what comes out by generalizing a field theory so as to include non-local fields, we start from a particular case of the non-local scalar field. A scalar operator U, which is supposed to describe a non-local scalar field, can be represented, in general, by a matrix with rows and columns, each characterized by a set of values of space and time coordinates. Alternatively, we can regard this operator U as a certain function of four space-time operators x^μ ($x'=x_1\equiv x$, $x^2=x_2\equiv y$, $x^3=x_3\equiv z$, $x^4=-x_4\equiv ct$) as well as of four space-time displacement operators p_μ, which satisfy well-known commutation relations

$$[x^\mu, p_\nu]=ih\delta_{\mu\nu}, \tag{1}$$

where

$$[A, B]\equiv AB-BA \tag{2}$$

for any two operators A and B. Usual local fields are included as the particular case, in which the field operator U is a function of x^μ alone, so that it can be represented by a diagonal matrix in the representation, in which the operators x^μ themselves are diagonal. In this particular case, it is customary to start from the second-order wave equation

$$\left(\frac{\partial^2}{\partial x_\mu \partial x^\mu}-\kappa^2\right)U(x^\mu)=0, \quad \kappa=mc/h \tag{3}$$

for the local field $U(x^\mu)$, in order that it can reproduce, when quantized, an assembly of identical particles with a definite mass m and the spin 0. Equation (3) is equivalent to the relation between the operator U and the operators p_μ

$$[p_\mu[p^\mu, U]]+m^2c^2U=0 \tag{4}$$

for this case. We assume that the non-local scalar field U in question satisfies the commutation relation of the same form as (4). However, in our case, we need further the commutation relation between U and x^μ, in contrast to the case of local field, in which U and x^μ are simply commutative with each other. In order to guess the correct form for it, some heuristic idea is needed. The principle of reciprocity seems to be very useful for this purpose. Namely, we assume that the commutation relation between U and x^μ has a form

$$[x_\mu[x^\mu, U]]-\lambda^2U=0, \tag{5}$$

where λ is a constant with the dimension of length and can be interpreted as the radius of the elementary particle in question, as will be shown below. The relations (4) and (5) are not exactly the same in form, but differ from each other by plus and minus signs of the last terms on the left-hand sides of (4) and (5). Thus, the two operator equations (4) and (5) can be said to be mutually reciprocal rather than perfectly symmetrical, indicating that the radius of the elementary particle λ must be introduced as something reciprocal to the mass m.

Now the operator U can be represented by a matrix $(x_\mu'|U|x_\mu'')$ in the representation, in which x_μ are diagonal matrices. The matrix elements, in turn, can be considered as a function $U(X_\mu, r_\mu)$ of two sets of real variables

$$X_\mu=\tfrac{1}{2}(x_\mu'+x_\mu''), \quad r_\mu=x_\mu'-x_\mu''. \tag{6}$$

Accordingly, the relations (4), (5) can be replaced by

$$(\partial^2/\partial X_\mu \partial X^\mu-\kappa^2)U(X_\mu, r_\mu)=0, \tag{7}$$

$$(r_\mu r^\mu-\lambda^2)U(X_\mu, r_\mu)=0, \tag{8}$$

[8] H. J. Bhabha, Proc. Ind. Acad. Sci. **A21**, 241 (1945); Rev. Mod. Phys. **17**, 200 (1945).

[9] M. Born, Nature **163**, 207 (1949); H. S. Green, Nature **163**, 208 (1949); M. Born and H. S. Green, Proc. Roy. Soc. Edinburgh **A92**, 470 (1949).

respectively. Equations (7) and (8) are obviously compatible with each other and the former implies that $U(X_\mu, r_\mu)$ is, in general, a superposition of plane waves of the form $\exp ik_\mu X^\mu$ with k_μ satisfying the condition

$$k_\mu k^\mu + \kappa^2 = 0, \tag{9}$$

whereas the latter implies that $U(X_\mu, r_\mu)$ can be different from zero only for those values of r_μ, which satisfy the condition

$$r_\mu r^\mu - \lambda^2 = 0. \tag{10}$$

Thus the most general solution of the simultaneous Eqs. (7) and (8) has the form

$$U(X_\mu, r_\mu) = \int \cdots \int (dk^4) u(k_\mu, r_\mu) \delta(\gamma_\mu r^\mu - \lambda^2) \times \delta(k_\mu k^\mu + \kappa^2) \exp(ik_\mu X^\mu), \tag{11}$$

where $u(k_\mu, r_\mu)$ is an arbitrary function of two sets of variables k_μ and r_μ.

The above considerations suggest us that one set X_μ of the real variables could be identified with the conventional space and time coordinates of the elementary particle regarded as a material point in the limit of $\lambda \to 0$, whereas the other set r_μ could be interpreted as variables describing the internal motion in general case, in which the finite extension of the elementary particle in question could not be ignored. Thus, we might expect that the field U of the above type is equivalent to an assembly of elementary particles with the mass m, the radius λ and the spin 0, if it is further quantized according to the familiar method of second quantization. However, we can easily anticipate that the equivalence is incomplete, because $U(X_\mu, r_\mu)$ is different from zero for arbitrary large values of r_μ, so far as they satisfy the condition (10), even when only one term of the right-hand side of (11) corresponding to a definite set of values of k_μ is taken into account. In other words, we need another condition for restricting the possible form of $U(X_\mu, r_\mu)$ or $u(k_\mu, r_\mu)$ in order to complete the equivalence above mentioned. For this purpose, we introduce an auxil ary condition

$$[p_\mu [x^\mu U]] = 0, \tag{12}$$

which can be said to be self-reciprocal in that the relation

$$[x^\mu [p_\mu, U]] = 0 \tag{13}$$

can be deduced from (12) immediately on account of the commutation relation (1). Both of (12) and (13) are equivalent to the condition

$$r_\mu \frac{\partial U(X_\mu, r_\mu)}{\partial X^\mu} = 0 \tag{14}$$

for $U(X_\mu, r_\mu)$, or the restriction that $u(k_\mu, r_\mu)$ should be zero unless k_μ and r_μ satisfy the condition

$$k_\mu r^\mu = 0. \tag{15}$$

Thus the most general form of $U(X_\mu, r_\mu)$, which satisfies all the relations (7), (8), and (14), is

$$U(X_\mu, r_\mu) = \int \cdots \int (dk)^4 u(k_\mu, r_\mu) \delta(k_\mu k^\mu + \kappa^2) \times \delta(r_\mu r^\mu - \lambda^2) \delta(k_\mu r^\mu) \exp(ik_\mu X^\mu), \tag{16}$$

where $u(k_\mu, r_\mu)$ is again an arbitrary function of k_μ and r_μ.[10]

Now a simple physical interpretation can be given to the non-local field of the form (16) by considering the corresponding particle picture: Suppose that the particle is at rest with respect to a certain reference system. In this particular case, the motion of the particle as a whole, or the motion of its center of mass, can be represented presumably by a plane wave in X-space with the wave vector $k_1 = k_2 = k_3 = 0$, $k_4 = -\kappa$. The corresponding form of $U(X_\mu, r_\mu)$ is, apart from the factor independent of X_μ, r_μ,

$$u(0, 0, 0, -\kappa; r_\mu) \delta(r_\mu r^\mu - \lambda^2) \delta(\kappa r_4) \exp(-i\kappa X^4) \tag{17}$$

which is different from zero only for those values of r_μ, which satisfy the conditions

$$r_1^2 + r_2^2 + r_3^2 = \lambda^2, \quad r_4 = 0. \tag{18}$$

Thus, the form of $U(X_\mu, r_\mu)$ in this case is determined completely by giving $u(0, 0, 0, -\kappa; r_\mu)$ as defined on the surface of the sphere with the radius λ in r-space. In other words, the internal motion can be described by the wave function $u(\theta, \varphi)$ depending only on the polar angles θ, φ, which are defined by

$$r_1 = r \sin\theta \cos\varphi, \quad r_2 = r \sin\theta \sin\varphi, \quad r_3 = r \cos\theta. \tag{19}$$

In general, $u(\theta, \varphi)$ can be expanded into series of spherical harmonics:

$$u(\theta, \varphi) = \sum_{l, m} c(0, 0, 0, -\kappa; l, m) P_l^m(\theta, \varphi), \tag{20}$$

which is equivalent to decomposing the internal rotation into various states characterized by the azimuthal quantum number l and the magnetic quantum number m.

In the case when the center of mass of the particle is moving with the velocity v_x, v_y, v_z, it can be described by a plane wave in X-space with the wave vector k_μ, which is connected with the velocity by the relations

$$v_x = -k_1 c/k_4, \quad v_y = -k_2 c/k_4, \quad v_z = -k_3 c/k_4, \quad k_4 = -(k_1^2 + k_2^2 + k_3^2 + \kappa^2)^{\frac{1}{2}}. \tag{21}$$

In this case, $U(X_\mu, r_\mu)$ has the form

$$u(k_\mu, r_\mu) \delta(r_\mu r^\mu - \lambda^2) \delta(k_\mu r^\mu) \exp(ik_\mu X^\mu), \tag{22}$$

which is different from zero only on the surface of the sphere with the radius λ in r-space, the sphere itself

[10] $U(X_\mu, r_\mu)$ as given by the expression (6) in I was not the most general form in that the coefficients $b(k_\mu)$ were independent of l_μ, which corresponded to ignore the internal rotation. The author is indebted to Professor R. Serber for calling attention to this point.

moving with the velocity v_x, v_y, v_z. Accordingly, we perform first the Lorentz transformation

$$x_\mu' = a_{\mu\nu} x_\nu \tag{23}$$

with the transformation matrix

$$(a_{\mu\nu}) \equiv \begin{pmatrix} 1+(k_1/K)^2 & k_1k_2/K^2 & k_1k_3/K^2 & k_1/\kappa \\ k_1k_2/K^2 & 1+(k_2/K)^2 & k_2k_3/K^2 & k_2/\kappa \\ k_1k_3/K^2 & k_2k_3/K^2 & 1+(k_3/K)^2 & k_3/\kappa \\ k_1/\kappa & k_2/\kappa & k_3/\kappa & -k_4/\kappa \end{pmatrix}, \tag{24}$$

where $K=(\kappa(\kappa-k_4))^{\frac{1}{2}}$. Then the wave function for the internal motion can be described by a function $u'(\theta', \varphi')$ of the polar angle θ', φ' defined by

$$\left.\begin{aligned} r_1' &= a_{1\nu} r_\nu = r' \sin\theta' \cos\varphi', & r_2' &= a_{2\nu} r_\nu = r' \sin\theta' \sin\varphi', \\ r_3' &= a_{3\nu} r_\nu = r' \cos\theta', & r_4' &= a_{4\nu} r_\nu = k_\mu r^\mu/\kappa. \end{aligned}\right\} \tag{25}$$

Incidentally, r_4' as defined by the last expression in (25) is nothing but the proper time multiplied by $-c$ for the particle, which is moving with the velocity v_x, v_y, v_z. Again, $u'(\theta', \varphi')$ can be expanded into series of spherical harmonics:

$$u'(\theta', \varphi') = \sum_{l,m} c(k_\mu, l, m) P_l^m(\theta', \varphi'). \tag{26}$$

Since the above arguments are in conformity with the principle of relativity perfectly, the non-local field in question can be regarded as a field-theoretical representation of a system of identical particles, each with the mass m, the radius and the spin 0, which can rotate as the relativistic rigid sphere without any change in shape other than the Lorentz contraction associated with the change of the proper time axis.

The non-local field U given by (16) reduces to the ordinary local scalar field in the limit $\lambda \to 0$, as it should be, provided that the rest mass m is different from zero. Namely, $(x_\mu'|U|x_\mu'')$ is different from zero only for $x_\mu' = x_\mu''$, because the only possible solution of the simultaneous Eqs. (9), (11), and (15) with $m \neq 0$ and $\lambda = 0$ is $r_1 = r_2 = r_3 = r_4 = 0$. On the contrary, the case of the zero rest mass $m=0$ is exceptional in that the non-local field U does not necessarily reduce to the local field in the limit $\lambda = 0$. This is because the simultaneous Eqs. (9), (11), and (15) with $m=0$ and $\lambda=0$ have solutions of the form

$$r_\mu = \pm(\lambda')^2 k_\mu, \quad k_4 = \pm(k_1^2+k_2^2+k_3^2)^{\frac{1}{2}}, \tag{27}$$

where λ' is an arbitrary constant with the dimension of length. More generally, the simultaneous equations with $m=0$ and $\lambda \neq 0$ has the general solution of the form

$$r_\mu = r_\mu' \pm (\lambda')^2 k_\mu, \quad k_4 = \pm(k_1^2+k_2^2+k_3^2)^{\frac{1}{2}}, \tag{28}$$

where r_μ' is any particular solution of the same equations. Thus the radius of the particle without the rest mass cannot be defined so naturally as in the case of the particle with the rest mass, corresponding to the circumstance that there is no rest system in the former case. Detailed discussions of this particular case will be made elsewhere.

III. QUANTIZATION OF NON-LOCAL SCALAR FIELD

In order to show that the non-local field above considered represents exactly the assembly of identical particles with the finite radius, we have to quantize the field on the same lines as the method of second quantization in ordinary field theory. For this purpose, it is convenient to write (16) in another form

$$U(X_\mu, r_\mu) = \int\cdots\int (dk)^4 (dl)^4 u(k_\mu, l_\mu) \times \delta(k_\mu k^\mu + \kappa^2)\delta(l_\mu l^\mu - \lambda^2)\delta(k_\mu l^\mu) \times \exp(ik_\mu X^\mu) \textstyle\prod_\mu \delta(r_\mu + l_\mu), \tag{29}$$

where l_μ is a four vector. The integrand is different from zero only for those values of k_μ, l_μ, which satisfy the relations

$$k_\mu k^\mu + \kappa^2 = 0, \quad l_\mu l^\mu - \lambda^2 = 0, \quad k_\mu l^\mu = 0. \tag{30}$$

Accordingly, the matrix elements for the operator U are

$$(x_\mu'|U|x_\mu'') = \int\cdots\int (dk)^4 (dl)^4 u(k_\mu, l_\mu) \times \delta(k_\mu k^\mu + \kappa^2)\delta(l_\mu l^\mu - \lambda^2) \exp(ik^\mu x_\mu'/2) \times \textstyle\prod_\mu \delta(x_\mu' - x_\mu'' + l_\mu) \exp(ik^\mu x_\mu''/2), \tag{31}$$

which is equivalent to the relation

$$U = \int\cdots\int (dk)^4 (dl)^4 \bar{u}(k_\mu, l_\mu) \exp(ik_\mu x^\mu/2) \times \exp(il^\mu p_\mu/\hbar) \exp(ik_\mu x^\mu/2), \tag{32}$$

between the operators x^μ, p_μ and U, where

$$\bar{u}(k_\mu, l_\mu) = u(k_\mu, l_\mu)\delta(k_\mu k^\mu + \kappa^2)\delta(l_\mu l^\mu - \lambda^2)\delta(k_\mu l^\mu). \tag{33}$$

As the operators $k_\mu x^\mu$ and $l^\mu p_\mu$ in the same term on the right-hand side of (32) are commutative with each other on account of the relations (1) and (30), (32) can also be written in the form

$$U = \int\cdots\int (dk)^4 (dl)^4 \bar{u}(k_\mu, l_\mu) \exp(ik_\mu x^\mu) \times \exp(il^\mu p_\mu/\hbar). \tag{32'}$$

Similarly the operator U^*, which is the Hermitian

conjugate of U, can be written in the form

$$U^*=\int\cdots\int(dk^4)(dl)^4\bar{u}^*(k_\mu, l_\mu)\times\exp(-ik_\mu x^\mu)\exp(-il^\mu p_\mu/\hbar). \quad (34)$$

Now the method of second quantization can be applied to our case in the following way: $\bar{u}(k_\mu, l_\mu)$ and $\bar{u}^*(k_\mu, l_\mu)$ in Eqs. (32′) and (34) are regarded as operators, which are Hermitian conjugate to each other and are non-commutative in general. The fact that the operators defined by

$$\left.\begin{aligned}U(k_\mu, l_\mu)&\equiv\exp(ik_\mu x^\mu)\exp(il^\mu p_\mu/\hbar);\\ U^*(k_\mu, l_\mu)&\equiv\exp(-ik_\mu x^\mu)\exp(-il^\mu p_\mu/\hbar)\end{aligned}\right\} \quad (35)$$

are unitary, i.e., satisfy the relation

$$U(k_\mu, l_\mu)U^*(k_\mu, l_\mu)=U^*(k_\mu, l_\mu)U(k_\mu, l_\mu)=1 \quad (36)$$

suggests us the commutation relations

$$\left.\begin{aligned}&[\bar{u}(k_\mu, l_\mu), \bar{u}^*(k_\mu', l_\mu')]\\ &=-\frac{k_4}{|k_4|}\prod_\mu\delta(k_\mu-k_\mu')\delta(l_\mu-l_\mu')\cdot\delta(k_\mu k^\mu+\kappa^2)\\ &\quad\times\delta(l_\mu l^\mu-\lambda^2)\delta(k_\mu l^\mu),\\ &[\bar{u}(k_\mu, l_\mu), \bar{u}(k_\mu', l_\mu')]=0,\\ &[\bar{u}^*(k_\mu, l_\mu), \bar{u}^*(k_\mu', l_\mu')]=0,\end{aligned}\right\} \quad (37)$$

which are obviously invariant with respect to the whole group of Lorentz transformations. In order to make the physical meaning of the relations (37) clear, we suppose the field in a cube with the edges of the length L, which is very large compared with λ. Then the effects of non-localizability of the field are negligible, because they are confined to small regions very near the surface of the cube.[11] In this case, the integrations with respect to k_μ on the right-hand side of Eqs. (32′) and (34) are replaced by the summations with respect to k_μ, which take the values

$$k_1=(2\pi/L)n_1,\quad k_2=(2\pi/L)n_2,\quad k_3=(2\pi/L)n_3,\quad k_4=\pm(k_1^2+k_2^2+k_3^2+\kappa^2)^{\frac{1}{2}}, \quad (38)$$

where n_1, n_2, n_3 are integers, either positive or negative, including zero. The integrations with respect to l_μ with fixed k_μ are replaced by those with respect to l_μ' defined by

$$l_\mu'=a_{\mu\nu}l_\nu, \quad (39)$$

where the coefficients $a_{\mu\nu}$ are given by (24). Further, we introduce the polar angle Θ, Φ, which are connected with l_1', l_2', l_3' just as θ', φ' are connected with r_1', r_2', r_3' by the relations (25). Thus we obtain

$$U=\sum_{k_1k_2k_3}\int\int\left(\frac{2\pi}{L}\right)^3\frac{\lambda\sin\Theta d\Theta d\Phi}{4\kappa(k^2+\kappa^2)^{\frac{1}{2}}}\times\{u(k,\Theta,\Phi)U(k,\Theta,\Phi)+v^*(k,\Theta,\Phi)U^*(k,\Theta,\Phi)\}, \quad (40)$$

[11] More precisely, L must be large compared with $\lambda/(1-\beta^2)^{\frac{1}{2}}$, where βc is the maximum velocity of particles in consideration.

where

$$\left.\begin{aligned}u(k,\Theta,\Phi)&\equiv u(k_1, k_2, k_3, -(k^2+\kappa^2)^{\frac{1}{2}}; l_\mu),\\ v^*(k,\Theta,\Phi)&\equiv u(-k_1, -k_2, -k_3, (k^2+\kappa^2)^{\frac{1}{2}}; -l_\mu),\\ U(k,\Theta,\Phi)&\equiv\exp(ikx+i(k^2+\kappa^2)^{\frac{1}{2}}x_4)\times\exp(i\lambda l^\mu p_\mu/\hbar),\\ U^*(k,\Theta,\Phi)&\equiv\exp(-ikx-i(k^2+\kappa^2)^{\frac{1}{2}}x_4)\times\exp(-i\lambda l^\mu p_\mu/\hbar).\end{aligned}\right\} \quad (41)$$

Finally, by expanding u and v^* into series of spherical harmonics, we obtain

$$U=\sum_{k_1k_2k_3}\sum_{l,m}\left(\frac{2\pi}{L}\right)^3\frac{\lambda}{4\kappa(k^2+\kappa^2)^{\frac{1}{2}}}\{u(k,l,m)\times U(k,l,m)+v^*(k,l,m)U^*(k,l,m)\}, \quad (42)$$

where

$$\left.\begin{aligned}u(k,l,m)&\equiv\int\int u(k,\Theta,\Phi)\times\bar{P}_l^m(\Theta,\Phi)\sin\Theta d\Theta d\Phi,\\ v^*(k,l,m)&\equiv\int\int v^*(k,\Theta,\Phi)\times P_l^m(\Theta,\Phi)\sin\Theta d\Theta d\Phi,\end{aligned}\right\} \quad (43)$$

$$\left.\begin{aligned}U(k,l,m)&\equiv\int\int U(k,\Theta,\Phi)\times P_l^m(\Theta,\Phi)\sin\Theta\, d\Theta d\Phi\\ U^*(k,l,m)&\equiv\int\int U^*(k,\Theta,\Phi)\times\bar{P}_l^m(\Theta,\Phi)\sin\Theta d\Theta d\Phi\end{aligned}\right\} \quad (44)$$

assuming that the spherical harmonics $P_l^m(\Theta,\Phi)$ and their complex conjugate $\bar{P}_l^m(\Theta,\Phi)$ are normalized according to the rule:

$$\int\int\bar{P}_l^m(\Theta,\Phi)P_l^m(\Theta,\Phi)\sin\Theta d\Theta d\Phi_m=1. \quad (45)$$

Similarly, U^* is transformed into the form

$$U^*=\sum_{k_1k_2k_3}\sum_{l,m}\left(\frac{2\pi}{L}\right)^3\frac{\lambda}{4\kappa(k^2+\kappa^2)^{\frac{1}{2}}}\{v(k,l,m)\times U(k,l,m)+u^*(k,l,m)U^*(k,l,m)\}, \quad (46)$$

where

$$\left.\begin{aligned}u^*(k,l,m)&\equiv\int\int u^*(k,\Theta,\Phi)P_l^m(\Theta,\Phi)\times\sin\Theta d\Theta d\Phi,\\ v(k,l,m)&\equiv\int\int v(k,\Theta,\Phi)\bar{P}_l^m(\Theta,\Phi)\times\sin\Theta d\Theta d\Phi.\end{aligned}\right\} \quad (47)$$

By the same transformation, we obtain from Eq. (37) the commutation relations

$$\left.\begin{aligned}&[a(k,l,m),\, a^*[k',l',m']]=\delta(k,k')\delta(l,l')\delta(m,m'),\\&[b(k,l,m),\, b^*(k',l',m')]=\delta(k,k')\delta(l,l')\delta(m,m'),\\&[a(k,l,m),\, b(k',l',m')]=0,\ \text{etc.}\end{aligned}\right\}\tag{48}$$

for the operators defined by

$$\left.\begin{aligned}a(k,l,m)&\equiv\left(\left(\frac{2\pi}{L}\right)^3\frac{\lambda}{4\kappa(k^2+\kappa^2)^{\frac{1}{2}}}\right)^{\frac{1}{2}}\cdot u(k,l,m),\\a^*(k,l,m)&\equiv\left(\left(\frac{2\pi}{L}\right)^3\frac{\lambda}{4\kappa(k^2+\kappa^2)^{\frac{1}{2}}}\right)^{\frac{1}{2}}\cdot u^*(k,l,m),\\b(k,l,m)&\equiv\left(\left(\frac{2\pi}{L}\right)^3\frac{\lambda}{4\kappa(k^2+\kappa^2)^{\frac{1}{2}}}\right)^{\frac{1}{2}}\cdot v(k,l,m),\\b^*(k,l,m)&\equiv\left(\left(\frac{2\pi}{L}\right)^3\frac{\lambda}{4\kappa(k^2+\kappa^2)^{\frac{1}{2}}}\right)^{\frac{1}{2}}\cdot v^*(k,l,m).\end{aligned}\right\}\tag{49}$$

Hence, each of the operators defined by

$$\begin{aligned}n^+(k,l,m)&\equiv a^*(k,l,m)a(k,l,m);\\n^-(k,l,m)&\equiv b^*(k,l,m)b(k,l,m)\end{aligned}\tag{50}$$

has eigenvalues 0, 1, 2, $\cdots$ and can be interpreted as the number of particles in the state characterized by the quantum numbers k, l, m with either positive or negative charge. Thus the non-local field above considered corresponds to the assembly of charged bosons with the mass m, the radius λ and the spin 0. It can easily be shown that in the limit $\lambda\to 0$, U reduces to the familiar quantized local field for bosons apart from the extra factor

$$\delta(x_1'-x_1'')\delta(x_2'-x_2'')\delta(x_3'-x_3'')\delta(x_4'-x_4'')\tag{51}$$

which must be omitted, whenever we go over from non-local to local field.

The non-local neutral field can be obtained, if we assume that the field operator U is Hermitian, i.e., $U=U^*$. In this case, we cannot discriminate between u and v, or a and b, so that we have instead of Eqs. (42) and (46) the relation

$$U=\sum_{k_1k_2k_3}\sum_{l,m}\left(\frac{2\pi}{L}\right)^3\frac{\lambda}{4\kappa(k^2+\kappa^2)^{\frac{1}{2}}}\{u(k,l,m)\times U(k,l,m)+u^*(k,l,m)U^*(k,l,m)\}.\tag{52}$$

It should be noticed, further, that we could start from the commutation relations

$$\left.\begin{aligned}&[\bar u(k_\mu,l_\mu),\,\bar u^*(k_\mu',l_\mu')]_+\\&\quad=\textstyle\prod_\mu\delta(k_\mu-k_\mu')\delta(l_\mu-l_\mu')\cdot\delta(k_\mu k^\mu+\kappa^2)\\&\qquad\qquad\times\delta(l_\mu l^\mu-\lambda^2)\delta(k_\mu l^\mu),\\&[\bar u(k_\mu,l_\mu),\,\bar u(k_\mu',l_\mu')]_+=0,\\&[\bar u^*(k_\mu,l_\mu),\bar u^*(k_\mu',l_\mu')]_+=0.\end{aligned}\right\}\tag{37}$$

instead of Eq. (37), where

$$[A,B]_+\equiv AB+BA\tag{53}$$

for any two operators A and B. However, in this case, we arrive at the well-known contradiction in the limit of $\lambda\to 0$, which prohibits the elementary particles with spin 0 from obeying Fermi statistics.

IV. NON-LOCAL SPINOR FIELD

The above considerations can easily be extended to the non-local vector field without introducing anything essentially new which needs detailed discussions. On the contrary, the case of the non-local spinor field must be investigated from the beginning. We start from the spinor operator ψ with four components, which transform as the components of Dirac wave function. Each of these components can be considered as a non-local operator just like the operator U in the case of the scalar field. As an extension of Dirac's wave equations for the local spinor field, we assume the relations between the operators x^μ, p_μ and ψ:

$$\gamma^\mu[p_\mu,\psi]+mc\psi=0,\tag{54}$$

$$\beta_\mu[x^\mu,\psi]+\lambda\psi=0,\tag{55}$$

where γ^μ are well-known Dirac matrices forming a four vector, which satisfy the commutation relations among themselves:

$$[\gamma^\mu,\gamma_\nu]_+=-2\delta_{\mu\nu}.\tag{56}$$

We assume similar commutation relations for matrices β_μ:

$$[\beta^\mu,\beta_\mu]_+=2\delta_{\mu\nu}.\tag{57}$$

Then, we obtain by iteration the relations

$$[p^\mu[p_\mu,\psi]]+m^2c^2\psi=0,\tag{58}$$

$$[x_\mu[x^\mu,\psi]]-\lambda^2\psi=0,\tag{59}$$

which have the same form as the relations (4) and (5) for the scalar field. However, the matrices β_μ have to be so chosen as to satisfy the demand that the relations (54) and (55) are compatible with each other. Namely, from the relations

$$\beta_\mu\gamma^\mu[x^\mu[p_\nu,\psi]]=\lambda mc\psi,\tag{60}$$

$$\gamma^\nu\beta_\mu[p_\nu[x^\mu,\psi]]=\lambda mc\psi,\tag{61}$$

which can be readily obtained by considering Eqs. (54) and (55), must have the same form, so that β_μ must satisfy an additional condition:

$$[\beta_\mu,\gamma^\nu][x^\mu[p_\nu,\psi]]=0.\tag{62}$$

This condition reduces to the form

$$[x^\mu[p_\mu,\psi]]=0,\tag{63}$$

which is the same as the condition (12) or (13) for the scalar field, if β_μ are so chosen as to satisfy the commutation relations

$$[\beta_\mu,\gamma^\nu]=C\delta_{\mu\nu},\tag{64}$$

where C is a matrix with the determinant different from zero. Equation (64) can be satisfied by matrices γ^μ, β_μ which are expressed in the form

$$\gamma^1=i\rho_2\sigma_1, \quad \gamma^2=i\rho_2\sigma_2, \quad \gamma^3=i\rho_2\sigma_3, \quad \gamma^4=\rho_3, \tag{65}$$
$$\beta_1=\rho_3\sigma_1, \quad \beta_2=\rho_3\sigma_2, \quad \beta_3=\rho_3\sigma_3, \quad \beta_4=-i\rho_2, \tag{66}$$

in terms of sets of mutually independent Pauli matrices σ_1, σ_2, σ_3 and ρ_1, ρ_2, ρ_3. It is well known that the matrices as given by (66) do not form an ordinary vector, but a pseudovector. Thus, if we confine our attention to the proper Lorentz transformation, the relations (54) and (55) are both invariant. However, if we perform the improper Lorentz transformation, for which the determinant of the transformation matrix has the value -1 instead of $+1$, the form of the relation (55) changes into

$$\beta_\mu[x^\mu, \psi]-\lambda\psi=0, \tag{67}$$

whereas the relation (54) is invariant. In other words, the fundamental equations for the non-local spinor field, which has similar properties as the non-local scalar field considered in the preceding sections, can be constructed so as to be invariant with respect to the whole group of Lorentz transformations including reflections, only if both forms (55) and (67) are put together into one relation for one spinor field with the components twice as many as the four components for the usual spinor field. This is equivalent to introduce one more independent set of Pauli matrices ω_1, ω_2, ω_3 and to assume that all of the matrices γ^μ, β_μ have each eight rows and columns characterized by eight combinations of eigenvalues of σ_3, ρ_3, ω_3. Therewith the spinor must have eight components, first four components and the remaining four corresponding respectively to the eigenvalues $+1$ and -1 of ω_3.

In order to establish the invariance of fundamental laws for the non-local spinor field with respect to the whole group of Lorentz transformations, we assume further that ω_2 and ω_3 change sign under improper Lorentz transformation, whereas ω_1 does not. We can now adopt the relation

$$\beta_\mu[x^\mu, \psi]+\omega_3\lambda\psi=0 \tag{68}$$

in place of Eq. (55). It is clear from the above arguments that the fundamental Eqs. (54) and (68) are invariant with respect to the whole group of Lorentz transformations. However, for the purpose of proving it more explicitly, we consider the transformation properties of ψ with respect to the Lorentz transformation, whereby we assume that the matrices γ^μ, β_μ have prescribed forms as defined by Eqs. (65), (66) independent of the coordinate system. In the usual theory, in which the spinor field ψ has four components, we have the linear transformation

$$\psi'=S\psi \tag{69}$$

associated with each of the Lorentz transformations for the coordinates:

$$x_\mu'=a_{\mu\nu}x_\nu, \tag{70}$$

where S is a matrix with four rows and four columns.[12] In our case, in which the spinor ψ has eight components, we assume the same form for S in Eq. (69) except that the numbers of rows and columns are doubled, when Eq. (70) is a proper Lorentz transformation with the determinant $+1$, whereas we have to replace Eq. (69) by

$$\psi'=\omega_1 S\psi, \tag{71}$$

when Eq. (70) is an improper Lorentz transformation with the determinant -1. This guarantees the invariance of the relation (68) with respect to improper as well as proper Lorentz transformations.

However, the above procedure is unsatisfactory, particularly because it is difficult to give a simple physical meaning to the new degree of freedom. As will be shown in the additional remark at the end of this paper, there is an alternative way, in which we have no need to increase the number of components of ψ from 4 to 8.

Now, each component ψ_i $(i=1, 2, 3, 4)$ of the spinor ψ can be represented as a matrix $(x_\mu'|\psi_i|x_\mu'')$ in the representation, in which x_μ are diagonal. $(x_\mu'|\psi_i|x_\mu'')$ can be regarded, in turn, as a function $\psi_i(X_\mu, r_\mu)$ of X_μ, r_μ, where X_μ, r_μ are defined by Eq. (6). Therewith the relations (54) and (68) can be represented by

$$\gamma^\mu(\partial\psi(X_\mu, r_\mu)/\partial X^\mu)+i\kappa\psi(X_\mu, r_\mu)=0, \tag{72}$$
$$\beta_\mu r^\mu\psi(X_\mu, r_\mu)+\lambda\psi(X_\mu, r_\mu)=0, \tag{73}$$

respectively, where $\psi(X_\mu, r_\mu)$ is a spinor with four components $\gamma_i(X_\mu, r_\mu)$ $(i=1, 2, 3, 4)$. The simultaneous Eqs. (72), (73) for $\psi(X_\mu, r_\mu)$ have a particular solution of the form

$$\psi(X_\mu, r_\mu)=\bar{u}(k_\mu, r_\mu)\exp(ik_\mu X^\mu), \tag{74}$$

where $\bar{u}(k_\mu, r_\mu)$ is a spinor with four components satisfying

$$\gamma^\mu k_\mu\bar{u}+\kappa\bar{u}=0, \quad \beta_\mu r^\mu\bar{u}+\lambda\bar{u}=0. \tag{75}$$

It follows immediately from (75) that $\bar{u}$ must satisfy

$$(k_\mu k^\mu+\kappa^2)\bar{u}=0, \quad (r_\mu r^\mu-\lambda^2)\bar{u}=0, \quad k_\mu r^\mu\bar{u}=0 \tag{76}$$

so that $\bar{u}$ can be written in the form

$$\bar{u}=u(k_\mu, r_\mu)\delta(k_\mu k^\mu+\kappa^2)\delta(r_\mu r^\mu-\lambda^2)\delta(k_\mu r^\mu). \tag{77}$$

Each of four components of u can be expanded in the same way as the scalar operator u in the preceding sections. The second quantization can be performed by assuming commutation relations of the type (37) between field quantities, so that the non-local field represents an assembly of fermions with the mass m, the radius λ and the spin $\frac{1}{2}$. Further analysis of the non-local spinor field will be made in Part II of this paper. At any rate it is now clear that there exist non-local scalar, vector, and spinor fields, each corresponding to the assembly of particles with the mass, radius, and the spin 0, 1, and $\frac{1}{2}$.

[12] See, for example, W. Pauli, *Handbuch der Physik* **24**, Part 1, 83 (1933).

Now the question, with which we are met first, when we go over to the case of two or more non-local fields interacting with each other, is whether we can start from Schrödinger equation for the total system (or any substitute for it), thus retaining the most essential feature of quantum mechanics. We know that Schrödinger equation in its simplest form is not obviously relativistic in that it is a differential equation with the time variable as independent variable, space coordinates being regarded merely as parameters. It can be extended to a relativistic form as in Dirac's many-time formalism or, more satisfactorily, in Tomonaga-Schwinger's super-many-time formalism, as long as we are dealing with local fields satisfying the infinitesimal commutation relations. However, if we introduce the non-local fields or the non-localizability in the interaction between local fields, the clean-cut distinction between space-like and time-like directions is impossible in general. This is because the interaction term in the Lagrangian or Hamiltonian for the system of non-local fields contains the displacement operators in the time-like directions as well as those in the space-like directions. Thus, even if there exists an equation of Schrödinger type, it cannot be solved, in general, by giving the initial condition at a certain time in the past. Under these circumstances, we must have recourse to more general formalism such as the S-matrix scheme, which was proposed by Heisenberg.[13] In other words, we had better start from the integral formalism rather than the differential formalism. In local field theory, the integral formalism such as that, which was developed by Feynman, can be deduced from the ordinary differential formalism.[14,15] In non-local field theory, however, it may well happen that we are left only with some kind of integral formalism. In fact it will be shown in Part II that the non-local fields above considered can be fitted into the S-matrix scheme.

[13] W. Heisenberg, Zeits. f. Physik **120**, 513, 673 (1943); Zeits. f. Naturforsch. **1**, 608 (1946); C. Møller, Kgl. Danske Vid. Sels. Math. Fys. Medd. **23**, Nr. 1 (1945); **22**, Nr. 19 (1946).

[14] R. P. Feynman, Phys. Rev. **76**, 749, 769 (1949).

[15] F. J. Dyson, Phys. Rev. **75**, 486, 1736 (1949). See also many papers by E. C. G. Stueckelberg, which appeared mainly in Helv. Phys. Acta.

This work was done during the author's stay at The Institute for Advanced Study, Princeton. The author is grateful to Professor J. R. Oppenheimer for giving him the opportunity of staying there and also for stimulating discussions. He is also indebted to Dr. A. Pais and Professor G. Uhlenbeck for fruitful conversation.

ADDITIONAL REMARKS ON NON-LOCAL SPINOR FIELD

The problem of invariance of the relation (55) with respect to improper Lorentz transformation can be solved without introducing extra components to the spinor field. Namely, we take advantage of the anti-symmetric tensor of the fourth rank with the components $\epsilon_{\kappa\lambda\mu\nu}$, which are $+1$ or -1 according as $(\kappa, \lambda, \mu, \nu)$ are even or odd permutations of (1, 2, 3, 4) and 0 otherwise. Further we take into account the relations

$$i\beta_\nu=\gamma^\kappa\gamma^\lambda\gamma^\mu, \tag{78}$$

where $(\kappa, \lambda, \mu, \nu)$ are even permutations of (1, 2, 3, 4). Then (55) can be written in the form

$$\tfrac{1}{6}\sum_{\kappa\lambda\mu\nu}\epsilon_{\kappa\lambda\mu\nu}\gamma^\kappa\gamma^\lambda\gamma^\mu[x^\nu, \psi]+i\lambda\psi=0, \tag{79}$$

which is obviously invariant with respect to the whole group of Lorentz transformation. The invariance can be proved more explicitly by associating a linear transformation

$$\psi'=S\psi, \tag{80}$$

with each of the Lorentz transformation (70), where S is a matrix with four rows and columns satisfying the relations

$$S\gamma^\mu S^{-1}=a_{\nu\mu}\gamma^\nu. \tag{81}$$

It should be noticed, however, that the relation (79) is a unification of the relations (55) and (67) rather than the simple reproduction of (55), because (79) must be identified with (67) in the coordinate system, which is connected with the original coordinate system by an improper Lorentz transformation with the determinant -1.

Multiple Compton Scattering II*

W. R. FAUST
Department of Physics, University of Maryland, College Park, Maryland
and
Nucleonics Division, Naval Research Laboratory, Washington, D. C.
(Received September 22, 1949)

An experimental and theoretical investigation has been made of the intensity and spectral distribution of gamma-radiation due to point and plane sources immersed in a homogeneous medium. The intensity is calculated by considering the multiple scattering as taking place in a succession of steps and the spatial distribution of the radiation is deduced from the equilibrium between quanta in a given group and those added to and removed from this group by scattering.

I. INTRODUCTION

IN a recent paper[1] the modifications due to the multiple scattering in the intensity and spatial distribution of gamma-rays from a source uniformly distributed throughout an infinite medium have been calculated and compared with the experiment. The approximation, made in this paper, that quanta which have experienced a given number of scatterings have the same energy leads to results in good agreement with the experiment. In these calculations complicating geometrical factors introduced by a beam or by inhomogeneties in the medium are avoided. The purpose of this paper is to extend the treatment to sources in a homogeneous medium which are concentrated at a point or on a plane.

In Section II the intensity from point and plane sources is calculated by considering the multiple scattering as taking place in a succession of steps. The distribution of radiation is deduced, under simplifying assumptions, from the equilibrium between the quanta in a given group and those added to or removed from this group by scattering. In Section III a description of the experimental method is given while in Section IV the approximate calculations of Section II are compared with experimental measurements.

II. THEORY

Part A. Suppose that a "point" source emitting $\eta\lambda$-gamma-rays per second of energy E_0 is immersed in an unbounded medium.[2] As in (I) the quanta are divided into groups determined by the number of scatterings they have experienced. If it is assumed that each quantum in the $k-1^{\text{th}}$ group loses the same energy (i.e., the mean energy loss at this frequency) upon being scattered into the k^{th} group, then it follows that the mean energy of the k^{th} group is

$$E_k=(\sigma_s/\sigma)E_{k-1}, \tag{1}$$

where σ_s/σ is evaluated at the energy E_{k-1} and σ_s/σ is the mean ratio of scattered to incident energy as calculated from the Klein-Nishima formula. The succession of energy values for an initial energy of 1.20 Mev is given in Table I.

In order to describe the spatial distribution of quanta, let $F_k(\rho)=F_k^+(\rho)+F_k^-(\rho)$ be the total number of quanta of group k passing through a sphere of radius ρ, per second, about the point source. Here F_k^+/F_k is the fraction of quanta with angles θ, relative to the radius vector, between zero and $\pi/2$ and F_k^-/F_k is the fraction with $\pi/2\leqslant\theta\leqslant\pi$.

The total cross section σ can be decomposed in a similar manner, i.e., $\sigma=\sigma^++\sigma^-$. The fraction of incident quanta scattered into directions with $0\leqslant\theta\leqslant\pi/2$ is σ^+/σ while σ^-/σ is the fraction scattered into $\pi/2\leqslant\theta\leqslant\pi$. Integration of the differential cross section between 0 and $\pi/2$ yields σ^+ while the integration is between $\pi/2$ and π for σ^-.

It will be assumed that the contribution to the positive component of group k from group $k-1$ scattered in

TABLE I. Scattered energies and linear absorption coefficients.

E Mev	σ_s/σ	μ cm^{-1}	μ^+ cm^{-1}	μ^- cm^{-1}
1.20	0.545	0.0643	0.0475	0.0166
0.654	0.63	0.0861	0.0603	0.0250
0.412	0.69	0.102	0.0705	0.0341
0.284	0.73	0.1178	0.0784	0.042
0.207	0.79	0.1333	0.0850	0.0524
0.064	0.825	0.143	0.0894	0.0574
0.135	0.845	0.155	0.0925	0.0634
0.113	0.86	0.159		
0.098	0.875	0.163		
0.086	0.89	0.167		

TABLE II. Distribution functions for a unit point source.

(a) $F_0^+=e^{-\mu_0\rho}$

(b) $F_1^+=2.179(e^{-\mu_0\rho}-e^{-\mu_1\rho})$
$F_1^-=0.1104(e^{-\mu_0\rho})$

(c) $F_2^+=3.5610e^{-\mu_0\rho}-8.2640e^{-\mu_1\rho}+4.7030e^{-\mu_2\rho}$
$F_2^-=0.3676e^{-\mu_0\rho}-0.2895e^{-\mu_1\rho}$

(d) $F_3^+=4.9244e^{-\mu_0\rho}-18.6850e^{-\mu_1\rho}+20.9530e^{-\mu_2\rho}-7.1924e^{-\mu_3\rho}$
$F_3^-=0.80770e^{-\mu_0\rho}-1.4812e^{-\mu_1\rho}+0.72790e^{-\mu_2\rho}$

(e) $F_4^+=6.0868e^{-\mu_0\rho}-32.3540e^{-\mu_1\rho}+53.4615e^{-\mu_2\rho}$
$-36.3730e^{-\mu_3\rho}+9.1787e^{-\mu_4\rho}$
$F_4^-=1.3676e^{-\mu_0\rho}-4.1062e^{-\mu_1\rho}+3.9830e^{-\mu_2\rho}-1.2030e^{-\mu_3\rho}$

* Part of a dissertation submitted to the graduate school of the University of Maryland in partial fulfillment of requirements for the degree of Doctor of Philosophy.

[1] W. R. Faust and M. H. Johnson, Phys. Rev. **75**, 467 (1949), designated hereafter as I.

[2] Pair production is neglected here

TABLE III. Distribution functions for a unit point source emitting 1.20 Mev quanta.

Z cm	F_0^+ No./S.	F_1^+ No./S.	F_2^+ No./S.	F_3^+ No./S.	F_4^+ No./S.	F_5^+ No./S.	F_6^+ No./S.	F_7^+ No./S.	F_8^+ No./S.
0	1.000	0.000	0.00	0.00	0.000	0.00	0.00	0.00	0.00
10	0.5257	0.2250	0.0719	0 0295	0.0247	0.0187	0.0164	0.0144	0.0130
20	0.2763	0.2120	0.1201	0.0750	0.0560	0.0456	0.0335	0.0282	0.0260
30	0.1454	0.1520	0.1134	0.0815	0.0677	0.0511	0.0411	0.043	0.035
40	0.0765	0.0977	0.0907	0.0803	0.0687	0.0588	0.0531	0.042	0.038
50	0.0404	0.0562	0.0605	0.0542	0.0454	0.0452	0.0437	0.041	0.036
60	0.0213	0.0387	0.0467	0.0377	0.0343	0.0344	0.0337	0.031	0.026
70	0.0111	0.0192	0.0235	0.0247	0.0240	0.0233	0.0233	0.023	0.022
80	0.0059	0.0105	0.0129	0.0149	0.0148	0.0152	0.0156	0.0157	0.0158
90	0.0031	0.0058	0.0078	0.0091	0.0100	0.0097	0.0101	0.0105	0.0106
100	0.0016	0.0031	0.0045	0.0053	0.0055	0.0057	0.0063	0.0066	0.0070
Z cm	F_0^- No./S.	F_1^- No./S.	F_2^- No./S.	F_3^- No./S.	F_4^- No./S.	F_5^- No./S.	F_6^- No./S.	F_7^- No./S.	F_8^- No./S.
0	0.00	0.1102	0.0789	0.0544	0.0411	0.0314	0.0265	0.0242	0.019
10	0.00	0.058	0.0708	0.0610	0.0489	0.045	0.0365	0.0349	0.031
20	0.00	0.031	0.0493	0.0534	0.0501	0.049	0.047	0.040	0.037
30	0.00	0.016	0.0312	0.0397	0.0411	0.0493	0.0487	0.045	0.041
40	0.00	0.0085	0.0167	0.0274	0.0322	0.0470	0.0359	0.034	0.030
50	0.00	0.0047	0.0108	0.0169	0.0230	0.0237	0.0244	0.027	0.024
60	0.00	0.0027	0.0069	0.0113	0.0133	0.0163	0.0175	0.018	0.018
70	0.00	0.00129	0.0034	0.0060	0.0090	0.0095	0.0111	0.012	0.0127
80	0.00	0.00068	0.0019	0.0034	0.0048	0.0058	0.0071	0.0070	0.0072
90	0.00	0.00036	0.00099	0.0019	0.0260	0.0038	0.0044	0.0051	0.0049
100	0.00	0.00019	0.00053	0.0011	0.0015	0.0026	0.0028	0.0032	0.0030

the spherical shell between ρ and $\rho+\delta\rho$ is

$$N\sigma_{k-1}\delta\rho F_{k-1}^+(\sigma_{k-1}^+/\sigma_{k-1}) + N\sigma_{k-1}\delta\rho F_{k-1}^-(\sigma_{k-1}^-/\sigma_{k-1}), \quad (2)$$

where N is the electron density. The first term represents the quanta scattered into the positive direction from F_{k-1}^+ while the last term is the contribution to the positive component from F_{k-1}^-.

This formulation is not entirely correct as it assumes that quanta traversing the shell travel a distance $d\rho$ while it is actually $d\rho/\cos\theta$, where θ is the angle at which the quanta are actually traveling. A still more serious difficulty is the assumption that $N\sigma_{k-1}F_{k-1}^+(\sigma_{k-1}^+/\sigma_{k-1})$ represents the outward going quanta. Actually quanta traversing the spherical shell in a solid angle $d\Omega$ about θ, will be scattered so that some will also be scattered inward. Similar remarks also apply to the negative group. In spite of these objections, expression (2) will be used in the following calculation.

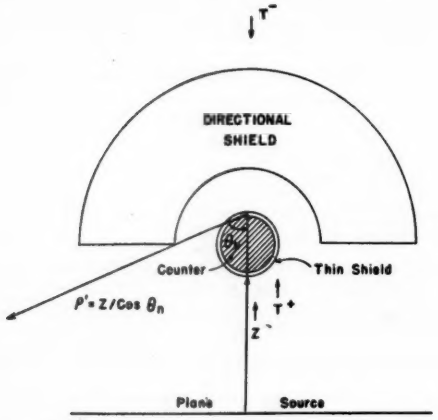

FIG. 1. Arrangement of counter shields.

The positive component of group k crossing a sphere of radius $(\rho+\delta\rho)$ is

$$F_k^+(\rho+\delta\rho)=F_k^+(\rho)-N\sigma_kF_k^+\delta\rho + N(\sigma_{k-1}^+F_{k-1}^+ + \sigma_{k-1}^-F_{k-1}^-)\delta\rho, \quad (3)$$

where $N\sigma_kF_k^+$ represents the quanta scattered out of group k. If terms of order $(\delta\rho)^2$ are neglected, then

$$\partial F_k^+/\partial\rho + N\sigma_kF_k^+ = N(\sigma_{k-1}^+F_{k-1}^+ + \sigma_{k-1}^-F_{k-1}^-). \quad (4)$$

In a similar manner it can be shown that

$$-\partial F^-/\partial\rho + N\sigma_kF_k^- = N(\sigma_{k-1}^-F_{k-1}^+ + \sigma_{k-1}^+F_{k-1}^-). \quad (5)$$

Particular solutions of Eqs. (4) and (5) that vanish exponentially at large distances and give $F_k^+(0)=0$, $(k\neq 0)$ with $F_k^-(0)$ finite are

$$F_k^+ = e^{-\mu_k\rho}\int_0^\rho e^{\mu_k\xi}\{\sigma_{k-1}^+F_{k-1}^+(\xi) + \sigma_{k-1}^-F_{k-1}^-(\xi)\}d\xi, \quad (6)$$

$$F_k^- = e^{+\mu_k\rho}\int_\rho^\alpha e^{-\mu_k\xi}\{\sigma_{k-1}^-F_{k-1}^+(\xi) + \sigma_{k-1}^+F_{k-1}^-(\xi)\}d\xi, \quad (7)$$

where for brevity $\mu_k^+=N\sigma_k^+$, etc., μ_k^+ and μ_k^- were computed from the Klein-Nishima formula, as described previously, for the electron density of water and are given in Table I. The quantity μ_k was computed from the total cross section and is also given in Table I.

Evidently the only physical solutions of Eqs. (4) and (5) for the zero group are $F_0^+=\eta\lambda e^{-\mu_0\rho}$ and $F_0^-=0$, where $\eta\lambda$ is the number of quanta emitted per second

by the point source. Equations (6) and (7) can now be evaluated successively and are given in Table II up to group 4. For groups of order greater than 4, the integrations were performed numerically and results are given in Table III.

Since $(F_k^+ + F_k^-)$ is the total number of quanta of group k passing through a sphere of radius ρ, the number crossing unit area is $(F_k^+ + F_k^-)/4\pi\rho^2$. Therefore a Geiger counter of area A and efficiency ϵ will register counts at a rate, due to all groups,

$$R = A/4\pi\rho^2 \sum_{k=0}^{k=\alpha} \epsilon_k (F_k^+ + F_k^-). \tag{8}$$

A is the area projected in a plane perpendicular to the radius vector.

If the counter characteristics are modified by means of a directional shield which has transmission coefficients T_k^+ and T_k^- (see Fig. 1) in the positive and negative directions respectively, the counter efficiency is reduced at each energy by just these coefficients, i.e.,

$$R = A/4\pi\rho^2 \sum_{k=0}^{k=\alpha} \epsilon_k (T_k^+ F_k^+ + T_k^- F_k^-). \tag{9}$$

The T_{-k}^+ are computed from the known mass absorption coefficients.[3]

Since photoelectric absorption in the detector wall causes the detector response to vanish at some energy E_P, the infinite sums in Eqs. (8) and (9) can be replaced by sums extending from zero to P where P corresponds to the detector cut-off energy. This energy can be estimated from the transmission curve of the detector wall. E_P is taken as the energy corresponding to $T = 0.50$.

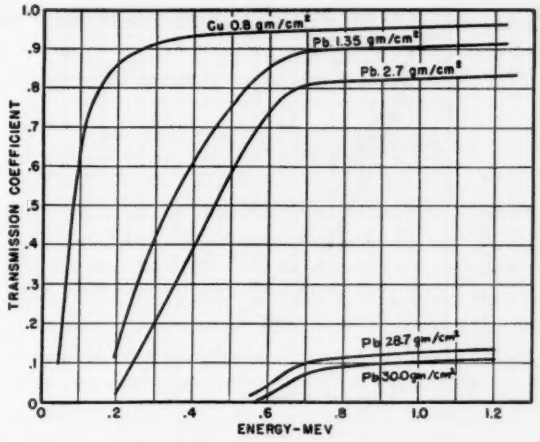

FIG. 2. Transmission coefficients of shields.

Part B. It is expedient to consider a plane source as a distribution of unit point sources of density $\eta\lambda$ over a surface. The number of quanta incident per second upon a cylindrical counter of unit projected area placed as shown in Fig. 1 is

$$I_k = \int_0^{2\pi} d\varphi \int_0^{\pi} \frac{F_k^+ + F_k^-}{4\pi\rho^2} \rho^2 \tan\theta d\theta. \tag{10}$$

φ is the longitude measured from the counter axis and θ is the polar angle measured relative to the negative direction. By an obvious transformation and integration

TABLE IV. Distribution of 1.20 Mev quanta due to a plane source emitting one quantum per cm² per second.

Z cm	I_0^+ No./cm²/S.	I_1^+ No./cm²/S.	I_2^+ No./cm²/S.	I_3^+ No./cm²/S.	I_4^+ No./cm²/S.	I_5^+ No./cm²/S.	I_6^+ No./cm²/S.	I_7^+ No./cm²/S.	I_8^+ No./cm²/S.
0	α	0.151	0.135	—	—	—	—	—	—
10	0.220	0.153	0.093	0.065	0.053	0.041	0.038	0.034	0.030
20	0.068	0.073	0.056	0.042	0.036	0.0311	0.029	0.027	0.024
30	0.027	0.034	0.031	0.026	0.024	0.022	0.0214	0.019	0.015
40	0.0135	0.0164	0.0173	0.015	0.0145	0.0143	0.0142	0.0136	0.013
50	0.0049	0.0079	0.0095	0.0090	0.0087	0.0086	0.0088	0.0091	0.0091
60	0.0025	0.0037	0.0048	0.0052	0.0050	0.0051	0.0052	0.0052	0.0051
70	0.00105	0.0019	0.0025	0.0027	0.0027	0.0029	0.0029	0.0031	0.003
80	0.0005	0.0087	0.0013	0.00155	0.00143	0.0017	0.0017	0.00179	0.0018
90	0.00025	0.0045	0.00065	0.00079	0.0071	0.00095	0.0009	0.00099	0.001
100	0.00011	0.00022	0.00032	0.00036	0.00038	0.00040	0.00048	0.00055	0.0005
Z cm	I_0^- No./cm²/S.	I_1^- No./cm²/S.	I_2^- No./cm²/S.	I_3^- No./cm²/S.	I_4^- No./cm²/S.	I_5^- No./cm²/S.	I_6^- No./cm²/S.	I_7^- No./cm²/S.	I_8^- No./cm²/S.
0	0.00	∞	∞	∞	∞	∞	∞	∞	∞
10	0.00	0.0243	0.035	0.0398	0.050	0.041	0.038	0.0355	0.032
20	0.00	0.0066	0.0149	0.0193	0.020	0.0243	0.0243	0.0225	0.022
30	0.00	0.0034	0.0065	0.0094	0.0107	0.0144	0.0137	0.0139	0.0014
40	0.00	0.0013	0.0030	0.0048	0.0059	0.0078	0.0077	0.0082	0.0088
50	0.00	0.00057	0.0014	0.0024	0.0028	0.0041	0.0043	0.0047	0.0051
60	0.00	0.00026	0.00066	0.0012	0.0017	0.0022	0.0025	0.0027	0.0029
70	0.00	0.00012	0.00033	0.00063	0.00089	0.0012	0.0014	0.0015	0.00165
80	0.00	0.000058	0.00016	0.00034	0.00048	0.00068	0.00077	0.00085	0.00096
90	0.00	0.000027	0.000078	0.00015	0.00024	0.00038	0.00043	0.00049	0.00057
100	0.00	0.000013	0.000037	0.000088	0.000117	0.00022	0.00024	0.00028	0.00032

[3] Compton and Allison, *X-Rays in Theory and Experiment* (D. Van Nostrand Company, Inc., New York, 1936), Appendix IX.

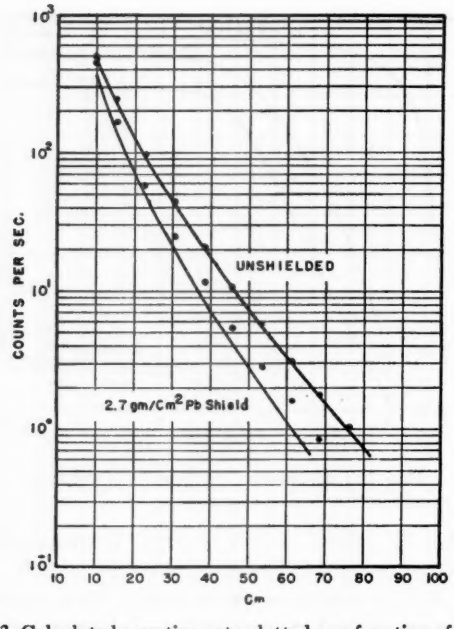

FIG. 3. Calculated counting rate plotted as a function of distance from a point source of 1.46 rd. The upper curve is the counting rate obtained for an unshielded counter, while the lower curve is the counting rate with a 2.7 g/cm² lead shield completely surrounding the counter. Circles are experimental data.

over φ, this can be written as

$$I_k=\frac{1}{\pi}\int_Z^\infty \frac{F_k^+ + F_k^-}{\rho} E(\cos^{-1}Z/\rho, \pi/2)d\rho, \quad (11)$$

where $E(\cos^{-1}Z/\rho, \pi/2)$ is the complete elliptic integral of the second kind. A good approximation to this integral for $Z>20$ is

$$I_k=\frac{1}{2}\int_Z^\infty \frac{F_k^+ + F_k^-}{\rho} d\rho. \quad (12)$$

Analogous to the description of the point source, the shielded counting rate for a counter of area A is

$$R=A\sum_{k=0}^{k=\rho} I_k T_k \epsilon_k. \quad (13)$$

Introduction of a directional shield as shown in Fig. 1 separates the quanta into components moving toward and away from the source. The positive component incident upon the cylindrical counter is approximately

$$I_k^+=\frac{1}{\pi}\int_Z^{Z/\cos\theta_n} \frac{F_k^+}{\rho} E(\cos^{-1}Z/\rho_1\pi/2)d\rho + \frac{1+T_k}{\pi}\int_{Z/\cos\theta_n}^\infty \frac{F_k^+}{\rho} E(\cos^{-1}Z/\rho_1\pi/2)d\rho \cong \frac{1}{2}\int_Z^\infty \frac{F_k^+}{\rho} d\rho, \quad (14)$$

provided Z is large. Similarly,

$$I_k^-=\frac{1}{2}\int_Z^\infty \frac{F_k^-}{\rho} d\rho. \quad (15)$$

These integrals were evaluated numerically and are given in Table IV.

The total counting rate for a counter of area A is

$$R=A\sum_{k=0}^{k=P} \epsilon_k(T_k^+ I_k^+ + T_k^- I_k^-). \quad (16)$$

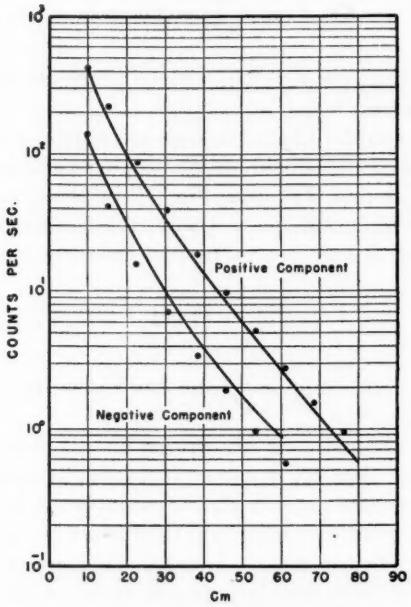

FIG. 4. Calculated directional counting rates plotted as a function of distance from a 1.46-rd. point source. The lower curve (negative component) represents the counting rate with a 30 g/cm² lead shield similar to that of Fig. 1 but positioned so that the shield was between the counter and source. The upper curve is the counting rate obtained for the case in which the unshielded portion of the counter was facing the source. Circles are experimental data.

III. DESCRIPTION OF EXPERIMENTS

Experimental conditions approximating those described in the theory may be realized in a large volume of water. Intensity measurements may be made with a Geiger counter. Sources of finite size must be used instead of the idealization of point and plane sources. Restrictions on the validity of such approximations require that intensity determinations cannot be made at extremities of the volume (within a mean free path) and that in the case of the plane radiator the maximum distance from the plane to the field point must be less than the linear dimension of the source.

Both point and plane source experiments were performed in a cylindrical tank six feet in diameter and six feet deep, filled with water. Counting rate measurements were made by a Geiger counter immersed in the water and held in position by means of an aluminum tube. In the point source experiment, the source was

placed at the tank center and the counter with its axis vertical was moved along a tank diameter in the plane of the source. Whereas in the case of the plane, the source was spread out over the bottom of the tank and the counter with its axis horizontal was moved away from the source. The counter tube was the same as that described in I; its efficiency is given by Fig. 3 of that reference.

Sources used in both experiments were made of Co^{60} which emit a β-ray and 2 γ-rays of 1.20-Mev mean energy per disintegration. A Bureau of Standards source contained in a small glass ampule having an activity of 1.46×10^6 disintegrations per second served as a point source. The plane source was prepared by plating $CoSO_4$ on thin copper turnings, measuring the mean activity per gram and spreading this material over a phenolic plane six feet in diameter. This source had an activity of 138 disintegrations per cm² per second.

Measurements of background were first taken after which the point source was introduced and counting rate determinations made at twelve different points

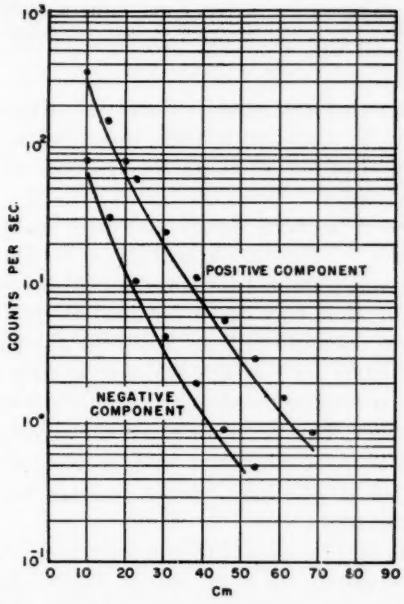

FIG. 5. Calculated directional counting rates with conditions similar to that of Fig. 4 but with an additional lead shield of 2.7 g/cm² completely surrounding the counter. Circles are experimental data.

along a tank radius. Estimates of the spectral distribution were made by a lead shield (2.7 g/cm²) placed completely around the counter. Directional data was taken with a thick lead shield of 30 g/cm², surrounding only half the counter; measurements were taken both with the shield facing toward and away from the source. These directional measurements were repeated with the 2.7 g/cm² shield completely surrounding the counter. Transmission coefficients of the various shields are given in Fig. 2 as a function of the energy.

Measurements identical in principle to those above were taken with the plane source. In this case the thin shield had a mass of 1.35 g/cm², while the directional shield was 28.7 g/cm².

IV. DISCUSSION OF RESULTS

Counting rates were computed from Eqs. (9) and (16) for the various shields and sources used. Results of such calculations[4] are represented in Figs. 3 to 8 by solid lines, and experimental data are denoted by circles.

Point source data are compared with theoretical results in Figs. 3, 4, and 5. Figure 3 shows that general agreement between theory and experiment was obtained for the unshielded counter, while a considerable discrepancy exists in the case of the shielded counter. This discrepancy is probably due to use of the mass absorption coefficient in computing the shield transmission. Since the mass absorption coefficient includes scattering as well as absorption, its use should overestimate the shielding because quanta scattered in the shield may not be deflected through an angle sufficiently large to miss the counter. The theory therefore should be lower than the experimental data in all cases in which a shield is used.

Figure 3 also shows that the data deviates further from the theory at great distances from the source. Because of the greater probability of high energy quanta scattering into the forward direction, those quanta of a

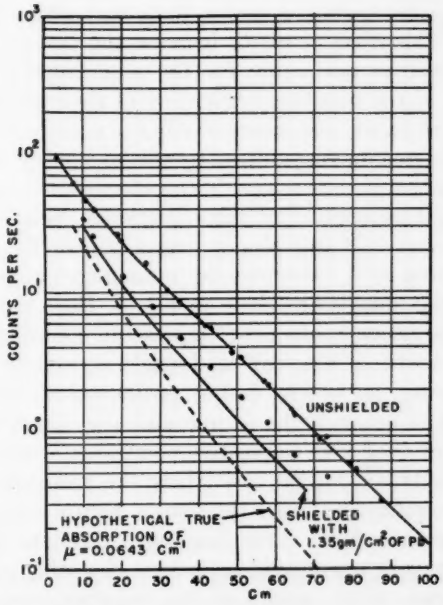

FIG. 6. Calculated counting rate plotted as a function of distance from a plane source having an activity of 138 disintegrations per second per cm². The upper curve represents the counting rate obtained for an unshielded counter, while the lower curve is the counting rate obtained with a 1.35 g/cm² lead shield completely surrounding the counter. Circles are experimental data.

[4] Since all parts of the counter were not equidistant from the "point" source, a correction factor $1/(1+(l/2\rho)^2)^{\frac{1}{2}}$, in which l is the counter length, was applied in calculating the counting rates from Eq. (9).

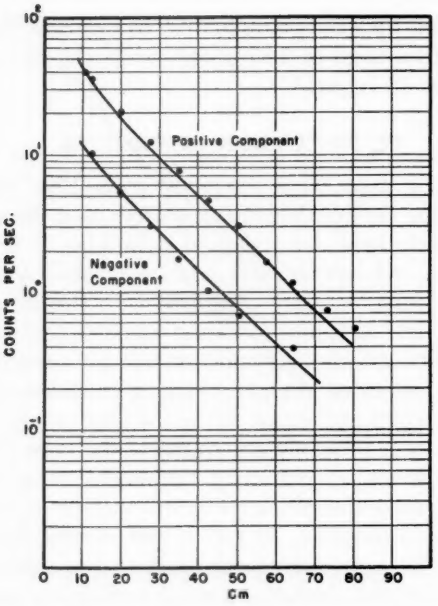

FIG. 7. Calculated directional counting rates plotted as a function of distance from the plane source. The upper curve (positive component) is the counting rate obtained for the arrangement of Fig. 1 with no thin shield present. The lower curve is the counting rate obtained with the directional shield placed between counter and source. Circles are experimental data.

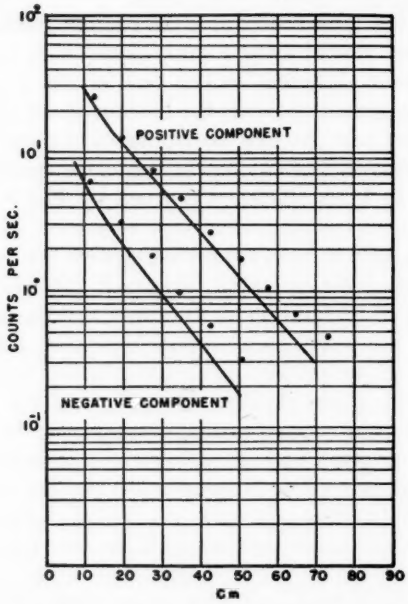

FIG. 8. Calculated directional counting rates obtained with conditions similar to that of Fig. 7 but with an additional lead shield of 1.35 g/cm² completely surrounding the counter. Circles are experimental data.

given group which have the highest energy travel farthest. Thus there are more high energy quanta at distances far from the source than that given by the theory. This effect tends to increase the counting rate but is not so noticeable for the unshielded counter because of the non-linear efficiency of the counter. On the other hand, the counter efficiency is practically linear for quanta transmitted by the lead shield so that the deviation is more noticeable for the shielded counter.

General agreement of the directional data for the point source with the theory was obtained. Results of calculations and experimental measurements for the directional shields are given in Fig. 4. Here the lower curve (negative component) represents counting rates obtained with a 30 g/cm² lead shield surrounding half the counter, as in Fig. 1, but positioned so that the shield was between the source and the counter. The upper curve of Fig. 4 (positive component) represents results obtained for the case where the unshielded side of the counter was facing the source. Figure 4 indicates that the theoretical curve lies above the data for the negative component and *vice versa* for the positive component. Since quanta in the negative component have been scattered through a larger angle than those in the positive component, they have a smaller energy than those in the positive component. Thus positive and negative components have respectively more and less energy than that calculated by Eq. (1). Experimental data should be displaced in these directions relative to the theory. Further shielding brings out the effects noted previously.

Comparison between theory and experiment for the plane source is illustrated in Figs. 6–8. Reasonable agreement was obtained for the unshielded counter. It is surprising that this curve beyond 20 cm from the source is exponential with an apparent absorption coefficient of 0.063 cm^{-1}, which is almost exactly equal to the linear scattering coefficient (Compton) of 0.0643 cm^{-1} for water. This is certainly a coincidence as radiation from a plane absorbed with a true absorption coefficient of 0.0643 cm^{-1} would produce the dotted curve of Fig. 6.

Shielding of the counter brought forth the same effects as was observed for the point source. Again these effects are due to overestimation of the shielding and to a slightly different energy distribution than was assumed in theory.

Counting rates from the spectral and spatial distribution of the scattered radiation as determined by the approximate theory of Section II thus yields results in agreement with the experiment. Deviations are easily explicable although difficult to include in the calculations.

The author is indebted to Professor M. H. Johnson for suggesting this problem and for his guidance during the course of the work.

The Disintegration of Ag^{110}

KAI SIEGBAHN
Nobel Institute for Physics, Stockholm, Sweden
(Received September 8, 1949)

The disintegration of Ag^{110} has been investigated using spectrometer and coincidence technique. The radiation contains a great number of β- and γ-components and the disintegration scheme is complicated. Four β-components and ten γ-rays have been found and their energies and intensities measured. The 225-day activity is due to an isomeric level in Ag, separated 116 kev from the 24-sec. ground level. The internal conversion coefficient of the γ-ray at 656 kev has been determined to be 2.5×10^{-3} by means of coincidence spectrometry. The disintegration scheme is discussed.

IN a recent communication[1] the author has reported some measurements on the β- and γ-radiation from long-lived Ag^{110} (225 days). It is the purpose of this paper to give a more complete description of the experiments and also to try to formulate a consistent disintegration scheme, which is unusually complicated due to the complex radiation.

β- AND γ-SPECTRUM

The soft part of the β-spectrum was investigated in a lens spectrometer having a G-M tube with a thin Nylon window and adjusted for high transmission and moderate resolution so that a thin sample could be used. The spectrum was then joined together with the harder part of the spectrum, investigated with a large double focusing spectrometer ($\rho=50$ cm) with high resolution. Figure 1 shows the complete spectrum, and Fig. 2 an enlarged part of the spectrum, where a number of internal conversion lines occur. If this spectrum is compared with the corresponding photo-electron (and Compton electron) spectrum as shown in Fig. 3 (obtained with a 3.7μ lead converter) one finds that the γ-radiation consists of 10 different γ-lines of measurable intensities. The energies of the γ-rays vary from 116 kev to 1516 kev. The results are shown in Table I.

Both the β-spectrum (β) and the photo-electron spectrum (γ) have been obtained with small statistical errors, the spectrometer investigations being extended over several weeks. The measurements have been repeated many times, especially over the part where most of the lines occur. All except two of the γ-lines appear in both spectra, in some cases as both K and L lines (conversion lines or photo-lines). The energy values, given in Table I are thus computed as the mean values of, in some cases, several independently obtained values of the γ-energies. (For instance the γ-energy of 885 kev is a mean value of four independent determinations i.e., from the K and L photo-lines and K and L internal conversion lines.) Any uncertainties in the energy determinations are therefore mostly due to difficulties of correcting accurately for straggling effects in the sample. The errors are smaller than 0.5 percent.

The intensities of the internal conversion lines are as expected small (α_K of the order of 10^{-3}) because of the relatively low Z value and the high energies. The softest line at 116 kev is, however, strongly converted. Furthermore the intensity ratio between the K and L conversion lines makes it quite probable that this line is due to a transition from a metastable state. The measured ratio between the intensities of the K and L lines is $\sim$1.3. To get at least some estimate of the half-life of the corresponding state, one can use the computations by Hebb and Nelson.[2] Assuming the radiation to be of essentially electric multipole type, the N_K/N_L ratio obtained for the energy in question is consistent with an effective l-value of 4. If this value is used in the formulas by Segrè-Helmholz[3] the half-life of the state can be estimated to be of the order of days. $l=5$ would give 10^4 years, which however cannot be excluded because of the small intensity of the isomeric transition. Since these formulas necessarily are of quite approximate nature (a deviation of one or two orders of magnitude may still be allowed), there are reasons to believe that the 116 kev level belongs to the 225-day activity of silver.

Since Ag^{110}, produced by slow neutron bombardment of Ag^{109}, is known to give two different half-lives of 225 days and 24 sec.,[4] the simplest explanation of this isomerism is to assume* that the 24-sec. level is the ground state of Ag^{110}. The 24-sec. activity of Ag^{110} is a β-emitter with an upper limit of 2.6 Mev (abs. Al)[5] or 2.8 Mev (cloud chamber).[6] If the 225-day activity partly decays via the 24-sec. ground level of the same nucleus, one would then expect to find also a β-component of the above energy in the radiation. Actually a very small intensity β-component of high energy was found (about 3 percent of the main spectrum), showing itself as a small background in the investigating of the internal conversion spectrum (Figs. 1 and 2). Taking a very strong sample and using a high transmission lens this component was investigated in more detail and treated by Fermi analysis. The upper limit was found

[1] K. Siegbahn, Phys. Rev. **75**, 1277 (1949) (cf. also references given in this paper).

[2] M. Hebb and E. Nelson, Phys. Rev. **58**, 586 (1940).

[3] A. Helmholz, Phys. Rev. **60**, 415 (1941).

[4] G. T. Seaborg and I. Perlman, Rev. Mod. Phys. **20**, 611 (1948).

* It is quite unlikely that the isomeric transition takes place after the β-emission since the following nucleus (Cd^{110}) contains an even number of protons and neutrons, which would violate the general rule found by Mattauch (Zeits. f. Physik **117**, 246 (1941)).

[5] O. Hirzel and H. Wäffler, Helv. Phys. Acta **19**, 214 (1946).

[6] Gaerttner, Turin, and Crane, Phys. Rev. **49**, 793 (1936).

to be 2.86 Mev and the spectrum is complex. The Fermi plot deviates from a straight line at 2.12 Mev, which would be the energy of the β-component next to the one at 2.86 Mev in energy.

The main part of the continuous β-spectrum was also treated by Fermi analysis. There is one strong β-component with an upper limit of 87 kev (abundance ~58 percent). The rest of the spectrum consists of essentially one component with the upper limit 530 kev (abundance ~35 percent), but the Fermi plot is not completely a straight line, which might indicate the presence of one or several β-components of very low intensities. The Fermi analysis was unable to give further information on these points.

INTENSITIES OF γ-LINES

The relative intensities of the γ-rays may be estimated from the photo-electron spectrum for those lines, which are completely resolved from each other and when there is no doubt about the form of the Compton electron background. These conditions are rather well satisfied for the lines at 656, 885, 935, 1389, and 1516 kev. These γ-lines happen to be the strongest in the γ-spectrum and are therefore of special importance for the disintegration scheme. The relative γ-intensities have been estimated by dividing the photo-lines by the photo-cross section at the corresponding energies. The result is given in Table II.

According to Table II the γ-lines at 656 and 885 kev

FIG. 1. Ag^{110} β-spectrum.

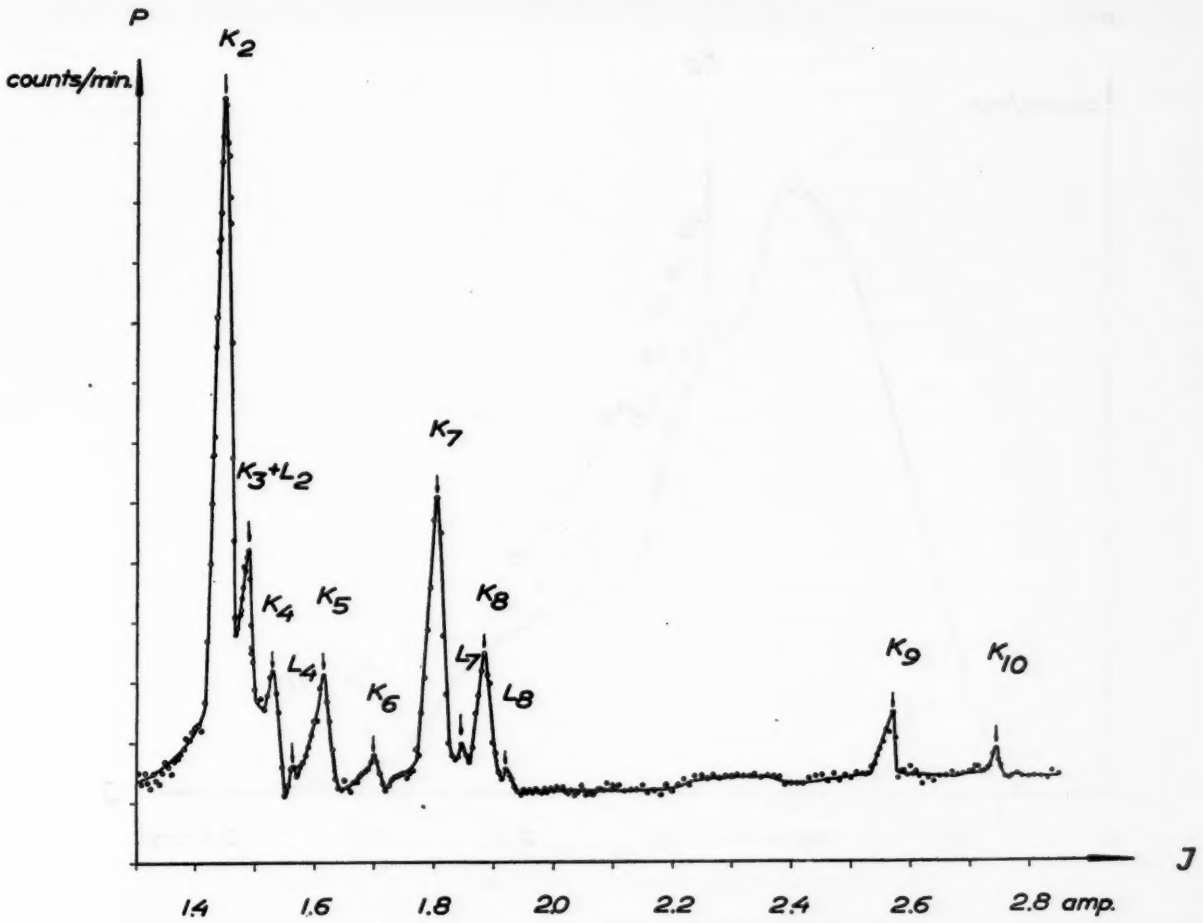

FIG. 2. Enlarged part of internal conversion spectrum of Ag^{110}.

are the most predominant transitions, the other being of less than half their intensities.

The intensities of the remaining part of the γ-rays are more difficult to estimate from the closely spaced photo-lines, since they appear on the slope of a number of Compton electron distributions. This latter spectrum could be taken separately (without lead foil) and then subtracted from the total spectrum but this would introduce great uncertainties since both the height and the form of the Compton spectrum change when the lead foil is removed. Some estimate can be made from the internal conversion spectrum if for simplicity it is assumed that the lines are of the same multipole order. This seems approximately to be the case with the lines in Table II. Under this special assumption one would conclude from the energy dependence of the internal conversion coefficients[7] that the lines at 676 kev (superimposed on the L line of the 656-kev γ-line), 706-kev and 759-kev lines are of almost the same intensity (the 759-kev line being somewhat stronger) and roughly equal to that of the 1516-kev line. The line at 814 kev could have about a third of this intensity.

[7] S. Dancoff and P. Morrison, Phys. Rev. 55, 122 (1939).

INTERNAL CONVERSION COEFFICIENT FOR THE 656-KEV γ-LINE

If the strong γ-line at 656 kev is emitted after all β- and γ-components, the internal conversion coefficient, α, can be determined by comparing the area of the line with the total β-spectrum. One then arrives at the value $\alpha_{656}=2.5\times10^{-3}$. This value for the coefficient can be obtained in another way. If coincidences ($C_{\beta e^-}$) between conversion electrons (e^-) focused in a spectrometer and the total β-spectrum (β) (β-tube immediately behind the sample) is investigated over the line, α can be computed, provided the efficiency (essentially the spectrometer transmission) of the e^- G-M-tube is known. The efficiency (e_{e^-}) is most easily determined from a βe^- coincidence line having a previously known internal conversion coefficient. Using the relation

$$C_{\beta e^-}/N_\beta = e_{e^-}\cdot\alpha$$

(N_β = counts in β-tube behind the sample) e_{e^-} can then be computed.

Figure 4 shows the K and L $_{\beta e^-}$ coincidence lines from the 411-kev γ-ray of Au^{198}. The spectrometer used was

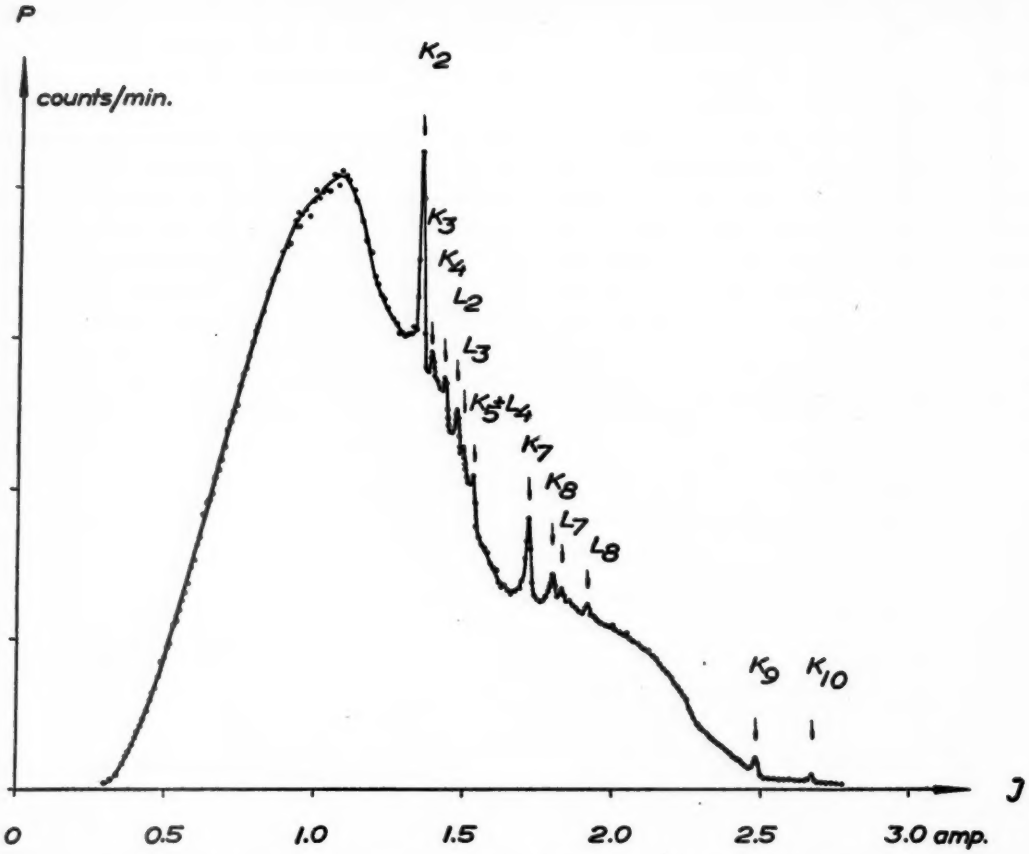

FIG. 3. Secondary electron spectrum of Ag^{110} from a 3.7μ lead converter.

of a high transmission "intermediate image" lens type,[8] which is especially well suited for this purpose, since the small coincidence effect is proportional to the transmission. From the top of the K coincidence line e_e- is determined once and for all. This value is then dependent on the knowledge of α_K for the 411-kev γ-ray. According to the two most recent spectroscopic measurements[9,10] α_K is 3.0×10^{-2} and 3.5×10^{-2} respectively. The maximum deviation from the mean value (3.25×10^{-2}) is thus less than 10 percent.

TABLE I. Energies and estimated intensities of the Ag^{110} γ-lines.

γ-line	γ-energy kev	Estimated intensity of γ-ray	Obtained from
1	116	weak (strongly conv.)	β
2	656	strong	β, γ
3	676	weak	β, γ
4	706	weak	β, γ
5	759	weak	β, γ
6	814	v. weak	β
7	885	strong	β, γ
8	935	medium	β, γ
9	1389	medium+	β, γ
10	1516	medium	β, γ

TABLE II. Relative intensities of the main γ-lines of Ag^{110}.

γ-energy in kev	656	885	935	1389	1516
Rel. intensity	100	81	31	33	17

Figure 5 shows the corresponding βe^- coincidence line for the Ag^{110} 656-kev γ-ray. The full curve is the conversion line itself, inserted in the figure for comparison. As can be seen the βe^- coincidences can be brought to fall on the β-line as expected. From the number of coincidences at the top of the line and with the value for e_e- obtained from the previous measurement on Au^{198} one gets $\alpha_K=2.5\times10^{-3}$ for this line. The full agreement with the above value of $\alpha_K(2.5\times10^{-3})$ is of course partly accidental, the experimental errors being around ±15 percent. In the coincidence experiment the window before the β-G-M counter (behind the sample) was not very thin and absorbed a big portion of the soft β-component ($E_{max}=87$ kev) but not so much of the harder one. If the 676-kev γ-line did not follow the whole β-spectrum, but for instance only the soft part, the number of βe^- coincidences would have been much less and thus also the computed value of α_K.

A value of $\alpha_K=2.5\times10^{-3}$ is consistent with a magnetic

[8] H. Slätis and K. Siegbahn, Phys. Rev. **75**, 1955 (1949), and Arkiv. f. Fys. **1**, No. 17, 339 (1949).

[9] K. Siegbahn and A. Hedgran, Phys. Rev. **75**, 523 (1949).
[10] D. Saxon and R. Heller, Phys. Rev. **75**, 909 (1949).

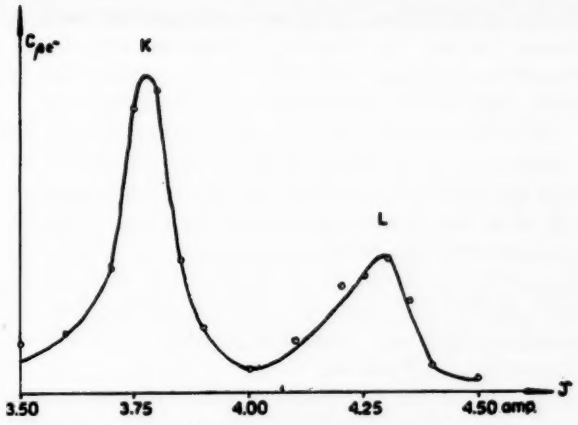

FIG. 4. βe^- coincidence lines of Au^{198} (K and L lines of γ-line at 411 kev).

or electric dipole radiation. According to present existing calculations[7] α_K for electric dipole radiation at this energy is 1.74×10^{-3} and for magnetic 2.74×10^{-3}. Electric quadrupole radiation would give $\alpha_K=5.18\times10^{-3}$.

In the coincidence spectrometer it was further possible to prove experimentally that the 116-kev γ-ray actually was due to a metastable level. The spectrometer resolution was 3 percent so that the K, L, and M lines were resolved. Coincidences were then taken on the lines and on the continuous spectrum around the lines. No βe^- coincidence lines could be found. A small effect due to $\beta\gamma$-coincidences was found between the continuous spectrum and γ-rays counted in the β-tube behind the sample. The effect was the same on the lines and the continuous spectrum. The expected computed coincidence rate if the level were not metastable was about six times the $\beta\gamma$-coincidence effect obtained, which was very far outside any statistical limits of error.

DISCUSSION OF THE DISINTEGRATION SCHEME

Naturally a disintegration scheme, which contains so many β- and γ-components must be expected to be quite complicated, and the scheme proposed here is justified only because it seems to fit the experimental data hitherto obtained.

According to M. Deutsch[11] K-capture constitutes less than 3 percent of all disintegrations, since no K x-rays could be observed. X-rays are of course to be expected because of the presence of the internal conversion lines (particularly those corresponding to the isomeric transition) but according to the above estimates, the intensity of these internal conversion lines is $\lesssim$3 percent of the total radiation, i.e., consistent with Deutsch's figure. Furthermore positron decay does not occur in any measurable amount since no annihilation radiation can be observed in the photo-electron spectrum.

The scheme shown in Fig. 6 is based on the following arguments:

[11] M. Deutsch, Phys. Rev. **72**, 527 (1947).

1. $\beta\gamma$- and $\gamma\gamma$-coincidence measurements

These measurements were performed with calibrated gold γ-tubes. The result for the $\beta\gamma$-coincidence measurements was $C_{\beta\gamma}/N_\beta=(3.62\pm0.20)\times10^{-3}$.

This value was obtained with a 10 mg/cm² Al absorber in front of the β-tube in order to absorb the soft component completely. According to the efficiency curve for the γ-tube, the scheme would give (one β-component followed by three γ-rays at 935, 885, and 656 kev) $C_{\beta\gamma}/N_\beta=(3.80\pm0.20)\times10^{-3}$.

The result of the $\gamma\gamma$-coincidence measurements was $C_{\gamma\gamma}/N_\gamma=(1.70\pm0.10)\times10^{-3}$. In this case it is somewhat harder to compare the result with an exact expected value, since all γ-intensities are not accurately known. Some of the transitions, however, are definitely less abundant than others, and with some reasonable assumptions regarding their relative intensities the expected value of $C_{\gamma\gamma}/N_\gamma$ is very likely to be $\sim1.80\times10^{-3}$.

Thus we find that the scheme is consistent with the coincidence measurements. A scheme with essentially two or four γ-rays in cascade instead of three, could not be expected to give agreement with the above results.

2. Energetic considerations

There is no γ-ray which is equal to the well-established difference in energy between the β-components of 87 kev and 530 kev. If the γ-line at 1389 is put after the 87-kev component and the 935-kev γ-ray after the 530-kev component, they end in the same level within the experimental errors. When the two strong γ-lines of 885 kev and 656 kev are put after this level one arrives to a total disintegration energy, which is very nearly the same as that obtained from the knowledge of the hard (but very faint) direct β-transition from the ground state in Ag^{110} ($\tau=24$ sec.) to the ground state in Cd^{110}. The small intensity β-spectrum of 24-sec. Ag^{110} is complex, with another β-component of $E_\beta=2.12$ Mev. This component would have to end at the first excited level in Cd^{110} (2.86−0.66=2.20 Mev, i.e., close to the energy

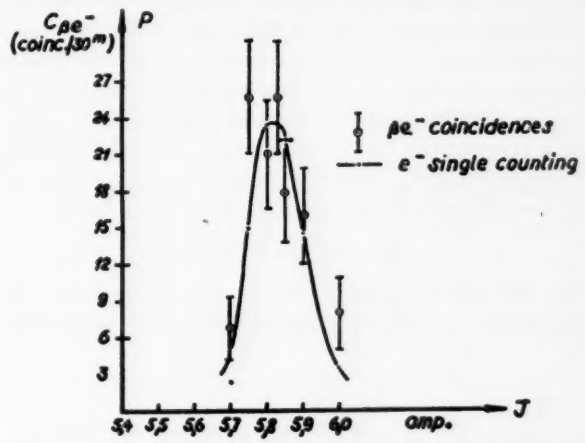

FIG. 5. βe^- coincidence line of Ag^{110} ($E_\gamma=656$ kev). Full line: the internal conversion line for comparison.

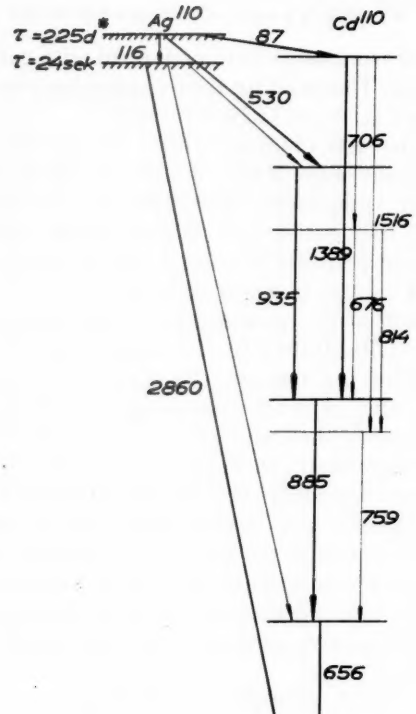

FIG. 6. Disintegration scheme of Ag^{110}, consistent with experimental material.

found above). Since the Fermi analysis offered some possibility for the main spectrum to contain another β-component, except the 87-kev and the 530-kev components, it may occur that a very small proportion of the ground state of Ag^{110} also decays to the level shown in the scheme, though spin considerations make this transition less probable.

The remaining γ-rays have been placed in the scheme according to the following considerations (faint lines in the scheme). Energetically the sum of the γ-rays at 706 kev and 676 kev is inside experimental errors equal to the energy of the γ-ray at 1389 kev and have therefore been put in cascade as an alternative two-step transition. If the 1516-kev γ-ray is assumed to go from the 87-kev level followed by the 759-kev γ-ray, one arrives to the first excited level (1516+759=2275; 1389+885=2274). The one remaining faint γ-ray of 814 kev fits in between two already existing levels.

3. *Intensity considerations*

In the above construction of the levels from the energies of the different γ-rays and β-components intensity considerations have been of important help. As stressed before the intensity estimates are of only approximate nature, and one cannot require the intensity relations in the scheme to fit quantitatively.

The total intensity of the γ-rays leaving the 87-kev β-component is in relative units (see Table II) 67, while the γ-intensity leaving the 530-kev β-component is 31. This has to be compared to the ratio of the two β-components, i.e., 58:35. Furthermore the γ-intensity arriving at the third excited level is 81 (γ-rays at 935, 1389 and 676 kev). Only one γ-ray is leaving this level namely the 885-kev γ-ray. The intensity of this is also 81 according to Table II.

The sum of the intensities of the 1516 kev and the 814 γ-rays is $17+\frac{1}{3}17\sim22$. The γ-intensity arriving at the first excited level is then $81+22=103$. Only the 656 γ-ray is leaving this level with the intensity 100.

Thus, the intensity relations fit the scheme surprisingly well. Together with the energetic and the additional coincidence data, the scheme describes the disintegration rather well in detail. One can of course not disregard the possibility of the emission of other components of very small intensity, not observed with the present technique. The fact that 7 percent of the β-spectrum did not fit to a straight Fermi plot may indicate the presence of such faint transitions. It is known, however, that deviations from straight lines in the Fermi analysis for forbidden spectra can be expected.

One further point may be briefly discussed here. The *ft.* value of the 2.86-Mev β-component from the 24-sec. level of Ag^{110} is about 10^4 and the transition is certainly allowed. The spin of the Cd^{110} ground state is presumedly zero and since a transition $0\rightarrow0$ is highly forbidden the spin of the 24-sec. state of Ag^{110} is 1 according to GT selection rules. The spin of the Ag^{109} is known to be $\frac{1}{2}$ and the addition of a slow neutron (for both isomers due to a resonance)[12] will give a spin of 1 or 0 to the nucleus after capture. It is most likely[13] that the neutron cross section connected to the isomer with the spin value, which comes nearest to the nucleus after capture will be the largest. Since the spin of the 225-day Ag must be at least 5 one would expect the 24-sec. cross section to be the largest. This is also the case according to the measurements by Seren, Friedlander, and Turkel,[14] who find the ratio σ 24 sec./σ 225 d to be ~47. The assignment of the lower state in Ag^{110} to be due to the 24-sec. isomer is thus consistent with the above picture.

[12] M. Goldhaber, Phys. Rev. **70**, 89 (1946).
[13] E. Segrè and A. C. Helmholz, Rev. Mod. Phys. **21**, 271 (1949).
[14] Seren, Friedlander, and Turkel, Phys. Rev. **72**, 888 (1947).

Recombination Spectrum and Electron Density Measurements in Neon Afterglows*

R. B. Holt, John M. Richardson, B. Howland, and B. T. McClure
Department of Physics, Harvard University, Cambridge, Massachusetts

(Received October 13, 1949)

The spectrum emitted by the recombination of positive ions and electrons in the afterglow of a pulsed microwave discharge through neon has been studied as a function of time. Simultaneous electron density measurements on the plasma were made by the cavity resonant frequency shift method, and the recombination coefficient was calculated from these data. The total radiated visible light was found to be proportional to the square of the observed electron density. The observation of light intensities allowed recombination measurements to be carried out at electron densities much too high to be observed directly by the cavity resonant frequency shift method. The *relative* intensities of several strong lines in the spectrum remained essentially constant during the afterglow, while the *relative* intensities of several others showed consistent changes.

INTRODUCTION

THE general problem of the mechanism of the disappearance of electrons from a gas discharge plasma by various processes has been the subject of an enormous amount of theoretical and experimental work.[1] In many cases, it is possible to choose experimental conditions such that virtually all of the electrons are lost by one process (*e.g.*, recombination with positive ions). In the present investigation simultaneous spectroscopic and electron density measurements were made on neon discharges under conditions favoring electron-positive ion recombination.

Recombination spectra have been studied in argon[2] and metal vapors.[3] The results of these studies have been used in conjunction with probe measurements to determine the recombination coefficient,[4] α, for electron-positive ion recombination. The values of α obtained were of the order of 10^{-10} cm^3/ion-sec., compared to a theoretical value (based on the use of hydrogen-like wave functions)[5] of about 10^{-12} cm^3/ion-sec. These values are in poor agreement with the values of α of the order of 10^{-6}–10^{-8} cm^3/ion-sec. which have recently been obtained[6] for several gases by means of microwave electron density measurements.

METHOD AND APPARATUS

A pulsed microwave (3000 mc/sec.) electrodeless discharge through spectroscopically pure neon at pressures between 10 and 30 mm Hg was used in this work. Any other method of exciting the original discharge would probably have been equally satisfactory; but, since it was desired to make microwave electron density measurements on the plasma, the microwave breakdown was selected for convenience. The measurements consisted of observing the spectrum as a function of time after cutting off the discharge, and measuring simultaneously the electron density by determining the shift of the resonant frequency of the cavity in which the discharge occurred. As can easily be seen from the definition of α, a plot of $1/n$ *vs.* time should result in a straight line provided virtually all of the electrons originally present in the plasma disappear due to recombination. If the electrons disappear due to ambipolar diffusion, it can easily be shown that the plot of log n *vs.* time should be a straight line—this gives a simple method of distinguishing experimentally between the two processes. If the total intensity of light emitted is simply proportional to the rate of disappearance of electrons, then a linear relationship between the square root of the intensity and time would be expected, for the range of conditions under which recombination is the principal process of electron removal.

Figure 1 is a block diagram of the apparatus used. The operating sequence, which repeated 200 times per second, follows. The timing of the sequence was controlled by a rotating wheel. Light from an incandescent bulb was sent through the slit in the wheel and reflected by a mirror onto a photo-multiplier, which generated an electrical trigger. The trigger was passed through a

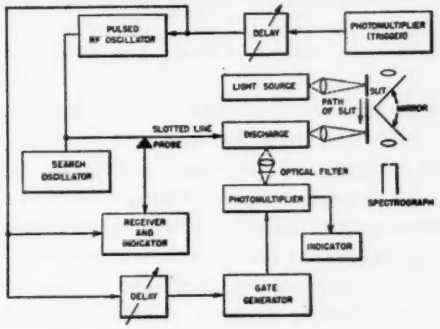

FIG. 1. Block diagram of apparatus used for studying recombination spectrum and variation of electron density in neon afterglow.

* The work described in this paper was assisted by the ONR.

[1] For a good summary of work before 1939, see L. B. Loeb, *Fundamental Processes of Electrical Discharge in Gases* (John Wiley and Sons, Inc., New York, 1939) Chapters II and III.

[2] C. Kenty, Phys. Rev. **32**, 624 (1928).

[3] F. L. Mohler and C. Boeckner, Bur. Stand. J. Research **2**, 489 (1929); C. Broeckner, Bur. Stand. J. Research **6**, 277 (1931); F. L. Mohler, Bur. Stand. J. Research **10**, 771 (1933); J. Research Nat. Bur. Stand. **19**, 447 (1937); and **19**, 559 (1937).

[4] Defined by the equation $dn/dt = -\alpha n^2$, where n is the electron concentration.

[5] Stueckelberg and Morse, Phys. Rev. **36**, 16 (1930).

[6] Quarterly Progress Report, Research Laboratory of Electronics, M.I.T. (January 15, 1949), p. 6 ff.

variable delay (0 to 3000 microseconds) and used to excite the pulsed r-f oscillator for 10 microseconds. The power thus generated (variable to approximately 1-kw peak) was passed through a slotted coaxial line and used to break down the vycor discharge tube, which was contained in a cylindrical cavity tuned near the pulsed oscillator frequency. The spectrum of the discharge was examined by allowing the light from the discharge to fall on the wheel a little distance from the triggering light and to pass through the same slit which was responsible for the generation of the trigger. After passing through this slit, the light from the discharge was reflected by a mirror onto the slit of a Kipp high intensity liquid prism spectrograph. The spectrographic plates obtained were run through a microphotometer to determine wave-lengths and relative intensities of spectral lines. Type 103a Eastman plates were used in some of the runs involving widely different exposure times to minimize reciprocity law failure. By varying the electrical delay, the light from the discharge could be examined during the discharge or at any time after the discharge up to a maximum of 3000 microseconds. The size of the slit and angular speed of the wheel were such that a time resolution of 2 microseconds could be achieved.

The apparatus was arranged so that the light from the discharge could also be viewed by a photo-multiplier (or, for the infra-red, by a Type 1P25 infra-red image tube). Because of the tremendous differences in light intensity encountered at various times after the discharge, it was necessary to "gate" the photo-multiplier or image tube so that it was sensitive only at the time after the discharge at which an observation was being made. This was accomplished by the use of a second variable delay circuit which operated from the original electrical trigger and furnished a delayed trigger to activate the photo-multiplier pulsing circuit. A synchroscope plus a calibrated video attenuator constituted the indicating equipment for the photo-multiplier.

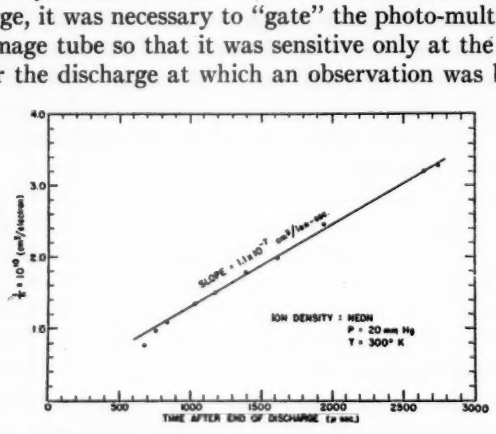

FIG. 2. Variation of electron density as a function of time.

Finally, the electron density in the plasma was measured in the following manner. A small signal from the search oscillator,[7] which was tuned to an accurately known frequency differing from the natural resonant frequency of the cavity by a few megacycles, was injected into the slotted line. The presence of electrons in the gas discharge plasma causes the resonant frequency of the cavity to be shifted from its normal value; and, in fact, it can be shown that under suitable experimental conditions, which were maintained here, the frequency shift is directly proportional to the concentration of electrons present, the exact factor of proportionality depending somewhat on the spatial distribution. By placing the probe of the slotted line at a suitable point in the standing wave pattern, it is possible to cause a minimum amount of power to flow into the receiver and indicator if the injected frequency and the cavity frequency coincide. Since the concentration of electrons in the plasma, and therefore the cavity frequency, was changing due to recombination, such a minimum did occur, and its development was fast enough to produce a pulse when receiver output was displayed on the indicator time base. It thus sufficed to observe the search frequency and the time after the discharge at which the pulse occurred in order to obtain one point on the electron density *vs.* time curve. To obtain other points, the search frequency was varied.

RESULTS

The variation of electron density as a function of time is shown in Fig. 2 for a typical run at a pressure of 20 mm Hg. The $1/n$ *vs.* time plot gives a good straight line, indicating that, in the range of experimental conditions used, recombination far exceeded diffusion as a mechanism of electron loss. The slope of the line gives $\alpha=1.1\times10^{-7}$ cm^3/ion-sec., and is considered in satisfactory agreement with the value 2.1×10^{-7} cm^3/ion-sec. obtained previously for neon with this same method at a lower peak input power.[6] We observed that the measured value of α increases with decreasing peak input power, varying over a 2:1 range which contains the previously reported figure. These observations are satisfactorily explained by noting that unless a large density of electrons are present initially in the plasma, a uniform spatial distribution (which is assumed in order to calculate the density) is not fully achieved from the non-uniform one existing at the end of the discharge by the time measurements begin. If such experimental conditions exist, some other distribution function may be reasonably assumed in order to preserve the value of α.

In order to test the assumption that the light intensity should be proportional to the square of the electron density, the data for total light intensity for two regions of the spectrum and the corresponding electron density data are plotted in Fig. 3. It should be remembered that the most that can be said of the light intensity is that the total energy radiated (regardless of the spectral distribution) should, in the absence of com-

[7] The method used was developed by S. C. Brown, M. A. Biondi, M. A. Herlin, E. Everhart, and D. E. Kerr, and is described in detail in Technical Report No. 66, Research Laboratory of Electronics, M.I.T. (1948).

plicating factors such as long-lived metastable levels, be proportional to the square of the electron density. The fact that the data show that this proportionality holds at least fairly well for two broad regions of the spectrum agrees with the assumption, and furthermore indicates that the mechanism of the recombination process probably does not change radically during the period of the afterglow studied, since a change in the mechanism would probably affect the spectral distribution. This is not intended to be a conclusive argument.

It should be noted that the light intensity measurements have allowed us to take data to shorter times after the discharge than would be possible with the electron density measurements. This is so because of the limitations imposed on the electron density method at relatively high electron densities (greater than about 10^{10} electrons/cm^3) because of the breakdown of the assumption (which is made in deriving the equations) that the presence of the electrons perturbs the cavity fields only slightly.

It was noted that the intensity of the afterglow at a particular time was the same whether the search signal was on or off for sufficiently low signal levels. This verifies the fact that it is possible to inject a signal large enough to make electron density measurements without affecting the plasma appreciably.

The microphotometer traces of the plates taken with the spectrograph showed several interesting features. Only lines identifiable as atomic neon were obtained. Secondly, the spectra were virtually pure line spectra. It would be expected that the initial process of an electron possessing thermal kinetic energy falling into a quantized level would give rise to a continuum within the resolution of our instrument beyond the series limit associated with the particular quantized level involved. Line spectra would then be expected as the secondary consequence of the atom (which would be left in an excited state unless the level into which the electron was captured was the ground state) returning to the ground state by the emission of one or more quanta. The absence of strong continua in the visible and near ultraviolet shows qualitatively that the upper quantum levels (which would give rise to continua in the far infra-red) are probably more important in the recombination process than has previously been supposed.

The *relative* intensities of various spectral lines were found to change very rapidly in the first few microseconds after the discharge, and then much more slowly during the remainder of the afterglow. The rapid change in the early part of the afterglow is to be expected, since a little time is required for the establishment of a stationary state of electron temperature in the plasma, etc. As an example of the type of change found in the spectrum of the later afterglow, the line 6678A ($^2P_4 3p8 - 3p4$ transition) gave a photographic density roughly twice that produced by the line 5852A ($^2P_4 3p10 - 3s4$ transition) at a time of 100 microseconds after the discharge, while the two lines produced the same photographic density 700 microseconds after the discharge. Similar somewhat smaller changes could be observed with many other lines, but the majority of the lines observed did not change appreciably in relative intensity, thus agreeing in detail with the photo-multiplier data already cited for various fairly wide regions of the spectrum. At any rate, a careful examination of the data did not reveal any striking *systematic* shift in the relative intensities of the lines which might have been correlated with a change in the relative importance of various quantum levels in the initial capture of electrons.

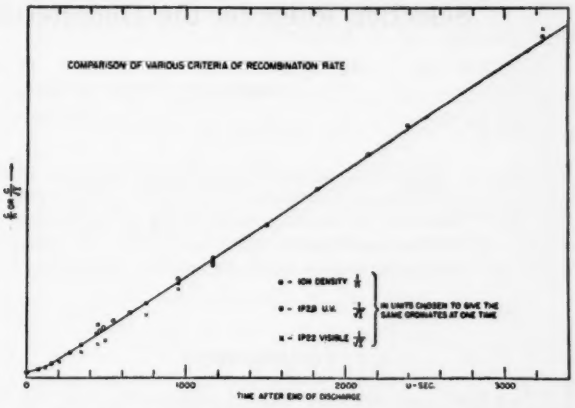

FIG. 3. Electron density; visible and ultraviolet light intensities, as a function of time.

ACKNOWLEDGMENT

The authors wish to express their thanks to Professor S. C. Brown of M.I.T. for his advice concerning the construction of the electron density measuring portion of the apparatus.

Selection Rules for the Dematerialization of a Particle into Two Photons

C. N. YANG*
Institute for Nuclear Studies, University of Chicago, Chicago, Illinois
(Received August 22, 1949)

Selection rules governing the disintegration of a particle into two photons are derived from the general principle of invariance under rotation and inversion. The polarization state of the photons is completely fixed by the selection rules for initial particles with spin less than 2. These results which are independent of any specific assumption about the interactions may possibly offer a method of deciding the symmetry nature of mesons which decay into two photons.

I. INTRODUCTION

IT has been pointed out[1] that a positronium in the ^3S state cannot decay through annihilation with the emission of two photons. Recent calculation[2] shows that also a vector or a pseudovector neutral meson cannot disintegrate into two photons. It is the purpose of the present paper to show that these facts are immediate consequences of certain selection rules which can be derived from the general principle of invariance under space rotation and inversion.

These selection rules also yield information on the polarization state of the two photons emitted. In particular, one concludes that the two photons resulting from the annihilation of slow positrons in matter always have their planes of polarization perpendicular to each other.[3] This has been pointed out by Wheeler who also proposed a possible experimental verification.[4]

An especially interesting consequence of these selection rules is that they could conceivably offer a means of studying the nature of particles which dematerialize into two photons. If, for example, neutral mesons are found which disintegrate into two photons,[5] one would conclude that they cannot be vector or pseudovector mesons. Besides, as will be apparent from the selection rules, the two disintegration photons from a scalar particle always have parallel planes of polarization while those from a pseudoscalar particle always have mutually perpendicular planes of polarization. An experimental determination of the relative orientation of the planes of polarization of the two disintegration photons would therefore decide whether the neutral meson is a scalar or a pseudoscalar meson.

In Section II we shall give a simple but mathematically somewhat incomplete treatment of the symmetry nature of a state of two photons propagating in opposite directions, the detailed mathematical treatment being discussed in Section IV. The selection rules are derived in Section III and are based on the symmetry nature of the two photon states discussed in Section II. In the last section the parity of mesons and of the positronium is discussed.

TABLE I. Eigenvalues of the rotations $\mathfrak{R}_\varphi$, $\mathfrak{R}_\xi$, and the inversion $\mathcal{P}$ for the four polarization states.

	$\Psi^{RR}+\Psi^{LL}$	$\Psi^{RR}-\Psi^{LL}$	Ψ^{RL}	Ψ^{LR}
$\mathfrak{R}_\varphi$ (rotation around z axis through an angle φ)	1	1	$e^{2i\varphi}$	$e^{-2i\varphi}$
$\mathfrak{R}_\xi$ (rotation around x axis through 180°)	1	1		
$\mathcal{P}$ (inversion)	1	−1	1	1

II. BEHAVIOR OF THE STATE OF TWO PHOTONS UNDER ROTATION AND INVERSION

Consider two photons of equal wave-length λ_0 propagating in opposite directions along the z axis. There are four such states which we shall denote by Ψ^{RR}, Ψ^{RL}, Ψ^{LR} and Ψ^{LL}. The first index refers to the circular polarization state of the photon propagating in the $+z$ direction, the second to that of the other photon. E.g., Ψ^{RL} would represent a state with a right circularly polarized photon propagating along the $+z$ axis and a left circularly polarized photon propagating along the $-z$ axis.

In order to investigate the behavior of these four states under a space rotation or an inversion let us first write down the electric field for a right circularly polarized electromagnetic wave propagating along the z axis,

$$(E_x)_+{}^R = E_0 \cos(kz-\omega t+\delta_+{}^R),$$
$$(E_y)_+{}^R = E_0 \sin(kz-\omega t+\delta_+{}^R). \quad (1)$$

TABLE II. Circular polarization of disintegration photons.

parity \ J	0	1	2, 4, 6⋯	3, 5, 7⋯
even	$\Psi^{RR}+\Psi^{LL}$	forbidden	$\Psi^{RR}+\Psi^{LL}$, Ψ^{RL}, Ψ^{LR}	Ψ^{RL}, Ψ^{LR}
odd	$\Psi^{RR}-\Psi^{LL}$	forbidden	$\Psi^{RR}-\Psi^{LL}$	forbidden

* Now at the Institute for Advanced Study, Princeton, New Jersey.

[1] J. A. Wheeler, Ann. N. Y. Acad. Sci. **48**, 219 (1946).

[2] S. Sakata and Y. Tanikawa, Phys. Rev. **57**, 548 (1948); R. Finkelstein, Phys. Rev. **72**, 415 (1947); J. Steinberger, Phys. Rev. **76**, 1180 (1949).

[3] They are not individually plane polarized. But if they are analyzed into plane polarized waves their planes of polarizations show the stated correlation.

[4] J. A. Wheeler, reference 1. See also M. H. L. Pryce and J. C. Ward, Nature **160**, 435 (1947), and Snyder, Pasternack and Hornbostel, Phys. Rev. **73**, 440 (1948). Experimental verification has been reported by E. Bleuer and H. L. Bradt, Phys. Rev. **73**, 1398 (1948).

[5] Bjorklund, Moyer, and York, Phys. Rev. **77**, 213 (1950).

TABLE III. Correlation of the planes (see reference 3) of polarization of disintegration photons ($\perp$ = planes of polarization perpendicular, $\parallel$ = planes of polarization parallel).

parity \ J	0	1	2, 4, 6⋯	3, 5, 7⋯
even	$\parallel$	forbidden	$\parallel \geqq 50\%$ $\perp \leqq 50\%$	$\parallel$ 50% $\perp$ 50%
odd	$\perp$	forbidden	$\perp$	forbidden

For a right circularly polarized wave propagating in the opposite direction,

$$(E_x)_-{}^R = E_0 \cos(-kz-\omega t+\delta_-{}^R),$$
$$(E_y)_-{}^R = -E_0 \sin(-kz-\omega t+\delta_-{}^R). \quad (2)$$

Under a rotation through an angle φ around the z axis,

$$x = x' \cos\varphi + y' \sin\varphi,$$
$$y = -x' \sin\varphi + y' \cos\varphi, \quad (3)$$
$$z = z'.$$

We have

$$(E_x)_+{}^{R'} = E_0 \cos(kz-\omega t+\delta_+{}^R+\phi),$$
$$(E_y)_+{}^{R'} = E_0 \sin(kz-\omega t+\delta_+{}^R+\phi); \quad (4)$$

$$(E_x)_-{}^{R'} = E_0 \cos(-kz-\omega t+\delta_-{}^R-\varphi),$$
$$(E_y)_-{}^{R'} = -E_0 \sin(-kz-\omega t+\delta_-{}^R-\phi). \quad (5)$$

Thus the phase of a right circularly polarized wave along the z axis changes by $+\varphi$ while that of a right circularly polarized wave along the $-z$ axis changes by $-\varphi$ under the rotation. For the quantum state Ψ^{RR} the total phase factor is the product of the two phase factors of the two photons. (This will become evident in Section IV.) Hence we conclude that the state Ψ^{RR} is an eigenstate of the rotation (3) with the eigenvalue 1.

Mathematically the states are changed under the rotation (3) by a unitary transformation which we shall call $\mathfrak{R}_\phi$. We conclude that:

$$\mathfrak{R}_\varphi \Psi^{RR} = \Psi^{RR}. \quad (6)$$

Similar conclusions are reached for a rotation around the x axis through 180° and for an inversion. We summarize the results in Table I.

It is of course evident that the angular momentum along the z axis for the different states is related to the eigenvalue of $\mathfrak{R}_\varphi$ in the usual way.

III. SELECTION RULES

The selection rules governing the disintegration of a particle into two photons follow immediately from Table I. We take the center-of-mass reference system and take the z axis along the direction of one of the outgoing photons.

(i) For an odd initial state the only possible mode of disintegration is to go into the state $\Psi^{RR}-\Psi^{LL}$. For an even initial state the three final states Ψ^{RL}, Ψ^{LR}, and $\Psi^{RR}+\Psi^{LL}$ are possible.

(ii) For an initial state with total angular momentum $J=1, 3, 5\cdots$ the only possible final states are Ψ^{RL} and Ψ^{LR}. This is so because $\Psi^{RR}+\Psi^{LL}$ and $\Psi^{RR}-\Psi^{LL}$ are both simultaneous eigenstates of $\mathfrak{R}_\varphi$ and $\mathfrak{R}_\xi$ with eigenvalues one, while the initial state that is an eigenstate of $\mathfrak{R}_\varphi$ with eigenvalue one has the rotation properties of the spherical harmonics Y_{J0} and therefore changes sign under $\mathfrak{R}_\xi$ for $J=1, 3, 5\cdots$.

(iii) For an initial state with $J=0, 1$ the only possible final states are $\Psi^{RR}+\Psi^{LL}$ and $\Psi^{RR}-\Psi^{LL}$, because the states Ψ^{RL} and Ψ^{LR} have angular momentum values $\pm 2\hbar$ along the z axis, which is too big for $J=0$ or 1.

These results are summarized in Table II.

It will be shown in the next Section that

(i) $\Psi^{RR}+\Psi^{LL}$ represents two photons with their planes of polarization always[3] parallel;

(ii) $\Psi^{RR}-\Psi^{LL}$ represents two photons with their planes of polarization always perpendicular; and

(iii) Ψ^{RL} and Ψ^{LR} both represent two photons with their planes of polarization 50 percent of the time parallel and 50 percent of the time perpendicular.

These facts combined with Table II lead to the conclusions summarized in Table III concerning the correlation of the planes of polarization of the disintegration photons.

IV. SPACE ROTATION AND INVERSION IN QUANTUM ELECTRODYNAMICS

In the electromagnetic field and the meson field, the number of particles is not a constant of motion. A complete formulation of the principle of invariance can only be made with the quantized field theory. Let us first consider the electromagnetic field described by the vector potential $\mathbf{A}(xyz)$. These are operators operating on state vectors Ψ which are usually represented as functions of occupation numbers. Under a space rotation ρ defined by

$$x_i = \sum_{j=1}^{3} \rho_{ij} x_j' \quad (x_1=x, x_2=y, x_3=z), \quad (7)$$

the operators $\mathbf{A}(xyz)$ and the wave function Ψ undergo a unitary transformation $\mathfrak{R}_\rho$ and the invariance under rotation requires that

$$\mathfrak{R}_\rho A_i(xyz) \mathfrak{R}_\rho{}^{-1} = \sum_{j=1}^{3} \rho_{ij} A_j(x'y'z'). \quad (8)$$

It is of course further required that the $\mathfrak{R}$'s form a group isomorphic to the group of rotations.

To see in detail what this means let us expand the vector potential $\mathbf{A}$ into plane waves as usual:

$$\mathbf{A}(xyz) = \sum_{\mathbf{k}} \sum_{\lambda=1}^{2} (2\pi\hbar c/vk)^{\frac{1}{2}} \mathbf{e}_{k\lambda} (a_{k\lambda} e^{i\mathbf{k}\cdot\mathbf{r}} + a_{k\lambda}{}^* e^{-i\mathbf{k}\cdot\mathbf{r}}), \quad (9)$$

where $\mathbf{e}_{k1}$ and $\mathbf{e}_{k2}$ are two unit vectors forming with $\mathbf{k}/k$ a right-handed orthogonal system of unit vectors. It will be more convenient to use circular polarization for the study of rotation and we define

$$(\mathbf{e}_{k1}+i\mathbf{e}_{k2})/\sqrt{2} = \mathbf{e}_k{}^L, \quad (\mathbf{e}_{k1}-i\mathbf{e}_{k2})/\sqrt{2} = \mathbf{e}_k{}^R; \quad (10)$$

$$(a_{k1}-ia_{k2})/\sqrt{2} = a_k{}^L, \quad (a_{k1}+ia_{k2})/\sqrt{2} = a_k{}^R. \quad (11)$$

TABLE IV. The parity of particles at rest.

Scalar meson	Vector meson	Pseudovector meson	Pseudoscalar meson	Positronium in ^1S and ^3S states
even	odd	even	odd	odd

Evidently

$$\mathbf{A}(xyz)=\sum_k(2\pi\hbar c/vk)^{\frac{1}{2}}(\mathbf{e}_k{}^L a_k{}^L e^{i\mathbf{k}\cdot\mathbf{r}}+\mathbf{e}_k{}^{L^*}a_k{}^{L^*}e^{-i\mathbf{k}\cdot\mathbf{r}})$$
$$+\sum_k(2\pi\hbar c/vk)^{\frac{1}{2}}(\mathbf{e}_k{}^R a_k{}^R e^{i\mathbf{k}\cdot\mathbf{r}}+\mathbf{e}_k{}^{R^*}a_k{}^{R^*}e^{-i\mathbf{k}\cdot\mathbf{r}}). \quad (12)$$

The operators $a_{k\lambda}$, $a_k{}^R$ and $a_k{}^L$ all satisfy the usual commutation relations

$$a_k{}^R a_k{}^{R^*}-a_k{}^{R^*}a_k{}^R=1, \quad \text{etc.}$$

We are particularly interested in those modes of electromagnetic waves propagating along the $+z$ or the $-z$ direction with a definite wave-length, There are four such modes and we shall write their a operators as $a_+{}^R$, $a_+{}^L$, $a_-{}^R$ and $a_-{}^L$; $+$ and $-$ meaning the direction $+z$ or $-z$ of propagation. For definiteness we choose the phases of those modes such that the $\mathbf{e}_{k1}$, $\mathbf{e}_{k2}$ vectors in Eqs. (10) have as their xyz components:

$$\mathbf{e}_{+,1}=\mathbf{e}_{-,1}=(1,0,0), \quad \mathbf{e}_{+2}=-\mathbf{e}_{-,2}=(0,1,0). \quad (13)$$

With the operators a one can express in a very convenient form the states Ψ^{RR}, Ψ^{RL}, Ψ^{LR} and Ψ^{LL} defined in Section II.

$$\begin{aligned}\Psi^{RR}&=a_+{}^{R^*}a_-{}^{R^*}\Psi_{00\ldots}, & \Psi^{RL}&=a_+{}^{R^*}a_-{}^{L^*}\Psi_{00\ldots},\\ \Psi^{LR}&=a_-{}^{R^*}a_+{}^{L^*}\Psi_{00\ldots}, & \Psi^{LL}&=a_+{}^{L^*}a_-{}^{L^*}\Psi_{00\ldots},\end{aligned} \quad (14)$$

where $\Psi_{00\ldots}$ is defined to be the state with no photons.

We make a digression here to prove the statement at the end of the last section about the correlation in the planes of polarization of the two photons for the states $\Psi^{RR}+\Psi^{LL}$, $\Psi^{RR}-\Psi^{LL}$, Ψ^{RL} and Ψ^{LR}. By (14) and (11),

$$\begin{aligned}\Psi^{RR}+\Psi^{LL}&=(a_+{}^{R^*}a_-{}^{R^*}+a_+{}^{L^*}a_-{}^{L^*})\Psi_{00\ldots}\\ &=(a_{+,1}{}^*a_{-,1}{}^*-a_{+,2}{}^*a_{-,2}{}^*)\Psi_{00\ldots},\\ \Psi^{RR}-\Psi^{LL}&=-i(a_{+,1}{}^*a_{-,2}{}^*+a_{+,2}{}^*a_{-,1}{}^*)\Psi_{00\ldots},\\ \Psi^{RL}&=\tfrac{1}{2}(a_{+,1}{}^*a_{-,1}{}^*+a_{+,2}{}^*a_{-,2}{}^*\\ &\quad +ia_{+,1}{}^*a_{-,2}{}^*-ia_{+,2}{}^*a_{-,1}{}^*)\Psi_{00\ldots},\\ \Psi^{LR}&=\tfrac{1}{2}(a_{+,1}{}^*a_{-,1}{}^*+a_{+,2}{}^*a_{-,2}{}^*\\ &\quad -ia_{+,1}{}^*a_{-,2}{}^*+ia_{+,2}{}^*a_{-,1}{}^*)\Psi_{00\ldots}.\end{aligned} \quad (15)$$

Noticing that e.g., $a_{+,1}{}^*a_{-,1}{}^*\Psi_{00\ldots}$ represents a state with two photons with parallel planes of polarization one completes the proof with no difficulty.

Returning to the investigation of the behavior of the states Ψ^{RR}, Ψ^{RL}, etc., under rotation let us consider the rotation around the z axis through an angle φ, as defined by (3). Substitution of (13) and (12) into (8) shows[6] that

$$\begin{aligned}\mathfrak{R}_\varphi a_+{}^R\mathfrak{R}_\varphi{}^{-1}&=e^{-i\varphi}a_+{}^R, & \mathfrak{R}_\varphi a_+{}^L\mathfrak{R}_\varphi{}^{-1}&=e^{+i\varphi}a_+{}^L,\\ \mathfrak{R}_\varphi a_-{}^R\mathfrak{R}_\varphi{}^{-1}&=e^{+i\varphi}a_-{}^R, & \mathfrak{R}_\varphi a_-{}^L\mathfrak{R}_\varphi{}^{-1}&=e^{-i\varphi}a_-{}^L.\end{aligned} \quad (16)$$

These and similar equations for the other annihilation operators and for a general rotation ρ determine the operators $\mathfrak{R}_\rho$ if the additional condition is imposed that $\mathfrak{R}_\rho$ form a group. It is not difficult to prove that

$$\mathfrak{R}_\rho\Psi_{00\ldots}=\Psi_{00\ldots}. \quad (17)$$

We can now prove Eq. (6) which asserts that Ψ^{RR} is an eigenstate of $\mathfrak{R}_\varphi$ with eigenvalue 1. Take the Hermitian conjugate of (16) and multiply from the right by $\mathfrak{R}_\varphi$:

$$\mathfrak{R}_\varphi a_+{}^{R^*}=e^{i\varphi}a_+{}^{R^*}\mathfrak{R}_\varphi, \quad \mathfrak{R}_\varphi a_-{}^{R^*}=e^{-i\varphi}a_-{}^{R^*}\mathfrak{R}_\varphi.$$

Hence,

$$\mathfrak{R}_\varphi a_+{}^{R^*}a_-{}^{R^*}=a_+{}^{R^*}a_-{}^{R^*}\mathfrak{R}_\varphi.$$

Operating on $\Psi_{00\ldots}$ with this last equation and making use of (17) and (14) one proves (6).

The other conclusions tabulated in the first row of Table I can be obtained in similar ways. For the rotation ξ:

$$x=x', \quad y=-y', \quad z=-z',$$

we have

$$\begin{aligned}\mathfrak{R}_\xi a_+{}^R\mathfrak{R}_\xi{}^{-1}&=a_-{}^R, & \mathfrak{R}_\xi a_+{}^L\mathfrak{R}_\xi{}^{-1}&=a_-{}^L,\\ \mathfrak{R}_\xi a_-{}^R\mathfrak{R}_\xi{}^{-1}&=a_+{}^R, & \mathfrak{R}_\xi a_-{}^L\mathfrak{R}_\xi{}^{-1}&=a_+{}^L.\end{aligned} \quad (18)$$

These lead to the results in the second row of Table I. Under an inversion the states are transformed by a unitary transformation $\mathcal{P}$ satisfying

$$\mathcal{P}\mathbf{A}(xyz)\mathcal{P}^{-1}=-\mathbf{A}(-x,-y,-z). \quad (19)$$

It is further required that

$$\mathcal{P}^2=1. \quad (20)$$

Expanding (19) into Fourier components we obtain

$$\begin{aligned}\mathcal{P}a_+{}^R\mathcal{P}^{-1}&=-a_-{}^L, & \mathcal{P}a_+{}^L\mathcal{P}^{-1}&=-a_-{}^R,\\ \mathcal{P}a_-{}^R\mathcal{P}^{-1}&=-a_+{}^L, & \mathcal{P}a_-{}^L\mathcal{P}^{-1}&=-a_+{}^R.\end{aligned} \quad (21)$$

It is to be noticed that (19) and (20) together do not completely determine the operator $\mathcal{P}$, as a change of sign of $\mathcal{P}$ does not affect either equation. However, changing the sign of $\mathcal{P}$ merely means a change in the name-calling of the even and odd states and is of no physical consequence. For definiteness we shall fix the sign by calling the vacuum an even state:

$$\mathcal{P}\Psi_{00\ldots}=\Psi_{00\ldots}. \quad (22)$$

Equations (21) and (22) lead to the third row of Table I.

[6] Actually since the Maxwell's equations are of the second order in $\partial/\partial t$, one should write together with (8)

$$\mathfrak{R}_\rho\frac{\partial A_i(xyz)}{\partial t}\mathfrak{R}_\rho{}^{-1}=\sum_j\rho_{ij}\frac{\partial A_j(x'y'z')}{\partial t}. \quad (A)$$

The operators $\partial A_i/\partial t$ are expanded into Fourier series similar to (12). Equation (A) together with (8) give Eq. (16).

V. PARITY OF MESONS AND THE POSITRONIUM

The above method for obtaining the symmetry nature of photon states can be easily extended to the meson field. In particular, if a_0 is the annihilation operator for a scalar meson at rest it is easy to see in analogy with Eq. (21) that

$$\mathcal{P}a_0\mathcal{P}^{-1}=a_0. \tag{23}$$

There is no change of sign of a_0 (see Eq. (21)) because the scalar meson field, unlike the vector potential of the electromagnetic field, retains its sign under an inversion. If we again call the state of no meson an even state, it is evident that a state with one scalar meson at rest is also even. This and similar conclusions concerning the parity of the vector, the pseudoscalar and pseudovector mesons are summarized in Table IV.

With the electron-positron field the situation is quite similar. The behavior of the field $\psi_i(xyz)$ under rotation and inversion is evidently given by

$$\mathcal{R}_\rho\psi_i(xyz)\mathcal{R}_\rho^{-1}=\sum_{j=1}^{4}S_{ij}(\rho)\psi_j(x'y'z'), \tag{24}$$

$$\mathcal{P}\psi_i(xyz)\mathcal{P}^{-1}=\sum_{j=1}^{4}\beta_{ij}\psi_j(x'y',z'), \tag{25}$$

where $S_{ij}(\rho)$ represents the spinor transformation corresponding to the rotation ρ and β_{ij} are the elements of Dirac's β-matrix.

If we expand ψ into plane waves and consider the particular mode representing an electron at rest in a positive or negative energy state it is evident that (25) shows

$$\mathcal{P}b_{0+}\mathcal{P}^{-1}=b_{0+},\quad \mathcal{P}b_{0-}\mathcal{P}^{-1}=-b_{0-}, \tag{26}$$

where b_{0+} and b_{0-} are the annihilation operators for an electron at rest with positive and negative energy values, respectively. The negative sign in (26) comes from the operation on ψ with the β-matrix. It is therefore evident that an electron-positron pair, both at rest, has an odd parity. Here, as before, we adopt the convention that the state of vacuum is to be called even.

Extension of the above argument to the ^1S and ^3S states of the positronium is evident. One gets for both states an odd parity. As mentioned in the introduction, Wheeler has pointed out[1] that the annihilation photons from the ^1S state of the positronium always have mutually perpendicular[3] planes of polarization. We see from Table III that the assignment of an odd parity to the ^1S state of positronium leads directly to the same conclusion.

The author is very much indebted to Professor E. Fermi for invaluable discussions and for his kind encouragement.

Note added in proof.—Some of the results of this paper have been obtained by L. D. Landau, Dokl. Akad. Nawk., USSR **60**, 207–209 (1948). See a summary in English in Phys. Abstracts **A52**, 125 (1949).

Thermionic Emission of Thin Films of Alkaline Earth Oxide Deposited by Evaporation

GEORGE E. MOORE AND H. W. ALLISON
Bell Telephone Laboratories, Murray Hill, New Jersey
(Received September 23, 1949)

Monomolecular films of BaO or SrO were deposited by evaporation on clean tungsten or molybdenum surfaces with precautions to eliminate effects caused by excess metal of the oxide or by heating. Thermionic emissions of the same order of magnitude as from commercial oxide cathodes have been obtained from these systems. The results can be explained qualitatively by considering the adsorbed molecules as oriented dipoles. Although the results may suggest a possible mechanism for a portion of the emission from thick oxide cathodes, there are serious obstacles against such thin film phenomena as a complete explanation.

MANY authors have discussed thermionic emission from thin films of electropositive metals deposited on either clean or oxidized metallic supports, such as tungsten. Others have investigated the oxide cathode, a much more complex system. Only two authors seem to have investigated thin films of alkaline earth oxide on clean support metals—a system intermediate in complexity between the first two. Of these, Davisson and Pidgeon[1] found that a tungsten ribbon was activated by material evaporated from a neighboring oxide-coated cathode. Hull[2,3] found that molybdenum, after receiving material evaporated from a mixture of BaO and Al_2O_3 in a porous molybdenum stocking, became a very satisfactory cathode for thyratrons as a result of this evaporated deposit. For reasons not given, both papers definitely attribute the activation to BaO, rather than to the barium metal, which, at least in Hull's work, certainly[4] evaporated with the BaO.

The present paper gives evidence that films of pure alkaline earth oxide from one to 25 molecular layers thick deposited by evaporation can lower the thermionic work function of clean receiver metals by as much as 3.5 volts. The results are compared with published data on oxide-coated cathodes.

EXPERIMENTAL

Tube Construction

Consistent results were obtained in a variety of tube structures which evolved into two designs, one used only for thermionic tests and the other for both thermionic and contact potential measurements. The essential features of the thermionic tube are shown in Fig. 1. Five filaments, F_0–F_4, were mounted inside the anode system, F_0 along the tube axis and the others parallel to it at intervals of 90° around the circumference of a circle of 0.75-in. radius. When the relative effects of two oxides on a given receiver surface were to be compared, the central filament acted as the receiver and was a ribbon with its plane at an angle of 45° to the planes of the outer filaments, as shown. Repeated runs could be made by cleaning the receiver by flashing. The outer filaments served as sources from which oxides evaporated onto the receiver, for example, BaO from F_1–F_3, SrO from F_2–F_4. When effects of equal quantities of a given oxide on four different receiver metals were to be investigated, the central filament served as a source from which the oxide was evaporated, the four outer filaments F_1–F_4 acting as receivers. In such experiments, the cross section of the central source filament was circular. The filaments were $6\frac{1}{4}$ in. long. They were supported by springs S from a system of mica insulators M. To minimize end cooling effects, the anode system was divided into three sections D, A, and D, the central 1.5-in. section A collecting the emission of the central section of the receiver filament, with D and D serving as guard rings. All three sections of the anode were usually operated 135 volts positive with respect to the filament on test, the small correction for Schottky effect being of the same order as that for clean tungsten. The baffles BB_1 mounted between the outer filaments prevent material evaporated from any side filament from depositing on those adjacent, the section B_1 protecting the sections between the anode and guards. The filaments used as sources of the alkaline earth oxide consisted of a support (or core) of chemically pure platinum coated with about 5 mg per cm² of an alkaline earth carbonate of high purity. The carbonate was converted to the oxide during exhaust. A sample analysis of $SrCO_3$ is given:

Spectrochemical qualitative		Estimated range
Major component	Sr	(percent)
Trace	Ba, Mg, Ca, Na	<0.03
Slight trace	Bi, Fe	<0.005
Very slight trace	Ag, Al, Co, Mn, Si	<0.001

Spectrochemical quantitative	Weight (percent)
Ba	0.023
Na	0.016
Ca	0.041
Mg	0.009

In the contact potential tube the same guard ring structure was used. A section is shown in Fig. 2. Filaments 1 and 3 were receivers while 2 and 4 were sources, respectively, of Sr metal and of SrO. The strontium metal sources resemble commercial oxide-coated filaments except that the coat was pure SrO

[1] Davisson and Pidgeon, Phys. Rev. **15**, 553 (1920).
[2] A. W. Hull, Phys. Rev. **56**, 86 (1939).
[3] A. W. Hull, U. S. Patent 2,246,176.
[4] Moore, Allison, and Morrison, Phys. Rev. **75**, 347 (1949).

and the support metal Konal or nickel containing approximately 0.1 percent by weight Mg. These are known[5,6] to reduce alkaline earth oxides to free metals. Tests which will be described elsewhere indicate that at least 100 atoms of strontium metal evaporated for each SrO molecule. The central filament 5 was a source of electrons for the contact potential tests and was usually clean tungsten operated at about 1800°K, although oxide-coated filaments were used in some tubes. Because of shields *SS*, material evaporated from one source could not strike either filament 5 or the other source. Filament 5 was heated by a biased half-wave rectifier so that electrons could leave[7] only during the non-heating half-cycle.

Chemical Preparation and Exhaust

All platinum filaments, either oxide sources or receivers, were treated at 1000°C for 30 min. in hydrogen saturated with water vapor to oxidize[8] any impurity present in the platinum which might otherwise form free alkaline earth metal by chemical reaction with the oxide coat. The platinum was prepared by Mr. H. T. Reeve and was unusually pure, the only impurity spectroscopically detectable being copper present to less than 0.03 percent.

During exhaust, the 702-EJ glass was baked for several hours at 470°C or above, the molybdenum or tantalum anode sections were heated inductively and all source filaments were thoroughly heated. This process was repeated several times throughout a two- or three-day exhaust period. The receiver filaments were then flashed, the barium-magnesium getters *G* were vaporized and the tube sealed off.

The stability of the work function of a receiver throughout long periods of idleness indicated that the pressure of thermionically important gases in the volume of the tubes was very low. Thus a contact potential test of a clean tungsten receiver in any tube tested could be repeated to within 0.02 volt after an idle period of more than a month. This fact, together with relations found by Langmuir[9] for the adsorption of gases on clean tungsten, indicates that no gas or gases in the volume of the tubes capable of affecting the work function by 0.1 volt or more were present to as much as 10^{-14} mm. This high vacuum is believed dependent on a severe exhaust schedule, the gettering action of zirconium applied to the outer anode surfaces and to the BaMg getters, *G*. The writers acknowledge the skill with which Mr. E. A. Thurber supervised the application of zirconium and several other features in the chemical preparation of these tubes.

Temperature Determination

Temperatures of source and receiver filaments were measured pyrometrically, correcting for emissivity and transmission of the glass. When possible, resistivity relations were used in combination with the Stefan-Boltzman law to extend the temperatures to values

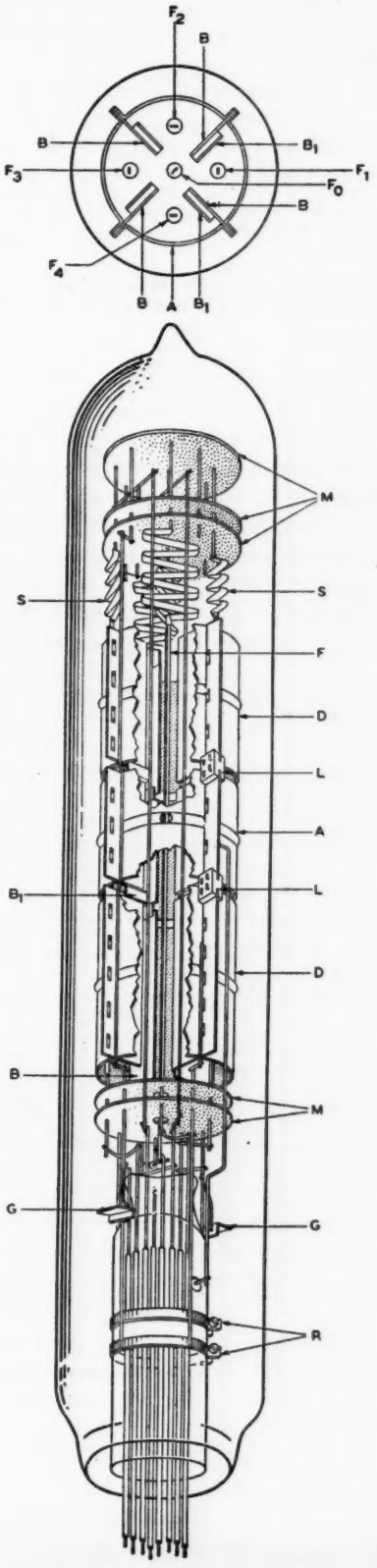

FIG. 1. Thermionic emission tube.

[5] E. F. Lowry, Phys. Rev. **35**, 1367 (1930).
[6] M. Benjamin, Phil. Mag. **20**, 1 (1935).
[7] L. H. Germer, Phys. Rev. **25**, 795 (1925).
[8] C. H. Prescott, Jr., J. Am. Chem. Soc. **60**, 3047 (1938).
[9] I. Langmuir, Chem. Rev. **13**, 167 (1933).

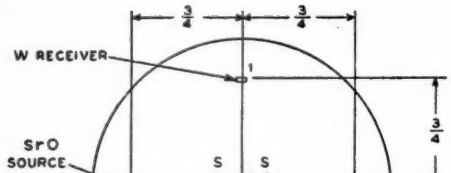

FIG. 2. Contact potential tube. (Filament 5 is electron source. $S-S$ are shields to prevent evaporated material from striking filament 5.)

inaccessible by optical pyrometers. A curve of corrected temperature as a function of filament current for a typical molybdenum filament is given in Fig. 3 and similar curves were obtained for tungsten. The data from two different optical pyrometers, from resistivity, and from power radiated, are in substantial agreement. The spectral emissivities of the coated filaments were measured by reflectometer methods. It is believed that the probable absolute error in any temperature given is not over 10°C and the probable relative error between any two observations of the same filament is not over 5°C. The precision of temperature determination limits the precision with which Richardson constants can be stated. With the present techniques, thermionic measurements of coated tungsten or molybdenum receivers can be made over a range of about 150°C; interelectrode conductance prevented measurement of emissions less than about 10^{-9} amp. It was assumed that the temperature scales determined for the clean receivers were unchanged for coverings up to about 50 layers. This assumption is difficult to justify experimentally but electromagnetic theory indicates that the effect on emissivity should be negligible for less than about 200 layers.

Thermionic Measurements

A modification of the method described by Becker[10] was used to express many of the activation measurements. The receiver filaments were first cleaned by heating for 10 sec. to approximately 2800°K for tungsten or 2300°K for molybdenum after which the observed thermionic emission was that appropriate for clean tungsten or molybdenum. The source filament F_0 was then operated for approximately an hour at a known temperature and allowed to cool. Each receiver filament in turn was then heated at gradually increasing

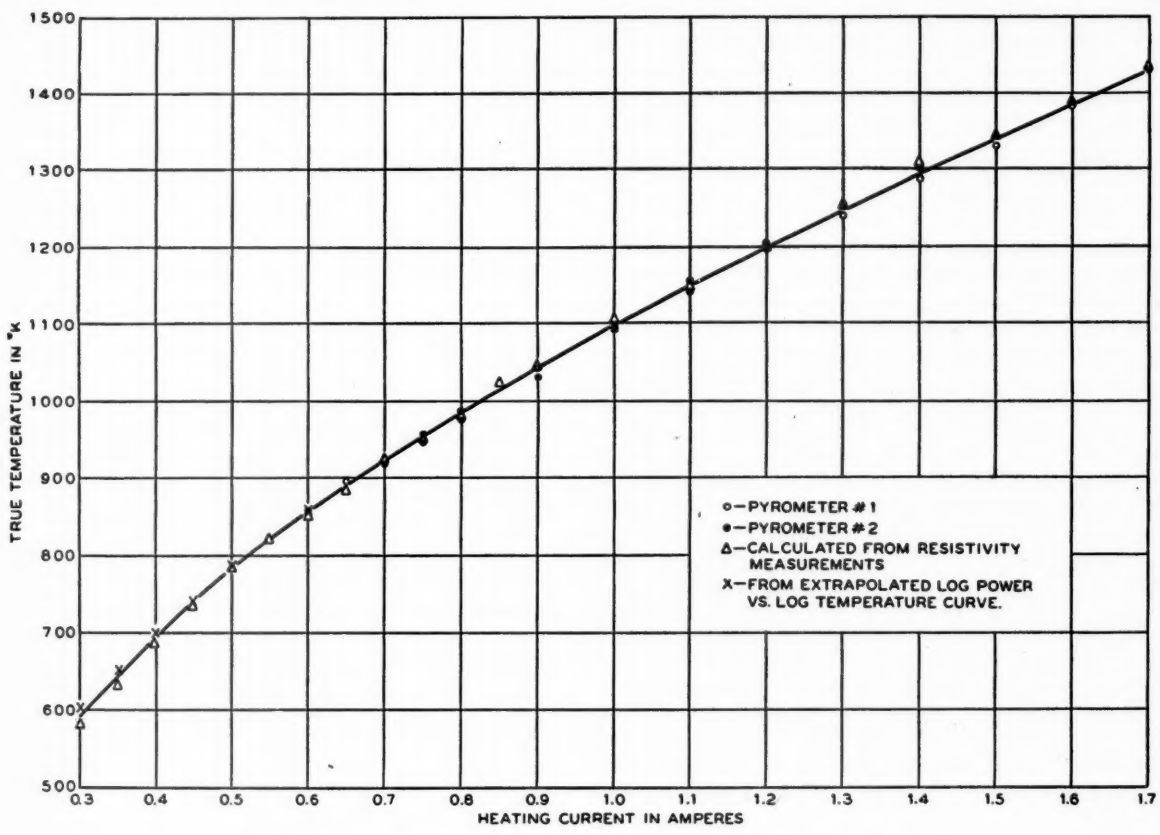

FIG. 3. Temperature-current characteristic for molybdenum receiver filament.

[10] J. A. Becker, Phys. Rev. 34, 1323 (1929).

temperatures until its emission reached a reference value (usually about 10^{-8} amp./cm^2). The receiver temperature required for this emission was recorded and the receiver then allowed to cool. The sources were again heated for approximately an hour and the receiver retested. The receivers were thus activated by successive deposits and the temperature required for reference emission was then plotted against the time for which the source filament had been operated. Several such runs were made with each experimental tube, the receiver filaments being cleaned by flashing before each run. This is a convenient method for representing the enormous range of activation observed in a single coating run.

In many runs, emissions were measured over a range of temperatures after each increment of deposit. The data were usually expressible in terms of Richardson's equation* $I=AT^2\exp(-\varphi e/kT)$, φ and A being determined with precisions of about five percent and 50 percent, respectively.

Determination of Amount of Oxide Deposited

The amount of oxide deposited on a receiver was determined by two methods, neither depending on assumptions regarding observed thermionic effects. The amount vaporized from the source can be computed from the vapor pressure-temperature curve of the oxide. Then from tube geometry and the assumption that no molecules are reflected from the receiver, the amount intercepted becomes known. This method is not very precise, the probable error of 10° in the determination of source temperature being equivalent to about 50 percent error in amount evaporated.

The amount present on a receiver ribbon can be determined with a precision of one or two percent by using radioactive tracers in coating the source filament. After deposit and thermionic test, the receivers are removed from the tube and their count compared with that of an aliquot of the mixture used to coat the source. The methods agree well within the 50 percent uncertainty of vapor pressure determinations indicating that not over 50 percent of the molecules are reflected from the receivers.

Many of the results are expressed in terms of molecular layers computed by assuming that the molecules are adsorbed with the line of centers perpendicular to the receiver surface, each molecule occupying a circle of radius r_0 as defined by Slater.[11] This configuration is assumed primarily for convenience rather than because of a strong belief in its correctness.

RESULTS

Activation as Shown by Richardson Lines

Ideally one would hope to find a continuous curve, reproducible from tube to tube, showing the behavior of the Richardson constants A and φ as a function of the amount of adsorbed oxide for each combination of oxide and receiver metal. This ideal was but imperfectly realized.

The activation of four receiver filaments in tube No. 5 by depositing BaO is shown in Figs. 4 and 5, the first giving φ and the second $\log_{10}A$ as a function of the amount of BaO deposited, determined by the vapor pressure-temperature method. φ decreases very rapidly for the first 0.1 layer and then only very gradually to about 24 layers—the maximum covering applied in this run. For tungsten, molybdenum, and tantalum, φ drops to 1.0 volt or less, but for zirconium, the lowest work function realized was about 1.5 volts. The behavior of A is less easily described. Perhaps the only safe generalization is that A for the coated receivers is usually at least one order of magnitude less than for the clean receiver metals.

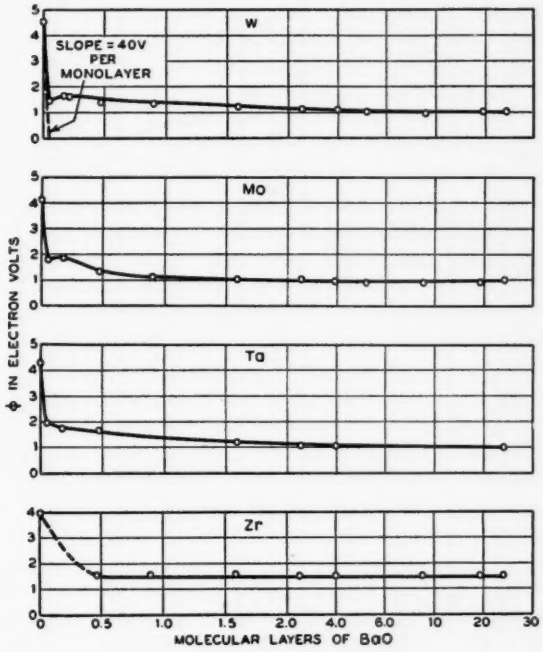

FIG. 4. Work function, φ, of receivers as a function of amount of BaO. Note change of scale in abscissas at 2.0 layers and at 6.0 layers.

More than 200 similar activation curves were taken. For successive runs on any particular receiver filament in a given tube, the emission current for a given amount of oxide and test temperature was reproducible to within less than ±50 percent for coverings of less than a monolayer, but became less reproducible for heavier coverings. In repeated runs on the same filament, the work functions usually agreed to within 0.1 volt but the reproducibility of A was poor. However, the experimental difficulty in obtaining reliable values for A, even for clean metals, is well known.

* Values of φ taken from Richardson lines have been designated as φ^* by Herring and Nichols, reference 15.

[11] J. C. Slater, *Introduction to Chemical Physics* (McGraw-Hill Book Company, Inc., New York, 1939), p. 381.

Activation by Modified Becker Method —Radioactive Tracers

Figure 6 shows a correlation between activation and amount of SrO evaporated onto three of the four tungsten receiver ribbons spaced around a SrO-coated platinum source filament. The amounts were determined with a precision of about two percent by tracers of radioactive fission strontium. The following results were obtained:

(1) During seven successive deposit runs, the emission *vs.* time of deposit data were reproducible for any one receiver but the time rates of activation differed by as much as a factor of two between individual receivers.

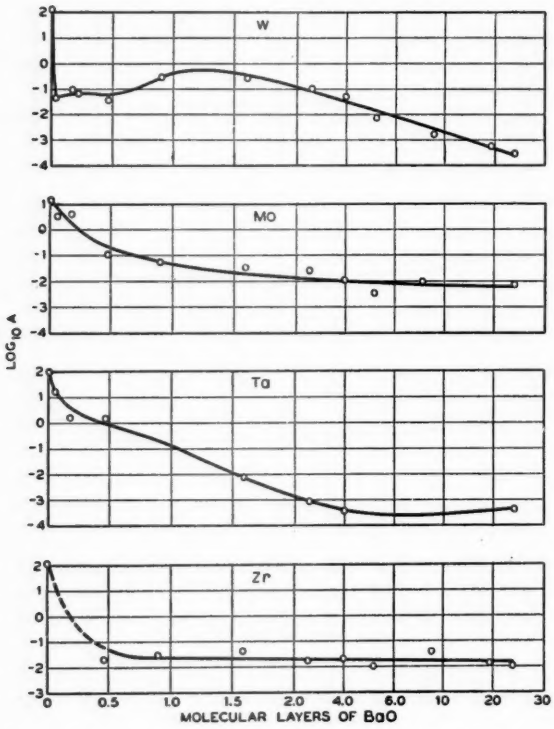

FIG. 5. $\log_{10}$ Richardson A for receivers as a function of amount of BaO. Note change of scale in abscissas at 2.0 layers and at 6.0 layers.

(2) Assuming a uniform rate of deposit, the amount of SrO required for any particular activation was determined directly by removing the receiver ribbons at the end of the seventh deposit run and comparing the radioactive count from each receiver with that from an aliquot of the mixture used to coat the source. That this resolved the discrepancy in time rates noted in (1) is indicated by the agreement of data for the three receivers shown in Fig. 6. Note that each gave an emission of 6.7×10^{-8} amp. cm^{-2} at $650°\pm10°$K for films from 0.3 to 1.0 μg cm^{-2}. In other tubes these same amounts of SrO often gave higher activation, the same emission requiring a temperature of 600°K or less. Heavier coverings, when accompanied by a treatment which consisted of heating the receiver for 2′ or 3′ at 900°K with or without space current, gave still higher activation (see Fig. 12, for example).

(3) Before opening the tube, the fourth tungsten receiver was heated at 1000°K for 60 hr. The resulting decay of emission was followed as a function of time; analysis then showed that the relationship of Fig. 6 held only for deposit. For simplicity in presentation, such decay phenomena will not be discussed further.[12]

Richardson Lines—Details

A few of the Richardson lines for one run in which a tantalum filament was exposed to BaO are shown in Fig. 7. One observes from the tabulated values in the figure that the work function and A both change during the run but not in a simple way. Occasionally, as the thickness of the deposited films increased and the filaments became more active, the Richardson lines were curved. In such cases, the curve was reproducible and always concave downward which is opposite to that expected for patch effects. The curvature is not caused by anode voltage effects, nor by inaccuracy in either temperature or current measurement. In all tubes studied, straight Richardson lines were obtained most consistently for films when the receivers were tantalum.

In Table I representative work functions and emissions are reported, together with values for oxide cathodes of the commercial type and various other emitters described in the literature. The first figure given for φ or emission for any thin film system applies to a monolayer while the second is for 10 to 30 molecular layers.

The data for the first three entries in Part C taken from Blewett,[13] are very conservative. When BaO and SrO are used together, the d.c. emissions realized commercially for the past decade are of the order 1–10 amp. In the present thin film experiments, emissions above about 150 ma/cm^2 were not directly observed; values above this level were obtained by extrapolation. By measurements in the temperature range 550–800°K, emissions above 2 amp./cm^{-2} at 1000°K were occasionally indicated.

Two similarities in Parts A and C of Table I are evident. First, the emissions for a commercial type of oxide layer are about equal to those found in the present work for thin layers of the same oxide on either tungsten or molybdenum. Second, CaO gives the least emission and BaO gives the highest in both the thick layers and the thin films. A difference not so evident in Table I should be noted; the best commercial cathodes use nickel as a support metal, but, in the one experiment with a nickel receiver, the emissions were low.

Contact Potential Measurements

The data of Table I were all obtained by thermionic measurements. However, the thermionic technique does not distinguish between the activation caused by the oxide as deposited, and any effects resulting from the required heating (to approximately 1000°K). Heating might cause physical or chemical changes in the struc-

[12] Some preliminary data on decay are given in Eisenstein's review. See *Advances in Electronics* (Academic Press, Inc., New York, 1949).

[13] J. P. Blewett, J. App. Phys. **10**, 668 (1939).

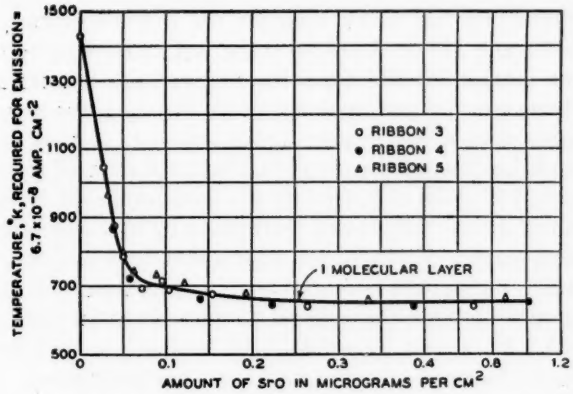

FIG. 6. Correlation between activation of tungsten and amount of SrO deposited.

ture of the system, which in turn could be partially responsible for the activations observed. By using contact potential tests, the nature of the active receiver system can be more definitely inferred. Since the measurement to be described depends on the shift in voltage-current characteristic for electrons flowing *into* the receiver against retarding fields, the activated specimens need never be heated after beginning a run. The effect of the oxide *as deposited* is therefore directly observed, and effects caused by heating can subsequently be evaluated. Answers to the following questions were sought: (1) How much activation is caused by heating the system during thermionic measurement? (2) The emission of a given layer of oxide on platinum is generally less than for the same layer on tungsten, molybdenum, or tantalum and also generally decays more rapidly during thermionic measurement. Is the tabulated lower activity for platinum receivers the result of decay before the measurement is complete, or inherent in the nature of the platinum surface? (3) Is

TABLE I. Emission constants.

System	ϕ-volts	Temperature range of measurements —°K	Indicated emission at 1000°K —amp. cm^{-2}
Part A—Thin oxide films in present work (1–30 monolayers)			
BaO on Mo	1.2–1.0	550–900	0.6–1.0
SrO on Mo	1.2–1.1	550–900	0.6–0.8
CaO on Mo	2.1	820–920	10^{-5}
BaO on W	1.2–1.0	550–900	0.6–1.0
SrO on W	1.2–1.1	550–900	0.6–0.8
CaO on W	2.1	820–920	10^{-5}
BaO on Ta	1.3–1.0	600–900	10^{-2}–10^{-3}
SrO on Ta	1.3	600–870	10^{-3}
BaO on Zr	1.5	670–870	10^{-3}
SrO on Pt	1.9	600–960	10^{-5}
SrO on Ni	2.0	675–850	10^{-9}
Part B—Thin films described in literature			
Hull's dispenser[a]			
Cathode—BaO on Mo	1.215		0.63
Ba metal on W[b]	2.1		0.002
Ba metal on oxygen on W[c,d]	1.34		0.03
Part C—Thick oxide films of commercial type			
BaO[e]	1.1±0.3		10^{-3} to 10^{-1}
SrO[e]	1.4±0.3		10^{-4} to 10^{-2}
CaO[e]	1.9±0.3		10^{-5} to 10^{-3}
Commercial oxide cathodes 1936 to present			
Mixed BaO-SrO on Ni	1.2–1.0		1–10
Prescott's nickelated filament —best activity[f]	1.37		0.25

[a] See reference 2.
[b] J. A. Becker, Trans. Faraday Soc. 28, 148 (1932).
[c] C. J. Smithells, *Tungsten* (D. Van Nostrand, Company, Inc., New York, 1936).
[d] A. L. Reimann, *Thermionic Emission* (John Wiley and Sons, Inc., New York, 1934).
[e] See reference 13.
[f] See reference 8.

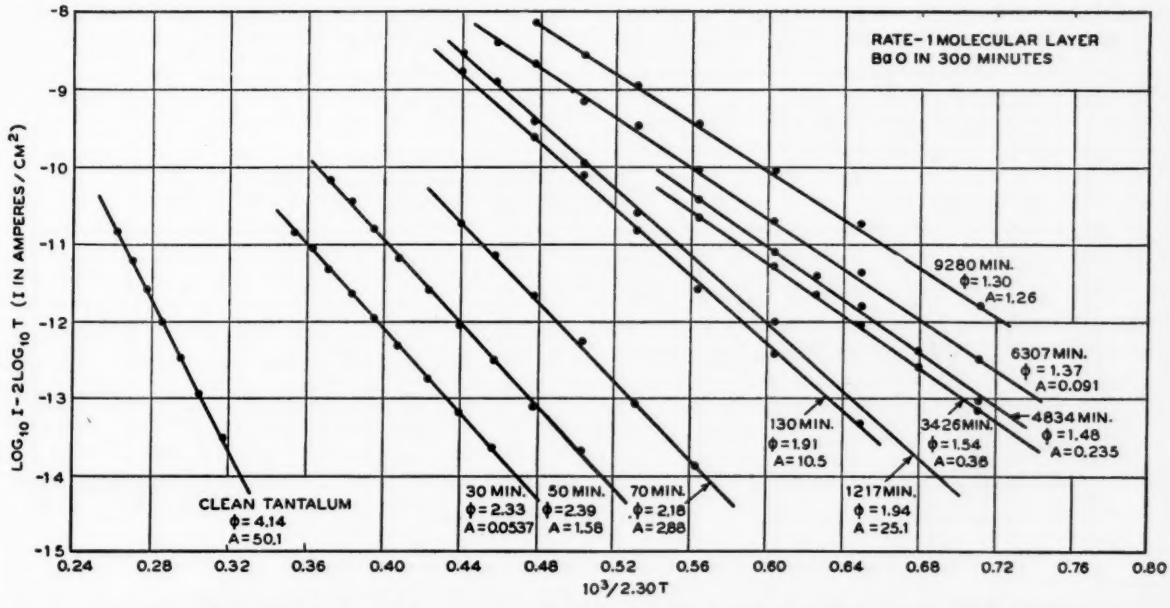

FIG. 7. Richardson lines for one run—BaO on tantalum. Each line represents a particular covering.

the deposited oxide in the form of agglomerates or a thin film?

These are taken up in turn:

(1) Four retarding field characteristics, corresponding to four different coverings (all less than monomolecular) of a molybdenum receiver during one coating run of SrO are shown on Fig. 8. The points for the curve farthest to the right represent clean molybdenum. The linear portion as drawn has a slope corresponding to an electron temperature[14] of 1826°K. The corrected pyrometer temperature of the electron source (a clean tungsten filament) was 1828°K. The difference between the two determinations is thus 2°K (less than the probable error of slope determination). When coating is applied to the receiver, the slope corresponds to a significantly higher electron temperature. The change of slope occurs even for the characteristic obtained after depositing oxide for 22.5 hr., corresponding to only 0.015 molecular layer. A line is then drawn through the lowest experimental point, parallel to the characteristic for the clean receiver.

Such changes of slope are probably a consequence of reflection caused by the known patch fields,[15] an effect which would prevent the method from indicating the full decrease in work function actually produced. Neglecting this effect, consider the characteristics for 133.3 and 317 hr. Until after the test corresponding to the deposit for 133.3 hr., the receiver was not tested thermionically and its temperature therefore was never more than a few degrees above ambient, so that the work function of the molybdenum had decreased by at least 1.20 volts as judged by the horizontal shift of the curve. It was then tested thermionically at a maximum temperature of 986°K for approximately 5 min. after which the contact potential test was repeated. The difference between the original contact potential test at 133.3 hr. shown by solid circles and the second test shown by small triangles indicated that φ increased by about 0.02 volt. A similar procedure was followed in the subsequent tests of this run. The thermionic tests never altered the work function of the receiver by more than 0.03 volt. At the 317-hr. test period shown, the thermionic test decreased φ, as measured by contact potential, by about 0.03 volt. These tests indicate that:

(a) Contact potential tests agree with Richardson plots in showing that thin films of the oxides activate the receivers and show, in addition, that the activation is caused almost entirely by the oxide *as deposited*, the heating during emission tests not being essential.

(b) For layers less than a monolayer, changes less than ±0.03

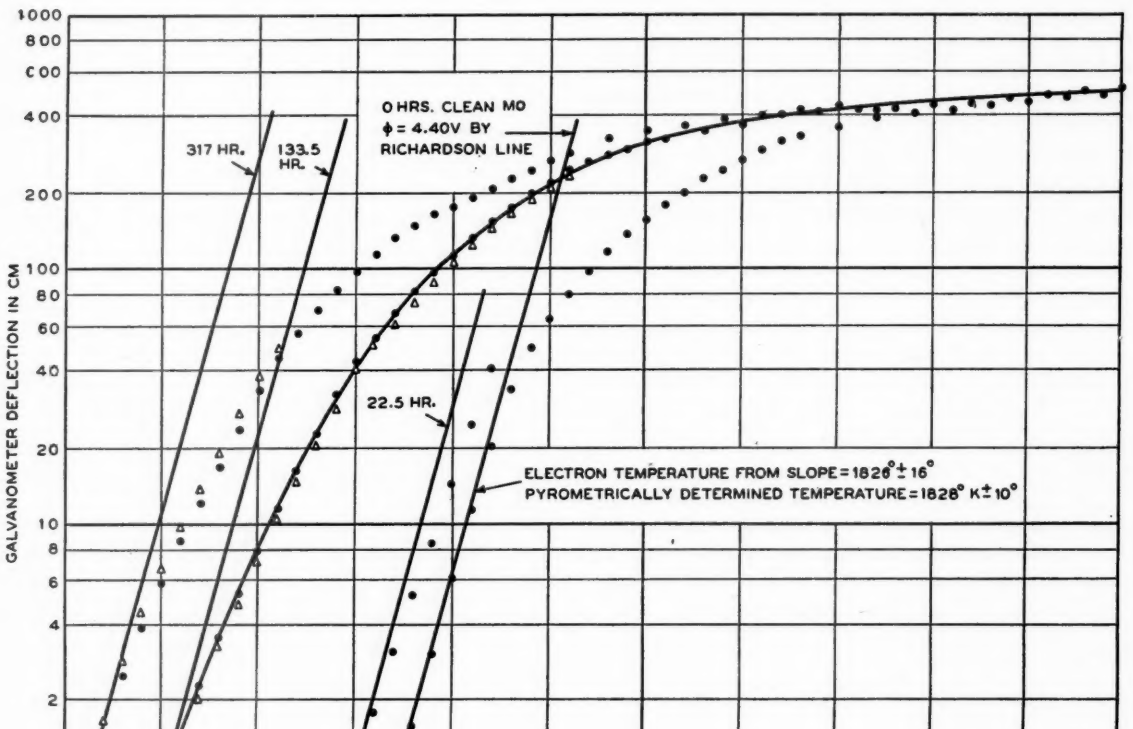

FIG. 8. Retarding potential lines as molybdenum receiver is coated with SrO.

[14] See for example Millman and Seeley, *Electronics* (McGraw-Hill Book Company, Inc., New York, 1941), p. 161 ff.
[15] C. Herring and M. H. Nichols, Rev. Mod. Phys. **21**, 185 (1949), see especially Fig. 18 and Chapter II.

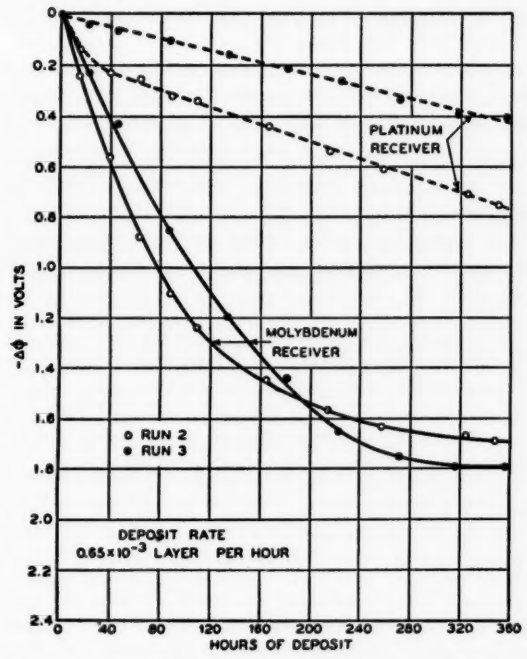

FIG. 9. Contact potential test—molybdenum and platinum receivers coated with SrO.

volt do occur as a result of incidental heating in thermionic tests. The corresponding change in the thermionic emission measured at low temperature is not more than a factor of three. For layers thicker than a monolayer, the activation by heating was often much greater than a factor of three.

Appreciable chemical reduction of adsorbed oxide to free strontium or barium is conceivable during thermionic tests. Contact potential tests, however, throw no light on this question because other experiments show that the change of work function is negligible when appreciable quantities of free strontium metal are deposited with the oxide. On this question one can therefore only conclude that if such reduction occurs, its effects are negligible for either contact potential or thermionic measurements of activation by monlayer films.

(2) Platinum activation was also studied in three tubes by contact potential tests in order to avoid heating the receiver during measurement. Contact potential curves, shown in Fig. 9, are derived from retarding potential curves such as Fig. 8 by plotting the shift of the retarding field characteristic against the amount of SrO deposited. Curves for platinum and molybdenum receivers on which the same amounts of SrO are deposited from the same source are shown in Fig. 9. No thermionic tests of the platinum were made during these runs except for the initial point, in which an attempt was made to obtain "clean" platinum. For run No. 2 the platinum was flashed for 10 sec. at $T=1800°K$ and the subsequent deposit of 0.23 molecular layer of SrO is seen to have decreased the work function by 0.775 volt. For run No. 3, the platinum was flashed 10 sec. at $T=1920°K$ and the deposit of the same amount of SrO decreased the work function by only 0.4 volt. Thermionic tests indicated that the platinum was considerably cleaner at the beginning of run No. 3 than for run No. 2. The contact potential tests thus indicate† that a given amount of SrO up to about 0.23 layer decreased the work function of platinum by much less than that of molybdenum.

(3) In contrast to Davisson and Pidgeon,[1] who concluded that the BaO on their receivers agglomerated, the deposit is here believed to form a thin film spread fairly uniformly over the receiver surface. This belief is based on the fact that the work function of a patchy surface as measured by contact potential is an arithmetical average of all patches, each weighted according to its area (reference 15, Eq. (II-4.3)). Thus, suppose that the deposited oxide became agglomerated into patches occupying about 10 percent of the area while the remaining 90 percent became uncoated. The work function of any patch must be positive so that the assumed agglomeration would give a contact potential only about 0.4 volt different from clean molybdenum. Such agglomeration is therefore inconsistent with the observed contact potential shift of 1.8 volts for 0.23 layer. The shift caused by a complete layer, if measured by a method not affected by reflection, would probably be considerably greater than 1.8 volts.

PURITY OF SYSTEMS

This work was intended as an examination of idealized thermionic systems, each containing in principle only a clean receiver metal adsorbing known amounts of pure alkaline earth oxide. The performance of these quantitatively specifiable systems was compared with that of the practical oxide cathode. The value of the comparison will depend on the degree to which the ideal system was experimentally realized.

Cleanliness of Receiver Metal Surfaces before Coating

If cleanliness is judged by agreement of observed thermionic data with generally accepted values in the literature, only tungsten, molybdenum, and tantalum receivers were made clean in these tubes. Filaments of less refractory metals, such as nickel, zirconium, or platinum, in general, could not be made clean at temperatures below melting, although many atomic layers of the support metal were vaporized from their surfaces. Because the emission from "soft" receivers in the cleanest condition attainable was always greater than the published values, it is believed that the residual higher activity is caused by alkaline earth oxide (deposited as a result of operating the source filament

† The work function of the "clean" platinum as measured by Richardson plots was about 2.7 volts, but as measured by contact potential, the work function of the molybdenum and platinum were nearly equal at the beginning of the run. This indicates patches of about 2.7 volts work function over a small part of the surface of this "clean" platinum.

during exhaust or subsequently) that remains in or on these receiver metals until fusion.

Of the three refractory metals, which could be thoroughly cleaned by flashing, tungsten and molybdenum activated to approximately the same extent for a given deposit of BaO or SrO and tantalum activated somewhat less. In general, the emission of coated platinum or nickel receivers was considerably less but lacked the stability required for reproducible Richardson plots.

However, in one test, a Richardson plot for clean platinum was obtained having a work function $\varphi=4.43$ ev and $A=25$. This was one of the closest approximations in the present experiments to the "clean" value of 5.3 volts quoted[16] in the literature. After depositing one monolayer of SrO, a Richardson plot at temperatures between 860°K and 960°K indicated a work function $\varphi=1.9$ ev and $A=0.01$. Measurement above 960°K caused deactivation. This was also one of the highest and most stable activities attained with a platinum receiver and was used for the platinum entry of Table I.

Only one nickel receiver was examined. It was flashed at higher and higher temperatures prior to each successive deposit run. Although this flashing increased the activation obtainable from a given deposit of SrO, the highest emission observed prior to burning out the nickel was that indicated in Table I. The nickel when last flashed was probably much cleaner than that in commercial cathodes.

In summary, the tungsten, molybdenum, and tantalum receivers are believed to have been clean before coating, the other receivers were not. Additional attempts will be made to prepare clean platinum receivers before coating.

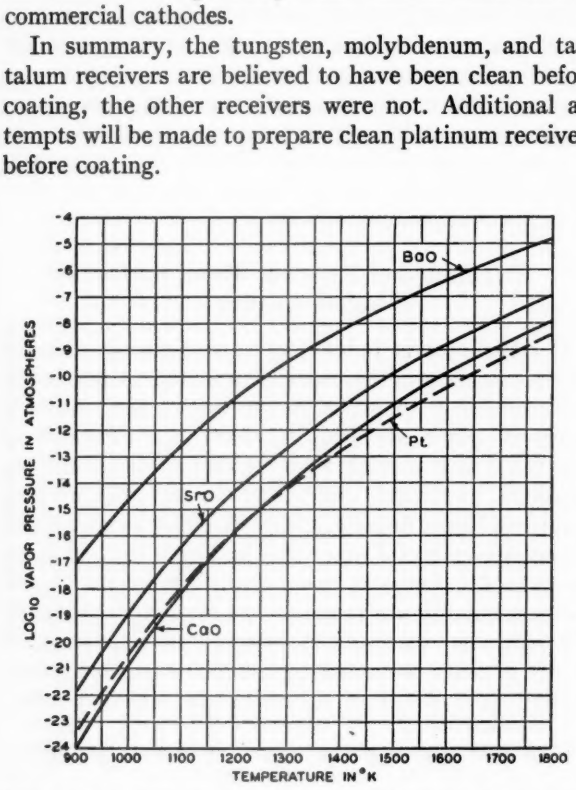

FIG. 10. Vapor pressure of alkaline earth oxides and of platinum.

[16] L. V. Whitney, Phys. Rev. 50, 1154 (1936).

Purity of Evaporated Product

The purity of the product evaporated from the source filaments is of paramount importance and was examined in four respects, listed (A), (B), (C), and (D).

(A) Is free calcium, strontium, or barium metal evaporated with the corresponding oxide? Three types of evidence combine to indicate that very little free metal is evaporated, and that any probable amount would have no appreciable effect on these thin film systems.

(a) Attempts were made to determine experimentally the amount of free metal evaporating with the oxide. Wooten's hydrogen evolution technique[17] was applied to special tubes containing only the pure platinum filament, treated in wet hydrogen and coated with the same pure alkaline earth carbonates as in the thermionic and contact potential tubes. Because of the present sensitivity limit of the method (about 1 μg), the results merely placed an upper limit of about 0.1 percent on the ratio of free metal to oxide evaporated. This ratio is sufficiently small to justify the working assumption, always tacitly made in measuring the vapor pressure, that the reduction of alkaline earth oxide either by heat alone or by contact with hot platinum is negligible. However, this experimental result in itself, is not sufficient to exclude the possible deposit of minute amounts of free metal which might be significant for semiconductor effects.

(b) A number of tubes were made in which the alkaline earth oxide was evaporated from a very pure Al_2O_3 ceramic source, with the thought that chemical reduction by such a ceramic would be even less probable than by platinum. Receivers were activated equally well by material evaporated either from the ceramic or from the platinum.

(c) Although the results will not now be given in detail, activation by evaporated free alkaline earth metal was compared with activation by evaporated oxides in several tubes of the contact potential design. It was shown that the deposit of appreciable quantities of free metal on a receiver already coated with the corresponding oxide caused very little or no additional activation. This same result occurred if the free metal were deposited at any time during the deposit of oxide and indicates that any free metal inadvertently evaporated from the oxide sources has no important effect.

(B) How much platinum evaporates with the oxide? Comparative vapor pressure curves, given in Fig. 10, were plotted from the measurements on the oxides by Claassen and Veenemans,[18] Blewett, Liebhafsky, and Hennelly,[19] and results from these Laboratories; the data of Jones, Langmuir, and Mackay[20] were used for platinum. The figure indicates that about one platinum atom evaporates for every CaO molecule, one for every 30 SrO molecules, and one for every 10^5 BaO molecules. Experience indicates that the rate of evaporation of support metals through these thick oxide layers may be about 30 percent as great as from the uncoated support metal. Accordingly, an appreciable amount of platinum

[17] This method was discussed orally by L. A. Wooten, Phys. Rev. 69, 248 (1946), but has never been adequately published. However, it has given good results in many tests over a 15-yr. period in these Laboratories; see, for example, G. E. Moore, J. Chem. Phys. 9, 427 (1941).

[18] Claassen and Veenemans, Zeits. f. Physik 80, 342 (1933).

[19] Blewett, Liebhafsky, and Hennelly, J. Chem. Phys. 1, 478 (1939).

[20] Jones, Langmuir, and Mackay, Phys. Rev. 30, 201 (1927).

is probably present in the evaporated deposits, especially from calcium oxide sources. Because Becker and Sears[21] showed that evaporated platinum deactivates tungsten, the observed activations are at present thought to be less than would have been observed in the absence of this platinum. Only for BaO is this deactivating effect believed negligible.

(C) How much electronegative gas is evaporated together with the oxide? The authors of all published thermionic measurements on clean platinum emphasize the difficulty in eliminating oxygen and other electronegative gases. All such authors treated their filaments far more severely than is practical for the coated sources of the present work. It is therefore believed that a small but undetermined fraction of the evaporated product is electronegative gas and because these are known to deactivate tungsten and molybdenum, the activations given above are believed less than would be expected in the absence of such gas. CO_2 from carbonates undissociated in exhaust would also cause deactivation.

(D) What other impurities evaporate with the oxides? The only important spectroscopically detectable impurities found present in any oxide is one or more of the other oxides. BaO, to the extent of even a fraction of one percent in either SrO or CaO, can introduce serious errors of interpretation because its vapor pressure is orders of magnitude higher than that of either SrO or CaO, and because BaO apparently vaporizes from such mixtures much more rapidly than predicted from Raoult's law. These effects are illustrated in Fig. 11 for a SrO source contaminated with 0.47 mole percent of BaO. The abscissas were calculated from the vapor pressure of SrO and the corrected temperature of the source filament, assuming that only SrO was evaporated. The curve marked "0 hours" suggests that tungsten could be fully activated by about 0.001 monolayer of SrO. Many such curves were obtained with different tubes and this result was originally so interpreted.[22] However, after heating the source filament for long periods at 1460°K, cleaning the receiver filaments, and repeating the experiments, curves such as those designated "100 hr." and "1540 hr." were obtained. Because of preferential evaporation of BaO, the SrO source was gradually purified until after 1540 hr. at 1460°K it was essentially free of BaO. That this source of error has been eliminated from the experiments discussed above is illustrated in Fig. 12, giving results for a SrO source containing only 0.025 percent BaO instead of the 0.47 percent in the preceding figure. Data are plotted for three runs at ages 0, 101, and 775 hr. The points show that there was essentially no disgreement in the data for these runs.

For the above reasons the systems studied are believed good approximations to the ideal of a clean

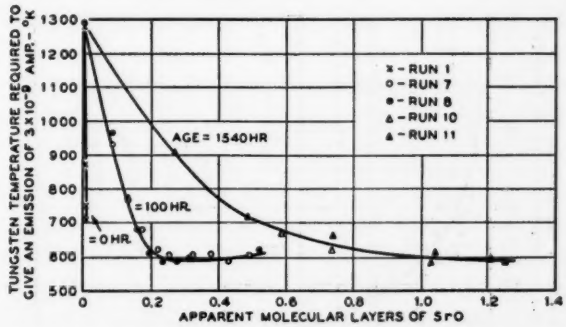

FIG. 11. Progressive purification of SrO source as indicated by time required for activation of tungsten ribbon. SrO contains 0.47 percent BaO.

receiver metal on which known amounts of pure alkaline earth oxides are adsorbed. Any experimental deviations from this ideal are believed to decrease the activation, yet the observed thermionic emissions from these approximations to the ideal are comparable in magnitude to that of the commercial oxide cathode.

DISCUSSION

The results may be explained tentatively by considering the alkaline earth oxide molecules to be strongly polar and preferentially adsorbed with the oxygen atom adjacent, and the line of centers perpendicular, to the receiver metal surface. Such an arrangement would appear probable if (1) other evidence indicates that the oxide molecules have a dipole moment with excess positive charge near the metal atom and (2) if the oxygen atom tends to be adsorbed preferentially toward the receiver surface.

Evidence for Polar Nature of Oxide Molecules

The three oxides in their crystalline state are usually considered ionic.[23] In contrast to DeBoer and Verwey,[24] the writers believe that the molecules are also ionic in the gaseous phase, and therefore probably in the adsorbed phase. The principal reason for disagreement with the above authors is their recognition of only two possibilities—that the molecule is formed either of doubly charged ions or of neutral atoms. The criteria for ionic nature given by Herzberg[25] were applied to the gaseous molecules considering the barium and oxygen as either doubly or singly charged ions. The results indicated that the gaseous molecule might not be doubly charged ionic but was almost surely singly charged ionic, and that the dipole strength was greatest for BaO and least for CaO. This same order also prevails in the dielectric constant[26] and in the tendency

[21] Becker and Sears, Phys. Rev. 43, 1058 (1933).
[22] Oral reports before the American Physical Society, Phys. Rev. 69, 248 (1946).
[23] See for example, Rice, *Electronic Structure and Chemical Binding* (McGraw-Hill Book Company, Inc., New York, 1940).
[24] DeBoer and Verwey, Rec. Trav. Chim. Pays-Bas 55, 443 (1946).
[25] G. Herzberg, *Molecular Spectra and Molecular Structure* (Prentice-Hall, Inc., New York, 1939), p. 400 ff.
[26] K. Hojendahl, Kgl. Danske Vid. Sels. Math.-fys. Medd (1938).

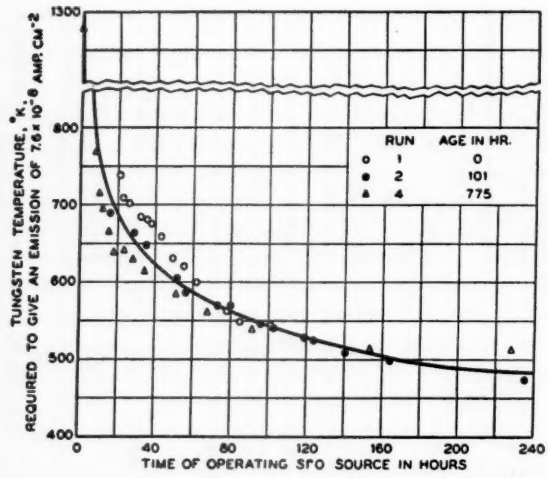

FIG. 12. Activation of tungsten receiver by SrO from source containing 0.025 percent BaO. Source temperature = 1470°K 0.058 molecular layers SrO deposited per hour.

of the oxide molecules to form compounds;[27] these differences could well account for the fact that BaO activates the receiver surfaces more than CaO. Furthermore, the differential rate of activation of a clean receiver (40 volts per monolayer in Fig. 4) is approximately that calculated if each adsorbed molecule lowers the work function by the amount expected from a singly charged ionic dipole in the most favorable orientation. The activation curves suggest that later arriving molecules are much less effective. It is therefore thought that the adsorbed molecules are strongly polar and as the distance between adjacent molecules decreases, there is a tendency for some of the molecules to reverse their orientation and form a "two-dimensional crystal."

Evidence That Oxygen Atom is Adjacent to Receiver Surface

One might infer that the oxygen would tend to be toward the receiver surface from the fact that Langmuir[9] has shown that only half of a monatomic film of oxygen atoms on tungsten will leave in 3 yr. at 1500°K while experiments by the writers suggest that nearly all Sr atoms will leave in 5 min. at this temperature.

Multilayer Films

The structure of the multilayer films is probably much more complex than for the monolayers; this would be expected from the strong affinity of one oxide molecule for another as indicated by the large heats of evaporation of the bulk oxides. However, one can infer that the semiconductor mechanism proposed for bulk oxide cathodes is probably not operative in even the thickest films examined in the present experiments. According to this theory,[13,28] the work function of the thick oxide layer in practical cathodes is determined essentially by the energy and concentration of impurity levels in the oxides. However, this does not seem probable‡ even in the thicker films of the present work. For example, 25 layers, shown in Fig. 4 to reduce the work function of tungsten from 4.5 volts to 1.0 volt, is about 10^{-6} cm thick, which is only a small fraction of the "exhaustion layer" within which the electrostatic potential in a semiconductor adjusts itself from the value at the plane of contact with the metal to the value characteristic of the bulk semiconductor. The change of potential V_D, in an exhaustion layer of thickness l and donor concentration n_D, is[29]

$$V_D = (2\pi e n_D l^2)/\epsilon,$$

where ϵ is the dielectric constant.[26] We take the values $\epsilon = 14.3$, $n_D = 10^{17}$, the upper limit for experiments on commercial-type coatings described by Wooten,[26,30] $l = 10^{-6}$ cm, for the thickness.

This gives 2×10^{-5} volt e.s.u. or 6×10^{-3} volt practical, an insignificant fraction of the change in work function which is produced by changes in activation of a thick coating. It seems safe to conclude therefore that the measured work functions shown in Fig. 4 are determined primarily by the nature of the double layers at the receiver-oxide and oxide-vacuum interfaces and have no particular relation to the existence of small amounts of volume impurities of the sort postulated in the semiconductor theory of the usual thick oxide coating.

Meaning of Thin Film Experiments for Practical Oxide Cathode

While the similarity in *magnitude* of emission is *not* intended as direct evidence for similarity in nature of the emission process in the two systems, the results are suggestive regarding one feature of current theories describing the oxide cathode as an electronic semiconductor in which excess barium (or strontium) metal governs both emission and conductivity. This emphasis on excess barium as an activating agent began with the papers of Koller[31] and Becker.[10] After about 1931,[13,32,33] emphasis shifted from barium on the outer surface of the oxide to barium in the lattice.

Turning to experimental evidence, one notes:

1. Results described above indicate that high thermionic emission is developed in thin oxide film systems containing essentially no excess alkaline earth metal either in the oxide layer or on its outer surface, and the addition of alkaline earth metal to these systems causes no appreciable increase of emission.

2. Widespread experience over the past 20 years has produced no satisfactory evidence that either the conductivity or emission

‡ The material in this section on multilayer films was largely suggested by Conyers Herring.

[27] Bichowsky and Rossini, *Thermochemistry of Chemical Substances* (Reinhold Publishing Corporation, New York, 1936).
[28] Hannay, McNair, and White, J. App. Phys. **20**, 669 (1949).
[29] W. Schottky, Zeits. f. Physik **118**, 539 (1942).
[30] See also Jenkins and Newton, Nature **163**, 572 (1949).
[31] L. R. Koller, Phys. Rev. **25**, 671 (1925).
[32] Becker and Sears, Phys. Rev. **38**, 2193 (1931).
[33] Fowler and Wilson, Proc. Roy. Soc. **137**, 503 (1932).

of thick oxide cathodes under practical operating conditions is related to excess barium, despite several attempts to produce such evidence. The most careful tests[17,30] show that if there is any correlation between barium content and emission, it can exist only for less than one atom of barium to 10^4 or 10^5 molecules of (BaSr)O.

3. Over the past 30 years, the emissions from thick layer, practical cathodes and from thin films of the type described above have both increased by a factor of more than 1000. For example, Arnold[34] stated that the commercial cathodes of 1920 emitted about 1 ma/cm² at 1000°K while today they emit at least 10^3 ma. Similarly, Davisson and Pidgeon[1] gave the emission of thin BaO films, prepared by methods nominally the same as those in the present experiments, as 0.3 ma at 1000°K; the films in the present work emit at least 10^3-fold more. This increase during the past 30 years in the emission of the thin film system cannot be related to barium metal and no published evidence justifies attributing the improvement in commercial cathodes to this cause.

While other analogous features of the two systems could be listed, a major point of dissimilarity should be emphasized. The evaporated deposits in the present work probably form true thin film systems, the adsorbed oxide acting entirely to lower the surface potential barrier for emission from clean receiver metals. In the practical oxide cathode, on the other hand, every experiment designed as a test indicates that the oxide layer is an electronic semiconductor; perhaps the most striking was performed by Hannay, McNair, and White,[28] who observed during activation the functional relationship between emission and conductivity implicit in the theory. One must conclude from their experiments that conductivity and emission of thick layers are governed by the same factors, although they do not necessarily support a mechanism based on excess barium.

If the thin film process is of importance in practical oxide cathodes the electrons could either be emitted at the interface, diffusing outward through pores without ever being incorporated into the lattice, or they could be conducted in the lattice to bits of support metal, or other substance which strongly adsorb the oxide, and then emitted by a thin film process from these particles which might be present in the outer layers of the oxide. The first mechanism would require a reflection coefficient of 0.9 or more for slow electrons striking oxide crystals. The work of Brown[35] suggests that such a reflection coefficient exists; however, this cannot yet be considered established. The great advantage of BaO, either pure or mixed with SrO, over either pure SrO or CaO as a coat for oxide cathodes is easily explained in terms of either mechanism as an equilibrium between molecules in the absorbed and crystalline phases; the relatively great energy binding the SrO or CaO molecules to their crystal lattice decreasing the fraction in the adsorbed phase. Further discussion of these speculations without additional evidence seems useless.

CONCLUSION

It has been established that the deposit of films in the range from one to 25 monolayers of BaO, SrO, or CaO on clean refractory metal surfaces reduces their thermionic work function, as measured by Richardson plots, by several electron volts. This effect can be qualitatively explained in terms of oriented dipoles.

Within the uncertainty of the experiment, the work functions obtained agree quantitatively with those published by others for bulk oxide coatings, which are ordinarily explained in terms of their properties as semiconductors. There is at present no theoretical reason for expecting such agreement. Further work is necessary before one can decide if the thin film mechanism is of any importance in practical cathodes, the present results being of the nature of necessary, but not sufficient, conditions for such importance.

The writers appreciate the help and advice of many colleagues, of whom only a few can be named. W. D. Stratton and H. W. Weinhart were responsible for mechanical design and construction. We acknowledge original ideas and other help resulting from discussions, especially with Conyers Herring, A. H. White, and J. A. Becker.

[34] H. D. Arnold, Phys. Rev. **16**, 70 (1920).

[35] B. B. Brown, thesis, M.I.T. (1942), not formally published.

A Theory of Dielectric Polarization in Alkali-Halide Crystals

SHEPARD ROBERTS
Research Laboratory, General Electric Company, Schenectady, New York
(Received August 8, 1949)

A theory of dielectric polarization is described in which each ion in an alkali-halide crystal is considered as a separate entity capable of being distorted internally by an electric field. Three stiffness coefficients suffice to describe the interaction between the local electric-field and the polarizable ion. The Lorentz internal field is shown to be valid for this calculation. Optical and dielectric polarizabilities per molecule and infra-red absorption frequencies in alkali-halide crystals calculated by this method are shown to be in substantial agreement with experiment. Electronic polarizabilities of free (gaseous) ions are also calculated, and a novel "pseudo-piezoelectric" effect is predicted.

I. INTRODUCTION

IT seems intuitively obvious that the dielectric properties of a solid material should be determined uniquely by the properties of the atoms or ions of which it is made, and by the way in which they are arranged. In respect to the atomic arrangement, the alkali-halide crystals are the simplest ionic solids and their pertinent dielectric and optical properties have generally been known for seventeen years. An interpretation of ionic polarization is now proposed which is inherently simple, explains all the experimental data to a good approximation and does not go beyond classical mechanical principles.

In order to study a single ion independently of the crystal, it is necessary to construct an imaginary boundary around it and to replace forces which formerly existed between particles inside the boundary and those outside by corresponding forces between the internal particles and the boundary. In this way a relation can be found between the forces acting on an ion and the distortion produced thereby. This relation may be expressed by three stiffness coefficients or "springs" connected between the nucleus, the electron cloud, and the boundary. All of these springs are necessary to explain the experimental results.

II. DISTORTION OF IONS BY ELECTRIC FIELDS

The arrangement and size of ions in ionic crystals are generally studied in the absence of an electric field by x-ray diffraction methods. In this way, it is determined, for example, that a sodium chloride crystal has a cubic unit cell with face-centered symmetry containing four ions of each type and having an edge 5.629 angstroms in length. This is the distance from the center of one sodium ion to the next, with a chlorine ion in between.

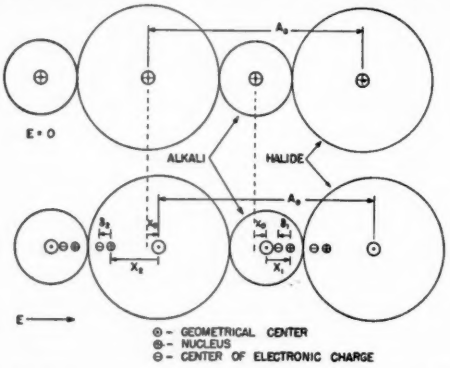

FIG. 1. Ionic arrangement in neutral crystal (upper diagram) and in polarized crystal (lower diagram) showing nuclear and electronic displacements.

It is convenient to think of each ion as a separate individual which just touches its neighbors. Then it is an experimental fact that the points of contact so defined between a given ion and its neighbors in the crystals being considered determine a sphere. This is what is meant by the spherical boundary of an ion. In crystals of the sodium chloride type it follows that the edge of the unit cube is equal to the sum of the diameters of the alkali and halide ions (if they do touch). From the regularity in the observed lattice spacings, it is found that each ion has very nearly the same diameter in different kinds of crystals.

When an electric field of ordinary magnitude is applied to an alkali-halide crystal, the ions are internally distorted, but their external spherical shape and size (as defined by the points of contact) as well as their arrangement are unaffected. This conclusion follows directly from the same symmetry considerations which are employed to prove the absence of the first-order piezoelectric effect. Since the ionic boundaries are not deformed by an electric field, there is no loss in generality for the present problem by considering the boundaries to be rigid spheres. A more complicated (non-rigid) ionic model would be needed if elastic deformation were to be considered in addition to electrical polarization.

In order to describe the internal distortion of an ion, it will be necessary to consider the relative displacements of certain reference points. The center of the spherical boundary is such a point. It is the center of charge, mass, etc., of the unpolarized ion and the geometrical center of the polarized ion. The position of the nucleus is another such point, which would be at the center in the unpolarized ion, but is displaced a distance X to one side of the center in the polarized ion. The third point is the center of charge of the electron cloud including all electrons, even those closely bound to the nucleus. In the unpolarized ion, the center of electronic

charge coincides with the position of the nucleus, but in the polarized ion, it is displaced a distance δ to one side of the nucleus.

These three points and the displacements X and δ for each of the two types of ions in an alkali-halide crystal are shown schematically in Fig. 1. A row of ions in an unpolarized crystal (upper diagram) is compared with a similar row of ions in a polarized crystal (lower diagram). The distance X_0, indicated in this figure, represents a displacement of the whole system of boundaries from its equilibrium position. Such a displacement is possible because, though rigid, the system of boundaries is not necessarily fixed in space. In this figure, positive vectors are drawn to the right.

III. EQUATIONS OF MOTION

The individual ion is distorted because forces operate on its component parts. The forces causing the distortion are due to the action of the local electric field on charge carriers. These forces are opposed by restoring forces depending on the magnitude of the ionic distortion. For simplification, the forces and displacements are to be considered small enough so that a relation analogous to Hooke's law is obeyed. In other words, the restoring forces are assumed proportional to the displacements. Three constants of proportionality b, c, and f are then needed to express the forces between the nucleus, the electron cloud and the ionic boundary due to their relative displacements. The equations for the total forces are given below.

1. *Force on nucleus:*

$$F_n=-bX+c\delta+peF_i, \tag{1}$$

where pe is the charge on the nucleus and F_i is the electrostatic field at the center of the ion.

2. *Force on electron cloud:*

$$F_e=-c\delta-f(X+\delta)-neF_i, \tag{2}$$

where n is the total number of electrons and e is the electronic charge.

3. *Force on boundary* (due to internal distortion):

$$F_b=bX+f(X+\delta). \tag{3}$$

Equation (2) involves the proposition that the average electric field effective in displacing the electron cloud is that at the center of the ion, or rather the field that would exist at this point if the ion itself were absent. The electric field in the space vacated by the ion is extremely unhomogeneous due to the close proximity of charged particles. However, in any such space where Laplace's equation is valid, the average potential on the surface of a sphere is equal to that at its center. Similarly, the average over the spherical surface of any Cartesian component of the potential gradient is equal to that at the center. If the distribution of electron probability density in the ion is uniform over each such concentric sphere, then the average field effective in causing electron polarization is that at the center. The assumption of radial symmetry follows from the picture of spherical ions adopted earlier.

The dipole moment induced on a given ion is obtained by multiplying the charge on each part of the ion by its total displacement in space from its initial or equilibrium position.

$$\begin{aligned}\mu_i&=pe(X+X_0)-ne(X+\delta+X_0)\\&=e(p-n)(X+X_0)-ne\delta.\end{aligned} \tag{4}$$

The mass of the electron cloud is negligible relative to that of the nucleus, hence the force on the electron cloud is effectively zero throughout the frequency range to be considered. Thus, Eq. (2) can be used to eliminate one of the variables, namely:

$$\delta=(-fX-neF_i)/(c+f). \tag{5}$$

Substituting this value of δ in Eqs. (1), (3), and (4), gives:

$$\left.\begin{aligned}F_n&=-\frac{bc+cf+fb}{c+f}X+\left(p-\frac{cn}{c+f}\right)eF_i\\F_b&=\frac{bc+cf+fb}{c+f}X-\frac{nf}{c+f}eF_i\\\mu_i&=\left(p-\frac{cn}{c+f}\right)eX+(p-n)eX_0+\frac{n^2}{c+f}e^2F_i\end{aligned}\right\}. \tag{6}$$

The form of these equations as well as all subsequent calculations can be greatly simplified by substituting three new parameters in place of the ionic stiffnesses b, c, and f. The new parameters are defined in terms of the old in the following way:

$$\left.\begin{aligned}A&=p-cn/(c+f)\\B&=e^2/\xi_0\cdot(c+f)/(bc+cf+fb)\\C&=e^2/\xi_0\cdot n^2/(c+f)\end{aligned}\right\}. \tag{7}$$

where ξ_0 is the permittivity of free space.

The fundamental equations then take the following form:

$$\left.\begin{aligned}F_n&=-1/B\cdot(e^2/\xi_0)X+AeF_i\\F_b&=1/B\cdot(e^2/\xi_0)X-(A-p+n)eF_i\\\mu_i&=AeX+(p-n)eX_0+C\xi_0F_i\end{aligned}\right\}. \tag{8}$$

Equations (8) are helpful in explaining the significance

TABLE I. Tentative ionic parameters.

	A	B (A³)	C (A³)
Li	—	0	0
Na	2.075	1.4	1.97
K	1.501	8.1	11.44
Rb	1.769	9.9	14.63
Cs	1.277	16.0	33.69
F	−0.867	35.2	11.05
Cl	−0.702	75.6	37.25
Br	−0.678	87.4	52.54
I	−0.614	109.2	79.90

TABLE II. Comparison of experimental and theoretical data for alkali-halide crystals.

	1 V (A³)	2 K	3 n (Na-D light)	4 α_D exp (A³)	5 α_D theor. (A³)	6 α_e exp (A³)	7 α_e theor. (A³)	8 λ_A exp (×10⁻⁶ m)	9 λ_A theor. (×10⁻⁶ m)	10 α_{sol} exp (A³)	11 α_g theor (A³)
LiF	16.21	9.27	1.391	35.7	37.5	11.55	11.05	32.6	32.3		11.7
LiCl	33.74	11.05	1.662	77.9	74.5	37.45	37.25		49.4	43.5	44.0
LiBr	41.36	12.1	1.784	97.6	92.7	52.26	52.54		55.5	61.1	61.6
LiI	54.00	11.03	1.955	124.7	121.1	78.52	79.90		57.2	93.4	96.2
NaF	24.65	6.0	1.326	46.2	45.5	14.92	14.98	40.6	40.6		15.8
NaCl	44.59	5.62	1.544	81.1	82.5	42.23	41.81	61.1	61.6	45.9	48.0
NaBr	52.95	5.99	1.641	99.3	100.7	57.32	57.20	74.7	74.1	64.1	65.7
NaI	67.46	6.60	1.774	131.7	129.1	84.41	84.82	85.5	85.5	96.3	100.3
KF	38.07	6.05	1.362	71.6	67.2	25.33	25.14		48.5	24.7	26.0
KCl	61.86	4.68	1.490	102.2	104.2	53.65	53.36	70.7	70.8	58.1	58.3
KBr	71.42	4.78	1.560	119.5	122.4	69.29	69.00	88.3	88.3	74.5	76.0
KI	87.67	4.94	1.667	149.4	150.8	97.92	97.27	102.0	101.8	107.3	110.5
RbF	44.85	5.91	1.398	83.6	83.1	32.47	31.97		53.4	31.9	32.9
RbCl	69.93	5.0	1.494	119.8	120.1	61.07	61.85	84.8	84.8	63.4	65.2
RbBr	80.50	5.0	1.553	137.9	138.3	77.28	77.76	114.0	113.7	81.0	82.9
RbI	98.30	5.0	1.647	168.4	166.7	107.19	106.64	129.5	135.4	113.3	117.4
CsF	54.22		1.478		97.3	46.03	46.59		48.1		46.4
CsCl	69.43	7.20	1.642	140.4	134.3	75.23	75.31	102.0	101.1	76.1	78.7
CsBr	78.95	6.51	1.698	153.2	152.5	91.33	91.09	134.0	135.1	94.3	96.3
CsI	94.94	5.65	1.788	173.2	180.8	120.40	119.72		155.9		130.9

of the new ionic parameters. According to this interpretation, Ae would be a sort of effective charge on the nucleus, while the remaining charge $-(A-p+n)e$ would be appropriately linked with the boundary. The parameter B, which has the dimensions of polarizability or volume, would be a measure of the displacement of the nucleus relative to the boundary for a given force between them.

If the boundary of an ion is restrained from moving, and if likewise its nucleus is held fixed, then only the inner electrons can move and the dipole moment is $C\xi_0F_i$, which corresponds to a polarizability, C. If the nucleus is released, the polarizability is increased by an amount proportional to the square of the nuclear charge times the parameter B. Then, the total polarizability is A^2B+C. Similarly, if only the nucleus is held fixed, the corresponding polarizability will be $(A-p+n)^2B+C$. A more detailed derivation of the polarizabilities is given in the next section.

A set of values of the parameters A, B, and C for alkali and halide ions is given in Table I. These values were obtained by successive approximations in order to achieve the most consistent agreement between experimental data and theoretical calculations. In order to resolve a certain indefiniteness in the absolute scale of values, the parameters B and C for lithium were arbitrarily set equal to zero. This should have a minimum effect on the results for other ions since the values for lithium are obviously much smaller, if different from zero.

IV. POLARIZABILITIES OF IONS IN CRYSTALS

In alkali-halide crystals, the subscripts 1 and 2 will be used to differentiate between the parameters of the alkali ion and the halide ion respectively. Then:

$$p_1=n_1+1; \quad p_2=n_2-1. \tag{9}$$

The equations of motion of the crystal comprise two sets of equations similar to (8), one set for each type of ion. Since X_0 is the same for both types of ion, it does not appear in the expression for the total dipole moment per molecule.

$$\mu=\mu_1+\mu_2=e(A_1X_1+A_2X_2)+\xi_0F_i(C_1+C_2). \tag{10}$$

The polarizability α is by definition the constant ratio of the dipole moment μ to the internal field F_i, divided by ξ_0.

$$\alpha=(\mu/\xi_0F_i)=(e/\xi_0F_i)(A_1X_1+A_2X_2)+C_1+C_2. \tag{11}$$

If the displacements are sinusoidal functions of time with a frequency $\omega/2\pi$, the force on the nucleus is:

$$F_n=ma=m(d^2/dt^2)(X+X_0)=-\omega^2m(X+X_0), \tag{12}$$

where m is the mass of the nucleus and a its acceleration.

At very low frequencies, the forces on the nucleus are nearly balanced so that the first part of Eq. (8) can be set equal to zero for each ion. Then:

$$X_1=A_1B_1(\xi_0F_i/e); \quad X_2=A_2B_2(\xi_0F_i/e). \tag{13}$$

The dielectric polarizability, α_D, valid at very low frequencies, is derived by substituting (13) in (11).

$$\alpha_D=(A_1^2B_1+C_1)+(A_2^2B_2+C_2). \tag{14}$$

Equation (14) indicates that the dielectric polarizability is an additive function expressible as a sum of polarizabilities of the separate ions.

The values of dielectric polarizability of alkali-halide

crystals calculated by means of this equation are shown in column 5 of Table II.

At wave-lengths in the range of visible light, the frequency is so high that the inertia of the nuclei effectively prevents them from moving, so that:

$$X_1+X_0=0; \quad X_2+X_0=0,$$

or
$$X_1=X_2=-X_0. \tag{15}$$

Since the system of ionic boundaries has no mass, the combined force on it per molecule must equal zero. Or:

$$F_{b1}+F_{b2}=1/B_1\cdot(e^2/\xi_0)X_1-(A_1-1)eF_1 \\ +1/B_2\cdot(e^2/\xi_0)X_2-(A_2+1)eF_i=0. \tag{16}$$

From this, one obtains:

$$X_1=X_2=\frac{A_1+A_2}{1/B_1+1/B_2}\cdot\frac{\xi_0F_i}{e}. \tag{17}$$

The electronic polarizability, α_e, so called because electrons are the only particles which move, is derived by substituting (17) in (11).

$$\alpha_e=\frac{(A_1+A_2)^2}{1/B_1+1/B_2}+C_1+C_2. \tag{18}$$

Since the boundaries have some freedom of motion, this electronic polarizability is greater than C_1+C_2, which corresponds to the hypothetical example of fixed boundaries. Equation (18) indicates that the electronic polarizability is not a strictly additive function since the first term involves cross products of the ionic parameters. However, this term is relatively small and the resulting departure from additivity is too slight to be observed experimentally.

Values of electronic polarizability calculated by means of Eq. (18) are shown in column 7 of Table II.

V. POLARIZABILITIES OF FREE IONS

It was formerly thought that the electronic polarizabilities of ions in crystals were smaller than those for ions in aqueous solutions.[1] Values of electronic polarizability of ions in solution were calculated by assuming the Lorentz value of internal field and were compared with theoretical polarizabilities of free ions calculated from data on the Stark effect.[2] Subsequent work by Böttcher[3] indicated that it was necessary to correct the Lorentz field to account for the interaction between a dissolved ion and its surroundings. When this was done the electronic polarizabilities of ions in solution were found to be more nearly equal to those of ions in crystals. So far no one has measured the polarizability of a "free" ion; however, it is now possible to calculate such polarizabilities from the data on solid crystals. Oddly enough, the resulting values turn out to be almost precisely equal to the original polarizabilities of ions in solution calculated by the Lorentz field assumption.

The polarizability of an unconstrained ion can be calculated by setting the force on its boundary equal to zero.

$$F_b=1/B\cdot(e^2/\xi_0)X-(A-p+n)eF_i=0. \tag{19}$$

Then:

$$X=(B/e)(A-p+n)\xi_0F_i. \tag{20}$$

At optical frequencies $X+X_0=0$, since the nucleus does not move. The dipole moment is derived from Eq. (8).

$$\mu_i=[B(A-p+n)^2+C]\xi_0F_i. \tag{21}$$

The polarizability of an alkali-halide ion pair is then obtained by adding the individual dipole moments and dividing by ξ_0F_i.

$$\alpha_g=B_1(A_1-1)^2+C_1+B_2(A_2+1)^2+C_2. \tag{22}$$

The electronic polarizability α_g of a pair of free (gaseous) ions has been calculated for each of the alkali-halides by using Eq. (22). These results are given in column 11 of Table II. For comparison, the polarizabilities α_{sol} of ionized molecules in dilute aqueous solutions as reported by Heydweiller[4] for the wave-length of sodium light are given in column 10. The conversion factor from his units to ours is $3/L\times10^{24}=4.981$, where L is Loschmidt's number and there are 10^{24} cubic angstroms per cubic centimeter.

VI. THE INTERNAL FIELD

In order to derive a relation between polarizability and dielectric constant or index of refraction, it is first necessary to establish the relation between the applied or macroscopic field E and the local field F_i which exists at the center of an ion in the crystal—or would exist there if the ion were removed without disturbing its neighbors. This calculation was originally carried out by Lorentz,[5] who assumed that the external field set up by a polarized ion was the same as that from a point dipole at its center.

The local field at a given position in a homogeneous crystal may be thought of as composed of four components. Of these, F_0 is the static field at equilibrium resulting from the Coulomb forces of the various charged particles making up the crystal. This component has been discussed in a previous paper[6] and has been shown to be zero at the centers of ions in the crystals under consideration.

The second component is just the applied field E, which needs no further comment.

The third component is the change in the Coulomb field due to displacement of charged particles from their equilibrium positions including only those particles

[1] K. Fajans and G. Joos, Zeits. f. Physik 23, 1 (1924).
[2] L. Pauling, Proc. Roy. Soc. A. 114, 181 (1927).
[3] C. J. F. Böttcher, Rec. des Trav. Chim. 65, 19 (1946).
[4] A. Heydweiller, Physik. Zeits. 26, 526 (1925).
[5] H. A. Lorentz, *Theory of Electrons*, Note 55, (B. G. Teubner, Leipzig, 1916), second edition, p. 308.
[6] S. Roberts, Phys. Rev. 76, 1215 (1949).

which are outside a sphere concentric with the ion in question, but of relatively large radius. This component is generally conceded to be $P/3\xi_0$, as derived by Lorentz and others, where P is the total polarization or dipole moment per unit volume.

Most of the discussion centers around the remaining term which is the change in the Coulomb field due to the displacement of charged particles (or induced dipoles) within the sphere. Lorentz found that this term vanishes in certain cubic crystals.

His calculation is based on the assumption of cubic symmetry with respect to each ionic position. A consequence of this symmetry requirement is that if the rectangular coordinates of the center of any one ion are (a, b, c) relative to any second ion, then there are two more ions like the first whose coordinates are (b, c, a) and (c, a, b). Only the "diagonal cubic"[7] types of crystals have this degree of symmetry. These include NaCl, CaCl, CaF_2, and ZnS.

The Z component of field at the origin due to a Z oriented dipole of strength μ located at the position (X, Y, Z) is:

$$E_Z=-\mu/4\pi\xi_0\cdot(X^2+Y^2-2Z^2)/(X^2+Y^2+Z^2)^{5/2}. \quad (23)$$

If one adds the components of field due to three equal dipoles at positions (a, b, c), (b, c, a), and (c, a, b), the result is evidently zero. Hence, one may conclude that there is no net contribution to the field at the center by all dipoles at a given distance from the ion in question in crystals having diagonal cubic symmetry. From this, it is also clear that the field component due to all dipoles within the sphere must vanish.

The external field of an ion may not necessarily be considered equivalent to that produced by a single point dipole at its center. In this event the ion needs to be represented by an assembly of point dipoles distributed throughout the space it occupies. In view of the spherical concept of the ion, it seems appropriate to assume that the dipoles are arranged inside in a manner at least consistent with cubic symmetry. In this, as in the previous example, the field at the center vanishes due to all polarized ions within the sphere.

Since only the second and third components of the internal field are non-vanishing, it may be expressed in the form derived by Lorentz.

$$F_i=E+P/3\xi_0. \quad (24)$$

In actual fact, it is not so simple to prove that the induced dipoles should be arranged inside the ion according to cubic symmetry. If true, this seems to imply a certain rigidity of the electron structure in which electrons are arranged in concentric spherical shells (or equivalent) which are displaced in relative position but not distorted in shape by the electric field. This is related to the previous assumption, based on the absence of a piezoelectric effect, that the spherical boundaries of ions are not distorted in shape by an electric field.

[7] M. Born and M. Goeppert-Mayer, *Handbuch der Physik* (1933), second edition, Vol. 24, No. 2, p. 625.

VII. DIELECTRIC CONSTANTS AND INDICES OF REFRACTION

The Lorentz internal field given by Eq. (24) is used in calculating the relations between the polarizabilities and the dielectric constant and index of refraction. If V is the volume per molecule in the crystal lattice, the total dipole moment per unit volume is:

$$P=\mu/V=\alpha\xi_0F_i/V=(\alpha\xi_0/V)E+(\alpha/3V)P=[\xi_0\alpha/(V-\alpha/3)]E. \quad (25)$$

Then, at low frequencies, α_D may be determined from measurements of the dielectric constant, K.

$$K=1+P/\xi_0E=(V+\tfrac{2}{3}\alpha_D)/(V-\tfrac{1}{3}\alpha_D),$$

or:

$$\alpha_D=3V(K-1)/(K+2). \quad (26)$$

This is the Clausius-Mosotti equation.

The corresponding equation relating the electronic polarizability to the optical index of refraction is that attributed to Lorentz and Lorenz.

$$\alpha_e=3V(n^2-1)/(n^2+2), \quad (27)$$

where n is the index of refraction.

The molecular volumes V of the alkali-halide crystals are calculated from the lattice constants compiled by Wyckoff.[8] The results are given in column 1 of Table II. The dielectric constants as compiled by Hojendahl[9] are listed in column 2. The indices of refraction for Na-D light as reported by Spangenberg[10] are listed in column 3. From these experimental data, values of dielectric polarizability α_D and electronic polarizability α_e are calculated by means of Eqs. (26) and (27). These results are shown in columns 4 and 6 respectively.

VIII. INFRA-RED ABSORPTION FREQUENCIES

The frequency, or wave-length, in the infra-red dispersion spectrum which seems to have been measured with greatest accuracy is that of maximum absorption. The experimental wave-length data for alkali-halide crystals reported by Barnes[11] are given in column 8 of Table II. At this frequency, $\omega_A/2\pi$, the dielectric constant or index of refraction is theoretically infinite and the applied field E vanishes corresponding to a finite polarization. Then, from Eq. (24):

$$E=F_i-P/3\xi_0=F_i-\mu/3\xi_0V=0,$$

or:

$$\mu=3V\xi_0F_i. \quad (28)$$

Then from Eq. (10):

$$A_1X_1+A_2X_2=(3V-C_1-C_2)\xi_0F_i/e. \quad (29)$$

[8] R. W. G. Wyckoff, *Crystal Structures, Section* I (Interscience Publications, Inc., New York, 1948).

[9] K. Hojendahl, Kgl. Danske Vid. Sels., Math.-Fys. Medd. **16** (2), 59 (1938).

[10] K. Spangenberg, Zeits. f. Krist. **57**, 494 (1923).

[11] R. B. Barnes, Zeits. f. Physik **75**, 723 (1932).

The forces on the nuclei are derived from Eqs. (8) and (12).

$$\left.\begin{aligned} F_{n1} &= -1/B_1\cdot(e^2/\xi_0)X_1+A_1eF_i \\ &= -\omega_A{}^2m_1(X_1+X_0) \\ F_{n2} &= -1/B_2\cdot(e^2/\xi_0)X_2+A_2eF_i \\ &= -\omega_A{}^2m_2(X_2+X_0) \end{aligned}\right\}. \quad (30)$$

Eliminating X_0 and solving for $\omega_A{}^2$ gives:

$$\omega_A{}^2=\frac{\left(\frac{X_1}{m_1B_1}-\frac{X_2}{m_2B_2}\right)\frac{e^2}{\xi_0}-\left(\frac{A_1}{m_1}-\frac{A_2}{m_2}\right)eF_i}{X_1-X_2}. \quad (31)$$

By solving Eqs. (16) and (29) for X_1 and X_2, substituting these values in (31) and by using Eqs. (14) and (18) for α_D and α_e to simplify the result, one finally obtains:

$$\omega_A{}^2=\frac{e^2(3V-\alpha_D)(1/m_1+1/m_2)}{\xi_0(3V-\alpha_e)(B_1+B_2)} =\frac{e^2(n^2+2)(1/m_1+1/m_2)}{\xi_0(K+2)(B_1+B_2)}. \quad (32)$$

The corresponding wave-length is:

$$\lambda_A=2\pi c/\omega_A, \quad (33)$$

where c is the velocity of light.

Wave-lengths calculated by this method are shown in column 9 of Table II. In this calculation, more consistent results were obtained by using the experimental values of α_D and α_e, or n and K, rather than the theoretical values. This is further evidence that the small deviations between theory and experiment are of real significance.

Equation (32) indicates that (B_1+B_2) may be calculated from observable properties of the crystal. Hence this equation leads to a second additivity relation, the first being the additivity of dielectric polarizabilities. A third additivity relation may be derived from Eqs. (14) and (18).

$$[(B_1+B_2)(\alpha_D+\alpha_e)]^{\frac{1}{3}}=A_1B_1-A_2B_2. \quad (34)$$

IX. THE PSEUDO-PIEZOELECTRIC EFFECT

A novel physical phenomenon is predicted by a further extension of the present theory. This is the "pseudo-piezoelectric" effect, which is similar to the ordinary piezoelectric effect in that it is a linear electromechanical phenomenon, but it differs in that it does not depend on crystalline anisotropy. In comparison with the ordinary piezoelectric effect, in which statically balanced forces applied to a crystal induce electric fields within it, a statically unbalanced force or acceleration is found to have the same effect on the isotropic crystals considered here.

In order to calculate the magnitude of the effect, the electric field will be considered which is set up in a crystal by raising its acceleration from zero to a uniform value "a." The surfaces of the crystal are to be electrically open, that is, no charge may flow to or from the surfaces from an external circuit. In this case, the electric field in the crystal turns out to be proportional to the acceleration.

$$E=\rho a, \quad (35)$$

where ρ is a new parameter equal to the following expression.

$$\rho=(m_1A_1B_1+m_2A_2B_2)/e(\tfrac{2}{3}\alpha_D+V). \quad (36)$$

The electric field produced by an acceleration equivalent to gravity in a sodium iodide crystal is, for example, -5.52 microvolt per meter according to the theory. In most of the alkali halides, the sign of the effect is negative. This is a result of the fact that the halide ions, having negative effective nuclear charges Ae, are the most highly polarizable. In view of the small magnitude of the effect, no attempt has been made to confirm it experimentally. However, if this were done, it would afford an independent means of testing the theory.

X. ADDITIONAL COMMENTS

The success in interpreting experimental results indicates that the theoretical assumptions are approximately valid in the case of alkali-halide crystals. However, these initial assumptions may be subject to certain limitations when applied to other types of crystals. For example, in many less symmetrical crystals, there are ions which are not in electrostatic equilibrium, hence F_0 is not zero. Such an ion may be distorted so much by this residual field that the relation between field strength and dipole moment is no longer linear. Owing to such a saturation effect the polarizability would be reduced. Experimental data for a number of crystals in this category are discussed in a previous paper.[6]

Since the theoretical derivation is based on the idea of contact between rigid spherical boundaries, it seems a little surprising that the experimental results should be consistent even in the case of certain lithium-halide crystals in which the lithium ions do not touch their neighbors. Evidently some other mechanism is needed to account for the constraint imposed on the lithium ions.

There would be a different complication in the case of piezoelectric crystals of the cubic ZnS type, since there would be relative motion between the respective ionic boundaries. These relative motions could be prevented by "clamping" the crystal, although this distinction probably makes little practical difference, since the clamped dielectric constant is only slightly different from that of the free crystal.

The foregoing theory was developed because existing theories did not explain the additivity of dielectric polarizabilities reported previously.[6] The author is indebted to Dr. F. E. Williams for urging him to find such an explanation. He also wishes to acknowledge the helpful discussions with Dr. M. H. Hebb.

The Theory of the Change in the Conductivity of Metals Produced by Cold Work

J. K. MACKENZIE AND E. H. SONDHEIMER*
H. H. Wills Physical Laboratory, University of Bristol, England
(Received September 22, 1949)

An attempt is made to calculate the increase in the residual electrical resistance of cold-worked metals by attributing the effect to an elastic distortion similar to that produced by the presence of edge type dislocations. It is shown that, in single crystals, the direction of the dislocation axes, the slip direction and the direction normal to the slip plane represent a set of principal axes of the conductivity tensor. The dislocation resistance parallel to the dislocation axes is zero, while the resistance in the slip direction exceeds the resistance normal to the slip plane by a factor which depends upon Poisson's ratio and which lies between 1 and 3. The mean density of dislocations in a highly cold-worked polycrystalline specimen of copper is estimated from the observed resistance change and is found to be in reasonable agreement with the value derived from the energy stored during work hardening. The formulation of the present theory follows the lines of a recent paper by J. S. Koehler; the results differ considerably from Koehler's, however, and it is shown that his treatment cannot be regarded as satisfactory.

1. INTRODUCTION

THE aim of the present paper is to give a theoretical discussion of the additional residual resistance of metals produced by cold working, it being assumed that the important change which occurs during cold work is the introduction of a large number of edge dislocations of the type discussed by Burgers[1] and Koehler.[2] This problem has recently been studied by Koehler,[3] and our formulation follows the general lines laid down in Koehler's paper; his treatment cannot, however, be regarded as satisfactory, and a re-examination of the problem seemed therefore to be desirable. The differences between our calculation and Koehler's will be pointed out at the appropriate stages during the development of our theory.

We consider a metal single crystal containing a large number of dislocations which have their axes parallel and which correspond to parallel slip planes. The resulting displacement of the lattice ions from their positions in the perfect lattice may be calculated approximately by means of elastic continuum theory. Owing to the elastic distortion the potential in the crystal lattice is no longer periodic, and a conduction electron moving through the crystal therefore undergoes scattering; the collisions are elastic, since the dislocations constitute a static perturbation. A rigorous evaluation of the scattering probability is difficult, since the displacements produced by a dislocation are such that the perturbation methods usual in the theory of metals cannot easily be applied; we therefore approximate by introducing a displacement function (Eq. (13)) which enables us to use the ordinary methods, and which at the same time reproduces to a considerable extent the actual elastic distortion present. It is hoped to investigate the error introduced by this procedure in a later paper; we shall here assume it to be unimportant.

When the scattering probability has been calculated, we can formulate the transport equation which determines the velocity distribution function, f, of the conduction electrons; this equation is formed by equating the rate of change in f due to an applied electric field to the rate of change due to the scattering mechanism, and it takes the form of a complicated integral equation. The general formulas required are collected together in §2, the matrix element for dislocation scattering is evaluated in §3, and the transport equation is set up in §4.1 in a form which includes the effect of thermal as well as dislocation scattering (Eq. (22)). The thermal scattering is assumed to take place isotropically.

In §4.2 we prove that the axes of the dislocation system represent a set of principal axes of the conductivity tensor, and in §5 we obtain explicit solutions of the transport equation for the limiting case in which the dislocation resistance is small compared with the thermal resistance. In §6 these solutions are used to set up general expressions (Eqs. (36) and (37)) for the dislocation resistance, based on the assumption that Matthiessen's rule concerning the additivity of the thermal and residual resistances is of general validity. The results are in reasonable quantitative agreement with the measured resistance change in polycrystalline copper. For single crystals the dislocation resistance is anisotropic, there being no resistance in the direction of the dislocation axes, and the resistance in the slip direction exceeding the resistance at right angles to it by a factor which lies between 1 and 3, and which is greater the smaller the value of Poisson's ratio.

2. GENERAL FORMULAS

2.1. As is usual in the theory of metallic conduction the conduction electrons will be regarded as free, in the sense that the energy E is related to the wave-vector $\mathbf{k}$ by $E=\hbar^2k^2/2m$, k being the magnitude of $\mathbf{k}$ and m being the effective mass of an electron. The distribution func-

* Now at the Research Laboratory of Electronics, Massachusetts Institute of Technology, Cambridge, Massachusetts.
[1] J. M. Burgers, Proc. Kon. Ned. Akad. Wet. 42, 293 (1939).
[2] J. S. Koehler, Phys. Rev. 60, 398 (1941).
[3] J. S. Koehler, Phys. Rev. 75, 106 (1949), hereafter referred to as K.

tion f of the electrons is conveniently written in the form

$$f=f_0-\frac{\hbar}{m}\mathbf{g}(\mathbf{k})\cdot\mathbf{k}\frac{\partial f_0}{\partial E}, \tag{1}$$

where f_0 is the Fermi function $1/\{e^{(E-\zeta)/kT}+1\}$ (ζ being the Fermi energy level and k being Boltzmann's constant**), and where $\mathbf{g}=(g_x, g_y, g_z)$ is an unknown vector function of $\mathbf{k}$ which is to be determined.

In the steady state, f is determined by the Boltzmann equation

$$-\frac{\epsilon\hbar}{m}\mathbf{E}\cdot\mathbf{k}\frac{\partial f_0}{\partial E}=\left[\frac{\partial f}{\partial t}\right]_{\text{coll.}}, \tag{2}$$

where $-\epsilon$ is the electronic charge. The term on the left-hand side denotes the rate of change of f due to an applied electric field $\mathbf{E}$; the product of $\mathbf{E}$ with $\mathbf{g}$ has as usual been neglected.

$[\partial f/\partial t]_{\text{coll.}}$ in Eq. (2) is the rate of change of f due to the mechanism which scatters the electrons. We shall suppose that the scattering in a highly cold-worked metal is due to two causes: first the presence of thermal vibrations, random impurities, etc., which scatter isotropically since the electrons are free,† and secondly the presence of a large number of dislocations, the scattering from which will possess directional features. It will be assumed that the first collision mechanism can be described in terms of a time of relaxation τ, so that we may write

$$\left[\frac{\partial f}{\partial t}\right]_{\text{coll.}}=-\frac{f-f_0}{\tau}+\left[\frac{\partial f}{\partial t}\right]_{\text{disl.}}, \tag{3}$$

where τ may be a function of the energy but is independent of the direction of $\mathbf{k}$. We must now find an expression for the dislocation term $[\partial f/\partial t]_{\text{disl.}}$.

2.2. Since the dislocations constitute a static perturbation, the collision operator is[4]

$$\left[\frac{\partial f}{\partial t}\right]_{\text{disl.}}=(2G+1)^3\frac{\Delta}{2\pi^3\hbar^2}\int\int\int\{f(\mathbf{k}')-f(\mathbf{k})\}\times\Omega(E_{\mathbf{k}}-E_{\mathbf{k}'})|(\mathbf{k}'|\Delta V|\mathbf{k})|^2dk_x'dk_y'dk_z', \tag{4}$$

where $(2G+1)^3$ is the number of atoms in the crystal, Δ is the volume of the unit cell, $\Omega(x)=\sin(xt/\hbar)/(x/\hbar)$, ($t$ being the time), and where $(\mathbf{k}'|\Delta V|\mathbf{k})$ is the matrix element for dislocation scattering, corresponding to a transition in which the wave-vector of an electron changes from $\mathbf{k}$ to $\mathbf{k}'$. The collisions are, of course, elastic, since $\Omega(E_{\mathbf{k}}-E_{\mathbf{k}'})$ is effectively different from zero only if $E_{\mathbf{k}}=E_{\mathbf{k}'}$. We may therefore, as usual, replace the integration in $\mathbf{k}$-space by an integration over the surface of a sphere of constant energy, and obtain

$$\left[\frac{\partial f}{\partial t}\right]_{\text{disl.}}=\frac{(2G+1)^3m\Delta}{2\pi^2\hbar^3k}\times\int\int\{f(\mathbf{k}')-f(\mathbf{k})\}|(\mathbf{k}'|\Delta V|\mathbf{k})|^2dS', \tag{5}$$

where dS' is an element of the surface $E_{\mathbf{k}'}=$ constant in $\mathbf{k}$-space. Using Eq. (1), this becomes

$$\left[\frac{\partial f}{\partial t}\right]_{\text{disl.}}=\frac{(2G+1)^3\Delta}{2\pi^2\hbar^2k}\frac{\partial f_0}{\partial E}\times\int\int\{\mathbf{g}(\mathbf{k})\cdot\mathbf{k}-\mathbf{g}(\mathbf{k}')\cdot\mathbf{k}'\}|(\mathbf{k}'|\Delta V|\mathbf{k})|^2dS', \tag{6}$$

and, combining (1), (2), (3), and (6), we obtain the following integral equation for $\mathbf{g}$

$$-\epsilon\mathbf{E}\cdot\mathbf{k}=\frac{1}{\tau}\mathbf{g}(\mathbf{k})\cdot\mathbf{k}+\frac{(2G+1)^3m\Delta}{2\pi^2\hbar^3k}\times\int\int\{\mathbf{g}(\mathbf{k})\cdot\mathbf{k}-\mathbf{g}(\mathbf{k}')\cdot\mathbf{k}'\}|(\mathbf{k}'|\Delta V|\mathbf{k})|^2dS'. \tag{7}$$

2.3. When Eq. (7) has been solved, the electric current density (J_x, J_y, J_z) can be obtained at once. For example, if $\mathbf{v}$ is the velocity of an electron, we have

$$J_x=-\frac{\epsilon}{4\pi^3}\int\int\int v_x f dk_x dk_y dk_z=\frac{\epsilon\hbar^2}{4\pi^3m^2}\int\int\int k_x\mathbf{g}(\mathbf{k})\cdot\mathbf{k}\frac{\partial f_0}{\partial E}dk_x dk_y dk_z,$$

using Eq. (1) and the relation $m\mathbf{v}=\hbar\mathbf{k}$ which holds for free electrons. For a degenerate electron gas, J_x can be expressed in the usual way as an integral over the surface of the Fermi sphere. Introducing polar coordinates k, θ, ϕ in the $\mathbf{k}$-space, the polar axis being in the z direction, we obtain

$$J_x=-\frac{3\epsilon n}{4\pi mk_0}\int\int\mathbf{g}(\mathbf{k})\cdot\mathbf{k}\sin^2\theta\cos\phi d\theta d\phi, \tag{8}$$

k_0 being the value of k at the surface of the Fermi sphere and $n=k_0^3/3\pi^2$ being the number of electrons per unit

** This is the only formula in the present paper in which k denotes Boltzmann's constant. In all other cases k is used to denote the magnitude of the wave-vector $\mathbf{k}$ and no confusion should therefore arise.

† Note that we disregard anisotropic conduction effects in the unstrained metal. The approximation of free electrons should be a reasonable one for the monovalent elements and for those metals in which the surface of the Fermi distribution does not approach close to the boundaries of the Brillouin zones (A. H. Wilson, reference 4, Chapter V).

[4] A. H. Wilson, *The Theory of Metals* (Cambridge University Press, London, 1936), p. 223.

volume. Similarly,

$$J_y=-\frac{3\epsilon n}{4\pi m k_0}\int\int \mathbf{g}(\mathbf{k})\cdot\mathbf{k}\sin^2\theta\sin\phi d\theta d\phi,$$
$$J_z=-\frac{3\epsilon n}{4\pi m k_0}\int\int \mathbf{g}(\mathbf{k})\cdot\mathbf{k}\sin\theta\cos\theta d\theta d\phi. \quad (9)$$

3. THE MATRIX ELEMENT FOR DISLOCATION SCATTERING

3.1. The matrix element which determines the transition $\mathbf{k}\rightarrow\mathbf{k}'$ is

$$(\mathbf{k}'|\Delta V|\mathbf{k})=\int\psi_{\mathbf{k}'}{}^*\Delta V\psi_{\mathbf{k}}d\tau, \quad (10)$$

where $\psi_{\mathbf{k}}$ is the electronic wave function corresponding to the state $\mathbf{k}$, ΔV is the deviation of the potential from its value in a perfectly periodic lattice, and where the integration extends over the whole crystal.

The potential in which the conduction electrons move in a perfect lattice may be written

$$V(\mathbf{r})=\textstyle\sum_j U_j(\mathbf{r}), \quad (11)$$

where the potential energy U_j is a function of the distance $\mathbf{r}-\mathbf{a}_j$ from the position $\mathbf{a}_j$ of the jth lattice point. U_j is large near the lattice point and falls off very rapidly with distance.

In the presence of dislocations the ions are displaced from their positions in the perfect lattice. If $\mathbf{u}_j$ is the displacement of the jth ion, the perturbing potential is

$$\Delta V=\textstyle\sum_j\{U_j(\mathbf{r})-U_j(\mathbf{r}+\mathbf{u}_j)\}=-\sum_j\mathbf{u}_j\cdot\mathrm{grad}U_j \quad (12)$$

approximately, provided that the displacements are small.

3.2. We shall consider the displacements to be produced by edge dislocations of the type discussed by Burgers[1] and Koehler.[2] Following K, we shall evaluate the matrix element for a positive-negative dislocation pair which has its axis parallel to the z axis, the positive dislocation being located at $x=0$, $y=\frac{1}{2}R$ and the negative dislocation at $x=0$, $y=-\frac{1}{2}R$. The x axis is the slip direction and the xz plane is the slip plane. R is of the order of 10^{-6} cm and is thus large compared with the interatomic distance.

The elastic problem corresponding to such a dislocation pair is a two-dimensional one, for which the displacement u_z vanishes and the displacements u_x and u_y are functions of x and y only. We take u_x and u_y to be given by

$$u_x=A\left\{\tan^{-1}\left(\frac{y-\frac{1}{2}R}{x}\right)-\tan^{-1}\left(\frac{y+\frac{1}{2}R}{x}\right)\right\}$$
$$+2Bx\left\{\frac{y-\frac{1}{2}R}{x^2+(y-\frac{1}{2}R)^2}-\frac{y+\frac{1}{2}R}{x^2+(y+\frac{1}{2}R)^2}\right\}$$
$$\text{for}\quad |y|\geqslant\tfrac{1}{2}R, \quad (13a)$$

$$u_x=A\left\{\tan^{-1}\left(\frac{\frac{1}{2}R-|y|}{x}\right)-\tan^{-1}\left(\frac{\frac{1}{2}R+|y|}{x}\right)\right\}$$
$$+2Bx\left\{\frac{y-\frac{1}{2}R}{x^2+(y-\frac{1}{2}R)^2}-\frac{y+\frac{1}{2}R}{x^2+(y+\frac{1}{2}R)^2}\right\}$$
$$\text{for}\quad |y|\leqslant\tfrac{1}{2}R, \quad (13b)$$

$$u_y=-C\log\left\{\frac{x^2+(y-\frac{1}{2}R)^2}{x^2+(y+\frac{1}{2}R)^2}\right\}^{\frac{1}{2}}$$
$$-2Bx^2\left\{\frac{1}{x^2+(y-\frac{1}{2}R)^2}-\frac{1}{x^2+(y+\frac{1}{2}R)^2}\right\}, \quad (13c)$$

where

$$A=\frac{\lambda}{2\pi},\quad B=\frac{\lambda}{8\pi}\frac{\nu}{\nu-1},\quad C=\frac{\lambda}{4\pi}\frac{\nu-2}{\nu-1}. \quad (14)$$

λ is the unit crystallographic slip distance, ν is the reciprocal of Poisson's ratio, and the principal value of the angles in (13a) and (13b) is taken $(-\frac{1}{2}\pi\leqslant\theta\leqslant\frac{1}{2}\pi)$.

3.21. The expressions (13) represent an approximation, since, for a true edge dislocation, u_z is given by (13a) for all values of y (compare K, Eq. (16)). If the correct expression is used, u_x is discontinuous across $x=0$ for $|y|\leqslant\frac{1}{2}R$ (i.e., across the line joining the two dislocations); such a discontinuity is of course the characteristic feature of a dislocation. This behavior of the displacement makes it very difficult to give a rigorous treatment of the problem, since the expression (12) for the perturbing potential cannot be used in the region close to the discontinuity. In representing the x-displacement by Eq. (13b) in the strip $|y|\leqslant\frac{1}{2}R$ we have effectively smoothed out the discontinuity. Note that our expression for u_x has the correct symmetry properties, being an odd function of x and an even function of y. Note also that the material near the origin is essentially a perfect lattice ($u_x=u_y=0$ for $x=y=0$) and that the first term in u_x vanishes on the line $y=0$; we are thus neglecting the contribution to the scattering of the region midway between the dislocations. It seems reasonable to suppose that this contribution will be small.††

In K the expression (12) is used for the perturbing potential, together with the exact expression for u_x. If this (inadmissible) procedure is followed, the dislocation resistance in the x direction is found to exceed that in the y direction by a (large) factor of the order of k_0R. Koehler does not obtain this result, and it seems to us that in deriving his expression (K, Eq. (26)) for the

†† An alternative approximation (suggested to us by Professor Koehler in a private communication) is to suppose that the first term in u_x is an even instead of an odd function of x, i.e., to replace it by its absolute value. This leads to the same expression (19) for the scattering probability as does our present procedure, and seems to indicate that the results are not very sensitive to the particular model adopted.

scattering probability, Koehler must at some stage have made an approximation of the type discussed here. This point is, however, not mentioned explicitly in K, and we have been unable to follow Koehler's calculation in detail.

3.3. Again following K, we shall take the potential of a single ion to be a screened Coulomb potential, so that

$$U_j(\mathbf{r})=-Z\epsilon^2\frac{e^{-q|\mathbf{r}-\mathbf{a}_j|}}{|\mathbf{r}-\mathbf{a}_j|}, \tag{15}$$

where $Z\epsilon$ is the effective charge of the ion and q is the screening constant. The electronic wave functions are assumed to be free electron wave functions (normalized in the whole crystal), so that

$$\psi_{\mathbf{k}}=e^{i\mathbf{k}\cdot\mathbf{r}}/\Delta^{\frac{1}{2}}(2G+1)^{\frac{1}{2}}. \tag{16}$$

Assuming further that the displacement of a lattice point at (x, y) is given by (13), and combining Eqs. (10), (12), (13), (15), and (16), we may now evaluate the matrix element, as in K, by integrating first over the electronic coordinates, and then converting the sum over j into an integral and performing another volume integration. The calculation follows the lines indicated by Koehler and the details will not be given here. The result is

$$\begin{aligned}(\mathbf{k}'|\Delta V|\mathbf{k})=&-\frac{32\pi^3Z\epsilon^2\delta(K_z)}{(2G+1)^3\Delta^2(q^2+K^2)(K_x^2+K_y^2)}\\&\times[A|K_x|\{\cos(\tfrac{1}{2}K_yR)-e^{-\frac{1}{2}R|K_x|}\}\\&+(2B-C)K_y\sin(\tfrac{1}{2}K_yR)],\end{aligned} \tag{17}$$

where $\mathbf{K}=\mathbf{k}'-\mathbf{k}$, K is the magnitude of $\mathbf{K}$, and where

$$\delta(K_z)=\frac{1}{2\pi}\int_{-\frac{1}{2}V^{\frac{1}{3}}}^{\frac{1}{2}V^{\frac{1}{3}}}e^{-iK_zz}dz=\frac{\sin(\frac{1}{2}K_zV^{\frac{1}{3}})}{\pi K_z}, \tag{18}$$

$V=(2G+1)^3\Delta$ being the volume of the crystal (note that Koehler's δ-function is defined in a slightly different way). The appearance of the δ-function means, of course, that, corresponding to the two-dimensional nature of the problem, only those transitions occur in which k_z' equals k_z.

3.4. The presence of the sine and cosine terms in the matrix element gives rise to diffraction effects which have been discussed in K. In normal metals the maximum value of $\frac{1}{2}K_yR$ is large compared with unity, and the square of the matrix element (i.e., the scattering probability) hence contains rapidly fluctuating terms which may be replaced by their average value. The scattering probability for a large number N of dislocation pairs all oriented similarly (i.e., having their axes parallel and corresponding to parallel slip planes) is then simply N times the average value for a single pair. We therefore obtain, neglecting the small term $e^{-\frac{1}{2}R|K_x|}$,*

$$\begin{aligned}|(\mathbf{k}'|\Delta V|\mathbf{k})|^2=&\frac{512\pi^6Z^2\epsilon^4N\{\delta(K_z)\}^2}{(2G+1)^6\Delta^4(q^2+K^2)^2(K_x^2+K_y^2)^2}\\&\times\{A^2K_x^2+(2B-C)^2K_y^2\},\end{aligned} \tag{19}$$

N being the total number of dislocation pairs in the specimen. Note that Eq. (19) differs from the corresponding expression in K (compare §3.21 above).

4. THE TRANSPORT EQUATION

4.1. Combining Eqs. (7) and (19), we obtain the transport equation

$$\begin{aligned}-\epsilon\mathbf{E}\cdot\mathbf{k}=&\frac{1}{\tau}\mathbf{g}(\mathbf{k})\cdot\mathbf{k}\\&+\frac{256\pi^4Z^2\epsilon^4mN}{(2G+1)^3\Delta^3\hbar^3k}\int\int\{\mathbf{g}(\mathbf{k})\cdot\mathbf{k}-\mathbf{g}(\mathbf{k}')\cdot\mathbf{k}'\}\\&\times\frac{A^2K_x^2+(2B-C)^2K_y^2}{(q^2+K^2)^2(K_x^2+K_y^2)^2}\{\delta(K_z)\}^2dS'.\end{aligned} \tag{20}$$

Introducing polar angles θ', ϕ' on the sphere $k'=k=$ constant, the polar axis being in the z direction, we have $dS'=k^2\sin\theta'd\theta'd\phi'$ and $K_z=k_z'-k_z=k(\cos\theta'-\cos\theta)$. The part of the integrals depending on θ' contains, apart from slowly varying quantities, the expression

$$\begin{aligned}\int_0^\pi\{\delta(K_z)\}^2\sin\theta'd\theta'=&\frac{1}{k}\int_{\theta'-\pi}^{\theta'-0}\{\delta(K_z)\}^2dK_z\\=&\frac{V^{\frac{1}{3}}}{2\pi^2k}\int_{\theta'-\pi}^{\theta'-0}\frac{\sin^2y}{y^2}dy,\end{aligned} \tag{21}$$

the upper limit of integration being

$$y=\tfrac{1}{2}V^{\frac{1}{3}}k(1-\cos\theta),$$

and the lower being

$$y=-\tfrac{1}{2}V^{\frac{1}{3}}k(1+\cos\theta).$$

Since these limits are of opposite sign, the integral in (21) is effectively

$$\int_{-\infty}^{\infty}\frac{\sin^2y}{y^2}dy=\pi,$$

and since the whole of the integral comes from regions near $y=0$ we may replace any slowly varying functions of θ' by their values when $y=0$, i.e., when $K_z=0$ and $\theta'=\theta$.

* It is easily shown that the contribution of this term to the resistivity is of order e^{-2k_0R} compared with the leading term, which is entirely negligible since k_0R is of order 100 for normal metals.

The transport equation therefore takes the final form

$$-\epsilon\mathbf{E}\cdot\mathbf{k}=\frac{1}{\tau}\mathbf{g}(\mathbf{k})\cdot\mathbf{k}+\frac{128\pi^3Z^2\epsilon^4mN}{(2G+1)^2\Delta^{8/3}\hbar^3}\times\int_0^{2\pi}\{\mathbf{g}(\mathbf{k})\cdot\mathbf{k}-\mathbf{g}(\mathbf{k}')\cdot\mathbf{k}'\}\times\frac{A^2K_x^2+(2B-C)^2K_y^2}{(q^2+K_x^2+K_y^2)^2(K_x^2+K_y^2)^2}d\phi', \quad (22)$$

all quantities in the integrand taking their value for $\theta'=\theta$.

4.2. When Eq. (22) has been solved, the electric current can be calculated by means of (8) and (9). The current is of course related to the electric field by a tensor relation of the form

$$J_i=\sum_{k=1}^{3}\sigma_{ik}\mathcal{E}_k, \quad i=1, 2, 3. \quad (23)$$

We shall now prove that the rectangular coordinate system formed by the direction of the dislocation axes, the slip direction and the direction perpendicular to these two represents a system of principal axes of the conductivity tensor σ_{ik}. If we put

$$\mathbf{g}=(g_x, g_y, g_z)=(h_x\mathcal{E}_x, h_y\mathcal{E}_y, h_z\mathcal{E}_z), \quad (24)$$

the integral equation (22) splits up into three equations, and from the symmetry of these equations it may easily be shown that h_x, h_y, and h_z are even functions of k_y and k_z. On substituting (24) into (8) and (9) it is therefore seen that h_y and h_z do not contribute to J_x, and there are corresponding results for J_y and J_z. Thus the only non-vanishing components of the conductivity tensor are the diagonal components σ_{11}, σ_{22}, and σ_{33}, which proves our result.

5. SOLUTION OF THE TRANSPORT EQUATION

We shall now obtain an explicit expression for the conductivity in the limiting case where the thermal resistance is large compared with the additional resistance due to dislocations.** In this case we may treat the second term on the right-hand side of (22) as small compared with the first and solve the equation by successive approximations. Putting $\mathbf{g}=\mathbf{g}_0+\mathbf{g}_1+\cdots$ and confining ourselves to the first two approximations, we obtain

$$\mathbf{g}_0\cdot\mathbf{k}=-\epsilon\tau\mathbf{E}\cdot\mathbf{k}, \quad (25)$$

$$\mathbf{g}_1\cdot\mathbf{k}=-\frac{128\pi^3Z^2\epsilon^5mN\tau^2}{(2G+1)^2\Delta^{8/3}\hbar^3}\times\int_0^{2\pi}\mathbf{E}\cdot\mathbf{K}\frac{A^2K_x^2+(2B-C)^2K_y^2}{(q^2+K_x^2+K_y^2)^2(K_x^2+K_y^2)^2}d\phi'. \quad (26)$$

Substituting these expressions into (8) and (9) and expressing $K_x=k_x'-k_x$ and $K_y=k_y'-k_y$ in polar coordinates (it should be remembered that $K_z=k_z'-k_z=0$), it is easily verified explicitly that the non-diagonal components of the conductivity tensor vanish, and that

$$\sigma_{11}=\sigma_i-\frac{3\pi^2Z^2\epsilon^6nN\tau^2}{(2G+1)^2\Delta^{8/3}\hbar^3k_0^6}\times\int_0^{\pi}d\theta\int_0^{2\pi}d\phi\int_0^{2\pi}d\phi'\frac{\sin\theta\cos\phi\sin\left(\frac{\phi'+\phi}{2}\right)\left\{A^2\sin^2\left(\frac{\phi'+\phi}{2}\right)+(2B-C)^2\cos^2\left(\frac{\phi'+\phi}{2}\right)\right\}}{\sin\left(\frac{\phi'-\phi}{2}\right)\left\{a^2+\sin^2\theta\sin^2\left(\frac{\phi'-\phi}{2}\right)\right\}^2}, \quad (27)$$

$$\sigma_{22}=\sigma_i+\frac{3\pi^2Z^2\epsilon^6nN\tau^2}{(2G+1)^2\Delta^{8/3}\hbar^3k_0^6}\times\int_0^{\pi}d\theta\int_0^{2\pi}d\phi\int_0^{2\pi}d\phi'\frac{\sin\theta\sin\phi\cos\left(\frac{\phi'+\phi}{2}\right)\left\{A^2\sin^2\left(\frac{\phi'+\phi}{2}\right)+(2B-C)^2\cos^2\left(\frac{\phi'+\phi}{2}\right)\right\}}{\sin\left(\frac{\phi'-\phi}{2}\right)\left\{a^2+\sin^2\theta\sin^2\left(\frac{\phi'-\phi}{2}\right)\right\}^2}, \quad (28)$$

where

$$a=q/2k_0, \quad (29)$$

and where

$$\sigma_i=n\epsilon^2\tau/m \quad (30)$$

is the conductivity caused by thermal scattering alone.

We further find that

$$\sigma_{33}=\sigma_i, \quad (31)$$

all the higher approximations vanishing. The conductivity measured parallel to the dislocation axes is therefore unchanged, as we should expect.

The triple integrals in (27) and (28) may be evaluated

** In K the transport equation is solved by a complicated numerical method in which the distribution function is expanded as a Fourier series. Only the first few terms of the series are retained, but the convergence of the procedure is not investigated. The present method of solution is much simpler; no numerical work is necessary, and the conductivity is obtained in the form of closed algebraic expressions.

by elementary methods, using $\frac{1}{2}(\phi'+\phi)$ and $\frac{1}{2}(\phi'-\phi)$ as variables of integration. The calculation is straightforward and the details will not be given here. The final results are

$$\sigma_{11}=\sigma_i-\frac{3\pi^4Z^2\epsilon^6nN\tau^2}{2(2G+1)^2\Delta^{8/3}\hbar^3k_0{}^6}\times\left\{\frac{\cot^{-1}a}{a^3}+\frac{1}{a^2(a^2+1)}\right\}\{3A^2+(2B-C)^2\}, \quad (32)$$

$$\sigma_{22}=\sigma_i-\frac{3\pi^4Z^2\epsilon^6nN\tau^2}{2(2G+1)^2\Delta^{8/3}\hbar^3k_0{}^6}\times\left\{\frac{\cot^{-1}a}{a^3}+\frac{1}{a^2(a^2+1)}\right\}\{A^2+3(2B-C)^2\}. \quad (33)$$

6. THE DISLOCATION RESISTANCE

6.1. Matthiessen's rule, applied to the present problem, states that the electrical resistance of a metal is the sum of an ideal resistance due to the lattice vibrations and a residual resistance due to dislocations. We shall assume that Matthiessen's rule holds for the resistance measured along any one of the principal axes, so that, for example,

$$1/\sigma_{11}=1/\sigma_i+1/\sigma_1,$$

where σ_i is given by (30) and $1/\sigma_1=\rho_1$ is the dislocation resistance in the x direction. For small values of σ_i/σ_1 this becomes

$$\sigma_{11}=\sigma_i-\sigma_i^2/\sigma_1,$$

and comparison with (30) and (32) shows that

$$\rho_1=\frac{1}{\sigma_1}=\frac{3\pi^4Z^2\epsilon^2m^2N}{2(2G+1)^2\Delta^{8/3}\hbar^3k_0{}^6n}\times\left\{\frac{\cot^{-1}a}{a^3}+\frac{1}{a^2(a^2+1)}\right\}\{3A^2+(2B-C)^2\}. \quad (34)$$

Similarly,

$$\rho_2=\frac{1}{\sigma_2}=\frac{3\pi^4Z^2\epsilon^2m^2N}{2(2G+1)^2\Delta^{8/3}\hbar^3k_0{}^6n}\times\left\{\frac{\cot^{-1}a}{a^3}+\frac{1}{a^2(a^2+1)}\right\}\{A^2+3(2B-C)^2\}. \quad (35)$$

6.11. Equations (34) and (35) have been derived only for the limiting case in which ρ_1 and ρ_2 are small compared with the thermal resistance. We shall, however, assume that Eqs. (34) and (35) may be taken to represent the dislocation resistance in the general case, regardless of the magnitude of the thermal resistance. It would be desirable to test this assumption by finding a more general solution of the transport equation; this, however, appears to involve considerable difficulties, and in the present paper we shall assume the general validity of (34) and (35) without attempting to supply a direct proof. Our expressions for the dislocation resistance are the simplest ones compatible with the assumption that Matthiessen's rule is of general validity.

6.12. For a metal of unit volume we have $(2G+1)^3\Delta=1$; also $k_0{}^3=3\pi^2n$ (see §2.3), and Eq. (14) may be used to express A, B, and C in terms of λ, the unit crystallographic slip distance, and ν, the reciprocal of Poisson's ratio. We therefore obtain, finally,

$$\rho_1=\frac{Z^2\epsilon^2m^2N\lambda^2}{24\pi^2\hbar^3n^3\Delta^2}\left\{\frac{\cot^{-1}a}{a^3}+\frac{1}{a^2(a^2+1)}\right\}\frac{3(\nu-1)^2+1}{(\nu-1)^2}, \quad (36)$$

$$\rho_2=\frac{Z^2\epsilon^2m^2N\lambda^2}{24\pi^2\hbar^3n^3\Delta^2}\left\{\frac{\cot^{-1}a}{a^3}+\frac{1}{a^2(a^2+1)}\right\}\frac{(\nu-1)^2+3}{(\nu-1)^2}. \quad (37)$$

We recall that ρ_1 is the dislocation resistance in the slip direction and ρ_2 the resistance normal to the slip plane, and that the dislocation resistance ρ_3 in the direction of the dislocation axes vanishes. n is the number of conduction electrons per unit volume, N the number of dislocation pairs per unit area normal to the axes, Δ the volume of the unit cell, and the potential of a lattice ion is taken to be of the form $-(Z\epsilon^2/r)e^{-qr}$; finally $a=q/2k_0$, where k_0 is the wave-vector at the surface of the Fermi distribution.

6.2. From (36) and (37) we obtain the following simple formula for the ratio of the dislocation resistances in and perpendicular to the slip direction:

$$\frac{\rho_1}{\rho_2}=\frac{3(\nu-1)^2+1}{(\nu-1)^2+3}. \quad (38)$$

The ratio thus depends only upon the value of Poisson's ratio. For all known materials ν (the reciprocal of Poisson's ratio) is positive, and its value cannot be less than 2; we see from Eq. (38) that, as ν increases from 2 to infinity, the ratio ρ_1/ρ_2 increases steadily from 1 to 3. A value $\frac{1}{3}$ of Poisson's ratio corresponds to $\nu=3$ and $\rho_1/\rho_2=13/7$.

6.21. The dislocation resistance measured in an arbitrary direction (α, β), as shown in Fig. 1, is given by the ordinary tensor rule‡

$$\rho_{\alpha,\beta}=\sin^2\alpha(\rho_1\cos^2\beta+\rho_2\sin^2\beta), \quad (39)$$

and the average resistance for a polycrystalline material, which is obtained by averaging (39) over all

‡ Equation (39) is entirely different from the corresponding Eq. (48) in *K*. Koehler's result is erroneous, as he does not take into account correctly the tensor character of the conductivity and calculates the resistance by means of a formula (*K*, Eq. (1)) which may be used for isotropic media only.

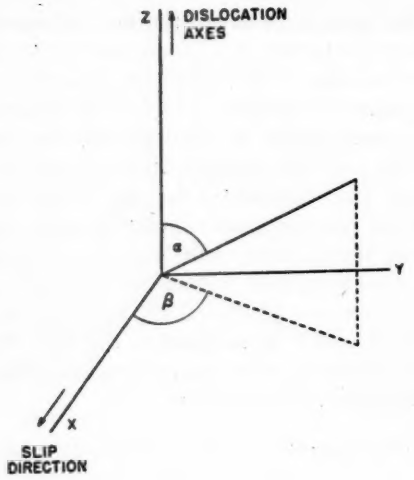

FIG. 1.

directions, is

$$\bar{\rho}=\tfrac{1}{3}(\rho_1+\rho_2)=\frac{Z^2\epsilon^2m^2N\lambda^2}{18\pi^2\hbar^3n^3\Delta^2}$$

$$\times\left\{\frac{\cot^{-1}a}{a^3}+\frac{1}{a^2(a^2+1)}\right\}\left\{1+\frac{1}{(\nu-1)^2}\right\}. \quad (40)$$

6.3. The experimental results on the change in the electrical resistance of metals produced by cold work all refer to room temperature and to polycrystalline specimens of undetermined purity. For a highly cold-worked specimen of copper, for example, the increase in resistance is 2 percent. If we assume that the cold work results in the introduction of a large number of dislocations of the type considered in the present paper, we may use Eq. (40) and the observed resistance change to estimate N, the mean density of dislocation pairs. For copper we take $n=1.2\times10^{23}$, $k_0=1.53\times10^8$, $\lambda=2.55\times10^{-8}$, $\Delta=\lambda^3/\sqrt{2}=1.17\times10^{-23}$, $\nu=2.94$, $Z=1$, and[5] $q\simeq2.5\times10^8$, so that $a=q/2k_0=0.82$. The thermal resistance of copper at 20°C is 1.89×10^{-18} gaussian unit. According to (40), an increase in resistance of 2 percent therefore corresponds to $N=5\times10^{12}$ dislocation pairs per cm^2. This value is considerably higher than the value $N=2.9\times10^{11}$ estimated from the energy stored during work hardening.[2] Our estimate of N is, however, somewhat too high, since the effective mass of a conduction electron in copper is probably greater than the mass of a free electron and the effective charge on an ion is greater than ϵ. These factors are difficult to estimate precisely, but they may reasonably be expected to reduce our estimate of N to about 10^{12}. In view of the artificial nature of our model and the many approximations made in the calculation, the agreement with the value derived from other evidence may be regarded as satisfactory.

In order to test our predictions for the angular dependence of the dislocation resistance, it is necessary to use pure single crystals and to carry out the experiments at low temperatures, where the main part of the resistance will be due to dislocation scattering. As mentioned in K, such experiments are at present in progress at the Physics Department of the Carnegie Institute of Technology.

We are indebted to various colleagues, and in particular to Mr. F. R. N. Nabarro, for much helpful comment and criticism. We also wish to thank Professor J. S. Koehler for valuable correspondence.

[5] N. F. Mott and H. Jones, *The Theory of the Properties of Metals and Alloys* (Oxford University Press, London, 1936), pp. 88, 294.

Theory of the "Forbidden" (222) Electron Reflection in the Diamond Structure

R. D. HEIDENREICH
Bell Telephone Laboratories, Murray Hill, New Jersey
(Received September 16, 1949)

The dynamical or wave-mechanical theory of electron diffraction is extended to include several diffracted beams. In the Brillouin zone scheme this is equivalent to terminating the incident crystal wave vector at or near a zone edge or corner. The problem is then one of determining the energy levels and wave functions in the neighborhood of a corner. The solution of the Schrödinger equation near a zone corner is a linear combination of Bloch functions in which the wave vectors are determined by the boundary conditions and the requirement that the total energy be fixed. This leads to a multiplicity of wave vectors for each diffracted beam giving rise to interference phenomena and is an essential feature of the dynamical theory.

At a Brillouin zone edge formed by boundaries associated with reciprocal lattice points S and G, the orthogonality of the unperturbed wave functions in conjunction with the periodic potential requires that another reciprocal lattice point λ be included in the calculation. The indices of λ must be such that $(\lambda_1\lambda_2\lambda_3)=(s_1s_2s_3)-(g_1g_2g_3)$. The perturbation at the zone edge results in non-zero amplitude coefficients Cg, Cs, and C_λ for the diffracted waves irrespective of whether or not the structure factor for λ, s or g vanishes. This is the basis of the explanation of the (222) reflection and since it arises through perturbation at a Brillouin zone edge or corner, the term "perturbation reflection" is advanced to replace the commonly used "forbidden reflection."

The octahedron formed by the (222) Brillouin zone boundaries exhibits an array of lines due to intersections with other boundaries to form edges. This array of lines is called a "perturbation grid" and the condition for the occurence of a (222) reflection is simply that the incident wave vector terminate on or near a grid line. Numerical intensity calculations are presented which show that a strong (222) can be accounted for by the dynamical theory.

An impedance network model is briefly discussed which may aid in qualitative considerations of the dynamical theory for the case of several diffracted waves.

INTRODUCTION

SINCE the discovery of electron diffraction some twenty years ago a number of examples of the occurrence of "forbidden" Bragg reflections have been reported. This, of course, has also been true for x-ray diffraction although not to the extent found in electron diffraction. An outstanding example has been the occurrence of a relatively strong (222) reflection from elements crystallizing with the diamond structure. It is the purpose of this paper to show that on the basis of the dynamical theory a (222) reflection is to be expected from diamond.

The term "forbidden" has generally been used to denote the appearance of Bragg reflections for which the structure factor is zero, thus leading to a zero intensity on the basis of the kinematic theory of diffraction. On the basis of the more general, dynamical theory, however, the term "forbidden" as applied to a reflection associated with a zero structure factor is not correct in the sense that zero intensity is no longer predicted. As will be seen, the term "perturbation reflection" would be a more accurate description applicable to the case of a zero structure factor in the dynamical theory.

It is perhaps advisable to consider very briefly the kinematic theory of diffraction and then mention some of the attempts to account for a perturbation reflection using the simple theory. The kinematic theory is actually a first-order approximation to the dynamical theory and amounts to assuming that the various diffracted and transmitted waves in a crystal are completely independent, i.e., no interactions. This approximation does not arise through the use of the Ewald construction in reciprocal space. The Ewald construction is a perfectly general method of predicting the *directions* of diffracted beams and is shown in Fig. 1; the approximation arises in the calculation of the intensities of these beams. The kinematic theory assumes that the amplitude of a wavelet scattered by an infinitesimal volume $dxdydz$ of the crystal is proportional to $Vdxdydz$ where V is the potential inside $dxdydz$. The amplitude of the wave scattered by the entire crystal in the direction RG is then

$$S=\int\int\int V(x,y,z)e^{2\pi i(g\cdot r)}dxdydz;$$

$$(g\cdot r)=g_1x+g_2y+g_3z, \quad (1)$$

with the integral being over the whole crystal. If V is expressed as a Fourier integral,

$$V=\int\int\int_{-\infty}^{+\infty} v_p e^{2\pi i(p\cdot r)}dp_1dp_2dp_3,$$

with $v_p=v_{p_1p_2p_3}$ and $(p\cdot r)=p_1x+p_2y+p_3z$, the scattered amplitude becomes

$$S=\int\int\int\left\{\int\int\int_{-\infty}^{+\infty} v_p e^{2\pi i(p\cdot r)}dp_1dp_2dp_3\right\}$$

$$\times e^{2\pi i(g\cdot r)}dxdydz. \quad (2)$$

In (2), the only terms of consequence are those for which the exponents vanish or $(p\cdot r)=-(g\cdot r)$ which requires that $g_1=-p_1$, $g_2=-p_2$, and $g_3=-p_3$. The amplitude S thus becomes proportional to v_p,

the Fourier coefficient of potential, and the intensity proportional to $|v_p|^2$. When the Ewald sphere touches some other reciprocal lattice point, say Q, the kinematic theory assumes that the intensities of the two beams are independent and are proportional to $|v_p|^2$ and $|v_q|^2$, respectively. As will be seen, this is not so in the dynamical theory where the weight of a reciprocal lattice point such as g is influenced by other points Q, etc., lying near or on the Ewald sphere.

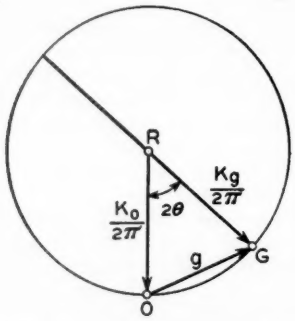

FIG. 1. Ewald construction in reciprocal space for diffracted wave vector. $K_0/2\pi=OR$ is incident crystal wave vector. Sphere of radius $|K_0/2\pi|$ centered at R touches reciprocal lattice point G giving rise to diffracted wave vector $K_g/2\pi=K_0+2\pi g/2\pi=RG$. If $|K_0|^2=|K_g|^2$, the Laue condition is fulfilled. θ is the Bragg angle. The plane of the paper can be viewed as a section through the Ewald sphere where it touches the reciprocal lattice point G so that K_0 and K_g are projected wave vectors.

It would appear at first sight that the interaction among reciprocal lattice points near or touching the Ewald sphere would be of the nature of a minor correction to the kinematic theory and not likely to produce a large effect. That a large correction to the kinematic theory is necessary is demonstrated in the electron diffraction patterns of Fig. 2. Figure 2(a) shows a very strong (222) Laue spot in the pattern from a single crystal of silicon. Over a narrow range of orientation, the (222) is the strongest reflection in the pattern. Figure 2(b) shows a Debye-Scherrer pattern obtained from an evaporated germanium film illustrating the high average intensity of the (222) ring. Figure 2(c) is a reflection pattern from a ground germanium surface in which the crystal size is sufficiently large to produce grainy rings. Local variations in the (222) intensity due to favorably oriented crystallites can be seen. From these and other patterns it is evident that any theory of the (222) reflection must account for a reasonably high intensity. It turns out that the interactions in the dynamical theory can be likened to resonance with coupled oscillators which may produce large responses even though the interaction or coupling is a first-order correction.

The (222) reflection in diamond (and other forbidden reflections) can be viewed as a result of a multiple reflection process. For example, a $(22\bar{2})$ could be considered as compounded from a $(11\bar{3})$ and a $(\bar{1}11)$. In general, compound reflections are those of indices (hkl) arising through diffracted beams of indices $(h_1k_1l_1)$, $(h_2k_2l_2)$ such that $h=h_2-h_1$, $k=k_2-k_1$, and $l=l_2-l_1$. This coupling or interaction condition relating the indices of primary and secondary reflections (to be considered here in detail) was recognized by Renninger[a] and used by him to explain observed (222) and (002) x-ray reflections in diamond. Renninger's conclusions are about the same as those arrived at in this paper, but the general treatment to be given here is considerably different and is based on the concept of Brillouin zones and perturbation of the energy levels at a zone corner. Raether[1] early attributed the forbidden (005) reflection observed in electron diffraction patterns of pyrites to dynamical coupling. Numerous other examples appear in the literature.

An alternative to the above discussion is the possibility that the accepted diamond lattice is not correct and that the structure factor is not zero for the (222). This alternative would seem preferable to the compound reflection theory in some cases. A weak (222) has been observed in x-ray patterns of diamond single crystals although apparently not from all crystals examined and is attributed to the configuration of the valence electrons. A (222) ring has not to the knowledge of the author been found in x-ray powder patterns of diamond, silicon, or germanium. However, this can be interpreted to mean that insufficient path length is available to build up the intensity as required in the dynamical theory. The contribution of the valence electrons to the electron scattering process is likely very small and not capable of accounting for the large intensities observed experimentally.

The conclusion would seem to be that a satisfactory explanation must be found in the dynamical theory. It has been demonstrated[2,3] that the wave-mechanical theory of electron diffraction is approximately correct and capable of explaining in a straightforward manner many experimental observations. The remainder of this paper will be concerned with demonstrating the capabilities of the theory.

I. GENERAL FORMULATION

Although the dynamical theory of electron diffraction has been developed[2] in terms of Brillouin zones, and the calculations carried out in detail for the simple case of a single diffracted wave, it seems

[a] M. Renninger, Zeits. f. Physik **106**, 141 (1937).
[1] H. Raether, Zeits. f. Physik **78**, 527 (1932).
[2] R. D. Heidenreich, J. App. Phys. **20**, 993 (1949).
[3] R. D. Heidenreich and L. Sturkey, J. App. Phys. **16**, 97 (1945). References to earlier work will be found in footnotes 1 and 2.

advisable to briefly state the problem and develop the general theory.

The problem to be considered here (the Laue case) assumes a slab of perfect crystal the front face of which is the x–y plane (Fig. 3). Incident from the left upon the front face is a monochromatic plane vacuum wave, $\varphi_v = A \exp[i(K_v \cdot r)]$, at approximately normal incidence. Inside the crystal the wave function is a linear combination of the various reflected and transmitted waves consistent with the total energy. At the back face, the crystal waves join up with vacuum transmitted and reflected waves. It is assumed that all waves travel in the positive direction of the z axis so that no reflected beams enter the vacuum from the front face.

Before undertaking the mathematical analysis, it is worth while to summarize the pertinent results of the mathematics to aid in understanding the fundamental features of the dynamical theory and to indicate the direction of the calculations. Since the kinematic theory is the first-order approximation to the dynamical theory, it is convenient to begin with the simplest case and show its relation to the more general one. This can be demonstrated schematically by considering the wave vectors in reciprocal space as shown in Fig. 4. In each illustration the wave vectors at the incident vacuum side, the crystal interior, and the exit vacuum side are shown. The incident vacuum wave vector K_v ($|K_v| = 2\pi/\lambda$) is the same in each case. If the crystal is oriented such that the Bragg condition is not realized for any crystal plane and if the inner potential is neglected, then there will be an incident crystal wave vector K_0 and a transmitted wave vector K_t, both of which are the same as K_v as shown in Fig. 4(a). If the incident vacuum wave is a plane wave, then the crystal wave and the transmitted wave are also plane waves joining at the crystal-vacuum surfaces. If now the incident crystal wave vector K_0 terminates on or near a Brillouin zone boundary, there will be a diffracted wave vector $K_g = K_0 + 2\pi g$ which can be drawn in either of the ways shown in Fig. 4(b). There is a transmitted vacuum and diffracted vacuum wave in this case. Figure 4(b) represents the kinematic case in which the waves are still plane waves. If K_0 has its terminus on the Brillouin zone boundary, then the Laue condition $|K_0|^2 = |K_g|^2$ is realized.

As will be seen later, the crystal waves which are solutions of the Schrödinger equation for the periodic potential inside the crystal are Bloch functions which have the form

$$\varphi_j = \sum_l C_l^j \exp[i(K_l^j \cdot r)],$$

with $K_l^j = K_0^j + 2\pi l$ and C_l^j the amplitude coefficient. When K_0 terminates on a Brillouin zone boundary, it turns out that the wave function inside the crystal is a linear combination of two Bloch functions φ_0 and φ_1. There are consequently two incident crystal wave vectors K_0^0 and K_0^1 and two diffracted wave vectors K_g^0 and K_g^1 since φ_0 and φ_1 must have the same energy. K_0^0 and K_g^0 form one Bloch function while K_0^1 and K_g^1 form the other. The boundary conditions require that the crystal wave vectors have tangential components which are equal to that of the incident vacuum wave vector or differ from it by the tangential component of a reciprocal lattice vector. Consequently, K_0^0 and K_0^1 have equal tangential components as do K_g^0 and K_g^1 with the normal components differing by a vector ΔK normal to

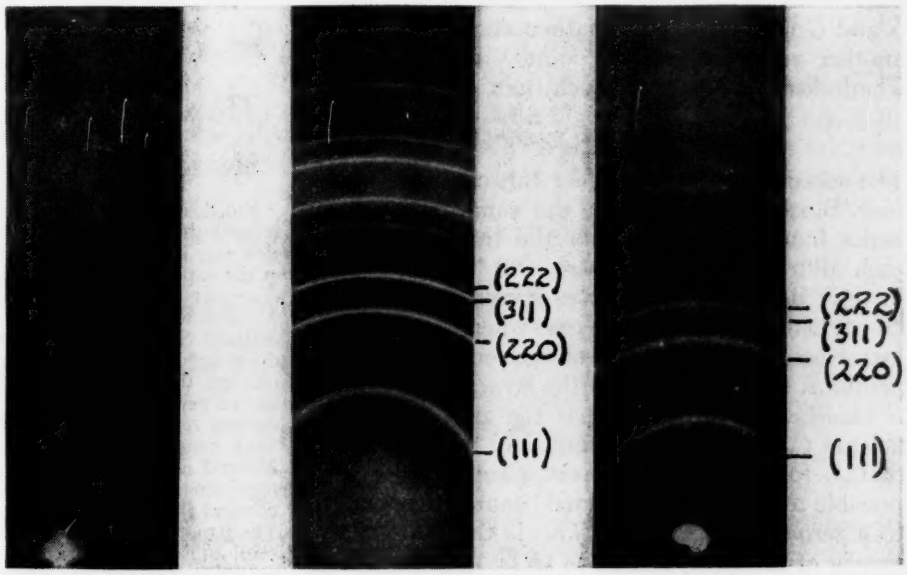

FIG. 2. Examples of the "forbidden" (222) reflection in electron diffraction patterns from silicon and germanium (40-kv electrons). (a) Strong (222) Laue spot from an etched single crystal of silicon. (Courtesy of K. H. Storks.) (b) Transmission pattern from an evaporated germanium film on a silica substrate. (c) Reflection pattern from a ground germanium surface showing grainy rings.

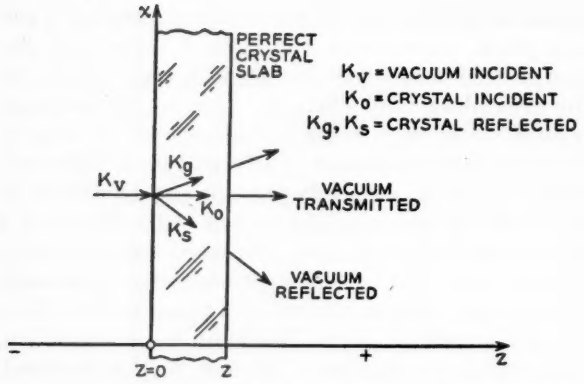

FIG. 3. Representation of the Laue case of the dynamical theory where no radiation emerges from same surface into which it enters. Electrons are incident from the left onto the front surface of a crystal slab bounded by the planes $z=0$ and $z=z$. The various transmitted and diffracted wave vectors are shown. In the case to be considered in detail, K_0 is approximately along the $[1\bar{1}0]$ crystal axis of germanium (Fig. 6).

the surface as shown in Fig. 4(c). K_g^0 and K_g^1 are out of phase at the incident surface so that the amplitude of the diffracted wave is zero at the surface and increases with penetration into the crystal.

The essential feature of the dynamical theory is the multiplicity of wave vectors such as K_g^0 and K_g^1 associated with a single diffracted wave. It is here that the interference phenomena arise with ΔK being the beat wave vector. The multiplicity of diffracted wave vectors can be viewed as multiple refraction (the crystal is doubly refracting in the case of Fig. 4(c)).

The extension to any number of diffracted waves is evident. The incident crystal wave vector may terminate at a Brillouin zone edge or corner and give rise to several diffracted waves. At a zone edge, however, formed by reciprocal lattice points S and G (Fig. 4(c)), the mathematics require that another reciprocal lattice point λ be considered. The indices of λ must be such that

$$(\lambda_1\lambda_2\lambda_3)=(s_1s_2s_3)-(g_1g_2g_3).$$

The solution in the crystal for this case consists of four Bloch functions with the same energy and hence four wave vectors for the transmitted and each diffracted beam. There will now be three distinct beat wave vectors as shown in Fig. 4(d). Of particular interest is the case when the structure factor associated with one of the reciprocal lattice points S, G, or λ is zero. If the structure factor for S vanishes, it turns out that the amplitude coefficients C_s^i do not vanish and may be comparable to C_g^i, for example. Thus, at a zone corner it is possible to produce a diffracted beam corresponding to a zero structure factor. This is the basis of the theory of the (222) reflection to be advanced. The following sections are concerned with the mathematical analysis leading to the calculation of intensities. The procedure is that commonly used in perturbation theory and is concerned with determining the energy levels at a corner, the amplitude coefficients, and finally the intensities.

A. Crystal Wave Functions

The general motion of an electron of total energy E in a region where the potential is $V(x, y, z)$ is described by the Schrödinger equation,

$$H\varphi=E\varphi \text{ with } H\equiv-\frac{h^2}{8\pi^2m}\nabla^2+V(x,y,z).$$

In a perfect crystal, the potential can be repre-

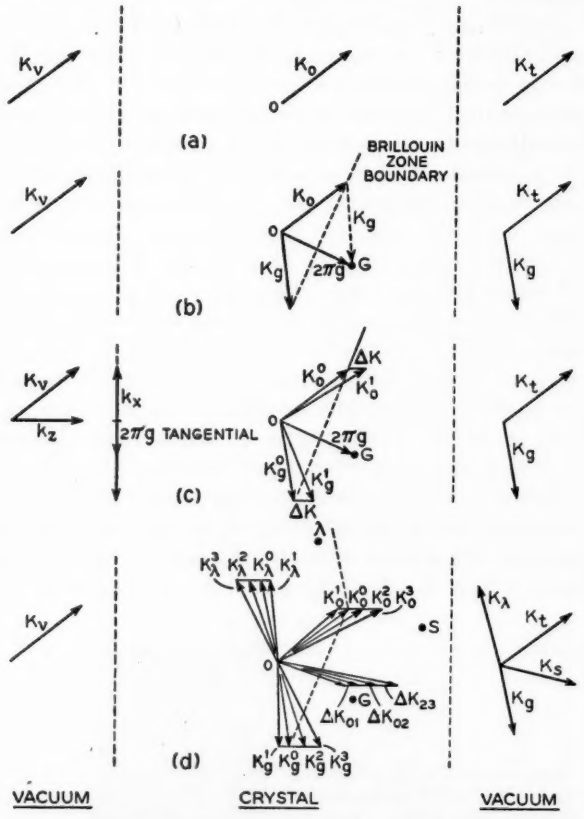

FIG. 4. Relations among wave vectors in reciprocal space for several approximations in diffraction theory. The representation may be taken as projections of the vectors onto the plane of the paper. The incident plane wave is from the left and the emergent plane waves on the right. (a) Zero approximation. No interaction with crystal. (b) Kinematic or first approximation. Single diffracted wave vector $K_g=K_0+2\pi g$. The diffracted wave in the crystal is a single plane wave. (c) Dynamical theory, single diffracted beam. The diffracted wave in the crystal now consists of two plane waves with wave vectors K_g^0 and K_g^1. The wave function in the crystal is a linear combination of two Bloch waves, one with wave vectors K_0^0 and K_g^0 and the other width K_0^1 and K_g^1. The boundary requirement for the tangential components is shown. (d) Dynamical theory, three diffracted beams (Brillouin zone edge). The structure factor of any one of the three reflections may be zero and still give rise to a non-zero amplitude for that reflection. (In (c) and (d), the beat wave vectors. ΔK, are normal to the crystal surface.)

sented by a Fourier series[b]

$$V(x, y, z) = -(V_0 + \sum_g{}' v_g e^{2\pi i(g\cdot r)}), \qquad (4)$$

where $g = g_1 b_1 + g_2 b_2 + g_3 b_3$ is a reciprocal lattice vector and $v_g \equiv v_{g_1 g_2 g_3}$ for brevity. The prime on the summation over the triple indices means that $g_1 = g_2 = g_3 = 0$ is excluded since it is written as V_0 (the inner potential).

In field-free space, $V = V_0$, the solution of the equation

$$H^{(0)}\varphi_j^{(0)} = E_j^{(0)}\varphi_j^{(0)} \text{ with } H^{(0)} \equiv \frac{-h^2}{8\pi^2 m}\nabla^2 + V_0 \qquad (5)$$

is a superposition of plane waves. Assume that the solution of (3) can be expanded in terms of the unperturbed wave functions φ_j^0 of (5) or

$$\varphi = \sum_j c_j \varphi_j^{(0)}, \qquad (6)$$

with the c_j's to be determined. Substituting (6) into (3) and using (5) obtain

$$\sum_j (V\varphi_j^{(0)} + \beta_j \varphi_j^{(0)}) C_j = 0, \qquad (7)$$

where $\beta_j = (E_j^{(0)} - E)$ and

$$E_j^{(0)} = h^2 |K_j|^2 / 8\pi^2 m.$$

Multiplying (7) on the left by $\varphi_m{}^{0*}$ (the complex conjugate of $\varphi_m{}^0$) and integrating over the unit cell, Ω,

$$\sum_j \left\{ \int_\Omega \varphi_m{}^{(0)*} V \varphi_j^{(0)} d\gamma + \beta_j \int_\Omega \varphi_m{}^{(0)*} \varphi_j^{(0)} d\gamma \right\} C_j = 0. \qquad (8a)$$

If the expression (4) for the potential is placed in (8a) and if the subscripts j and m of (8a) are identified with reciprocal lattice vectors,[c] there is obtained upon integration

$$\beta_m \quad C_m = \sum_{j,\, j \neq m} v_{m-j} \cdot C_j. \qquad (8b)$$

The Fourier coefficient v_{m-j} occurs in (8b) as a result of the orthogonality of the unperturbed wave functions $\varphi_j^{(0)}$. Equation (8b) is the desired relation between the amplitude coefficients, the Fourier coefficients and the energy and is sometimes called the "dispersion equation." In (8b),

$$\beta_j \equiv \left(\frac{h^2 |K_j|^2}{8\pi^2 m} - E \right)$$

rather than $[|K_j|^2 - (8\pi^2 m/h^2)E]$ as employed in reference 2.

Suppose now that the Ewald sphere passes in the neighborhood of reciprocal lattice points g and s. In (8b), j and m then take on the values, 0, g, and s. The Fourier coefficient v_{m-j} will take on not only the values v_g, $v_{-g}{}^*$, v_s, $v_s{}^*$ but also v_{s-g} and $v_{s-g}{}^*$. If $\lambda = s - g$, C_λ must be taken into account if the reciprocal lattice point λ lies near the Ewald sphere. The set of Eqs. (8) for the case of amplitudes C_0, C_g, C_s, and C_λ with $\lambda = s - g$ then becomes

$$\begin{bmatrix} \beta_0 & -v_g{}^* & -v_s{}^* & -v_\lambda{}^* \\ -v_g & \beta_g & -v_\lambda{}^* & -v_{\lambda-g}{}^* \\ -v_s & -v_\lambda & \beta_s & -v_g \\ -v_\lambda & -v_{\lambda-g} & -v_g{}^* & \beta_\lambda \end{bmatrix} \begin{Bmatrix} C_0 \\ C_g \\ C_s \\ C_\lambda \end{Bmatrix} = 0. \qquad (9)$$

The roots of the secular determinant[d] of (9) are the eigenvalues from which the possible crystal wave vectors and energy gaps are determined. The amplitude coefficients C_g, C_s, C_λ are obtained from (9) in terms of C_0, the Fourier coefficients and the eigenvalues. The solution is thus a one-electron Bloch function reducing to a plane wave when the Fourier coefficients of potential approach zero.

There will be one Bloch function for each root of the secular determinant (9) which, for a given K_0, will have different energies corresponding to the different roots. It is possible to choose a set of distinct vectors $K_0{}^0$, $K_0{}^1$, $K_0{}^2$, and $K_0{}^3$ (one for each root of the secular determinant) which have the same tangential components as the incident vacuum wave vector and correspond to the same total energy. (The total energy is fixed in a diffraction experiment.) With the tangential components fixed, the normal components are adjusted to satisfy the requirement for fixed E so that $K_0{}^1$, for example, can be written

$$K_0{}^1 = K_0{}^0 + \Delta K_{01},$$

where ΔK_{01} is normal to the surface. The various wave vectors and ΔK's are illustrated in Fig. 4(d).

A Bloch solution exists for each allowed wave vector $K_0{}^0$, $K_0{}^1$, etc., so that the possible solutions are

$$\begin{aligned} \varphi_0 &= \sum_{p=0,\, g,\, s,\, \lambda} C_p{}^0 \exp[i(K_p{}^0 \cdot r)], \\ &\cdots \\ \varphi_3 &= \sum_{p=0,\, g,\, s,\, \lambda} C_p{}^3 \exp[i(K_p{}^3 \cdot r)] \end{aligned} \qquad (10)$$

and the crystal wave function is a linear combination of such solutions

$$\psi_e = a_0\varphi_0 + a_1\varphi_1 + a_2\varphi_2 + a_3\varphi_3, \qquad (11)$$

where the a's are coefficients to be determined by the boundary conditions.

[b] Reference 1, Appendix I.

[c] If K_0 denotes the incident wave vector and m a reciprocal lattice vector, then $K_m = K_0 + 2\pi m$ is a diffracted wave vector.

[d] The matrix in (9) is Hermitian and hence the secular determinant possesses four real roots.

From the linear combination of Bloch functions (11), the transmitted and diffracted waves associated with K_0^0, K_0^1, K_0^2 and K_0^3 can be sorted out according to the subscripts and written separately as

$$\begin{aligned}\zeta_t &= \sum_{l=0,1,2,3} a_l C_0^l \exp[i(K_0^l\cdot r)],\\ &\cdots\cdots\cdots\cdots\\ \zeta_\lambda &= \sum_{l=0,1,2,3} a_l C_\lambda^l \exp[i(K_\lambda^l\cdot r)].\end{aligned} \tag{12}$$

Here ζ_t is the transmitted wave amplitude and ζ_g, ζ_s, ζ_λ are diffracted amplitudes. In this case a diffracted wave, say ζ_g, is now characterized by four wave vectors (Fig. 4(d)) rather than the single one of the kinematic theory, and consists of a series of terms, one from each Bloch function.

The amplitude coefficients, a, in Eq. (12) are determined by the boundary conditions at the incident crystal surface ($z=0$). If $A\exp[i(K_v\cdot r)]$ denotes the incident plane wave, then the following equations apply at $z=0$.

$$\begin{bmatrix} C_0^0 & C_0^1 & C_0^2 & C_0^3\\ C_g^0 & C_g^1 & C_g^2 & C_g^3\\ C_s^0 & C_s^1 & C_s^2 & C_s^3\\ C_\lambda^0 & C_\lambda^1 & C_\lambda^2 & C_\lambda^3 \end{bmatrix} \begin{Bmatrix} a_0\\ a_1\\ a_2\\ a_3 \end{Bmatrix} = \begin{Bmatrix} A\\ 0\\ 0\\ 0 \end{Bmatrix}. \tag{13}$$

Equations (13) are immediately obtained from (12) at $z=0$ where $\zeta_t=A$ and $\zeta_g=\zeta_s=\zeta_\lambda=0$. The exponentials do not occur since the tangential components of all wave vectors are equal or differ by a reciprocal lattice vector at $z=0$. The same boundary conditions apply at the exit surface but need not be considered since all the coefficients and amplitudes are determined at the incident surface and by the potential inside the crystal.

B. Intensities

Having obtained explicit wave functions (12) for the transmitted and diffracted beams, the calculation of the intensities is straightforward. If I_n is the intensity associated with the indices n, then

$$\begin{aligned} I_n &= \zeta_n\zeta_n^*\\ &= \sum_{l,s=0,1,2,3} \{a_l a_s^* C_n^l C_n^{s*} \exp[i(K_n^l - K_n^s)\cdot r]\\ &\quad + a_l^* a_s C_n^{l*} C_n^s \exp[-i(K_n^l - K_n^s)\cdot r]\}. \end{aligned} \tag{14a}$$

Since the coefficients of the exponentials are complex conjugates, the intensity is real and (14a) can be simplified and written

$$\begin{aligned} I_n &= |a_0 C_n^0 + a_1 C_n' + a_2 C_n^2 + a_3 C_n^3|^2\\ &\quad - 2\sum_{\substack{l,s=0,1,2,3\\ l\neq s}} a_l a_s^* C_n^l C_n^{s*} \sin^2 \tfrac{1}{2}(k_0^l - k_0^s)_z z, \end{aligned} \tag{14b}$$

where the term $l=s$ has been removed from the summation and $(k_0^l - k_0^s)_z$ is the z or normal component of $K_0^l - K_0^s$.

The fine structure of a Laue spot can be obtained by evaluating the intensities for each of the wave vectors K_n^0, K_n^1, etc. The angular spread between K_n^0 and K_n^1, etc. is of the order of $\Delta E/E$ where ΔE is the energy gap at the zone boundary and is about 10^{-4} rad. for 40-kv electrons. Such a procedure may be necessary in interpreting diffraction patterns where high resolution is obtained.

The first term on the right of Eq. (14b) vanishes for all but the transmitted beam as seen from (13). The intensity of a diffracted beam thus consist of a sum of $\sin^2$ terms such as is obtained in treating interference phenomena in light optics. The arguments of the $\sin^2$ terms in (14b) can be written $\frac{1}{2}(k_0^l - k_0^s)_z z = \frac{1}{2}|\Delta K_{sl}|z$ where ΔK_{sl} is determined from the secular roots[5] and is the beat wave number or "anpassung" in Bethe's original theory.[4]

In using (14b) it must be remembered that the following assumptions are incorporated:

(a) A perfect crystal in which the potential is represented by a Fourier series.

(b) An abrupt discontinuity in potential at the crystal-vacuum interface. Laue[5] has shown that this assumption is valid for fast electrons.

(c) No attenuation due to inelastic scattering. The possibility of including inelastic scattering into the dynamical theory using Slater's[6] complex potential method has yet to be investigated.

II. EQUIVALENT CIRCUIT FOR ELECTRON DIFFRACTION

The foregoing discussion is equivalent to an extension of Bethe's treatment,[4] the difference being chiefly one of terminology and the explicit use of energy levels as a means of determining the permissible crystal wave vectors. In the Brillouin zone scheme, the Laue conditions are equivalent to requiring that the incident wave vector, K_0, terminate on a Brillouin zone boundary. The existence of one or more diffracted beams is determined by the details of the energy discontinuities at the zone boundary. A single energy gap allows one and only one diffracted beam and is realized when the terminus of K_0 is not near a zone edge or corner. The multiple energy gap arising in the vicinity of a zone corner gives rise to two or more diffracted beams; in the case of Eq. (9) there will be four energy levels at the corner and three diffracted beams. The number of diffracted beams is always one less than the number of roots of the secular determinant. However, the relative intensities of

[5] For example: If E_0 and E_1 are two of the secular energy roots, then ΔK_{01} is determined by $E_0(K_0^0)=E_1(K_0^1)=E_1(K_0^0+\Delta K_{01})$. $|\Delta K_{01}|^2$ can be neglected as can $(\Delta K_{01}\cdot g)$ for most approximations.

[4] H. A. Bethe, Ann. d. Physik **87**, 55 (1928).

[5] M. von Laue, Phys. Rev. **37**, 53 (1931).

[6] J. C. Slater, Phys. Rev. **51**, 74 (1937).

the possible beams is not simply related to the magnitudes of the energy gaps at the boundary. A detailed calculation is necessary to obtain the intensities as will be demonstrated in a later section. Although the use of Eqs. (9), (13), and (14b) is sufficient to determine the energy levels at a zone corner and the intensities of the diffracted beams, the model is strictly formal and does not appeal to the intuition. For this reason, the use of a coupled oscillator model in the form of an equivalent circuit will be mentioned which presents a relatively simple physical model for the dynamical theory.

The impedance network model for the diffraction problem is obtained directly from the energy matrix (9) for the specific case of a periodic potential and is not as general as that employed by Kron.[7] If the energy matrix (9) is viewed as an electrical network matrix whose meshes contain inductance and capacitance, the off-diagonal terms represent the elastances of the coupling condensers. If the correspondence is carried out it is found that the Fourier coefficients of potential in (9) behave as couplings between the various beams which correspond to the meshes of the network. The condition for resonance between two meshes (identical natural frequencies) is just the Laue condition in the diffraction case.

A network can be drawn for the matrix (9) only if one or more of the Fourier coefficients vanish. If $v_{\lambda-g}=0$, the network is that shown in Fig. 5(a). If $v_\lambda=0$, in addition, where λ might be (222), the network is that shown in Fig. 5(b). Mesh λ is no longer directly coupled to the incident or driver mesh 0 but still may be driven through the coupling condensers v_g and v_s, providing that $\lambda=s-g$. If $\lambda=(222)$, then a possibility is $g=(\bar{1}\bar{1}1)$ and $s=(113)$. If mesh g is detuned sufficiently that its response can be neglected, the matrix of the system can be reduced in order from four to three. This reduction in order through neglecting the response of one mesh (or beam) greatly facilitates the calculation of intensities when such an approximation is valid as will be seen. No computational advantages are gained from the network analogy unless a network analyzer can be used. A more detailed consideration of the analogy is not justified at this time.

III. (222) INTENSITIES

In order to compute the diffracted intensities, it is necessary to know the details of the reciprocal lattice geometry and the Brillouin zone corners. All the numerical calculations in this paper will be made for germanium ($a_0=5.65$A), but either diamond or silicon would do as well. Since the (222) reflection is of primary interest, it is convenient to consider a plane section of the reciprocal lattice normal to the $[1\bar{1}0]$ zone axis as shown in Fig. 6. The reciprocal lattice points are located to scale and the Brillouin zone boundaries drawn as the perpendicular bisectors of the respective reciprocal lattice vectors.[8] The zone boundaries of interest are parallel to the $[1\bar{1}0]$ crystal axis. The edges influencing the $(22\bar{2})$ reflection are then those such as A, B, C, D of Fig. 6. In the first example to be considered, the incident crystal wave vector, K_0, is drawn from the origin so that it terminates at the $(111)|(22\bar{2})$ zone corner.[f] $K_0{}^p/2\pi$ is the projection of the incident crystal wave vector on the plane of the paper (containing the labeled reciprocal lattice points). The third reciprocal lattice point involved must be such that $\lambda=s-g$. Thus, if $g\equiv(111)$, $s\equiv(22\bar{2})$, then $\lambda=(11\bar{3})$. If a circle of radius $|K_0{}^p/2\pi|$ is drawn with C as center, it will be seen that the reciprocal lattice point $\lambda=(11\bar{3})$ lies some distance off the circle. The point (220) lies somewhat nearer the circle but does not interact since the indices do not satisfy the condition $\lambda=s-g$. Since $(11\bar{3})$ is considerably off from the Laue condition, its amplitude is assumed sufficiently weak that it can be neglected as a first approximation. Neglecting C_λ and setting $v_s=0$ in (9) gives, for point C,

$$\begin{bmatrix} \beta_0 & -v_g^* & 0 \\ -v_g & \beta_g & -v_\lambda^* \\ 0 & -v_\lambda & \beta_s \end{bmatrix} \begin{Bmatrix} C_0 \\ C_g \\ C_s \end{Bmatrix} = 0. \qquad (15)$$

Since $|K_g|^2=|K_s|^2=|K_0|^2$, $\beta_0=\beta_g=\beta_s$, and the

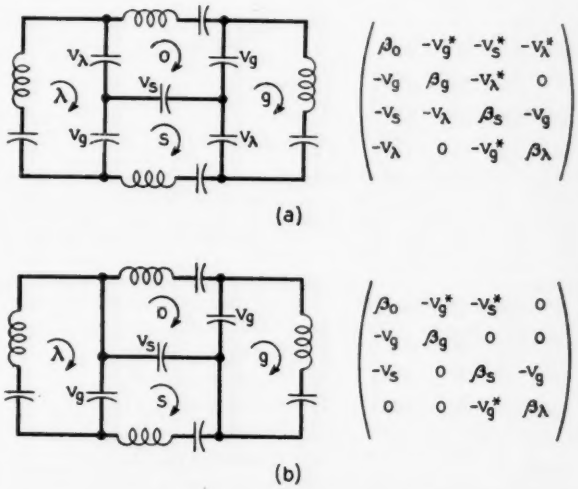

FIG. 5. Equivalent networks for dynamical theory based on the matrix (9) for the periodic potential. (a) $v_{\lambda-g}=0$. (b) $v_{\lambda-g}=v_\lambda=0$. The coupling condensers are labeled with the Fourier coefficients to which they correspond. Mesh 0 is taken to be the "driver." In (b), mesh λ corresponds to the case of the (222) reflection which responds through the couplings v_s and v_g even though not directly coupled to the driver.

[7] G. Kron, Phys. Rev. 67, 39 (1945).

[8] See L. Brillouin, *Wave Propagation in Periodic Structures* (McGraw-Hill Book Company, Inc., New York, 1946).

[f] The symbol $(h_1k_1l_1)|(h_2k_2l_2)$ will be used to denote the intersection of zone boundaries $(h_1k_1l_1)$ and $(h_2k_2l_2)$.

secular determinant yields the cubic

$$\beta_0^3-\beta_0|v_\lambda|^2-\beta_0|v_g|^2=0, \tag{16}$$

with the roots $\beta_0{}^0=0$, $\beta_0{}^1=+(|v_g|^2+|v_\lambda|^2)^{\frac{1}{2}}=+\Delta E$, $\beta_0{}^2=-(|v_g|^2+|v_\lambda|^2)^{\frac{1}{2}}=-\Delta E$. The energies are then[g]

$$E^0=h^2|K_0|^2/8\pi^2m,$$

$$E^1=\frac{h^2|K_0|^2}{8\pi^2m}-(|v_g|^2+|v_\lambda|^2)^{\frac{1}{2}}=\frac{h^2|K_0|^2}{8\pi^2m}-\Delta E, \tag{17}$$

$$E^2=\frac{h^2|K_0|^2}{8\pi^2m}+(|v_g|^2+|v_\lambda|^2)^{\frac{1}{2}}=\frac{h^2|K_0|^2}{8\pi^2m}+\Delta E.$$

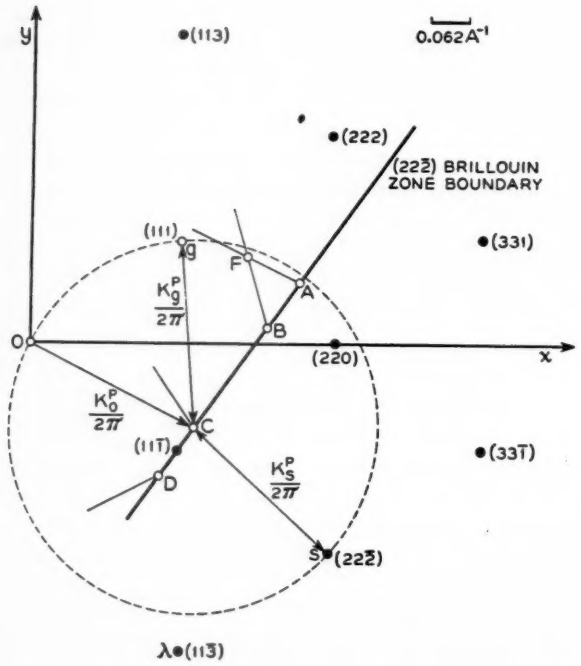

FIG. 6. Plane section through germanium reciprocal lattice drawn to scale with Miller indices of reciprocal lattice points given. The plane of the paper is normal to the [1$\bar{1}$0] crystal axis. Brillouin zone edges A, B, C, and D are all common to the (22$\bar{2}$) zone boundary. $K_0{}^p/2\pi$ is the projection of the incident crystal wave vector on the plane of the paper and terminates at the (111)|(22$\bar{2}$) corner. The circle of radius $|K_0{}^p/2\pi|$ passes through reciprocal lattice points (22$\bar{2}$) and (111) but misses (11$\bar{3}$). The edges are as follows

A....(113)|(22$\bar{2}$). Couples with (331).
B....(331)|(22$\bar{2}$). Couples with (113).
C....(111)|(22$\bar{2}$). Couples with (11$\bar{3}$).
D....(11$\bar{3}$)|(22$\bar{2}$). Couples with ($\bar{1}\bar{1}\bar{1}$).
F....(113)|(331). Couples with (22$\bar{2}$).

The permissible incident wave vectors are found by equating the roots (17) with $K_0{}^1=K_0{}^0+\Delta K_{01}$, $K_0{}^2=K_0{}^0+\Delta K_{02}$ so that[h]

$$\Delta K_{01}\simeq K_0{}^1-K_0{}^0\simeq\frac{\Delta E}{2}\frac{8\pi^2m}{h^2K_0}=\frac{\pi\Delta E}{\lambda E^{(0)}},$$

$$\Delta K_{02}\simeq K_0{}^2-K_0{}^0\simeq-\frac{\Delta E}{2}\frac{8\pi^2m}{h^2K_0}=-\frac{\pi\Delta E}{\lambda E^{(0)}}, \tag{18}$$

$$\Delta K_{12}\simeq K_0{}^2-K_0{}^1\simeq-\Delta E\frac{8\pi^2m}{h^2K_0{}^0}=-\frac{2\pi\Delta E}{\lambda E^{(0)}}.$$

It is not necessary to calculate the crystal wave functions explicitly when using (14b) to compute the intensities. The boundary Eqs. (13) are for this case ($a_3=0$),

$$\begin{Bmatrix} C_0{}^0 & C_0{}^1 & C_0{}^2 \\ C_g{}^0 & C_g{}^1 & C_g{}^2 \\ C_s{}^0 & C_s{}^1 & C_s{}^2 \end{Bmatrix}\begin{Bmatrix} a_0 \\ a_1 \\ a_2 \end{Bmatrix}=\begin{Bmatrix} A \\ 0 \\ 0 \end{Bmatrix}.$$

Writing $C_g=\alpha_gC_0$, $C_s=\alpha_sC_0$, etc., the constants a_0, a_1, and a_2 are found to be

$$a_0=A\frac{\alpha_s{}^1\alpha_g{}^2-\alpha_s{}^2\alpha_g{}^1}{|c|}C_0{}^1C_0{}^2;$$

$$a_1=-A\frac{(\alpha_s{}^0\alpha_g{}^2-\alpha_s{}^2\alpha_g{}^0)}{|c|}C_0{}^0C_0{}^2; \tag{19}$$

$$a_2=A\frac{(\alpha_s{}^0\alpha_g{}^1-\alpha_s{}^1\alpha_g{}^0)}{|c|}C_0{}^0C_0{}^1,$$

with

$$|c|=C_0{}^0C_0{}^1C_0{}^2[(\alpha_s{}^1\alpha_g{}^2-\alpha_s{}^2\alpha_g{}^1)-(\alpha_s{}^0\alpha_g{}^2-\alpha_s{}^2\alpha_g{}^0)+(\alpha_s{}^0\alpha_g{}^1-\alpha_s{}^1\alpha_g{}^0)].$$

The α's are easily found from (15) to be

$$\alpha_g=\frac{\beta_sv_g-\beta_0v_\lambda{}^*}{\beta_s\beta_g-v_\lambda{}^*(v_g{}^*+v_\lambda)};\quad \alpha_s=-\frac{\beta_g\beta_0-v_g(v_g{}^*+v_\lambda)}{\beta_g\beta_s-v_\lambda{}^*(v_g{}^*+v_\lambda)}.$$

Since $\beta_0=\beta_g=\beta_s$, there is finally obtained the relations

$$\begin{aligned} &\alpha_g{}^0=0;\quad(\beta_0{}^0=0), && \alpha_s{}^0=-v_g/v_\lambda{}^*,\\ &\alpha_g{}^1=\beta_0{}^1/v_g{}^*, && \alpha_s{}^1=v_\lambda/v_g{}^*,\\ &\alpha_g{}^2=\beta_0{}^2/v_g{}^*=-\alpha_g{}^1, && \alpha_s{}^2=\alpha_s{}^1. \end{aligned} \tag{20}$$

By (19) and (20)

$$a_0a_1{}^*=-\frac{1}{2}\frac{|A|^2}{C_0{}^0C_0{}^{1*}}\frac{\alpha_s{}^1\alpha_s{}^{0*}}{|\alpha_s{}^1-\alpha_s{}^0|^2},$$

$$a_0a_2{}^*=-\frac{1}{2}\frac{|A|^2}{C_0{}^0C_0{}^{2*}}\frac{\alpha_s{}^1\alpha_s{}^{0*}}{|\alpha_s{}^1-\alpha_s{}^0|^2}, \tag{21}$$

$$a_0a_2{}^*=+\frac{1}{4}\frac{|A|^2}{C_0{}^1C_0{}^{2*}}\frac{|\alpha_s{}^0|^2}{|\alpha_s{}^1-\alpha_s{}^0|^2},$$

with $\alpha_0{}^*\alpha_1=(\alpha_0\alpha_1{}^*)^*$ etc. The relative intensities

[g] Since $\beta_0\equiv[(h^2|K_0|^2/8\pi^2m)-E]\equiv[E^{(0)}-E]$.

[h] The approximation $(\Delta K\cdot K)\cong|\Delta K||K|$ is employed for the case of nearly normal incidence where the direction cosines of the incident wave vector is nearly unity. Otherwise, the expressions (18) will contain the direction cosines in the denominator.

are found from (14b) to be

$$I_{(22\bar{2})}=\frac{|\alpha_s{}^1|^2|\alpha_s{}^0|^2}{|\alpha_s{}^1-\alpha_s{}^0|^2}[4\sin^2\tfrac{1}{2}(\Delta K_{01}z)-\sin^2\tfrac{1}{2}(\Delta K_{12}z)],$$

$$I_{(111)}=\frac{|\alpha_g{}^1|^2|\alpha_s{}^0|^2}{|\alpha_s{}^1-\alpha_s{}^0|^2}\sin^2\tfrac{1}{2}(\Delta K_{12}z), \tag{22a}$$

$$I_t=1+\frac{2(\alpha_s{}^1\alpha_s{}^{0*}+\alpha_s{}^{1*}\alpha_s{}^0)}{|\alpha_s{}^1-\alpha_s{}^0|^2}\sin^2\tfrac{1}{2}(\Delta K_{01}z)-\frac{|\alpha_s{}^0|^2}{|\alpha_s{}^1-\alpha_s{}^0|^2}\sin^2\tfrac{1}{2}(\Delta K_{12}z).$$

Introducing numerical values for the Fourier coefficients (Appendix I), the final result is

$$\begin{aligned}I_{(22\bar{2})}&=0.23[4\sin^2\pi z/z_0-\sin^2\pi 2z/z_0],\\ I_{(111)}&=0.59\sin^2\pi 2z/z_0,\\ I_t&=1-0.90\sin^2\pi z/z_0-0.37\sin^2\pi 2z/z_0,\end{aligned} \tag{22b}$$

where, by (18),

$$z_0=\frac{2\lambda E^{(0)}}{\Delta E}(\Delta E=(|v_g|^2+|v_\lambda|^2)^{\frac{1}{2}}=10.5\text{ volts}).$$

Figure 7 shows a plot of the intensities (22b) as a function of penetration in the crystal, z, for 40-kv electrons ($\lambda=0.061$A). The intensities averaged over thickness or path length in the crystal are found by setting $\sin^2=\frac{1}{2}$ in (22b) or $\langle I_{(111)}\rangle_{Av}=0.30$ and $\langle I_{(22\bar{2})}\rangle_{Av}=0.32$. Hence, not only is there a $(22\bar{2})$ reflection at the $(111)|(22\bar{2})$ zone corner, but the intensity is about the same as that of the (111) intensity. It will be noted that the intensity of the reflection builds up more slowly than does that of the allowed reflection.

The energy as a function of wave vector along the vector K_0 to $(111)|(22\bar{2})$ is of interest. Returning to (15) with $\beta_0\neq\beta_g\neq\beta_s$ and writing $\beta_g=\beta_0+\Delta_g$ and $\beta_s=\beta_0+\Delta_s$ where

$$\Delta_g\equiv(h^2/8\pi^2m)(|K_g|^2-|K_0|^2)$$

and

$$\Delta_s\equiv(h^2/8\pi^2m)(|K_s|^2-|K_0|^2)$$

the secular determinant is ($g\equiv(111)$, $s\equiv(22\bar{2})$, $\lambda\equiv(11\bar{3})$ as before)

$$\begin{vmatrix}\beta_0 & -v_g^* & 0\\ -v_g & \beta_0+\Delta_g & -v_\lambda^*\\ 0 & -v_\lambda & \beta_0+\Delta_s\end{vmatrix}=0 \tag{23}$$

yielding a cubic. The roots are most conveniently evaluated by numerical calculation for various values of $|K_0|^2$. The deviations, Δ_g and Δ_s, can be found from Fig. 6 by measuring the projections of K_0, K_g, and K_s and computing the differences of the squares. The energies so obtained are in the form of that for a free electron, $E^{(0)}=h^2|K_0|^2/8\pi^2m$, plus a correction term. Two of the roots possess a positive correction and one a negative correction. A plot of energy *versus* wave number along K_0 is shown in Fig. 8 using the reduced zone scheme.

If the amplitude coefficient C_λ ($\lambda\equiv(11\bar{3})$) had not been neglected, the secular determinant at point C would have been

$$\begin{vmatrix}\beta_0 & -v_g^* & 0 & -v_\lambda^*\\ -v_g & \beta_g & -v_\lambda^* & -v_{\lambda-g}^*\\ 0 & -v_\lambda & \beta_s & -v_g\\ -v_\lambda & -v_{\lambda-g} & -v_g^* & \beta_\lambda\end{vmatrix} \tag{24}$$

rather than (23). The Fourier coefficient $v_{\lambda-g}=v_{(00\bar{4})}$ now occurs as a coupling between meshes g and λ. The plot of energy *vs.* wave number $|K_0|$ (along K_0) to the corner will now appear as in Fig. 9 as compared to Fig. 8. The retention of C_λ has increased the perturbation.

The cubic approximation demonstrated for point C of Fig. 6 can be applied at corners A, B, and D along the $(22\bar{2})$ zone boundary. The intensities obtained at corners A, B, and D are as follows:

Corner A: $(113)|(22\bar{2})$;
$s\equiv(331)$; $g\equiv(113)$; $\lambda=(22\bar{2})$; $v_{\lambda-g}=v_{11\bar{5}}$.
C_{331} neglected: $\Delta E=(|v_g|^2+|v_{\lambda-g}|^2)^{\frac{1}{2}}=7$ volts.
$I_{(22\bar{2})}=0.14[4\sin^2\pi z/z_0-\sin^2\pi 2z/z_0]$; $z_0=2\lambda E/\Delta E=700$A,
$I_{(113)}=0.93\sin^2\pi 2z/z_0$,
$I_t=1-0.56\sin^2\pi z/z_0-0.76\sin^2\pi 2z/z_0$,
$\langle I_{(22\bar{2})}\rangle_{Av}=0.21$; $\langle I_{(113)}\rangle_{Av}=0.46$.

Corner B: $(331)|(222)$;
$s\equiv(331)$, $g\equiv(113)$, $\lambda=(22\bar{2})$.
C_{113} neglected; $\Delta E=(|v_g|^2+|v_s|^2)^{\frac{1}{2}}=7.3$ volts.
$I_{(22\bar{2})}=0.17[4\sin^2\pi z/z_0-\sin^2\pi 2z/z_0]$,
$I_{(331)}=0.24\sin^2\pi 2z/z_0$,
$I_t=1-0.68\sin^2\pi z/z_0-0.06\sin^2\pi 2z/z_0$,
$\langle I_{(22\bar{2})}\rangle_{Av}=0.27$; $\langle I_{(331)}\rangle_{Av}=0.11$.

Corner D: $(11\bar{3})|(22\bar{2})$;
$s\equiv(11\bar{3})$, $g\equiv(\bar{1}11)$, $\lambda=(22\bar{2})$.
$C_{(111)}$ neglected: $\Delta E=(|v_g|^2+|v_s|^2)^{\frac{1}{2}}=10.7$ volts.
$I_{(22\bar{2})}=0.23[4\sin^2\pi z/z_0-\sin^2\pi 2z/z_0]$; $z_0=450$A,
$I_{(11\bar{3})}=0.36\sin^2\pi 2z/z_0$,
$I_t=1-0.93\sin^2\pi z/z_0-0.13\sin^2\pi 2z/z_0$,
$\langle I_{(22\bar{2})}\rangle_{Av}=0.35$; $\langle I_{(11\bar{3})}\rangle_{Av}=0.18$.

The values of $I_{(22\bar{2})}$ can be computed for points along the $(22\bar{2})$ zone boundary other than the corners (Appendix II). $I_{(22\bar{2})}$ will generally decrease upon leaving a corner and moving along the $(22\bar{2})$ boundary. A strong $(22\bar{2})$ reflection is thus obtained only from restricted regions of the $(22\bar{2})$ boundary.

Having investigated the behavior at zone corners formed by Brillouin zone boundaries, one of which has a zero structure factor, the question arises as to the behavior at a corner where both structure

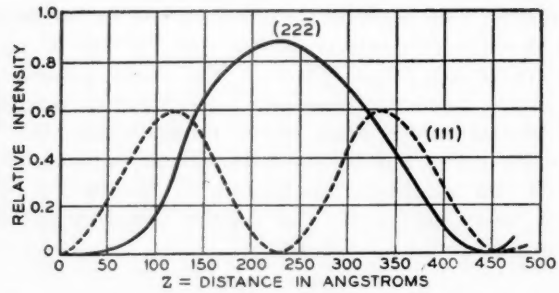

FIG. 7. Intensities of the (111) and (22$\bar{2}$) reflections as a function of depth of penetration in crystal. Incident crystal wave vector terminates at (111)|(22$\bar{2}$) boundary (point C, Fig. 6). Amplitude of (11$\bar{3}$) reflection neglected. The (222) intensity builds up more slowly than the (111). 40-kv electrons, $\lambda=0.061$A.

factors are non-zero. Point F (Fig. 6) or the (331)|(113) corner will serve as an example. Here $s\equiv(331)$, $g(113)$ and $\lambda=(22\bar{2})$. Since $v_\lambda=0$ and $|K_\lambda|^2>|K_0|^2$, the amplitude coefficient C_λ can be neglected. The intensities are found to be

$$I_{(113)}=0.77\sin^2\pi z/z_0 \text{ with } z_0=\lambda E/\Delta E;$$
$$\Delta E=(|v_g|^2+|v_s|^2)^{\frac{1}{2}},$$
$$I_{(331)}=0.23\sin^2 z/z_0.$$

Both intensities possess the period $z_0=\lambda E/\Delta E$ in contrast to the mixed periods found at points A, B, C, and D. The reason lies in the matrix since the root $\beta_0{}^0=0$ requires $C_0{}^0=0$. There are thus only two incident crystal wave vectors, $K_0{}^1$ and $K_0{}^2$. If K_0 moves away from the corner (331)|(113) along the (113) boundary, $I_{(113)}$ becomes

$$I_{(113)}=\sin^2\pi z/z_0 \text{ with } z_0=\lambda E/(V_{113}).$$

Along the (331) boundary away from the corner,

$$I_{(331)}=\sin^2 z/z_0 \text{ with } z_0=\lambda E/(v_{331}).$$

Thus, at the corner, not only is the intensity partitioned between the two diffracted beams, but the period z_0 is reduced to a lower value than it would be for either reflection alone. This suggests that the values of z_0 measured from electron micrographs of regular crystals [8,9] should be interpreted cautiously. In the case of MgO crystals, the calculated value of $z_0{}^1$ is 410A for the (200) reflection. The value measured by Hall[9] is about 300A (although an observed value of 420A was reported by the author,[3] it has since been found that an error was made in the measurement and the value in this case is also about 300A). It seems likely that for the orientation of electron beam and MgO crystal at which the effect is observed, the incident crystal wave vector is near the (200)|(220) corner. In this case $z_0=320$A for 60-kv electrons or a value much nearer the experimental value than the 410A. Thus, in interpreting experimental observations on the basis of the dynamical theory, it now appears that the simple results for only one diffracted beam may often be inadequate.

Only a fraction of the Brillouin zone edges involving the (222) boundaries have been considered. The ones shown in Fig. 6 are typical but not complete even for the (22$\bar{2}$) boundary. The (33$\bar{1}$)|(22$\bar{2}$) boundary occurs between A and B, for example, and couples with ($\bar{1}\bar{1}$1).

If the structure factors for two of the indices satisfying the relation $\lambda=s-g$ are zero, a "forbidden" reflection does not occur. For example, if $s\equiv(22\bar{2})$, $g\equiv(220)$, and $\lambda\equiv(00\bar{2})$, a step matrix results

$$\begin{pmatrix} \beta_0 & -v_g{}^* & 0 & 0 \\ -v_g & \beta_g & 0 & 0 \\ 0 & 0 & \beta_s & -v_g \\ 0 & 0 & -v_g{}^* & \beta_\lambda \end{pmatrix}$$

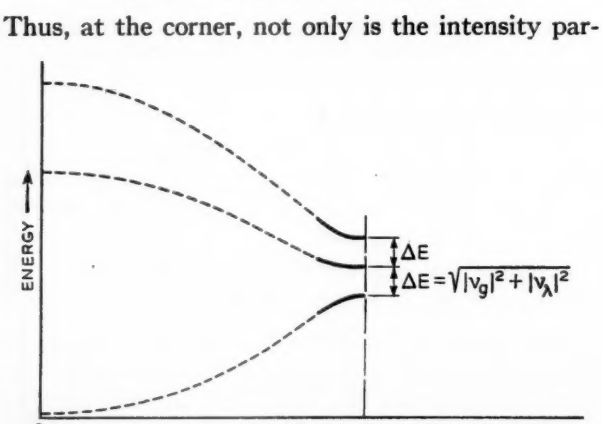

FIG. 8. Plot of energy *vs.* incident wave number $|K_0|$ along the wave vector K_0 to the (111)|(22$\bar{2}$) Brillouin zone edge in the reduced zone scheme. C_λ is neglected here to yield the cubic approximation (Eq. (23)). The solid portions of the curves are calculated from (23) while the dotted regions are schematic since the solutions hold only in the neighborhood of a zone edge. For this case, $\Delta E=10.5$ volts.

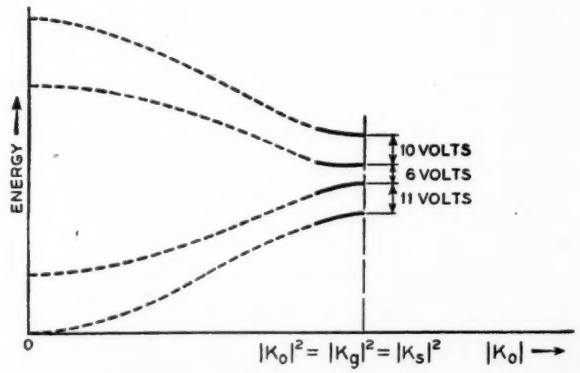

FIG. 9. Plot similar to Fig. 8 for the (111)|(22$\bar{2}$) zone corner with C_λ not neglected yielding the quartic approximation (Eq. (24)). The quadratic approximation (Fig. 2 of reference 1) gives two distinct energy levels and a single gap far from a zone edge. The cubic approximation at an edge results in three levels and two gaps while the quartic gives four levels and three gaps. The perturbation increases as the order of approximation increases.

[9] C. E. Hall, J. App. Phys. 19, 198 (1948).
[1] Using the quadratic approximation (reference 3).

and the only reflection that will occur is (220) since there is no perturbation at the (220)|(22$\bar{2}$) corner.

The dynamical theory seems to be at least in semiquantitative agreement with experimental observations on the intensity of the (222) Laue spot obtained from single crystals of silicon and germanium. As previously mentioned, for certain settings of the crystal, the strongest spot in the pattern is found to be the (222). This is evidently possible when the incident crystal wave vector terminates at the corner formed by the (222) Brillouin zone boundary and another boundary such as (111), (113), or (331). In the case of a powder pattern (Debye-Scherrer rings), such as Fig. 2(b), it is difficult to predict the (222) intensity averaged over all orientations.[j] An idea as to the procedure necessary to obtain an average intensity for a perturbation reflection can be obtained from Fig. 10. Figure 10 shows the (222) Brillouin zone boundary for the diamond lattice. The dark shaded lines are the neighborhoods of the intersections of Brillouin zone boundaries of the form (111), (113), and (331) with the (222) boundary and represent the regions in which the perturbation (222) reflection will result.[k] On the basis of the network analogy, the dark regions are those in which there is effective coupling to the (222) mesh while in the white region the (222) mesh is isolated. For lack of any other name, the dark region of Fig. 10 will be called a "perturbation (or coupling) grid." The total perturbation grid extends over all faces of the (222) octahedron. (The octahedron so formed is not strictly a Brillouin zone as the term is used in solid state physics. It might be termed a "pure zone," however, since all faces have indices of the same form, i.e., (222), ($\bar{2}\bar{2}\bar{2}$), (22$\bar{2}$), etc. for this case.) The average intensity of a (222) Debye-Scherrer ring is then obtained by averaging over the entire (222) octahedron. The fraction of the total area of a pure zone occupied by the perturbation grid would be a rough measure of the average intensity of a Debye-Scherrer ring. In Appendix II it is shown that the widths of the grid lines are of the order of 2°.

Having demonstrated that a (222) reflection is to be expected from the diamond lattice, the question arises as to whether or not other perturbation reflections may not arise in the same way. For example, the (200) structure factor for diamond is also zero. Calculations for several corners ((002)|(33$\bar{1}$), (002)|(111), (002)|(113), and (002)|(331)) have been made and indicate that a strong (002) should occur at these corners and others. Diffraction patterns from evaporated germanium and silicon

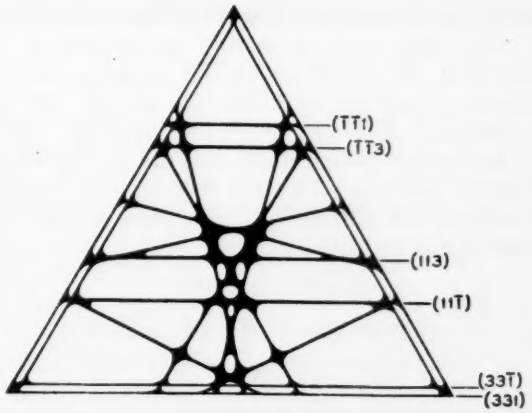

FIG. 10. View normal to the (22$\bar{2}$) Brillouin zone face of the (222) octahedron in reciprocal space. The array of intersecting lines consists of zone edges formed by intersections of the (22$\bar{2}$) face with other zone boundaries and is termed a "perturbation grid." The widths of the grid lines are of the order of a degree or so (Appendix II) with increased broadening near intersections as shown schematically above. The perturbation grid extends over all faces of the octahedron.

generally show a weak (200) ring but a strong Laue spot from a single crystal has not been reported. With a suitably oriented crystal, a strong (200) reflection should be obtained if the theory is correct. The multiplicity for (200) is six as compared to eight for (222) which reduces the change of finding the correct orientation in randomly oriented crystals. An experiment to find the (200) Laue spot seems called for.

A perturbation grid occurs for all zone boundaries in any crystal whether or not the structure factor vanishes. If the structure factor is not zero, then the effect of the perturbation grid is not so evident since an appreciable change in intensity from that expected with the kinematic theory is unlikely and would be difficult to detect experimentally due to complications arising from factors such as preferred orientation, distortion, etc. Cases in which the structure factor is zero should be the most fruitful in this type application of the dynamical theory.

IV. GENERAL REMARKS

The presence of the (222) reflection in electron diffraction patterns of elements possessing the diamond structure seems at present to be adequately explained by the dynamical theory. Experimental verification[2,3,9] of the approximate correctness of several of the salient features of the dynamical theory leads to a reasonable amount of confidence in the foregoing explanation of the (222) reflection. The general approach and treatment is not unique to electrons, however, and could be carried out for x-rays as well.* The case of a single diffracted beam in x-ray diffraction was worked out some thirty

[j] For the case of only one strong diffracted beam, the integration has been carried out to obtain the intensities of Debye-Scherrer rings. M. Blackman, Proc. Roy. Soc. (London) A174, 68 (1939).

[k] See Appendix II for calculations pertaining to the width of the lines.

* See J. Weigle and H. Müksam, Helv. Phys. Acta. 10, 139 (1937).

years ago by Darwin and Ewald.[10] The transition to the x-ray case can be readily accomplished by noting that the quantity $|v_g|/E$ occuring in the argument of the $\sin^2$ term for the simple electron case becomes $(K/(|\gamma_0\gamma_g|)^{\frac{1}{2}})|\sigma_g|$ for x-rays,[10] where $K=1$ for normal polarization, σ_g is the polarizability coefficient, and γ_0, γ_g are the direction cosines for the incident and diffracted beams, respectively. If α denotes the polarizability, then

$$\sigma \equiv 4\pi\alpha = \sum_g \sigma_g e^{2\pi i(g\cdot r)}$$

(the x-ray counter part of Eq. (4)) and

$$|\sigma_g| = (e^2\lambda^2/m\pi^2\Omega)|F_g|,$$

e is the electronic charge, λ the wave-length, m the electron mass, c the ratio of the electrostatic and electromagnetic units, Ω the volume of the unit cell, and F_g the x-ray structure factor. For the case when the Ewald sphere touches reciprocal lattice points (111) and $(22\bar{2})$, Eqs. (22a) may be applied with

$$z_0 \simeq \frac{2\lambda}{(|\sigma_g|^2+|\sigma|^2)^{\frac{1}{2}}} = 1.44\times10^{-4}\text{ cm for }\lambda=1.5\text{A}.$$

The two cases, electron and x-ray, thus differ only by a change of scale as can be seen. The x-ray $(22\bar{2})$ reflection does not reach maximum intensity until the depth of penetration is about 8000A in germanium as compared to 225A in the electron case. From the equivalent circuit point of view, the couplings in the x-ray case are much weaker than in the electron case.

The period $z_0 \simeq 1.4\times10^{-4}$ cm (in germanium) for 1.5A x-rays is of the same order as the estimates of mosaic size. If the coherent path length in a crystal is l, then the relative intensity of a reflection will be dependent upon l. In the case of diamond, z_0 is about 4×10^{-4} cm for the (222) and the intensity should be sensitive to the mosaic size of the crystal. This appears to be in qualitative agreement with experimental observation.[11] However, the dependence of intensity upon mosaic size does not require that the x-ray (222) in diamond originate primarily through the perturbation grid on the (222) octahedron (Fig. 10). The simple case for only a single diffracted beam wherein the (222) structure factor is not zero (due to valence electron distribution) would also predict a dependence of intensity upon coherent path length. The width of the perturbation grid lines for the x-ray case will be of the order of about one-fifth of those for the electron case according to a rough calculation. The region in which a perturbation (222) can occur in the x-ray case is then smaller than for the electron case. It would appear desirable to carry through the perturbation calculation in detail for the x-ray case in an effort to determine whether or not the dynamical theory alone is sufficient to account for the (222).

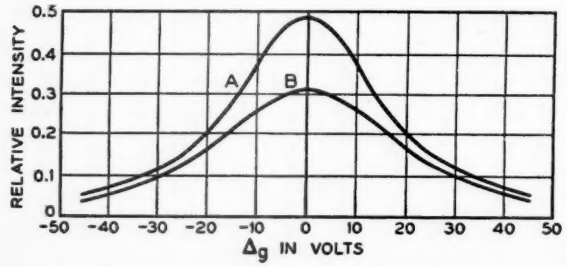

FIG. 11. Rocking curves for the Ge (111) reflection averaged over thickness showing the difference in width far from a Brillouin zone edge, A, and at the $(111)|(22\bar{2})$ edge, B. Curve A is the quadratic approximation for only one diffracted beam. Curve B is the cubic approximation with the incident wave vector maintaining its terminus on the $(22\bar{2})$ boundary and running either direction away from the $(111)|(22\bar{2})$ edge. The deviation from the Laue condition, Δg, is given in volts which can be converted to radians, $\Delta\theta$, through the relation $\Delta\theta=\Delta_g d/2E\lambda$ where d is the interplanar spacing, E the total energy, and λ the wave-length. For 40-kv electrons, $\Delta\theta=1.3\times10^{-3}\Delta g$.

In the electron case it seems clear that the origin of the (222) is a perturbation phenomenon. Application of the theory to a number of cases in addition to the (222) would be desirable as a check.

The author is indebted to various members of the technical staff for aid and criticism and particularly to Dr. C. Herring for help in developing the general theory and to Dr. R. L. Dietzold for aid in the equivalent circuit treatment.

APPENDIX I. FOURIER COEFFICIENTS

The Fourier coefficients of potentials are given by†

$$v_g = (e/\pi\Omega|g|^2)\Sigma_j (Z_j - f_j)\exp[2\pi i(g_j\cdot r_j)]\text{ e.s.u.} \quad \text{(I-1)}$$

and $v_{hkl}(\text{volts}) = 300\, v_g$. Ω is the volume of the unit cell.

Some of the coefficients for germanium used in the text are displayed below and were calculated using formula (I-1).

Germanium:	Silicon:	Diamond:
$a_0=5.65$A	$a_0=5.42$A	$a_0=3.56$A
$\Omega=180$A^3	$\Omega=159$A^3	$\Omega=45$A^3.

The unit cells contain eight atoms with the basis

(000), $(\frac{1}{2}\frac{1}{2}0)$, $(\frac{1}{2}0\frac{1}{2})$, $(0\frac{1}{2}\frac{1}{2})$, $(\frac{1}{4}\frac{1}{4}\frac{1}{4})$, $(\frac{3}{4}\frac{3}{4}\frac{1}{4})$, $(\frac{1}{4}\frac{3}{4}\frac{3}{4})$, $(\frac{3}{4}\frac{1}{4}\frac{3}{4})$.

Germanium:

hkl	(111)	$(11\bar{1})$	$(\bar{1}\bar{1}1)$	(113)
v_{hkl}	$6(1-i)$	$6(1+i)$	$6(1+i)$	$4.5(1-i)$
$\lvert v_{hkl}\rvert$	8.5 volts	8.5	8.5	6.4
hkl	$(11\bar{3})$	(331)	$(33\bar{1})$	$(11\bar{5})$
v_{hkl}	$4.5(1-i)$	$2.5(1-i)$	$2.5(1+i)$	$1.9(1+i)$
$\lvert v_{hkl}\rvert$	6.4	3.5	3.5	2.7

APPENDIX II. ROCKING CURVES

The behavior of the diffracted intensities in the neighborhood of a Brillouin zone corner is important in considering

[10] See W. Zachariasen, *Theory of X-ray, Diffraction in Crystals* (John Wiley and Sons, Inc., New York, 1945), Sections 3, 8–11.

[11] Robertson, Fox, and Martin, Phil. Trans. **A232**, 474 (1934).

† The deviation, Δ_g, can be converted to radians through the relation $\Delta\theta=\Delta_g d/2E_\lambda$ where d is the interplanar spacing.

the widths of the perturbation grid lines of Fig. 10. A calculation of the intensities as a function of the deviation, Δg from the Laue condition is required and can be carried out readily for the cubic approximation. For corner C (Fig. 6, the (111)|(22$\bar{2}$) corner) the matrix (15) becomes

$$\begin{pmatrix} \beta_0 & -v_g^* & 0 \\ -v_g & \beta_0+\Delta_g & -v_\lambda^* \\ 0 & -v_\lambda & \beta_0 \end{pmatrix}, \quad \begin{matrix} g\equiv(111) \\ s\equiv(22\bar{2}) \\ \lambda\equiv(11\bar{3}) \end{matrix} \qquad \text{(II-1)}$$

where $\Delta_g\equiv(h^2/8\pi^2m)(|K_g|^2-|K_0|^2)$ is the deviation from the Laue condition for the wave vector Kg. In this $\Delta_s=0$ since K_0 is to maintain its terminus on the (22$\bar{2}$) zone boundary but may move away from the corner in either direction. The secular determinant of (II-1) yields the roots

$$\begin{aligned} \beta_0^0&=0, \\ \beta_0^1&=-(\Delta_g/2)+[(\Delta_g/2)^2+(\Delta E)^2]^{\frac{1}{2}}, \\ \beta_0^2&=-(\Delta_g/2)-[(\Delta_g/2)^2+(\Delta E)^2]^{\frac{1}{2}}, \end{aligned}$$

with $\Delta E=(|v_g|^2+|v_\lambda|^2)^{\frac{1}{2}}$ as before (Fig. 8). Using the roots (II-2), the beat wave vectors are found to be

$$\begin{aligned} \Delta K_{01}&=K_0^1-K_0^0=(\pi/\lambda E^{(0)})\{-(\Delta_g/2)+[(\Delta_g/2)^2+(\Delta E)^2]^{\frac{1}{2}}\}, \\ \Delta K_{02}&=K_0^2-K_0^0=(\pi/\lambda E^{(0)})\{-(\Delta_g/2)-[(\Delta_g/2)^2+(\Delta E)^2]^{\frac{1}{2}}\}, \\ \Delta K_{12}&=K_0^2-K_0^1=(-2\pi/\lambda E^{(0)})[(\Delta_g/2)^2+(\Delta E)^2]^{\frac{1}{2}}. \end{aligned} \qquad \text{(II-3)}$$

The ratios of the amplitude coefficients $\alpha_g=C_g/C_0$, etc. are now

$$\begin{aligned} \alpha_g^0&=0, \\ \alpha_g^1&=\frac{1}{v_g^*}\left\{-\frac{\Delta_g}{2}+\left[\left(\frac{\Delta_g}{2}\right)^2+(\Delta E)^2\right]^{\frac{1}{2}}\right\}, \quad \alpha_s^0=-\frac{v_g}{v_\lambda^*}, \\ \alpha_g^2&=\frac{1}{v_g^*}\left\{-\frac{\Delta_g}{2}-\left[\left(\frac{\Delta_g}{2}\right)^2+(\Delta E)^2\right]^{\frac{1}{2}}\right\}, \quad \alpha_s^1=\alpha_s^2=\frac{v_\lambda}{v_g^*}, \end{aligned} \qquad \text{(II-4)}$$

in contrast to Eq. (20). From (14b) and (21) the diffracted intensities are found to be

$$\begin{aligned} I_{\substack{(222)\\ s}}&=\frac{|\alpha_s^0|^2|\alpha_s^1|^2}{|\alpha_s^1-\alpha_s^0|^2|\alpha_g^2-\alpha_g^1|^2}[4(|\alpha_g^2|^2-\alpha_g^{2*}\alpha_g^1) \\ &\quad\times\sin^2\tfrac{1}{2}\Delta K_{01}z+4(|\alpha_g^1|^2-\alpha_g^2\alpha_g^{1*})\sin^2\tfrac{1}{2}\Delta K_{02}z \\ &\quad+2(\alpha_g^2\alpha_g^{1*}+\alpha_g^{2*}\alpha_g^1)\sin^2\tfrac{1}{2}\Delta K_{12}z], \end{aligned} \qquad \text{(II-5)}$$

$$\begin{aligned} I_{\substack{(111)\\ g}}&=4\frac{|\alpha_s^0|^2|\alpha_g^2|^2|\alpha_g^1|^2}{|\alpha_s^1-\alpha_s^0|^2|\alpha_g^2-\alpha_g^1|^2}\sin^2\tfrac{1}{2}\Delta K_{12}z \\ &=\frac{|v_g|^2}{(\Delta_g/2)^2+(\Delta E)^2}\sin^2\tfrac{1}{2}\Delta K_{12}z, \end{aligned}$$

in place of Eqs. (22a).

It is of interest to consider first the (111) intensity as given by (II-5). If $v_\lambda=v_{113}$ is neglected, $I_{(111)}$ reduces to the case for only one diffracted wave (reference 1) since now $(\Delta E)^2=|v_g|^2$ with

$$\Delta_g\equiv\frac{h^2}{8\pi^2m}(|K_g|^2-|K_0|^2)=2\frac{h^2}{8\pi^2n}|K|^2\Delta\theta\ \sin2\theta=2E^{(0)}\Delta\theta\ \sin2\theta,$$

where $\Delta\theta$ is the deviation from the Bragg angle θ. If the average value of $\sin^2=\frac{1}{2}$ is employed, the effect of thickness is eliminated and average rocking curves are obtained as shown in Fig. 11. The width at half-maximum intensity for the approximation of only one diffracted wave (far from a corner) is about 32 volts as compared to about 42 volts at the (111)|(22$\bar{2}$) corner.[1] The width at half-maximum can be

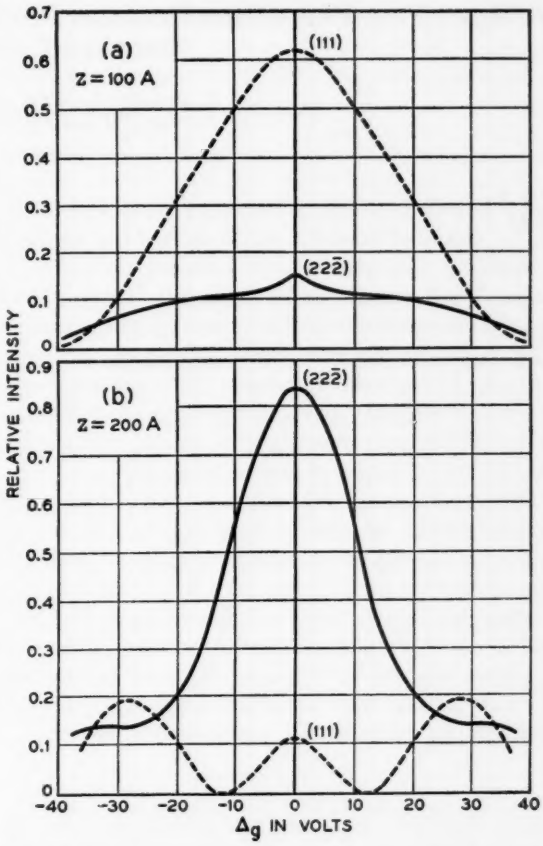

FIG. 12. Ge (111) and (22$\bar{2}$) rocking curves for two thicknesses of crystal as computed using the cubic approximation. The incident wave vector terminus is maintained on the (22$\bar{2}$) zone boundary and in the neighborhood of the (111)|(22$\bar{2}$) edge.

obtained directly from (II-5) as $[\Delta_g]_{\frac{1}{2}}=4\Delta E$ and is seen to be proportional to the energy gap at the zone boundary. The width of a Kikuchi line would then be greater for large energy gaps and hence greater if the incident wave vector terminates near a zone corner.

The width of the (222) reflection is not obtained quite as simply due to the presence of several periods in the expression (II-5) for the intensity. Equation (II-5) has been plotted for two different thicknesses, 100A and 200A, and is shown in Fig. 12. The (111) is also plotted for the same thickness for comparison. The subsidiary maxima are evident for the (111) reflection in Fig. 12(b) and are more intense than the primary. The half-widths of the (222) rocking curve from germanium are seen to be about 54 volts with a thickness of 100A and 26 volts at 200A. The (222) exhibits in both cases a greater half-width than does the (111). Experimentally, this should show up as a broader (222) Kikuchi line.

The half-widths of the grid lines of Fig. 10 are thus seen to be of the order of 5×10^{-2} rad. or about 2° for 40-kv electrons.

Mean Free Path of the Particles Produced in Nuclear Explosions and Comparison between Explosions in C and Pb

A. LOVATI, A. MURA, G. SALVINI, AND G. TAGLIAFERRI
Institute of Physics of the University of Milan, Milan, Italy
(Received December 2, 1949)

WE give here the preliminary results of a cloud-chamber research made during the spring and summer of this year at the Laboratorio della Testa Grigia (3500 meters above sea level). There were two aims of our research: (a) Measurement of the mean free path in Pb for nuclear interaction of the penetrating particles of nuclear explosions; (b) comparison of the nuclear explosions produced in nuclei of different size (C and Pb) so as to have an experimental choice between the different theories of meson production.[1]

Our experimental disposition is given in Fig. 1. The cloud-chamber expansions were controlled with G-M counters. At least one counter in the tray A and at least two counters in each of the trays B, C, and D had to be discharged. In the cloud chamber (32 cm in diameter and 10 cm of illuminated depth) there are seven Pb and C plates, of the thicknesses indicated in the figure. Present results were obtained from a total of 1980 photographs taken in 570 hours of measurement.

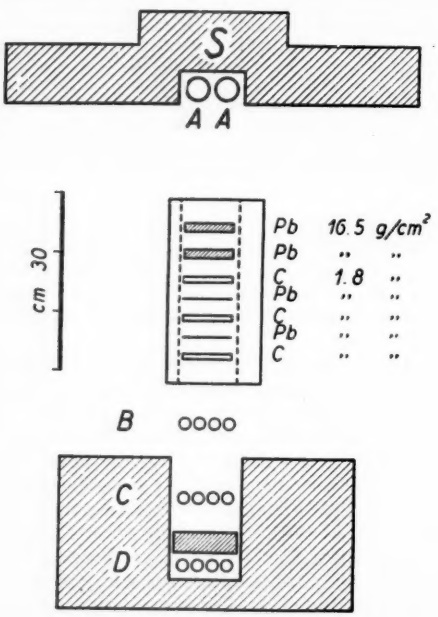

FIG. 1. Arrangement of apparatus.

(A) In the 223 nuclear explosions produced in the lead S above the cloud chamber (so-called penetrating and mixed showers) we counted 614 penetrating particles which traversed the Pb plates of the cloud chamber for a total of 23,300 g/cm². On the other hand, we counted 29 nuclear explosions produced by these penetrating particles in the Pb plates of the cloud chamber, and 7 scatterings with a projected angle $\geqslant 10°$. Hence we obtained an uncorrected mean free path $\lambda_{unc}=650$ g/cm².

The nuclear explosions produced inside the cloud chamber were recognized (i) by the emission of at least two particles, one of them at least heavily ionizing, (ii) by the emission of at least four relativistic particles from a thin plate, (iii) by the emission of two penetrating particles at least from the first thick plate. The events (i) are by far the highest percentage. Our λ_{unc} is certainly larger than the true value, for the larger part of the nuclear explosions were produced in the thick plates, but a part of them were not revealed because they did not emerge with heavily ionizing particles. The simultaneous presence in the cloud chamber of 16.5 and 1.8 g/cm² Pb plates enabled us to correct the above value of the mean free path. Let us consider only the nuclear explosions revealed on the basis of criterion (i). The probability p_i to reveal a nuclear explosion in the thin plates by criterion (i) is rather close to unity; on the basis of previous works[2] we have estimated it at about 0.85. To estimate the probability p_T of revealing a nuclear explosion in the thick plates on basis of criterion (i) we have assumed (as appeared directly) that all the nuclear explosions observed in the cloud chamber and produced by ionizing particles in the thick and thin plates (55 and 17 nuclear explosions respectively) are of the same type as those produced by the penetrating particles of a preceding nuclear event in the Pb S. Thus it resulted:

$$p_T=0.85(55\times 1.8):(17\times 16.5)=0.3.$$

On the basis of the above values of p_T and p_i, and introducing a further small correction to take into account the instrumental selection in favor of the nuclear explosions with successive production, we could calculate $\lambda=300$ g/cm², with a possible error of ± 30 percent. This value is in a good accord with that which we estimated (350 g/cm²) by a less direct correction in a preceding work.[3] Later, Fretter[4] published a maximum mean free path of 750 g/cm², in agreement with our uncorrected value.

Fretter too, in his measurements, revealed the nuclear explosions with criteria (i) and (iii). On the basis of the

[1] W. Heitler and L. Jànossy, Congress of Como (1949); W. Heisenberg, Congress of Como (1949); G. Wataghin, Phys. Rev. 74, 975 (1948), and 75, 693 (1949).

[2] Harding, Lattimore, and Perkins, Proc. Roy. Soc. A196, 325 (1949); Bridge, Hazen, Rossi, and Williams, Phys. Rev. 74, 1083 (1948).

[3] Lovati, Mura, Salvini, and Tagliaferri, Nuovo Cimento 6, 207 (1949) and Nature 163, 1004 (1949).

[4] W. B. Fretter, Phys. Rev. 76, 511 (1949).

TABLE I. Number of nuclear explosions observed in the thin C and Pb plates, distributed according to the number of relativistic particles.

n	0	1	2	3	4	5	6	7	8	9	10
C	8	11	5	3	6	3	2	2	1	—	—
Pb	1	5	12	9	10	7	5	—	—	—	1

results of Powell and co-workers[5] we evaluated the number of the events of type (i) observed by Fretter. Then we estimated his probability corresponding to our p, finally obtaining for him $\lambda=360$ g/cm^2, which is rather consistent with our value of λ.

It is rather probable that the penetrating particles of the nuclear explosions be mainly π-mesons and protons. If we should admit, on basis of Piccioni's result,[6] a mean free path for the π-mesons larger than the geometrical at least by a factor say 4, it could be deduced that about $\frac{1}{3}$ of the penetrating particles emitted in the nuclear explosions at 3500 meters above sea level are protons.

(B) In Table I the distribution is given of the nuclear explosions produced in the three C and in the two Pb thin plates, according to the number of relativistic particles. Our statistics are still insufficient, and the theories are too qualitative. We only note here that we obtained an experimental ratio,

$$\frac{\text{nuclear explosions with } n\geqslant 4 \text{ relativistic particles in C}}{\text{nuclear explosions with } n\geqslant 4 \text{ relativistic particles in Pb}} = 0.6\pm 0.3.$$

(For $n\geqslant 4$, the numbers of nuclear explosions in C and Pb may be directly compared, for their revelation (criterion ii) is independent of the presence of the heavy ionizing particles.) This result seems to indicate that many nucleons may be accelerated to a relativistic velocity in a nuclear explosion, eventually giving rise to mesons, at least in the nucleus of Pb. In fact, should the nuclear explosions be a single nucleon-nucleon impact inside a nucleus, than we should have, assuming geometrical cross sections for the production of nuclear explosions, a value of 3.5 for the above ratio. This value might vary from 3.5 to 2, owing to the transparency of the C nucleus.

We are grateful to Professor B. Ferretti for many helpful discussions.

[5] Brown, Camerini, Fowler, Heitler, King, and Powell, Phil. Mag. **40**, 862 (1949).
[6] O. Piccioni, Congress of Como (1949).

Letters to the Editor

PUBLICATION of brief reports of important discoveries in physics may be secured by addressing them to this department. The closing date for this department is five weeks prior to the date of issue. No proof will be sent to the authors. The Board of Editors does not hold itself responsible for the opinions expressed by the correspondents. Communications should not exceed 600 words in length.

An Extension of the Theory of Diabatic Flow

BRUCE L. HICKS
Ballistic Research Laboratories, Aberdeen Proving Ground, Maryland
November 8, 1949

OUR work on two- and three-dimensional diabatic flow began in 1945 with a search both for a general formulation of the subject and a specific calculation of forces on bodies in the fields of flow. The general study was completed first and has been presented in three papers.[1] Results have also been obtained by other workers.[2–5] We can now report the calculation of diabatic forces.

On thermodynamic grounds, as we suggested in 1945, one would expect that a body immersed in a moving fluid containing a heat source would experience a force; for the fluid pressure, owing to the presence of the body, is changed in the region where the fluid is heated, and is returned to its upstream value at a point far downstream from the body.* Both general theory and a specific example indicate[1(b),(c),4] that the effects of a heat source are much like those of a fluid source. Also on aerodynamic grounds, therefore, a heat source should produce a force since the velocity over the surface of the body is changed by the source more on the side near the source than on the far side. Similarly one can see that the force in the x direction will vary approximately as $\cos 2\theta_0$ where θ_0 gives the angular position of the source measured at the body from the direction of flow or x axis.

To these qualitative arguments we add, as typical of results that can be obtained, a specific calculation of the force on a circular cylinder. The complex potential Ψ for an incompressible, irrotational flow field that contains a cylinder Γ of radius a with center at $z=0$, a fluid source of strength m at $z=z_0=R_0\exp i\theta_0$, and has uniform velocity in the x direction $(-V_0)$ at $+\infty$ is,[6] if there is no circulation about the cylinder,

$$\Psi=-V_0(z+a^2z^{-1})+(m/2\pi)\log(z-z_0)(a^2z^{-1}-\bar{z}_0). \quad (1)$$

If ρ is the fluid density, the complex force F_x-iF_y per unit length on the cylinder $(\rho i/2)\int_\Gamma \Psi'^2 dz$, becomes, when the integration is carried through,

$$F_x-iF_y=\rho m a^2 z_0^{-2}[V_0+(z_0 m/2\pi)(R_0^2-a^2)^{-1}]. \quad (2)$$

The terms on the right correspond to the interaction of the source with, respectively, the flow induced by the body and by the source itself. For a continuous distribution of sources of density σ in a neighborhood ΔA of z_0 the second term drops out. If also we use the known connection[1(c),4] between the heat source strength per unit mass and time, Q, and the (effective) fluid source strength σ, we find

$$F_x-iF_y=\rho V_0(a^2R_0^{-2})(Q/c_pT_0)\Delta A\exp(-2i\theta_0), \quad (3)$$

c_pT_0 being the entropy per unit mass of the fluid before heating. The $\cos 2\theta_0$ dependence for F_x is thus confirmed. The calculation is less accurate for source positions in front of the cylinder than for other positions because the equations do not make allowance for vorticity in the wake of the source. The correct value of ρ to use in Eq. (3) depends on the relative positions of the streamline passing around the body and the heated region.

We have thus shown that a force both in and perpendicular to the direction of the flow can be produced in diabatic flow of a perfect fluid over a body. The calculation is of course applicable both to the diabatic flow and to the case of mass addition to an incompressible fluid. The classical adiabatic flow only produces forces normal to the flow and then only if there is circulation about the body. If both circulation and heat (or fluid) sources are present it can be shown that there are additional forces in both directions.

Further fundamental investigation of these diabatic forces seems warranted. The size of the computed force arising from the heating is not inconsiderable. An order of magnitude calculation shows that the force is $(2\eta q\Delta A/V_0)$ where q is the dynamic pressure and $\dot{\eta}$ is the heating rate expressed as the fractional time rate of change of enthalpy. The corresponding result for a sphere can be obtained. Since the whole calculation is based on first-order perturbation treatment of the (non-linear) diabatic flow equations, and since a compressible fluid does not admit fluid sources of finite strength and infinitesimal extent, further extension of the theory is required when the heat source strength is not small or when compressible fluids are considered at any but the lowest Mach numbers. Some idea of the range of the validity of the perturbation treatment and of the magnitude of the compressibility corrections can be gained from references 1(c) and 4. For a realistic calculation, allowance must also be made for the departure of the fluid from the inviscid, non-turbulent model considered here.

I am indebted to Dr. W. C. Taylor and Mr. W. H. Hebrank for helpful discussions during these investigations, and to Professors Starr, Platzman, and Tsien for sending me prepublication copies of their papers.

[1(a)] B. L. Hicks, Quart. App. Math. **6**, 221 (1948); [(b)] Quart. App. Math. **6**, 407 (1949); [(c)] Third Symposium on Combustion, Flame and Explosion Phenomena. Paper No. 25 (Williams and Wilkins).
[2] Victor P. Starr, J. Meteor. **6**, 188 (1949).
[3] George W. Platzman (private communication).
[4] H. S. Tsien and Milton Beilock (private communication).
[5] Chan-Mou Tchen, Phys. Rev. **76**, 883 (1949).
* This argument can be formalized to show that the work done on the body per second because of the fluid element Δm is nearly equal to $(\mathbf{R}V_2\cdot\nabla T_1)$ where V_2 is the velocity induced at Δm by the body and T_1 is the temperature rise of the fluid owing to the heat release at Δm.
[6] Compare Milne-Thomson, *Theoretical Hydrodynamics* (1938), Chapter VIII.

The Inelastic Scattering of Neutrons by Light Nuclei

L. E. BEGHIAN, M. A. GRACE, G. PRESTON, AND H. HALBAN
Clarendon Laboratory, Oxford University, Oxford, England
November 29, 1949

WE have investigated the inelastic scattering of 2.5 Mev neutrons by light nuclei. In many such elements the level spacing is so wide that only the lowest level is excited by neutrons of this energy. Thus the γ-rays produced in this process are homogeneous and this facilitates the determination of their energy and intensity. Furthermore, theoretical calculations of cross section for inelastic scattering are simplified when only a single transition to the ground-state of the scattering nucleus occurs.

The neutrons were produced by the d-d reaction using an occluded target with deuterons of 100-kev energy. Considerable care was taken to minimize scattering in the vicinity of the target which was made of $\frac{1}{8}$-mm aluminum foil, soldered to the end of an aluminum tube of $\frac{1}{4}$-mm wall thickness. This tube was waxed to the glass end of the accelerator column. In this way not more than 4.3 γ-rays/1000 neutrons originated in the target.*

Disk-shaped scatterers, 2 cm in diameter and 5 mm thick, were placed directly in contact with the target. With deuteron currents of the order of 100 μA air cooling was found to be adequate.

The γ-rays from the scatterer were detected in a pair of thin-walled glass Geiger-Müller counters set up in coincidence, using a polystyrene converter in front of the counter to produce the secondary electrons. The absolute sensitivity of this arrangement was measured with γ-rays from Co^{60} and Na^{24}. By placing aluminum foils between the two counters, the absorption curve of the secondary electrons was found. Knowledge of the form of this curve and its end-point enabled us to determine the energy and estimate the degree of homogeneity of the γ-rays.

The absolute neutron intensity was determined using a proton recoil ionization chamber[1] (4 cm in diameter, 16 cm in length, 1-mm wall thickness of a special aluminum alloy). This was filled to 20 atmospheres pressure with highly purified methane and gave electron collection.

Table I shows the results for three materials and it can be seen

TABLE I. Comparison of the results for three materials.

Scatterer	Inelastic scattering cross section (barns)	Total cross section (barns)	Energy of γ-ray (Mev)	Observation of same excitation level by other methods (Mev)
Magnesium	1.0 $\pm$0.15	2.2	1.35$\pm$0.1	1.38[2] 1.32[3] 1.36[4,5]
Sulfur	0.44$\pm$0.06	2.5	2.35$\pm$0.1	2.25[3]
Fluorine (polytetrafluoro-ethylene)	0.62$\pm$0.1	2.0	1.3 $\pm$0.1	1.6[6]

that the γ-ray energy compares well with that obtained by other methods. A test with a carbon scatterer showed no significant effect (inelastic cross section $<6\times10^{-3}$ barn).

It is of interest to note that in the case of magnesium the cross section of inelastic scattering is approximately half the total cross section at this energy.

Investigations are now proceeding on materials which emit more than one γ-ray line. We wish to express our gratitude to Professor Lord Cherwell for his interest in the work and for the facilities afforded to us.

* We cannot exclude the existence of γ-rays from the d-d reaction which has been discussed by several authors: these would be caused by an excited state of He^5 or H^3 which theoretically is extremely unlikely. However, from a measurement of the number of γ-rays caused by inelastic scattering in the target material itself, we can give an upper limit of 2.5 γ-rays per 1000 neutrons from such a reaction.

[1] L. E. Beghian and H. Halban, Proc. Phys. Soc. **62A**, 395 (1949).
[2] K. Siegbahn, Phys. Rev. **70**, 127 (1946).
[3] R. H. Dicke and J. M. Marshall, Phys. Rev. **63**, 86 (1943).
[4] E. H. Rhoderick, Nature **163**, 848 (1949).
[5] E. H. Rhoderick *et al.*, Nature **164**, 663 (1949).
[6] E. Bleuler and W. Zunti, Helv. Phys. Acta **20**, 195 (1947).

Optical Effects in Bulk Silicon and Germanium

H. B. BRIGGS
Bell Telephone Laboratories, Murray Hill, New Jersey
November 25, 1949

PURE bulk silicon and germanium are highly transparent to infra-red energy of wave-lengths greater than their photo-electric long wave limits, i.e., 1.2×10^{-4} cm for silicon and 2.2×10^{-4} cm for germanium.[1] As examples of the transmission through thick samples it may be noted that a germanium slab, part of a standard high back-voltage melt, and of thickness 6.0 mm showed very little absorption in the wave-length range from 2 microns to 6.5 microns. A sample of high purity Du Pont silicon, of thickness 5.2 mm, showed little absorption in the wave-length range from 1.2 microns to 6 microns.

The high transparency suggested the measurement of the refractive indices by the prism method. Two prisms were made, one of silicon and the other of germanium. The silicon used was part of a commercial Electromet melt, with a purity of 99.8 percent. Samples of Du Pont silicon that have since come to hand have a lower impurity content. The germanium used was part of a standard high back-voltage melt, and is typical of the purest germanium now available. From spectrochemical tests the total impurity content is estimated as less than 0.01 percent.

Measurements of the prism angle were made with a Gaertner spectrometer equipped with a Gauss eyepiece. Measurements of the angle of minimum deviation were made with the aid of a lead sulfide photo-conducting cell fitted in the eyepiece holder of the spectrometer. The procedure consisted in isolating a narrow spectral band with a Perkin-Elmer monochromator; focusing this energy on the entrance slit of the Gaertner spectrometer, and adjusting the telescope angle so that on rotation of the prism table the photo-cell response indicated minimum deviation.

TABLE I. Silicon: Prism angle 11° 24′ 7″.

λ	n
1.05×10^{-4} cm	3.565
1.10	3.553
1.20	3.531
1.40	3.499
1.60	3.480
1.80	3.466
2.00	3.458
2.20	3.451
2.40	3.447
2.60	3.443

TABLE II. Germanium: Prism angle 17° 6′ 30″.

λ	n
1.80×10^{-4} cm	4.143
1.85	4.135
1.90	4.129
2.00	4.116
2.10	4.104
2.20	4.092
2.30	4.085
2.40	4.078
2.50	4.072
2.60	4.068

The range of measurements is limited on the short wave side by absorption in the prism, and on the long wave side by absorption in the glass of the optical system.

The results of the measurements of refractive indices are shown in Tables I and II.

Consideration of the errors involved in the settings from which the indices were calculated indicates that the values above are accurate for the samples tested to within a few tenths of one percent. Some qualitative tests on germanium at λ 1.8×10^{-4} cm showed a definite increase in refractive index with increasing temperature.

It is to be noted that these values of refractive index for bulk germanium are somewhat lower than we obtained for evaporated films by interference methods.[2] A review of the data on thin film measurements indicates that a possible cause of the discrepancy lies in the assumption of equal densities for the evaporated films and the bulk material.

The high transparency and high refractive indices make possible the construction of unique optical elements for infra-red use. As an example, a plano-convex lens of germanium was made. The radius of curvature of the convex side of this lens is 3.52 inches. The calculated focal length, using the refractive index of 4.1 at 2 microns, is 1.13 inches. This checked well with the experimentally determined focal length. The F-number of this lens is 1.5. The F-number of a glass lens of identical geometry is 9.5.

A further property of these lenses is that they are opaque to visible and ultraviolet light.

As a consequence of the high refractive indices, the reflection losses for windows or lenses of Si or Ge are high, amounting roughly to 50 percent of the incident beam. Such losses may be reduced by the usual non-reflecting film technique. As an example, the transmission of a germanium window was increased from 43 percent to 90 percent of the incident energy at 4 microns by films of selenium on the two surfaces of the window.

[1] This transparency was observed independently by M. Becker and H. Y. Fan, Bull. Am. Phys. Soc. **24**, 29 (No. U5) (1949).
[2] W. H. Brattain and H. B. Briggs, Phys. Rev. **75**, 1705 (1949).

Erratum: Short Range Alpha-Particles from Fluorine and Lithium Bombarded by Protons

[Phys. Rev. **75**, 1756 (1949)]
W. E. BURCHAM AND JOAN M. FREEMAN
Cavendish Laboratory, Cambridge, England

AN error was made in the calculation of the energy of the excited state of Be^8 from observation of the short range alpha-particles in the $Li^7(p\gamma)Be^8$ reaction. The emission of alpha-particles of energy 1.38$\pm$0.08 Mev at 104° with the incident proton beam of energy 0.44 Mev requires an energy release in the break-up of Be^8 of 3.0$\pm$0.2 Mev. The energy of the excited state is 2.9$\pm$0.2 Mev instead of 2.6$\pm$0.2 Mev as previously given.

Proton-Proton Scattering and the Triplet Range of Nuclear Force

P. SWAN
University of Melbourne, Melbourne, Australia
October 24, 1949

IT is well known that the interaction between two protons, and that between a neutron and a proton, depends on whether the spins are parallel (triplet interaction) or anti-parallel (singlet interaction), giving four separate interactions between the fundamental nuclear particles. In the scattering of high energy nucleons, a non-central component of force becomes important, but if consideration is restricted to the analysis of scattering experiments below about 10 Mev, its effect is not appreciable,[1] and furthermore the calculated results are insensitive to the shape of the interaction potential,[2] so that one may use a rectangular potential well.

Considering first the singlet interaction, the s wave scattering of protons in hydrogen leads fairly conclusively to a singlet p-p well width of about 2.8×10^{-13} cm, and depth 10.5 Mev. It is then found that a singlet interaction of the same range for the n-p case is compatible with the binding energy of the virtual state of the deuteron, as found from low energy n-p scattering data. This is in accordance with the idea of charge independence of the forces between nucleons.

For the triplet interaction, the scattering of sub-thermal neutrons by ortho- and para-hydrogen[3] and by NaH[4] gives a range of about 1.6×10^{-13} cm for the n-p interaction; and the corresponding well depth is found from the known binding energy of the deuteron. Information on the p-p triplet interaction may be obtained by analysis of R. R. Wilson's experiments[5] on p-p scattering at 10 Mev, at which energy p wave scattering first becomes important. One first deduces the p wave scattering phase K_1 required to fit the experimental angular distribution, but two widely divergent values have previously been quoted, *viz.* $-0.8°$ by Peierls and Preston,[6] and $-0.4°$ by Foldy.[7] The present calculations lead to the value $K_1=(-0.4\pm0.1)°$ in good agreement with Foldy. We now see whether charge independence of forces can be preserved for the triplet interaction. A relation may be obtained between the depth and width of the n-p triplet well by utilizing the known binding energy of the deuteron, and the curve showing this relation is plotted in Fig. 2 (curve a). To obtain a similar curve, (b), for the p-p triplet well dimensions corresponding to $K_1=-0.4°$, it is first necessary to graph K_1 as a function of well depth for a number of well widths (Fig. 1). Associated values of range and depth of the repulsive potential, yielding the required value of K_1 may then be read off the graph. A correction must here be made to the well depth, for in calculating the values of K_1, the Coulomb interaction was ignored inside the well. To allow for this, an amount $\delta D=1.14$ Mev (cm) calculated at 10 Mev (lab.) from the approximate formula $\delta D=\psi^*V\psi d\tau/\psi^*\psi d\tau$, was added to the p-p repulsive potential. This corrected curve (b) is shown in Fig. 2.

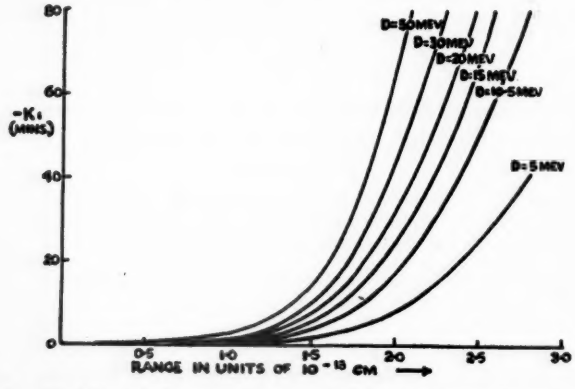

FIG. 1. Variation of phase shift K_1 as a function of well range for various well potentials, for the scattering of protons by protons.

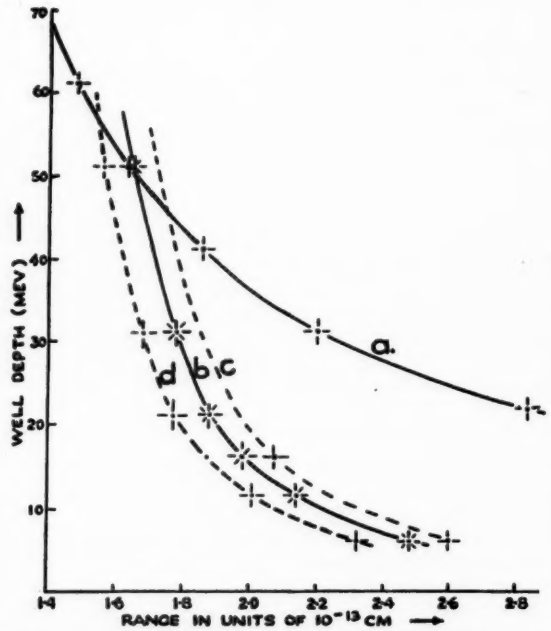

FIG. 2. Relation between well depth and range for the neutron proton interaction, as deduced from: (a) The binding energy of the deuteron; (b) the p wave scattering of protons by protons, taking $K_1=-0.4°$; (c) and (d) taking $K_1=-0.5°$ and $-0.3°$ respectively, and assuming charge independence of the nuclear interaction.

The intersection of curves (a) and (b) in Fig. 2 gives a unique value for a common range of the n-p and p-p triplet interactions satisfying both the experimental p-p scattering and the deuteron binding energy. This range is seen to be $1.65(\pm0.10)\times10^{-13}$ cm, a value almost identical with that given by the experiments on the scattering of neutrons by ortho- and para-hydrogen and by NaH. The corresponding triplet potential for the n-p interaction is 50.6 Mev, and for the p-p interaction 49.5 Mev.

[1] W. Rarita and J. Schwinger, Phys. Rev. **59**, 436 (1941).
[2] J. M. Blatt and J. D. Jackson, Phys. Rev. **76**, 18 (1949).
[3] Sutton, Hall, Anderson, Bridge, DeWire, Lavatelli, Long, Snyder, and Williams, Phys. Rev. **72**, 1147 (1947).
[4] Shull, Wollan, Morton, and Davidson, Phys. Rev. **73**, 842 (1948).
[5] R. R. Wilson, Phys. Rev. **71**, 384 (1947).
[6] R. E. Peierls and M. A. Preston, Phys. Rev. **72**, 250 (1947).
[7] L. L. Foldy, Phys. Rev. **72**, 731 (1947).

Upper Limit of Spin-Spin Interaction Factor

G. J. BENE, P. M. DENIS, AND C. R. EXTERMANN
Institut de Physique, Université de Genève, Geneva, Switzerland
November 29, 1949

WE applied the method of nuclear induction[1] to determine the gyromagnetic ratio of protons in water, at a fixed frequency, first in an iron-cored electro-magnet (field X), then in air-cored Helmholtz coils (field Y). The frequency used was 3 Mc, the resonance field being then about 750 gauss.

Using the flip-coil method, we were not able to detect any difference between the resonance fields X and Y. The error was in this case smaller than one percent. This sets a superior limit for the spin-spin interaction factor introduced by Stueckelberg.[2]

It is possible to attain a higher accuracy by determining the ratio μ_0F^{19}/μ_1H^1 of the nuclear moments for fluorine and hydrogen nuclei successively in fields X and Y. By using this method, we found the same ratio 0.9416 to three significant figures, confirming the previous negative result.

[1] F. Bloch, Phys. Rev. **70**, 460 (1946).
[2] E. C. G. Stueckelberg, Phys. Rev. **73**, 808 (1948).

Determination of the Maximum Energy of Beta-Rays from Cu 62 by a New Method of Analyzing Absorption Data

L. KATZ, A. S. PENFOLD, H. J. MOODY, R. N. H. HASLAM, AND H. E. JOHNS
Betatron Group, University of Saskatchewan, Saskatoon, Saskatchewan, Canada
November 14, 1949

LARGE discrepancies exist between various published values for the end-point energy of the beta-ray spectrum from Cu 62. The published values are 2.6 Mev,[1] 2.5 Mev,[2] and 3.42 Mev.[3] Absorption measurements of the beta-particles from Cu 62 were made by us in an effort to resolve these discrepancies.

It soon became apparent to us that a determination of the end point by visual inspection of the absorption curve or the graphical analyses found in the literature was inaccurate or cumbersome. We have developed a method of analyzing aluminum absorption curves which is an extension of a method given by Widdowson and Champion,[4] embodies some principles of the method of Bleuler and Zünti,[5] and has the advantage of yielding a straight line similar to a Fermi plot.

An aluminum absorption curve for beta-rays may be plotted as in Fig. 1, curve *A*, where the percent transmission of the rays

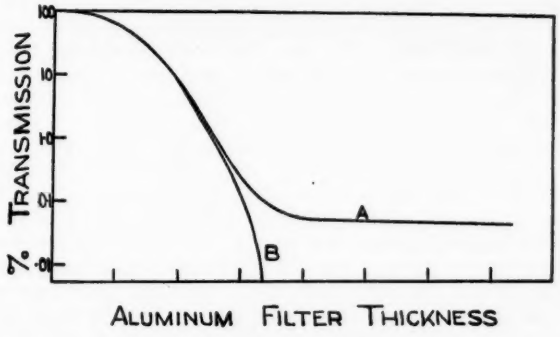

FIG. 1. Aluminum absorption curve for β-rays.

is plotted against filter thickness in mg/cm². If the gamma-ray background is subtracted, the curve *B* results.

Our method assumes that the lower part of the absorption curve follows a power law of the form:

$$y=K_1(E_0-E)^n, \tag{1}$$

where y is the fractional transmission, E_0 is the end-point energy, E is the energy of particles just absorbed at a given thickness of filter, and n is a positive constant greater than unity, and either integral or fractional. The expression can be transformed to give:

$$y^{1/n}=K_2(E_0-E). \tag{2}$$

If the logarithm of each side of (1) is taken, the resulting expression is

$$\log y=\log K_1+n\log(E_0-E).$$

From the absorption data of Fig. 1B an end point E_0' is assumed. A plot on log-log paper is then made of y *vs.* $(E_0'-E)$ and the slope of the curve is determined to give a value of n, say n'. Using this value n' a plot on linear paper is made of $y^{1/n'}$ *vs.* E. From expression (2) it can be seen that when the ordinate is zero a value for the end point, say E_0'' can be obtained. Using this value E_0'' a new value n'' of the exponent is obtained. This new value of the exponent is then used to get a more accurate value for the maximum beta-energy. These approximations are repeated until a sufficiently accurate value is obtained.

In all determinations done here successive approximations to E_0 have formed a convergent series. If a graph is plotted of the change in E_0 assumed against the E_0 obtained, then an extrapolation to $\Delta E=0$ will give the end energy exactly.

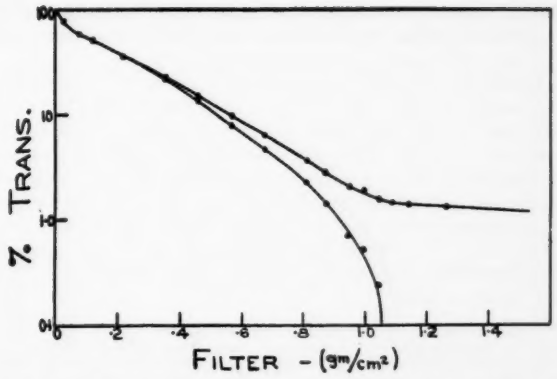

FIG. 2. Absorption curve for β-rays from Cu^{62}. Kink in curve at small filter thickness seems to indicate another component; this is being investigated.

Copper samples of 418 mg/cm² thickness were irradiated for 20 minutes at 70 *R*/min. in front of the University's 22-Mev betatron. An absorption curve was obtained and after corrections for loss of counts, the absorption curves were analyzed by this method as shown in Figs. 2, 3, and 4.

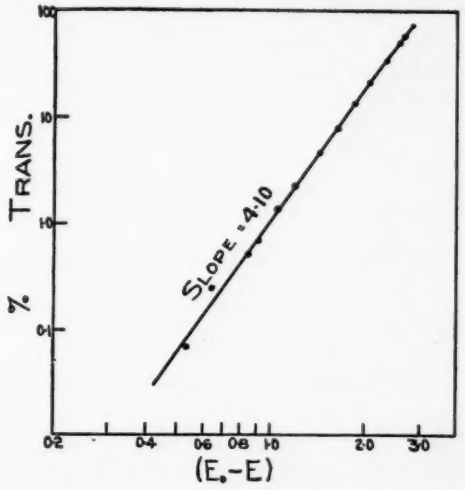

FIG. 3. Method of determining the value of n. The abscissas are the energies corresponding to given filter thicknesses as obtained from the range-energy curve.

Three separate determinations gave end points of 2.91, 2.94, and 2.92 Mev. The mean of these values is 2.92 Mev and the possible error was estimated to be ±0.06 Mev. This value is in

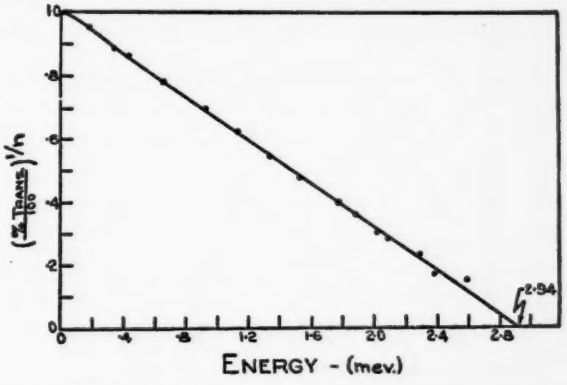

FIG. 4. Plot of $y^{1/n}$ against E to obtain E_0, the maximum β-energy.

essential agreement with a value reported by Becker and Kirn[6] who obtained as a "preliminary" value 2.80±0.05 Mev. This value was determined by spectrometric means.

In analyzing this data the range-energy curve for the absorption of electrons in aluminum as given in *The Science and Engineering of Nuclear Power*,[7] was used. All beta-spectra analyzed to date have indicated that this is the most reliable range-energy curve.

The above method of curve analysis may be used to obtain the end-energies of complex spectra. A paper is in preparation outlining the method in detail and giving further examples.

This work was carried out with the aid of a grant from the Canadian National Research Council, whose assistance is gratefully acknowledged.

[1] E. C. Crittenden, Jr., Phys. Rev. **56**, 709 (1939).
[2] G. T. Seaborg and I. Perlman, Rev. Mod. Phys. **20**, 596 (1948).
[3] K. Simma and F. Yamaski, Sci. Pap. Inst. Phys. Chem. Res. Japan **35**, 16 (1938).
[4] E. E. Widdowson and F. C. Champion, Proc. Phys. Soc. London **50**, 185 (1938).
[5] E. Bleuler and W. Zünti, Helv. Phys. Acta **19**, 375 (1946).
[6] R. A. Becker and F. S. Kirn, Phys. Rev. **76**, 182 (1949).
[7] *The Science and Engineering of Nuclear Power* (Addison-Wesley Press Inc., Cambridge, 1947), Vol. 1.

Photo-Disintegration of Rhodium*

N. W. Curtis, J. Hornbostel, D. W. Lee, and E. O. Salant
Brookhaven National Laboratory, Upton, New York
November 28, 1949

ANGULAR and energy distributions of protons from nuclei disintegrated by collimated x-rays produced with a 20-Mev betatron have been studied, some preliminary results of rhodium disintegrations being presented here.

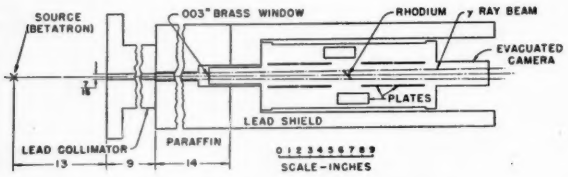

FIG. 1. Experimental arrangement, schematic.

A diagrammatic sketch of the apparatus is shown in Fig. 1. Alignment was checked optically and with x-ray shadowgraphs. Particles emitted from the target enter photographic emulsions (200μ Ilford) in an evacuated "camera." Only those tracks beginning at the surface are measured; neutron-proton recoil tracks originating in the body of the emulsion are sparse enough and evenly enough distributed so that they contribute negligibly to surface tracks, which are observed to have the correct directions for the protons to originate in the target. Energies are evaluated by the usual range relationship[1] and are corrected for loss in the 0.025-mm target.

TABLE I. Ratios of small-angle to right-angle intensities.

Proton energies, Mev	3.5–5.5	5.5–7.5	7.5–9.5	9.5–11.5
Ratios	0.69±0.14	0.75±0.10	0.54±0.10	0.23±0.08

Figure 2 shows histograms of observed intensities I (=number of protons per hundredth steradian) for 3 plate positions, 20° (forward)±7°, 90°±12°, and −20° (=160°)±7°, the factor to convert I to N, the number of observed tracks, being stated on each histogram. Fore and aft intensities do not differ within present statistical errors, but right-angle emission predominates over emission at small angles, particularly at the higher proton energies. The small-angle intensity is averaged from the fore-and-aft positions and its ratio to right-angle intensity is shown in Table I.

Some such angular asymmetry might be expected from either of the dipole theories,[2,3] though the effect has yet to be estimated quantitatively, either with these or the compound-nucleus models.[4]

A similar irradiation with a heavy paraffin target served to check the betatron x-ray spectrum[5] which, with the theoretical deuteron cross sections,[6] is consistent with our observed proton spectrum. From the upper limit of the x-ray energies and the highest energy rhodium proton tracks on the 90° plate, a threshold of 8±1 Mev is obtained. By comparing intensities on the 90° plates from the two targets (monitoring the beam with an ion chamber), it is found that the rhodium γ-p cross section is 4.0±0.5 times the deuteron γ-p cross section for the 15–20-Mev gamma-energy range. Using the value from the symmetrical theory for the deuteron cross section[7] at 17.5 Mev and 90°, then, with the foregoing rhodium—deuteron ratio, the rhodium cross section for 17.5±1.0 Mev and 90° comes out to be $3.6(\pm 0.5)\times 10^{-28}$ cm²/sterad. With this value and with the observed angular distribution, the integral cross section for the same energy is $3.5(\pm 0.6)\times 10^{-27}$ cm². These cross sections apply to disintegration into a normal Ru^{102} nucleus; that excited states of the latter are not much involved in disintegrations by 15—20-Mev gamma-rays is

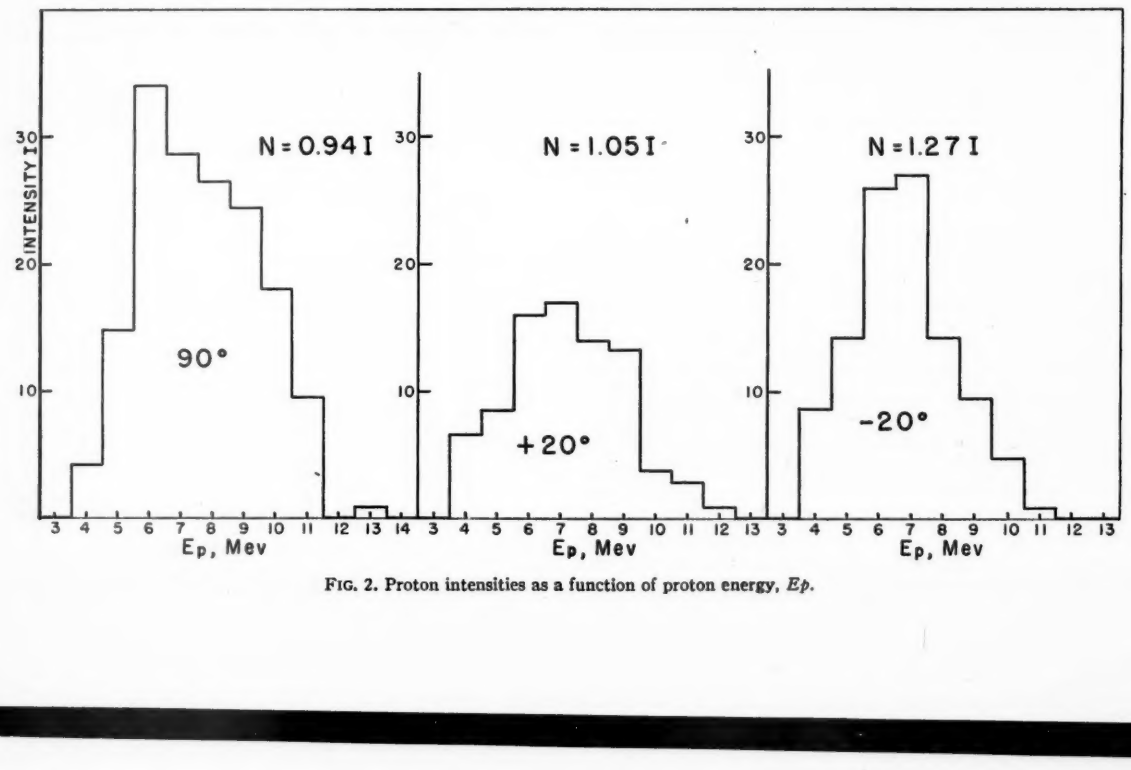

FIG. 2. Proton intensities as a function of proton energy, E_p.

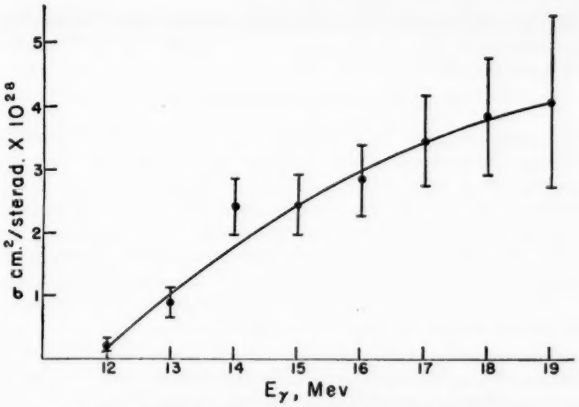

FIG. 3. Cross sections for proton emission at 90° as a function of γ-ray energy.

implied by the closeness of this value to the total photo-proton cross sections of neighboring elements determined by the radioactive-product method.[8]

With the threshold, the 90° cross section and the betatron intensity spectrum, the 90° excitation curve, calculated for a normal product nucleus, is shown in Fig. 3.

An upper limit to the neutron flux from the betatron was obtained in the heavy paraffin irradiation. Upper limits to Rh n-p cross sections at large and small angles were determined for 11–14-Mev neutrons, with coincidence proportional counters.[9] These values show that only a negligible fraction of our observed protons could come from an n-p reaction.

We take pleasure in acknowledging our indebtedness to Colonel C. R. Dutton of Picatinny Arsenal for permission to use the betatron and to Dr. B. A. Lloyd of the Arsenal for invaluable aid.

* Research carried out at the Brookhaven National Laboratory under the auspices of the AEC.
[1] C. M. G. Lattes, P. H. Fowler, and P. Cuer, Proc. Phys. Soc. (London) 59, 883 (1947).
[2] M. Goldhaber and E. Teller, Phys. Rev. 74, 1046 (1948).
[3] E. D. Courant, Phys. Rev. 74, 1226 (1948).
[4] V. F. Weisskoff and D. H. Ewing, Phys. Rev. 57, 472 (1940).
[5] H. W. Koch and R. E. Carter, Phys. Rev. 75, 1950 (1949).
[6] A. Pais, Kgl. Danske Vid. Sels. Math.-fys. Medd. 20, 1 (1943).
[7] W. Rarita and J. S. Schwinger, Phys. Rev. 59, 556 (1941).
[8] O. Hirzel and H. Wäffler, Helv. Phys. Acta 20, 373 (1947); 21, 200 (1948).
[9] E. Wantuch, this Laboratory (private communication).

A Delayed Coincidence Counting Measurement of $Hg^{203,205}$*

DANIEL BINDER
Sloane Physics Laboratory, Yale University, New Haven, Connecticut
December 5, 1949

AN attempt has been made to measure the half-life of the γ-ray in the beta-gamma-cascade emission from $Hg^{203,205}$ by a delayed coincidence measurement. The experimental arrangement makes use of a proportional counter as the beta-ray detector and a 931A photo-multiplier tube with an anthracene crystal as the gamma-detector. A resolution curve for the detectors and coincidence circuits was obtained by sending beta-rays from a P^{32} source through the proportional counter into the anthracene scintillation counter. The resulting plot of coincidence counting rate *versus* delay (placed in either channel) resulted in a symmetrical curve with a half-width of 7×10^{-8} sec.

The $Hg^{203,205}$ source was placed between the two counters with an absorber to stop the beta-rays from entering the scintillation counter and a similar curve taken. A compilation of two runs is shown in Fig. 1, and the curve is quite symmetrical. An upper limit for the half-life may be obtained by using theoretical expressions[1] for the coincidence *versus* delay curves. Increasingly larger

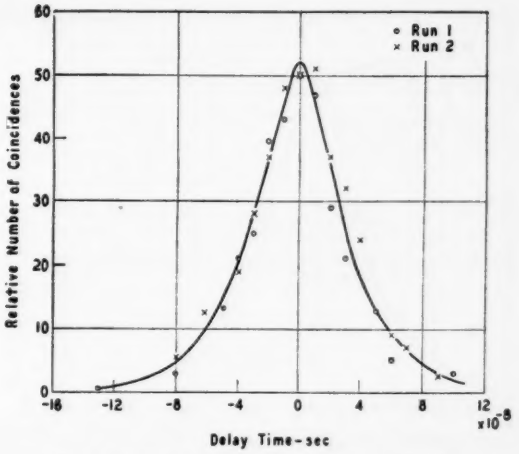

FIG. 1. Coincidence counting rate *versus* delay curve for the $Hg^{203,205}$ decay.

values for the half-lives were inserted in these expressions until a distinct asymmetry appeared in the curve. This occurred at 2×10^{-8} sec., which is then the upper limit.

From the work of Inghram, Hess, and Hayden,[2] the observed activity is probably due to Hg^{203}. Using this fact and the γ-ray energy given by Saxon[3] in Segré's formula,[4] an upper limit for the l-change may be determined. For $\Delta l=2$, the computed half-life is 9×10^{-10} sec., and for $\Delta l=3$, 2×10^{-5} sec. The l-change is thus not greater than 2, in agreement with Saxon's value[3] of 2 from the ratio of K and L conversion coefficients.

The author would like to thank Professors E. C. Pollard and H. L. Schultz for valuable discussions and Mr. F. G. Timperley for technical assistance.

* Assisted by the Joint Program of the ONR and the AEC.
[1] D. Binder, Phys. Rev. 76, 856 (1949).
[2] Inghram, Hess, and Hayden, Phys. Rev. 71, 561 (1947).
[3] D. Saxon, Phys. Rev. 74, 849 (1948).
[4] E. Segré and A. C. Helmholz, Rev. Mod. Phys. 21, 271 (1949).

Coherent Neutron-Proton Scattering by Liquid Mirror Reflection*

D. J. HUGHES
Brookhaven National Laboratory, Upton, Long Island, New York
AND
M. T. BURGY AND G. R. RINGO
Argonne National Laboratory, Chicago, Illinois
December 7, 1949

THE importance of the coherent scattering of slow neutrons by protons in the determination of the range of nuclear forces has been emphasized recently by Blatt,[1] Blatt and Jackson,[2] and Bethe.[3] These authors show that the main uncertainty in the determination of the singlet as well as the triplet n-p range is the coherent n-p scattering. The coherent scattering has been measured with an accuracy of three percent in the parahydrogen experiment[4] and slightly less accurately by the scattering from hydrogen in crystals.[5] The former experiment contains a possible additional systematic error caused by the presence of orthohydrogen and the latter experiment possesses the uncertainty of the correction for temperature diffuse scattering (which lessens the observed coherent scattering). About a year ago, when plans for a repetition of the parahydrogen measurement were being considered, Hamermesh[6] and Wattenberg suggested that the coherent hydrogen scattering might be measured with the neutron mirror techniques then in use at Argonne Laboratory.[7,8] Hamermesh pointed out that the coherent scattering amplitude could be obtained from the critical angle of a hydrogen mirror with no theoretical uncertainty (no effect of inelastic scattering because only forward scattering is involved in glancing reflection), but

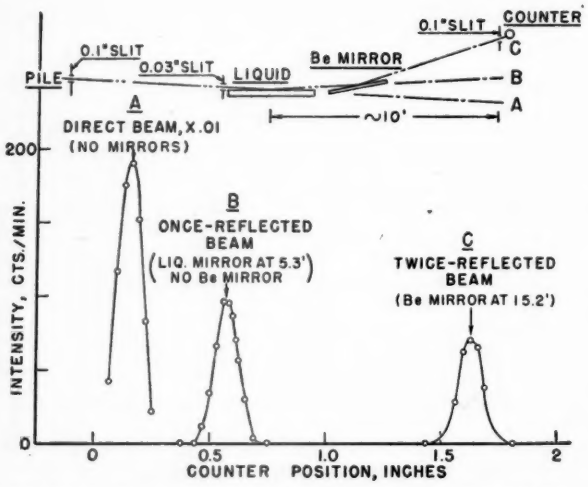

FIG. 1. Experimental arrangement of mirrors and the variation of the beam intensity with counter position.

that an accuracy of one percent in the amplitude would require measurement of a 10′ critical angle to 0.05′. Because of the difficulty of such an experiment, no plans for its performance were made.

Recently, however, we have devised a method which gives the coherent hydrogen amplitude very exactly with only a moderately accurate measurement of the critical angle. In this method, neutrons are specularly reflected from tri-ethyl benzene, a liquid containing a hydrogen to carbon ratio of 1.5 ($C_{12}H_{18}$). This compound is chosen because the (positive) amplitude of carbon is slightly greater than 1.5 times the (negative) amplitude of hydrogen. The critical angle, θ_c, for neutron reflection from the liquid is then proportional to $(a_C+1.5a_H)^{\frac{1}{2}}$, and a certain error in θ_c implies a much smaller error in a_H (approximately $\frac{1}{10}$th the error in θ_c for tri-ethyl benzene). If the two amplitudes are balanced more closely by changing the C—H ratio, the required accuracy in the critical angle becomes even less, but the angle would be so small that its measurement would not be feasible. With a carbon to hydrogen ratio of 1.5 and the previously accepted value for a_H, a critical angle of 6′ for a neutron wave-length of 8A was expected.

In spite of many misgivings, it proved to be extremely simple to reflect neutrons from the liquid surface. A thermal neutron beam (obtained from the Argonne pile) was collimated by 0.1-in. slits 10 ft. apart, and was incident on the liquid surface at an angle of 5.3′, as measured by the position of the reflected neutron beam relative to the direct beam (Fig. 1). The incident neutrons contained all the wave-lengths of the Maxwell distribution, hence all wave-lengths longer than the wave-length, λ_c, whose critical angle is 5.3′, were reflected. In order to measure λ_c, the beam of neutrons leaving the liquid was in turn reflected at a Be mirror. The intensity reflected by the Be mirror remains constant until the angle of incidence reaches the Be critical angle for the wave-length λ_c. The critical angle for the Be mirror as a function of wave-length had already been determined with monochromatic neutrons, hence λ_c could be obtained from the observed Be critical angle. As a second method of obtaining λ_c the transmission of the reflected neutrons in a standardized plate of gold was measured and λ_c calculated from the transmission and the known (Maxwellian) velocity distribution. The angle of incidence at the liquid mirror was then changed and the new λ_c measured again by both methods.

The critical wave-length, λ_c, for a particular angle, θ_c, at the liquid mirror then gives the amplitude $(a_C+1.5a_H)$:

$$\theta_c=\lambda_c[N(a_C+1.5a_H/\pi]^{\frac{1}{2}},$$

where N is the number of C atoms per cm³. The value of a_C is known to 0.5 percent from total cross-section measurements at energies slightly above thermal[9] and is taken to be 6.63×10^{-13} cm (corresponding to a free atom cross section of 4.7 barns). The value for a_H then becomes

$$a_H=-(3.75\pm0.03)\times10^{-13}\text{ cm}.$$

The standard error, 0.9 percent, is based on the statistics of the present measurement alone and does not include the (smaller) uncertainty in the carbon amplitude. Although there is no known source of systematic error, the measurement could be repeated with a different liquid to lessen the possibility of unknown errors and to push the accuracy even higher. Our result is five percent lower than the value of the hydrogen amplitude obtained in references 4 and 5 and is outside the error of those experiments as quoted by Blatt and Jackson[2] and Bethe.[3]

The changes in the nuclear force constants which will result from the present experiment can be estimated roughly from the curves given by Blatt, and Blatt and Jackson. From Fig. 2, reference 1, and Fig. 7, reference 2, it is seen that the new value of the hydrogen amplitude will raise the triplet n-p range to 1.71×10^{-13} cm and produce an increase in the singlet range of about 1×10^{-13} cm. This change in the singlet range is about half the amount needed to make the n-p range equal to the p-p range. Errors which are involved in the other constants necessary to infer the ranges may well make up the rest of the difference and thus attain consistency of the experimental constants with charge-independence of nuclear forces.

We wish to extend our thanks to Dr. R. Dodson, H. Prosser, and R. C. Anderson of the Brookhaven National Laboratory Chemistry Department for the purification of the tri-ethyl benzene, to Dr. M. Hamermesh for valuable help in the planning and analysis of the experiment, and to Dr. A. Wattenberg for his assistance while the measurements were being made at Argonne Laboratory.

* Work performed under the auspices of the AEC.
[1] J. M. Blatt, Phys. Rev. **74**, 92 (1948).
[2] J. M. Blatt and J. D. Jackson, Phys. Rev. **76**, 18 (1949).
[3] H. A. Bethe, Phys. Rev. **76**, 38 (1949).
[4] Sutton, Hall, Anderson, Bridge, De Wire, Lavatelli, Long, Snyder, and Williams, Phys. Rev. **72**, 1147 (1947).
[5] Shull, Wollan, Morton, and Davidson, Phys. Rev. **73**, 842 (1948).
[6] M. Hamermesh, Phys. Rev. **77**, 140 (1950).
[7] E. Fermi and L. Marshall, Phys. Rev. **71**, 666 (1947).
[8] D. J. Hughes and M. T. Burgy, Phys. Rev. **76**, 1413 (1949).
[9] W. W. Havens and L. J. Rainwater, Phys. Rev. **75**, 1296 (1949); W. B. Jones, Phys. Rev. **74**, 364 (1948); C. T. Hibdon and C. O. Muelhause, Phys. Rev. **76**, 100 (1949); C. G. Shull and E. O. Wollan (private communication); W. Selove (private communication).

Interatomic Distances in CF_3Br, CF_3I, and CF_3CN*

JOHN SHERIDAN** AND WALTER GORDY
Department of Physics, Duke University, Durham, North Carolina
December 2, 1949

INVESTIGATIONS of the microwave spectra of CF_3Br, CF_3I, and CF_3CN have been made which allow a partial determination of the structures of these molecules. Attempts are being made to obtain molecules with other stable isotopes concentrated so that an unambiguous assignment of the atomic distances can be made.

$C^{12}F_3Br^{79}$ and $C^{12}F_3Br^{81}$.—Measurements of the $J=8\rightarrow9$, $10\rightarrow11$, and $11\rightarrow12$ transitions have been made. The analysis of the hyperfine structure is incomplete. The moments of inertia I_B are 399.9×10^{-40} g/cm² for CF_3Br^{79} and 403.7×10^{-40} g/cm² for CF_3Br^{81}. If tetrahedral bond angles to the carbon are assumed, the distance $d_{CF}=1.32_6$A and $d_{CBr}=1.93_3$A are obtained. These are in close agreement with the corresponding values in fluoroform,[1] $d_{CF}=1.326$A, and in methyl bromide,[2] $d_{CBr}=1.936$A. The CF distance is considerably smaller than the added covalent radii[3] (1.51A), while the CBr distance is, within experimental error, equal to the added covalent radii (1.94A) of C and Br.

CF_3I.—The $J=14\rightarrow15$ and $11\rightarrow12$ transitions were observed for CF_3I. Analysis of the hyperfine structure has not been completed. The moment of inertia I_B is equal to 551.0×10^{-40} g/cm². If tetra-

hedral angles are assumed and $d_{CF}=1.326$A, as in fluoroform and CF_3Br, the resulting value for d_{CI} is 2.16$_2$A. This is significantly longer than the added covalent radii (2.12A). A plausible explanation for the larger d_{CI} is that ionic structures of the type,

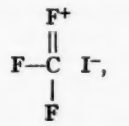

make significant contributions to the ground state. Though in this structure the positive charge is on the most electronegative atom, the unfavorable charge distribution may be counterbalanced by the strong tendency of F to form double bonds. As has been pointed out by Pauling,[4] the tendency of atoms to form multiple bonds decreases rapidly with descending rows in the periodic table. In this connection, it is of interest that the d_{CCl} distance 1.765A in CF_3Cl recently determined from microwave spectroscopy by Coles and Hughes[5] is slightly less than the added covalent radii, and that d_{CF} in CF_3F is considerably less than that in CH_3F.[6] It seems plausible that d_{CX} in CF_3X is lengthened or shortened in accord with the relative contributions of the above type of ionic structure and those containing $C=X^+$, the latter gaining predominance in the sequence X=I, Br, Cl, F.

CF_3CN.—The $J=5\rightarrow6$ and $7\rightarrow8$ transitions have been observed and the moment of inertia, $I_B=284.7\times10^{-40}$ g/cm^2 obtained for $C^{12}F_3C^{12}N^{14}$. If tetrahedral angles, $d_{CF}=1.326$A (as in CHF_3), and $d_{CN}=1.160$ are assumed, the d_{CC} obtained is 1.49$_2$A. The hyperfine structure due to N^{14} quadrupole coupling was barely resolvable.

* The research reported in this document has been made possible through support and sponsorship extended by the Geophysical Research Directorate of the Air Force Cambridge Research Laboratories under Contract No. W19(122)ac-35. It is published for technical information only and does not represent recommendations or conclusions of the sponsoring agency.

** On leave from Department of Chemistry, University of Birmingham, Birmingham, England.

[1] Gilliam, Edwards, and Gordy, Phys. Rev. **75**, 1014 (1949).
[2] Gordy, Simmons, and Smith, Phys. Rev. **74**, 243 (1948).
[3] For F the revised radius proposed by Shomaker and Stevenson (J. Am. Chem. Soc. **63**, 37 (1941)) and for C the revised value suggested by Gordy (J. Chem. Phys. **15**, 81 (1947)) is employed.
[4] L. Pauling, *The Nature of the Chemical Bond* (Cornell University Press, Ithaca, 1940), p. 232.
[5] D. K. Coles and R. H. Hughes, Phys. Rev. **76**, 858 (1949).
[6] L. O. Brockway, J. Phys. Chem. **41**, 185 (1937).

The Scattering of Light by Light

J. C. WARD
The Clarendon Laboratory, Oxford, England
November 7, 1949

IN a recent paper, F. J. Dyson[1] has shown that the divergencies which occur in quantum electrodynamics may be consistently eliminated by the use of mass and charge renormalization, to all orders of approximation. One of the processes which might be thought to give rise to divergencies and which has to be discussed is the scattering of light by light. The divergence may be isolated in a logarithmically divergent integral which is not gauge invariant, and it is conjectured that this term vanishes for reasons of symmetry as is the case to lowest order in e^2. It seems that a formal proof can be given as follows.

The integral in question, in Dyson's notation, is $\int R_{\lambda\mu\nu\sigma}(0, p^i)dp^i$, where p^i represent the internal variables corresponding to the degrees of freedom of a certain irreducible graph having only four external photon lines incident, and therefore a finite number of closed electron loops connected by internal photon lines. The energy-momenta of the external photons is put equal to zero. From the independent variables p^i, we may take a set t^j, one for each of the closed loops, corresponding to the energy-momenta with which the virtual electrons propagate within their own loops. The effect of the incident external photon lines will now be to replace $S_F(p)$ by $S_F(p)\gamma_\mu S_F(p)$ in particular electron lines of the reduced graph obtained by leaving out the external photon lines entirely. But there is the relation $(1/2\pi)(\partial/\partial t_\mu{}^j)S(p)=S(p)\gamma_\mu S(p)$ for electron lines in the loop carrying the variable t^j.

Hence the total effect of inserting external photon lines in all electron lines of the reduced graph is to give

$$\sum_{jklm}\int\frac{\partial}{\partial t_\lambda{}^j}\frac{\partial}{\partial t_\mu{}^k}\frac{\partial}{\partial t_\rho{}^l}\frac{\partial}{\partial t_\nu{}^m}[M(p^i)]dp^i,$$

where this expression also accounts correctly for the possible insertion of two or more photon lines at one electron line.

Since M is uniformly small for large t, this vanishes on integration over the energy momenta of the virtual electrons.

[1] F. J. Dyson, Phys. Rev. **75**, 1736 (1949).

Ferromagnetic Resonance Absorption by Mo Permalloy at 2920 Mc/Sec.

JUNKICHI ITOH AND TETSUO AKIOKA
Department of Physics and Research Institute of Acoustical Science, Osaka University, Osaka, Japan
September 6, 1949

FERROMAGNETIC resonance absorption at microwave frequency has been studied by several authors.[1,2] Except in the first experiment, the frequency used was greater than 8000 mc/sec. usually about 30,000 mc/sec. We performed the experiment at 2920 mc/sec.

The resonance condition for plane specimen is given by the equation:[3]

$$\omega=\gamma(BH)^{\frac{1}{2}}, \tag{1}$$

where ω is the angular frequency of microwave, γ is the gyromagnetic ratio of electron, B is the magnetic induction, and H is the magnetic field strength. Since the resonance field is very low for 2920 mc/sec., we used Mo Permalloy for the absorbing material,* which saturates magnetically at few oersteds and whose saturation magnetic induction is 8500 gauss.

The apparatus used is a magic tee and a high Q resonant cavity of rectangular cross section (7.0×3.5 cm^2). The cavity is of one wave-length size and is connected to a wave guide which forms one branch of the magic tee, by a rectangular slot. On the end plate, a thin plate of Mo Permalloy is sometimes soldered and sometimes set by screws. On the front half of the cavity, a finely adjustable plunger is put on, by which the resonant frequency of the cavity can be changed very finely.

First, keeping the cavity always at resonance by adjusting the plunger, the absorption by Mo Permalloy is measured as a function of static magnetic field which is perpendicular to the high frequency magnetic field. The result obtained is shown in Fig. 1.

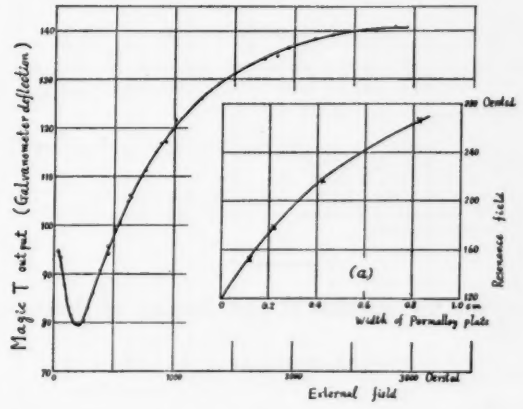

FIG. 1. Absorption curve by Mo Permalloy (2.9×3.4 cm^2 in area and 0.053 cm in thickness) at 2920 mc/sec. (a) Magnetic field strength at maximum absorption.

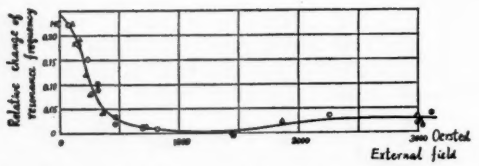

FIG. 2. Relative change in resonant frequency measured by a sample of 2.9×3.4 cm² in area and 0.053 cm in thickness. (Various marks indicate different series of experiments.)

Since the demagnetizing factor of the sample is not known accurately, we determined the true resonance field experimentally by the following procedure. The samples whose length is 2.9 cm and whose thickness is 0.053 cm, having various widths, are screwed on the end plate and resonance fields are measured successively. The values of resonance field are plotted against the width of the samples, as shown in Fig. 1(a). The value of resonance field extrapolated to zero width must correspond to the true resonance field with zero demagnetization field. The value thus obtained is 120 oersted, and the calculated g value of electron using (1) is 2.05, the error being about three percent.

Next, keeping the frequency of microwave constant, the plunger length corresponding to the resonance of the cavity is measured as a function of magnetic field. The relation between the plunger length and the change of resonant frequency of the cavity is calibrated by comparing it with a standard cavity wave-length meter. From these measurements we can calculate the change of resonant frequency of the cavity as a function of magnetic field, as shown in Fig. 2, in which the resonant frequency at 1200 oersted is accepted as a standard frequency.

From the above two experiments, we can calculate μ_R and μ_L, assuming that at very high field both μ_R and μ_L coincide with static μ. By the relation between complex permeability, $\mu=\mu'-j\mu''$, and μ_R and μ_L,[3] we calculated the values of μ' and μ'' as functions of magnetic field, which are shown in Fig. 3. The

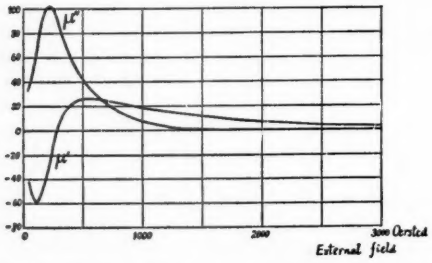

FIG. 3. μ' and μ'', measured by a sample of 2.9×3.4 cm² in area and 0.053 cm in thickness. Demagnetizing field is about 120 oersted.

result does not coincide quantitatively with the theoretical prediction by Kittel,[3] even if the relaxation force is assumed to be given by $-\lambda[\mathbf{M}-\chi_0\mathbf{H}]$, where λ/H is a constant, as Yager did.[2]

Further work is now going on.

[1] J. H. E. Griffiths, Nature 158, 670 (1946); W. A. Yager and R. M. Bozorth, Phys. Rev. 72, 80 (1947).
[2] W. A. Yager, Phys. Rev. 75, 316 (1949).
[3] C. Kittel, Phys. Rev. 71, 270 (1947); 73, 155 (1948).
* We are indebted to Professor Y. Shirakawa of Tohoku University for obtaining these samples.

On the Calculation of Self-Energy of Particles

SURAJ N. GUPTA*
Cavendish Laboratory, Cambridge, England
December 2, 1949

IT has been shown in recent years that the self-energy of particles may be obtained in a covariant form by using an invariant perturbation theory developed by Tomonaga, Schwinger, Feynman, and others. However, it will be of interest to show that the covariant self-energy may be obtained even with the ordinary perturbation theory by using our generalization of a transformation due to Pauli and Rose.[1]

For instance, the calculation of the mesic self-energy of a nucleon with momentum $\mathbf{p}$ involves a summation over virtual states containing a pair of a nucleon and a meson with momenta $(\mathbf{p}-\mathbf{k})$ and $\mathbf{k}$, and energies E and ϵ respectively, where

$$E=\{M^2+(\mathbf{p}-\mathbf{k})^2\}^{\frac{1}{2}}, \quad \epsilon=(\mu^2+k^2)^{\frac{1}{2}}. \tag{1}$$

Since $(\mathbf{p}-\mathbf{k}, E)$ and $(\mathbf{k}, \epsilon)$ are 4-vectors, their sum $(\mathbf{p}, E+\epsilon)$ is also a 4-vector, and hence

$$z\equiv\{(E+\epsilon)^2-p^2\}^{\frac{1}{2}} \tag{2}$$

is a Lorentz-invariant quantity. We can, therefore, obtain a covariant result by expressing the self-energy integral in terms of the variable z.

For this, we carry out the transformation from the variables $\mathbf{k}$ to the variables ϕ, v, and ω, where ϕ is the azimuthal angle around the axis parallel to $\mathbf{p}$, and

$$v=E-\epsilon, \quad \omega=E+\epsilon. \tag{3}$$

Computing the functional determinant, we obtain for the elements of volume the relation

$$d\mathbf{k}/E\epsilon=(1/2p)d\phi dv d\omega. \tag{4}$$

The limits of integration of ϕ are

$$0\leqslant\phi\leqslant 2\pi. \tag{5}$$

To obtain the limits of v, we note that

$$(E^2-\epsilon^2-p^2-M^2+\mu^2)^2=4(\mathbf{k}\cdot\mathbf{p})^2\leqslant 4k^2p^2,$$

or

$$(v\omega-p^2-M^2+\mu^2)^2\leqslant p^2\{(\omega-v)^2-4\mu^2\},$$

or

$$v^2(\omega^2-p^2)+2v\omega(\mu^2-M^2)+(p^2+M^2-\mu^2)^2+4\mu^2p^2-p^2\omega^2\leqslant 0.$$

Hence the two limits of v are given by

$$v=\frac{(\omega(M^2-\mu^2)\pm pF(z))}{z^2}, \tag{6}$$

where

$$F(z)\equiv\{z^4-2(M^2+\mu^2)z^2+(M^2-\mu^2)^2\}^{\frac{1}{2}}. \tag{7}$$

The limits of ω are

$$\{(\mu+M)^2+p^2\}^{\frac{1}{2}}\leqslant\omega\leqslant\alpha, \tag{8}$$

the least value of ω corresponding to $\mathbf{k}=\mu/(\mu+M)\mathbf{p}$. Since according to (2)

$$z=(\omega^2-p^2)^{\frac{1}{2}} \tag{9}$$

it follows that the limits of z are

$$(\mu+M)\leqslant z\leqslant\alpha. \tag{10}$$

It should be noted that the transformation given above is the most general one, and covers all possible cases. If we put $\mu=M$, we obtain the transformation given by Pauli and Rose[1] for the treatment of vacuum polarization. On the other hand, if we put $\mu=0$, we get the transformation used by the present writer[2] to calculate the self-energy of the electron.

Using the above general transformation, we have calculated the self-energy of the nucleons due to the pseudoscalar as well as the vector meson field with the two types of coupling in each case (Moller-Rosenfeld-Schwinger mixture). It is found that the self-energy W is in general of the form

$$W=\delta M\cdot\frac{M}{(M^2+p^2)^{\frac{1}{2}}}+\delta N\cdot\frac{p^2}{(M^2+p^2)^{\frac{1}{2}}}, \tag{11}$$

where δM and δN are divergent functions of z but independent of p. The first term in (11) may be absorbed by a renormalization of the mass of the nucleon. On the other hand, the second term in (11), which arises from the direct coupling terms in the interaction, disappears on regularization developed by Feynman[3] and

by Pauli and Villars.[4] It will be interesting to compare the present situation with the electromagnetic self-energy of the mesons as investigated by Heitler and McConnell.[5]

I wish to express my thanks to Dr. S. T. Ma for many stimulating discussions. I am also indebted to Professor H. A. Bethe for some valuable comments.

* State Scholar of the Government of India.
[1] W. Pauli, and M. E. Rose, Phys. Rev. **49**, 462 (1936).
[2] S. N. Gupta, Proc. Phys. Soc. (to be published).
[3] R. P. Feynman, Phys. Rev. **74**, 1430 (1948).
[4] W. Pauli and F. Villars, Rev. Mod. Phys. **21**, 434 (1949).
[5] W. Heitler and J. McConnell, Nature **164**, 218 (1949).

Nuclear Gamma-Radiation of Cu^{61}

F. Boehm, J. P. Blaser, P. Marmier, and P. Preiswerk
Department of Physics, Swiss Federal Institute of Technology, Zürich, Switzerland
December 5, 1949

THE positron spectrum of Cu^{61} has been examined recently by Cook and Langer[1] with a large magnetic spectrometer. The experimental curves of these authors show a deviation from the Fermi distribution which is much larger than for Cu^{64} and it seems possible that not all of this deviation arises from instrumental factors. It is pointed out by different authors[2,3] that Cu^{61} does not emit nuclear gamma-rays which means that the spectrum of Cu^{61} must be simple. On the other hand the measurements of Cook and Langer can hardly be understood without the assumption of a complex spectrum. To examine this discrepancy, we started a search for gamma-radiation in Cu^{61}.

By irradiation of a nickel target with protons from the cyclotron we get very strong sources of Cu^{61}. After chemical separation and precipitation as chloride the Cu^{61} samples have been examined in a magnetic lens spectrometer for conversion-electrons and for photo-electrons. The following gamma-rays have been found:

$$E_{\gamma 1} = (0.652 \pm 0.005) \text{ Mev}$$
$$E_{\gamma 2} = (0.279 \pm 0.005) \text{ Mev}$$
$$E_{\gamma 3} = (0.070 \pm 0.001) \text{ Mev}.$$

The first and the second of these gamma-rays, γ_1 and γ_2, have been detected by photo-electron conversion from a lead radiator (Fig. 1). The relative intensity of these gamma-rays may be estimated by comparison with the photo-lines of the annihilation radiation taking into account the variation of the photoelectric cross section with energy, and the fact that two gamma-rays of the annihilation radiation are due to one positron. One gets for the intensity of γ_1 and γ_2 relative to the total number of decays respectively (9 ± 4) percent and (5 ± 3) percent. The ratio of K-capture to positrons in the 1.205 Mev transition has previously been assumed to be 0.3.

The intensities of γ_1 and γ_2 decay with the half-life of 3.35h characteristic of Cu^{61}. Contaminations can therefore be excluded.

The line γ_3 has been found as an internal conversion line in both a magnetic lens and a magnetic semicircular spectrometer. Its K/L conversion ratio was found to be 10 ± 3. Therefore this transition probably has a dipole character. Assuming a K internal conversion coefficient of about 10 percent (Hebb and Nelson), and comparing the line area with that of the positron spectrum, we find the intensity of this gamma-line relative to the number of decays to be (4 ± 2) percent. No harder gamma-radiation than 0.652 Mev could be found.

These gamma-rays give evidence for a complex decay of Cu^{61}. We may assume that the complexity arises from a positron transi-

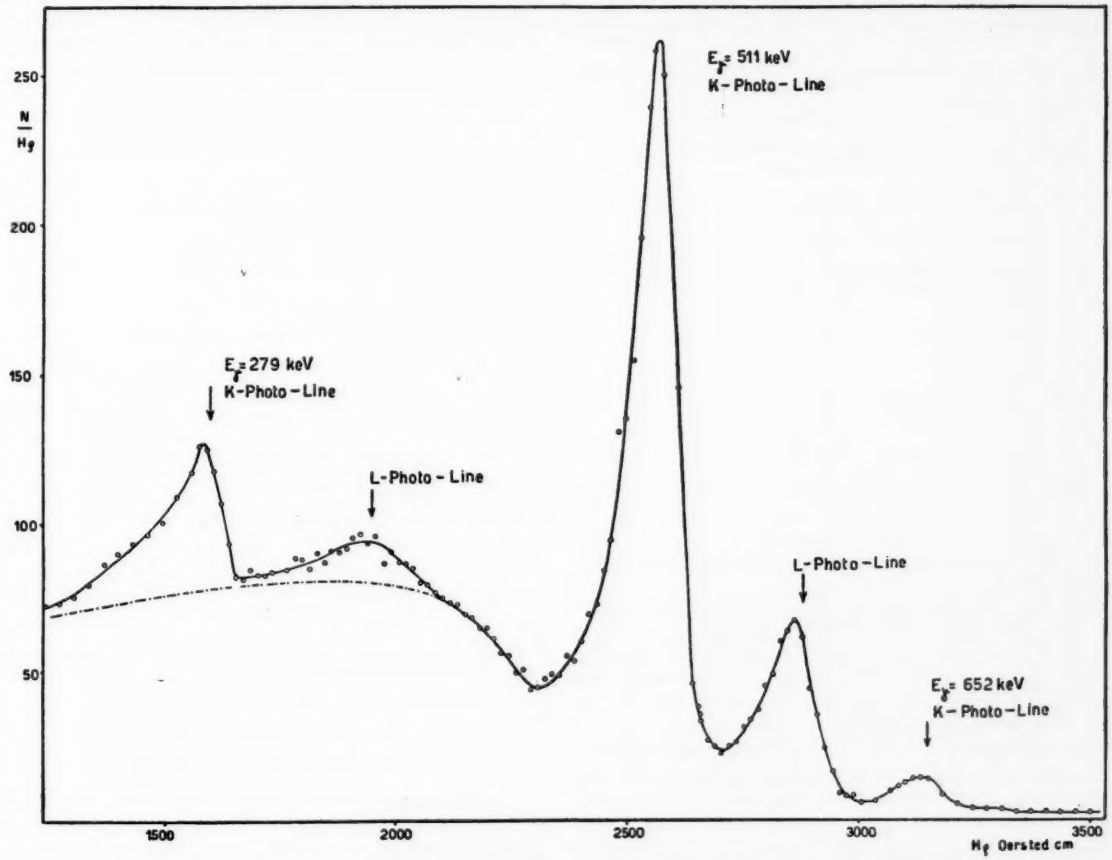

FIG. 1. Photo-electron spectrum of Cu^{61} with lead converter. Dotted curve shows the Compton electron background as measured in Zn^{65} in the same geometry.

tion to a state of Ni^{61} 0.652 Mev above the ground state. The end point energy of this spectrum would be 1.205−0.652=0.553 Mev. This assumption is in agreement with the findings of Cook and Langer that the positron spectrum shows a deviation for energies lower than about 0.511 Mev. For this energy the ratio of K-capture to positron emission is about 5, which means that in the momentum distribution of the positrons a complexity of about 1–2 percent must be expected.

We wish to thank Professor Scherrer for his kind interest in and active support of this work.

[1] C. S. Cook and L. M. Langer, Phys. Rev. **74**, 227 (1948).
[2] W. Gentner and E. Segrè, Phys. Rev. **55**, 814 (1939).
[3] Bradt, Gugelot, Huber, Medicus, Preiswerk, and Scherrer, Helv. Phys. Acta **18**, 252 (1945).

Half-Life for Double Beta-Decay*

C. A. LEVINE, A. GHIORSO, AND G. T. SEABORG
Department of Chemistry and Radiation Laboratory, University of California, Berkeley, California
November 28, 1949

FIREMAN[1] has reported the results of a rather difficult beta-particle coincidence counting experiment in which the decay of $_{50}Sn^{124}$ to $_{52}Te^{124}$ by the simultaneous emission of two negative beta-particles, with a half-life between 4×10^{15} and 9×10^{15} years, seems to have been observed. This note reports the results obtained from a different and somewhat simpler method of looking for the phenomenon of simultaneous emission of two beta-particles. These results are negative so far and show that this process is considerably less probable in the case chosen by us than in that reported by Fireman.

Our method consists of looking in uranium samples for 90-year Pu^{238} which would come from U^{238} by the double beta-particle mechanism since Np^{238} is heavier than U^{238}, which in turn is substantially heavier than Pu^{238}, in the isobaric triplet $_{92}U^{238}-{}_{93}Np^{238}-{}_{94}Pu^{238}$. This chemical method of investigation is particularly applicable to this isobaric triplet because there appears to be no other mechanism to account for the Pu^{238} should it be found. The energetics of the situation are summarized in the following diagram, where the disintegration energies (in Mev) are derived from sources which may be traced through a recent compilation.[2]

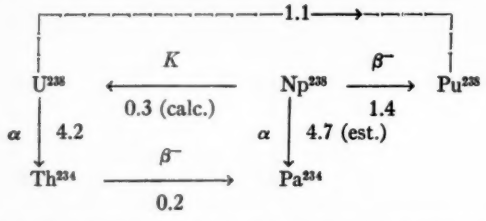

The alpha-disintegration energy of Np^{238} is estimated from alpha-decay systematics.[3]

Our experiment consisted of taking 14 kg of very pure, 6-year old, UO_3 and extracting and separating the plutonium fraction by chemical means. The method consisted essentially of dissolving the oxide in nitric acid and precipitating Pu(IV) with lanthanum fluoride, followed by solution of the lanthanum fluoride and oxidation of the plutonium to Pu(VI), which was extracted into diethyl ether and then re-extracted into water. Similar cycles were repeated five times in order to separate completely from UX_1 and to reduce the amount of lanthanum carrier, after which the final sample was plated out on flat platinum with total carrier weight probably less than 50 micrograms. The use of tracer Pu^{239} in this separation established that the chemical yield amounted to 10 percent.

This final sample was measured for the presence of the 5.51-Mev alpha-particles of Pu^{238} on the alpha-pulse analyzer apparatus in this laboratory.[4] This analysis showed that the counting rate of the Pu^{238} alpha-particles at essentially 50 percent counting yield amounted to 0.00±0.01 counts per minute above background. This indicates that the "half-life" of U^{238} for simultaneous emission of two beta-particles, for which a total energy of 1.1 Mev is available, is greater than 6×10^{18} years.

This experiment could be extended to reach longer half-lives through the use of larger and older sources of uranium such as pitchblende ore. In this case, of course, the plutonium fraction so isolated will contain a certain amount of Pu^{239} as has already been demonstrated.[5] The extraction of plutonium from a ton of pitchblende (50 percent uranium) with 10 percent yield could detect a half-life as long as some 10^{22} years for the same limits of counting accuracy.

This result appears to disagree with that of Fireman although it may not be possible to be positive about this in view of the difference in energies and atomic numbers and possible difference in degree of prohibition involved. The theory for the double beta-decay process sets widely differing ranges of half-life depending upon whether the process can take place without neutrino emission.[6] Fireman's results are in the range predicted for double beta-decay without neutrino emission while our half-life limit seems to be above this predicted range and perhaps points toward the emission of two neutrinos in this process.

A recent investigation[7] of the double beta-transition $_{52}Te^{130}\rightarrow{}_{54}Xe^{130}$, by a similar method in which the xenon present with a tellurium ore was analyzed, also points toward a two-neutrino process, but is subject to experimental uncertainty with respect to the age of and the degree of xenon retention by the ore.

It is a pleasure to acknowledge the assistance of Dr. L. B. Magnusson in the chemical procedure.

* This work was performed under the auspices of the AEC.
[1] E. L. Fireman, Phys. Rev. **75**, 323 (1949).
[2] G. T. Seaborg and I. Perlman, Revs. Mod. Phys. **20**, 585 (1948).
[3] Perlman, Ghiorso, and Seaborg, Phys. Rev. **74**, 1730 (1948); Phys. Rev. **77**, 26 (1950).
[4] Ghiorso, Jaffey, Robinson, and Weissbourd, National Nuclear Energy Series, Plutonium Project Record Vol. 14B "The Transuranium Elements: Research Papers," Paper No. 16.8 (McGraw-Hill Book Company, Inc., New York, 1949).
[5] G. T. Seaborg and M. L. Perlman, J. Am. Chem. Soc. **70**, 1571 (1948); National Nuclear Energy Series, Plutonium Project Record Vol. 14B "The Transuranium Elements: Research Papers," Paper No. 1.3 (McGraw-Hill Book Company, Inc., New York, 1949).
[6] W. H. Furry, Phys. Rev. **56**, 1184 (1939).
[7] M. G. Inghram and J. H. Reynolds, Phys. Rev. **76**, 1265 (1949).

On the Reaction $Mg^{24}(p, \gamma)Al^{25}$

T. GROTDAL, O. M. LÖNSJÖ, AND R. TANGEN
University of Oslo, Oslo, Norway
AND
I. BERGSTRÖM
Nobel Institute for Physics, Stockholm, Sweden
December 5, 1949

THE bombardment of ordinary magnesium with protons gives the following reactions:

(1) $Mg^{24}(p, \gamma)Al^{25}$ Q=2.3 Mev
(2) $Mg^{25}(p, \gamma)Al^{26}$ Q=8.4 Mev
(3) $Mg^{26}(p, \gamma)Al^{27}$ Q=7.3 Mev.

These reactions have been investigated by Curran and Strothers.[1] They separated the reactions by the positrons accompanying some of the resonances, ascribing these resonances to reaction (2). Hole, Holtsmark, and Tangen[2] found eight sharp resonances between 200 and 500 kv. Tangen,[3] using the same technique as

Curran and Strothers, found resonances in reaction (3) at 290, 314, 336, 388, 430, 451, and 494 kv, and resonances at 222, 310, 392, 417, 492, 508, and 525 kv accompanied by positron activity. Finding the γ-radiation from the strongest of the latter resonances, those at 222 and 417 kv, to have a mean energy of 1.5 Mev or less, he concluded that these resonances probably belong to reaction (1).

To solve this problem targets of separated Mg isotopes have been prepared in the isotope separator of the Nobel Institute in Stockholm,[4] and exposed to protons from the 500 kv van de Graaff machine of the University of Oslo. The thickness of the targets was about 35 μg/cm^2 Mg^{24}, for Mg^{25} and Mg^{26} the isotopic quantities corresponded to twice the amount of Mg^{24}. The targets were bombarded for 20 sec., giving saturation intensity of the positron activity, and the positrons escaping through a thin window in the target tube were counted for 15 sec. with a thin-walled G-M tube. As the proton current at present does not exceed 2 μA, only the strong resonances at 222 and 417 kv could be investigated. Positron activity corresponding to these resonances was found only on the Mg^{24} target, showing that the reaction $Mg^{24}(p, \gamma)Al^{25}$ is that actually taking place. Of course, there may also be resonances yielding positrons from the Mg^{25} reaction, such as suggested by Curran and Strothers.

[1] S. C. Curran and J. E. Strothers, Proc. Roy. Soc. London **A172**, 72 (1939).
[2] N. Hole, J. Holtsmark, and R. Tangen, Naturwiss. **28**, 399 (1940).
[3] R. Tangen, Kgl. Norske Vid. Selsk. Skr., No. 1 (1946).
[4] I. Bergström, S. Thulin, N. Svartholm and K. Siegbahn, Arkiv f. Fysik 1, 11 (1949).

Pd Film Fast Neutron Detector

B. R. Gossick
NEPA Division of the Fairchild Engine and Airplane Corporation, Oak Ridge, Tennessee
November 28, 1949

PRELIMINARY information has been obtained on resistance variations of a palladium film fired on a ceramic core due to recoil-proton bombardment. In view of the large magnitude of resistance changes, it is proposed here that this resistor might be employed to measure the energy absorbed per gram of tissue as a result of fast neutron flux, after L. H. Gray.[1] The resistors which have been exposed this far were manufactured by Continental Carbon, Inc., according to a process described in "Printed Circuit Techniques."[2] Through the courtesy of Dr. J. W. Jira, of Continental Carbon, resistors with exposed palladium films were obtained before the protective coats of vitreous enamel and paint were applied. One of these resistors was coated with paraffin and placed in an-air-cooled hole in the Oak Ridge pile. A fifteen-hour exposure at full power reduced the resistance from 48,300 to 234 ohms. A similar resistor in a chamber evacuated to approximately nine microns showed a resistance change of from 51,000 to 252 ohms within two minutes after 44 centimeters of hydrogen were applied to the system. The resistors were maintained at approximately room temperature during both the proton-recoil and hydrogen gas experiments.

Another resistor of the same type was placed in a stream of nitrogen within an oven which was brought to 900°C, and then allowed to cool. Again the resistance change was approximately from 50,000 to 200 ohms.

The resistance film initially has a dull gray appearance, and a negative temperature coefficient of resistance, indicating the presence of palladium oxide, but, after the resistance has been reduced by any one of the three treatments described above, the film is bright and shiny and the temperature coefficient of resistance is positive. This would suggest that the oxide has been reduced to the metal. The surface of the film is rough as seen under a low power microscope, both before and after the resistance has been reduced. It is doubtless important to the mechanism that palladium itself is a reducing catalyst, and can also occlude large quantities of hydrogen.

This phenomenon was first observed in the fall of 1947 at Argonne National Laboratory, when NEPA conducted radiation damage tests on electronic components under the direction of Mr. E. S. Bettis and Dr. E. R. Mann. In these tests, and again recently at the Oak Ridge pile, the vitreous enamel covered palladium film resistors of Continental Carbon were exposed in jackets of paraffin, polystyrene, graphite, cadmium, and aluminum. The resistance decreased substantially in the case of the hydrogenous covered resistors, sometimes to 4 percent of the initial value. The agreement in the results between resistors of the same value exposed under identical conditions was poor, and it seems probable that this was due to variations in the thickness of the protective vitreous enamel. Under the same bombardment the resistors covered with graphite, aluminum, and cadmium did not suffer an appreciable change in resistance.

[1] L. H. Gray, Proc. Camb. Phil. Soc. **40**, 72 (1944).
[2] Nat. Bur. Stand., Circular No. 468, November 15, 1947, page 16.

Nuclear Induction Due to Free Larmor Precession*

E. L. Hahn
Physics Department, University of Illinois, Urbana, Illinois
December 5, 1949

IN the study of transient and steady state phenomena concerning nuclear magnetic resonance it is well known that the nuclear magnetic moment possesses a flipped spin state having a phase memory of the order of T_2, the total relaxation time, which ranges from $\sim 10^{-5}$ to a few seconds in various substances. On the basis of this property Bloch[1] has pointed out that one can expect to obtain a nuclear induction signal in the absence of an applied r-f field after having suddenly perturbed the spin ensemble by the application of an r-f field pulse of short duration at the resonance condition $\omega = \omega_0 = \gamma H_0$. ω is the applied r-f angular frequency, γ is the gyromagnetic ratio, H_0 is the large d.c. magnetic field applied to a given ensemble of spins, and ω_0 designates the natural Larmor frequency of this ensemble. Directly following the removal of the pulse a resultant component of nuclear magnetization M_{xy} will remain the xy plane perpendicular to the large field H_0, which formerly established this magnetization in the z direction at thermal equilibrium. An inductive coil with its axis in the xy plane first provides the pulse, and thereafter has induced in it a nuclear induction r-f voltage as a consequence of the free Larmor precession of the magnetic moment M_{xy}.

Reported here is an experiment which displays this effect using conventional r-f techniques for providing r-f pulses and amplifiers capable of fast response in conjunction with typical nuclear induction apparatus. Only a single LC tuned circuit is essential for

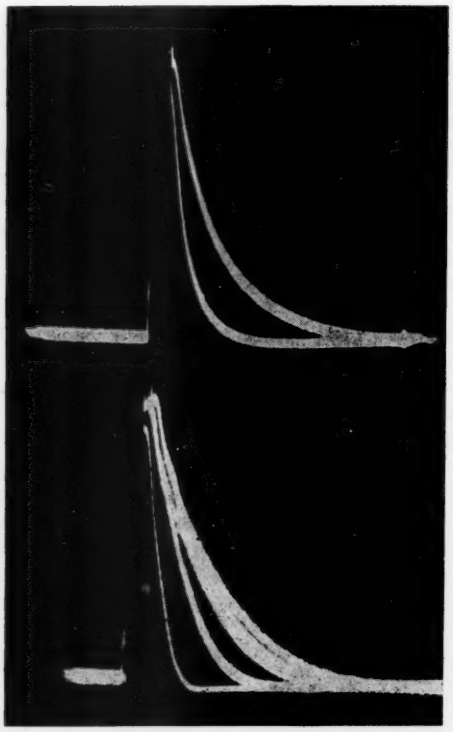

FIG. 1. The top oscillographic trace indicates by double exposure the nuclear induction decay due to protons in two water solutions of $Fe(NO_3)_3$ of different concentrations. The longer decay corresponds to 2×10^{19} Fe^{+++}/cc and the shorter decay corresponds to 9×10^{19} Fe^{+++}/cc, causing a T_2 of 0.0018 sec. and 0.0004 sec. respectively. T_2^* for both cases is $\sim$0.00046 sec. and $t_w\sim100$ μsec. H_1 is adjusted to an intensity such that $\omega_1 t_w\sim\pi/2$ and nutation provides an appreciable $M_{xy}(t_w)$.

Multiple exposures in the bottom photograph show various values of $T_m\sim T_2^*\ll T_2$ for protons in glycerine as T_2^* is arbitrarily changed from a maximum of 6.7×10^{-4} sec. (longest decay) to a minimum of 1.9×10^{-4} sec. (shortest decay). The slight dip following the pulse is due to momentary saturation of the receiver. The exposures are slightly displaced to indicate how $M_{xy}(t_w)$ is affected by changes in T_2^* as well as T_2 (upper photograph) due to decay of nutation during the pulse.

transmitting and receiving r-f energy, and critical balancing procedures are no longer a necessity. R-F pulses are applied at time intervals $>T_1\gtrsim T_2$ at pulse width $t_w<T_2$, at a maximum r-f field intensity H_1 (T_1 is the spin-lattice relaxation time).[2] *Following the pulse an exponential nuclear induction signal (Figs. 1 and 2) appears whose decay time depends upon (1) the extent of external magnetic field inhomogeneities over the sample, and (2) the intrinsic T_2 of the spin ensemble due to lattice conditions.* The condition brought about by (1) obscures a direct measurement of T_2 since the oscillations of M_{xy} over a spectrum of Larmor frequencies begin to interfere destructively and cause the integrated nuclear signal to decay more quickly than would otherwise be effected by T_2. T_1 can be directly measured, similar to a previous method,[3] by comparison of initial decay amplitudes for various known times between pulses. It will be shown in a later paper that (1) is the principal condition contributing to the spin echo effect,[4] which, however, permits direct measurement of T_2. The mechanism of free precession reported here is fundamental to obtaining the echo effect.

A qualitative prediction of the decay is indicated by integrating a simple solution (for M_{xy}) of Bloch's equations[1] over all Larmor frequencies imposed by the magnet, using a symmetric distribution function $g(\Delta\omega)$, where $\Delta\omega=\omega_0-\omega$ and $g(\Delta\omega)$ is maximum for $\Delta\omega=0$. The maximum voltage, V_{max}, of free induction is proportional to the following:

$$V_{max}\sim\omega\, e^{-(t-t_w)/T_2}\int_{-\infty}^{\infty} g(\Delta\omega)M_{xy}(\Delta\omega,t_w)\times\cos[\Delta\omega(t-t_w)+\phi]d(\Delta\omega),$$

where $\phi=\arctan(\Delta\omega/\beta\tan\beta t_w/2)$, $\beta=(\omega_1^2+(\Delta\omega)^2)^{\frac{1}{2}}$, and $\omega_1=\gamma H$. It is convenient to assume

$$g(\Delta\omega)=\frac{2T_2^*}{1+(\Delta\omega)^2T_2^{*2}},$$

where $T_2^*=2/(\Delta\omega)_{\frac{1}{2}}$ and $(\Delta\omega)_{\frac{1}{2}}$ is the total width at half-maximum of the spectrum due to external field inhomogeneities. If we further assume $\omega_1\gg(\Delta\omega)_{\frac{1}{2}}$ then $\phi\to0$ and $M_{xy}(\Delta\omega,t_w)$ is nearly constant in the region of $\Delta\omega\sim0$ where the integral does not vanish. Therefore, integration gives approximately

$$V_{max}\sim M_{xy}(t_w)\omega\exp\left[-t\left(\frac{1}{T_2}+\frac{1}{T_2^*}\right)\right],$$

where t is measured from the end of the pulse. The decay times T_m directly measured from oscillographic traces appear to obey the relationship $1/T_m=1/T_2+1/T_2^*$. A systematic variation in T_2 for protons in water solutions of ferric ions of known concentrations C has been obtained to confirm the known relationship $T_2\sim1/C$, having the knowledge of T_2^*. The values of T_2 so obtained are in agreement with results obtained by Bloembergen *et al.*,[5] using the line width method.

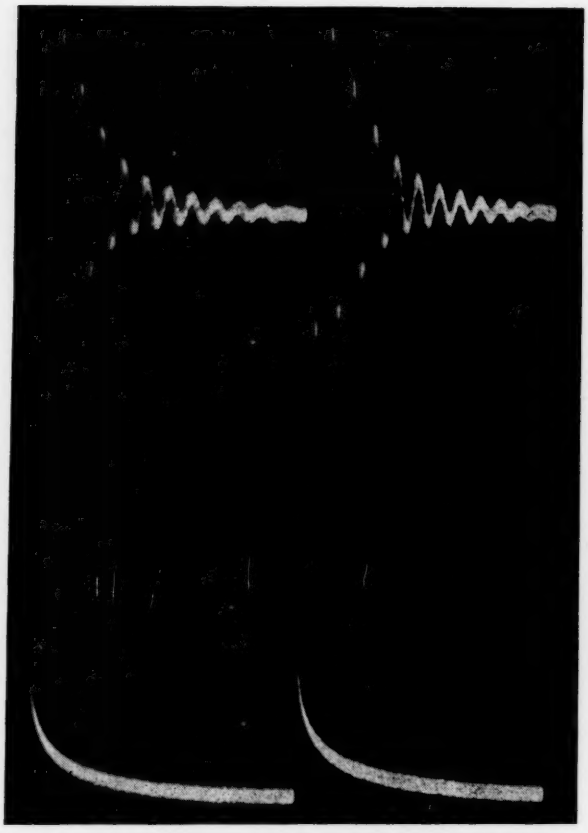

FIG. 2. The top trace indicates a beat note between an external r-f signal generator (near the Larmor frequency, loosely coupled to the inductive coil) and the nuclear signal shown alone (after detection) on the bottom trace. This beat note is identical in principle with the "wiggle effect" (see reference 5) except that H_0 is held constant in this case.

The author is indebted to H. W. Knoebel for his valuable assistance in the arrangement and design of the apparatus.

* Supported in part by ONR.

[1] F. Bloch, Phys. Rev. 70, 460 (1946).

[2] T_2 includes the effect of T_1 in limiting the phase memory of Larmor precession.

[3] E. L. Hahn, Phys. Rev. 76, 145 (1949).

[4] E. L. Hahn, Bull. Am. Phys. Soc. 24, No. 7, 13 (1949).

[5] Bloembergen, Purcell, and Pound, Phys. Rev. 73, 679 (1948).

The Isotopic Constitution of Erbium and Lutecium

RICHARD J. HAYDEN, DAVID C. HESS, JR., AND MARK G. INGHRAM
Argonne National Laboratory, Chicago, Illinois
December 5, 1949

DURING the past two years measurements of the isotopic composition of many of the rare earths have been made. These measurements have recently been extended to cover the elements erbium and lutecium. The mass analyses were made with a 60°, six-inch radius of curvature mass spectrometer using a heated filament ion source and other techniques previously described.[1]

The erbium analyzed was a column separated sample obtained from Dr. D. H. Harris of the Oak Ridge National Laboratory. The extreme purity of this sample made possible a significant search for undiscovered rare isotopes. The observed abundances along with the probable error are quoted in the third row of Table I. The earlier photometric results of Aston[2] (corrected for Dempster's 162 and 164 values) and Wahl[3] are also quoted in the table.

TABLE I. Isotopic constitution of erbium (percent).

Observer	162	164	166	167	168	170
Aston*	0.25	2	35	24	29	10
Wahl	0.1	1.5	32.9	24.4	26.9	14.2
Authors	0.136±0.003	1.56±0.03	33.41±0.3	22.94±0.2	27.07±0.3	14.88±0.2

* Values at 162 and 164 were obtained by A. J. Dempster, Phys. Rev. 53, 727 (1938).

The following limits for other possible erbium isotopes were obtained:

160, 161 < 0.0008 percent,
163 < 0.0009 percent, 165 < 0.003 percent,
169 < 0.008 percent, 171 < 0.005 percent, and
172 < 0.0014 percent.

Based on the new values, on the assumption of zero packing fraction for the erbium isotopes, and on a conversion factor of 1.000275 between physical and chemical scales, the chemical atomic weight of erbium becomes 167.28. The international value, chemically determined, is 167.2.

Lutecium was first thought to be a simple element, but the work of Mattauch and Lichtblau[4] showed that, in addition to the main peak at 175, a 2.5 percent isotope exists at 176. Our lutecium analysis was made on a sample purified by Dr. J. K. Marsh of Oxford and obtained from Johnson, Matthey and Company as Catalog number 320. The 176 isotope was found to be present to 2.60±0.03 percent and consequently the 175 was 97.40±0.03 percent. The following limits for other possible lutecium isotopes were set: 177 and 178 < 0.006 percent, 173 < 0.008 percent, and 174 < 0.008 percent. With this isotopic abundance and assuming zero packing fraction for lutecium and the 1.000275 conversion factor, the chemical atomic weight of lutecium is 174.98. The international value is 175.0.

[1] Inghram, Hayden, and Hess, Jr., Phys. Rev. 72, 967 (1947).
[2] F. W. Aston, Nature 133, 327 (1934).
[3] W. Wahl, Finska Kemistsomfundets Medd. 50, 10 (1941).
[4] Mattauch and Lichtblau, Zeits. f. Physik 111, 514 (1939).

Production of Gamma-Rays in Nuclear Interactions of Cosmic Rays*

B. P. GREGORY, B. ROSSI, AND J. H. TINLOT
Department of Physics and Laboratory for Nuclear Science and Engineering, Massachusetts Institute of Technology, Cambridge, Massachusetts
December 2, 1949

THE evidence presented in this letter is based on a preliminary statistical analysis of forty-seven cloud-chamber pictures showing nuclear interactions in which electronic showers were produced. The cloud chamber contained seven lead plates ($\frac{1}{4}$ inch thick) and six aluminum plates ($\frac{5}{16}$ inch thick) placed alternately, and was triggered by a counter telescope shielded with lead placed underneath the chamber, in anticoincidence with a large double tray of counters placed above.

The mixed shower shown in Fig. 1 was produced by a neutral particle in the fourth (AL) plate. Four penetrating particles, *a*, *b*, *c*, and *d*, appear at this point and traverse the chamber; one of these is responsible for the triggering. (The track marked *x* is not connected with the interaction since it is not of counter age.) The shower *A* starts in the seventh (Pb) plate and is observed to traverse the remaining plates while maintaining a uniform density of particles of 9 to 10. The shower *B* appears in the fifth (Pb) plate and dies out after multiplying in the seventh plate. The axes of these showers reproject to the center of the nuclear event, and are in a well-illuminated region of the chamber. We have in this picture two clear examples of a non-ionizing link between the center of a nuclear event and the starting point of a shower. A similar example was presented by one of us (B.P.G.) at the June, 1949, Cosmic Ray Conference, Idaho Springs, Colorado.

A preliminary analysis of showers of more than five particles gave the following result:

(a) Events originating in aluminum show 16 cases of non-ionizing link, 8 cases in which the starting point of the shower could not be located, and no case in which one could identify an electron coming out of the aluminum plate. This result is in agreement with the hypothesis that all showers originate as a gamma-ray, since an aluminum plate is equivalent to only 0.08 radiation length.

(b) Events originating in lead show 10 cases in which the shower starts in the same lead plate, 14 cases of non-ionizing link, and 18 cases in which the starting point of the shower could not be located. Assuming that nuclear events are produced in a random position in a lead plate (whose thickness corresponds to 1.2 radiation lengths) and that all showers are produced by initial gamma-rays, the probability of observing a non-ionizing link from an event in lead is calculated to be 65 percent. This is in agreement with the numbers stated above.

The angle in space between the two showers *A* and *B* of Fig. 1 lies between 14 and 18 degrees. A slight displacement due to turbulence in the chamber is responsible for the poor accuracy in

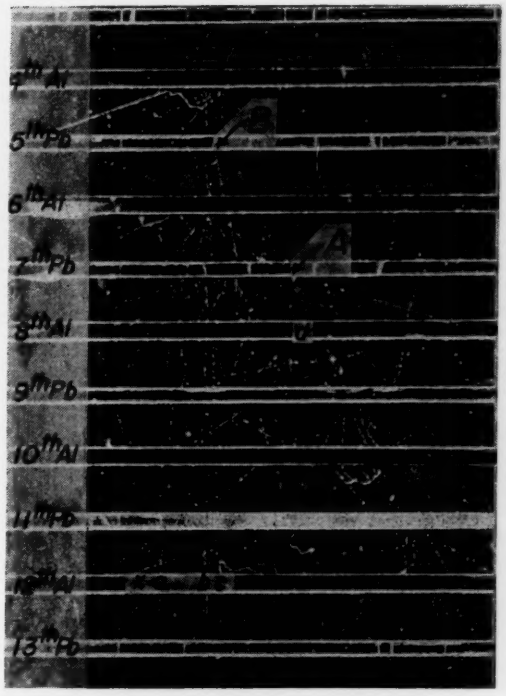

FIG. 1. Photograph of a mixed shower.

this measurement. The energy of shower A was estimated to be 1 Bev from the number of electrons observed at the maximum. If we consider that showers A and B originate from two gamma-rays which are the decay products of a neutral meson of 300 electron masses and having very short lifetime, the energy of shower B can be calculated from the energy of shower A and the angle between the showers; one finds this energy to be 300 ± 100 Mev. This value is not unreasonable with regard to the appearance of shower B.

* Assisted by the Joint Program of the ONR and the AEC.

Erratum: Quasi-Chemical Method in the Statistical Theory of Regular Mixtures

[Phys. Rev. 76, 977 (1949)]

YIN-YUAN LI
University of Illinois, Urbana, Illinois

IN a private communication Dr. C. N. Yang (The Institute For Advance Study, Princeton) wrote:

"In my paper[1] (hereafter called I) it was shown that from the quasi-chemical method one derives the approximate combinatorial formulas (56) and (59) . . . That the converse is true (namely, that the non-interference of local configurations leads to the quasi-chemical method) is evident from the derivation in I of (56) and (59). It goes without saying that, assuming (56) and (59), the free energy of the crystal calculated therefrom is proportional[2] to the free energy of the imaginary gaseous mixture (see equation immediately preceeding (54) in I) and that therefore the equilibrium values of $[q]$ are given by the Eq. (31) of I . . ."

With apologies I withdraw the following comment which appears in the concerned paper at the end of the first paragraph in page 977.

"Yang implicity followed the exact line of the hypothesis of non-interference of local configurations. He also tried to deduce his quasi-chemical method by adopting the hypothesis although with little success (§6 of reference 1)."

[1] C. N. Yang, J. Chem. Phys. 13, 66 (1945).
[2] Except for a constant term which is independent of the $[q]$'s for given w.

Effect of Light on a Diamond Conduction Counter*

R. K. WILLARDSON AND G. C. DANIELSON
Institute for Atomic Research and Department of Physics, Iowa State College, Ames, Iowa

December 5, 1949

ONE of the disadvantages of using a crystal conduction counter is the accumulation of space charge field resulting from the trapping of charge carriers. This space charge field opposes the applied field and may lower the pulse height below the noise level of the amplifier. Several methods of minimizing this difficulty have been suggested. Wouters and Christian[1] and McKay[2] used periodic reversals of the applied field; Hofstadter[3] suggested heat or light to release trapped charges; Chynoweth[4] increased the counting rate using light from a Nernst filament; and McKay[5] used the barrier layer in a semiconductor.

We have found in our counting of Co^{60} gamma-rays and Sr^{90}-Y^{90} beta-particles that the reduction of counting rate by the space charge field can be completely eliminated in some diamonds. This is accomplished by violet light irradiation of the diamond, which is normally in the dark. After this light treatment the diamond is in an activated condition and the counting rate is maintained indefinitely (as long as the external field is applied) at a value equal to or greater than the initial rate. This effect is quite different from the ordinary release of space charge by red light and to our knowledge has neither been predicted nor observed.[6]

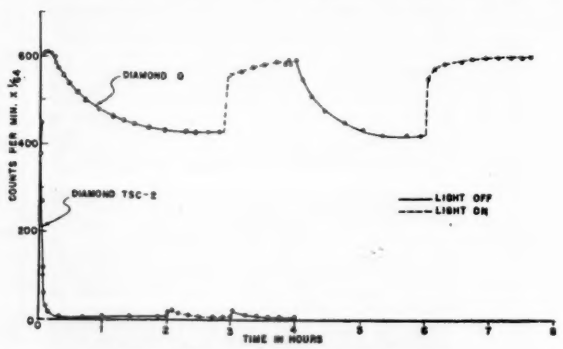

FIG. 1. Effect of red light on counting rate ($\lambda = 6500$A, $E_A = 10$ kv/cm, $Co^{60}\gamma$).

Figure 1 shows the effect of red light on two diamonds which count gamma-rays. Diamond Q is typical of several of our better counters. The counting rate increases slightly at first and then decreases finally approaching a relatively high equilibrium value. If a beam of monochromatic red light (6500A) is focused on the diamond, the counting rate increases very rapidly to a high value which seems to be maintained as long as the light is applied. Upon removal of the light source the counting rate again decreases.

Diamond TSC-2 is typical of our poor counters. In this case, the space charge effects are severe, and the counting rate decreases to a value approaching zero. Red light does not increase the counting rate appreciably.

Figure 2 shows the effect of violet light on the same two diamonds. If a beam of monochromatic violet light (4046A) is focused on diamond Q, the counting rate is observed to decrease rather than increase as it did for red light. Following the decrease there is an increase in counting rate to an equilibrium value. Upon removal of the light source the counting rate increases rapidly to a still higher value and then more slowly to a constant value. After several hours this final value equals or exceeds the initial counting rate. This rate appears to be maintained indefinitely with saturation fields. The source can be removed for several hours and then replaced without appreciable change in counting rate; but lower field strengths may result in a temporary lower counting rate. For fields less than 2 kv/cm it was not possible to put this diamond into the activated condition.

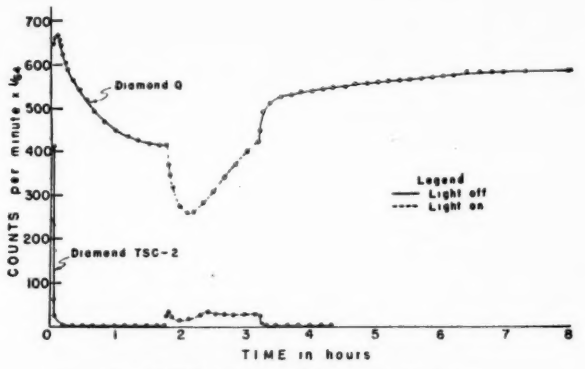

FIG. 2. Effect of violet light on counting rate ($\lambda = 4047$A, $E_A = 10$ kv/cm, $Co^{60}\gamma$).

Diamond TSC-2 does not show this response to violet light. The effect of violet light appears to be similar to the slight effect observed for red light on poor counting diamonds.

Using a Nernst filament as a strong light source, diamond Q may be put into the activated state more rapidly. A temporary initial rise in counting rate occurs and may be attributed to the longer wave-lengths. Unfiltered light from an ordinary projection lantern can also be used.

An explanation of these effects must involve a consideration of photo-conductivity as well as space charge. The decrease in counting rate when using violet light is probably caused by the trapping of photo-conducting carriers which adds to the space charge field. The following increase in counting rate may be caused by a smoothing out of the energy band boundaries[7] which will increase the average distance charges travel before being trapped.

In the activated condition the band boundaries may be nearly straight lines. The small rise at the beginning of the curves for diamond Q may have a similar origin; a slight smoothing out of the energy bands would temporarily predominate over the effect of space charge, especially when the applied field is one of saturation.

We wish to thank Mr. Louis Small, president of Service Diamond Tool Company for his cooperation in supplying these diamonds.

* Contribution No. 88 from the Institute for Atomic Research and Department of Physics, Iowa State College, Ames, Iowa. Work was performed at the Ames Laboratory of the AEC.
[1] L. F. Wouters and R. S. Christian, Phys. Rev. **72**, 1127 (1947).
[2] K. G. McKay, Phys. Rev. **74**, 1606 (1948).
[3] R. Hofstadter, Nucleonics **4**, 14 (1949).
[4] A. G. Chynoweth, Phys. Rev. **76**, 310 (1949).
[5] K. G. McKay, Phys. Rev. **76**, 1537 (1949).
[6] However, this effect is probably related to the unusual photo-conductivity properties of diamond; see the classical papers by Gudden and Pohl or by R. Robertson, J. J. Fox, and A. E. Martin, Phil. Trans. **232**, 465 (1934).
[7] Irregular band boundaries in an insulating crystal containing lattice defects have been suggested by G. H. Wannier, Phys. Rev. **76**, 438 (1949) and by H. M. James, Science **110**, 254 (1949).

Beta-Spectrum of Be^{10}*

P. R. Bell and J. M. Cassidy
Oak Ridge National Laboratory, Oak Ridge, Tennessee
November 25, 1949

THE scintillation spectrometer[1,2] has been used to determine the beta-spectrum of Be^{10}. The sample was made by activating Be in the pile and then enriching the sample in Be^{10} by magnetic separation at *Y*-12. The results obtained confirm the earlier result reported at the 1949 Washington meeting of the Physical Society.

Approximately 1.5 milligrams of BeO were mounted on 100 microgram per cm² Formvar film; the area was about 3 cm². An anthracene crystal was used with an RCA-5819 photo-multiplier. The pulse height distribution is shown in Fig. 1. The sample activity was so large that the background was negligible. Our first sample separated from a cyclotron target had a specific activity of 18 disintegrations per second per milligram of Be. The pile sample after electromagnetic enrichment had a specific activity of 855 disintegrations per second per milligram of Be.

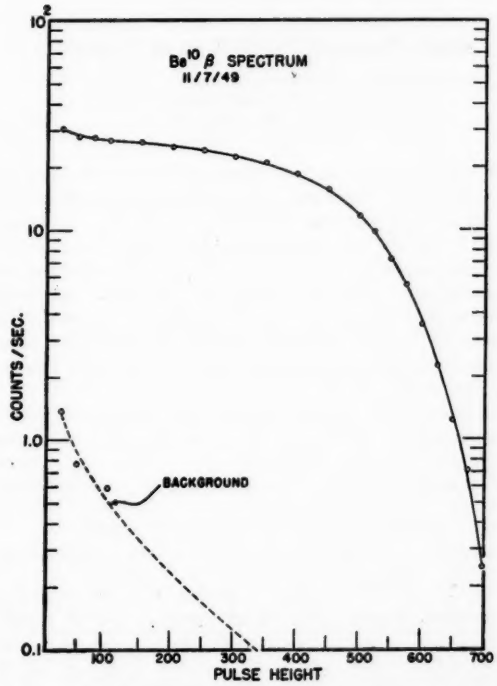

FIG. 1. Pulse height distribution of Be^{10} beta-ray pulses. Pulse height interval was 33 pulse height divisions.

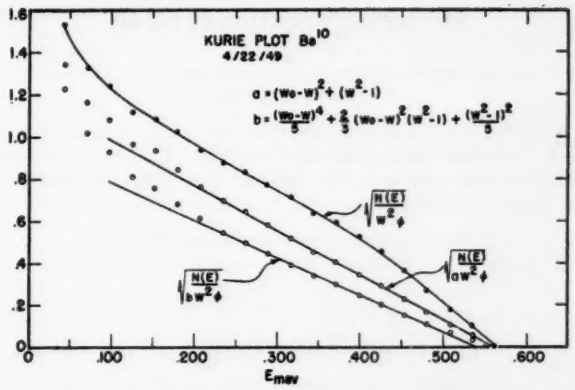

FIG. 2. Kurie plot of cyclotron Be^{10}. Sample thickness about 2 mg/cm² on 0.5 mg/cm² polyethylene.

Figure 2 shows the Fermi-Kurie plots reported previously. It was not possible to decide whether the first or second forbidden axial vector or tensor correction gave the best approach to a straight line near the end point. Figure 3 shows the results obtained with the present sample. It is now possible to see that the second forbidden correction gives the best fit, as is expected theoretically. The strong turn-up at low energies is found generally with the scintillation spectrometer and is probably due to scattering out from the crystal. The maximum energy of the beta-ray as given by the corrected Kurie plot is 0.535±0.02 Mev for the original sample and 0.545±0.010 Mev for the more active sample. The more precise value agrees with other recent measurements.[3,4]

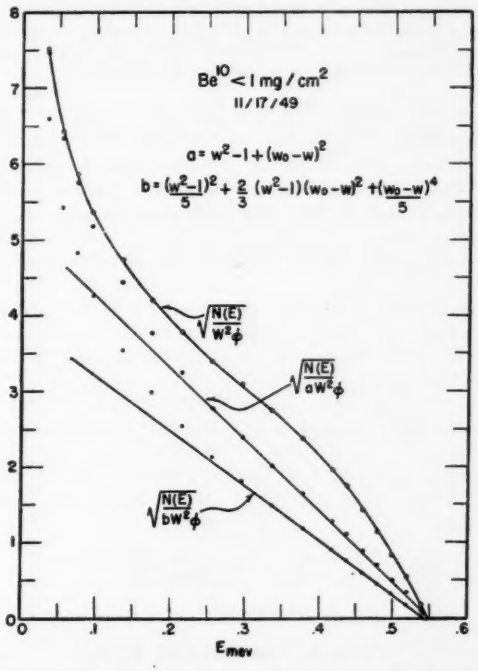

FIG. 3. Kurie plot of pile activated and electromagnetically separated Be.

* This document is based on work performed under Contract No. W-7405, eng. 26 for the Atomic Energy Project at Oak Ridge National Laboratory.
[1] W. H. Jordan and P. R. Bell, Nucleonics **5**, 30 (1949).
[2] Bell, Ketelle, and Cassidy, Phys. Rev. **76**, 574 (1949).
[3] C. S. Wu and L. Feldman, Phys. Rev. **76**, 698 (1949).
[4] H. W. Fulbright and J. C. D. Milton, Phys. Rev. **76**, 1271 (1949).

Microwave Spectrum of CF_3Br

A. H. SHARBAUGH, B. S. PRITCHARD, AND T. C. MADISON
General Electric Research Laboratory, Schenectady, New York
December 5, 1949

ABOUT forty lines, arising from the $J=4\rightarrow5$ and $J=5\rightarrow6$ rotational transitions of CF_3Br^{79} and CF_3Br^{81}, have been measured and analyzed. The nuclear and molecular constants are listed in Table I.

TABLE I. Nuclear and molecular constants of CF_3Br.

		ν_0 (mc/sec.)	$I_B\times10^{40}$ (g-cm²)	B_0 (mc/sec.)	$eQ(\partial^2V/\partial Z^2)$
$J=4\rightarrow5$	CF_3Br^{79}	20,981.25	399.86	2098.12	618.4 ±7
	CF_3Br^{81}	20,785.49	403.63	2078.55	517.3 ±4
$J=5\rightarrow6$	CF_3Br^{79}	25,177.46	399.86	2098.12	624.5 ±5
	CF_3Br^{81}	24,942.87	403.63	2078.57	514.7 ±6

Using a nuclear spin of $\frac{3}{2}$ for bromine and neglecting second-order quadrupole corrections, Fig. 1 shows the excellent agreement

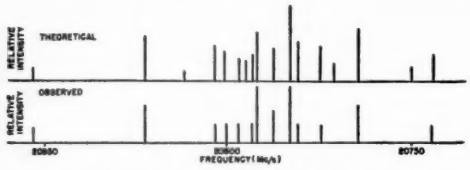

FIG. 1. Comparison of the theoretical and experimental spectrum for the $J=4\rightarrow5$ transition of CF_3Br^{81}.

between the calculated and experimental spectrum for the $J=4\rightarrow5$ transition of CF_3Br^{81}. Assuming tetrahedral bond angles to the carbon; *viz.*, 109° 28′, we compute $d_{CF}=1.321$A and $d_{CBr}=1.936$A. The moment of inertia of the CF_3 group about an axis through its center of mass and perpendicular to the symmetry axis, I_{CF_3}, is computed to be 46.14 at. wt. A², and the distance of the center of gravity of this group to the nucleus of the Br atom becomes 2.300A.

Calculated from measurements on CF_3Cl in a manner similar to ours, Coles and Hughes[1] report $d_{CF}=1.323$A and $I_{CF_3}=46.31$ at. wt. A² which agrees well with our measurements of the corresponding quantities of CF_3Br.

From measurements on the $J=8\rightarrow9$, $10\rightarrow11$, and $11\rightarrow12$ transitions, Sheridan and Gordy[2] compute the values $I_B=399.9\times10^{-40}$ g-cm² for CF_3Br^{79} and $I_B=403.7\times10^{-40}$ g-cm² for CF_3Br^{81}. Assuming tetrahedral bond angles, they find $d_{CF}=1.326$A and $d_{CBr}=1.933$A. These results are seen to be in good agreement with ours.

[1] D. K. Coles and R. H. Hughes, Phys. Rev. **76**, 858 (1949).
[2] Sheridan and Gordy (private communication).

The Active Coaxial Tube

PHILIPPE A. CLAVIER
Sylvania Electric Products Inc., Bayside, New York
November 25, 1949

IN a recent paper,[1] J. A. Roberts indicated the possibility of obtaining gain in a wave tube in the direction opposite to that of the electron beam.

This effect was considered some time ago by the present writer in connection with a study of certain aspects of the traveling-wave tube for the Bureau of Ships. Certain conclusions were drawn which are summarized briefly below, from which it is deduced that such a condition is indeed possible.

Considering a hollow wave guide through which is passing an electron beam, it may be shown that any wave having an electric component in the direction of the beam will not be cut off. In fact, some of these waves may actually undergo amplification. The Larmor frequency enters as a parameter into the propagation constant of the waves. In the case of a cylindrical guide pure *TE* or *TM* waves do not exist except where the Larmor frequency is zero or infinity. For a finite Larmor frequency, gain may be achieved in the direction of the electron beam or in the opposite direction. The latter may be quite large; larger, in fact, than the 76 db/cm mentioned by Roberts.

The gain parameters have been derived by the writer for such a system. These are functions of the Larmor frequency, the electron plasma frequency, wave-length, and guide diameter. The simplest case is that for which the Larmor frequency is infinite, the voltage gain being only in the backward direction and having the value per unit length of

$$\frac{110}{D}[1+(1.53\times10^{10}I)/((66\phi/D^2+3.55\times10^7/\lambda^2)^2D^2\lambda^2\phi)]^{\frac{1}{2}},\quad \text{(db)}$$

in which D and ϕ are the diameter and potential respectively of the cylinder, λ is the wave-length and I the beam current. The units are centimeters, volts and milliamperes.

The different solutions of the wave equation are not orthogonal to each other, and "cross terms" will appear in the computation of the Poynting vector. It can be shown, however, that in the case of "backward" gain, the average power flow at the output (cathode) end of the tube is in the backward direction.

Of major importance in the application of these principles in what the writer calls an "active coaxial" tube, is the design of a proper matching system. With the signal entering the guide at the collector end and power being taken at the cathode end, one may deduce that, for stability, a part of the power at the output end is to be reflected toward the input end. It can be shown that the reflected power can be kept small compared to the signal input power. The ideal input matching device is one that divides the input power equally between the two "backward" propagating waves. It should be noted that, under any condition, there remains a mismatch factor which increases as the cold cut-off frequency is approached from either direction.

[1] J. A. Roberts, Phys. Rev. **76**, 340 (1949).

Some Physical Properties of Titanium

HERBERT I. FUSFELD AND JOSEPH T. GILBERT
Pitman-Dunn Laboratory, Frankford Arsenal, Philadelphia, Pennsylvania
November 25, 1949

THIS Laboratory received three titanium rods from a commercial facility for tests of internal friction and velocity of sound. The rods as received were thirty inches long and of circular cross section 0.232 inch in diameter. The treatment given to the rods by the company consisted of a 66 percent reduction in area, followed by an anneal at 1200°F for one hour. Spectroscopic analysis of the material showed the presence of from 0.01 to 0.1 percent of Fe, Si, and Cu, 0.001 to 0.01 percent of Mn, less than 0.01 percent of Mg, Al, and Ni, and no detectable amounts of Cr, V, Mo, W, Co, or As.

Measurements of internal friction or damping were conducted utilizing apparatus previously described.[1] All such measurements were made at a pressure less than 0.1 mm of mercury. The fundamental resonant frequency was used to evaluate the velocity of

TABLE I. Data for four specimens of titanium.

Spec.	Damping	Velocity of Sound ft./sec.	Velocity of Sound met./sec.	Density lb./ft.³	Density g/cc	Modulus of Elasticity lb./in.²	Modulus of Elasticity dyne/cm²
1	2.24×10^{-4}	16,350	4983.5	282.4	4.523	16.30×10^6	11.24×10^{11}
2	2.39×10^{-4}	16,349	4983.2	282.4	4.523	16.30×10^6	11.24×10^{11}
3	1.88×10^{-4}	16,273	4960.0	282.8	4.530	16.17×10^6	11.15×10^{11}
4	1.48×10^{-4}	16,299	4968.0	281.5	4.509	16.17×10^6	11.15×10^{11}

sound, v, measurements of mass and volume were made to determine the density, d, and the modulus of elasticity was computed from the formula $E=dv^2$.

Of the three rods received, one was cut into two 15-in. pieces, referred to as specimens 1 and 2, respectively. A piece 20 in. in length was cut from each of the two remaining rods, and comprise specimens 3 and 4, respectively. The results are given in Table I.

[1] H. I. Fusfeld, Phys. Rev. **75**, 1626 (1949).

Erratum: Electrical Properties of Pure Silicon and Silicon Alloys

[Phys. Rev. 75, 865 (1949)]

G. L. PEARSON AND J. BARDEEN
Bell Telephone Laboratories, Murray Hill, New Jersey

November 25, 1949

EQUATION (61) should read

$$1/\mu=(16\pi^2e^3m^2/3_k{}^2h^3)f(y). \qquad (61)$$

Equation (67) should read

$$1/\mu=(h/4e)(3/\pi)^{\frac{1}{2}}n^{\frac{1}{3}}. \qquad (67)$$

There appears to be a numerical error of a factor of 2π in Mott's derivation[1] of the mobility resulting from scattering by screened ions, and a correction was made in our numerical calculations. The uncorrected form was inadvertently placed in the text as Eq. (61) instead of the correct expression given above.

[1] N. F. Mott, Proc. Camb. Phil. Soc. **32**, 281 (1936).

Electron Screening and Ionization Potentials of Neutral and Singly Ionized Atoms

WOLFGANG FINKELNBURG
Engineer Research and Development Laboratories, Fort Belvoir, Virginia
AND
FRANK STERN
Princeton University, Princeton, New Jersey

December 2, 1949

IN spite of the considerable interest in the ionization potentials of atoms and ions, there are still neutral and singly ionized atoms for which this important constant is either entirely unknown or very uncertain and doubtful. Therefore, it may be of interest to note that it is possible to interpolate, often at least with a fair degree of accuracy, unknown ionization potentials and to correct wrong ones. This can be done by using regularities in the change of the screening constant $Z-Z_{eff}$ from element to element in the Periodic Table which one of us has recently published.[1] The improved spectroscopic ionization potentials, published by C. E. Moore[2] and F. W. Meggers,[3] were used to correct the formerly published data and to check our regularities more closely. While all details will be discussed later in a more extensive paper, our method is outlined here briefly and a number of new and corrected ionization potentials are presented.

If the screening constants

$$s=Z-Z_{eff}=Z-n(E_i/R)^{\frac{1}{2}} \qquad (1)$$

for the outermost electron of an atom or ion are computed in the conventional manner from the empirical ionization potentials E_i and the shell number n of the outermost electron,[4] and if the change of these s-values from element to element

$$\Delta s=s_N-s_{N-1}$$

is tabulated in the Periodic Table, regularities become evident which can be understood theoretically. Table I shows the regular trend of the Δs-values in the main groups of the Periodic Table. These regularities are the more pronounced, the more similar the chemical behavior of the group elements is (e.g., Cd−Zn−Hg),

TABLE I. Trend of Δs-values in the main groups of the "Periodic Table."

Group	I	II	III	IV	V	VI	VII	VIII
n								
2	1.09	0.60	1.09	0.74	0.75	1.07	0.74	0.75
3	1.67	0.59	1.26	0.67	0.68	1.02	0.68	0.71
4	1.97	0.58	1.67	0.56	0.68	1.02	0.65	0.68
5	2.29	0.54	1.81	0.59	0.68	0.92	0.69	0.66
6	2.51	0.50	2.24	0.59	0.73	1.0	0.7	0.67

whereas changes in the electron configuration, as they occur in the transition elements and the rare earths, result in marked irregularities. Making use of the known regularities, unknown Δs-values and ionization potentials can be computed using Eq. (1). It seems of interest to note that our method is ***not*** based on extrapolation or interpolation along ***one*** group, but is based on the regularities in two neighboring groups in the Periodic Table.

The case of the new alkali atom francium may serve as an example. The extrapolation along the alkali group alone would result in a Δs-value of 2.70 ± 0.2 (corresponding to an ionization potential of 3.7 ev) which, however, would make the Δs for the following element, radium, with 0.27 far too low. The very regular trend of Δs in the chemically very similar group Ca−Sr−Ba−Ra clearly indicates for Ra a Δs of 0.46 ± 0.03, thus making Δs for Fa 2.52, still in line with the alkali group trend. The corresponding ionization potential of Fa thus is 4.0 ± 0.1 ev. In an analogous way, the new or corrected ionization potentials of Table II have been determined.

TABLE II. New and corrected ionization potentials of neutral and singly ionized atoms in ev.

New E_i-values				Corrected E_i-values			
Tc	7.3 ± 0.2	Po^+	18.2 ± 0.5	P	10.55 ± 0.15	As^+	18.7 ± 0.5
Po	8.4 ± 0.3	At^+	18.2 ± 0.8	As	9.85 ± 0.1	Br^+	21.6 ± 0.3
At	9.5 ± 0.2	Rn^+	19.9 ± 1.0	Bi	$8.3\ \pm0.2$	Sb^+	16.7 ± 0.5
Fa	4.0 ± 0.1	Fa^+	21.5 ± 0.7			Te^+	18.8 ± 0.5
		Ac^+	11.5 ± 0.3				

In those cases where spectroscopic ionization potentials are also known for the higher atomic ions, the trend of the Δs along the isoelectronic sequences can be used as a third check, as may be seen from Table III. The system of the ionization potentials of all

TABLE III. Δs-values in the first isoelectronic sequences of the "Periodic Table" (element symbols indicating first member of isoelectronic sequence).

		I	II	III	IV	V	VI
He	$1s^2$	0.66	0.64	0.65	0.63	0.63	0.63
Li	$2s$	1.09	1.04	1.02	1.01	1.00	1.00
Be	$2s^2$	0.60	0.59	0.59	0.58	0.58	0.57
B	$2p$	1.09	1.04	1.02	1.00	0.99	0.98
C	$2p^2$	0.74	0.73	0.72	0.71	0.70	0.70
N	$2p^3$	0.75	0.74	0.73	0.72	0.71	0.71
O	$2p^4$	1.07	1.01		0.95	0.94	0.93
F	$2p^5$	0.74	0.73		0.72	0.72	0.72
Ne	$2p^6$	0.75	0.75	0.73	0.73	0.72	0.72

atoms and atomic ions thus actually is interconnected by a sort of three-dimensional lattice in which each ionization potential is the cross point of three "curves," the change of the screening constant along the period, along the group and along the isoelectronic sequence.

The authors appreciate greatly the advice and help of the spectroscopy group of the National Bureau of Standards, particularly of Mrs. C. E. Moore, and an enlightening letter of Dr. H. N. Russell.

[1] W. Finkelnburg, Zeits. f. Naturforschung **2a**, 16 (1947).
[2] C. E. Moore, *Atomic Energy Levels* (U. S. Department of Commerce, Nat. Bur. of Stand., 1949), Vol. I.
[3] W. F. Meggers, "Periodic Chart of the Atoms" (W. M. Welch Scientific Co., 1947).
[4] W. Finkelnburg, *Atomic Physics* (McGraw-Hill Book Company, Inc., New York, 1950), Sections 3-16.

Ionization Potentials of Higher Atomic Ions

WOLFGANG FINKELNBURG
Engineer Research and Development Laboratories, Fort Belvoir, Virginia
December 2, 1949

IONIZATION potentials of higher atomic ions can be determined from spectroscopic data, with good accuracy, only in those cases where a considerable number of lines of a Rydberg series is known. In all other cases where empirical ionization potentials are known, they have been extrapolated from the isoelectronic sequences. There are several methods for doing this, the best one having been developed and used extensively by Eldén.[1] All these methods basically amount to the same: A figure which is directly related to the ionization potential, mostly the screening constant $s=Z-Z_{eff}$, is plotted against some function of Z, and the extrapolation then is carried through graphically under the plausible assumption of a monotonic trend of this curve. In these customary methods, an extrapolated ionization potential thus is determined by the *one* condition that its representative point falls on a smooth curve with the corresponding points of other members of the same isoelectronic sequence.

The author has refined this method by taking into account two more regularities which must be fulfilled by the correct ionization potential, and thus may serve for its determination. Not only the screening constants s, but also the changes of these screening constants from element to element in the periodic table, called Δs, must fall on a smooth curve. These Δs-values connect the different isoelectronic sequences among each other, so that actually the whole system of ionization potentials of all atoms and atomic ions is interconnected in a regular way like a network. While in the customary methods only the extrapolation of the s-values along each single isoelectronic sequence was used to determine an unknown figure, the accuracy is increased considerably by making use of the requirement that the Δs-values show a regular behavior too, and that their absolute values follow a certain sequence for all ions of the same ionization stage.[2] The extrapolation of the Δs-values provides a particularly sensitive check of extrapolated figures, because they are small differences of the s-values, and a regular arrangement of them thus guarantees an even more regular behavior of the interesting s-values themselves.

TABLE I. Corrected and new values of ionization potentials of higher atomic ions of the first 23 elements (new values italicized).

	III	IV	V	VI	VII	VIII	IX	X	XI	XII	XIII	XIV	XV
F							*1102*						
Ne	63.43				207.3	239.0	*1196*	*1360*					
Na								*1465*	*1646*				
Mg										*1959*			
Al										2085	*2299*		
Si											*2436*	*2666*	
P												*2815*	*3061*
S	34.7							448.6	*506.4*	*564.6*	*651.7*	*706.4*	*3220*
Cl		53.3		96.75				455.8	*531.4*	*594.0*	*656.6*	*749.6*	*808.2*
A		59.8	74.97	91.41	124.20		422.6	*480.0*	*539.5*	*621.1*	*688.5*	*755.5*	*854.4*
K	46.1	61.3	*82.5*	99.88	118.24	154.6	175.8	504.1	*566.2*	*630.2*	*717.7*	*789.9*	*861.4*
Ca		67.7		*109*	128.0	148.1	188.2	211.3	592.5	659.3	*727.8*	821.2	*898.3*
Se		74.3	92.0	111	*138*	159.3	181.2	224.8	250.0	687.9	*759.5*	*832.3*	*931.7*
Ti				120	141	*171*	193.8	*217.2*	264.5	291.6	790.2	866.5	*943.8*
V				129	151	174	*206*	*231.0*	*256.3*	307.4	336.4	899.4	*980.6*

The details of the method and its inherent accuracy will be discussed in a later paper. However, we have reason to believe that our extrapolated ionization potentials have the same relative accuracy as the first three or four members of the respective isoelectronic sequence which makes them much more accurate than those extrapolated by the older methods.

We have used our method to recompute about 50 extrapolated or uncertain ionization potentials, and to compute the missing 50 ionization potentials of the ions of the first 23 elements of the Periodic Table as covered in the recent book by C. E. Moore.[3] The data of this excellent book have been used as the basis of our extrapolations, and the figures of Table I are intended to supplement the ionization potentials presented in that book.

The author is greatly indebted to Mrs. C. E. Moore of the National Bureau of Standards for clarifying discussions and suggestions, and for the communication of her tables prior to publication.

[1] B. Edlén, Zeemann-Verhandlungen 1935, page 88, and numerous papers in Zeits. f. Physik and Zeits. f. Astrophysik.
[2] W. Finkelnburg, Phys. Rev. **77**, 000 (1949).
[3] C. E. Moore, *Atomic Energy Levels* (U. S. Department of Commerce, Nat. Bur. Stand., 1949), Vol. I.